FOREWORD

This report was prepared by the Research Laboratories Division of The Bendix Corporation as part of the research and study program performed under Air Force Contract No. AF 33(657)-10998.

The project engineer for the Air Force is Mr. James Morris.

The work described in this report was performed by the Attitude Controls Group of the Dynamic Controls Department. Mr. J. G. Rivard is the group supervisor and Mr. L. B. Taplin is the department head. Supervision and technical direction of the program was the responsibility of Mr. R. H. Larson.

Several individuals contributed to this research and study program. Mr. J. H. Tarter analyzed the re-entry trajectory and defined the attitude maneuvers required. Mr. J. T. Kasselmann analyzed the control requirements of the re-entry maneuver and selected and designed an attitude control loop to meet these requirements. Mr. L. L. Evans investigated the feasibility of using momentum exchange devices for generating control moments. Mr. J. C. Walberer was responsible for the design of the attitude control engines and associated components. Messrs. R. W. Presley and E. Rappaport conducted the analogue computer simulations of control system dynamics. Mr. R. H. Larson analyzed the orbital transfer and rendezvous maneuvers and performed the work on secondary injection thrust vector control.

ABSTRACT

This study is concerned with the application of high moment-producing techniques for the attitude control of manned space vehicles which perform orbital transfer, rendezvous, and lifting re-entry maneuvers. The specific accomplishments were:

(a) Establishment of control system, subsystem and component requirements for critical vehicle flight phases.

(b) Analysis of promising techniques for performing the flight control functions required during the various maneuvers.

A hypothetical vehicle was selected and its space mission was analyzed to determine the attitude control requirements. The rendezvous and re-entry maneuvers were found to be especially demanding on the attitude control system.

The production of control moments by means of reaction wheels, gyros, mass expulsion, secondary injection thrust vector control, and aerodynamic surfaces was investigated. Reaction engines, secondary injection thrust vector control, and aerodynamic flaps were selected for use in the required attitude control systems, and specific designs were made. The control loops were analyzed with regard to response, accuracy, and fuel consumption. A substantial amount of this analysis was accomplished by means of analog computer simulation.

This technical documentary report has been reviewed and is approved.

C. R. Bryan

C. R. BRYAN
Asst. for Research & Technology
Flight Control Division
AF Flight Dynamics Laboratory

TABLE OF CONTENTS

LIST OF ILLUSTRATIONS

LIST OF TABLES

SECTION 1

INTRODUCTION AND SUMMARY

1.1 OBJECTIVE

The objective of this study is to provide methods and techniques for achieving control and stabilization of large manned vehicles during orbital rendezvous and re-entry maneuvers. The following general tasks have been accomplished:

(a) Establishment of the control system, subsystem, and component requirements for critical vehicle flight phases.

(b) Detailed analysis of certain promising techniques for performing the flight control functions required during the various phases and maneuvers.

1.2 PROBLEM DEFINITION

1.2.1 Hypothetical Vehicle and Requirements

The vehicle and associated requirements assumed for this study are defined below.

(a) Vehicle initial weight - 200,000 lbs

(b) Vehicle initial orbit altitude - 150 n.m.

(c) Maximum orbit altitude - 1000 n.m.

(d) Vehicle length - approximately 200 ft.

(e) Capability for rendezvous

(f) Vehicle is manned

(g) Aerodynamic control during re-entry

1.2.2 Vehicle Maneuvers

The manned space vehicle performs several maneuvers during its mission. These are described briefly and in sequence as follows:

Manuscript released by author February 1964 for publication as an FDL Technical Documentary Report.

(a) Boost - The main rocket engine or a booster engine launches the vehicle from the earth and puts it into a parking orbit considerably below that of the target with which it is to rendezvous, and possibly in a different plane. Ideally, both the vehicle and target are in circular orbits at this point.

(b) Change of Plane - At the intersection of the vehicle and target orbital planes, the velocity vector of the vehicle is rotated so that the orbits of the vehicle and target become coplanar. The altitude of the vehicle will not be changed. This maneuver is preceded by rotating the vehicle about its yaw axis to properly position the thrust vector.

(c) Orbital Transfer (ascent) - When the vehicle and target are at the proper relative position, a thrusting period is introduced to put the vehicle into an elliptical orbit, with the apogee at the same altitude and position as the target. At the apogee, an additional thrust pulse may be used to increase the vehicle velocity nearer to that of the target.

(d) Rendezvous - The rendezvous phase begins as soon as the vehicle reaches the target altitude. The vehicle is initially ahead of the target and with a lower velocity, therefore the distance between the bodies decreases with time. Rendezvous is achieved by applying a series of thrust pulses to the vehicle to bring the vehicle velocity up to that of the target as the distance between them decreases. During this phase, the attitude control system maintains proper thrust vector alignment with the line-of-sight between the two bodies.

(e) Docking - Docking is the terminal phase of rendezvous and is one of the most critical maneuvers because non-destructive physical contact must be achieved. The docking maneuver begins when the relative velocity and range are very small. It involves orienting the vehicle and making vernier thrust corrections. At physical contact a latching scheme absorbs the impact energy and locks the bodies together.

(f) Separation - Separation is somewhat the reverse of docking because vernier control is used to separate the bodies until larger engines can be used.

(g) Change of Plane - If it is necessary to put the vehicle into a different orbital plane in preparation for re-entry, it would be accomplished before reducing orbital altitude. It is most efficient to change the orbital plane at a high altitude because the velocity is lower and requires less correction.

(h) Orbital Transfer (descent) - The descent orbital transfer is the reverse of that used in ascent. The velocity is decreased to generate an elliptical orbit, and at the perigee a velocity decrement circularizes the orbit.

(i) Re-entry - The re-entry phase begins by decreasing the velocity and allowing the vehicle to enter the atmosphere. Aerodynamic surfaces control the velocity-altitude relationships within allowable limits for safe re-entry.

Insofar as performance of the attitude control system is concerned, the most critical maneuvers are rendezvous and re-entry. This report will be concerned with the initial portions of rendezvous and re-entry where fully automatic control of the vehicle is imperative.

1.3 SUMMARY

The vehicle mission was analyzed with regard to the attitude control requirements imposed by orbital transfer, rendezvous, and re-entry. For orbital transfer, the attitude errors during thrusting periods cannot exceed one degree, while during rendezvous, the most critical requirement restricts the attitude error to a maximum value of one-half degree. The complexity of the re-entry maneuver does not lend itself to definition of attitude control requirements in terms of only accuracy. In essence, the attitude control system must rapidly and accurately respond to the attitude commands of the guidance system while under varying load conditions imposed by changes in velocity and atmospheric density.

Various methods for producing large control moments on the hypothetical vehicle have been studied. While control moment gyros are preferable to reaction wheels from the standpoint of torque and power requirements, no momentum exchange system of any kind was proposed for the vehicle because adequate attitude control can be maintained using reaction engines. Secondary injection thrust vector control is a convenient means for compensating for engine misalignment and maintaining vehicle attitude during main engine firing. Moveable aerodynamic surfaces are mandatory for controlling the attitude of a lifting re-entry vehicle.

The optimum attitude control system for orbital transfer and rendezvous uses mass expulsion moment producers incorporated in a control loop which functions in an on-off mode with rate feedback. When the control moments are small, reaction engines are used, but when the main engine fires, secondary injection thrust vector control must be employed to compensate for engine misalignment. The valve-combustor system proposed for the reaction engines uses a two-stage solenoid-operated poppet valve which feeds the propellants into a vortex doublet combustor. An all-fluid vortex valve system is defined for controlling the secondary injection flow rate.

The attitude control of a lifting re-entry vehicle requires the use of both mass expulsion and aerodynamic surfaces. At high altitudes where the dynamic pressure is low, aerodynamic control is insufficient and requires augmentation by control moments created by mass expulsion. At a later time, however, the dynamic pressure reaches a sufficient level to allow complete aerodynamic control of attitude. The actuator selected for driving the aerodynamic flaps is an expansion vane motor controlled by a spool-type servo valve. A piston-cylinder lacks the performance and fuel economy of an expansion vane motor. Reaction jets are completely out of the question for flap control because of the enormous quantities of fuel required.

SECTION 2

MISSION EQUATIONS

2.1 ORBITAL TRANSFER

2.1.1 Assumptions

(a) The target is in a circular orbit.

(b) The manned vehicle is initially in a circular parking orbit below that of the target.

(c) The orbital planes of the traget and vehicle do not coincide.

(d) The thrust magnitude of the main engine is high enough so that the use of impulsive velocity increments is a good approximation. (Ref. (1)*, p. 2-21 states, "The assumption of instantaneous addition of the velocity tangentially is a realistic approximation for accelerations greater than 1/2 g.")

2.1.2 Equations for Ascent

Simple orbital transfer maneuvers are used to bring the vehicle to the proximity of the target. First the relative inclination of the orbital planes is reduced to zero, then a Hohman-type elliptical transfer maneuver is employed to reach the target. All of the equations used are taken from Ref. (2).

Initially, the orbital planes may have a differential inclination as illustrated in Figure 2-1. To make the planes coincide, the velocity vector of the vehicle must be rotated through the angle ψ when the vehicle is at one of the nodes. This is accomplished by applying a velocity increment with the proper magnitude and direction. The velocity of the vehicle in its initial circular orbit is:

---

*Numbers in parentheses refer to the references listed in Section 10.

$$V_{ic} = \sqrt{\frac{\mu}{R_i}} \qquad (2\text{-}1)$$

where: $\mu = g_c R_e^2$

The magnitude of the corrective velocity increment is:

$$\Delta V_1 = 2V_{ic} \sin \frac{\psi}{2} \qquad (2\text{-}2)$$

and the direction of the thrust is $\xi = \psi/2$ measured from the normal to the original velocity vector. In this maneuver, only the direction of the velocity vector is changed. Figure 2-2 illustrates the vector addition.

The transfer maneuver to the target altitude involves producing the following velocity increment:

$$\Delta V_2 = V_{tc} \left(\frac{R_i}{R_t}\right)^{-1/2} \left\{ \left[\frac{1}{2} \left(1 + \frac{R_i}{R_t} \right) \right]^{-1/2} - 1 \right\} \qquad (2\text{-}3)$$

and is directed tangentially to the parking orbit. This impulse is applied when the vehicle lags the target by the angle:

$$\eta_t - \eta_v = \pi \left\{ 1 - \left[\frac{1}{2} \left(1 + \frac{R_i}{R_t} \right) \right]^{3/2} \right\} \qquad (2\text{-}4)$$

so that the vehicle will "meet" the target at the apogee of its transfer ellipse. (Refer to Figure 2-3.) If it is desired to put the vehicle into circular orbit with the target, the following velocity change is directed tangentially to the orbit path:

$$\Delta V_3 = V_{tc} \left\{ 1 - \left(\frac{R_i}{R_t}\right)^{1/2} \left[\frac{1}{2} \left(1 + \frac{R_i}{R_t} \right) \right]^{-1/2} \right\} \qquad (2\text{-}5)$$

where: $$V_{tc} = \sqrt{\frac{\mu}{R_t}} \qquad (2\text{-}6)$$

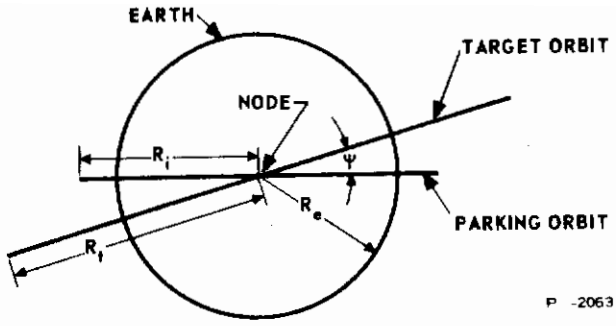

Figure 2-1 - Differential Inclination of Orbit Planes

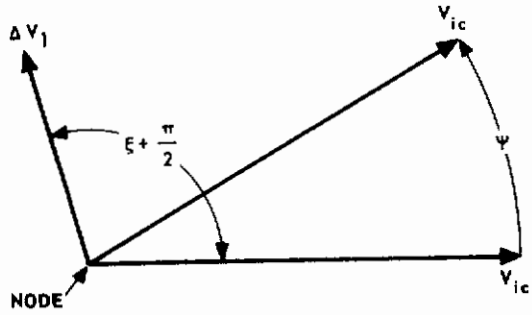

Figure 2-2 - Orbit Plane Rotation

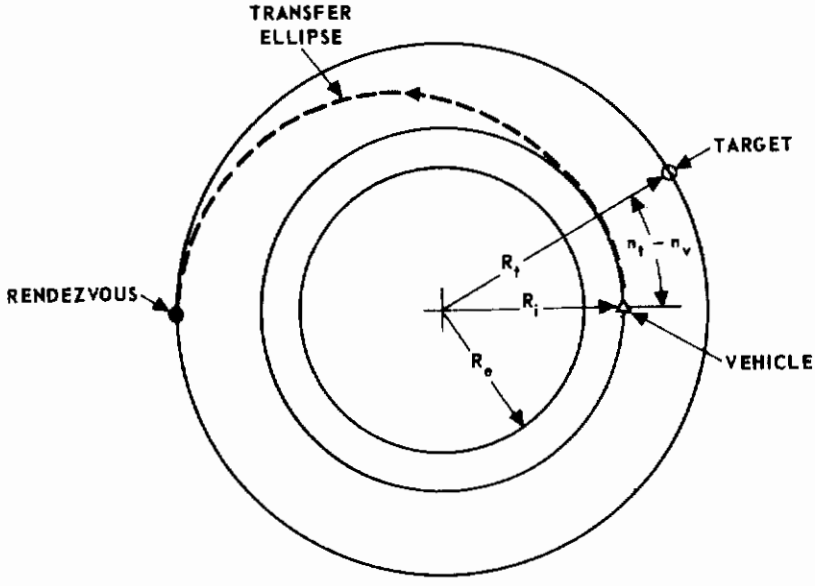

Figure 2-3 - Ascent Orbital Transfer

In most maneuvers a circularizing increment would not be incorporated because it is not generally desirable to equalize the velocities of the target and vehicle. By not circularizing, the target and vehicle will have a relative velocity of $-\Delta V_3$ which is advantageous for rendezvous. In essence, ΔV_3 is applied during rendezvous but not as one impulse.

2.1.3 Equations for Descent

At the completion of rendezvous, it will be necessary to return to a low parking orbit before proceeding with re-entry. The maneuvers are nearly the reverse of those used for ascent to the target altitude.

If a change of orbital plane is required for re-entry, it would be most efficiently accomplished at the target altitude, since the velocity is less and is more easily corrected than in a low orbit. Using the angle terminology of Figure 2-2, the corrective velocity change for this maneuver is:

$$\Delta V_4 = 2V_{tc} \sin \frac{\psi}{2} \qquad (2\text{-}7)$$

directed at the angle, $\xi = \psi/2$

The next two velocity impulses are directed against the prevailing velocity vector to reduce the vehicle speed. The magnitudes of the sequential velocity decrements are:

$$\Delta V_5 = V_{fc} \left(\frac{R_t}{R_f}\right)^{-1/2} \left\{1 - \left[\frac{1}{2}\left(1 + \frac{R_t}{R_f}\right)\right]^{-1/2}\right\} \qquad (2\text{-}8)$$

$$\Delta V_6 = V_{fc} \left\{\left(\frac{R_t}{R_f}\right)^{1/2} \left[\frac{1}{2}\left(1 + \frac{R_t}{R_f}\right)\right]^{-1/2} - 1\right\} \qquad (2\text{-}9)$$

where R_t is the radius of the target orbit, R_f is the radius of the circular parking orbit to be used for the re-entry maneuver, and V_{fc} is the vehicle velocity in the parking orbit. The operation is illustrated by Figure 2-4. ΔV_5 is applied to initiate the transfer ellipse, and ΔV_6 is applied at the perigee of the ellipse to circularize the orbit.

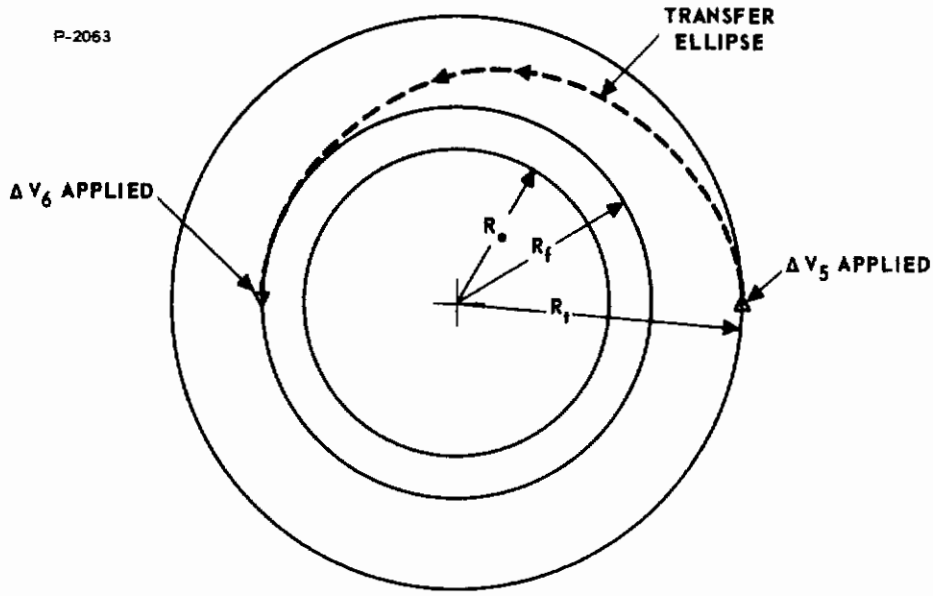

Figure 2-4 - Descent Orbital Transfer

2.1.4 Equations for De-boost Into Re-entry Trajectory

The re-entry maneuver involves moving the vehicle out of a low parking orbit into an earth-bound trajectory followed by suitable altitude-velocity control in the atmosphere to effect a safe landing. The execution of the maneuver depends upon the vehicle's aerodynamic characteristics and the structural and crew limitations. For the case at hand, a lifting re-entry configuration is used, which requires that a corridor be flown which avoids conditions of insufficient lift, excessive lift, and excessive physical abuse.

The first phase of re-entry is to leave the parking orbit and properly adjust the velocity and the angle of the path from the horizontal. If the orbit is low enough, this can be accomplished by using a drag brake. A simpler method is to use retro-rocket thrust to change the velocity vector as illustrated in Figure 2-5. The angle and magnitude of the velocity correction are:

$$\Delta V_7 = \left[(V_f \cos\theta - V_{fc})^2 + (V_f \sin\theta)^2 \right]^{1/2} \qquad (2\text{-}10)$$

$$\zeta = \arctan \frac{V_f \sin\theta}{V_f \cos\theta - V_{fc}} \qquad (2\text{-}11)$$

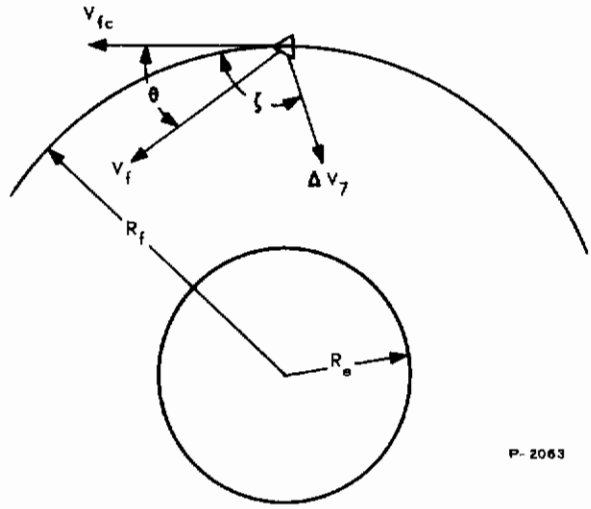

Figure 2-5 - Initial Re-Entry Maneuver, Departure from Orbit

2.1.5 Error Analysis

This analysis is concerned with determining the errors which will result at the end of the orbital transfer maneuver as the result of attitude errors at the initiation of maneuver. The error coefficients used are first order linear approximations but are sufficiently accurate for initial error estimates. Some of the equations are taken from Ref. (3).

The first step in the over-all transfer maneuver is to correct the differential inclination of the orbital planes. Appendix I shows that for errors in the magnitude and direction of the velocity impulse, the residual differential inclination is:

$$\delta\psi = (1 - \cos\psi)\,\delta\,\xi + \cos\frac{\psi}{2}\,\frac{\xi(\Delta V_1)}{V_{ic}} \qquad (2\text{-}12)$$

For this angular error, a maximum lateral horizontal error of

$$b = (\delta\psi)\,R_t \qquad (2\text{-}13)$$

would be present at the inception of the rendezvous maneuver.

In the orbital transfer, the initial and final states correspond to the perigee and apogee of the transfer ellipse. For this case, the inplane error coefficients are listed in Table 2-1. θ is the angle

between velocity and horizontal, η is the geocentric angle measured from the perigee, and A is defined by:

$$A = \frac{R_1 V_1^2}{\mu}$$

The initial state variations are those which exist immediately after the velocity impulse for orbital transfer has been applied.

Table 2-1

Error Coefficients for Orbital Transfer

Final State Variations	Initial State Variations			$\delta\eta_1$
	$\delta R_1/R_1$	$\delta V_1/V_1$	$\delta\theta_1$	
$\delta R/R$	$(4-A)/(2-A)$	$4/(2-A)$	0	0
$\delta V/V$	$-2/(2-A)$	$-(2+A)/(2-A)$	0	0
$\delta\theta$	0	0	$-A$	0
$\theta\eta/\pi$	$-3/A^{3/2}(2-A)^{1/2}$	$-3/A^{1/2}(2-A)^{1/2}$	$-4/A$	1

Of particular interest is the effect which the attitude error will have on rendezvous. Using Table 2-1 and Figure 2-6, it can be deduced that th angular rate of the line-of-sight between the vehicle and target when they initially reach the same altitude is:

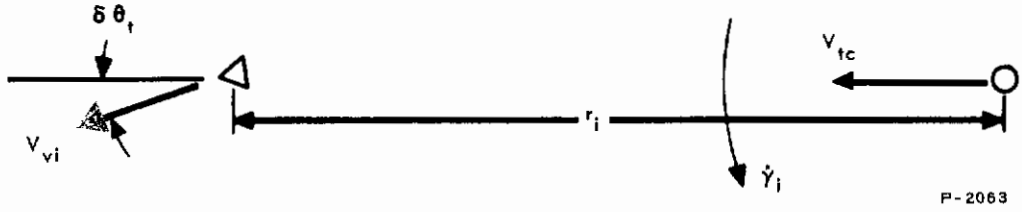

Figure 2-6 - Rendezvous Initial Conditions

$$\gamma_i = \frac{V_{vi}\,\delta\theta_t}{r_i} = \frac{V_{vi}\,R_i\,(V_{ic} + \Delta V_2)^2\,\delta\theta_i}{\mu\, r_i} \qquad (2\text{-}14)$$

The equations presented above can be used for both ascent and descent maneuvers, but for the case at hand only ascent is of interest. This is because small errors in position at the inception of the re-entry maneuver can be readily corrected during re-entry.

2.1.6 Nomenclature

b = Lateral range at rendezvous initiation

g_c = Acceleration of gravity at sea level, ft/sec^2

r = Range between vehicle and target, ft

r_i = Range at initiation of rendezvous, ft

R = Radius from earth's center, ft

R_e = Earth's radius, ft

R_f = Radius of re-entry circular parking orbit, ft

R_i = Radius of initial circular parking orbit, ft

R_t = Radius of target circular parking orbit, ft

V = Vehicle velocity, ft/sec

V_f = Vehicle velocity at initiation of re-entry maneuver, ft/sec

V_{fc} = Orbital velocity, re-entry circular parking orbit, ft/sec

V_{ic} = Orbital velocity, initial circular parking orbit, ft/sec

V_{tc} = Orbital velocity, circular target orbit, ft/sec

V_{vi} = Vehicle velocity at rendezvous initiation, ft/sec

ΔV_1 = Velocity application for orbital plane change (ascent phase), ft/sec

ΔV_2 = Velocity increment for initiating orbital transfer, (ascent phase), ft/sec

ΔV_3 = Velocity increment required to circularize at the apogee of the orbital transfer ellipse (ascent phase), ft/sec

ΔV_4 = Velocity application for orbital plane change (descent phase), ft/sec

ΔV_5 = Velocity decrement for initiating orbital transfer (descent phase), ft/sec

ΔV_6 = Velocity decrement for circularizing at the perigee of the orbital transfer ellipse (descent phase), ft/sec

ΔV_7 = Velocity application for leaving re-entry parking orbit, ft/sec

$\dot{\gamma}$ = Angular rate of line-of-sight during rendezvous, rad/sec

$\dot{\gamma}_i$ = Initial angular rate of line-of-sight, rad/sec

δ = Error increment prefix

ζ = Angle between velocity vector and thrust vector when leaving re-entry parking orbit, rad

η = Geogentric angle, rad

η_t = Angle between target and inertial reference plane, rad

η_v = Angle between vehicle and inertial reference plane, rad

θ = Angle between velocity vector and horizontal, rad

$\delta\theta_i$ = Error angle when leaving initial parking orbit for transfer to target orbit, rad

$\delta\theta_t$ = Error angle at interception of target orbit, rad

μ = Gravitational constant, $g_c R_e^2$, ft^3/sec^2

ξ = $\xi + \pi/2$ = rotation of the thrust vector from the velocity vector for change of orbital plane, rads

π = 3.14159265358979 . . .

ψ = Angular inclination of vehicle and target orbits, rad

2.2 RENDEZVOUS

2.2.1 Assumptions

(a) The vehicle and target are at nearly the same altitude.

(b) The vehicle is initially ahead of the target and traveling at a lower velocity

(c) The relative motion is essentially coplanar.

(d) All maneuvers are performed by the vehicle.

(e) All control engines have constant thrust.

2.2.2 Guidance Philosophy

The guidance system for the rendezvous maneuver incorporates three control systems. The range rate control system acts to attenuate the closing rate as the range between the vehicle and target decreases, the goal being to prevent damage at impact. The angular rate control system establishes the vehicle on a collision course with the target by nulling the angular rate of the line-of-sight between the two bodies. The attitude control system properly orients the thrust vectors of the control engines with respect to the line-of-sight.

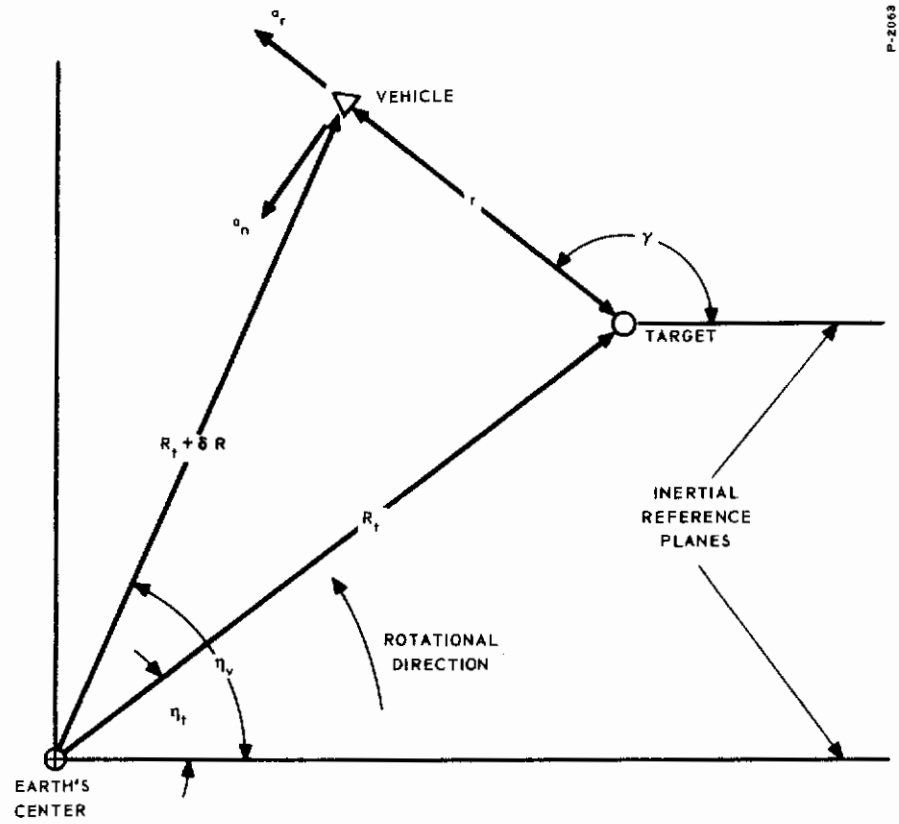

Figure 2-7 - Rendezvous Geometry

The geometry of the problem is shown in Figure 2-7. The vehicle is ahead of the target but traveling at a lower velocity so that $\dot{r}$ is negative. $\dot{\gamma}$ is the angular rate of the line-of-sight between the two bodies. Generally, $r << R_t$ so that $\eta_t \simeq \eta_v$ and $\dot{\eta}_t \simeq \dot{\eta}_v$.

The longitudinal engine is a part of the range rate control system and acts along the line-of-sight to produce the acceleration a_r. A transverse-mounted engine acts normal to the line-of-sight through the vehicle center of gravity. It is the prime mover of the angular rate control system and produces a_n.

The rendezvous maneuver involves the use of multiple corrections for bringing the two bodies together. The angular rate and range rate control systems operate at somewhat regular intervals to correct for errors introduced by each other as well as errors which grow as functions of time. The sequence is such that the time between

corrections allows adequate data filtering and smoothing by the guidance computer. The attitude control system can be either continuous or on-off in nature, so long as the vehicle is in proper orientation during the application of the normal and longitudinal corrections.

The rendezvous maneuver begins when the vehicle's radar picks up and begins to track the target. The range at this point could be 10 to 50 miles or more and the range rate could be -200 to -2000 fps, depending on altitude. Immediately, the attitude control system puts the longitudinal axis on the line-of-sight, and the angular rate control system applies the necessary lateral pulse to reduce the angular rate of the line-of-sight to near zero. This logic continues until the range is reduced to a few miles. From this point on, the time-to-go parameter,

$$\tau = \frac{r}{-\dot{r}}$$

plays a major role in that the logic used with the range rate control system is to maintain τ within specified limits. When τ reaches the lower limit, the longitudinal engine is turned on to increase the vehicle velocity a sufficient amount to bring τ to the upper limit. This continues until the range is reduced to one hundred feet or less, and the range rate is 1 or 2 fps. At this point the docking system takes over and no more velocity changes are made except to maintain a collision course. When the bodies are a few feet apart, a mechanical or magnetic system controls the impact and hook-up.

2.2.3 Equations of Motion

The equations for coplanar motion along the line-of-sight and normal to the line-of-sight are given in Ref. (2) and (6):

$$\ddot{r} - r\dot{\gamma}^2 = a_r - B\,r\left[1 - 3\cos^2(\gamma - \eta_t)\right] \qquad (2\text{-}15)$$

$$r\ddot{\gamma} + 2\dot{r}\dot{\gamma} = a_n - 3\,B\,r\,\sin(\gamma - \eta_t)\cos(\gamma - \eta_t). \qquad (2\text{-}16)$$

B is a term which accounts for the effect of gravity gradient upon the relative motion and is defined as:

$$B = \frac{G\,M_e}{R_t^3}, \qquad (2\text{-}17)$$

where G is the universal gravitational constant and M_e is the earth's mass. For a rendezvous when the total maneuver time is small, the gravity term has a small effect and can be eliminated, at least for a first order analysis. The simplified equations then are:

$$\ddot{r} - r\dot{\gamma}^2 = a_r , \tag{2-18}$$

$$r\ddot{\gamma} + 2r\dot{\gamma} = a_n . \tag{2-19}$$

A general analytic solution of these equations is not possible because of the nonlinearities present. Appendix II contains linearized forms of these equations which are useful for first approximations.

Equations (2-15) through (2-19) represent the ideal case where the a_r vector lies on the line-of-sight and the a_n vector is perpendicular to the line-of-sight. Included in these equations should be the effect of attitude error upon the relative motion. Figure 2-8 defines the error angle ϵ which can exist about the pitch axis with respect to the line-of-sight. Using the small-angle approximation, the simplified equations for coplanar motion become:

$$\ddot{r} - r\dot{\gamma}^2 = a_r - a_n \epsilon \tag{2-20}$$

$$r\ddot{\gamma} + 2\dot{r}\dot{\gamma} = a_r \epsilon + a_n \tag{2-21}$$

We can go one step further than the above equations to include errors about the roll and yaw axes as well as the pitch axis. Using the nomenclature defined in Figure 2-9, the equations of motion become:

$$\ddot{r} - r(\dot{\gamma}_y^2 + \dot{\gamma}_p^2) = a_r - a_n \epsilon \tag{2-22}$$

$$r\ddot{\gamma}_p + 2\dot{r}\dot{\gamma}_p = a_n + a_r \epsilon \tag{2-23}$$

$$r\ddot{\gamma}_y + 2\dot{r}\dot{\gamma}_y = a_r \epsilon' - a_n \epsilon'' \tag{2-24}$$

Equations (2-22) through (2-24) are the most general of the simplified expressions developed, but their use is cumbersome because of the large number of variable terms. It is seen that Equations (2-22) and (2-23) are identical with Equations (2-20) and (2-21) except for the

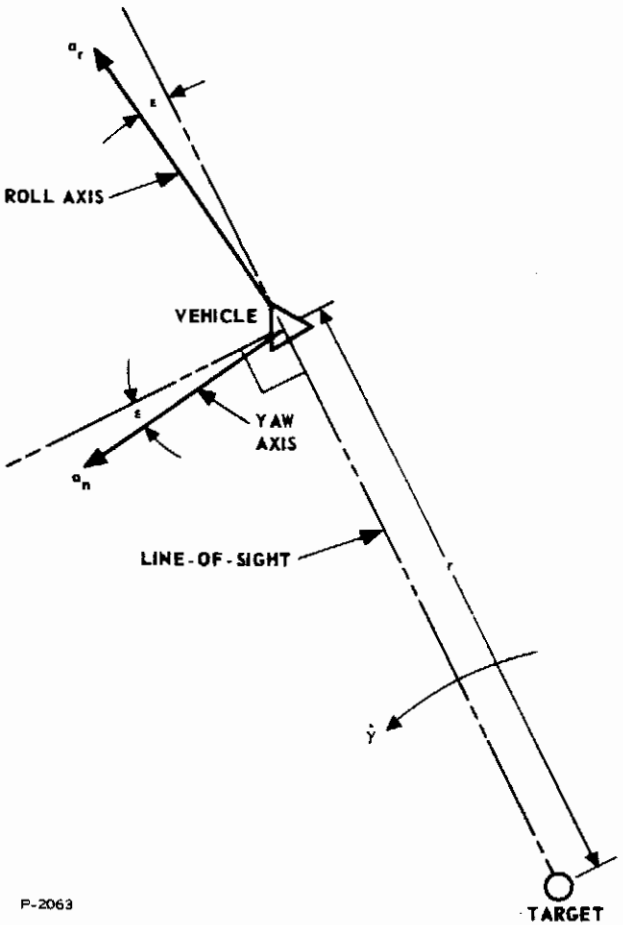

Figure 2-8 - Rendezvous Motion with Pitch Error

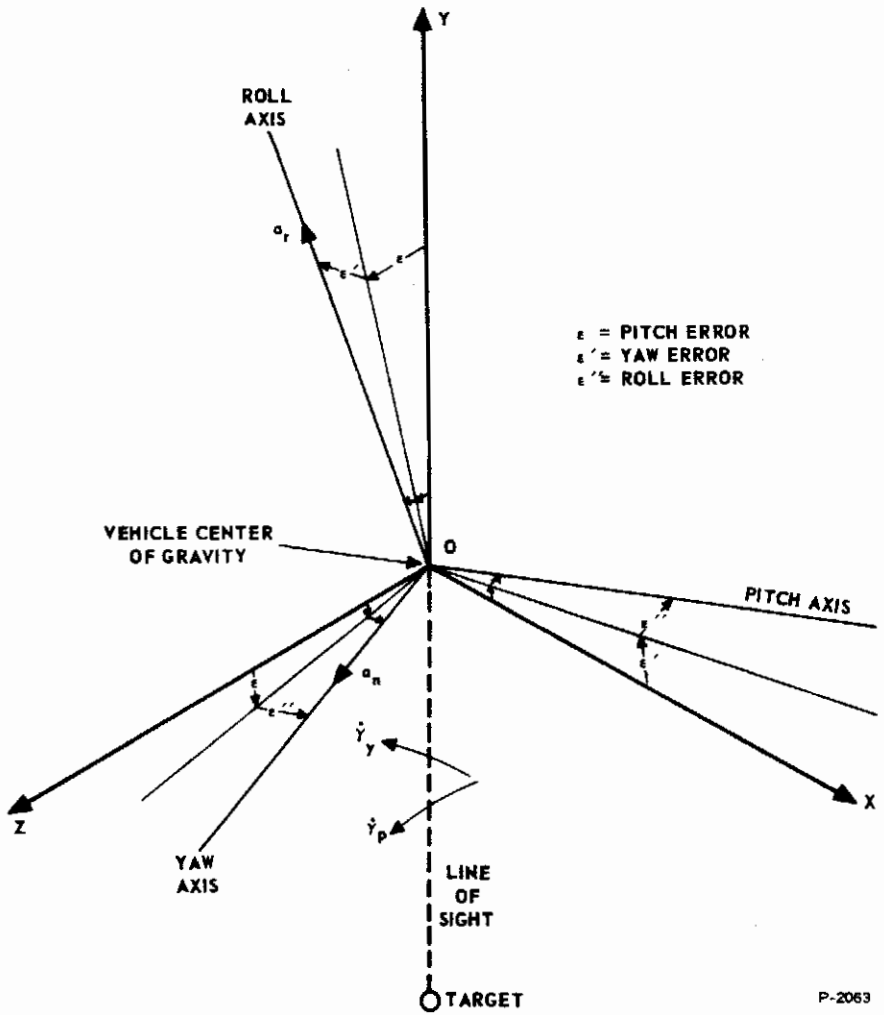

Figure 2-9 - Three-Axes Attitude Errors

presence of the $r\dot{\gamma}_y^2$ term. It is obvious that if ϵ' and ϵ'' are maintained sufficiently small, $\dot{\gamma}_y^2 << \dot{\gamma}_p^2$, thus making Equations (2-20) and (2-22) equivalent. For purposes of analyzing and defining the rendezvous control logic, ϵ' and ϵ'' will be assumed to be small enough so that Equations (2-20) and (2-21) adequately define the relative motion.

2.2.4 Guidance Logic

The initiation of corrective thrusts occurs when τ and $\dot{\gamma}$ reach pre-set limits. $\dot{\gamma}$ is the angular rate of the line-of-sight and is not allowed to exceed $\dot{\gamma}_{max}$. $\tau = -r/\dot{r}$, where r is the range and $\dot{r}$ is the range rate; it is not allowed to drop below τ_{min}. The logic is such that when either $\dot{\gamma}_{max}$ or τ_{min} is reached, both orthogonal engines fire to correct τ and $\dot{\gamma}$ to or near predetermined values designated τ_b and $\dot{\gamma}_b$. If $\tau \geqq \tau_b$ or $\dot{\gamma} \leqq \dot{\gamma}_b$, the respective engine will not be allowed (or needed) to fire

The thrust terminations of the orthogonal engines are not simultaneous. The firing time of each engine is controlled by the integrated output of a single axis accelerometer and a pre-computed velocity increment requirement. For the normal (angular rate) correction, the thrust is terminated when

$$\Delta V_{no} = \int_o^{\Delta t_n} a_n \, dt = -(\dot{\gamma}_o - \dot{\gamma}_b) \, r_o \qquad (2\text{-}25)$$

where: a_n = acceleration normal to line-of-sight,

Δt_n = thrusting time,

$\dot{\gamma}_o$ = angular rate at thrust initiation,

$\dot{\gamma}_b$ = pre-set bias angular rate,

r_o = initial range,

For the longitudinal (range rate) correction, the thrust is terminated when:

$$\Delta V_{ro} = \int_o^{\Delta t_r} a_r \, dt = r_o \left[\frac{1}{\tau_o} - \frac{1}{\tau_b}\right] \qquad (2\text{-}26)$$

where: Δt_r = thrusting time,

a_n = acceleration along line-of-sight

τ_o = initial time-to-go

τ_b = pre-set corrected time-to-go

Equations (2-25) and (2-26) are accuracte only when the velocity corrections are instantaneous, but they do provide an adequate control law and they are easily handled by spaceborne computers. They are discussed further in Appendix II.

For the rendezvous maneuver of a large vehicle it becomes necessary to reduce the levels of the corrective thrusts as the range decreases in order to maintain acceptable accuracy of the angular rate and range rate control systems. This can be achieved by incorporating clustered engines or by taking advantage of the various engine sizes used for pitch, yaw and roll control. The logic which follows allows for two changes of normal and longitudinal thrust. Initially, $a_n = a_{ni}$ and $a_r = a_{ri}$. When r_o reaches r', $a_n = a_n'$ and $a_r = a_r'$. When r_o reaches r'', $a_n = a_n''$ and $a_r = a_r''$. In each case, the accelerations are decreased by nearly an order of magnitude.

A functional block diagram of the guidance system is shown in Figure 2-10. For this study, all delays and dynamic lags are assumed to be negligible to facilitate computation on a digital computer. Peculiar features of the system are the following:

(a) The main ON-OFF controllers sense two signals. They are turned on only by limiting values of $\dot{\gamma}$ and τ, and they are turned off only at the command of the secondary ON-OFF controllers. Only one of the controllers need be on to actuate normal and longitudinal corrections.

(b) The secondary ON-OFF controllers react to the integrated outputs of the body-mounted accelerometers. They are normally ON, but during the coast periods do not pass any signals to the engines since the main controllers are OFF. The cut-off points of the relays are variable in that they are the computed values of ΔV_n and ΔV_r at the initiation of the correction.

(c) The functions of the hold circuits are to maintain the ΔV_n and ΔV_r signals at the values computed when the correction began.

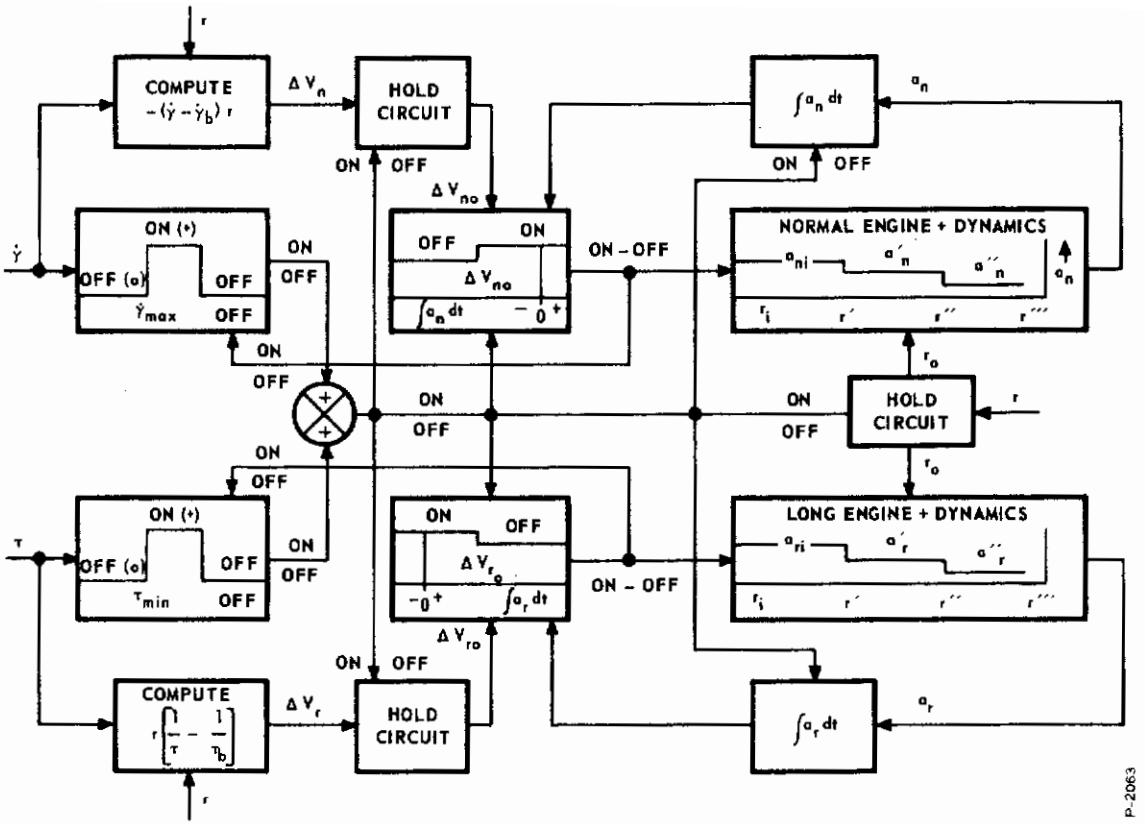

Figure 2-10 - Rendezvous Guidance System - Block Diagram

(d) The integration circuits for the accelerometers operate as commanded by the main ON-OFF controllers. When the circuits are turned off, their outputs return to zero.

2.2.5 Nomenclature

a_n = Acceleration created by transverse engine, ft/sec^2

a_{ni} = Value of a_n at start of rendezvous and $r_o > r'$

a'_n = Value of a_n for $r' \geq r_o \geq r''$

a''_n = Value of a_n for $r'' \geq r_o \geq r'''$

a_r = Acceleration created by longitudinal engine, ft/sec^2

a_{ri} = Value of a_r at start of rendezvous and for $r_o > r'$

a'_r = Value of a_r for $r' \geq r_o > r''$

a''_r = Value of a_r for $r'' \geq r_o > r'''$

r = Range between vehicle and target during rendezvous, ft

r_o = Range at initiation of correction maneuver, ft

r' = Range at first change of normal and longitudinal engine sizes, ft

r'' = Range at second change of normal and longitudinal engine sizes, ft

r''' = Range at which the initial closure phase of the rendezvous maneuver gives way to the docking phase, ft

$\dot{r}$ = Range rate, ft/sec

$\dot{r}_o$ = Range rate at the initiation of a corrective maneuver, ft/sec

R_t = Radius of target orbit, ft

t = Time, sec

Δt_n = Thrusting time of normal engine, sec

Δt_r = Thrusting time of longitudinal engine, sec

ΔV_{no} = Commanded change in normal velocity, ft/sec

ΔV_{ro} = Commanded change in longitudinal velocity, ft/sec

$\dot{\gamma}$ = Angular rate of rendezvous line-of-sight, rad/sec

$\dot{\gamma}_p$ = Angular rate about pitch axis, rad/sec

$\dot{\gamma}_y$ = Angular rate about yaw axis, rad/sec

$\dot{\gamma}_b$ = Commanded angular rate during correction, rad/sec

$\dot{\gamma}_o$ = Angular rate at the initiation of a corrective maneuver, rad/sec

$\dot{\gamma}_{max}$ = Maximum allowable angular rate, rad/sec

ϵ = Pitch attitude error angle during rendezvous, rad

η = Geocentric angle, rad

η_t = Angle between target and inertial reference, rad

η_v = Angle between vehicle and inertial reference, rad

τ = Time-to-go parameter, $-r/\dot{r}$, sec

τ_b = Commanded time-to-go during correction, sec

τ_o = Time-to-go at the initiation of a corrective maneuver, sec

τ_{min} = Minimum allowable time-to-go, sec

$(\dot{})$ = Denotes first derivative with respect to time

$(\ddot{})$ = Denotes second derivative with respect to time

2.3 RE-ENTRY

2.3.1 Basic Vehicle Shape

A detailed study to arrive at an optimum re-entry shape is outside the scope of this project which is, after all, directed toward studying moment-producing techniques. It was thus decided to assume the use of a delta winged glider configuration. This decision was based on the fact that considerable data on the hypersonic aerodynamic characteristics of such configurations have been accumulated. As a result, not only is much of the basic information required to evaluate various moment producing techniques readily available, but also confidence may be expressed that if the configuration selected is not the absolute optimum, it is at least quite practical and reasonable.

Some of the unclassified and declassified data on the aerodynamic characteristics of delta winged gliders published by NASA.[16-21] These publications cover delta wings with sweepback angles, Λ, from 70 to 80 degrees. Since some of the most specific data deals with shapes having $\Lambda = 70°$, this value will be assumed for the work in this study.

2.3.2 Trajectory Equations

Before a study of moment producing techniques for a re-entering vehicle can be begun, some information on probable re-entry trajectory parameters must be available. The equations of motion in the pitch plane for a re-entry vehicle are given in Appendix III. These are:

$$m \frac{dV}{dt} = - \frac{C_D A_R \rho V^2}{2} + mg \sin \theta \qquad (2\text{-}27)$$

$$-mV \frac{d\theta}{dt} = \frac{C_L A_R \rho V^2}{2} - mg \cos \theta + \frac{m V^2 \cos \theta}{R} \qquad (2\text{-}28)$$

The geometry of the motion is shown in Figure 2-11.

Strictly speaking, every term in Equation (2-27) and (2-28) with the possible exception of A_R is a variable. However, the range of variation of some of the terms is such that they may be considered constant. It has been stated in Appendix III that g and R will be assumed

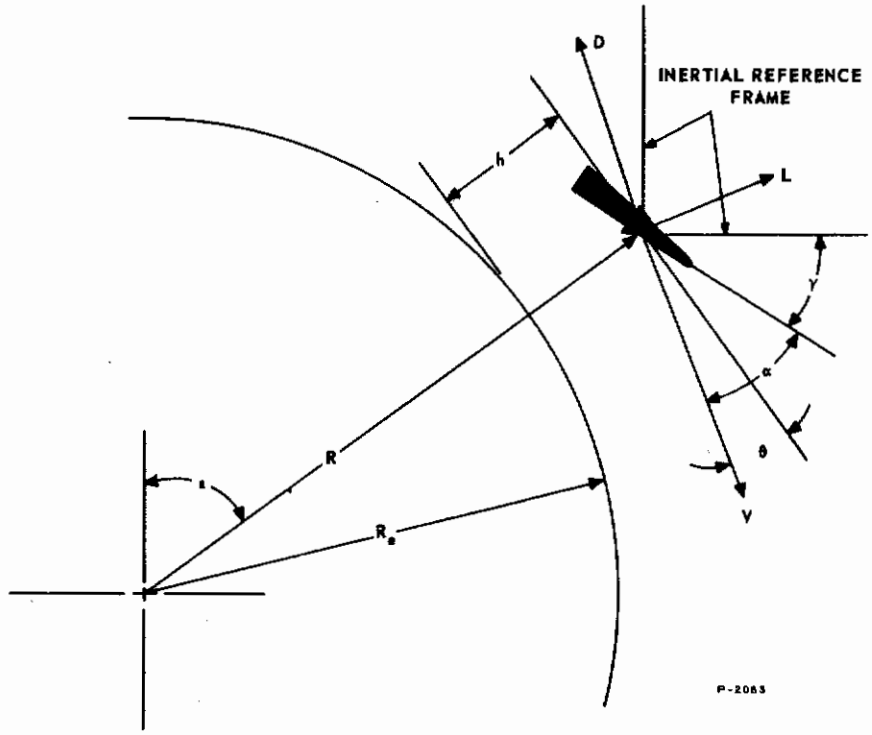

Figure 2-11 - Geometry of Re-Entry Motion in Pitch Plane

to be constant. The thermal protection system may be presumed to at least partially involve ablation or the use of expendable cooling. Vehicle electrical power and power for the actuation of aerodynamic surfaces may be expected to be supplied from a chemically fueled power system. Any actual vehicle design should take the loss of mass from these sources into account. However, the effects of this variable should be much less than some of the others under consideration and in this study, m will be taken as a constant.

In addition to Equations (2-27) and (2-28), Appendix III also gives:

$$\rho = \rho_B \, e^{-\beta h} \qquad (2\text{-}29)$$

and

$$\frac{dh}{dt} = -V \sin \theta \qquad (2\text{-}30)$$

Equations (2-27) through (2-30) contain 7 variables, namely V, θ, h, C_D, C_L, ρ, and t. In order to express the first 6 variables in terms of t, two more relationships between these variables will have to be defined without introduction of new variables. One of these relationships may be obtained from knowledge of the aerodynamic characteristics of the vehicle. The various aerodynamic coefficients, such as C_L and C_D, are functions of the basic vehicle shape, angle of attack, position of the various aerodynamic control surfaces, vehicle size, velocity, and the characteristics of the fluid through which the vehicle is traveling. Aerodynamic data is correlated through use of the various similarity relationships, notably Reynolds number and Mach number. At higher values of the Mach number, its effect on the aerodynamic coefficients is small. For the range of velocities under consideration in this study, (5000 to 26000 fps), Mach number effects on aerodynamic coefficients can be ignored. The effect of Reynolds number is more difficult to assess. If the vehicle is assumed to have a velocity of 26000 fps at 300,000 ft altitude and a velocity of 5000 fps at 180,000 ft, the change in Reynolds number can be calculated.

$$N_R = \frac{\rho V L_R}{\mu} \qquad (2\text{-}31)$$

and from Ref. (22):

at 300,000 ft $\rho = 1.488 \times 10^{-7}$ lb/ft^3

$\mu = 8.343 \times 10^{-6}$ lb/ft-sec

at 180,000 ft $\rho = 3.558 \times 10^{-5}$ lb/ft^3

$\mu = 1.1288 \times 10^{-5}$ lb/ft^3

The mean aerodynamic chord, $\bar{c}$, which is equal to 2/3 of the root chord for a triangular wing is frequently used as the reference length. Substitution of the appropriate values into Equation (2-31) gives a Reynolds number of 62000 at 300,000 ft and 2,100,000 at 180,000 ft for a 200 ft long delta wing. This is not an insignificant variation. Data for viscosities above 300,000 ft are not given in [21] but it is quite evident that Reynolds number is very small at the higher altitudes. The state of knowledge regarding the effect of Reynolds number on aerodynamic characteristics does not appear to be too satisfactory at this time. However, it is indicated in [23] that the greatest Reynolds number effects occur above 300,000 ft. Since the most important portions of the reentry occur below this altitude, the effect of variations in Reynolds number will be neglected in this study.

If it is accepted that the aerodynamic coefficients C_L and and C_D are functions only of the basic vehicle shape, angle of attack, and aerodynamic control position, then it is possible to express C_L as a function of C_D. For example,[19] gives plots of C_L and C_D as a function of α for various deflections of a trailing edge flap for a 70 degree sweep delta wing at a Mach number of 6.83 and a Reynolds number of 0.60×10^6 and large angles of attack. Data is also given for the pitching moment coefficients corresponding to various control deflections. From the latter, the equilibrium values of angles of attack for a given control deflection may be determined. By crossplotting of the values of C_L and C_D corresponding to the flap deflection for a given value of α, a curve C_L and C_L/C_D versus C_D for equilibrium conditions may be constructed. Such a set of curves is shown in Figure 2-12. The data for this curve has been obtained from Ref. (19) and corresponds to a 70 degree delta wing with a nose incidence of 10 degrees and angles of attack of 28 to 77 degrees.

One other relationship is required to solve for the re-entry trajectory. Such a relationship can be obtained by defining a control law to be followed by the vehicle during its re-entry. This control law will set some variable to be either held constant, limited to a maximum or minimum value, or to follow some program. Implementation of the control law requires the measurement of at least one parameter associated with the trajectory. A number of parameters could be considered for use as the controlled variable. These include altitude, h, dynamic pressure, q, path angle, θ, path velocity, V, and either the path of resultant acceleration. There are distinct difficulties associated with the measurement of most of these variables which require some sort of transducer external to the vehicle envelope. It would appear that very serious problems with calibration would exist because of aerodynamic heating, ionization, shock waves, and other effects on external probes. The one set of variables which can be measured by transducers located entirely in the vehicle under protected conditions are the accelerations. In addition, limitation of deceleration forces to tolerable values is one of the major requirements for the re-entry trajectory. On these grounds, control of accelerations has been selected as the basis of the control law assumed in this study.

Either the resultant acceleration or the path acceleration represent mathematically convenient measured variables. Because of changes in angle of attack and lift-to-drag ratio, the angles with the

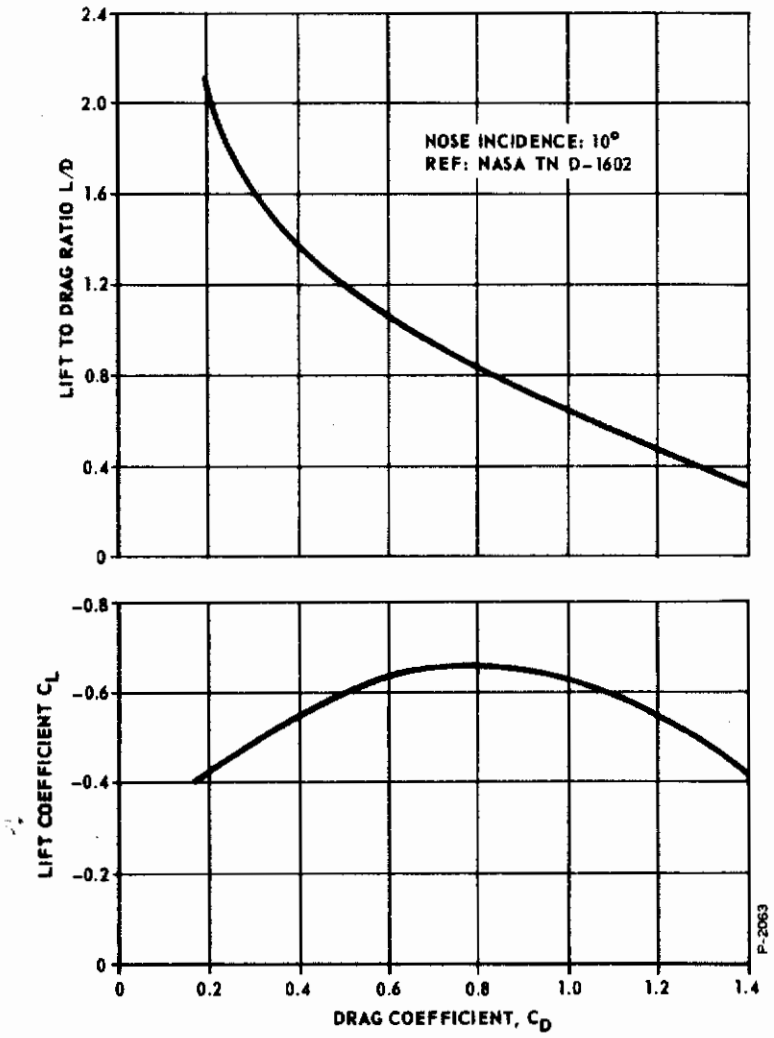

Figure 2-12 - Aerodynamic Characteristics of 70° Delta Wing Controlled by Trailing Edge Flap

vehicle axis of the vectors representing both accelerations will be variable. As a result, a single fixed position accelerometer will not be capable of exactly measuring these accelerations at all angles of attack unless some means of compensation is used. Except for the fact that resultant acceleration will be larger than the path acceleration there seems to be no over-riding reason to select one over the other. For the purposes of this study, the values of path acceleration was selected as the controlled variable. It was assumed that some means of compensating the accelerometer output for changes in angle of attack is used. Some means of determining angle of attack to feed into

the compensation circuit is required. If aerodynamic control is used, equilibrium angle of attack will be a function of control surface position and can thus be easily measured. If mass expulsion is used for producing the required moments, means of measuring angle of attack is not so obvious. However, some method of angle of attack measurement will be required as an input to a supplementary control loop which will limit thrust to values which will maintain the vehicle within the desired angle of attack range. This will be available as a means of correcting accelerometer output for changes in α.

The assumed control law may be stated as:

$$\left(\frac{dV}{dt}\right)_d = -k_d g_c \qquad (2\text{-}32)$$

At initial entry, although velocity is high, atmospheric density is very small. The drag force $D = C_D A_R \rho V^2/2$ cannot be built up to a large enough value to bring path deceleration immediately to its desired value. However, the attitude control system will pitch the vehicle up to the maximum allowable angle of attack in order to obtain the greatest possible value of C_D. This will also give a minimum value of L/D. As the vehicle descends, the drag force will build up as atmospheric density increases. The increased drag will gradually bring the path deceleration up to the desired value. When the condition $dV/dt = (dV/dt)_d$ is reached, the vehicle will begin to pitch down in order to maintain a value of C_D which will give the desired value of path deceleration. With the aerodynamic characteristics assumed here, a decrease of C_D causes an increase in L/D. As L/D increases the vehicle will pull up and start to climb. As atmospheric density decreases, the vehicle will commence to pitch up to maintain deceleration at its desired value. This will cause a decrease in L/D, the vehicle will descend again and the whole process will start over.

2.3.3 Nomenclature

A_R = Reference or wing area - ft

$\bar{c}$ = Mean aerodynamic chord - ft

C_D = Gasdynamic drag coefficient - dimensionless

C_L = Gasdynamic lift coefficient - dimensionless

D = Drag force - lbs

g = Gravitational acceleration - ft/sec^2

g_c = Gravitational acceleration at sea level = 32.174 fps

h = Geometric Altitude - ft

k_d = Factor in control law - dimensionless

L_R = Reference length in Reynolds No. - ft

L = Lift force - lbs

m = Vehicle mass - slugs

N_R = Reynolds number - dimensionless

R = Distance from vehicle to center of earth - ft

t = Time - seconds

V Vehicle velocity along flight path - fps

$(dV/dt)_d$ = Desired value of path acceleration - ft/sec^2

α = Angle of attack - radians

β = Exponential factor used in Equation (2-29) = (1/24100)ft

θ = Path angle with horizontal - radians

Λ = Sweepback angle - degrees

μ = Dynamic viscosity - lb/ft sec

ρ = Atmospheric density - $slugs/ft^3$

ρ_B = Base density used in atmospheric density approximation - $slugs/ft^3$

SECTION 3
MISSION COMPUTATIONS

3.1 ASSUMPTIONS AND CONSTANTS

The over-all vehicle mission, involving orbital transfer, rendezvous, and re-entry, is predicted on the basis of the following parameters.

(a) Altitude of initial parking orbit

$$h_i = 150 \text{ nautical miles}$$

(b) Altitude of target orbit

$$h_t = 300 \text{ nautical miles}$$

$$h_t = 600 \text{ nautical miles}$$

$$h_t = 1000 \text{ nautical miles}$$

(c) Differential inclination of initial parking orbit and target orbit

$$\psi = 10^\circ \text{ maximum}$$

(d) Altitude of final parking orbit at initiation of re-entry

$$h_f = 66 \text{ nautical miles}$$

(e) Average acceleration of gravity during re-entry

$$g = 31.4 \ \frac{\text{ft}}{\text{sec}^2} \quad (22)^*$$

(f) Base density for atmospheric approximation, Equation (2-29)

$$\rho_B = 0.00238 \ \frac{\text{slug}}{\text{ft}^3} \quad (24)$$

---

*Numbers in parentheses refer to the references listed in Section 10.

(g) Exponential factor for atmosphere approximation, Equation (2-29)

$$\beta^{-1} = 24{,}000 \text{ ft}^{(24)}$$

(h) Average distance from vehicle to earth's center during re-entry

$$R = 21.1 \times 10^6 \text{ ft}$$

(i) Weight of vehicle in initial parking orbit

$$W_i = 200{,}000 \text{ lb}$$

(j) Thrust of main engine

$$T_{ri} = 400{,}000 \text{ lb}$$

(k) Specific impulse of all engines

$$I_{sp} = 400 \text{ sec}$$

(l) Gravitational constant

$$\mu = 1.4069 \times 10^{16} \quad \frac{\text{ft}^2}{\text{sec}^2}$$

(m) Earth's radius

$$R_e = 20.9 \times 10^6 \text{ ft}$$

(n) One nautical mile = 6076 ft

3.2 ORBITAL TRANSFER

3.2.1 Orbit Velocities

The velocities associated with the various orbit altitudes are calculated from:

$$V_c = \sqrt{\frac{\mu}{R}} \tag{3-1}$$

where a circular orbit is assumed for all cases.

The results are:

Altitude nautical miles	Velocity ft/sec
66	25,698
150	25,396
300	24,881
600	23,940
1000	22,836

3.2.2 Plane Change

A 10 degree rotation of the orbital plane occurs while moving at a velocity of 25,396 ft/sec. From Equation (2-2), the required corrective velocity increment is $\Delta V_1 = 4420$ ft/sec.

Errors incurred during the execution of the maneuver will contribute a lateral horizontal error at the initiation of rendezvous. From Equations (2-12) and (2-13), it is found that for a 100 nautical mile target altitude the lateral error will be:

$$b = 67.4\ \delta\xi + 0.174\ \delta\ (\Delta V_1)$$

For every degree of angular error, the resulting lateral error will increase 1.2 miles, and for every 10 ft/sec of velocity error, the lateral error will increase 1.7 miles.

3.2.3 Ascent

To move the vehicle from the parking orbit of 150 nautical miles altitude to the target altitude, a Hohman transfer ellipse is followed. From Equations (2-3) and (2-6) the following required values of velocity increments are obtained:

Target Altitude nautical miles	Velocity Increase ft/sec
300	254
600	735
1000	1320

When the vehicle and target are at the same altitude, a relative velocity exists between them. Equation (2-5) defines the velocity increment required to bring the vehicle velocity up to that of the target, and therefore defines the maximum magnitude of the relative velocity which can exist. Assuming the vehicle to be ahead of the target, we see that the minimum relative velocity between the two bodies at the inception of rendezvous is:

Target Altitude nautical miles	Minimum Relative Velocity ft/sec
300	- 256
600	- 716
1000	-1242

The angular rate of the line-of-sight at the inception of rendezvous is a function of the errors incurred during the ascent transfer maneuver. Using Equation (2-14) and assuming that $\delta\theta_i = 0.0175$ rad and $\tau_i = 300$ sec, the angular rate is:

Target Altitude nautical miles	Angular Rate (Line-of-Sight) rad/sec
300	0.0057
600	0.0020
1000	0.0011

The vehicle weight at the end of the ascent maneuver and at the inception of the rendezvous maneuver can be obtained from the following equation:

$$W = W_i \exp. \left(- \Sigma \frac{\Delta V}{I_{sp}\, g_c} \right) \qquad (3\text{-}2)$$

where:
- W = weight, lb
- W_i = initial weight
- ΔV = velocity increment, ft/sec
- I_{sp} = specific impulse, 1/sec
- g_c = acceleration of gravity at sea level, in./sec^2

The results are as follows:

Target Altitude nautical miles	$\Sigma\Delta V$ ft/sec	W lbs
300	4674	139,000
600	5155	134,000
1000	5740	128,000

3.2.4 Descent

The transfer maneuver from the target orbit to the re-entry parking orbit is described by Equations (2-8) and (2-9). The respective velocity decrements are:

Target Altitude nautical miles	ΔV_5 ft/sec	ΔV_6 ft/sec
300	400	440
600	840	950
1000	1400	1470

3.2.5 De-Boost

The velocity of the vehicle in the re-entry parking orbit is 25,700 ft/sec. If the vehicle velocity vector is maintained at this magnitude but rotated through an angle of 2.5 degrees, the magnitude of the velocity correction is found from Equation (2-10) to be:

$$\Delta V_7 = 1120 \text{ ft/sec}$$

3.3 RENDEZVOUS

3.3.1 Computation Procedure

The numerical analysis of the rendezvous maneuver must be performed with the assistance of a computer because of the complexity of the equations and the number of solutions required. A digital computer can be used for the complete maneuver, so long as the attitude dynamics are not included. An analogue computer can effectively simulate the

complete dynamics during a thrust period, but its use for the over-all maneuver would be extremely difficult because of the large number of discontinuities which occur. It was decided to use a digital computer to establish and verify the rendezvous control logic wherein the effect of attitude dynamics is approximated by using various fixed values of attitude error.

Equations (2-20) and (2-21) provide a fairly accurate description of coplanar motion. Repeating here, they are:

$$\ddot{r} - r\dot{\gamma}^2 = a_r - a_n \epsilon \qquad (3\text{-}3)$$

$$r\ddot{\gamma} + 2\dot{r}\dot{\gamma} = a_r \epsilon + a_n \qquad (3\text{-}4)$$

ϵ is the attitude error about the pitch axis as shown in Figure 2-8. a_r and a_n are discontinuous functions of time.

Starting with the initial conditions: r_i, $\dot{r}_i$, and $\dot{\gamma}_i$, Equations (3-3) and (3-4) are solved with a digital computer according to the following commands:

(a) When $\tau \geq \tau_{min}$ and $\dot{\gamma} < \dot{\gamma}_{max}$, $a_r = 0$ and $a_n = 0$.

(b) When τ reaches τ_{min} or $\dot{\gamma}$ reaches $\dot{\gamma}_{max}$, a_r and a_n assume the values tabulated below:

Condition	a_r	a_n
$\dot{\gamma}_o \leq \dot{\gamma}_b$	does not apply	0
$\tau_o \geq \tau_b$	0	does not apply
$r_o > r'$	a_{ri}	a_{ni}
$r' \geq r_o > r''$	a_r'	a_n'
$r' \geq r_o > r'''$	a_r''	a_n''

The first two conditions override all others.

(c) a_r and a_n are maintained at the above values for the following time durations.

$$\Delta t_n = \frac{(\dot{\gamma}_o - \dot{\gamma}_b)\, r_o}{a_n} \tag{3-5}$$

$$\Delta t_r = \frac{r_o}{a_r}\left[\frac{1}{\tau_o} - \frac{1}{\tau_b}\right] \tag{3-6}$$

a_r and a_n are not changed during a thrusting period, therefore command (a) is violated during each correction.

(d) The above commands are obeyed until $r = r'''$, at which time the computation is terminated.

3.3.2 Control Parameters

The various control parameters associated with the rendezvous maneuver were initially sized or estimated using the linearized rendezvous equations contained in Appendix II. Many of the values were refined during the computer simulation study, but this initial step facilitated a rapid convergence to the final solution. For example, Equation (II-15) gives a good approximate relationship between the extreme values of $\dot{\gamma}$ and τ, and Equations (II-8) and (II-19) relate the parameters associated with range rate correction and angular rate correction.

The time-to-go parameter τ was chosen to vary between 40 seconds and 60 seconds. The 20 seconds difference provides a reasonably long coasting period between corrections so that data smoothing can be accomplished. The low nominal value of τ insures that the over-all maneuver time is reasonably short.

Values for $\dot{\gamma}$ were selected in conjunction with τ, because the two parameters are related. Upper and lower limits for $\dot{\gamma}$ were selected as 0.0010 rad/sec and 0.0004 rad/sec, respectively.

As the range decreases, the thrust levels of the control engines must be decreased in order to maintain controllable thrust

duration. The following table presents the minimum thrusting times allowed for various engine sizes:

engine thrust, lb	1000	10,000	100,000	500,000
minimum pulse width, sec	0.1	0.3	1.0	2.0

It is assumed that the main engine is used for the first angular rate correction to insure that enough thrust capacity is available to put the vehicle on course. The values of a_n and a_r after the first angular rate correction are

$$a_{ni} = -13 \text{ ft/sec}^2 \text{ and } a_{ri} = 100 \text{ ft/sec}^2$$

When the range reaches r' = 15,000 feet, the engine sizes are changed such that $a_n' = -2$ ft/sec^2 and $a_r' = 13$ ft/sec^2. When the range reaches r'' = 1500 ft, the accelerations become $a_n'' = -0.150$ ft/sec^2 and $a_r'' = 2$ ft/sec^2. Note that each thrust change is by approximately an order of magnitude.

It is seen that the rendezvous maneuver is comprised of four phases with regard to the thrust levels of the control engines. They are:

1. Main engine thrust (400,000 pounds) is used to correct initial angular rate error.
2. For r > 15,000 feet, main engine thrust is used for range rate control and a 50,000 pound thrust normal engine is used for angular rate control.
3. For 15,000 ft > r > 1500 ft, a 50,000 pound thrust auxiliary engine is used for range rate control and an 8000 pound thrust normal engine is used for angular rate control.
4. For 1500 ft > r > 60 ft, an 8000 pound thrust auxiliary engine is used for range control and a 600 pound thrust normal engine is used for angular rate control.

3.3.3 Rendezvous Simulation and Pitch Error

Simulated maneuvers were made for the most ciritical case, i.e., rendezvous at an altitude of 1000 nautical miles. The various parameters contained in Subsections 3.2.2, 3.2.3, and 3.3.2 were initially used with the computation procedure described in Subsection 3.3.1. The control parameters were varied somewhat from their initial values to provide the most desirable maneuver performance. Various values of pitch attitude error were used to determine the effect upon the maneuver and to establish tolerable pitch error limits.

The results of the computer simulation of rendezvous are condensed and presented in Tables 3-1 through 3-5. The final values of the parameters used are defined below:

r_i = 372,600 ft for 1000 nautical miles target altitude

$\dot{r}_i$ = -1242 ft/sec for 1000 nautical miles target altitude

$\dot{\gamma}_i$ = 0.0004 rad/sec

τ_i = 300 sec

ϵ = 0, ±0.010, ±0.020 rad

τ_{min} = 40 sec

τ_b = 65 sec

$\dot{\gamma}_{max}$ = 0.0010 rad/sec

$\dot{\gamma}_b$ = 0.0003 rad/sec

a_{ri} = 100 ft/sec^2 (400,000 lb thrust)

a_r' = 13 ft/sec^2 (50,000 lb thrust)

a_r'' = 2 ft/sec^2 (8,000 lb thrust)

a_{ni} = -13 ft/sec^2 (50,000 lb thrust)

a_n' = -2 ft/sec^2 (8,000 lb thrust)

a_n'' = -0.150 ft/sec^2 (600 lb thrust)

r' = 15,000 ft

Table 3-1 - Rendezvous Maneuver at 1000 Nautical Mile Altitude with Zero Attitude Error

CYCLE	Δt_c sec.	t_o sec.	r_o ft.	τ_o sec.	$\dot{\gamma}_o$ rad/sec.	Δt_r sec.	a_r ft/sec^2	Δt_n sec.	a_n ft/sec^2	r_1 ft.	τ_1 sec.	$\dot{\gamma}_1$ rad/sec.	t_1 sec.
1	110.7	111	236,000	191.8	0.00100	0	100	12.69	-13	220,000	179.4	0.00037	123
2	70.3	194	134,000	109.6	0.00100	0	100	7.21	-13	125,000	102.4	0.00038	200
3	39.6	240	76,800	62.9	0.00100	0.39	100	4.14	-13	71,900	60.8	0.00038	245
4	20.8	265	47,300	40	0.00088	4.55	100	2.10	-13	42,900	59.0	0.00038	270
5	19.1	289	29,100	40	0.00082	2.80	100	1.17	-13	27,400	61.3	0.00035	292
6	21.3	313	17,900	40	0.00082	1.72	100	0.72	-13	17,300	62.7	0.00032	315
7	22.8	337	11,000	40	0.00079	8.14	13	2.69	-2	9,200	54.1	0.00046	346
8	14.1	360	5,000	40	0.00085	5.03	13	1.86	-2	6,100	58.0	0.00040	365
9	18.0	383	4,200	40	0.00084	3.11	13	1.13	-2	3,900	60.9	0.00036	386
10	20.9	407	2,600	40	0.00083	1.92	13	0.69	-2	2,500	62.1	0.00034	409
11	22.1	431	1,600	40	0.00082	1.19	13	0.41	-2	1,500	63.0	0.00033	432
12	23.1	455	990	40	0.00081	4.78	2	3.38	-0.15	900	58.7	0.00039	460
13	18.8	479	610	40	0.00084	2.94	2	2.18	-0.15	580	61.0	0.00036	482
14	21.0	503	377	40	0.00085	1.81	2	1.37	-0.15	363	62.5	0.00033	502
15	22.5	527	232	40	0.00080	1.12	2	0.78	-0.15	227	63.3	0.00031	528
16	23.3	551	143	40	0.00099	0.69	2	0.47	-0.15	141	64.1	0.00031	552
17	24.1	576	90	40									

P-1853

Table 3-2 - Rendezvous Maneuver at 1000 Nautical Mile Altitude with + 0.010 Radian Attitude Error

CYCLE	Δt_c sec.	t_o sec.	r_o ft.	τ_o sec.	$\dot{\gamma}_o$ rad/sec.	Δt_r sec.	a_r ft/sec^2	Δt_n sec.	a_n ft/sec^2	r_1 ft.	τ_1 sec.	$\dot{\gamma}_1$ rad/sec	t_1 sec.
1	110.7	111	236,000	191.8	0.00100	0	100	12.69	-13	220,000	179.6	0.00037	123
2	70.4	194	134,000	109.7	0.00100	0	100	7.21	-13	125,000	102.6	0.00038	201
3	39.7	241	76,800	63.1	0.00100	0.36	100	4.14	-13	71,900	61.2	0.00038	245
4	21.3	266	47,000	40.0	0.00090	4.52	100	2.18	-13	42,700	59.0	0.00049	271
5	17.5	288	30,000	41.6	0.00100	2.61	100	1.62	-13	28,500	61.6	0.00044	291
6	20.5	311	19,000	41.1	0.00100	1.70	100	1.02	-13	18,400	62.7	0.00043	313
7	21.6	335	12,000	41.1	0.00100	8.29	13	4.21	-2	10,050	54.1	0.00061	343
8	12.0	355	7,830	42.2	0.00100	5.02	13	2.74	-2	7,060	58.4	0.00051	360
9	16.9	377	5,020	41.5	0.00100	3.36	13	1.76	-2	4,680	60.7	0.00047	380
10	19.1	399	3,200	41.6	0.00100	2.13	13	1.12	-2	3,070	62.0	0.00044	401
11	20.9	422	2,040	41.2	0.00100	1.40	13	0.71	-2	1,980	63.2	0.00043	424
12	21.9	445	1,300	41.4	0.00100	4.69	2	6.06	-0.15	1,140	56.8	0.00055	452
13	14.8	466	847	42.1	0.00100	3.55	2	3.95	-0.15	783	59.6	0.00048	470
14	18.4	489	541	41.2	0.00100	2.41	2	2.53	-0.15	514	61.2	0.00045	491
15	20.3	511	344	41.0	0.00100	1.55	2	1.61	-0.15	333	62.4	0.00043	513
16	21.6	535	214	40.7	0.00100	1.00	2	1.01	-0.15	213	63.1	0.00041	536
17	22.5	558	137	40.6	0.00100	0.63	2	0.64	-0.15	135	63.6	0.00041	557
18	23.0	582	865	40.6	0.00100								

P-1853

Table 3-3 - Rendezvous Maneuver at 1000 Nautical Mile Altitude with -0.010 Radian Attitude Error

CYCLE	Δt_c sec.	t_o sec.	r_o ft.	τ_o sec.	$\dot{\gamma}_o$ rad/sec	Δt_r sec.	a_r ft/sec^2	Δt_n sec.	a_n ft/sec^2	r_1 ft.	τ_1 sec.	$\dot{\gamma}_1$ rad/sec.	t_1 sec.
1	110.7	111	236,000	191.8	0.00100	0	100	12.69	-13	220,000	179.1	0.00037	123
2	70.2	194	134,000	109.4	0.00100	0	100	7.21	-13	125,000	102.2	0.00038	201
3	39.5	240	76,800	62.8	0.00100	0.41	100	4.14	-13	71,900	60.8	0.00038	244
4	20.8	265	47,300	40.0	0.00086	4.55	100	2.05	-13	42,900	58.9	0.00027	270
5	19.0	289	29,100	40.0	0.00059	2.80	100	0.65	-13	27,500	61.2	0.00024	292
6	21.2	313	18,000	40.0	0.00056	1.73	100	0.36	-13	17,300	62.7	0.00023	314
7	22.7	337	11,060	40.0	0.00057	8.18	13	1.42	-2	9,200	54.3	0.00032	345
8	14.3	360	6,800	40.0	0.00058	5.03	13	0.97	-2	6,100	57.9	0.00027	365
9	17.9	383	4,220	40.0	0.00057	3.12	13	0.56	-2	3,950	60.4	0.00024	386
10	20.4	406	2,620	40.0	0.00056	1.94	13	0.34	-2	2,520	59.5	0.00021	408
11	19.4	430	1,625	40.0	0.00049	1.20	13	0.15	-2	1,586	62.8	0.00022	431
12	22.9	454	1,009	40.0	0.00054	4.85	2	1.65	-0.15	910	58.6	0.00027	459
13	18.6	478	621	40.0	0.00057	2.99	2	1.14	-0.15	584	60.7	0.00024	481
14	20.7	501	385	40.0	0.00056	1.85	2	0.68	-0.15	370	62.6	0.00022	504
15	22.6	526	237	40.0	0.00053	1.14	2	0.36	-0.15	231	63.0	0.00021	527
16	23.1	550	147	40.0	0.00052	0.71	2	0.21	-0.15	145	64.1	0.00020	550
17	24.1	574	90	40.0	0.00052								

P-1853

Table 3-4 - Rendezvous Maneuver at 1000 Nautical Mile Altitude with + 0.020 Radian Attitude Error

CYCLE	Δt_c sec.	t_o sec.	r_o ft.	τ_o sec.	$\dot{\gamma}_o$ rad/sec.	Δt_r sec.	a_r ft/sec^2	Δt_n sec.	a_n ft/sec^2	r_1 ft.	τ_1 sec.	$\dot{\gamma}_1$ rad/sec	t_1 sec.
1	110.7	111	236,000	191.8	0.00100	0	100	12.69	-13	220,000	179.9	0.00037	123
2	70.5	194	134,000	110.0	0.00100	0	100	7.21	-13	125,000	102.9	0.00037	201
3	40.3	241	76,100	62.6	0.00100	0.44	100	4.10	-13	71,306	60.9	0.00039	246
4	20.9	266	46,800	40.0	0.00091	4.50	100	2.19	-13	42,600	59.1	0.00060	271
5	13.3	284	33,000	45.8	0.00100	2.13	100	1.78	-13	31,700	62.4	0.00048	286
6	19.2	306	21,900	43.2	0.00100	1.70	100	1.18	-13	21,200	62.9	0.00050	307
7	18.5	326	15,000	44.4	0.00100	8.19	13	5.23	-2	12,600	55.0	0.00067	334
8	10.1	344	10,300	44.9	0.00100	5.45	13	3.61	-2	9,270	58.4	0.00056	350
9	14.7	364	6,930	43.7	0.00100	4.00	13	2.43	-2	6,400	59.9	0.00053	368
10	16.2	385	4,670	43.7	0.00100	2.69	13	1.63	-2	4,430	61.5	0.00052	387
11	17.1	404	3,195	44.4	0.00100	1.75	13	1.12	-2	3,090	62.7	0.00049	406
12	18.8	425	2,165	44.0	0.00100	1.22	13	0.76	-2	2,114	63.3	0.00048	426
13	19.3	445	1,470	44.1	0.00100	5.37	2	6.86	-0.15	1,286	56.5	0.00063	452
14	11.5	464	1,024	45.0	0.00100	3.50	2	4.78	-0.15	937	59.7	0.00056	469
15	15.2	484	698	44.5	0.00100	2.47	2	3.26	-0.15	657	60.8	0.00052	487
16	16.9	504	474	43.8	0.00100	1.76	2	2.21	-0.15	455	62.6	0.00050	506
17	18.2	524	323	44.4	0.00100	1.15	2	1.51	-0.15	314	62.8	0.00048	526
18	19.4	545	217	43.4	0.00100	0.83	2	1.01	-0.15	213	63.3	0.00048	546
19	19.6	566	147	43.7	0.00100	0.55	2	0.69	-0.15	145	63.7	0.00046	567
20	20.5	588	985	43.2	0.00100								

P 1853

Table 3-5 - Rendezvous Maneuver at 1000 Nautical Mile Altitude with -0.020 Radian Attitude Error

CYCLE	Δt_c sec.	t_o sec.	r_o ft.	τ_o sec.	$\dot{\gamma}_o$ rad/sec.	Δt_r sec.	a_r ft/sec^2	Δt_n sec.	a_n ft/sec^2	r_1 ft.	τ_1 sec.	$\dot{\gamma}_1$ rad/sec.	t_1 sec.
1	110.7	111	236,000	191.8	0.00100	0	100	12.69	-13	220,000	178.9	0.00037	123
2	70.1	193	134,000	109.3	0.00100	0	100	7.21	-13	125,000	102.0	0.00038	201
3	39.4	240	76,800	62.7	0.00100	0.44	100	4.14	-13	71,900	61.1	0.00035	244
4	21.2	265	47,000	40.0	0.00082	4.52	100	1.90	-13	42,700	59.0	0.00016	269
5	19.0	289	29,000	40.0	0.00035	2.79	100	0.10	-13	27,400	61.3	0.00013	292
6	21.3	313	17,800	40.0	0.00030	1.72	100	0.003	-13	17,200	62.6	0.00011	315
7	22.5	337	11,000	40.0	0.00028	run terminated							
8													
9													
10													
11													
12													

P-1853

r'' = 1500 ft

r''' = 60 ft

W = 128,000 lb (assumed constant)

Analysis of the data obtained from the computer provides the steady-state pitch error limits for the attitude control system. The criteria used for determining these limits are as follows:

(1) Δt_c should not be less than 10 sec, so as to allow sufficient time for data smoothing.

(2) $\dot{\gamma}_1$ should not be less than 0.0002 rad/sec, for the simple reason that a value this small could be induced by disturbances to cross the zero point into the negative region. This then would necessitate rotating the normal engine 180 degrees prior to the next correction.

(3) The pulse widths, Δt_r and Δt_n, should not be reduced to the point where actual implementation of the pulses becomes impractical. Arbitrary minimum limits used are:

a_n or a_r, ft/sec^2	100	13	2	0.15
Thrust, lb	400,000	52,000	8,000	600
Minimum Δt_n or Δt_r, sec	1.5	0.4	0.2	0.1

Examination of Tables 3-1 through 3-5 reveals that, except for minor violations of the third criterion above, a steady-state error of ±0.010 rad is acceptable. We will use this pitch error range since the anticipated steady-state limit cycle will tend to reduce adverse effects. It should be pointed out that only the angular rate correction is appreciably affected by the pitch error because the longitudinal engine is nearly an order of magnitude larger than the normal engine.

The computer was not programmed to include attitude dynamics or the effects of overshoot beyond the limit cycle, but a reasonable estimate of the overshoot magnitude can be obtained from the information available. The expression for the velocity change in the normal direction is:

$$\Delta V_n = a_n \Delta t_n + a_r \Delta t_r \epsilon_{ss} + a_r \int \Delta \epsilon_{os} \, dt \qquad (3\text{-}7)$$

where ϵ_{ss} is the steady-state pitch error and $\Delta\epsilon_{os}$ is the overshoot beyond ϵ_{ss}. Where there is no overshoot, the percentage change in ΔV_n due to the presence of ϵ_{ss} is

$$\frac{a_r \Delta t_r \epsilon_{ss}}{a_n \Delta t_n} \times 100$$

Using values from Table 3-1 where no error is present, we see that a sudden introduction of $\epsilon_{ss} = \pm 0.010$ radians causes a 17 to 20 percent change in ΔV_n from its "optimum" value of $a_n \Delta t_n$. It seems reasonable that an overshoot which contributes only an additional 2 percent to this change would not be detrimental to performance. For this assumption then, the integral in Equation (3-7) is defined by:

$$\int \Delta \epsilon_{os} \, dt = 0.02 \, \frac{a_n \Delta t_n}{a_n} \qquad (3\text{-}8)$$

The minimum value of this integral (from Table 3-1, Cycle 16) is 0.0007 rad-sec which, for example, means that an overshoot of 0.010 rad beyond a steady-state error of 0.010 rad can only last 0.07 second.

The above defined allowable limit-cycle and overshoot errors of the attitude control system need not be considered fixed. If the limit cycle can be made to be within ±0.010 rad, then the overshoot integral can be increased so long as the net change ΔV_n from $an\Delta t_n$ does not exceed approximately 20 percent. Also, if a high frequency limit cycle with a period less than that of the smallest Δt_n is used, the errors will tend to cancel out thus allowing a larger limit cycle to be used. This technique would be excessively wasteful of fuel, however.

The attitude control system must operate under conditions of varying angular velocity and acceleration. Essentially, it must follow the angular rate control system which periodically creates an angular acceleration to keep the angular rate within limits. The maximum angular rate which the pitch channel of the attitude control system must follow is 0.001 rad/sec. The angular acceleration disturbances vary with range and engine size, the maximum values for each normal acceleration being:

a_n, ft/sec^2	-13	-2	-0.15
r, ft	15,000	1500	60
$\ddot{\gamma}$, rad/sec^2	-8.66×10^{-4}	-13.3×10^{-4}	-25.0×10^{-4}

It is seen that the most severe condition imposed upon the attitude control system by the rendezvous logic is that of following a linear ramp of 0.001 rad/sec which changes to a parabolic trajectory superimposed upon the ramp as the result of an applied angular acceleration of -0.0025 rad/sec^2.

3.3.4 Roll and Yaw Errors

Figure 2-9 shows the attitude errors which can exist about the pitch, yaw, and roll axes. The effect of pitch errors has been investigated and discussed. Here we will examine the effects of yaw and roll errors upon the rendezvous maneuver.

In the figure, the XYZ orthogonal coordinate system is referred to the target, with the Y axis being on the line-of-sight between the vehicle and target. The center 0 of this coordinate system is the center of gravity of the vehicle. The orthogonal coordinate system referred to the vehicle is defined by the pitch, yaw, and roll axes, and the center of this coordinate system is the vehicle center of gravity also. The two coordinate systems are related by angles of rotation about the pitch, yaw, and roll axes, designated by ϵ, ϵ', and ϵ'' respectively. These angles represent attitude errors which must be maintained within narrow limits to facilitate proper vehicle performance.

A study of Figure 2-9 reveals that the pitch error ϵ causes the range rate control to cross couple into the angular rate control and vice versa. This effect was studied in Subsection 3.3.3. The yaw error ϵ' acts with the range rate control to create an angular rate of line-of-sight which is normal to that being corrected by the angular rate control. The roll error ϵ'' acts with the angular rate control to also create a normal angular rate. The problem at hand is to determine acceptable limits for ϵ' and ϵ''.

The equations of motion for the case illustrated in Figure 2-9 are:

$$\ddot{r} - r(\dot{\gamma}_y^2 + \dot{\gamma}_p^2) = a_r - a_n \epsilon \qquad (3\text{-}9)$$

$$r\ddot{\gamma}_p + 2\dot{r}\dot{\gamma}_p = a_n + a_r \epsilon \qquad (3\text{-}10)$$

$$r\ddot{\gamma}_y + 2\dot{r}\dot{\gamma}_y = a_r \epsilon' - a_n \epsilon'' \qquad (3\text{-}11)$$

where r = range to target,

$\dot{\gamma}_y$ = angular rate about yaw axis,

$\dot{\gamma}_p$ = angular rate about pitch axis.

The effect of gravity is ignored, and the following small angle approximations are made:

$$\cos(\epsilon, \epsilon', \epsilon'') = 1 \tag{3-12}$$

$$\sin(\epsilon, \epsilon', \epsilon'') = \epsilon, \epsilon', \epsilon'' \tag{3-13}$$

Equation (3-9) and (3-10) are identical to Equations (3-3) and (3-4), except for the presence of the $r\dot{\gamma}_y^2$ term. It is obvious that if ϵ' and ϵ'' are maintained sufficiently small, $\dot{\gamma}^2 << \dot{\gamma}_p^2$, thus making Equations (3-3) and (3-9) equivalent. In addition to preserving the rendezvous logic defined in Subsections 2.2.4 and 3.3.1, the condition that $\dot{\gamma}_y^2 << \dot{\gamma}_p^2$ simplifies the problem of positioning the normal engine (by rolling) prior to a correction. The basic requirements for the roll and yaw channels of the attitude control system are thus defined.

Simultaneous numerical solutions of Equations (3-9), (3-10), and (3-11) could be obtained via a digital computer, but it does not appear to be necessary. Rather, an approach will be taken similar to that used in Appendix II where nonlinear equations are linearized and solved analytically. The validity of this approach is supported by the close similarity of results obtained for the linearized and nonlinear rendezvous equations of motion.

To determine $\dot{\gamma}_y$, it becomes necessary to simultaneously solve Equations (3-9) and (3-11). For the case at hand, Equation (3-9) can be written with good accuracy as:

$$\ddot{r} = a_r, \tag{3-14}$$

since $r(\dot{\gamma}_y^2 + \dot{\gamma}_p^2) << a_r$ and $a_n \epsilon << a_r$. Expressions for $\dot{r}$ and r are then:

$$\dot{r} = \dot{r}_o + a_r \Delta t \tag{3-15}$$

$$r = r_o + \dot{r}_o \Delta t + \frac{1}{2} a_r (\Delta t)^2, \tag{3-16}$$

where Δt is the time from the initiation of the longitudinal acceleration. Substitution of Equations (3-15) and (3-16) into Equation (3-11) gives:

$$\left[r_o + \dot{r}_o \Delta t + \frac{1}{2} a_r (\Delta t)^2\right] \ddot{\gamma}_y + 2\left[\dot{r}_o + a_r \Delta t\right] \dot{\gamma}_y = a_r \epsilon' - a_n \epsilon'' \qquad (3\text{-}17)$$

Equation (3-17) is a nonhomogeneous linear first order differential equation in $\ddot{\gamma}_y$ with variable coefficients. The solution was attempted but found to be extremely complex, so a simpler form was used. Since we are interested in the time duration Δt_r, the average velocity during this time is

$$\bar{\dot{r}} = \dot{r}_o + \frac{1}{2} a_r \Delta t_r, \qquad (3\text{-}18)$$

which when substituted into Equation (3-11) gives:

$$\left[r_o + (r_o + \frac{1}{2} a_r \Delta t_r)\Delta t\right] \ddot{\gamma}_y + 2\left[\dot{r}_o + \frac{1}{2} a_r \Delta t_r\right] \dot{\gamma}_y = a_r \epsilon' - a_n \epsilon'' \qquad (3\text{-}19)$$

The solution for the case where $\Delta t = \Delta t_r$ is:

$$\dot{\gamma}_{y1} = \frac{(a_r \epsilon' - a_n \epsilon'')\Delta t_r (r_o + \frac{\dot{r}_o}{2} \Delta t_r + \frac{a_r}{4} \Delta t_r^2)\, r_o^2\, \dot{\gamma}_{yo}}{\left[r_o + \dot{r}_o \Delta t_r + \frac{1}{2} a_r \Delta t_r^2\right]^2} \qquad (3\text{-}20)$$

Equation (3-20) will be examined for typical values of parameters obtained from the rendezvous computer study. The following table shows results for the case where $\dot{\gamma}_{yo} = 0$.

r_o	47,300	17,900	11,000	990
$\dot{r}_o$	-1182	-447	-275	-25
a_r	100	100	13	2
a_n	-13	-13	-2	-0.15
Δt_r	4.55	1.72	8.14	4.78
Δt_n	2.10	0.72	2.69	3.38
$\frac{\dot{\gamma}_{y1}}{a_r \epsilon' - a_n \epsilon''}$	1.11×10^{-4}	1.04×10^{-4}	9.7×10^{-4}	5.7×10^{-3}

These are the most restrictive cases. If we set $\dot{\gamma}_{y1} = 0.0001$ rad/sec to insure that $\dot{\gamma}_y^2 << \gamma_p^2$, then the expressions defining ϵ' and ϵ'' become:

$$100\,\epsilon' + 6\,\epsilon'' = 0.900 \qquad (3\text{-}21)$$

$$13\,\epsilon' + 0.66 = 0.104 \qquad (3\text{-}22)$$

$$2\,\epsilon' + 0.106 = 0.0176 \qquad (3\text{-}23)$$

The values of a_n were adjusted to allow for their lower duration by multiplying by $\Delta t_n/\Delta t_r$. Considering the above relationships plus the fact that ϵ' and ϵ'' are not constant nor necessarily in phase, it is concluded that the following error limits are realistic:

$$\epsilon' = \pm 0.010 \text{ rad}$$

$$\epsilon'' = \pm 0.020 \text{ rad}$$

3.3.5 Nomenclature

a_n = Acceleration created by transverse engine, ft/sec^2

a_{ni} = Value of a_n at start of rendezvous and for $r_o > r'$

a_n' = Value of a_n for $r' \geq r_o > r''$

a_n'' = Value of a_n for $r' \geq r_o > r'''$

a_r = Acceleration created by longitudinal engine ft/sec^2

a_{ri} = Value of a_r at start of rendezvous and for $r_o > r'$

a_r' = Value of a_r for $r' \geq r_o > r''$

a_r'' = Value of a_r for $r'' \geq r_o > r'''$

r = Range between vehicle and target during rendezvous, ft

r_i = Range at initiation of rendezvous, ft

r_o = Range at initiation of correction maneuver, ft

r_1 = Range at termination of correction, ft

r' = Range at first change of normal and longitudinal engine sizes, ft

r'' = Range at second change of normal and longitudinal engine sizes, ft

r''' = Range at which the initial closure phase of the rendezvous maneuver gives way to the docking phase, ft

$\dot{r}$ = Range rate, ft/sec

$\dot{r}_i$ = Range rate at initiation of rendezvous, ft/sec

$\dot{r}_o$ = Range rate at the initiation of a corrective maneuver, ft/sec

t = Time, sec

t_o = Total elapsed time at initiation of a correction, sec

t_l = Total elapsed time at termination of a correction, sec

Δt_c = Time duration between corrections, sec

Δt_n = Thrusting time of normal engine, sec

Δt_r = Thrusting time of longitudinal engine, sec

ΔV_n = Change in normal velocity, ft/sec

ΔV_r = Change in longitudinal velocity, ft/sec

W = Vehicle weight, lb

$\dot{\gamma}$ = Angular rate of rendezvous line-of-sight, rad/sec

$\dot{\gamma}_b$ = Commanded angular rate during correction, rad/sec

$\dot{\gamma}_i$ = Angular rate at start of rendezvous, rad/sec

$\dot{\gamma}_o$ = Angular rate at the initiation of a corrective maneuver, rad/sec

$\dot{\gamma}_l$ = Angular rate at the termination of the normal correction, rad/sec

$\dot{\gamma}_{max}$ = Maximum allowable angular rate, rad/sec

$\dot{\gamma}_p$ = Angular rate of line-of-sight about pitch axis, rad/sec

$\dot{\gamma}_y$ = Angular rate of line-of-sight about yaw axis, rad/sec

$\dot{\gamma}_{yl}$ = Angular rate at termination of correction, rad/sec

ϵ = Pitch attitude error angle, rad

ϵ_{ss} = Steady state pitch error, rad

$\Delta\epsilon_{os}$ = Overshoot beyond ϵ_{ss}, rad

ϵ' = Yaw attitude error angle, rad

ϵ'' = Roll attitude error angle, rad

τ = Time-to-go parameter, $-r/\dot{r}$, sec

τ_b = Commanded time-to-go during correction, sec

τ_i = Time-to-go at start of rendezvous, sec

τ_o = Time-to-go at the initiation of a corrective maneuver, sec

τ_l = Time-to-go at the termination of the longitudinal correction, sec

τ_{min} = Minimum allowable time-to-go, sec

$(\dot{})$ = Denotes first derivative with respect to time

$(\ddot{})$ = Denotes second derivative with respect to time

3.4 RE-ENTRY

3.4.1 Trajectory Computations

Equations (2-27), (2-28), (2-29), (2-30), and (2-32) together with the data contained in Figure 2-12 were programmed for solution on an IBM 650 computer. The numerical values and the sources of the constants used are as follows:

g = 31.4 ft/sec^2 (Average of values at 400,000 and 120,000 ft)(22)

ρ_B = 0.00238 slugs/ft^3 (Ref.(24), page 2-26)

β^{-1} = 24,000 ft (Ref (24), page 2-76)

R = 20,900,000 + 200,000 = 21,100,00 ft (Ref.(25), page 2-37)

h_o = 400,000 ft (Appendix III)

V_i = 26,000 fps

m = 3110 slugs

A_R = 14,500 ft^2 (Area of 20° isosceles triangle 200 ft long)

The vehicle weight during re-entry was chosen as 100,000 lb, since this is the approximate average of the values obtained for the three cases involving different target altitudes.

Figures 3-1 through 3-12 are plots of the numerical results of re-entry trajectory computations. Figures 3-1 through 3-6 show the effect of changes in the initial entry angle θ_i for $k_d = 2$ and $A_R = 14500$ feet^2. Figures 3-7 through 3-12 indicate the effect of changes in k_d and A_R for $\theta_i = 2.5$ degrees.

Figure 3-1 most clearly shows the important effect of θ_i on the trajectory. It is evident that undesirable skipping occurs as θ_i increases and that 5 degrees is about as large a value of θ_i as can be tolerated.

At first it seems paradoxical that an increase in θ_i increases the severity of the skipping. However, this effect is easily explained. The greater the value of θ_i, the deeper the vehicle descends into the atmosphere on its first plunge. As a result the values of C_D required to maintain $dV/dt = (dV/dt)d$ reach smaller values, giving as a consequence, larger values of L/D. Once the vehicle starts to climb, it rapidly returns to the angle of attack giving the maximum C_D and minimum L/D. However the higher lift accelerations imposed at the beginning of the climb enable the vehicle to reach higher altitudes during the skip. This is shown by Figure 3-2 which gives the L/D ratios required during re-entry. As can be seen, the vehicle is at the minimum value of L/D for the majority of the time in all three cases. Periodically, a transient increase in L/D occurs, the apex of which coincides with the point of deepest descent for a given skip. The greater the value of θ_i, the greater the value of maximum L/D required. At $\theta_i = 7°$, the maximum value of L/D = 2.25 is actually somewhat beyond the capabilities of the assumed vehicle.

Figures 3-3 and 3-4 give the values of resultant and path accelerations experienced by the vehicle during re-entry. These figures are another representation of what has already been said and required little additional comment. It should be noted that for the two larger values of θ_i, there is a considerable period of time in which the vehicle is essentially in a zero g state and is thus on the verge of returning to orbit. The value of controlled path deceleration is slightly less than the even value of 2. This is a consequence of the control law being programmed as $(dV/dt)_d = -k_d g$ instead of $(dV/dt)_d = -k_d g_c$.

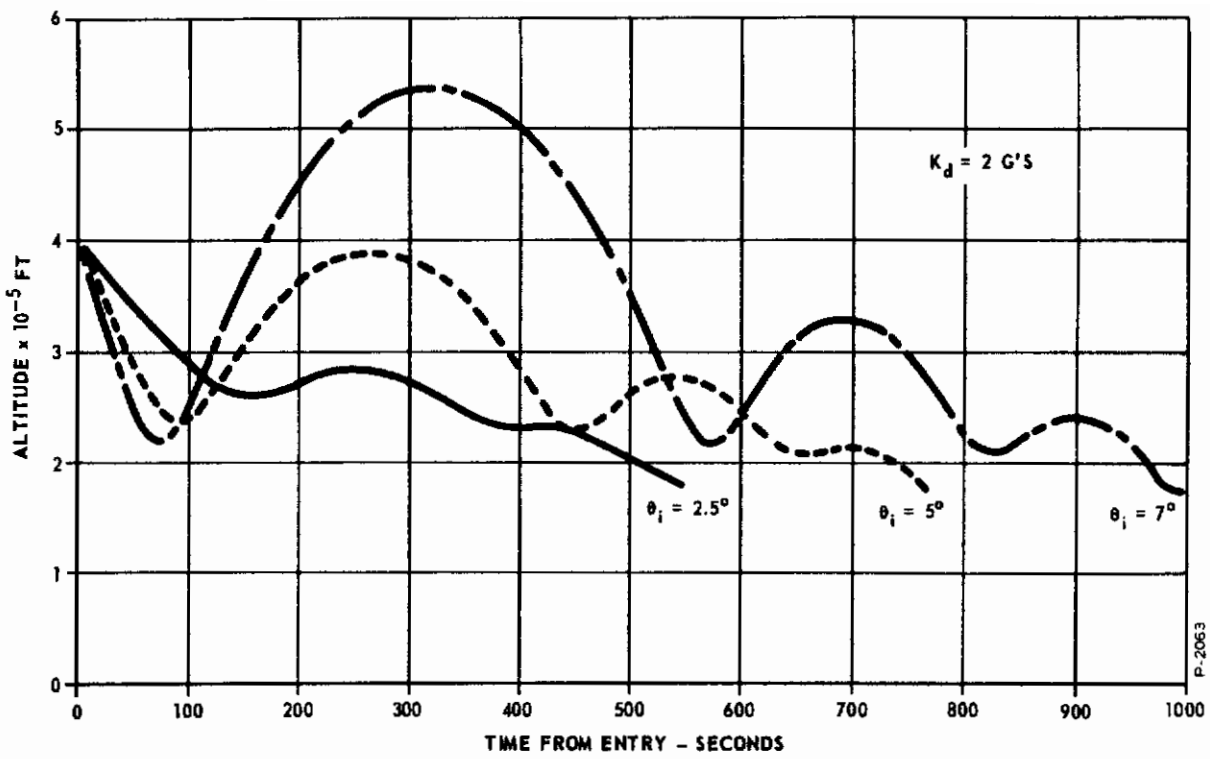

Figure 3-1 - Re-Entry Trajectory Characteristics;
Altitude Versus Time

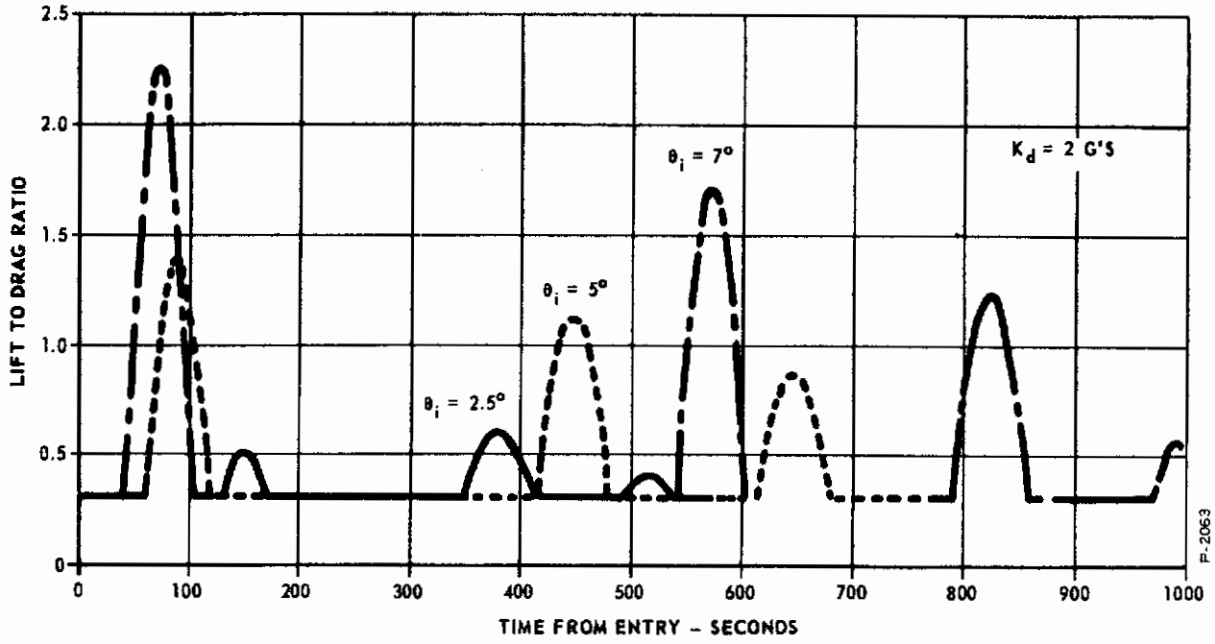

Figure 3-2 - Re-Entry Trajectory Characteristics;
Resultant Acceleration Versus Time

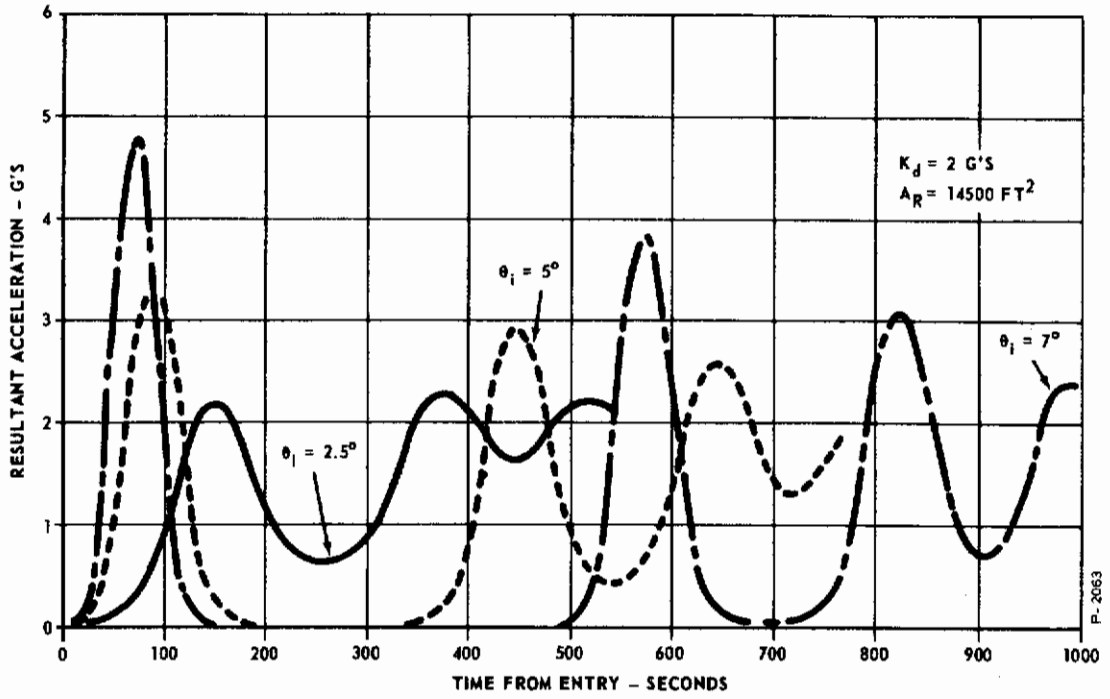

Figure 3-3 - Re-Entry Trajectory Characteristics;
Resultant Acceleration Versus Time

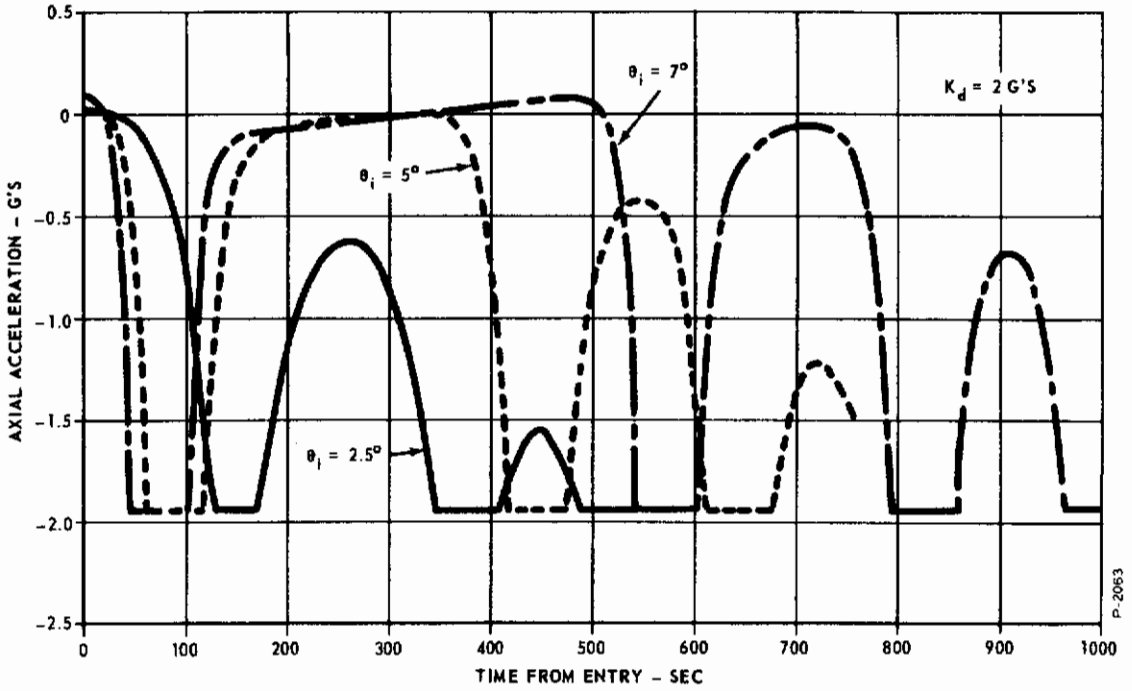

Figure 3-4 - Re-Entry Trajectory Characteristics;
Axial Acceleration Versus Time

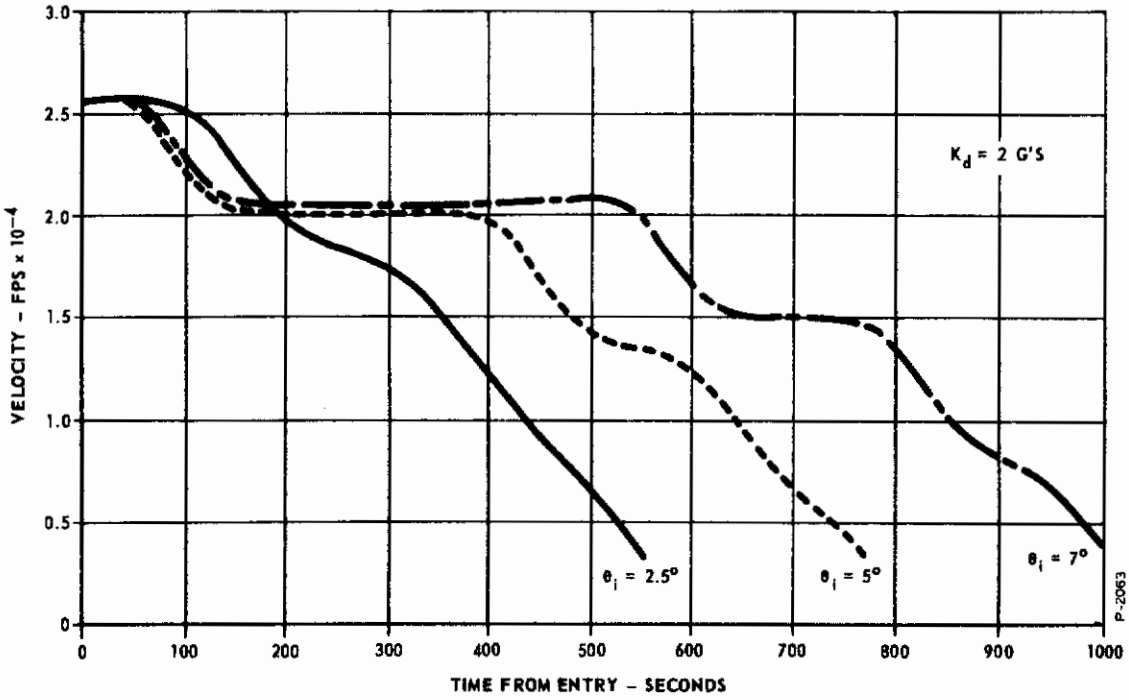

Figure 3-5 - Re-Entry Trajectory Characteristics; Velocity Versus Time

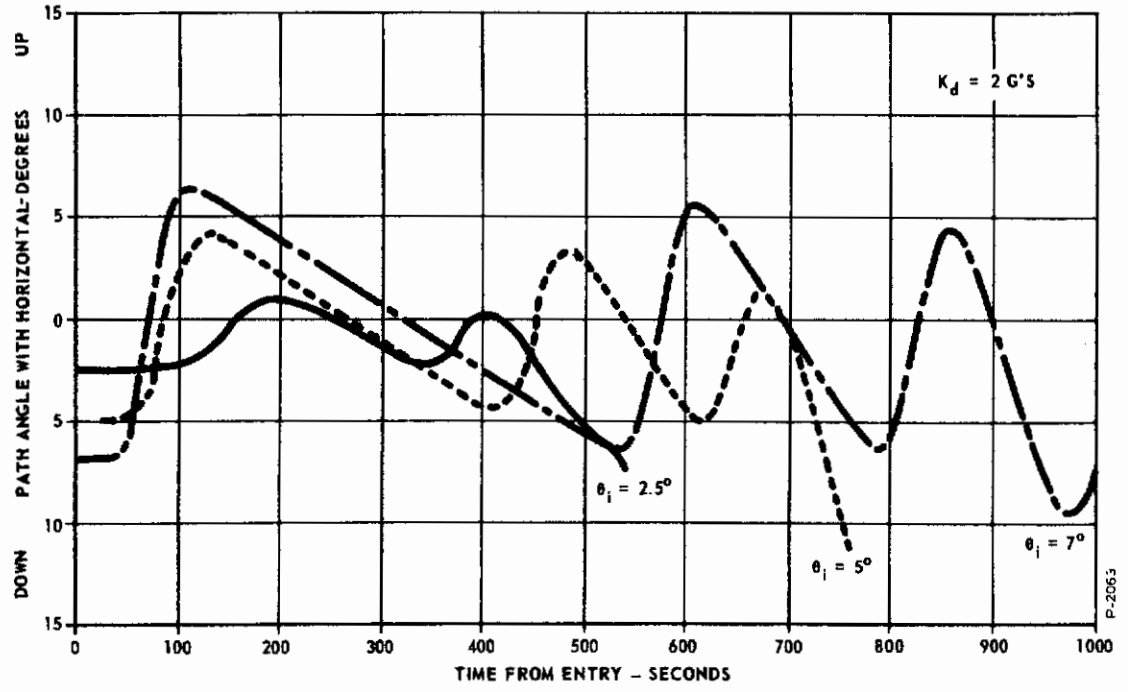

Figure 3-6 - Re-Entry Trajectory Characteristics; Path Angle Versus Time

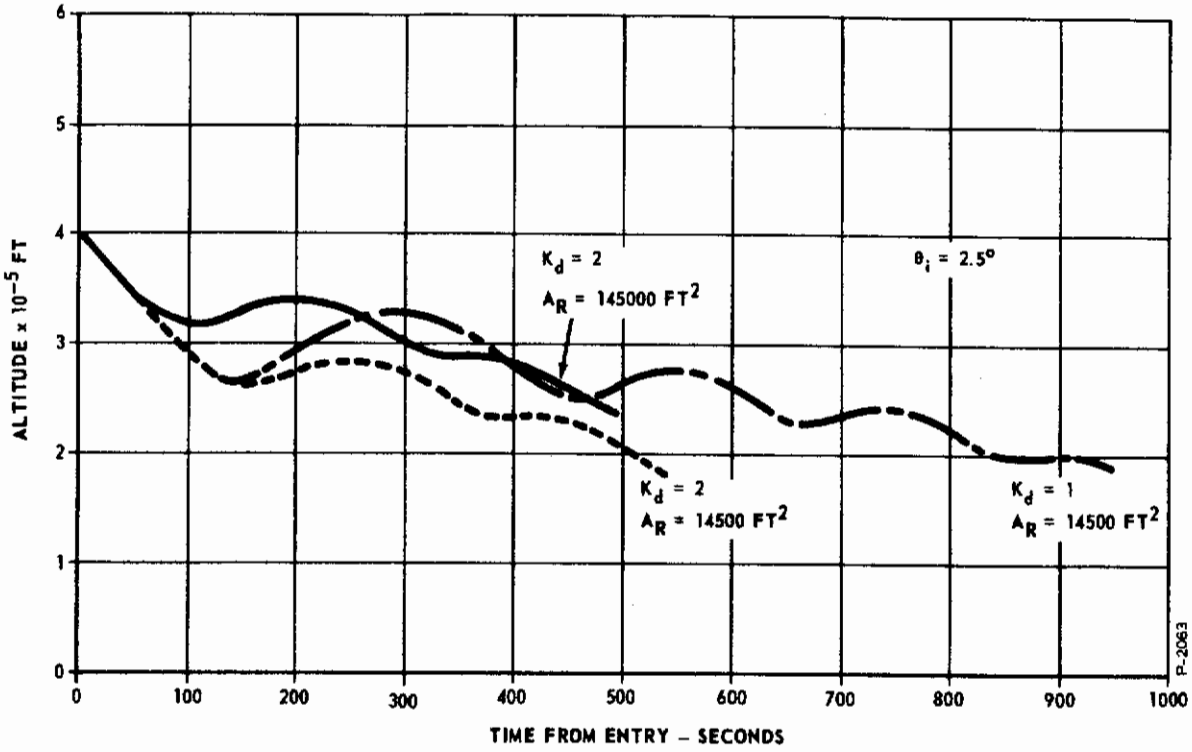

Figure 3-7 - Re-Entry Trajectory Characteristics;
Altitude Versus Time

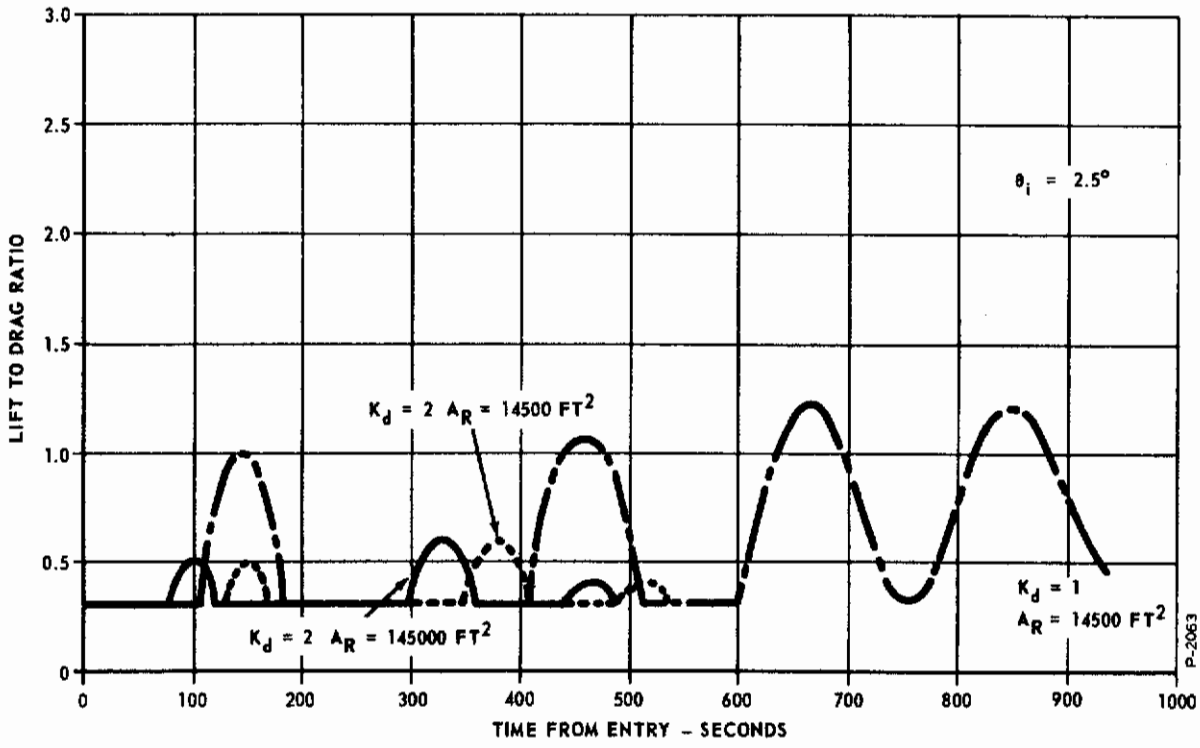

Figure 3-8 - Re-Entry Trajectory Characteristics;
Lift-to-Drag Versus Time

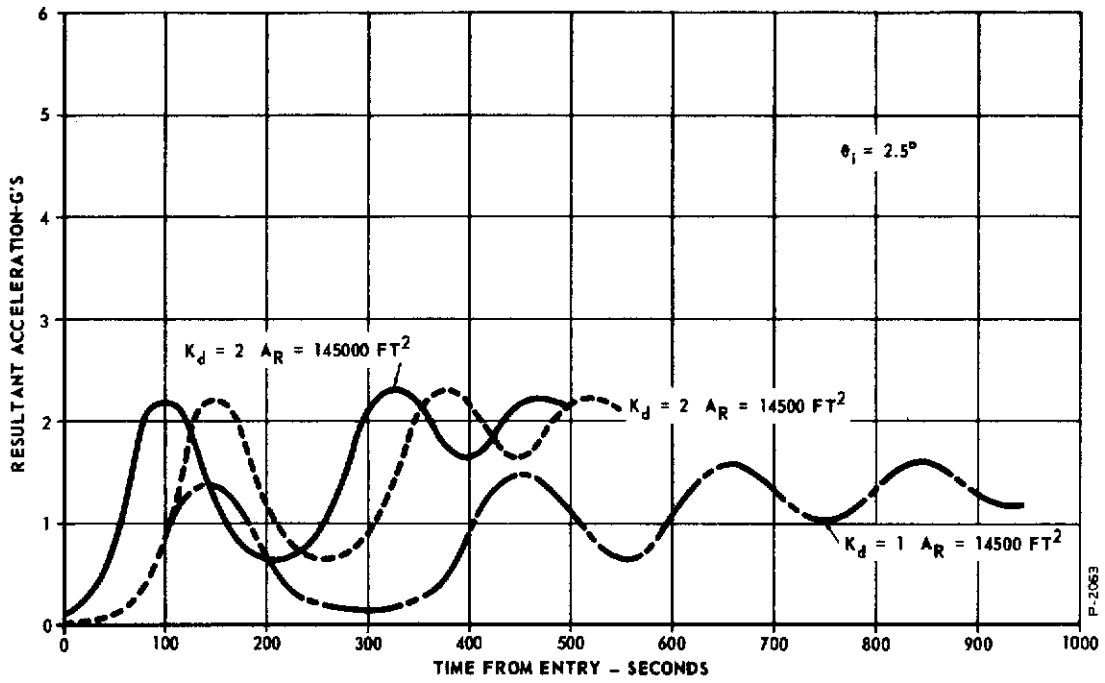

Figure 3-9 - Re-Entry Trajectory Characteristics;
Resultant Acceleration Versus Time

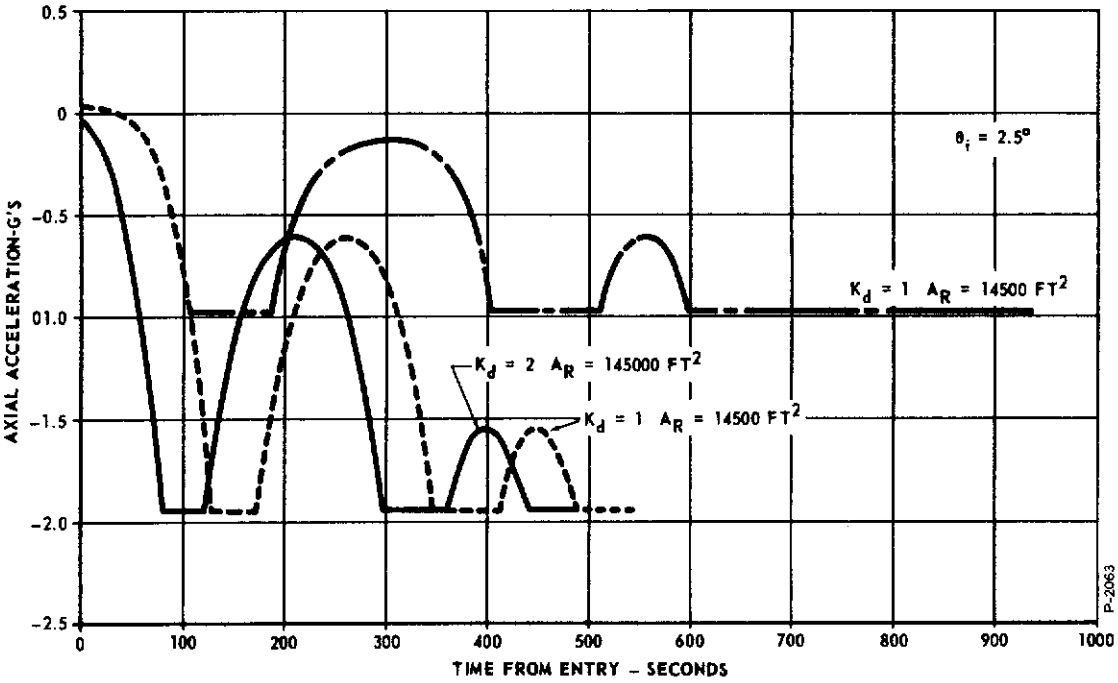

Figure 3-10 - Re-Entry Trajectory Characteristics;
Axial Acceleration Versus Time

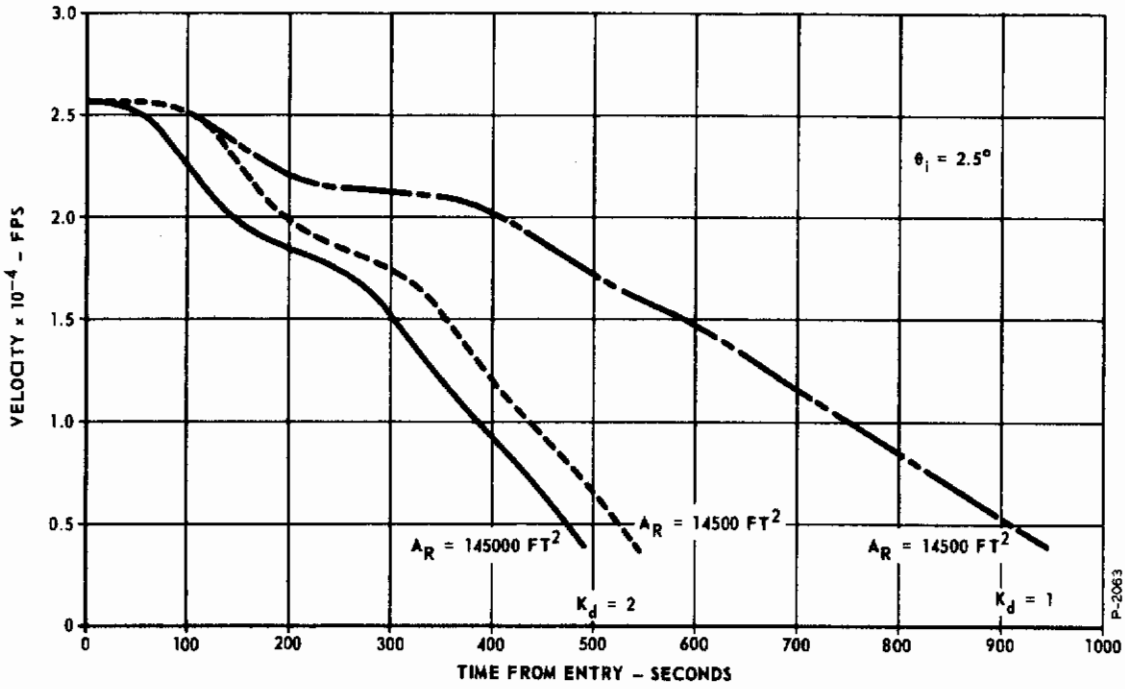

Figure 3-11 - Re-Entry Trajectory Characteristics;
Velocity Versus Time

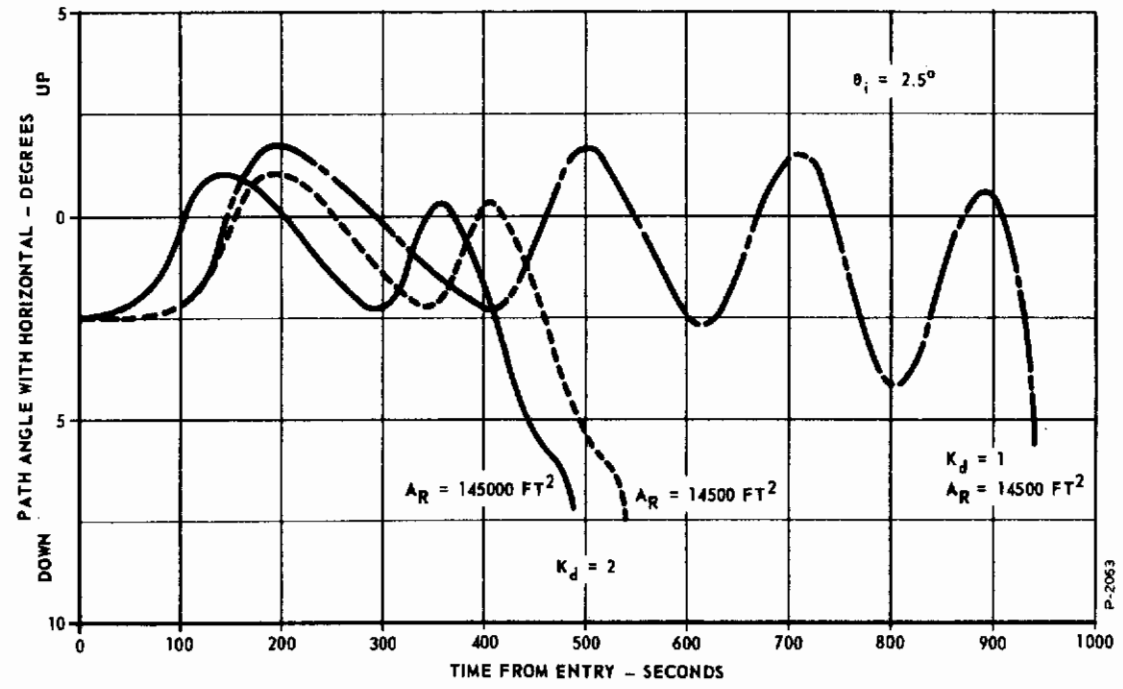

Figure 3-12 - Re-Entry Trajectory Characteristics;
Path Angle Versus Time

Since a value of g somewhat less than that at sea level was used to correct for the high altitudes, an odd value of controlled path deceleration resulted. This situation was of no great significance and was not reprogrammed after it was discovered.

Figures 3-5 and 3-6 give the values of V and θ during re-entry. This data, especially that relating to V, is required for selection of the final trajectory and for evaluation of the various moment producing methods.

Figures 3-7 through 3-12 show the effect of increasing A_R and decreasing k_d on the trajectory for $\theta_i = 2.5°$. As can be seen, increasing A_R by a factor of 10 does not exert a great effect. The curves of the various parameters for $A_R = 145{,}000$ ft^2 are similar in shape to those for $A_R = 14{,}500$ and are displaced by only a relatively small amount on the time and altitude scales. If Equations (2-27) and (2-28) are divided by m, the terms A_R and m appear only in the grouping $A_R/2m$. Thus, the trajectories for $A_R = 145{,}000$ ft^2 and m = 100,000/32.2 slugs are identical to those that would be obtained with $A_R = 14{,}500$ ft^2 and m = 10,000/32.2 slugs. As would be expected, reduction of the value of k_d demands more frequent and greater corrections in vehicle attitude. It is of interest that for the last 300 seconds of the $k_d = 1$ trajectory, the L/D ratio is continuously corrected.

As the angle of attack of a delta wing in hypersonic flow is increased from 0 toward 90 degrees, both L/D and C_D will at first increase. Eventually a point of maximum L/D will be reached, and thereafter L/D will decrease as α and C_D increase. Thus there are two aerodynamic regimes in which the vehicle may operate during re-entry.

The trajectory parameters plotted in Figures 3-1 through 3-12 are based on a vehicle operating in that range of angles of attack in which L/D decreases and C_D increases as α increases. This operating region is characterized by the fact that drag coefficients are large and that pitching the vehicle up acts to increase deceleration since both effects produced, namely an increase in C_D and a decrease L/D, act in this direction.

A trajectory solution was attempted for a vehicle operating in the low angle of attack region. The most significant feature of this regime is the fact that increasing angle of attack now increases L/D. Also, much lower values of C_D are obtained. As a consequence of the

reversal of the slope of the L/D versus α curve, the sign of the control system pitch correction used for the original trajectory computations must be changed. The computer program was modified by changing to essentially on-off control in which a minimum angle of attack was assumed when path deceleration was less than a desired value and maximum angle of attack was assumed when path deceleration was greater than a desired value. Typical aerodynamic characteristics for a 70 degrees sweep delta winged glider at low angles of attack were taken from Ref (23).

The trajectory for the low drag vehicle was characterized by excessive skipping and long flight time. The computer was not allowed to carry the computation down to V = 4000 fps. At t = 2144 seconds, V was still 13,786 fps. The first three skips reached altitudes of 516,000, 410,000 and 359,000 feet respectively. This was felt to be unsatisfactory and the low angle of attack region was not explored further.

3.4.2 Trajectory Selection

Three factors of major importance during re-entry are deceleration, dynamic pressure, and aerodynamic heating. These must be maintained within proper limits if the vehicle and its payload are to survive re-entry. The resultant decelerations experienced by the vehicle and its contents are shown in Figures 3-3 and 3-9. From these, it can be seen that the lowest deceleration forces are experienced by those vehicles following trajectories with θ_i = 2.5 degrees. With these trajectories, a peak deceleration of 2.3 g's is experienced, which is well within human tolerances.

A useful device for studying the relationships between re-entry trajectory, dynamic pressure, and aerodynamic heating is a plot of velocity versus altitude. The velocities and altitudes of trajectories corresponding to A_R = 14500 ft^2 and θ_i = 2.5 degrees have been plotted in Figure 3-13. Also shown on Figure 3-13, is the locus of a constant dynamic pressure, q = 50 psf, where

$$q = \frac{1}{2} \rho V^2 \qquad (3\text{-}24)$$

Atmospheric data (22) have been used in the calculations of the points for this curve of constant q. As can be seen, the two trajectories under

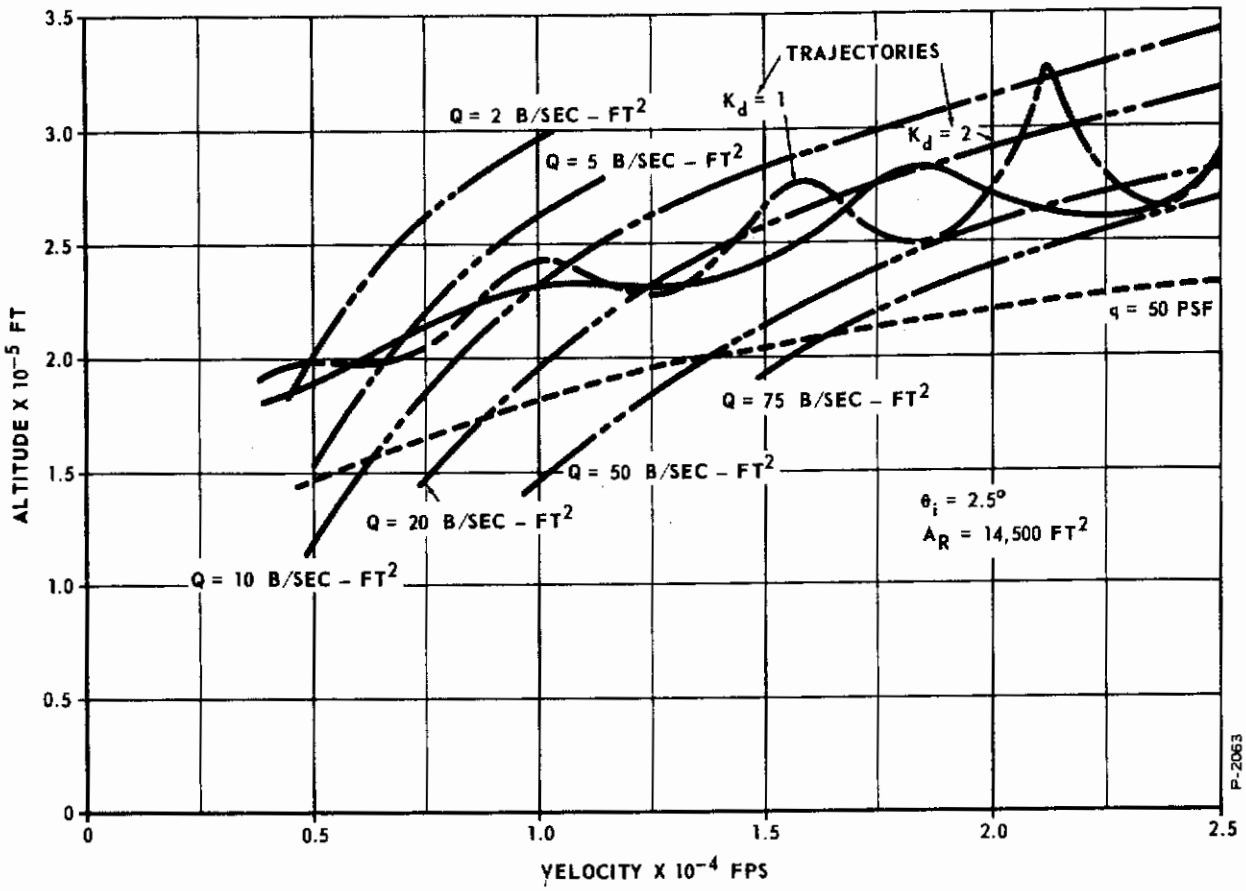

Figure 3-13 - Re-Entry Trajectory Characteristics; Heating Rate and Dynamic Pressure Versus Functions of Altitude and Velocity

consideration lie well above the q = 50 psf line. This corresponds to a very light loading. For example the X-15 has been designed for q = 2500 psf and has been operated in excess of 2000 psf. (26) From this, it may be concluded that dynamic pressure will present no serious problems for the trajectories under consideration.

From page 5-30 of (25), and from (27) and (28) the following relationship for stagnation point convective heat transfer is obtained:

$$Q = 865 \left(\frac{V}{10^4}\right)^{3.15} \sqrt{\frac{\rho/\rho_{sl}}{R_n}} \qquad (3\text{-}25)$$

The loci of Q = 75, 50, 20, 10, 5, and 2 B/ft^2 sec have been plotted on Figure 3-13 for R_n = 0.5 ft using atmospheric data from (22).

In order to obtain a relationship between Q and t, a cross-plot of Figure 3-13 and either Figure 3-7 or 3-11 may be made. This is shown in Figure 3-14. From this it can be immediately seen that the total heat input, represented by the areas under the Q versus t curves, is considerably greater for the $k_d = 1$ trajectory. This is a consequence of the longer time required to decelerate the vehicle. Graphical integration of the two curves given in Figure 3-14 gives approximate values of total heat input of $\Sigma Q \Delta t = 13{,}000$ B/ft^2 for $k_d = 2$ and $\Sigma Q \Delta t = 21{,}000$ B/ft^2 for $k_d = 1$. On the basis of the significantly lesser total heat input, the trajectory corresponding to $k_d = 2$ will be used for the study.

The total heat input of 13,000 B/ft^2 will be applied to the nose and to the leading edges of the wing. As can be seen by comparison of Figures 5.24 and 5.25 of (25) even with large angles of attack, heat inputs on the underside of the wing can be expected to be considerably

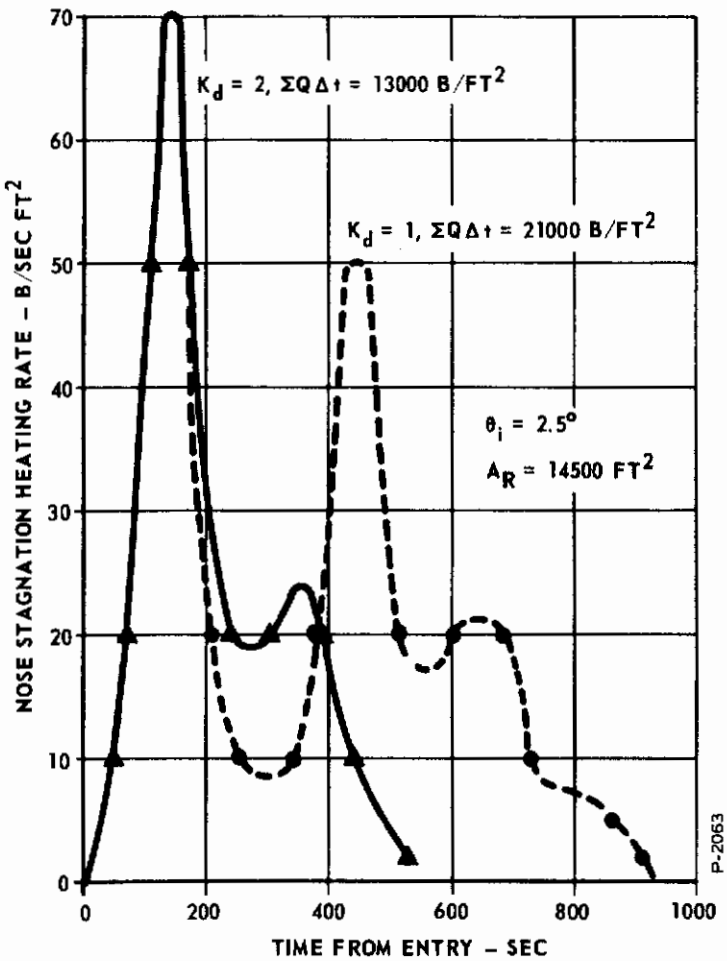

Figure 3-14 - Re-Entry Characteristics; Stagnation Heating Rate Versus Time

less than those at the nose and leading edges. See also (21). Since effective heats of ablation in excess of 6000 B/lb are possible (29), it will be assumed that aerodynamic heating presents no difficulty for the trajectory corresponding to $k_d = 2$.

In conclusion, for a wing area of 14,500 ft^2, an acceptable trajectory is obtained when the initial path angle is 2.5 degrees and $k_d = 2$.

3.4.3 Nomenclature

A_R	=	Reference or wing area - ft^2
C_D	=	Gasdynamic drag coefficient - dimensionless
C_L	=	Gasdynamic lift coefficient - dimensionless
D	=	Drag force - lbs
g	=	Gravitational acceleration - ft/sec^2
g_c	=	Gravitational acceleration at sea level = 32.174 fps
h	=	Geometric Altitude - ft
h_o	=	Geometric altitude at initial entry - ft
k_d	=	Factor in control law - dimensionless
L	=	Lift force - lbs
m	=	Vehicle mass - slugs
q	=	Dynamic pressure - psf
Q	=	Stagnation point heat transfer - B/ft^2 sec
R	=	Distance from vehicle to center of earth - ft
R_n	=	Radius of nose of vehicle - ft
t	=	Time - seconds
V	=	Vehicle velocity along flight path - fps
V_i	=	Path velocity at initial entry - fps
$\left(\frac{dV}{dt}\right)_d$	=	Desired value of path acceleration - ft/sec^2

α	=	Angle of attack - radians
β	=	Exponential factor used in Equation (2-29), $(1/24100)ft^{-1}$
θ	=	Path angle with horizontal - radians
θ_i	=	Initial entry angle - radians
Λ	=	Sweepback angle - degrees
μ	=	Dynamic viscosity - lb/ft sec
ρ	=	Atmospheric density - slugs/ft^3
$\rho_{s\ell}$	=	Atmospheric density at sea level = 0.00238 slugs/ft^3
ρ_B	=	Base density used in atmospheric density approximation - slugs/ft^3

3.5 SUMMARY

3.5.1 Attitude Control Requirements

The required accuracy of the attitude control system depends upon the particular flight maneuver being executed. The most critical requirements defined thus far occur during rendezvous, with the least critical in effect during orbital coasting. It was not possible to predict the attitude control requirements from the simplified re-entry mission analysis because the effect of variations of angle of attack is a complex function of velocity and atmospheric density. The analysis of attitude control during re-entry is discussed in Section 8.

When the vehicle is following a parking orbit, there may be no reason at all for maintaining a certain attitude orientation, particularly if a large number of rotations about the earth are required to properly phase the vehicle with the target. Even when it is necessary to direct antenna toward the earth for communications or ephemeris determination, the attitude accuracy tolerance would be no less than 30 degrees. The major problem during periods of coasting, then, is that of maintaining attitude stability for the sake of personnel comfort.

The maneuver which accomplishes the rotation of the vehicle orbital plane to coincide with the target orbit requires

moderately accurate positioning of the engine thrust vector. In Subsection 3.2.2, it was shown that an angular error of one degree would create a lateral error of approximately one mile at the inception of rendezvous. This would be acceptable and does not appear to be difficult to achieve.

Angular errors at the initiation of the ascent maneuver affect the angular rate of the line-of-sight at the inception of rendezvous. Subsection 3.2.3 shows that an angular error of one degree will create line-of-sight angular rates of 0.0011 rad/sec at a 1000 nautical mile attitude and 0.0057 rad/sec at 300 nautical miles. An error of one degree is certainly the maximum permissible, since the resulting angular rates are sufficiently large to require the use of the main engine for making the first angular rate correction.

Attitude accuracy requirements during descent and deboost are not as critical as those associated with ascent, since the re-entry maneuver can tolerate moderate deviations of initial conditions. It will be assumed that attitude accuracies of within one degree are adequate.

The accuracy requirements of the attitude control system during rendezvous were determined on the basis of a constant error persisting during a given correction. This study revealed that average pitch errors of +0.010 rad or -0.010 rad during each correction would permit a successful rendezvous. It was also found that yaw accuracies within ±0.010 rad and roll accuracies within ±0.020 rad would be acceptable.

The requirements of the attitude control system during re-entry cannot be explicitly defined because they are a function of the vehicle velocity and atmospheric density as well as the guidance law. For example, when the vehicle is at a high attitude where the atmospheric density is low, greater errors in angle of attack can be tolerated than when the density and accompanying aerodynamic effects become large. In essence, during re-entry, attitude control requirements are not adequately defined in terms of only position error because of the complete integration of the attitude control system into the guidance system. This problem is investigated further in Section 8.

3.5.2 Vehicle Inertia

The mission analysis was based upon a total vehicle weight of 200,000 pounds in an initial parking orbit at 150 nautical miles.

Assumptions made concerning the space maneuvers required to reach the orbit of the target resulted in a vehicle weight of approximately 128,000 pounds during rendezvous. The weight during re-entry was estimated to be 100,000 pounds.

A study of the re-entry maneuver has defined the vehicle shape which in turn has allowed the principal moments of inertia to be estimated. Figure 3-15 shows a plan view of the vehicle. The ranges of the principal moments of inertia as determined by full and empty fuel tanks are analyzed in Appendix IV. They are:

$$J_p = 4.94 \times 10^6 \text{ lb-sec}^2\text{-ft to } 4.13 \times 10^6 \text{ lb-sec}^2\text{-ft}$$

$$J_y = 5.78 \times 10^6 \text{ lb-sec}^2\text{-ft to } 5.00 \times 10^6 \text{ lb-sec}^2\text{-ft}$$

$$J_r = 1.06 \times 10^6 \text{ lb-sec}^2\text{-ft to } 0.95 \times 10^6 \text{ lb-sec}^2\text{-ft}$$

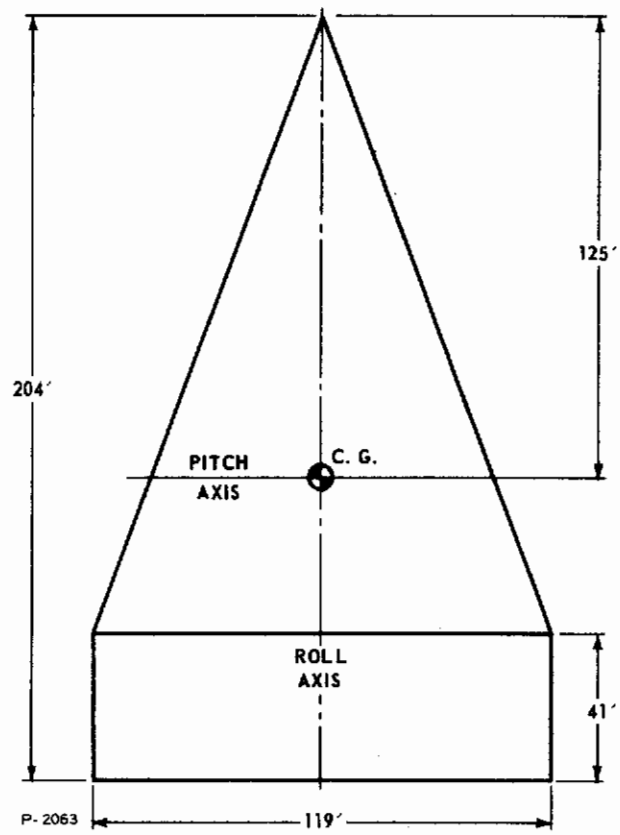

Figure 3-15 - Vehicle Plan View

where the subscripts p, y, and r refer to pitch, yaw, and roll axis respectively. The center of gravity does not move along either the pitch or roll axis, but does move a total of 1.10 feet along the yaw axis as the fuel is consumed.

3.5.3 Engine Orientation

The thrust levels required for vehicle guidance at various times during the flight are:

(a) 400,000 pounds

(b) 50,000 pounds

(c) 8,000 pounds

(d) 600 pounds

The 400,000 pound thrust is used for plane change, orbital transfer and re-entry de-boost, while all thrust levels are required during the

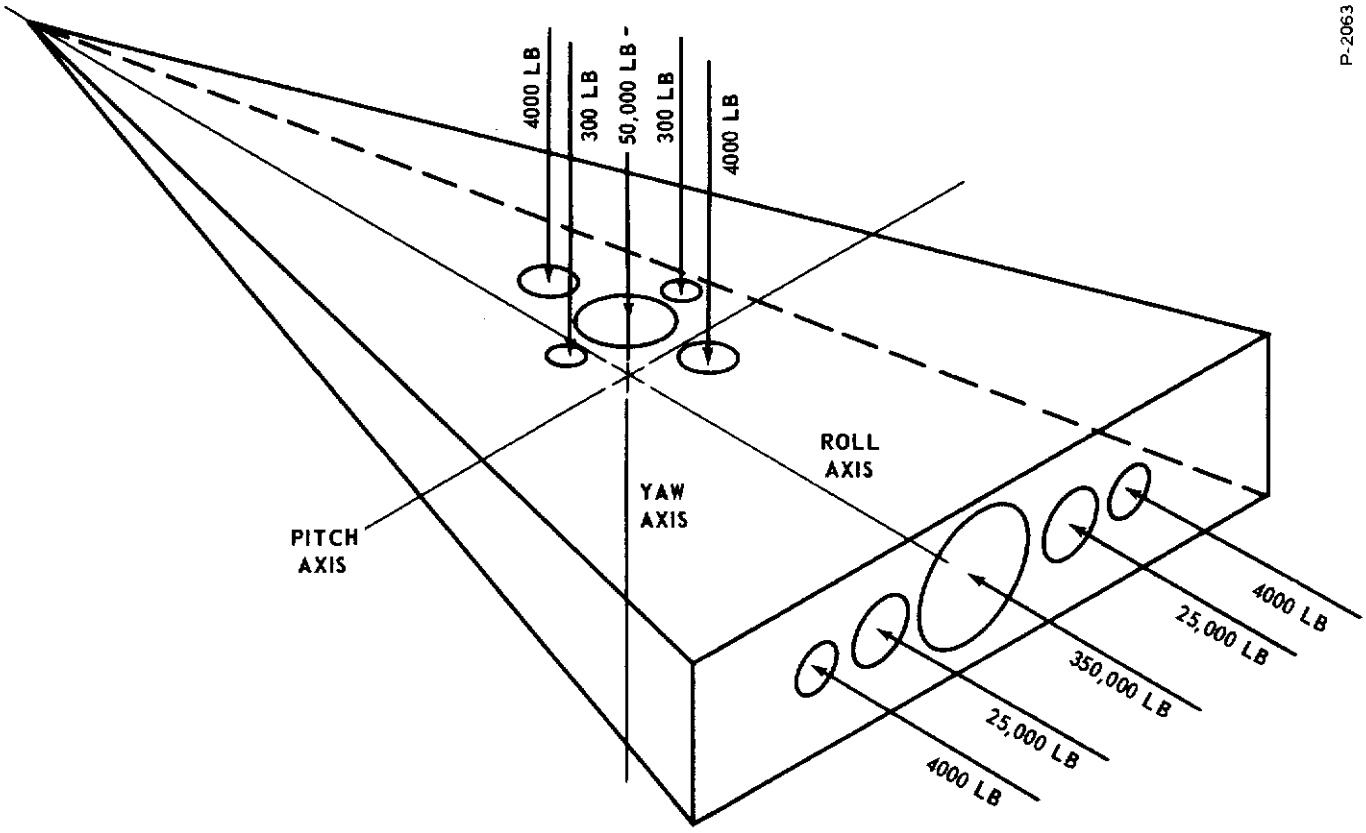

Figure 3-16 - Schematic Diagram of Guidance Engine Locations

rendezvous maneuver. During rendezvous the following thrust combinations are required:

(a)	Longitudinal thrust:	400,000 pounds
	Normal thrust:	50,000 pounds
(b)	Longitudinal thrust:	50,000 pounds
	Normal thrust:	8,000 pounds
(c)	Longitudinal thrust:	8,000 pounds
	Normal thrust:	600 pounds

Figure 3-16 shows schematically the locations and sizes of the guidance engines. The engines are clustered to provide net thrust vectors along the vehicle principal axes. A detailed discussion of the guidance engine orientation is contained in Appendix V.

3.5.4 Disturbance Torques

It is highly unlikely that the guidance engines and vehicle structure can be so mated that the thrust vectors always pass through the vehicle center of gravity. The firing of the guidance engines, therefore, produces disturbance torques which must be counteracted by the attitude control system. Table 3-6 contains the estimated maximum

Table 3-6 - Engine Misalignment Estimates

ENGINE SIZE, LB	400,000	50,000	50,000	8,000	8,000	600
AXIS LOCATION	ROLL	ROLL	YAW	ROLL	YAW	YAW
MAX MOMENT ARM ABOUT ROLL, FT	0	0	0.5	0	0.5	0.5
MAX ROLL MOMENT FT-LB	0	0	25,000	0	4,000	300
MAX MOMENT ARM ABOUT PITCH, FT	1	1	1	1	1	1
MAX PITCH MOMENT, FT-LB	400,000	50,000	50,000	8,000	8,000	600
MAX MOMENT ARM ABOUT YAW, FT	0.5	0.5	0	0.5	0	0
MAX YAW MOMENT, FT-LB	200,000	25,000	0	4,000	0	0

P-2063

moment arms which could exist and the resulting disturbance torques exerted on the vehicle for each of the various engines.

Secondary injection thrust vector control will be incorporated into a separate attitude control loop to handle the large disturbance torques produced during the 400,000 pound thrust. The smaller engines will not use thrust vector control, consequently their disturbance torques will be imposed upon the normal attitude control system. The maximum total disturbance torques exerted by the smaller guidance engines are estimated to be:

Maximum pitch Moment, ft-lb	25,000
Maximum yaw Moment, ft-lb	58,000
Maximum roll Moment, ft-lb	25,000

SECTION 4

MOMENTUM EXCHANGE SYSTEMS FOR ATTITUDE CONTROL

4.1 INTRODUCTION

A momentum exchange system employs a rotating device which generates a control moment by virtue of an exchange of angular momentum between the vehicle and the device. The most effective systems utilize either reaction wheels or single-degree-of-freedom gyros. Rotating spheres and fluid gyros have been studied, but their development has not progressed far enough for them to be considered practical. This study is concerned with the application of gyros and reaction wheels as moment-producing devices in the hypothetical vehicle defined in Subsections 1.2 and 3.5.

4.2 DESIGN ANALYSIS OF CONTROL-MOMENT GYRO

This analysis is concerned with the use of single-degree-of-freedom gyros for exerting control moments about the vehicle major axes. The design equations and curves evolved are based upon the simplified equations developed in Appendix VII.

Consider the single-degree-of-freedom gyro as shown in Figure 4-1 with axes $\bar{e}_1$, $\bar{e}_2$, and $\bar{e}_3$ locked in the gyro and the vehicle represented by the $\bar{a}_1$, $\bar{a}_2$ and $\bar{a}_3$ axes. The gyro is free to rotate about the $\bar{e}_1$ axis which coincides with the vehicle $\bar{a}_1$ axis and has the spin angular momentum vector $\bar{H}_1$ along the $\bar{e}_3$ axis. The $\bar{e}_3$ axis and the $\bar{a}_3$ axis are initially aligned.

The moment vector $\bar{M}_{V_1}$ which is produced on the vehicle by precessing the gyro around the $\bar{a}_1$ axis, is approximated by the expression:

$$\bar{M}_{V_1} = H_1 \cos\theta_1 \dot{\theta}_1 \bar{a}_2 + H_1 \sin\theta_1 \dot{\theta}_1 \bar{a}_3 \qquad (4\text{-}1)$$

The momentum impulse vector obtained by precessing the gyro is then:

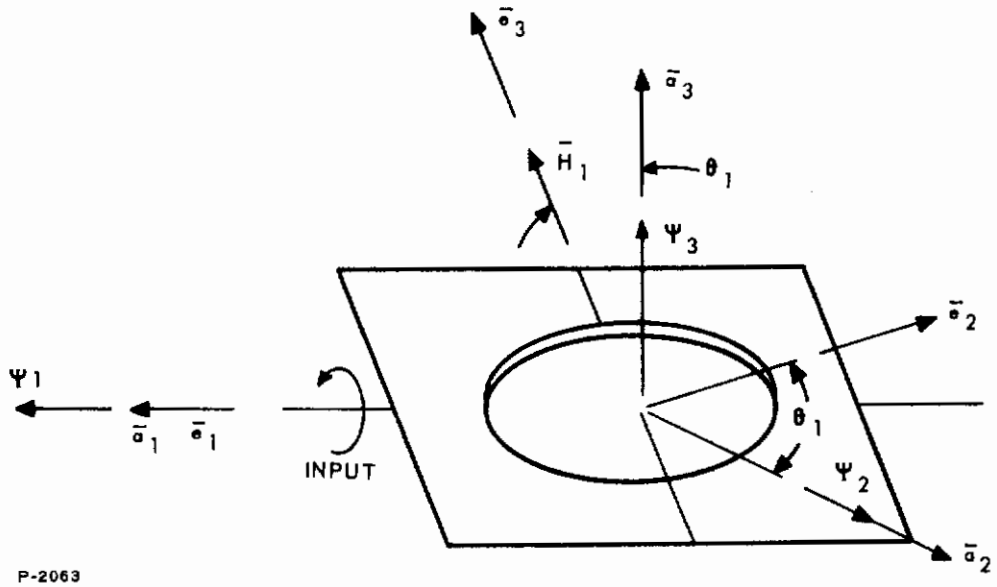

Figure 4-1 - Single-Degree-of-Freedom Gyro Schematic

$$\bar{I}_{m_1} = \int_o^t \bar{M}_{V_1}\, dt = \int_o^t \left[H_1 \cos\theta_1\, \dot{\theta}_1\, \bar{a}_2 + H_1 \sin\theta_1\, \dot{\theta}_1 \bar{a}_3 \right] dt \tag{4-2}$$

and substituting $\dot{\theta}_1 = \dfrac{d\theta_1}{dt}$:

$$\bar{I}_m = \int_0^{\theta_1} H_1 \cos\theta_1\, d\theta_1\, \bar{a}_2 + H_1 \sin\theta_1\, d\theta_1\, \bar{a}_3 \tag{4-3}$$

with the result:

$$\bar{I}_m = H_1 \sin\theta_1\, \bar{a}_2 - H_1 (1 - \cos\theta_1)\, \bar{a}_3 \tag{4-4}$$

The first term, $H_1 \sin\theta_1$ is the desired control impulse about the $\bar{a}_2$ axis, and the second term, $-H_1 (1 - \cos\theta_1)$, is the cross-coupling impulse about the $\bar{a}_3$ axis. For either impulse, the saturation value

occurs at θ_1 = 90 degrees. The magnitudes of the produced impulses versus the precession angle are shown as a percentage of the saturation value H_1 in Figure 4-2. From Figure 4-2 it is obvious that single-axis control can be realized only if the gyro precession angles are very small or some form of compensation is included in the system. This compensation can be either in the form of two gyros back-to-back in which case the cross-coupling terms will cancel, or by commanding alternate gyros to cancel the cross-coupling effect. In either case, the control inpulse a along the vehicle $\bar{a}_2$ axis is:

$$I_{m_2} = H_1 \sin \theta_1 \tag{4-5}$$

Since this is a conservative angular momentum transfer, this impulse must equal the change in angular momentum of the vehicle; i.e.:

$$H_1 \sin \theta_1 = J_2 \Delta \psi_2. \tag{4-6}$$

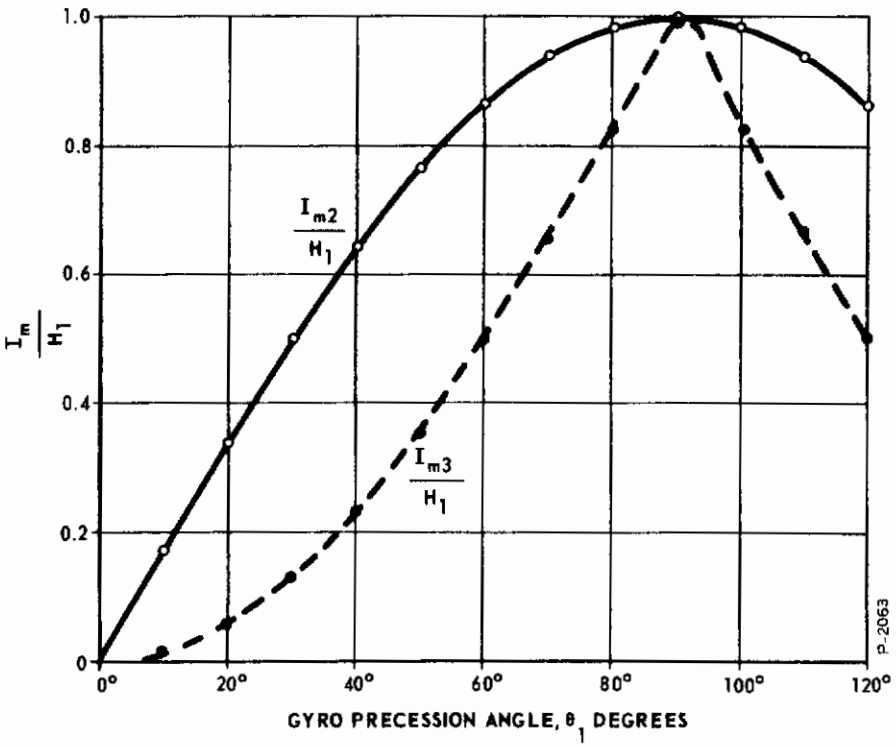

Figure 4-2 - Effect of Precession Angle upon Momentum Impulse

The spin angular momentum of the gyro, H_1, has the magnitude $C\Omega$ and if a perfectly cylindrical gyro is assumed, then:

$$H_1 = \frac{1}{2} m R^2 \Omega \qquad (4\text{-}7)$$

where:

m = mass of the gyro rotor, lb-sec^2/ft

R = outside radius of the rotor, ft

Ω = spin velocity of the rotor, rad/sec

A relation for R and Ω can be found by considering the stresses involved. The maximum stress for a rotating cylinder occurs as a hydrostatic stress at the center and has the magnitude:

$$\sigma_{max} = \frac{3 + \mu}{8} \rho \ (\Omega R)^2 \qquad (4\text{-}8)$$

where:

σ_{max} = maximum tensile stress, lb/ft^2

μ = Poisson's ratio

ρ = the specific density of the material, lb-sec^2/ft^4

Rewriting Equation (4-8) gives:

$$(\Omega R) = \sqrt{\frac{8 \sigma_{max}}{(3+\mu)\rho}} \qquad (4\text{-}9)$$

Referring to Equation (4-7)

$$H_1 = \frac{1}{2} \frac{w}{g} R^2 \Omega = \frac{1}{2} \frac{w}{g} R \sqrt{\frac{8 \sigma_{max}}{(3+\mu)\rho}} \qquad (4\text{-}10)$$

and Equation (4-6) becomes:

$$\Delta\psi_2 = \frac{H_1 \sin\theta_1}{J_2} \tag{4-11}$$

$$\Delta\psi_2 = \frac{1}{2}\,\frac{w}{g}\,R\sqrt{\frac{8\sigma_{max}}{(3+\mu)\rho}}\,\frac{\sin\theta_1}{J_2} \tag{4-12}$$

Equation (4-12) can be used to establish a relationship between the gyro weight w and radius R necessary to produce a given vehicle rate change $\Delta\psi_{2max}$ for a given precession angle θ_{max}.

$$(wR) = \frac{2g\,J_2\,\Delta\psi_{2_{max}}}{\frac{8\,\sigma_{max}}{(3+\mu)\rho}\,\sin\theta_{1_{max}}} \tag{4-13}$$

Since the gyro rotor is assumed to be cylindrical with radius R and width h, the gyro moments of inertia are:

$$A = \frac{w}{g}\left(\frac{R^2}{4} + \frac{h^2}{12}\right) \tag{4-14}$$

$$C = \frac{1}{2}\,\frac{w}{g}\,R^2 \tag{4-15}$$

The gyro rotor width, h, can be eliminated by considering the weight of the gyro:

$$\therefore\quad h = \frac{w}{\pi R^2 \rho\, g} \tag{4-16}$$

Substituting Equation (4-16) into Equation (4-14) gives the following expression for A in terms of w and R.

$$A = \frac{w}{g}\left(\frac{R^2}{4} + \frac{w^2}{12\,\pi^2 R^4 \rho^2 g^2}\right) \tag{4-17}$$

If Equations (4-6), (4-13), and (4-17) are combined and used with Equation (VII-24) of Appendix VII, the following approximate expression for the gyro input torque results:

$$T_{C_1} = \left[\frac{g}{w} \frac{H_1^2}{Y} + \frac{w^7}{192 \pi^2 g^7 \rho^2} \frac{Y^2}{H_1^4} \ddot{\theta}_1 \right] \tag{4-18}$$

where H_1 and Y are defined as:

$$H_1 = \frac{J_2 \Delta \psi_{2_{max}}}{\sin \theta_{1_{max}}} \tag{4-19}$$

$$Y = \frac{8 \sigma_{max}}{(3 + \mu) \rho} \tag{4-20}$$

An approximate expression for $\ddot{\theta}_1$ for Equation (4-18) can be obtained in terms of the maximum precession angle and the required response time t_o. The gyro precession can be approximated by two methods which represent the minimum and maximum values of torquer size required for a given response time. In the first method the torquer both accelerates and decelerates the gyro to a new position by applying a constant torque for one half of the precession angle, with the torque then reversed to stop the gyro at the desired position. In the second method, the torquer will accelerate the gyro to the desired final position and then some form of an external braking mechanism is used to stop the gyro at this position. Assuming $\ddot{\theta}$ to be constant, approximate mathematical expressions for the above conditions can be written as

Method 1

$$\frac{\theta_{1_{max}}}{2} = \frac{1}{2} \ddot{\theta}_1 \left(\frac{t_o}{2} \right)^2 \tag{4-21}$$

$$\ddot{\theta}_1 = \frac{4 \theta_{1_{max}}}{t_o^2} \tag{4-22}$$

$$\dot{\theta}_{max} = \frac{2\theta_{max}}{t_o} \tag{4-23}$$

Method 2

$$\theta_{1_{max}} = \frac{1}{2} \ddot{\theta}_1 (t_o)^2 \tag{4-24}$$

$$\ddot{\theta}_1 = \frac{2\theta_{1_{max}}}{t_o^2} \tag{4-25}$$

$$\dot{\theta}_{max} = \frac{2\theta_{max}}{t_o} \tag{4-26}$$

For any given response time t_o, the second method would require less torque since the gyro accelerations would be reduced. However, both of the above methods will be analyzed.

For the two methods of torquing, Equation (4-18) becomes:

1. Torque source used for acceleration and deceleration of gyro:

$$T_{C_1} = \left[\frac{g}{w}\frac{H_1^2}{Y} + \frac{w^7}{192\rho^2\pi^2 g^7}\frac{Y^2}{H_1^4}\right]\frac{4\theta_{1_{max}}}{t_o^2} \tag{4-27}$$

2. Torque source used for acceleration of gyro only:

$$T_{C_1} = \left[\frac{g}{w}\frac{H_1^2}{Y} + \frac{w^7}{192\rho^2\pi^2 g^7}\frac{Y^2}{H_1^4}\right]\frac{2\theta_{1_{max}}}{t_o^2} \tag{4-28}$$

The equations as stated relate the weight and torque requirements of a gyro system capable of producing a given vehicle angular rate

change $\Delta\psi_{2_{max}}$ in time t_o on a vehicle with an inertia J_2 about the axis of the produced rate. The angle $\theta_{1_{max}}$ is the total precession angle of the gyro. Also, as shown by the Y term, the material used in the gyro construction must be considered.

The analysis of the mission requirements for the rendezvous maneuver has dictated the following conditions:

$$\Delta\psi_{2_{max}} = -1 \times 10^{-3} \text{ rad/sec}$$

$$J_2 = 4.36 \times 10^{6} \text{ ft lb sec}^2$$

$$t_o = 0.4 \text{ sec}$$

$$\theta_{1_{max}} = \frac{\pi}{2} \text{ rad for gyro pairs}$$

$$\theta_{1_{max}} = \frac{\pi}{6} \text{ rad for single gyro}^*$$

Using these values, Equation (4-27) and (4-28) can be plotted as the torque required versus the gyro weight for various values of the material parameter Y. The curves for the first torquing method are shown in Figure 4-3 and for the second torquing method in Figure 4-4. Six curves are shown on each graph, the upper grouping of curves pertaining to a single gyro along each axis and the lower or encircled grouping of curves pertaining to one gyro of a gyro pair along each axis. The three curves in each grouping show the effects of the following three materials:

---

*This value of θ_1 was selected to minimize the cross-coupling effect of the gyro precession. This angle will produce 50 percent of the saturation impulse around the primary axis and only 14 percent of the saturation impulse on the orthogonal axis; a figure which lends readily to compensation by alternate gyros. For gyro pairs, however, a full 90 degree precession is possible.

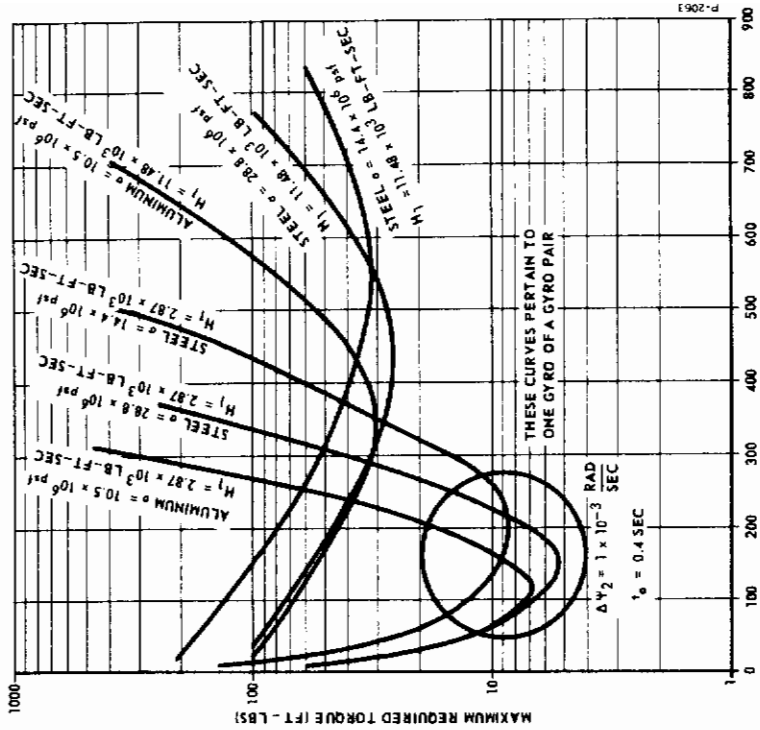

Figure 4-3 - Torque vs. Weight for Gyro Precession (Method 1)

Figure 4-4 - Torque vs. Weight for Gyro Precession (Method 2)

1. Aluminum with a maximum allowable stress of 10.5 x 10^6 psf (73,000 psi).
2. Steel with a maximum allowable stress of 14.4 x 10^6 psf (100,00 psi).
3. Steel with a maximum allowable stress of 28.8 x 10^6 psf (200,000 psi).

The gyro radius and spin velocity can be obtained for any point on the curves from the following relationships:

$$R = \frac{2 g H_l}{w\sqrt{Y}}, \text{ ft} \tag{4-29}$$

$$\Omega = \frac{\sqrt{Y}}{R} = \frac{w Y}{2 g H_l}, \quad \frac{\text{rad}}{\text{sec}}. \tag{4-30}$$

The maximum energy and power requirements for a full maneuver can be obtained by assuming that the torque will be applied for the full maneuver. The maximum energy required to precess a gyro through an angle θ_l is then:

$$E_{l_{max}} = T_{C_l} \theta_{l_{max}}. \tag{4-31}$$

and is independent of the torquing method. This energy will be expressed in ft. lbs. The maximum power required is:

$$P_{l_{max}} = T_{C_l} \dot{\theta}_{l_{max}} = T_{C_l} \frac{2 \theta_{l_{max}}}{t_o} \tag{4-32}$$

The power and energy requirements as described by Equation (4-31) and (4-32) are for a single gyro which is torqued through a given precession angle. However, the total system energy and power requirements must also consider the particular gyro configuration. The gyro pair arrangement will require two torque sources since the two gyros

must be precessed to execute the maneuver. With the single gyro, on the other hand, the energy requirements must consider any cross-coupling correction by the alternate gyros. Figure 4-5 shows the arrangement where one gyro is used per axis. The full 30 degree precession of the single gyro will produce 14 percent of the saturation impulse along the orthogonal axis. To correct this impulse, the gyro on this axis must precess 8 degrees. (This can be verified from Figure 4-2.) The cross-coupling due to the second gyro would in turn require a precession angle of 0.5 degrees on the third gyro, a value which will produce a negligible feedback to the original control axis. Thus to produce a 30 degree precession on any axis, the total energy required is:

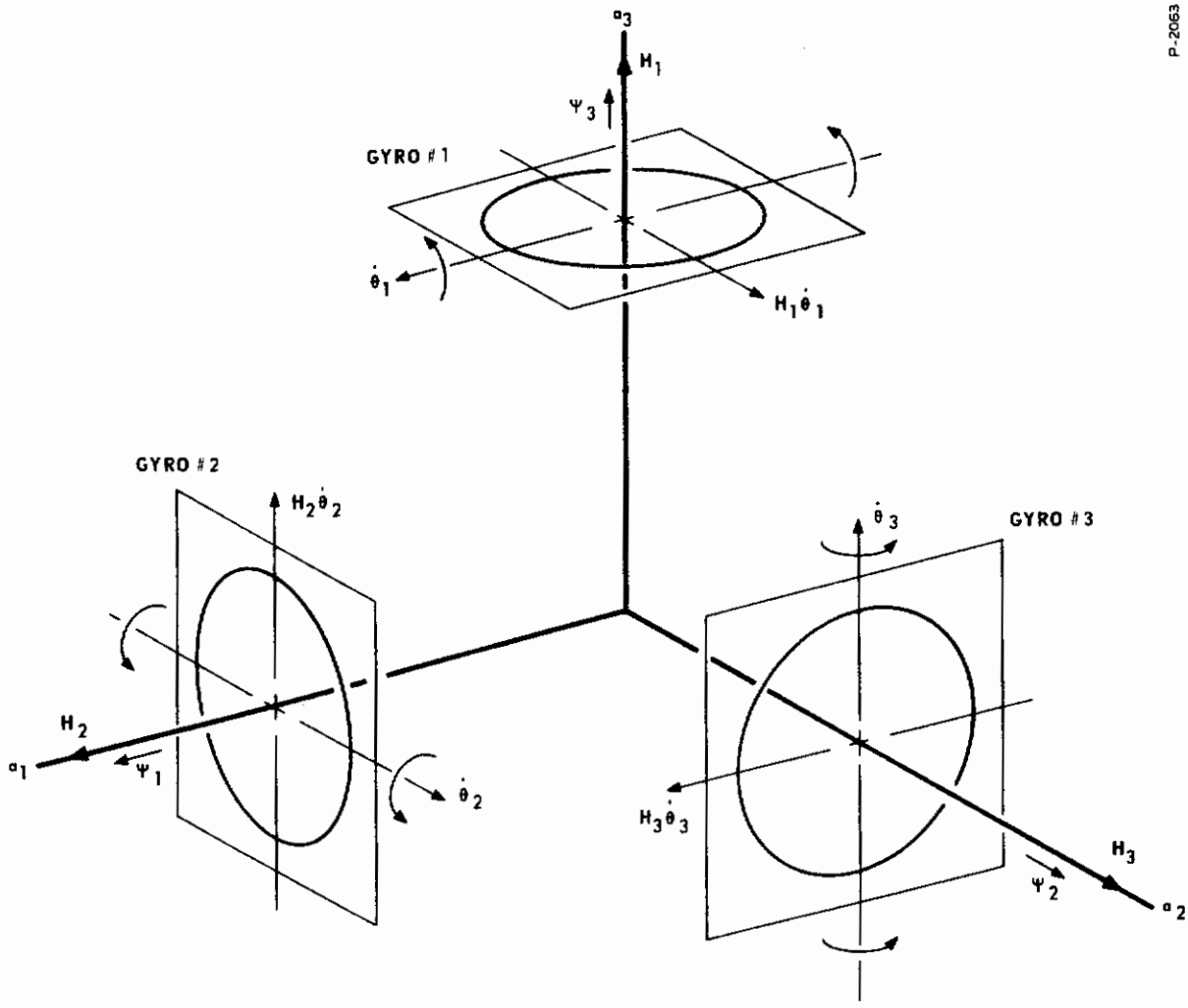

Figure 4-5 - Three-Axis Gyro System Geometry

$$E_{tot} = \text{Energy of gyro 1} + \text{Energy of gyro 2} + \text{Energy of gyro 3}$$

$$= T_{C_1} \theta_{1_{max}} + T_{C_2} \theta_{2_{max}} + T_{C_3} \theta_{3_{max}} \qquad (4\text{-}33)$$

Then for

$$\theta_{1_{max}} = \frac{\pi}{6} \text{ rad}, \quad \theta_{2_{max}} = 0.135 \text{ rad}, \text{ and } \theta_{3_{max}} = 0.009 \text{ rad},$$

$$E_{tot} = 0.668\, T_{C_1} \qquad (4\text{-}34)$$

The above analysis has ignored the power required to overcome the losses resulting from the high rotor speeds. With gas bearings and proper streamlining to minimize windage losses, this could be acceptably low. For purposes of comparing the performance of the gyro system with a reaction wheel system, the information contained in the above analysis is sufficient.

4.3 COMPARISON OF CONTROL-MOMENT GYRO AND REACTION WHEEL

The requirements of the rendezvous maneuver are such that the vehicle must have at most an average acceleration of 2.5×10^{-3} rad/sec^2 during an attitude correction. If this acceleration is to be produced by a reaction wheel, the necessary reaction torque is:

$$T_{w_2} = J_2 \dot{\psi}_3 = 11{,}900 \text{ ft-lbs}$$

If a cylindrical reaction wheel equivalent to the gyro pair arrangement is used,* then:

---

*The two gyros produce the desired vehicle rate $\dot{\psi}$ by creating an angular momentum impulse $2H_o$ along the given vehicle axis. A comparable reaction wheel must also be capable of this total impulse and therefore should be equivalent to the gyro pair.

$$J_w = \frac{1}{2} \frac{(2w)}{g} R^2 = \frac{w}{g} R^2 \qquad (4\text{-}35)$$

where w and R would be the same as for the gyro pair system. Since this is strictly an energy comparison, a single point is sufficient. For example, the minimum torque point on the curves for the gyro pair as given in Figure 4-4 corresponds to gyros which have a weight of 160.2 lb and a radius of 0.53 ft. From the data presented, the energy required by the gyros to produce the vehicle rate of 1×10^{-3} rad/sec in 0.4 sec is 10 ft lb. This includes the 2.87 ft lb of kinetic energy attained by the vehicle. A reaction wheel of this size would have an inertia J_w where:

$$J_w = \frac{160.2}{32.2} \times (0.539)^2 = 1.145 \text{ lb-ft-sec}^2$$

The wheel acceleration $\dot{\Omega}$ is:

$$\dot{\Omega} = \frac{T_{w_2}}{J_w} = 10{,}180 \text{ rad/sec}^2$$

The maximum angular velocity for this wheel is:

$$\dot{\Omega} = \frac{\sqrt{Y}}{R} = \frac{\sqrt{4.6 \times 10^6}}{0.539} = 3980 \text{ rad/sec.}$$

The time required to accelerate to this maximum acceleration is then:

$$t_o = \frac{\Omega}{\dot{\Omega}} = 0.40 \text{ second}$$

and the resulting vehicle velocity is:

$$\psi_2 = \dot{\psi}_2 \; t_o = 1 \times 10^{-3} \text{ rad/sec.}$$

In other words, both the gyro controller and the equivalent reaction wheel will produce the same vehicle control rates. The major difference between the two systems is the energy requirement.

The energy required by the equivalent reaction wheel for the same response and rate is the kinetic energy attained by the vehicle as well as the kinetic energy attained by the reaction wheel. That is:

$$E_w = \frac{1}{2} J_2 \psi_2^2 + \frac{1}{2} J_w \Omega_w^2 \qquad (4\text{-}36)$$

$$= 2.87 + \frac{1}{2} \times 1.45 \times 1.585 \times 10^6$$

$$= 1.143 \times 10^6 \text{ ft lb.}$$

In other words, the energy requirement for the reaction wheel is approximately 1.14×10^5 times greater than the energy requirement for the gyro, both systems producing identical vehicle rates and response times. Also, the reaction wheel requires a torque source of 11,900 ft lb while the gyro pair requires two torquers in the 5 to 10 ft lb range.

While this comparison was made for only one particular gyro configuration, the same difference in energies required will apply in general.* From this analysis, the reaction wheel control source is

---

*This energy difference can also be shown in a general manner. The maximum energy required by the gyro system is approximately the energy required to accelerate the vehicle; i.e.:

$$E_w = \frac{1}{2} J_2 \psi_2^2$$

With the reaction wheel on the other hand, the energy must be supplied to both the wheel and the vehicle; i.e.:

$$E_w = \frac{1}{2} J_2 \psi_2^2 + \frac{1}{2} J_w \Omega_w^2$$

and the energy for the reaction wheel system will always be greater by

$$\frac{1}{2} J_w \Omega_w^2$$

seen to be unacceptable for control of a large vehicle. This control means has been successfully employed in small satellites, however, where high response is not required.

4.4 NOMENCLATURE

Symbol	Definition
A	Moment of inertia of gyro rotor about transverse axis, lb-ft-sec^2
C	Moment of inertia of gyro rotor about spin axis lb-ft-sec^2
D	Damping factor, ft-lb-sec
E	Energy, ft-lb
g	Acceleration of gravity, ft/sec^2
h	Width of gyro rotor, ft
H_l	Angular momentum of one gyro rotor, lb-ft-sec
I_m	Momentum impulse, ft-lb-sec (subscripts 1, 2, 3 refer to vehicle principal axes)
J	Moment of inertia of vehicle, lb-ft-sec^2 (subscripts 1, 2, 3 refer to vehicle principal axes)
J_w	Moment of inertia of reaction wheel about spin axis, lb-ft-sec^2
M_{V_l}	Moment exerted on vehicle by gyro, ft-lb
P	Power, ft-lb/sec
R	Radius of gyro rotor, ft
T_c	Control torque exerted upon gyro, ft-lb (subscripts 1, 2, 3 refer to gyro principal axes)
T_w	Control torque exerted upon reaction wheel, ft-lb (subscripts 1, 2, 3 refer to vehicle principal axes)
t_o	Response time, sec.
w	Weight of gyro rotor, lb.
Y	Lumped parameter (see text)

Symbol	Definition
Δ	Prefix indicates incremental change
θ	Gyro precession angle, rad. (Subscripts 1, 2, 3 refer to gyro principal axes)
μ	Poisson's ratio
π	3.1416
ψ	Vehicle angular rate, rad/sec. (subscripts 1, 2, 3 refer to vehicle principal axes)
ρ	Mass density, $lb\text{-}sec^2/ft^4$
Ω	Gyro spin angular velocity, rad/sec
σ	Material tensile stress, lb/ft^2
$\bar{(\ )}$	Indicates vector quantity
$\dot{(\ )}$	Indicates first derivative with respect to time
$\ddot{(\ )}$	Indicates second derivative with respect to time

SECTION 5

SECONDARY INJECTION THRUST VECTOR CONTROL

5.1 INTRODUCTION

Thrust vector control, by means of secondary injection, is under intensive study by industry and government. This method for producing control moments on a spacecraft is basically simple and offers increased reliability, reduced weight, and increased response when compared with mechanical methods such as swivel nozzles, gimballed engines, jet vanes, or jetavators. In secondary injection, the injectant fluid is fed into the diverging section of the rocket nozzle where it causes a bow shock. The resulting asymmetrical pressure distribution within the nozzle, plus the jet reaction force of the injectant, creates a side thrust. In effect, the thrust vector of the main rocket nozzle is increased in magnitude and canted in the plane of the injector nozzle through an angle equal to the arctangent of the ratio of the side thrust to the axial thrust. A schematic diagram of secondary injection is shown in Figure 5-1.

Although secondary injection can be qualitatively described, a reasonably accurate theoretical analysis has not yet been achieved. This situation exists because of the difficulty in describing the complex

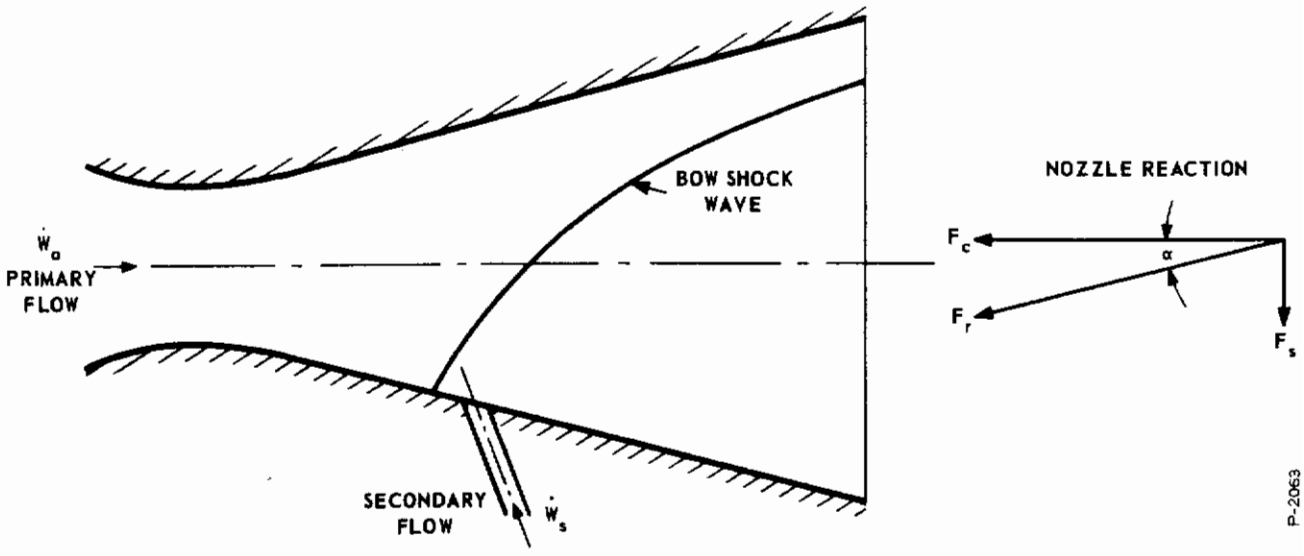

Figure 5-1 - Diagram of Secondary Injection

interaction which occurs between the primary and secondary fluids. Some investigators have achieved rather good correlation between theory and experiment but only within certain limits of operation as dictated by the initial assumptions. Nevertheless, the sizeable inroads which have been made so far, plus the extent of the effort being put forth, indicate that a strong theory will evolve before too long.

Up to the present, the work on secondary injection leading to successful designs has been almost totally empirical. As a result, empirical equations and rules-of-thumb have been developed for some of the important design parameters. It has been found that the side thrust developed is strongly affected by:

(a) the injected fluid properties,
(b) the injection flow rate,
(c) the injected fluid momentum,
(d) the injector axial position,
(e) the injector angle,
(f) the injected fluid pressure,
(g) the injector nozzle shape,
(h) the primary flow rate,
(i) the primary axial thrust.

The secondary injection of inert liquids has received the most attention thus far because a liquid system is simple to operate and uses essentially state-of-the-art components. The only successful applications of secondary injection in rocket engines have been with inert liquid injectants. Freon has been the most common liquid used because it possesses a low boiling point, low specific heat, high density, and low heat of vaporization; all desirable injectant characteristics.

The initial concept of secondary injection involved the use of gas. While liquid injection has received considerably more attention, gas injection has superior performance. The main reason why development of gas injection systems has proceeded at a slower pace involves the state-of-the-art of the necessary components. For cold gas injection, high pressure storage tanks or a gas generation system are required in addition to special gas regulators and injector valves which can function under the cooling effects of gas expansion. Hot gas is by far the most effective injectant, but it is the most difficult to handle and control.

Two sources of hot gas are available for injection. Gas can be bled from the main engine or a separate hot gas generator can be used. The combustion chamber bleed system is the most attractive because of its high performance, light weight, and basic simplicity; however, it operates at the highest temperature. It is reasonable to assume however, that a reliable hot gas system using by-pass gas from the engine combustion chamber will be developed in the near future. We will be concerned solely with such a system because it represents the ultimate in secondary injection thrust vector control.

5.2 PERFORMANCE CHARACTERISTICS

Figure 5-2 shows a schematic diagram of a by-pass hot gas secondary injection thrust vector control system. $\dot{W}_a$ is the steady weight flow rate into the main nozzle, and $\dot{W}_s$ is the metered flow rate of the injectant. An assumption will be made that the variation of $\dot{W}_s$ from zero to maximum has no significant effect upon $\dot{W}_a$ or combustion stability.

The effective specific impulse of the secondary injectant is defined as:

$$I_{sps} = \frac{F_s}{\dot{W}_s} \qquad (5\text{-}1)$$

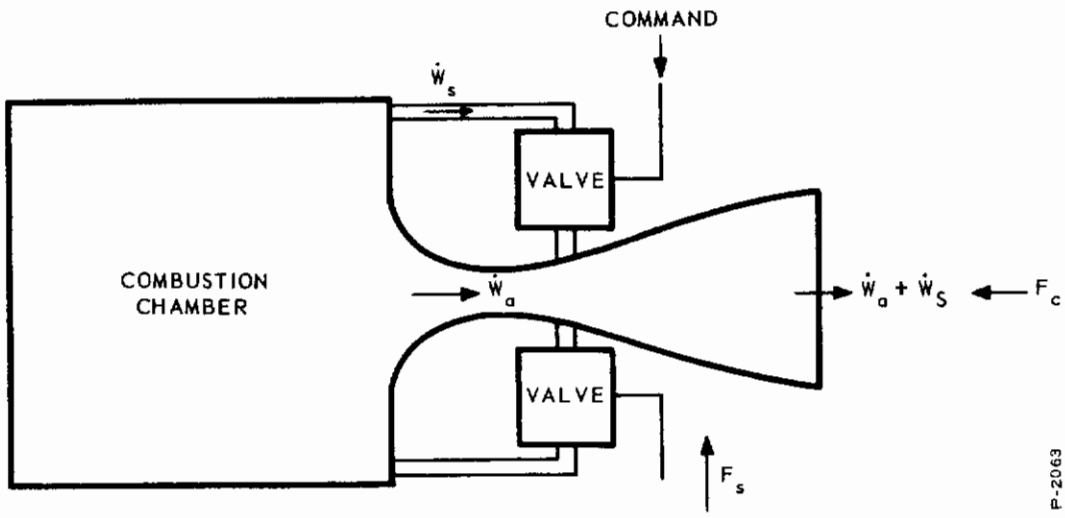

Figure 5-2 - Schematic Diagram of By-Pass Secondary Injection Thrust Vector Control

where $\dot{W}_s$ is the injectant weight flow rate and F_s is the net side thrust acting on the main rocket nozzle. The specific impulse of the main engine without secondary injection is:

$$I_{spa} = \frac{F_a}{\dot{W}_a} \tag{5-2}$$

while the specific impulse with secondary injection is:

$$I_{spc} = \frac{F_c}{\dot{W}_a + \dot{W}_s}, \tag{5-3}$$

where F_a and F_c are the axial thrusts acting on the main nozzle. Due to the flow separation and accompanying shock created by secondary injection, $I_{spc} < I_{spa}$, the magnitude of the difference being a function of the secondary flow rate.

$$\frac{I_{spc}}{I_{spa}} = f_1(\dot{W}_s, \dot{W}_a) < 1 \tag{5-4}$$

It has been found empirically that the ratio of the side flow specific impulse to the axial flow specific impulse is fairly constant over most of the useful injectant flow range. Most researchers have used the ratio, I_{sps}/I_{spa}, but as implied,[73] the ratio I_{sps}/I_{spc} is more constant. We will therefore define an amplification factor by:

$$K_a = \frac{I_{sps}}{I_{spc}} = \frac{F_s(\dot{W}_a + \dot{W}_s)}{F_c \dot{W}_s} \tag{5-5}$$

or,

$$K_a = \frac{F_s}{W_s I_{spa} f_1(\dot{W}_s, \dot{W}_a)} \tag{5-6}$$

These equations describe the static gain of the secondary injection phenomenon.

For a given mission, the total required axial impulse is defined by:

$$I_{at} = \int_o^{t_f} F_c \, dt = I_{spa} \int_o^{t_f} f_1(\dot{W}_s, \dot{W}_a)(\dot{W}_a + \dot{W}_s)\, dt, \tag{5-7}$$

where t_f is the total firing time of the engine.

An estimate of the additional fuel requirements for the mission due to secondary injection can be obtained from Equation (5-7) by letting $\dot{W}_s$ assume a constant average value, $\overline{\dot{W}_s}$.

Integration gives:

$$I_{at} = I_{spa}\, f_1 (\overline{\dot{W}_s}, \dot{W}_a)\, (\dot{W}_a + \overline{\dot{W}_s})\, t_f \qquad (5-8)$$

The total fuel consumption is then:

$$W_t = \frac{I_{at}}{I_{spa}\, f_1 (\overline{\dot{W}_s}, \dot{W}_a)} \qquad (5-9)$$

If no secondary injection system were used, then the total fuel consumption would be simply I_{at}/I_{spa}, so the increased fuel consumption due to secondary injection is:

$$\Delta W_{si} = \frac{I_{at}}{I_{spa}} \left[\frac{1}{f_1 (\overline{\dot{W}_s}, \dot{W}_a)} - 1 \right] \qquad (5-10)$$

The values of K_a, I_{spa}, and $f_1 (\dot{W}_s, \dot{W}_a)$ depend upon the gas characteristics and the design of the nozzles and secondary injection system. Much work has yet to be done in this area, but the references indicate that amplification factors of near 2 should be realized for vector angles of up to 5 or 6 degrees. Reference (73) uses a value for $f_1 (\dot{W}_s, \dot{W}_a)$ of 0.98 in weight computations.

5.3 SYSTEM REQUIREMENTS

The basic function of the secondary injection thrust vector control system is to correct for thrust vector misalignments, the maximum imposed moment being 400,000 ft-lb. Since the engine is located approximately 40 feet from the vehicle center of gravity, this represents a side thrust of 10,000 pounds and a vector angle of 1.4 degrees. Other important parameters, assumed and otherwise, which define the system are:

(a) Specific impulse: $I_{spa} = 400$ sec

(b) Specific impulse efficiency: $f_1(\dot{W}_s, \dot{W}_a) = 0.98$

(c) Amplification factor: $K_a = 2.0$

(d) Main engine thrust: 350,000 lbs

(e) Thrust of engine cluster: 400,000 lbs

The secondary injectant flow rate required to maintain a 10,000 pound side force is 12.8 lb/sec, as obtained from Equation (5-6). The effective side thrust specific impulse is 776 seconds. From Equation (5-10) it is found that the fuel requirement of the 350,000 pound thrust engine is increased by approximately 2 percent due to secondary injection. For the 400,000 pound thrust engine cluster, this represents an approximately 1.8 percent increase in fuel consumption.

The most critical item involved in implementing thrust vector control is the injectant flow control valve, because the performance of the control loop is directly dependent upon the accuracy, response, and reliability of this device. Two types of valves are investigated for this application in the articles which follow. They are a simple poppet valve and a multi-stage vortex valve.

5.4 SECONDARY INJECTION POPPET VALVE

5.4.1 Description

The poppet valve under consideration is shown schematically in Figure 5-3. It is a two-stage device which uses control gas from a source other than the main engine combustion chamber. A practical problem associated with this valve is the compatibility of materials with the hot gases. The use of a relatively cool control gas will promote reliability, but the extreme corrosive and erosive characteristics of the combustion chamber gas strain the capabilities of presently available materials. The assumption is therefore made that materials technology will progress sufficiently in the next few years to make this valve practical.

5.4.2 Basic Equations

The assumptions upon which the valve analysis is based are:

(a) Isothermal conditions prevail,

(b) The fluid medium behaves as a perfect gas

(c) All gas flow is frictionless

(d) Combustion chamber temperature and pressure are constant during a thrust period.

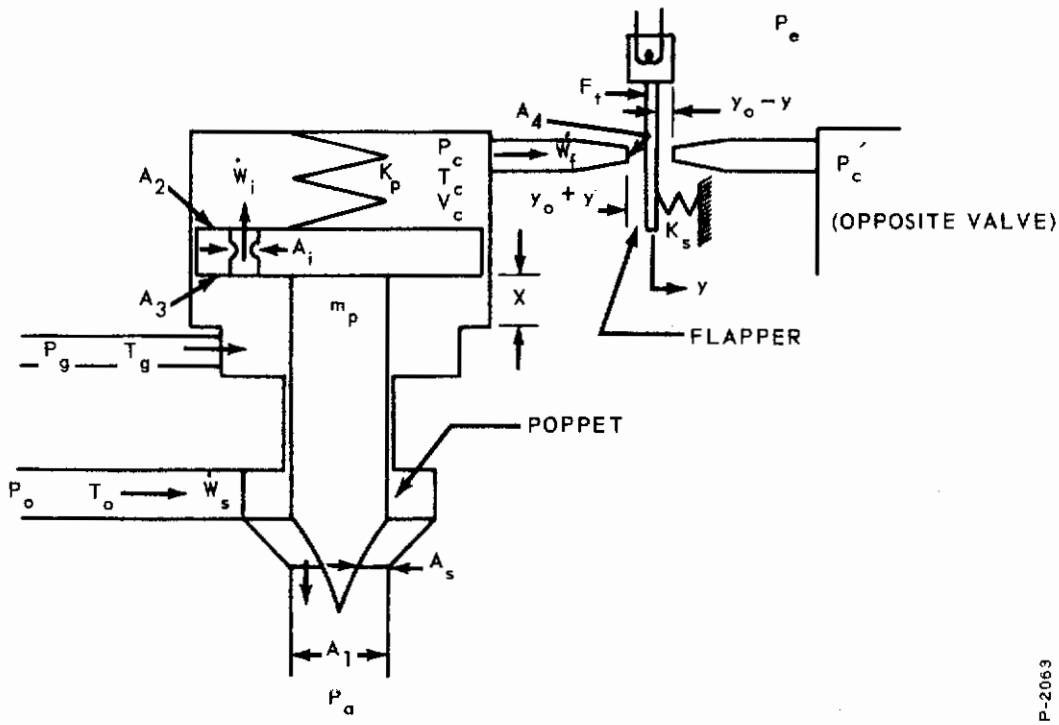

Figure 5-3 - Schematic Diagram of Secondary Injection Poppet Valve

The weight flow rates through the various orifices are:

$$\dot{W}_i = \frac{C_g P_g A_i}{\sqrt{T_g}} f_1\left(\frac{P_c}{P_g}\right) \qquad (5\text{-}11)$$

$$\dot{W}_f = \frac{C_g P_c A_f}{\sqrt{T_g}} f_1\left(\frac{P_e}{P_c}\right) \qquad (5\text{-}12)$$

$$\dot{W}_s = \frac{C_o P_o A_s}{\sqrt{T_g}} f_1\left(\frac{P_a}{P_o}\right) \qquad (5\text{-}13)$$

where:

$$C_{o,g} = g\left(\sqrt{\frac{k}{R}\left(\frac{2}{k+1}\right)^{\frac{k+1}{k-1}}}\right)_{o,g}$$

g = acceleration of gravity, in./sec^2

k = ratio of specific heats

R = gas constant, in.^{2}/sec^2-°R

P_a, P_g, P_c, P_o = pressures, psia

A_i, A_c, A_s = effective orifice areas, in.^{2}

T_g, T_o = absolute gas temperatures, °R.

$f_1(P_n/P_m)$ are the conventional orifice flow functions, sometimes referred to by A*/A.

The variable orifice areas are defined by:

$$A_s = C_s x \tag{5-14}$$

$$A_f = C_f (y + y_o) \tag{5-15}$$

$$A_f' = C_f (y_o - y) \tag{5-16}$$

C_s and C_f being constants. A_f' is the area of the flapper orifice for the opposing poppet valve. All "primed" symbols refer to the other valve.

The valve dynamics are inherent in the motion of the poppet and the pressure variation behind the piston. The continuity equation for gas flow is:

$$\dot{W}_i - \dot{W}_f = \frac{d}{dt} (\rho_c V_c), \tag{5-17}$$

where ρ_c is gas density, and V_c is the enclosed gas volume.

Flapper position is defined by:

$$P_c A_4 + F_t = P_c' A_4 + K_s \dot{y}, \tag{5-18}$$

and poppet motion is given by:

$$P_g A_3 + P_o A_s + P_a (A_1 - A_s) = m_p \ddot{x} + K_p x + F_p + P_c A_2, \tag{5-19}$$

where: A_4 = area of flapper nozzle, in.^{2}

F_t = effective control force on flapper, lb

y = flapper gap, in.

K_s = effective flapper mechanical stiffness, lb/in.

A_2, A_3 = piston areas, $in.^2$

m_p = poppet mass, $lb\text{-}sec^2/in.$

K_p = poppet spring stiffness, lb/in.

F_p = poppet spring preload, lb

Expanding and rearranging these equations results in:

$$\frac{dP_c}{dt} = \left[\frac{C_g P_g A_i \sqrt{T_g} R_g f_1\left(\frac{P_c}{P_g}\right)}{V_{co}}\right] - P_c A_f \left[\frac{C_g R_g \sqrt{T_g} f_1\left(\frac{P_e}{P_c}\right)}{V_{co}}\right] + \left[\frac{A_2}{V_{co}}\right] x \frac{dP_c}{dt} + \left[\frac{A_2}{V_{co}}\right] P_c \frac{dx}{dt} \quad . \tag{5-20}$$

$$y = \frac{(P_c - P'_c) A_4 + F_t}{K_s} \tag{5-21}$$

$$x = \frac{(F_p - P_a A_1 - P_g A_3) - A_2 P_c}{m_p S^2 + K_e} \tag{5-22}$$

where:

$V_{co} = V_c$ at $x = 0$

$K_e = K_p - P_o C_s + P_a C_s$

The nonlinearities inherent in Equation (5-20) preclude the development of a useful analytic expression, so simplification is necessary.

5.4.3 Linearized Performance

The steady-state performance is obtained by dropping all time-variant terms from Equations (5-20) and (5-22). The result of this manipulation is:

$$P_c = \frac{P_g A_i f_1\left(\frac{P_c}{P_g}\right)}{C_f (y + y_o) f_1\left(\frac{P_e}{P_c}\right)} \tag{5-23}$$

$$P'_c = \frac{P_g A_i f_1\left(\frac{P'_c}{P_g}\right)}{C_f (y_o - y_o) f_1\left(\frac{P_e}{P'_c}\right)} \tag{5-24}$$

$$(P_c - P'_c) A_4 + F_t = K_s y \tag{5-25}$$

$$P_c A_2 + (K_p + P_a C_s - P_o C_s) x = P_g A_3 + P_a A_1 - F_p \tag{5-26}$$

For the preliminary analysis of the valve dynamics, a linearized expression is sufficient. Considering small perturbations about a steady-state operating point, Equations (5-20), (5-21), and (5-22) become:

$$\Delta P_c = \frac{G_1}{1 + \tau_b S}\left[\tau_a S\, \Delta x - \Delta y\right] \tag{5-27}$$

$$\Delta P'_c = \frac{G'_1\, \Delta y}{1 + \tau_c S} \tag{5-28}$$

$$\Delta y = \frac{1}{K_s}\left[\Delta P_c A_4 - \Delta P'_c A_4 + F_t\right] \tag{5-29}$$

$$\Delta x = -\frac{A_2}{K_e}\left(\frac{1}{\tau_d^2 S^2 + 1}\right) \Delta P_c \tag{5-30}$$

where P_{ci}, P'_{ci}, x_i, and y_i are initial conditions, and

$$\tau_c = \frac{A_2}{R_g \sqrt{T_g}\, C_g C_f f_1\left(\frac{P_e}{P_{ci}}\right)}$$

$$\tau_b = \frac{V_{co} - A_2 x_i}{C_g R_g \sqrt{T_g}\left[C_f(y_i+y_o) f_1\left(\frac{P_e}{P_{ci}}\right) - C_f(y_i+y_o)\frac{P_e}{P_{ci}} f_1'\left(\frac{P_e}{P_{ci}}\right) - A_i f_1'\left(\frac{P_{ci}}{P_g}\right)\right]}$$

$$G_1 = \frac{C_f P_{ci} f_1\left(\frac{P_e}{P_{ci}}\right)}{C_f(y_i+y_o) f_1\left(\frac{P_e}{P_{ci}}\right) - C_f(y_i+y_o)\frac{P_e}{P_{ci}} f_1'\left(\frac{P_e}{P_{ci}}\right) - A_i f_1'\left(\frac{P_{ci}}{P_g}\right)}$$

$$G_1' = \frac{C_f P'_{ci} f_1\left(\frac{P_e}{P'_{ci}}\right)}{C_f(y_o - y_i) f_1\left(\frac{P_e}{P'_{ci}}\right) - C_f(y_o - y_i)\frac{P_e}{P'_{ci}} f_1'\left(\frac{P_e}{P'_{ci}}\right) - A_i f_1'\left(\frac{P'_{ci}}{P_g}\right)}$$

$$\tau_c = \frac{V_{co}}{C_g R_g \sqrt{T_g}\left[C_f(y_o - y_i) f_1\left(\frac{P_e}{P'_{ci}}\right) - C_f(y_o - y_i)\frac{P_e}{P'_{ci}} f_1'\left(\frac{P_e}{P'_{ci}}\right) - A_i f_1'\left(\frac{P'_{ci}}{P_g}\right)\right]}$$

$$\tau_d = \sqrt{\frac{m_p}{K_e}}$$

$$K_e = K_p + P_a C_s - P_o C_s$$

S = Laplace operator

The valve dynamics are illustrated by the block diagram of Figure 5-4. Using the transfer function notation shown in the figure, the over-all transfer function is:

$$\frac{\Delta \dot{W}_s}{\Delta F_t} = \frac{G_a G_b G_c G_d}{(1 + G_a H_b H_c)(1 + G_c G_b H_d) + G_a G_b H_a} \qquad (5\text{-}31)$$

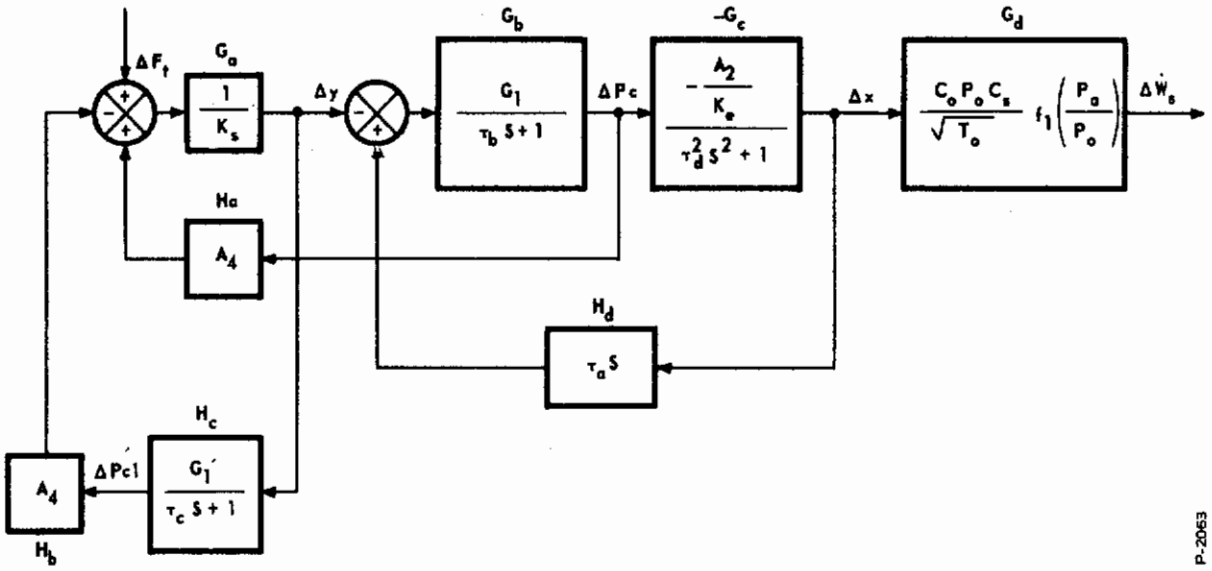

Figure 5-4 - Block Diagram of Linearized Poppet Valve Dynamics

The numerator reduced to:

$$\frac{G_1 A_2}{K_s K_e}(\tau_c S+1)\ \frac{C_o P_o C_s}{\sqrt{T_o}}\ f_1\left(\frac{P_a}{P_o}\right)$$

and the denominator becomes:

$$\left[\tau_b \tau_c \tau_d^2\right] S^4 + \tau_d^2\left[\tau_b\left(1+\frac{A_4 G_1'}{K_s}\right)+\tau_c\left(1+\frac{A_4 G_1}{K_s}\right)\right] S^3$$

$$+\left[\tau_c\left(\tau_b+\frac{A_2 G_1}{K_e}\tau_a\right)+\tau_d^2\left(\frac{A_4 G_1'}{K_s}+\frac{A_4 G_1}{K_s}\right)\right] S^2$$

$$+\left[\frac{A_2 G_1}{K_e}\tau_a\left(1+\frac{A_4 G_1'}{K_s}\right)+\tau_b\left(1+\frac{A_4 G_1'}{K_s}\right)+\tau_c\left(1+\frac{A_4 G_1}{K_s}\right)\right] S$$

$$+\ 1+\frac{A_4 G_1'}{K_s}+\frac{A_4 G_1}{K_s}$$

For stability, Routh's criterion requires that:

$$a_3 a_2 > a_4 a_1 \tag{5-32}$$

$$a_3 a_2 a_1 > a_3^2 a_0 + a_1^2 a_4 \tag{5-33}$$

$$a_0 > 0 \tag{5-34}$$

where $a_0 \ldots\ldots a_4$ are the coefficients of the corresponding powers of S in the denomenator.

5.4.4 Preliminary Design

The design of the poppet valve is based upon the following assumed conditions and parameters:

$T_o = 5000°F$

$P_o = 200$ psia

$k_o = 1.25$

Combustion gas molecular weight = 10.5 lb/mole

$R_o = 6.9 \times 10^5$ in^2/sec^2 °R

$C_o = 0.324$

$T_g = 2000°F$

$P_g = 600$ psia

$k_g = 1.324$

Control gas molecular weight = 4.8 lb/mole

$R_g = 15.0 \times 10^5$ in^2/sec^2 °R

$C_g = 0.212$

$$P_e \approx 0 \text{ psia}$$

$$P_a = 20 \text{ psia}$$

The basic requirement of the valve is to meter flow rates of from zero to 12.8 lb/sec as a direct function of the input command. Specific requirements for response are undefined, except that it be stable.

The assumption is made that $\dot{W}_s$, y, and x must be zero when F_t is zero. For this case, Equations (5-23) through (5-26) become:

$$P_{co} = P'_{co} = \frac{P_g A_i f_1\left(\frac{P_{co}}{P_g}\right)}{C_f y_o f_1\left(\frac{P_e}{P_{co}}\right)} \qquad (5\text{-}35)$$

$$F_p = P_g A_e + P_a A_1 - P_{co} A_2 \qquad (5\text{-}36)$$

The various parameters, in the order in which they were selected or computed are as follows:

$$A_1 = (A_s)_{max} = 15 \text{ in.}^2$$

$$(x)_{max} = 5.0 \text{ in.}$$

$$C_s = 3.0 \text{ in.}$$

$$P_{co} = 310 \text{ psia}$$

$$A_3 = 15 \text{ in.}^2$$

$$A_2 = 30 \text{ in.}^2$$

$$F_p = 0 \text{ lb}$$

$$(P'_c)_{max} = 500 \text{ psia}$$

$$(y)_{max} = 0.020 \text{ in.}$$

$$y_o = 0.038 \text{ in.}$$

$$(P_c)_{min} = 204 \text{ psia}$$

$$A_4 = 0.049 \text{ in.}^2$$

$$C_f = 0.785 \text{ in.}$$

$$K_s = 25 \text{ lb/in.}$$

$$(F_t)_{max} = 15 \text{ lb}$$

$$A_i = 0.015 \text{ in.}^2$$

$$\dot{W}_i = 0.039 \text{ lb/sec}$$

$$K_p = 1180 \text{ lb/in.}$$

$$V_{co} = 180 \text{ in.}^3$$

$$m_p = 0.0934 \text{ lb-sec}^2/\text{in.}$$

$$K_e = 1180 - (180)3 = 640 \text{ lb/in.}$$

The values of the time constants and gains at the condition of zero injectant flow are:

$$\tau_a = 2.42 \times 10^{-6} \text{ sec}$$

$$\tau_b = 3.82 \times 10^{-4} \text{ sec}$$

$$\tau_c = 3.82 \times 10^{-4} \text{ sec}$$

$$\tau_d = 0.012 \text{ sec}$$

$$G_1 = 8.15 \times 10^3 \text{ lb/in.}^3$$

$$G'_1 = 8.15 \times 10^3 \text{ lb/in.}^3$$

The over-all transfer function is:

$$\left(\frac{\Delta \dot{W}_s}{\Delta F_t}\right)_{\text{zero flow}} = \frac{1.23\,(3.82 \times 10^{-4} S + 1)}{\left[0.636 \times 10^{-12}\right]S^4 + \left[5.67 \times 10^{-8}\right]S^3 + \left[1.395 \times 10^{-4}\right]S^2 + \left[8.70 \times 10^{-4}\right]S + 1} \tag{5-37}$$

The values of the time constants and gains at the condition of maximum injectant flow are:

$$\tau_a = 2.42 \times 10^{-6} \text{ sec}$$

$$\tau_b = 4.18 \times 10^{-5} \text{ sec}$$

$$\tau_c = 2.32 \times 10^{-4} \text{ sec}$$

$$\tau_g = 0.012 \text{ sec}$$

$$G_1 = 3.52 \times 10^{3} \text{ lb/in.}^3$$

$$G_1' = 7.96 \times 10^{3} \text{ lb/in.}^3$$

The over-all transfer function is:

$$\left(\frac{\Delta \dot{W}_s}{\Delta F_t}\right)_{\text{zero flow}} = \frac{0.69\,(2.32 \times 10^{-4} S + 1)}{\left[0.547 \times 10^{-12}\right]S^4 + \left[1.42 \times 10^{-8}\right]S^3 + \left[1.27 \times 10^{-4}\right]S^2 + \left[3.34 \times 10^{-4}\right]S + 1} \tag{5-38}$$

The application of Equations (5-32), (5-33), and (5-34) show the valve to be stable at both of the extreme flow conditions. A computer simulation of the valve, however, shows that its reponse is highly oscillatory. This requires additional damping, which can be obtained by closing the loop around the poppet valve or by using s suitable compensation in the over-all thrust vector control loop. It was determined that sufficient damping will result if a flow transducer is used to close the loop around the valve, and lead-lag compensation defined by:

$$\Delta F_t = \frac{1 + 0.10\,S}{1 + 0.01\,S}\,(\Delta i - \Delta \dot{W}_s)$$

is used. With this compensation, the valve loop transfer function can be approximated by:

$$\frac{\Delta \dot{W}_s}{\Delta i} = \frac{0.854}{1 + (0.046)S + (0.0058)S^2}$$

where Δi is the input current for actuating the flapper.

The practicability of closing the loop around the poppet valve is open to some question because of the high temperatures to which the flow transducer would be exposed. A flow meter directly in the injectant gas stream would be pretty much out of the question since 5000°F gas is used. A potentiometer connected to the poppet would be more reasonable, but it would have to be insulated from the environment and most likely cooled by a special system. A scheme which appears to offer greatest reliability is to pneumatically sense the poppet position, pass the signal through a pneumatic lead-lag network, and direct the resulting pneumatic pressure against a piston or bellows attached to the flapper.

5.4.5 Nomenclature

Symbol	Definition
$a_0, \ldots a_4$	Coefficients of corresponding powers of S in characteristic equation
A_1	Effective area of exit nozzle, in.^{2}
A_2	Rear area of poppet piston, in.^{2}
A_3	Frontal area of poppet piston, in.^{2}
A_4	Area of flapper nozzle, in.^{2}
A_f	Effective restricting area of flapper valve, in.^{2}
A_i	Effective area of by-pass orifice, in.^{2}
A_s	Effective area of poppet opening, in.^{2}
C_f	Flapper valve coefficient, in.
C_g	A gas constant for control gas
C_o	A gas constant for supply gas
C_s	Poppet area coefficient, in.

Symbol	Definition
F_p	Preload on poppet spring, lb
F_t	Control force on flapper, lb
g	Acceleration of gravity, in./sec^2
G_l	Lumped constant, lb/in.^{3}
G_a,...G_d	Transfer functions (see Figure 5-4)
H_a,...H_4	Transfer functions (see Figure 5-4)
k_g	Ratio of specific heats for control gas
k_o	Ratio of specific heats for supply gas
K_e	Lumped constant, lb/in.
K_p	Stiffness of mechanical poppet spring, lb/in.
K_s	Stiffness of mechanical flapper spring, lb/in.
m_p	Mass of poppet, lb-sec^2/in.
P_a	Pressure downstream of poppet, psia
P_c	Control pressure behind poppet piston, psia
P_e	Ambient pressure at valve, psia
P_g	Control gas pressure, psia
P_o	Supply gas pressure, psia
R_g	Universal gas constant for control gas, in.^{2}/sec^2 °R
R_o	Universal gas constant for supply gas, in.^{2}/sec^2 °R
S	Laplace operator, 1/sec
T_o	Supply gas temperature, °R
T_g	Control gas temperature, °R
V_c	Volume behind poppet piston, in.^{3}
V_{co}	Volume behind poppet piston when x = 0, in.^{3}
$\dot{W}_f$	Flow rate through flapper valve, lb/sec
$\dot{W}_i$	Flow rate through valve by-pass orifice, lb/sec

Symbol	Definition
$\dot{W}_s$	Injectant flow rate, lb/sec
x	Displacement of poppet, in.
y	Displacement of flapper, in.
y_o	Flapper gap at y = 0, in.
Δ	Prefix to denote small change
ρ_c	Density of gas behind poppet piston lb-sec^2/in.^{4}
$\tau_a, \ldots \tau_d$	Time constants (see text)
$f_1\left(\frac{P_x}{P_y}\right)$	Orifice flow function
$f'_1\left(\frac{P_x}{P_y}\right)$	Derivative of orifice flow function with respect to P_x/P_y
$(\,)'$	Primed symbols refer to the opposing poppet valve
$(\,)_i$	Subscript i refers to the operating point about which the linearized dynamics pertain
$(\dot{})$	Denotes first derivative with respect to time
$(\ddot{})$	Denotes second derivative with respect to time

5.5 SECONDARY INJECTION VORTEX VALVE

5.5.1 Description

A vortex valve is an "all-fluid" control element having no moving mechanical parts. The valving action is produced by interaction between the control flow and supply flow. A schematic diagram of the valve is shown in Figure 5-5. In the absence of control flow, the main flow proceeds radially toward the central outlet orifice of the vortex chamber. This condition produces the maximum total flow through the valve. The addition of control flow imparts a rotational flow component to the supply flow as it passes the control inlet orifice. The supply flow entering the vortex chamber then has a tangential velocity component in addition to the radial velocity. As the flow proceeds toward the center of the valve the tangential

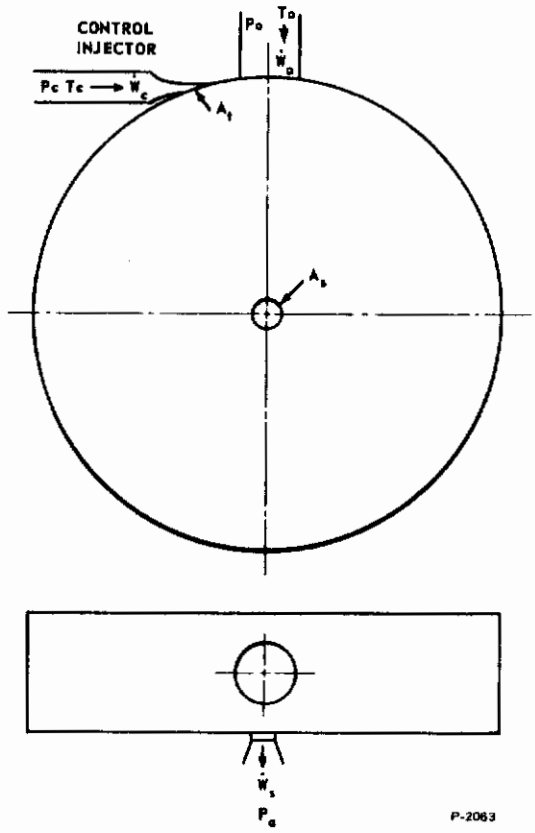

Figure 5-5 - Schematic Diagram of Vortex Valve

velocity increase is required for the inward moving gas to maintain its original angular momentum. The effect is similar to the increase in rotational velocity when a person rotating, with arms stretched out, pulls his arms toward his body. In the vortex valve the effect is complicated by the viscous coupling of the gas and by the compressibility of the gas. The faster rotating gas, located toward the center of the valve, tends to drive the slower moving outer layers. The two-dimensional vortex flow in the chamber thus bootstraps itself. Near the outlet hole the flow field changes from two-dimensional flow into a three-dimensional vortex by the sink effect of the center hole. Maximum velocities occur near the center of the vortex chamber.

The complete valve system can consist of one or more vortex valve stages, depending upon the gain required. For a valve with three vortex stages, for example, the final stage is sized to handle the range of flow required. The control flow port is connected to the inlet of a smaller vortex second stage, and the control port of the second stage is in turn connected to the inlet of a still smaller, but similar, vortex first stage. The control flow from the first stage can be controlled by a flapper nozzle valve in accordance with an electrical signal.

Power gain in each vortex stage is achieved through the ability of a small change in angular momentum of the fluid in the chamber to greatly affect the flow through the chamber. The angular momentum is induced by tangential jets near the outer wall of the chamber which bias the valve at the high gain portion of its operating range. Changes in angular momentum are created by bleeding off a small flow to reduce the effect of the bias flow. When vortex stages are coupled they must be properly matched so that the flow range of each driving stage is compatible with the control flow requirements of its following stage at the existing operating pressure level.

This is basically an all-fluid system with no moving parts other than the flapper nozzle valve pilot stage which is used to generate a low level pneumatic input signal. This approach results in inherent simplicity and potentially high reliability. Control system development trends indicate that all-fluid techniques will find wide application in space. The basic vortex valve phenomena has been demonstrated, and vortex valve characteristics appear to be particularly desirable for systems requiring flow control with relatively high gain. It is anticipated that the vortex valve will become an extremely useful control device for many severe applications, including those where the control fluid is extremely hot and highly contaminated and accelerations are extremely high.

5.5.2 Simplified Performance Equations

A purely analytical approach to the general solution of a physical three-dimensional viscous vortex flow is not practical. The three-dimensional compressible flow and the internal losses in the valve due to viscous drag are not predictable by purely analytical means. A simplified analysis, based on a number of assumptions verified by simple basic experiments, serves as an excellent guide in the initial design of vortex devices and gives an insight into the basic capabilities and limitations of the vortex valve.

In a vortex valve, near maximum flow occurs at zero control flow. The design of the valve is such that the outlet port is the flow restricting area. This flow may be calculated using the adiabatic flow equation for a compressible gas.

$$\dot{W}_{so} = \frac{C_o A_s P_o}{\sqrt{T_o}} f_1\left(\frac{P_a}{P_o}\right), \qquad (5\text{-}39)$$

where:

$$C_o = g\sqrt{\frac{k}{R_o}\left(\frac{2}{k+1}\right)^{\frac{k+1}{k-1}}}$$

A_s = Effective area of outlet orifice restriction (includes orifice coefficient), $in.^2$

P_o and T_o are the inlet gas pressure and temperature. $f_1(P_a/P_o)$ is the conventional orifice flow function, sometimes referred to as A*/A:

$$f_1\left(\frac{P_a}{P_o}\right) = \sqrt{\frac{2}{k-1}\left(\frac{k+1}{2}\right)^{\frac{k+1}{k-1}}}\left(\frac{P_a}{P_o}\right)^{\frac{1}{k}}\sqrt{1-\left(\frac{P_a}{P_o}\right)^{\frac{k-1}{k}}}$$

when:

$$\frac{P_a}{P_o} \geq \left(\frac{2}{k+1}\right)^{\frac{1}{k-1}}$$

and,

$$f_1\left(\frac{P_a}{P_o}\right) = 1$$

when:

$$\frac{P_a}{P_o} \leq \left(\frac{2}{k+1}\right)^{\frac{k}{k-1}}$$

The expression for the control flow is:

$$\dot{W}_c = \frac{C_g A_t P_c}{\sqrt{T_c}} f_1\left(\frac{P_o}{P_c}\right) \qquad (5\text{-}40)$$

where: $C_g = g\sqrt{\frac{k}{R_g}\left(\frac{2}{k+1}\right)^{\frac{k+1}{k-1}}}$

A_t = Effective orifice area restricting the control gas, $in.^2$

The normalized linearized steady flow characteristic of an optimum single vortex valve stage is shown in Figure 5-6. As the control flow is increased from zero, the total flow initially increases very slightly (1 to 2 percent), and then abruptly drops to the minimum level. This region of abrupt change is the operating region of the valve, therefore the control pressure is manipulated in the vicinity of 1.3 P_o to 1.5 P_o. For the valve characteristics assumed here, the gain of the stage is:

$$K_v = -\frac{\Delta\dot{W}_s}{\Delta P_c} = 5\,\frac{\dot{W}_{so}}{P_o} \qquad (5\text{-}41)$$

It is also seen that the control flow at maximum cut-off is 10 percent of the maximum primary flow.

The dynamic performance of a single vortex valve stage is predicted on the basis of the simplified flow path shown in Figure 5-7. The assumption is made that the only significant volume in the valve occurs just upstream of the outlet restriction. It is also assumed that isothermal conditions prevail.

The significant equations then are:

$$\dot{W}_{so} - K_v\,(P_c - 1.34\,P_o) - \frac{C_o A_s P_v}{\sqrt{T_o}}\, f_1\left(\frac{P_a}{P_v}\right) = \frac{V_v}{R_o T_o}\,\frac{dP_v}{dt}. \qquad (5\text{-}42)$$

$$\dot{W}_s = \frac{C_o A_s P_v}{\sqrt{T_o}}\, f_1\left(\frac{P_a}{P_v}\right) \qquad (5\text{-}43)$$

Linearizing and combining Equations (5-42) and (5-43) gives the following result:

$$\frac{\Delta\dot{W}_s}{\Delta P_c} = \frac{-K_v}{\tau_v S + 1} \qquad (5\text{-}44)$$

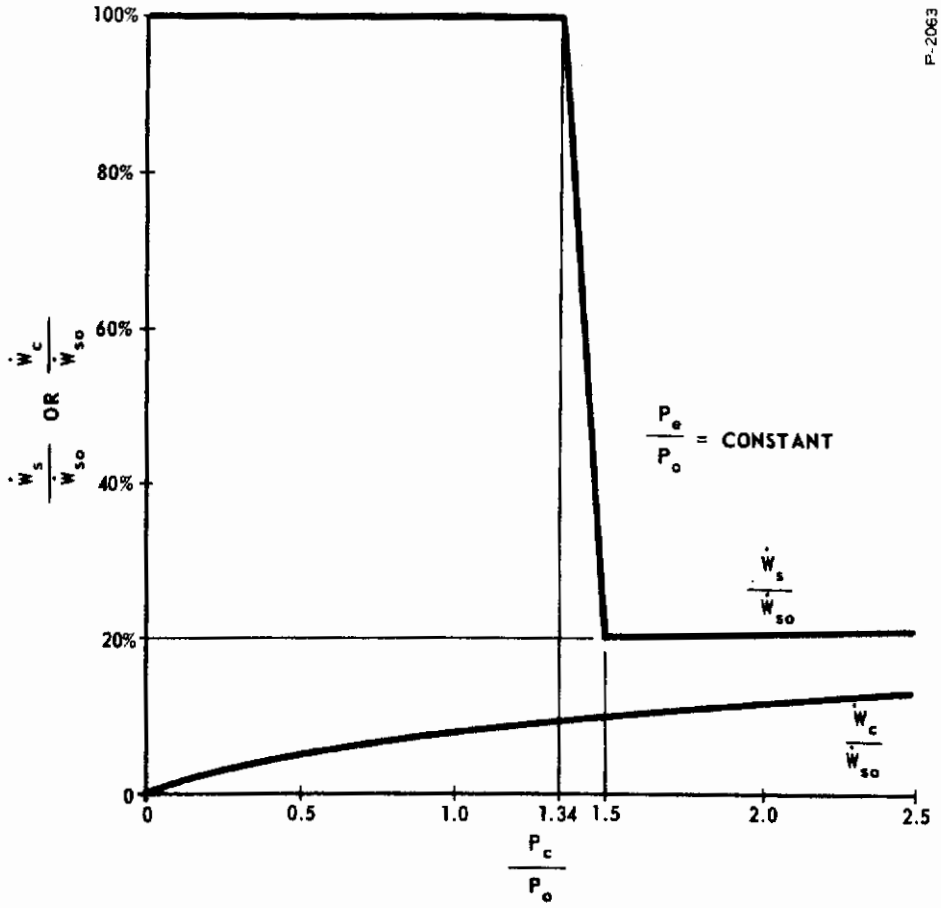

Figure 5-6 - Linearized Vortex Flow Characteristics

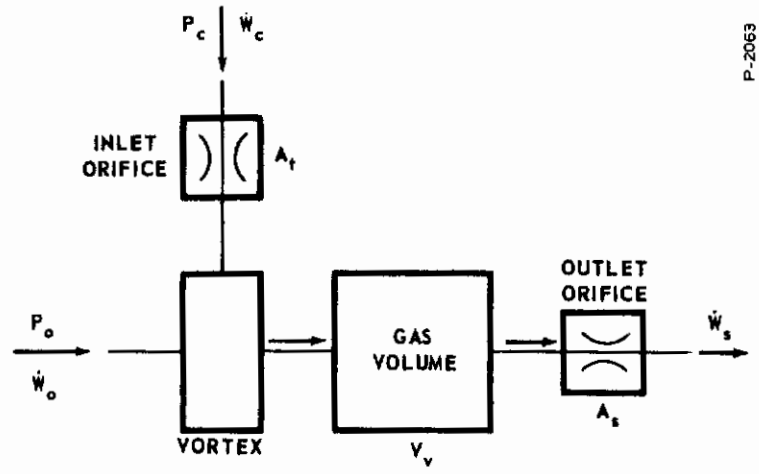

Figure 5-7 - Schematic Diagram of Simplified Vortex Valve Flow Path

where:
$$\tau_v = \frac{V_v}{R_o C_o A_s \sqrt{T_o}\left[f_1\left(\frac{P_a}{P_{vi}}\right) - \frac{P_a}{P_{vi}} f_1'\left(\frac{P_a}{P_{vi}}\right)\right]}$$

P_{vi} is determined from Equation (5-43) for a given initial value of $\dot{W}_s$. Insofar as $\dot{W}_o$ is concerned, we have assumed the response to be instantaneous, whereby the expression is then simply,

$$\dot{W}_o = W_{so} - K_v (P_c - 1.34 P_o) - \frac{C_g A_t P_c}{\sqrt{T_c}} f_1\left(\frac{P_o}{P_c}\right) \qquad (5\text{-}45)$$

In linearized form, Equation (5-45) is:

$$\frac{\Delta \dot{W}_o}{\Delta P_c} = -\left[K_v + \frac{C_g A_t}{\sqrt{T_c}} f_1\left(\frac{P_o}{P_{ci}}\right) - \frac{C_g A_t}{\sqrt{T_c}} \frac{P_o}{P_{ci}} f_1'\left(\frac{P_o}{P_{ci}}\right)\right] \qquad (5\text{-}46)$$

5.5.3 Three-Stage Valve

The dynamics of a three-stage valve is next investigated. Using the system shown in Figure 5-8, the following equations based upon isothermal flow are obtained.

$$\frac{C_g A_{g3} P_g}{\sqrt{T_g}} f_1\left(\frac{P_{c3}}{P_g}\right) - \frac{C_g A_{t3} P_{c3}}{\sqrt{T_g}} f_1\left(\frac{P_o}{P_{c3}}\right) - \dot{W}_{b3} = \frac{V_3}{R_g T_g} \frac{dP_{c3}}{dt} . \qquad (5\text{-}47)$$

$$\frac{C_g A_{g2} P_g}{\sqrt{T_g}} f_1\left(\frac{P_{c2}}{P_g}\right) - \frac{C_g A_{t2} P_{c2}}{\sqrt{T_g}} f_1\left(\frac{P_{c3}}{P_{c2}}\right) - \dot{W}_{b2} = \frac{V_2}{R_g T_g} \frac{dP_{c2}}{dt} . \qquad (5\text{-}48)$$

$$\frac{C_g A_{g1} P_g}{\sqrt{T_g}} f_1\left(\frac{P_{c1}}{P_g}\right) - \frac{C_g A_{t1} P_{c1}}{\sqrt{T_g}} f_1\left(\frac{P_{c2}}{P_{c1}}\right) - \dot{W}_{b1} = \frac{V_1}{R_g T_g} \frac{dP_{c1}}{dt} . \qquad (5\text{-}49)$$

$$\dot{W}_{b3} = \dot{W}_{eo2} - K_{v2}(P_{c2} - 1.34 P_{c3}) - \frac{C_g A_{t2} P_{c2}}{\sqrt{T_g}} f_1\left(\frac{P_{c3}}{P_{c2}}\right) \qquad (5\text{-}50)$$

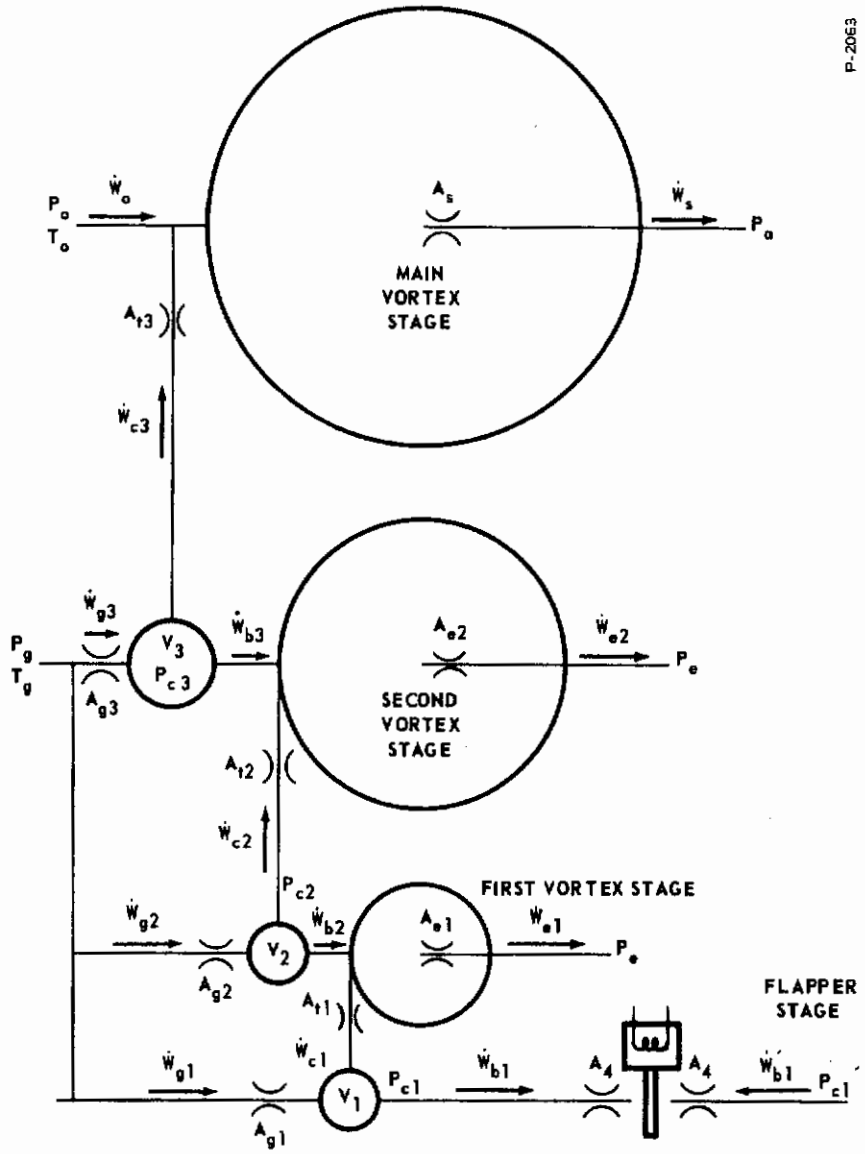

Figure 5-8 - Schematic Diagram of Secondary Injection Valve with Three Vortex Stages

$$\dot{W}_{eo2} = \frac{C_g A_{e2} P_{c3}}{\sqrt{T_g}} f_1\left(\frac{P_a}{P_{c3}}\right) \qquad (5\text{-}51)$$

$$\dot{W}_{b2} = \dot{W}_{eo1} - K_{v1}(P_{c1} - 1.34 P_{c2}) - \frac{C_g A_{t1} P_{c1}}{\sqrt{T_g}} f_1\left(\frac{P_{c2}}{P_{c1}}\right) \qquad (5\text{-}52)$$

$$\dot{W}_{eo1} = \frac{C_g A_{e1} P_{c2}}{\sqrt{T_g}} f_1\left(\frac{P_a}{P_{c2}}\right) \tag{5-53}$$

$$\dot{W}_{b1} = \frac{C_g A_t P_{c1}}{\sqrt{T_g}} f_1\left(\frac{P_a}{P_{c1}}\right) \tag{5-54}$$

$$A_f = \sqrt{4\pi A_4}\,(y_o + y) \tag{5-55}$$

$$y = \frac{F_t - (P'_{c1} - P_{c1})\,A_4}{K_s} \tag{5-56}$$

Note that the flapper valve is the same as that used with the poppet valve shown in Figure 5-3. By combining Equations (5-47) through (5-56), the following expressions relating the control pressure are obtained:

$$\Delta P_{c3} = \frac{K_x \Delta P_{c2}}{\tau_x S + 1} \tag{5-57}$$

$$\Delta P_{c2} = \frac{K_{y1} \Delta P_{c1} + K_{y2} \Delta P_{c3}}{\tau_y S + 1} \tag{5-58}$$

$$\Delta P_{c1} = \frac{K_{z1} \Delta P_{c2} - K_{z2} \Delta A_f}{\tau_z S + 1} \tag{5-59}$$

$$\Delta A_f = \left(K_{t1} - \frac{K_{t2}}{\tau_t S + 1}\right)(\Delta F_t + A_4 \Delta P_{c1}) \tag{5-60}$$

The lumped constants used in Equations (5-57) through (5-60) are defined as follows:

$$K_x = \frac{K_3 K_{d3}}{1 + K_3 K_{c3}}$$

$$\tau_x = \frac{\tau_3}{1 + K_3 K_{c3}}$$

$$K_{y1} = \frac{K_2 K_{d2}}{1 + K_2 K_{c2}}$$

$$K_{y2} = \frac{K_{23}}{1 + K_2 K_{c2}}$$

$$\tau_y = \frac{\tau_2}{1 + K_2 K_{c2}}$$

$$K_{z1} = \frac{K_{12}}{1 + K_1 K_{c1}}$$

$$K_{z2} = \frac{K_1 K_f}{1 + K_1 K_{c1}}$$

$$\tau_z = \frac{\tau_1}{1 + K_1 K_{c1}}$$

$$K_{t1} = \frac{\sqrt{4\pi A_4}}{K_s}$$

$$K_{t2} = \frac{K_1' K_f' 4\pi A_4^2}{K_s (K_s + K_s K_1' K_{c1}' + K_1' K_f' A_4 \sqrt{4\pi A_4})}$$

$$\tau_t = \frac{K_s \tau_1'}{K_s + K_s K_1' K_{c1}' + K_1' K_f' A_4 \sqrt{4\pi A_4}}$$

$$K_3 = \frac{1}{\frac{C_g A_{t3}}{\sqrt{T_g}}\left[f_1\left(\frac{P_o}{P_{c3i}}\right) - \frac{P_o}{P_{c3i}} f_1'\left(\frac{P_o}{P_{c3i}}\right)\right] - \frac{C_g A_{g3}}{\sqrt{T_g}} f_1'\left(\frac{P_{c3i}}{P_g}\right)}$$

$$\tau_3 = \frac{V_3/R_g T_g}{\frac{C_g A_{t3}}{\sqrt{T_g}}\left[f_1\left(\frac{P_o}{P_{c3i}}\right) - \frac{P_o}{P_{c3i}} f_1'\left(\frac{P_o}{P_{c3i}}\right)\right] - \frac{C_g A_{g3}}{\sqrt{T_g}} f_1'\left(\frac{P_{c3i}}{P_g}\right)}$$

$$K_{c3} = \frac{C_g A_{e2}}{\sqrt{T_g}}\left[f_1\left(\frac{P_a}{P_{c3i}}\right) - \frac{P_a}{P_{c3i}} f_1'\left(\frac{P_a}{P_{c3i}}\right)\right] + 1.34 K_{v2} - \frac{C_g A_{t2}}{\sqrt{T_g}} f_1'\left(\frac{P_{c3i}}{P_{c2i}}\right)$$

$$K_{d3} = K_{v2} + \frac{C_g A_{t2}}{\sqrt{T_g}}\left[f_1\left(\frac{P_{c3i}}{P_{c2i}}\right) - \frac{P_{c3i}}{P_{c2i}} f_1'\left(\frac{P_{c3i}}{P_{c2i}}\right)\right]$$

$$K_2 = \frac{1}{\frac{C_g A_{t2}}{\sqrt{T_g}}\left[f_1\left(\frac{P_{c3i}}{P_{c2i}}\right) - \frac{P_{c3i}}{P_{c2i}} f_1'\left(\frac{P_{c3i}}{P_{c2i}}\right)\right] - \frac{C_g A_{g2}}{\sqrt{T_g}} f_1'\left(\frac{P_{c2i}}{P_g}\right)}$$

$$K_{23} = \frac{-A_{t2} f_1'\left(\frac{P_{c3i}}{P_{c2i}}\right)}{A_{t2}\left[f_1\left(\frac{P_{c3i}}{P_{c2i}}\right) - \frac{P_{c3i}}{P_{c2i}} f_1'\left(\frac{P_{c3i}}{P_{c2i}}\right)\right] - A_{g2} f_1'\left(\frac{P_{c2i}}{P_g}\right)}$$

$$\tau_2 = \frac{V_2/R_g T_g}{\frac{C_g A_{t2}}{\sqrt{T_g}}\left[f_1\left(\frac{P_{c3i}}{P_{c2i}}\right) - \frac{P_{c3i}}{P_{c2i}} f_1'\left(\frac{P_{c3i}}{P_{c2i}}\right)\right] - \frac{C_g A_{g2}}{\sqrt{T_g}} f_1'\left(\frac{P_{c2i}}{P_g}\right)}$$

$$K_{c2} = \frac{C_g A_{e1}}{\sqrt{T_g}}\left[f_1\left(\frac{P_a}{P_{c2i}}\right) - \frac{P_a}{P_{c2i}} f_1'\left(\frac{P_a}{P_{c2i}}\right)\right] + 1.34 K_{v1} - \frac{C_g A_{t1}}{\sqrt{T_g}} f_1'\left(\frac{P_{c2i}}{P_{c1i}}\right)$$

$$K_{d2} = K_{v1} + \frac{C_g A_{t1}}{\sqrt{T_g}}\left[f_1\left(\frac{P_{c2i}}{P_{c1i}}\right) - \left(\frac{P_{c2i}}{P_{c1i}}\right) f_1'\left(\frac{P_{c2i}}{P_{c1i}}\right)\right]$$

$$K_1 = \frac{1}{\frac{C_g A_{t1}}{\sqrt{T_g}}\left[f_1\left(\frac{P_{c2i}}{P_{c1i}}\right) - \frac{P_{c2i}}{P_{c1i}} f_1'\left(\frac{P_{c2i}}{P_{c1i}}\right)\right] - \frac{C_g A_{g1}}{\sqrt{T_g}} f_1'\left(\frac{P_{c1i}}{P_g}\right)}$$

$$K_{12} = \frac{-A_{t1} f_1'\left(\frac{P_{c2i}}{P_{c1i}}\right)}{A_{t1}\left[f_1\left(\frac{P_{c2i}}{P_{c1i}}\right) - \frac{P_{c2i}}{P_{c1i}} f_1'\left(\frac{P_{c2i}}{P_{c1i}}\right)\right] - A_{g1} f_1'\left(\frac{P_{c1i}}{P_g}\right)}$$

$$\tau_1 = \frac{V_1/R_g T_g}{\frac{C_g A_{t1}}{\sqrt{T_g}}\left[f_1\left(\frac{P_{c2i}}{P_{c1i}}\right) - \frac{P_{c2i}}{P_{c1i}} f_1'\left(\frac{P_{c2i}}{P_{c1i}}\right)\right] - \frac{C_g A_{g1}}{\sqrt{T_g}} f_1'\left(\frac{P_{c1i}}{P_g}\right)}$$

$$K_{c1} = \frac{C_g A_{fi}}{\sqrt{T_g}} \left[f_1\left(\frac{P_e}{P_{cli}}\right) - \frac{P_e}{P_{cli}} f_1'\left(\frac{P_e}{P_{cli}}\right)\right]$$

$$K_f = \frac{C_g P_{cli}}{\sqrt{T_g}} f_1\left(\frac{P_e}{P_{cli}}\right)$$

τ_1', K', K_{c1}', K_f' are the same as τ_1, K_1, K_{c1}, K_f, except that the P_c terms are replaced by P_c' terms.

The linearized dynamics of the system shown in Figure 5-8 is represented by the block diagram of Figure 5-9. The over-all transfer function is:

$$\frac{\Delta \dot{W}_s}{\Delta F_t} = \frac{G_{num.}}{G_{denom.}} \qquad (5\text{-}61)$$

where:

$$G_{num.} = K_{v3} K_x K_{y1} K_{z2} \left[(\tau_t S+1) K_{t1} - K_{t2}\right]$$

$$G_{denom.} = (\tau_{v3} S+1)\Big\{\left[(\tau_x S+1)(\tau_y S+1) - K_x K_{y2}\right]\left[-A_4 K_{z2} K_{t2} + (\tau_t S+1)(\tau_z S+1 + A_4 K_{z2} K_{t1})\right] - (\tau_x S+1)(\tau_t S+1) K_{y1} K_{z1}\Big\}$$

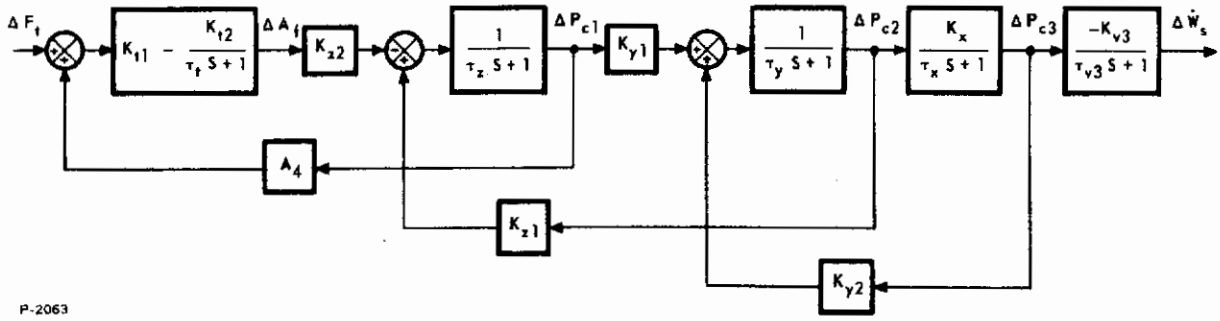

Figure 5-9 - Block Diagram of Injection Valve with Three Vortex Stages

The characteristic equation is:

$$\left[\tau_t \tau_x \tau_y \tau_z\right]S^4+\left[\tau_t \tau_z (\tau_x+\tau_y)+\tau_x \tau_y (\tau_t+\tau_t A_4 K_{z2} K_{t1}+\tau_z)\right]S^3+\left[\tau_x \tau_y (1+A_4 K_{z2} K_{t1} - A_4 K_{z2} K_{t2})+\tau_t \tau_z+(\tau_x+\tau_y)(\tau_t+\tau_t A_4 K_{z2} K_{t1}+\tau_z)-K_{y1} K_{z1} \tau_t \tau_x - K_x K_{y2} \tau_t \tau_z\right]S^2+\left[(\tau_x+\tau_y)(1+A_4 K_{z2} K_{t1}-A_4 K_{z2} K_{t2})+\tau_t+\tau_t A_4 K_{z2} K_{t1}+\tau_z-K_{y1} K_{z1}(\tau_t+\tau_x)-K_x K_{y2}(\tau_t+\tau_t A_4 K_{z2} K_{t1}+\tau_z)\right]S+\left[1+A_4 K_{z2} K_{t1} - A_4 K_{z2} K_{t2}-K_{y1} K_{z1}-K_x K_{y2}(1+A_4 K_{z2} K_{t1}-A_4 K_{z2} K_{t2})\right] = 0 \qquad (5\text{-}62)$$

For stability, the conditions defined by Equations (5-32), (5-33), and (5-34) must be met.

5.5.4 Two-Stage Valve

If the second vortex stage shown in Figure 5-8 is eliminated such that $P_{c2} = P_{c3}$ and $\dot{W}_{b2} = \dot{W}_{b3}$, then the significant relationships are:

$$\Delta P_{c3} = \frac{K_m \Delta P_{c1}}{\tau_m S+1} \qquad (5\text{-}63)$$

$$\Delta P_{c1} = \frac{K_{n1} \Delta P_{c3} - K_{n2} \Delta A_f}{\tau_n S+1} \qquad (5\text{-}64)$$

$$\Delta A_f = K_{t1} - \frac{K_{t2}}{\tau_t S+1}(\Delta F_t + A_4 \Delta P_{c1}) \qquad (5\text{-}65)$$

and the corresponding block diagram is as shown in Figure 5-10. The constants are defined as:

$$K_m = \frac{K_3 K_{d2}}{1+K_3 K_{c2}}$$

$$\tau_m = \frac{\tau_3}{1+K_3 K_{c2}}$$

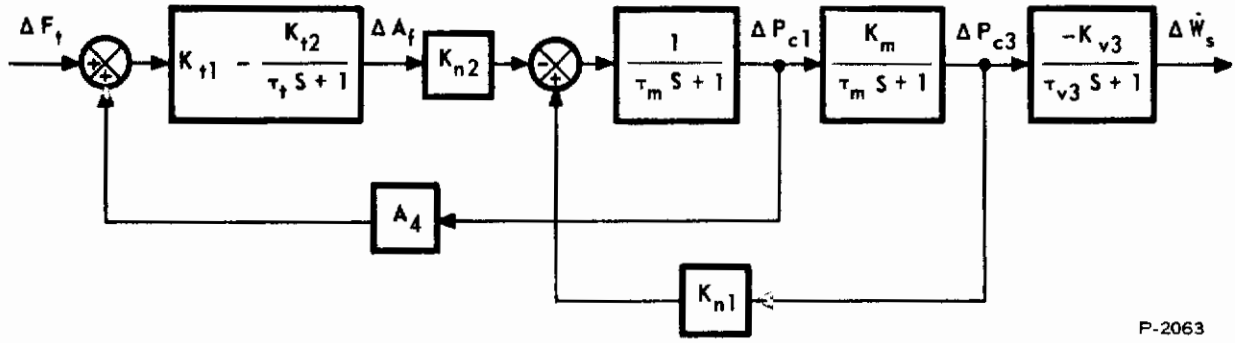

Figure 5-10 - Block Diagram of Injection Valve with Two Vortex Stages

$$K_{n1} = \frac{K_{12}}{1 + K_1 K_{c1}}$$

$$K_{n2} = \frac{K_1 K_f}{1 + K_1 K_{c1}}$$

$$\tau_n = \frac{\tau_1}{1 + K_1 K_{c1}}$$

$$K_{t1} = \frac{\sqrt{4\pi A_4}}{K_s}$$

$$K_{t2} = \frac{4\pi K'_1 K'_f A_4^2}{K_s (K_s + K_s K'_1 K'_{c1} + K'_1 K'_f A_4 \sqrt{4\pi A_4})}$$

$$\tau_t = \frac{K_s \tau'_1}{K_s + K_s K'_1 K'_{c1} + K'_1 K'_f A_4 \sqrt{4\pi A_4}}$$

The terms, K_1, K'_1, K_3, etc., are as previously defined, except that P_{c2} is replaced by P_{c3}, and P'_{c2} by P'_{c3}. The over-all transfer function is:

$$\frac{\Delta \dot{W}_s}{\Delta F_t} = \frac{K_{v3} K_m K_{n2} \left[K_{t1} (\tau_t S+1) - K_{t2}\right]}{(\tau_{v3} S+1)\left[(\tau_m S+1)(\tau_t S+1)(\tau_n S+1 + A_4 K_{n2} K_{t1}) - (\tau_m S+1) K_{n2} K_{t2} A_4 - K_m K_{n1} (\tau_t S+1)\right]} \qquad (5\text{-}66)$$

The characteristic equation is

$$\left[\tau_m \tau_n \tau_t\right]S^3+\left[\tau_n \tau_t+\tau_m(\tau_n+\tau_t+\tau_t A_4 K_{n2} K_{t1})\right]S^2+\left[\tau_m(1+A_4 K_{n2} K_{t1}-A_4 K_{n2} K_{t2})\right.$$

$$\left.+\tau_t(1+A_4 K_{n2} K_{t1}-K_m K_{n1})+\tau_n\right]S+1+A_4 K_{n2} K_{t1}-A_4 K_{n2} K_{t2}-K_m K_{n1}=0 \quad (5\text{-}67)$$

For stability, Ronth's criterion requires that:

$$a_1 a_2 > a_o a_3 \quad (5\text{-}68)$$

$$a_o > 0 \quad (5\text{-}69)$$

where a_o, a_1, a_2, and a_3 are the coefficients of the corresponding powers of S.

5.5.5 Preliminary Design

The requirements and operating conditions used for the design of the vortex valve are essentially the same as those used in the design of the poppet valve, reported in Subsection 5.4.4. Repeating here, they are:

$$\Delta\dot{W}_{s\,max} = 12.8 \text{ lb/sec}$$

$$T_o = 5000°F$$

$$P_o = 200 \text{ psia}$$

$$k_o = 1.25$$

$$R_o = 6.9 \times 10^5 \ \frac{\text{in.}^2}{\text{sec}^2 °R}$$

$$C_o = 0.324$$

$$T_g = 2000°F$$

$$P_g = 600 \text{ psia}$$

$$k_g = 1.324$$

$$R_g = 15.0 \times 10^5 \ \frac{\text{in.}^2}{\text{sec}^2 °R}$$

$$C_g = 0.212$$

$$P_e \approx 0 \text{ psia}$$

$$P_a = 20 \text{ psia}$$

Isothermal conditions are assumed, and in the main vortex stage the temperature of the mixed gas is assumed to be that of the primary flow. Using the linearized performance characteristic shown in Figure 5-6 we find that:

$$(P_{c3})_{min} = 268 \text{ psia}$$

$$(P_{c3})_{max} = 300 \text{ psia}$$

$$\dot{W}_{so} = 16.0 \text{ lb/sec}$$

$$(\dot{W}_s)_{min} = 3.2 \text{ lb/sec}$$

$$(\dot{W}_{c3})_{max} = 1.6 \text{ lb/sec}$$

The above values serve as the starting point for the valve design. Using the equations developed in Subsection 5.5.4 the valve constants are determined. It is found that two vortex stages and one flapper stage are required, the respective parameters being as follows:

$$A_s = 18.3 \text{ in.}^2$$

$$A_{t3} = 1.31 \text{ in.}^2$$

$$(\dot{W}_{c3})_{min} = 1.34 \text{ lb/sec}$$

$$(\dot{W}_{b3})_{min} = 0.075 \text{ lb/sec}$$

$$(\dot{W}_{b3})_{max} = 0.336 \text{ lb/sec}$$

$$A_{g3} = 0.655 \text{ in.}^2$$

$$(P_{c1})_{min} = 359 \text{ psia}$$

$$(P_{c1})_{max} = 450 \text{ psia}$$

$$A_{e1} = 0.293 \text{ in.}^2$$

$$(\dot{W}_{c1})_{max} = 0.0375 \text{ lb/sec}$$

$$A_{t1} = 0.0205 \text{ in.}^2$$

$$(\dot{W}_{c1})_{min} = 0.0280 \text{ lb/sec}$$

$$(A_f)_{min} = 0.0150 \text{ in.}^2$$

$$(A_f)_{max} = 0.0300 \text{ in.}^2$$

$$y_o = 0.020 \text{ in.}^2$$

$$(y)_{max} = 0.020 \text{ in.}$$

$$A_4 = 0.0447 \text{ in.}^2$$

$$(P'_{c1})_{min} = 450 \text{ psia}$$

$$(P'_{c1})_{max} = 540 \text{ psia}$$

$$(F_t)_{max} = 9 \text{ lb}$$

$$K_s = 45 \text{ lb/in.}$$

$$(\dot{W}_{b1})_{min} = 0.0288 \text{ lb/sec}$$

$$(\dot{W}_{b1})_{max} = 0.0459 \text{ lb/sec}$$

$$A_{g1} = 0.0306 \text{ in.}^2$$

$$V_{v3} = 900 \text{ in.}^3$$

$$V_{v1} = 20 \text{ in.}^3$$

$$V_3 = 200 \text{ in.}^3$$

$$V_1 = 10 \text{ in.}^3$$

The dynamic constants are computed to be:

A. For P_{c3} = 300 psia, P_{c1} = 450 psia: (minimum flow)

$$K_{t1} = 0.01667 \text{ in.}^2/\text{lb}$$

$$K_{t2} = 0.01354 \text{ in.}^2/\text{lb}$$

$$\tau_t = 1.541 \times 10^{-6} \text{ sec}$$

$$K_m = 0.370$$

$$\tau_m = 3.15 \times 10^{-6} \text{ sec}$$

$$K_{n1} = 0.161$$

$$K_{n2} = 5940 \text{ lb/in.}^4$$

$$\tau_n = 8.35 \times 10^{-6} \text{ sec}$$

$$\tau_{v3} = 2.98 \times 10^{-6} \text{ sec}$$

$$K_{v3} = 0.400 \text{ in.}^2/\text{sec}$$

B. For P_{c3} = 268 psia, P_{c1} = 359 psia: (maximum flow)

$$K_{t1} = 0.01667 \text{ in.}^2/\text{lb}$$

$$K_{t2} = 0.01320 \text{ in.}^2/\text{lb}$$

$$\tau_t = 1.255 \times 10^{-6} \text{ sec}$$

$$K_m = 0.334$$

$$\tau_m = 2.82 \times 10^{-6} \text{ sec}$$

$$K_{n1} = 0.308$$

$$K_{n2} = 4950 \text{ lb/in.}^4$$

$$\tau_n = 8.80 \times 10^{-6} \text{ sec}$$

$$\tau_{v3} = 2.98 \times 10^{-6} \text{ sec}$$

$$K_{v3} = 0.400 \text{ in.}^2/\text{sec}$$

Substitution of the above constants into Equation (5-66) gives the linearized valve transfer function at conditions of minimum and maximum flow. They are:

$$\frac{\Delta \dot{W}_s}{\Delta F_t} = \frac{1.556\left[(8.22 \times 10^{-6})S + 1\right]}{\left[(2.98 \times 10^{-6})S+1\right]\left[(22.8 \times 10^{-18})S^3 + (37.0 \times 10^{-12})S^2 + (12.65 \times 10^{-6})S+1\right]} \tag{5-70}$$

when $\dot{W}_s = 3.2$ lb/sec and $F_t = 0$ lb, and

$$\frac{\Delta \dot{W}_s}{\Delta F_t} = \frac{1.376\left[(6.03 \times 10^{-6})S + 1\right]}{\left[(2.98 \times 10^{-6})S+1\right]\left[(18.75 \times 10^{-18})S^3 + (31.5 \times 10^{-12})S^2 + (11.74 \times 10^{-6})S+1\right]} \tag{5-71}$$

when $\dot{W}_s = 16.0$ lb/sec and $F_t = 9.0$ lb.

The application of Equations (5-68) and (5-69) to the above transfer functions shows that the valve is stable. Further study of the transfer functions shows that the valve is critically damped, and therefore, requires no compensation loop around it.

The general character of the valve response can be obtained by examining the third order polynomial in the denominator. This cubic is of the form:

$$\frac{1}{a_3 S^3 + a_2 S^2 + a_1 S + a_o}$$

Rewrite it to put it into the form:

$$\frac{B}{\left(\frac{S}{\omega_{ns}}\right)^3 + A\left(\frac{S}{\omega_{ns}}\right)^2 + \frac{S}{\omega_{ns}} + B}$$

where:

$$\omega_{ns}^2 = \frac{a_1}{a_3}$$

$$A\omega_{ns} = \frac{a_2}{a_3}$$

$$B\omega_{ns} = \frac{a_o}{a_1}$$

For the two valve transfer functions, these coefficients are:

$\omega_{ns}^2, \frac{rad^2}{sec^2}$	Minimum Flow Condition 55.5×10^{10}	Maximum Flow Condition 62.5×10^{10}
A	2.27	1.88
B	0.106	0.107

These values are characteristic of a system which is nearly critically damped. This can be further demonstrated by dropping the third order term, whereby the damping ratio of the resulting second order system is essentially unity.

5.5.6 Nomenclature

Symbol		Definition
$a_o,\ldots,a_3$	=	Coefficients of corresponding powers of S
A_e	=	Effective exit orifice area of secondary vortex stage, $in.^2$
A_f	=	Effective restricting area of flapper valve, $in.^2$
A_g	=	Effective area of control gas throttling orifice, $in.^2$
A_s	=	Effective exit orifice area of main vortex stage, $in.^2$.
A_t	=	Vortex inlet orifice area, $in.^2$

Symbol		Definition
C_g	=	A gas constant for control gas
C_o	=	A gas constant for supply gas
F_t	=	Control force on flapper, lb
g	=	Acceleration of gravity, in./sec^2
k	=	Ratio of specific heats
$K_1, K_{12}, K_2, K_{23}, K_3$	=	Lumped constants (see text)
$K_{c1}, K_{c2}, K_{c3}, K_{d2}, K_{d3}, K_f$	=	Lumped constants (see text)
$K_m, K_{n1}, K_{n2}, K_{t1}, K_{t2}$	=	Lumped constants (see text)
$K_x, K_{y1}, K_{y2}, K_{z1}, K_{z2}$	=	Lumped constants (see text)
K_s	=	Stiffness of mechanical flapper spring, lb/in.
K_v	=	Gain of vortex stage, in.^{2}/sec
P_a	=	Pressure downstream of main vortex stage, psia
P_c	=	Control pressure at each vortex inlet, psia
P_e	=	Ambient pressure at valve, psia
P_g	=	Control gas pressure, psia
P_o	=	Supply gas pressure, psia
P_v	=	Effective pressure upstream of vortex exit orifice, psia
R_g	=	Universal gas constant for control gas, in.^{2}/sec^2-°R
R_o	=	Universal gas constant for supply gas, in.^{2}/sec^2-°R
S	=	Laplace operator, 1/sec
T_g	=	Temperature of control gas, °R
T_o	=	Temperature of supply gas, °R
V	=	Gas volume upstream of vortex inlet orifice, in.^{3}
V_v	=	Volume upstream of vortex exit orifice, in.^{3}

Symbol		Definition
$\dot{W}_b$	=	Flow rate between valve stages, lb/sec
$\dot{W}_c$	=	Flow rate of control gas into vortex stage, lb/sec
$\dot{W}_e$	=	Flow rate out of secondary vortex stage, lb/sec
$\dot{W}_o$	=	Flow rate of supply gas into main vortex stage, lb/sec
$\dot{W}_s$	=	Injectant flow rate, lb/sec
$\dot{W}_{so}$	=	Maximum injectant flow rate, lb/sec
y	=	Displacement of flapper, in.
y_o	=	Flapper gap at y = 0, in.
Δ	=	Prefix to denote small change
$\tau_1, \tau_2, \tau_3, \tau_m, \tau_n$	=	Time constants (see text)
$\tau_v, \tau_x, \tau_y, \tau_z$	=	Time constants (see text)
$f_1(P_x/P_y)$	=	Orifice flow function
$f_1'(P_x/P_y)$	=	Derivative of orifice flow function with respect to P_x/P_y
$(\ )'$	=	Primed symbols refer to the opposing valve system
$(\ )_1$	=	Subscript 1 refers to first vortex stage
$(\ )_2$	=	Subscript 2 refers to second vortex stage
$(\ )_3$	=	Subscript 3 refers to main vortex stage
$(\ )_i$	=	Subscript i refers to the operating point about which the linearized dynamics pertain
$(\dot{})$	=	Denotes first derivative with respect to time
$(\ddot{})$	=	Denotes second derivative with respect to time

5.6 VALVE COMPARISON

From Subsections 5.4.4 and 5.5.5, it is found that the rates of gas consumption of the two valves when the main engine is firing but no thrust vector deflection is taking place are:

Poppet valve quiescent flow = 0.078 lb/sec

Vortex valve quiescent flow = 6.68 lb/sec

This sizeable difference is not as serious as it appears at first glance, since 6.4 lb/sec of the vortex valve flow rate is directed into the main engine nozzle where it acts to increase the net thrust. As pointed out in Article 5.2, however, secondary injection lowers the specific impulse by a small but sufficient amount to make some of the injectant flow appear to be wasted. Accurate information on this effect is not available, so for the present comparison, it will be assumed that no attenuation in axial specific impulse occurs. We then have a vortex valve quiescent flow rate of 0.28 lb/sec.

When the main engine is not firing, the poppet valve quiescent flow ideally does not change. The vortex valve, however, passes a net flow rate of 1.76 lb/sec, none of which does any useful work. This high leakage from the vortex valve is not permissible since it would allow a loss of 6300 pounds of fuel per hour, which for an eight hour mission would require additional 50,000 pounds of fuel. The eight hour requirement of the poppet valve is 2200 pounds of fuel, which may also be excessive. For either valve, a means for cutting off the control gas supply during coast periods seems necessary. We will assume that this is incorporated.

For comparative purposes, we now have quiescent flow rates of 0.078 lb/sec for the poppet valve and 0.280 lb/sec for the vortex valve. When maximum thrust vector deflection is taking place, the wasted flow to the poppet valve remains at 0.078 lb/sec, but the lost flow to the vortex valve increases to 0.551 lb/sec. The flow rate through the main engine is 1000 lb/sec, thus these leakages are small and can be considered to be of no significance. We therefore conclude that, having proper flow control to the valves, there is no significant difference between the flow requirements of the two valves.

The final selection of the injectant metering valve depends upon considerations of weight, reliability, and response. Without going into detailed design, only a qualitative comparison can be made. As stated in Subsection 5.4.9, the reliability of the poppet valve would be poor, based upon the present state-of-the-art. Conversely, the reliability of the vortex valve can be expected to be excellent, because of the absence of moving parts in contact with the main gas flow. With regard to weight, the vortex valve will undoubtably be heavier, but this disadvantage may

be of secondary consideration. Insofar as response is concerned, the vortex valve is significantly faster than the poppet valve and requires no compensation loop around it to obtain acceptable stability. In view of the fact that a study such as this cannot properly weigh all of the advantages and disadvantages, a conclusive selection of one valve in preference to the other cannot be made. It does appear, however, that the vortex valve has the greatest potential for success.

SECTION 6

ATTITUDE CONTROL REACTION ENGINES

6.1 INTRODUCTION

The mass expulsion attitude control system, while being one of the more conventional means of developing space vehicle control torques, is nonetheless an ultimate choice in meeting the requirements for response, efficiency, weight, reliability and versatility. The system basically consists of propellant tankage, manifolding, a positive shut-off control valve, a combustor and a converging-diverging nozzle. This section is concerned with propellant selection, tankage evaluation, system design and definition, and dynamic analysis including analogue computer simulation. Weight estimates have been made of the propellant and tankage of the controller.

The valve design is discussed with regard to optimizing certain parameters to achieve optimum performance: Two possible modes of control, on-off and proportional, are discussed and possible system design concepts presented. In addition to the basic control system dynamic analysis and simulation discussed in this section, the computer program for valve-combustor simulation is described in Appendix VIII.

6.2 PROPELLANT SELECTION

6.2.1 Introduction

The selection of a propellant combination for the reaction attitude control system involves considerable tradeoff with regard to the other vehicle systems. It is especially influenced by the possible use of the main propulsion system propellants. Liquid hydrogen and liquid oxygen have been chosen for the propulsion system because of their high specific impulse. They do have an inherent problem however in not being hypergolic and thus requiring an ignition system. The control system analytical studies show that the on-off or pulsing mode of control operation is the most desirable. This conclusion is then complicated by the requirement for the fairly sophisticated ignition system when capitalizing on the already available non-hypergolic propellants.

It was decided to make a tradeoff involving both a storable hypergolic bipropellant and the cryogenic liquid hydrogen - liquid oxygen combination. This comparison is made on the basis of performance, storage requirements, handling and contribution to system weight. Considerable analysis and application data is available for the variety of propellant combinations available.

6.2.2 Propellant Properties and Characteristics as Related to Performance

Several convenient parameters are available for comparing the various promising propellant combinations. Those parameters chosen for this study are specific impulse, characteristic velocity, and density impulse.

A combustion chamber pressure of 200 psia along with an expansion ratio of 150:1 has been selected to be compatible with minimizing the control system weight. All basic propellant tradeoffs are made assuming isentropic thermodynamic processes.

The ideal specific impulse I_{SP} is a measure of the available energy in a given quantity of propellant. It is defined as the thrust per unit weight of propellant.

$$I_{SP} = \sqrt{\frac{2 R_b}{g}\left(\frac{k_b}{k_b - 1}\right)\frac{T_b}{M}\left[1 - \left(\frac{P_e}{P_b}\right)^{\frac{k_b - 1}{k_b}}\right]} \qquad (6\text{-}1)$$

The characteristic velocity C^* is a measure of the available energy in the gas and it differs from specific impulse in being independent of thrust, thus it is easily measured in an actual experiment. It is expressed as:

$$C^* = \frac{g P_b A_t}{\dot{W}_p} \qquad (6\text{-}2)$$

The density impulse I_D is a comparative parameter for relating the available propellant energy to its liquid density. It is significant when considering storage volume and its influence on system weight. Density impulse is calculated from Equation 6-3:

$$I_D = I_{SP}\left[\frac{1+r}{\frac{1}{\delta_f}+\frac{r}{\delta_o}}\right] \qquad (6\text{-}3)$$

where: r = oxidizer to fuel ratio by weight

δ_f = specific gravity of fuel

δ_o = specific gravity of oxidizer

Several bipropellant combinations were evaluated based on the above assumptions and performance criterion. Table 6-1 gives these performance parameters for the propellants considered. A survey of the technical literature along with the parameter tradeoff resulted in a choice of a hypergolic combination of nitrogen tetroxide as an oxidizer and a fuel mixture of UDMH and hydrazine 50-50 by weight. Another hypergolic combination, liquid fluorine and liquid hydrogen was considered because of its high specific impulse, however it will not be used because of lack of sufficient performance data to prove feasibility and because of its extreme toxicity which poses a hindrance to logistics on a vehicle of this type.

Physical parameters for the two bipropellant combinations selected are shown in Table 6-2. These are required for nozzle, combustor, and injector design.

It was previously mentioned that an expansion ratio of 150:1 would be used in system design. Reference to Equation (6-1) indicates that increasing the expansion ratio P_b/P_e results in an increase in specific impulse. Ideally when operating in space where the atmospheric pressure approaches zero we could expand the gases completely with an appropriate nozzle length. Figure 6-1 shows a plot of ideal specific impulse versus expansion ratio for the propellants being considered. Specific impulse increases rapidly up to an expansion ratio of 150:1. Above this ratio little gain in specific impulse is realized. Nozzle size and weight, however, continue to increase and in most cases the small additional gain in specific impulse is nullified by the increase in system weight. The nozzle area relationship is given by Equation (6-4).

Table 6-1 - Specific Impulse of Various Bipropellants

Oxidizer	Fuel	O/F	I_{SP} Sec	I_{SPD} Sec	C* ft/sec
90% Hydrogen Peroxide	UDMH	4.40	273	234	4210
90% Hydrogen Peroxide	Hydrazine	2.04	275	302	4240
Mixed Oxides of N_2	UDMH	2.5	285	334	4430
Nitrogen-Tetroxide	Hydrazine	1.25	286	352	4450
RFNA	Hydrazine	1.40	278	352	4230
RFNA	UDMH	2.7	269	331	4100
WFNA	Hydrazine	1.22	278	342	4160
Nitrogen-Tetroxide	50/50 UDMH-Hydrazine	1.62	290	338	4500
Fluorine	Hydrogen	5.67	410	157	6530
Oxygen	Hydrogen	4.5	396	121	6100

P-2063

* Chamber pressure = 200 psia, expansion ratio = 150:1

Table 6-2 - Bipropellant Properties

Liquid	N_2O_4 + 50/50 UDMH Hydrazine	Liquid Oxygen-Liquid Hydrogen
1. Density of Oxidizer	90.5 lb/ft^3	70.2 lb/ft^3
2. Density of Fuel	56.0 lb/ft^3	4.44 lb/ft^3
3. O/F Ratio	1.62	4.45
Gas		
1. Ratio Specific Heats (k)	1.28	1.25
2. Molecular Weight (M)	21	10.5
3. Gas Constant (R_b)	74.0 ft-lb_m/°R-lb_f	147 ft-lb_m/°R-lb_f
4. Combustion Temperature (T_b)	5815°R	5460°R

P-2063

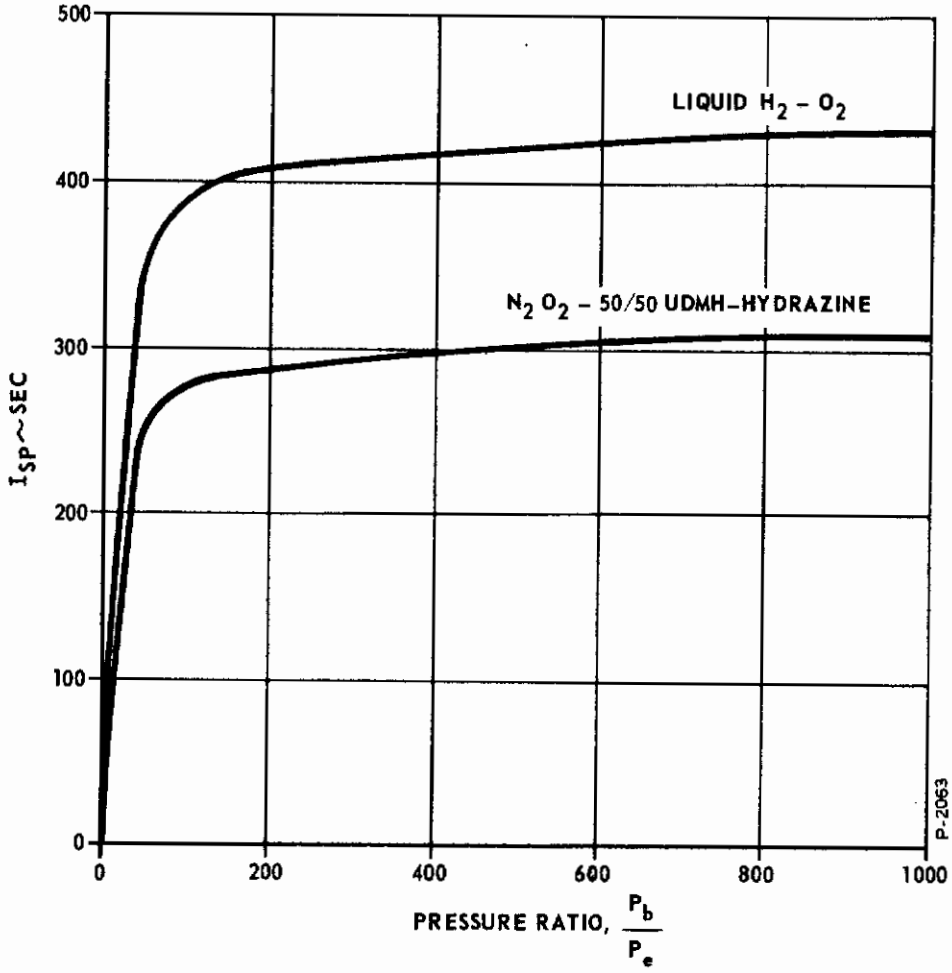

Figure 6-1 - Variation of Specific Impulse with Pressure Ratio

$$\frac{A_t}{A_e} = \left(\frac{k_b + 1}{2}\right)^{\frac{1}{k_b - 1}} \left(\frac{P_e}{P_b}\right)^{\frac{1}{k_b}} \sqrt{\frac{k_b + 1}{k_b - 1}\left[1 - \left(\frac{P_e}{P_b}\right)^{\frac{k_b - 1}{k_b}}\right]} \qquad (6\text{-}4)$$

6.2.3 Storage Requirements

The propellants are stored and transported in the liquid state until reaching the combustor. The N_2O_4 and the 50/50 mixture will require temperature control to prevent freezing since the freezing point of N_2O_4 is 12°F and for 50/50 it is -65°F. A minimum amount of

insulation is needed to maintain these propellants in the liquid state. Conventional spherical pressurized tankage would be used. The liquid hydrogen and oxygen are much more difficult to maintain since their boiling points are so low. The insulation necessary to maintain these propellants below their boiling points will add significantly to the total weight.

The storage of liquid hydrogen and liquid oxygen in space vehicles can be accomplished by several techniques. The most common methods considered are: (1) ambient temperature gas storage at high pressure, (2) single-phase cryogenic fluid storage at super-critical (higher than fluid critical) pressure, and (3) two-phase cryogenic fluid storage at subcritical (lower than fluid critical) pressure. A brief discussion of each of these methods is presented here in order of their mention.

High pressure storage has the advantage of system simplicity and almost indefinite standby (non-use) capability. Its disadvantage is the large volume and weight required for a relatively low payload or usable storage capacity. Generally, high pressure systems are used for either small payload or low-consumption, long duration missions.

Supercritical cryogenic storage of fluids ensures single-phase vapor delivery under all gravity conditions just as high pressure gas storage does, however supercritical cryogenic storage permits large payload quantity storage in a minimum system volume and weight. Therefore, supercritical cryogenic storage is used for large payload capacity, high consumption applications which require minimum storage volume and weight.

Even greater weight savings could be realized if subcritical cryogenic storage systems were to be used, since vessel pressure requirements would be lower, resulting in less vessel weight. However, the operational reliability of subcritical cryogenic storage methods has not been established due to phase - separation problems associated with zero gravity operations and is therefore not under consideration for present space applications.

Supercritical storage of cryogenic fluids is illustrated in Figure 6-2. The initial tank fill condition is indicated by point 1 in the figure. The fill state represented here is a mixture of saturated liquid and vapor at atmospheric pressure. After fill, heating results in

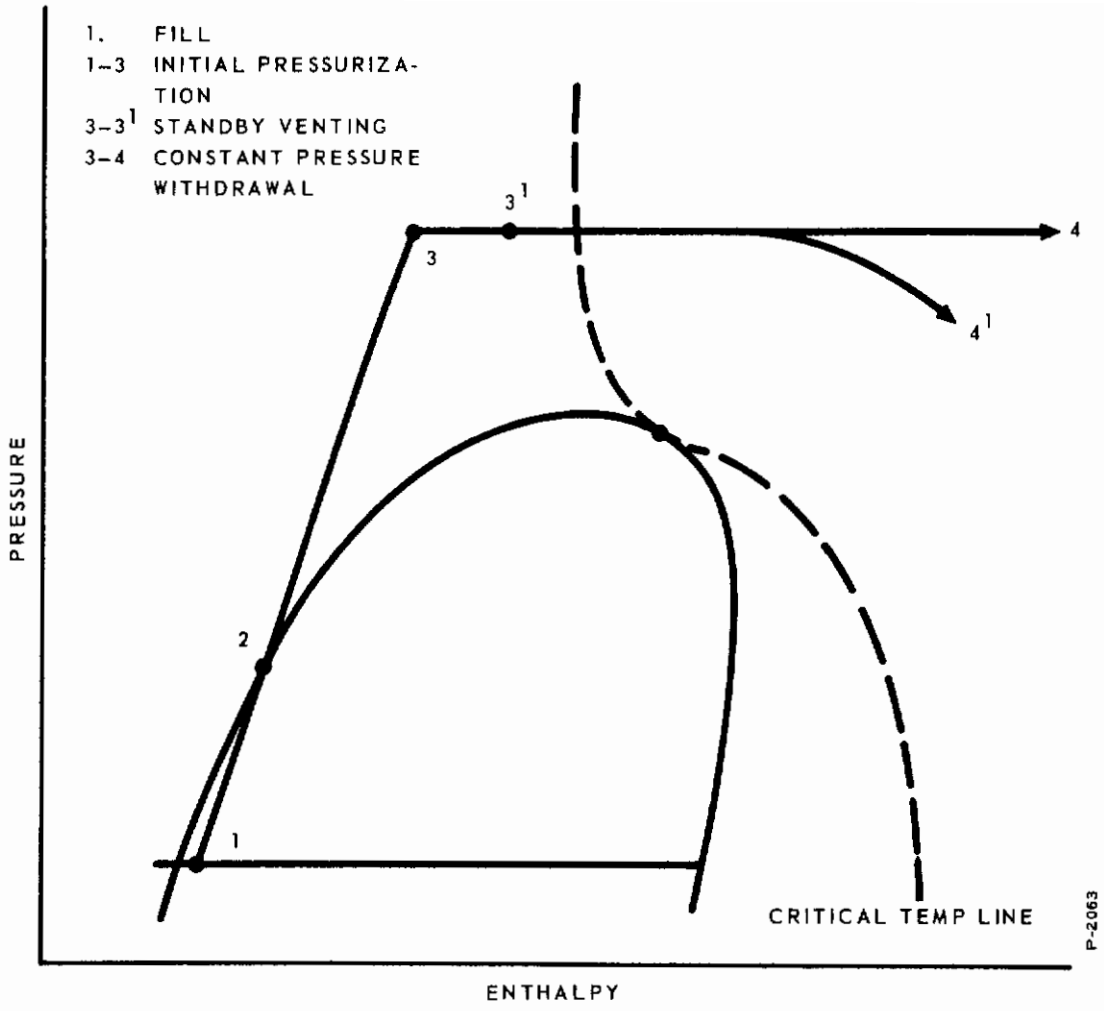

Figure 6-2 - Pressure-Enthalpy Diagram - Thermally Pressurized Supercritical Storage

pressurization at constant density. During this process (1 to 2), the liquid expands until it fills the entire container. Once the desired supercritical pressure is reached at point 3, fluid delivery can be initiated. Constant pressure operation, as indicated by path 3-4, is achieved by the simultaneous addition of heat to the storage volume. Here, as long as supercritical pressures are maintained, the stored mass remains as a homogenous, single-phase fluid.

As shown in Figure 6-2, the fluid temperature rises during operation. When the temperature of the fluid in the vessel becomes significantly higher than the critical temperature, controlled heat input

is not necessary for maintenance of a single phase. The ambient heat leak into the vessel in most cases is adequate to maintain a somewhat isothermal path to 4' while vessel pressure is free to decay. Nearly full utilization of the stored fluid is still realized, since the difference in residual densities at points 4 and 4' is of secondary importance compared to the total charge.

During constant pressure operation, the heat input requirements $\underline{Q}_H$, are found by evaluating the following equation:

$$\underline{Q}_H = \underline{H}_2 - \underline{H}_1 - \int_{m_1}^{m_2} H_a \, dm - \underline{Q}_L \qquad (6\text{-}5)$$

If the pressure is allowed to vary while fluid is being delivered, then the pressure energy must be considered. Equation (6-5) has been evaluated for hydrogen and oxygen and the results presented in Figures 6-3 and 6-4. Here, the total heat input, $\underline{Q}_H + \underline{Q}_L$, has been evaluated for a unit change in mass as a function of the density of the fluid remaining in the storage vessel.

The insulations used for current supercritical cryogenic storage applications are almost exclusively of the superinsulation class. These consist of alternate layers of a good reflector material, such as aluminum, and poor conductive material, such as Fiberglas paper. Evacuation of the insulation space is necessary to obtain low conductivities and to prevent liquefaction of atmospheric constituents.

Supercritical storage of low-boiling point fluids is a lighter, more compact method of fluid storage than the previously used high pressure gas technique. Although subcritical storage is more preferable from a weight standpoint, until more testing of these systems has been completed, they cannot be considered usable.

Design of optimum supercritical vessels requires a knowledge of: (1) ambient heat leak through vessel insulation, (2) minimum fluid use rates, and (3) the properties of the materials of construction. For applications where use rates are high enough that minimum thicknesses of insulation are adequate to prevent unwanted venting, supercritical storage is an exceptionally straightforward, light and reliable storage method.

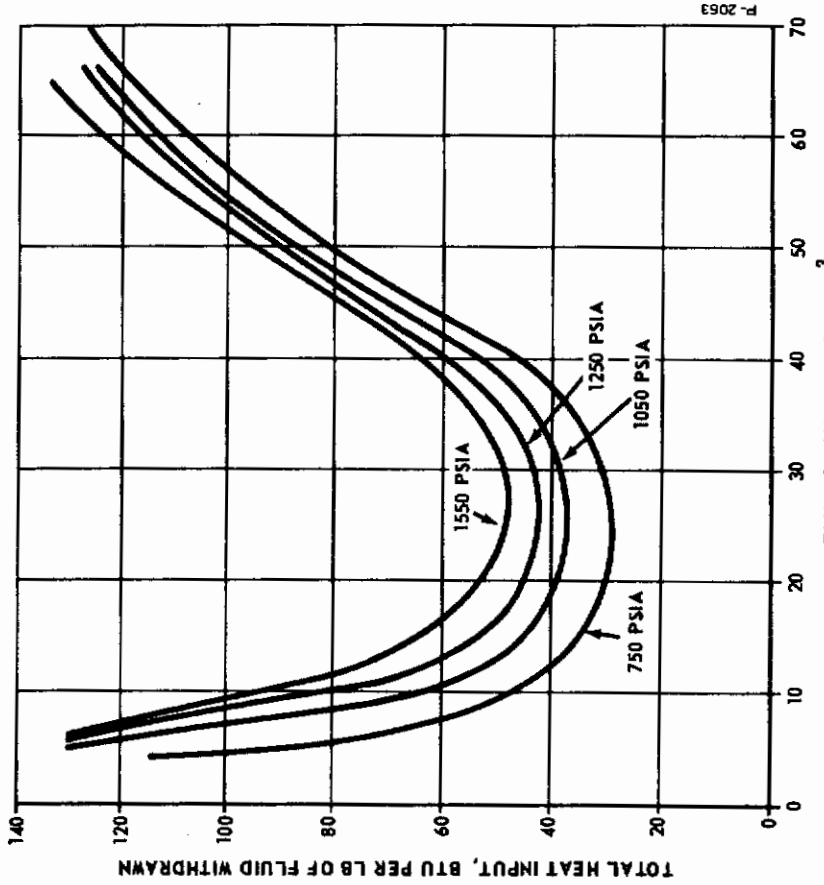

Figure 6-4 - Specific Heat Input for Constant Pressure Delivery, Supercritical Oxygen Storage

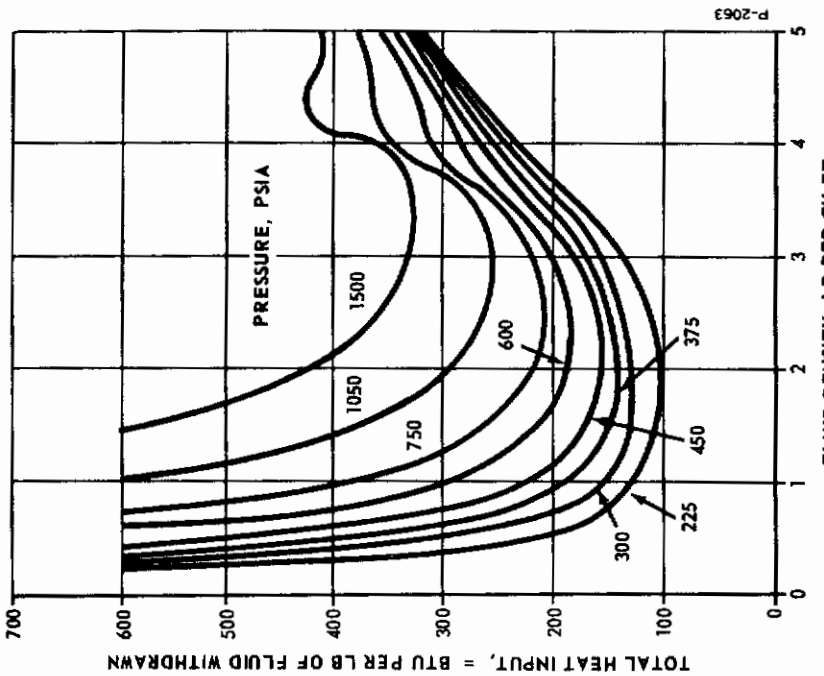

Figure 6-3 - Specific Heat Input for Constant Pressure Delivery, Supercritical Hydrogen Storage

6.2.4 Handling Problems

All of the propellants considered have unique handling problems. Some of these are discussed as follows:

Nitrogen Tetroxide - Contact with the skin causes severe burns. Breathing the vapors will cause poisoning. Spillage may produce fire, and contact with fuels can result in an explosion. Nitrogen tetroxide is stored as a liquid without refrigeration. The liquid will not burn by itself, but will support combustion. It is very corrosive and the metals used in the storage container are selected based on the water content. With a water content of under 0.1 percent, carbon steel, aluminum, nickel, or inconel may be used. Above 0.1 percent water a 300 series stainless steel is recommended.

Liquid Hydrogen - Skin contact with liquid hydrogen causes severe frostbite and burns. It is extremely inflammable and all or part of the flame may be invisible. Explosions can occur when solid air collects in liquid hydrogen and when gaseous hydrogen is mixed with air in a confined space. Storage presents a problem because hydrogen in a liquid state must be kept at a temperature below -424°F. Most metals show a higher strength and modulus of elasticity at low temperature but become very brittle. Ferrous alloys, excepting the austenite nickel chrome alloys, are too brittle and cannot be used. Stainless steel (300 series), copper, bronze, aluminum, monel and brass are suitable, but in all cases, stainless steel is preferred.

Liquid Oxygen - Contact with the skin causes frostbite and burns as with liquid hydrogen. Liquid oxygen itself does not burn but vigorously supports combustion. Mixing with fuels causes a dangerous explosion hazard, particularly if the threat of a spark is present. A mixture of frozen fuel and liquid oxygen is shock sensitive and will react violently.

The materials problems are similar to those associated with liquid hydrogen since the oxygen must be kept at - 298°F to remain a liquid. Stainless steels, copper, bronze, brass, monel, and aluminum are compatible with liquid oxygen.

6.2.5 System Weight Comparison

An accurate system weight comparison must include propellant, tankage, and insulation weights. The rest of the control system would be basically the same for both propellant combinations.

The values of I_{SP} for the two propellant combinations are obtained from Figure 6-1 for an expansion ratio of 150 to 1. These are:

$$(I_{SP})_{HBP} = 290 \text{ seconds (hypergolic bipropellant)}$$

$$(I_{SP})_{LOH} = 410 \text{ seconds (liquid hydrogen-oxygen)}$$

For an estimated total impulse of 1,500,000 lb-sec, the propellant weights are:

$$(W_P)_{HBP} = 5180 \text{ pounds}$$

$$(W_P)_{LOH} = 3660 \text{ pounds}$$

Adding 15 percent for tankage, the comparative weight of the hypergolic bipropellant system is 5950 pounds. Adding 80 percent for tankage and 440 pounds for insulation, the comparative weight of the hydrogen-oxygen system is 7028 pounds. The comparative weight of the hydrogen-oxygen system is seen to be 18 percent greater than that of the bipropellant system.

This comparison was made assuming the hydrogen and oxygen for the attitude control system would be stored at supercritical pressures in separate tanks. However, if they were stored in the main engine tanks and pumped to the A.C.S., the weight necessary for comparison would essentially consist only of the propellant and insulation. When this is done the LOH system provides a 30 percent weight saving. It is therefore desirable to use liquid hydrogen and oxygen from the main engine tanks as the propellant for the mass expulsion attitude control system.

6.3 SYSTEM DESCRIPTION AND DESIGN

6.3.1 Introduction

A schematic diagram of the reaction control system selected for this application is shown in Figure 6-5. This system is unique in that it can be operated in either on-off or proportional modes or a combination of both. This provides unlimited flexibility in the design of the over-all attitude control loop. Detailed descriptions of the critical components which make up the system are given in the subsections which follow.

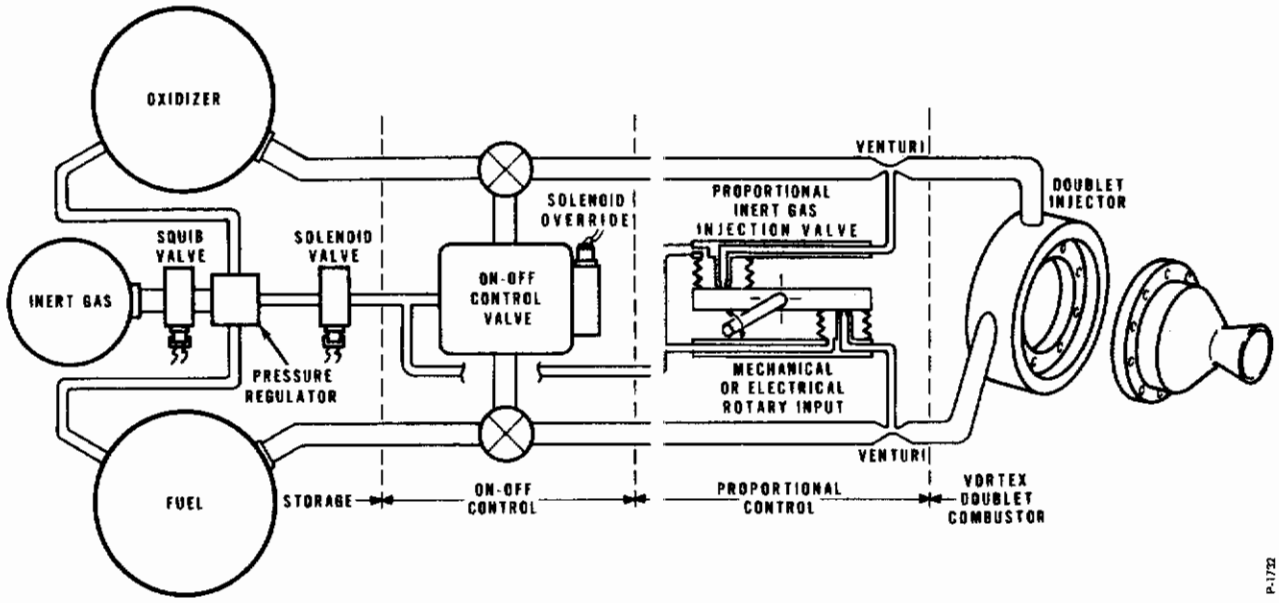

Figure 6-5 - Reaction Control System

6.3.2 Nozzle

The ideal thrust from a nozzle is expressed as:

$$F_n = C_F A_t P_b \qquad (6\text{-}6)$$

where:

F_n = thrust, lbs

C_F = thrust coefficient, dimensionless

P_b = chamber pressure, psia

A_t = throat area, in^2.

This equation assumes that the combustion gases are homogeneous, obey the perfect gas law and that the flow is one-dimensional. A correction factor is introduced to take into account heat losses, three-dimensional flow effects, friction losses and imperfect combustion. This correction factor is 0.96 for a well-designed nozzle operating in space.

The thrust coefficient C_I is expressed as a function of ratio of specific heats and expansion ratio $\frac{P_e}{P_b}$ as follows:

$$C_F = \sqrt{\frac{2\,k_b^2}{k_b - 1}\left(\frac{2}{k_b + 1}\right)^{\frac{k_b + 1}{k_b - 1}}\left[1 - \left(\frac{P_e}{P_b}\right)^{\frac{k_b - 1}{k_b}}\right]} \qquad (6\text{-}7)$$

This coefficient determines the amplification of thrust due to the gas expansion in the nozzle as compared to the thrust that would be expected if the chamber pressure acted over the throat area. Pressure ratio and area ratio are related by Equation (6-4).

A suitable chamber is first selected, and Equation (6-6) is employed to determine the throat area. Expansion ratio or area ratio is then selected and the other is computed. If the nozzle weight or length is too large, then a higher value of P_b should be chosen keeping in mind that while this will make the nozzle smaller it may mean a greater increase in the size of the pumps and tanks.

An alternative to raising the chamber pressure is to use a nozzle which is designed to produce the same expansion as the conical design but in a shorter length. Examples of these are the Rao nozzle, the variable area nozzle, and the expansion-deflection nozzle. References (88), (89), and (90) discuss these designs and others.

Nozzle cooling must also be taken into account. There are four cooling methods available: radiation, regeneration, ablation, and film cooling. A radiation-cooled nozzle is also called an uncooled nozzle since all heat is transferred by forced convection from the combustion gases to the wall and then through the wall by conduction. This method becomes ineffective if the nozzle wall reaches a temperature where the materials lose their strength. One solution is to coat the inside walls with a refractory liner. This retards the heat transfer so that the metal does not reach the higher temperature until after the engine stops firing and the nozzle is unpressurized. Materials with minimum high temperature strength should always be used with this cooling method.

Regenerative cooling is another method where either the fuel or oxidizer is used as the coolant. One scheme using liquid hydrogen is to pump the liquid, which is at -423°F, through tubes running up the outside of the nozzle. After picking up heat, the hydrogen will vaporize and assume some high temperature. This gas is then expanded through a turbine which drives the pumps supplying fuel and oxidizer to the main engine.

Ablation cooling uses materials on the inside periphery of the nozzle which decompose and produce a high temperature differential. This method requires very careful design of, not only the nozzle, but also the injector. Film cooling utilizes a cooling fluid introduced directly into the chamber to absorb heat and thicken the effective boundary layer between the hot gases and the walls of the chamber.

In this study, radiation cooling will be assumed to be used in the design of the attitude control nozzles to minimize weight and complexity.

6.3.3 Injector and Combustion Chamber

This system will use a novel vortex doublet combustion chamber which is shown schematically in Figure 6-6. The oxidizer is admitted radially and the fuel tangentially so that a vortex is induced with combustion occurring as the liquids spiral toward the center. Excellent mixing is accomplished and a long average burning path is inherent. The mixing is done as the liquids swirl away from the injector holes which allows the igniter to be positioned so that combustion does not affect the propellant flow into the chamber. Another advantage of this design is that the walls of the chamber operate cooler because the higher temperature gases are confined to the center of the combustor.

The total propellant weight flow rate is found from:

$$\dot{W}_p = \frac{F_n}{I_{SP}} \tag{6-8}$$

The oxidizer and fuel flow rates depend on the oxidizer-to-fuel ratio as follows:

$$\dot{W}_o = \dot{W}_p \left(\frac{r}{1 + r}\right) \tag{6-9}$$

$$\dot{W}_f = \dot{W}_p - \dot{W}_o \tag{6-10}$$

Injector areas are found from the expression:

$$A_{io}, A_{if} = \frac{\dot{W}_{o,f}}{C_{dp}\sqrt{2\, g\, \rho_{o,f}\, (P_i - P_b)}} \tag{6-11}$$

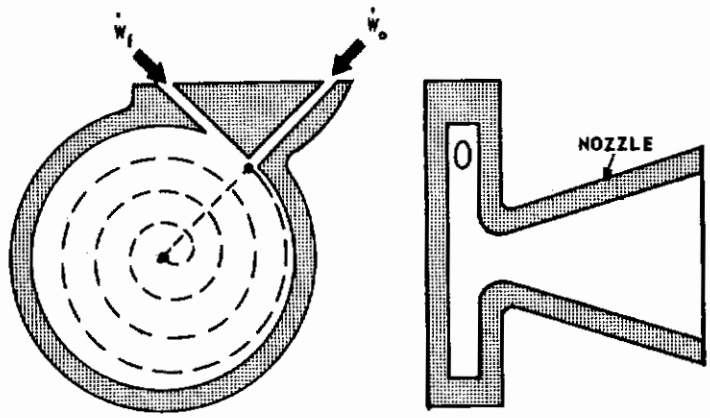

Figure 6-6 - Vortex Doublet Combustor

where:
C_{dp} = orifice discharge coefficient for propellant
$\rho_{o,f}$ = density of fuel or oxidizer, lb-sec^2/in.^{4}
P_i = pressure upstream of injectors, psia
P_b = combustion chamber pressure, psia

A 20:1 length-to-diameter ratio is normally employed for these injectors. A series of doublets will be used, all of which are controlled by the same valve.

Characteristic length L^* is a measure of the chamber volume and is used in calculating residence time. It is defined as chamber volume divided by throat area. Chamber volume takes into account all the volume up to the nozzle throat. The vortex doublet combustion chamber can operate efficiently over a wide range of thrust for any given chamber pressure. For this reason the choice of L^* should not present a problem.

6.3.4 Control Valve

An on-off control valve is shown in Figure 6-7. The pilot-operated, two-stage configuration was chosen to meet response requirements. A single-stage valve capable of handling the large flows dictates excessively large electrical actuation devices. Such large electrical actuation devices must be avoided due to their limited response capabilities. The proposed valve utilizes a small solenoid capable of working from conventional power supplies.

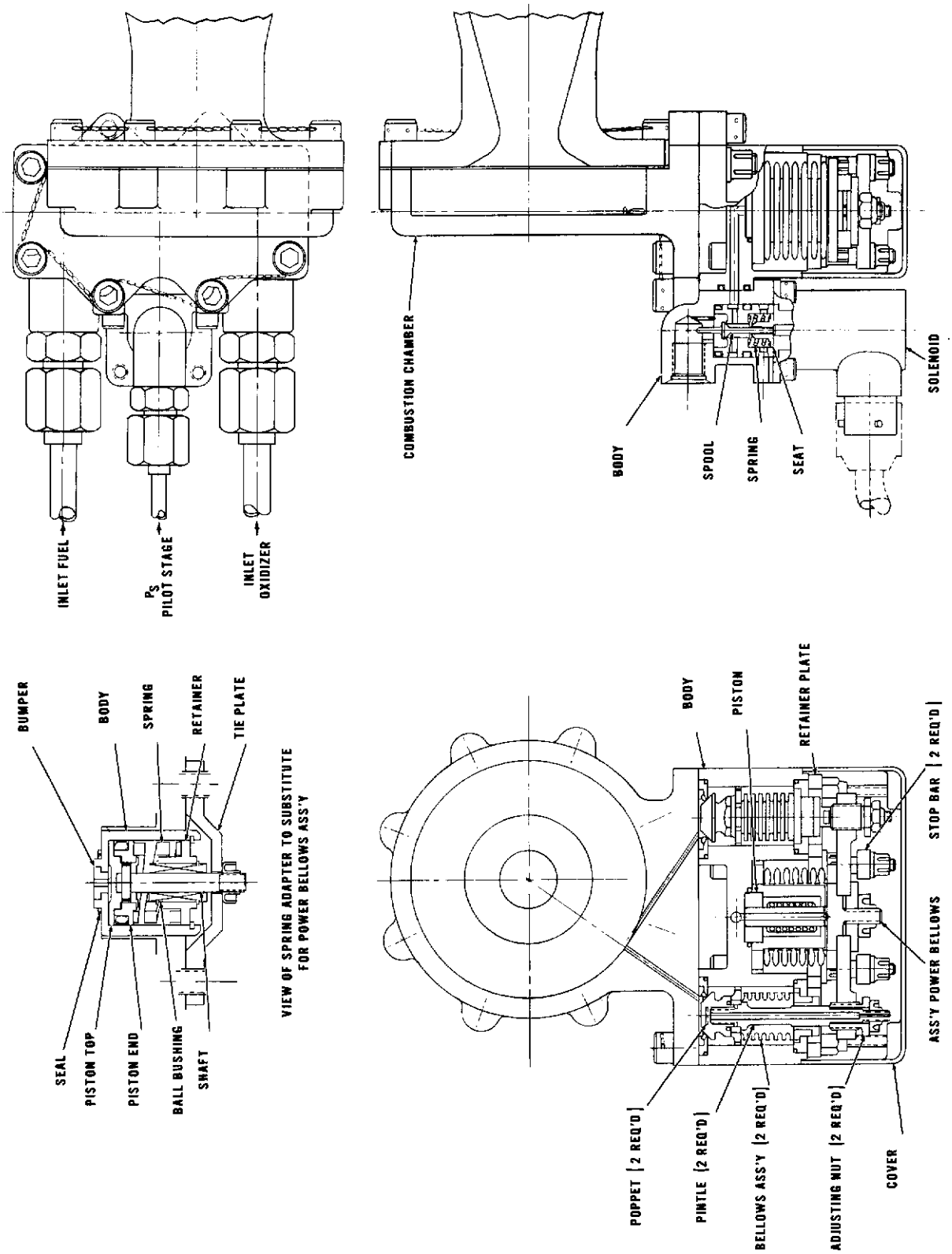

Figure 6-7 - Reaction Control Valve

The valve operation is as follows: The pilot stage consists of a simple unbalanced area poppet actuated by a solenoid, as shown in Figure 6-8. The control signal actuates this solenoid allowing the control gas to flow into the main stage. When this pressure force builds up to a point sufficient to overcome the restraining forces, the main stage piston is actuated. Attached to this piston by a tie bar are the main stage poppets. The flow of fuel and oxidizer into the combustor is controlled by these poppets. The main stage is illustrated in Figure 6-9. When the signal is removed, the pilot stage poppet is closed by the gas acting on the unbalanced area, the gas in the main stage exhausts, and the spring preload closes the main stage. Symmetry in opening and closing response is a function of the mechanical parameters.

The required valve poppet flow area of the main stage is calculated as follows:

$$(A_v)_{o,f} = \frac{\dot{W}_{o,f}}{C_{dp}\sqrt{2\, g\, \rho_{o,f}\, (P_s' - P_i)}} \qquad (6\text{-}12)$$

where P_s' = propellant supply pressure at the valve. From the valve geometry, the stroke is calculated for a given poppet diameter. The choice of the poppet diameter is somewhat arbitrary and crossplots are made to optimize stroke to diameter ratio. The expression for poppet area is:

$$A_v = \pi y \sin\theta\, (2 r_b - y/2) \qquad (6\text{-}13)$$

as determined from Figure 6-10.

A force balance on the valve must be done to assure adequate valve seat preload and also to provide the forces required for opening and closing the valve. This must be done in conjunction with the dynamic analysis to assure the required response.

The gas weight flow rate through the pilot stage valve area A_u is :

$$\ddot{W}_a = \frac{C_i\, C_{di}\, A_u\, P_a}{\sqrt{T_i}} \qquad (6\text{-}14)$$

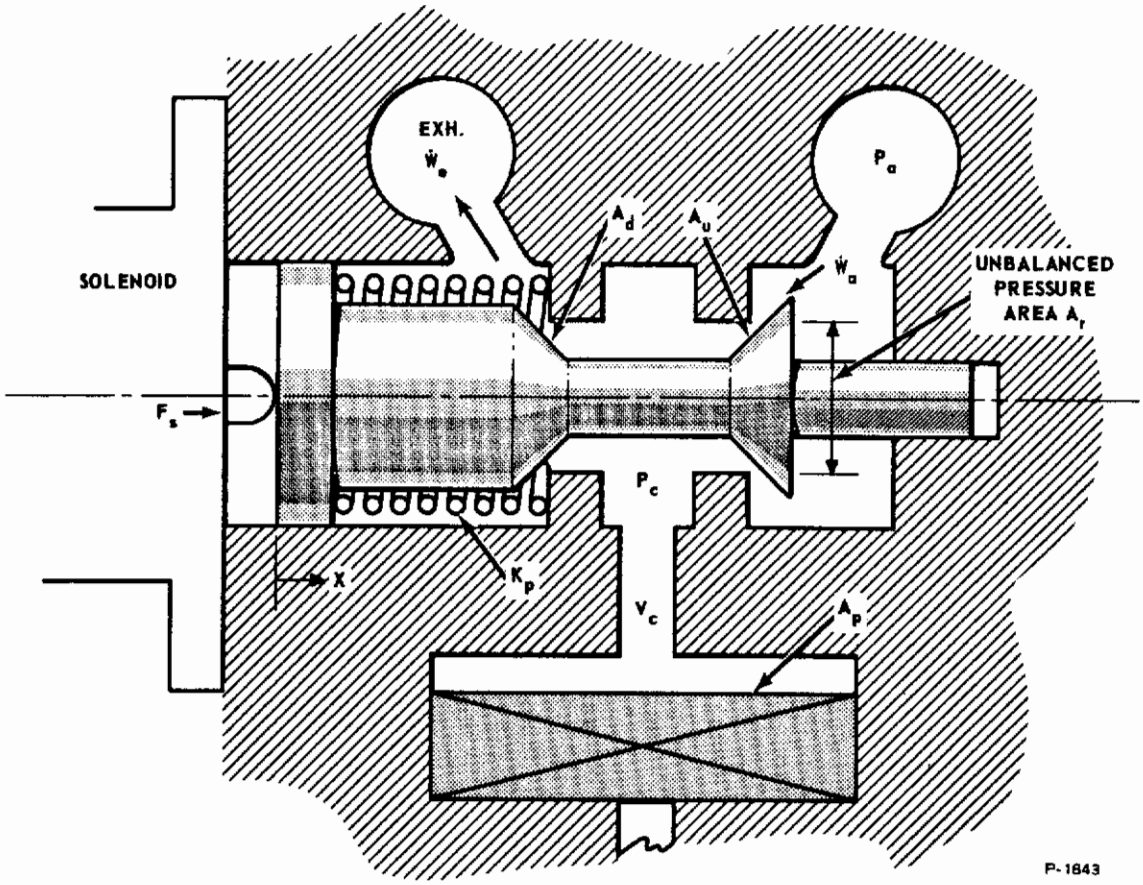

Figure 6-8 - Pilot Stage Characteristics

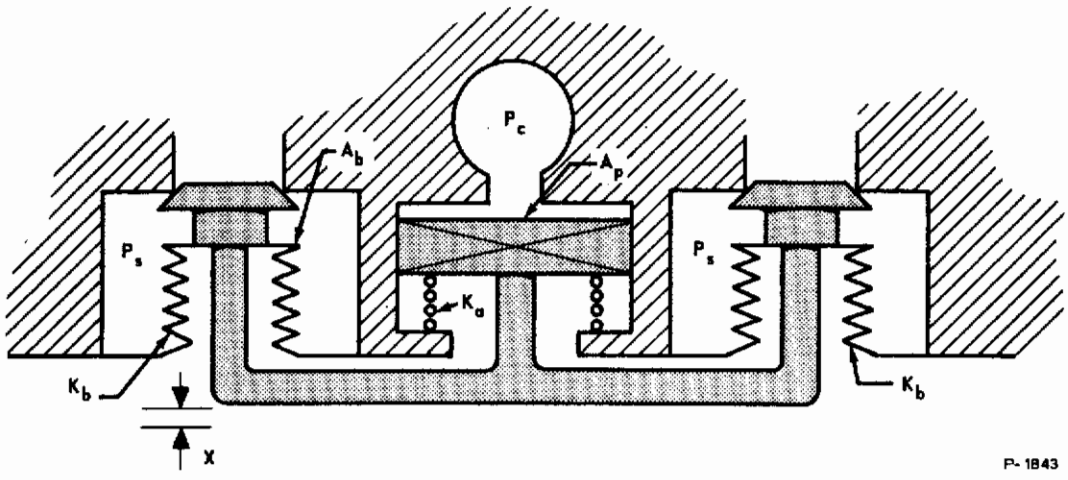

Figure 6-9 - Main Stage Schematic

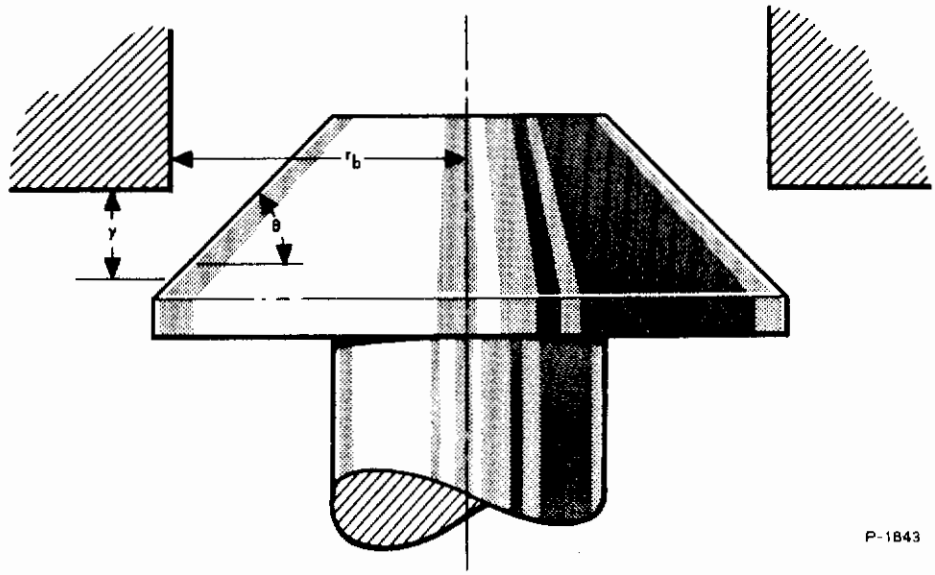

Figure 6-10 - Poppet Flow Area

The compressibility flow is:

$$\dot{W}_c = \frac{V_c}{R_i T_i} \frac{d P_c}{dt} \tag{6-15}$$

Equating these two flows gives an expression for evaluating A_u:

$$\frac{d P_c}{dt} = \frac{R_i \sqrt{T_i} C_i C_{di} P_a A_u}{V_c} \tag{6-16}$$

This assumes that the flow across the orifice is sonic, which is valid for $P_c \leq P_a/2$. The main stage is then designed so that it will move with $P_a/2$ applied to the piston. A_u is related to the stroke x by:

$$A_u = \pi x \sin\theta \left(2 r_u - \frac{x}{2}\right) \tag{6-17}$$

where r_u = radius of poppet hole.

The exhaust gas flow rate across the pilot stage poppet is:

$$\dot{W}_e = \frac{C_i\, C_{di}\, A_d\, P_c}{\sqrt{T_i}}\, f_1\left(\frac{P_e}{P_c}\right) \tag{6-18}$$

where $f_1\left(\frac{P_e}{P_c}\right)$ is the orifice flow function.

The compressibility flow is:

$$\dot{W}_c = \frac{V_c}{R_i\, T_i}\,\frac{d\,P_c}{dt} \tag{6-19}$$

Equating these two flows and assuming sonic flow we get the expression:

$$\frac{d\,P_c}{P_c} = \frac{C_i\, C_{di}\, A_d\, R_i \sqrt{T_i}\, dt}{V_c} \tag{6-20}$$

Integrating the above gives:

$$\ell n\, P_a - \ell n\, P_c = \frac{C_i\, C_{di}\, A_d\, R_i \sqrt{T_i}\, t}{V_c} \tag{6-21}$$

from which the exhaust area is:

$$A_d = \frac{V_c\,(\ell n\, P_a - \ell n\, P_e)}{C_i\, C_{di}\, R_i \sqrt{T_i}\, t} \tag{6-22}$$

The exhaust area should be approximately 6 times the inlet area to insure symmetrical opening and closing.

6.3.5 Proportional Control

Thrust is a function of chamber pressure, nozzle throat area, and specific heat ratio. Variation of throat area can be accomplished by inserting a tapered plug into the approach section of the nozzle or by aerodynamically restricting the area by means of a high-pressure jet. Even if the chamber pressure can be independently varied to maintain it at the desired level, the variation in throat area will affect the propellant flow rate. In addition, variable throat area devices are complex and are seldom used in practice.

Many methods exist for varying chamber pressure. Turbopumps can be used which give a throttling ratio of approximately 4 to 1. Varying the injector areas by mechanical means is very complex and unreliable. Most methods require that the chamber pressure be high to ensure stable combustion at low flow rates.

The method to be used in this system is an all-fluid technique which promotes good mixing and stable combustion even at low chamber pressures. The fuel and oxidizer are passed through cavitating venturis just prior to entering the injectors. An inert gas is injected at the throat of the venturis. The injected gas displaces some of the propellant and flows into the combustor. The amount of fluid displacement is proportional to gas flow. The system is designed for symmetrical supply pressure on each side and the oxidizer-to-fuel ratio is maintained constant throughout the throttling range. The proportional valve, shown schematically in Figure 6-5, controls the gas flow to both sides. This valve is a very simple device and will not add significant complexity to the system. The on-off valve allows the system to be operated in the on-off mode at different thrust levels by varying the gas pressure.

6.3.6 System Design

The system design is based upon a 1000 pound thrust engine operating at a chamber pressure of 200 psia. A pressure ratio of 150:1 is initially selected since no appreciable increase in specific impulse is obtained above this value.

The thrust coefficient C_F is found from Equation (6-7) to be 1.79. Inserting this value and P_b = 200 psia into Equation (6-6), the nozzle throat area is calculated as 2.83 in^2. At P_b/P_e = 150, the specific impulse is 410 seconds. The ratio of nozzle exhaust area to throat area is computed from Equation (6-4) as 14.5 to 1.

The total propellant flow rate at the 150:1 pressure ratio is:

$$\dot{W}_p = \frac{1000}{410} = 2.43 \text{ lb/sec}$$

Oxidizer flow rate is:

$$\dot{W}_o = \dot{W}_p \times \frac{4.5}{1 + 4.5} = 1.99 \text{ lb/sec}$$

and the fuel flow rate is 0.44 lb/sec. The combustion chamber volume is calculated to be 56 in^3.

The areas of the injectors are found from Equation (6-11), assuming a pressure drop of 100 psig.

$$A_{io} = 0.0441 \text{ in.}^2$$
$$A_{if} = 0.0393 \text{ in.}^2$$

The poppet flow areas for the main stage are calculated from Equation (6-12) by assuming a maximum pressure drop of 10 psi across the oxidizer poppet.

$$A_{vo} = 0.169 \text{ in.}^2$$

This area is a function of the poppet radius and stroke as given by Equation (6-13). Choosing the radius equal to 0.375 inch, the maximum stroke is 0.100 inch.

The fuel side poppet is made with the same diameter and stroke as the oxidizer poppet to preserve symmetry. The pressure drop is calculated to be 5.4 psi. The pressure drops across both poppets are within 4.6 psi of each other and, therefore, will not significantly effect the force balance on the valve.

The pilot stage is sized assuming a gas supply pressure of 600 psi. Refer to Figure 6-8 for the basic geometry of this stage. In Equation (6-16) which equates the flow across the poppet to the compressibility flow into the main stage, a time response of 1 millisecond is chosen to achieve 300 psi control pressure in the main stage. The temperature T_i of the control gas is assumed to be 100°R due to the presence of the cryogenic propellants in the valve.

V_c is estimated to be 0.050 in.^3, thus making:

$$(A_u)_{max} = 0.00645 \text{ in.}^2$$

Let the radius of the poppet r be 0.0625 inch and let the poppet angle θ be 45 degrees. Solving for x in Equation (6-17) gives the maximum stroke as:

$$x_m = 0.027 \text{ in.}$$

The pilot stage exhaust area is sized to insure a 0.001 second decay time. For a pressure decay of 600 psia, Equation (6-22) dictates that $(A_d)_{max} = 0.0406$ in.^{2} r_d then becomes 0.156 inch.

The remaining parameters were determined by experience and through dynamic simulation of the system on a computer. The complete list of constants is found in Table 6-3 contained in Subsection 6.4.3.

6.4 DYNAMIC ANALYSIS

6.4.1 Valve Dynamics

The elements which make up the valve are a solenoid, pilot stage, and main stage. The dynamics associated with each are analyzed and described in the following paragraphs.

The steady-state force developed by the solenoid is a linear function of position and is given by:

$$(F_e)_{ss} = K_s E \left[1 - k_s (x_m - x)\right] \qquad (6\text{-}23)$$

where:

$$K_s = 23.6 \times 10^{-5} \frac{B_p r_s^2 N}{R_s}, \text{ lb/volt}$$

E = input voltage

k_s = solenoid displacement gain, 1/in.

x_m = maximum displacement of solenoid, in.

x = displacement of solenoid, in.

B_p = maximum flux density, webers/meter^2

N = number of coil turns

r_s = solenoid radius, meters

R_s = coil resistance, ohms

Including the solenoid dynamics, the expression for the force is:

$$F_e = \left[\frac{K_s E}{1 + \tau_s S}\right] \left[1 - k_s (x_m - x)\right] \qquad (6\text{-}24)$$

Table 6-3 - Values of Computer Constants

Symbol	Value	Units
A_{it}	0.0834	$in.^2$
A_p	1.225	$in.^2$
A_t	2.79	$in.^2$
C_d	0.85	
C_f	0.3075	$°R^{1/2}/sec$
C_h	0.000178	$in.^5/lb$
C_i	0.523	$°R^{1/2}/sec$
C_2	3.16	lb/in.-sec
E	28.0 (max.)	volts
F_{s1}	5.19	lb
F_{s2}	85.0	lb
k_i	1.4	
k_b	1.25	
k_s	18.5	1/in.
K_a	1500.0	lb/in.
K_b	300.0	lb/in.
K_c	6530	lb/sec
K_p	50	lb/in.
K_s	0.643	lb/volt
L_h	17.32	lb $sec^2/in.^5$
M_2	0.00145	lb-sec^2/in.
M_p	8.663×10^{-5}	lb-sec^2/in.
P_a	600.0	psia
P_e	≈ 0	psia
P_s	300.0	psia
r_b	0.375	in.
r_d	0.156	in.
r_u	0.0625	in.
R_h	12.47	$sec/in.^2$
R_i	662.0	in./°R
R_b	1820.0	in./°R
T_b	5460.0	°R
T_i	100.0	°R
V_b	56.2	$in.^3$
V_c	0.050	$in.^3$
x_m	0.030	in.
y_m	0.100	in.
θ	45.0	deg
τ_b	1.5×10^{-3}	sec
τ_i	0.001	sec
τ_s	0.003	sec

P-2063

where:

$$\tau_s = \frac{\text{coil inductance } L_s}{\text{coil resistance } R_s}$$

The equation of motion for the pilot stage poppet shown in Figure 6-8 is:

$$M_p \ddot{x} + K_p \dot{x} + F_{sl} = F_e \qquad (6\text{-}25)$$

where: M_p = poppet mass, lb-sec^2/in.

K_p = rate of solenoid return spring, lb/in.

F_{sl} = pilot stage preload, lb

When the pilot stage poppet moves, gas enters the volume upstream of the main stage piston or bellows and begins to increase the pressure P_c from its original level P_e. Until the poppet reaches full stroke, however, gas also flows out of the main stage through the area A_d. The general expression for the weight flow rate into the main stage control volume is:

$$\dot{W}_a = \pi \sin\theta \left(2 r_u x - \frac{x^2}{2}\right) \frac{C_{di} C_i P_a}{\sqrt{T_i}} \qquad (6\text{-}26)$$

and the weight flow rate of the gas leaving the control volume is:

$$\dot{W}_e = \pi \sin\theta \left[2 r_d (x_m - x) - 1/2 (x_m - x)^2\right] \frac{C_{di} C_i P_c}{\sqrt{T_i}} \qquad (6\text{-}27)$$

where

θ = poppet angle, degree

r_u = upstream metering radius, in.

r_d = downstream metering radius, in.

C_{di} = orifice discharge coefficient

C_i = flow coefficient of control gas = $2\sqrt{\frac{k_i}{R_i}\left(\frac{2}{k_i+1}\right)^{\frac{k_i+1}{k_i-1}}}$

The difference between inlet and outlet flow rates is the rate-of-change of gas weight within the volume, expressed as:

$$\dot{W}_a - \dot{W}_e = \frac{V_c}{R_i T_i}\frac{dP_c}{dt} \qquad (6\text{-}28)$$

where:

V_c = control volume, $in.^3$

R_i = gas constant for control gas, in./°R

T_i = temperature of control gas.

By combining Equations (6-26), (6-27), and (6-28) and letting $\theta = 45°$, the following expression is obtained:

$$\frac{dP_c}{dt} = \frac{K_c}{V_c}\left\{\left[2 r_u x - x^2/2\right] P_a - \left[2 r_d (x_m - x) - 1/2 (x_m - x)^2\right] P_c\right\}, \qquad (6\text{-}29)$$

where:

$$K_c = \frac{\pi}{\sqrt{2}} C_{di} C_i R_i \sqrt{T_i}$$

Equation (6-29) relates the pressure P_c in the main stage control volume to the displacement of the poppet.

The equation of motion for the main stage is:

$$M_2 \ddot{y} + F_{s2} + (2K_b + K_a) y = A_p P_c + 2\pi r_b^2 P_i \qquad (6\text{-}30)$$

where

M_2 = main stage mass, $lb\text{-}sec^2/in.$

y = displacement of main stage poppets, in.

F_{s2} = total preload on main stage poppets, lb

K_b = spring rate of main stage poppet bellows, lb/in.

K_a = rate of main stage return spring, lb/in.

A_p = area of main stage piston, $in.^2$

P_c = pressure acting on main stage piston, psig

r_b = radius of main stage poppet ports, in.

P_i = pressure downstream of main stage poppets, psig.

The total flow rate of propellant out of the main stage is given by:

$$\dot{W}_p = C_2 A_{vt} \sqrt{P_s' - P_i} \qquad (6\text{-}31)$$

where

C_2 = flow coefficient for propellant

$A_{Vt} = \sqrt{2}\ \pi\ (r_b\ y - y^2/2)$ = total flow area, $in.^2$

P_s' = supply pressure of propellants at the valve, psia

P_i = pressure upstream of injector nozzle, psia.

Since the flow is incompressible, it is also given by:

$$\dot{W}_p = C_2 A_{it} \sqrt{P_i - P_b} \qquad (6\text{-}32)$$

where

A_{it} = total injector orifice area, $in.^2$

P_b = combustion chamber pressure, psia.

Combining Equations (6-31) and (6-32) gives the following expression for P_i:

$$P_i = \frac{A_{vt}^2 P_s' + A_{it}^2 P_b}{A_{vt}^2 + A_{it}^2} \qquad (6\text{-}33)$$

6.4.2 Combustion Dynamics

The gas flow process in the combustion chamber is assumed to be isothermal. With this assumption, the following linear relationship describes the process:

$$\dot{W}_{cp} = \frac{V_b}{R_b T_b} \frac{d P_b}{dt} \qquad (6\text{-}34)$$

where:

$\dot{W}_{cp}$ = rate of change of weight of combustion products, lb/sec

V_b = combustion chamber volume, $in.^3$

R_b = gas constant for combustion products, in./°R

T_b = temperature of combustion products, °R

P_b = combustion chamber pressure, psia

Integrating Equation (6-34) gives:

$$P_b = \frac{R_b T_b}{V_b} W_{cp} \qquad (6\text{-}35)$$

Test results for representative engines indicate that combustion can be represented as a linear process with a single time constant after ignition occurs. Before ignition, propellant accumulates in the combustion chamber. Thus:

$$W_{cp} = \frac{\delta}{1 + \tau_b S} W_b \qquad (6\text{-}36)$$

where τ_b is the combustion time constant and δ is a switching function used to represent the ignition time delay:

δ = o when $t < \tau_i$

= 1 when $t \geq \tau_i$

W_b is the total weight of propellants and gas in the combustion chamber, and W_{cp} is the weight of combustion products. Substitution of Equation (6-36) into (6-35) gives:

$$P_b = \frac{\delta}{1+\tau_b S} \frac{R_b T_b}{V_b} W_b \tag{6-37}$$

The weight flow rate of gas out of the combustion chamber is:

$$\dot{W}_g = \frac{C_{di} C_f A_t P_b}{\sqrt{T_b}} \tag{6-38}$$

where:

C_{di} = discharge coefficient

C_f = flow coefficient

A_t = nozzle throat area.

The rate of change of total weight within the combustion chamber is then:

$$\dot{W}_b = \dot{W}_p - \dot{W}_g = A_{it} C_2 \sqrt{P_i - P_b} - \frac{C_{di} C_f A_t P_b}{\sqrt{T_b}} \tag{6-39}$$

The calculations for determining the combustion time constant τ_b are based on the following simplified model of the combustion process:

(A) The fuel and oxidizer travel at injection velocity to the center of the combustion chamber.

(B) Combustion occurs instantaneously at the center of the combustion chamber.

(C) The combustion products travel at sonic velocity to the nozzle throat.

The injection velocity into the combustion chamber is given by:

$$V_1 = \sqrt{\frac{2g}{\rho} \Delta P_i} \tag{6-40}$$

The velocity of the combustion products is given by:

$$V_2 = \sqrt{k_b g R_b T_b} \tag{6-41}$$

The combustion time constant is then:

$$\tau_b = \frac{2}{V_1} + \frac{2}{V_2} \tag{6-42}$$

The equivalent electrical circuit used to represent the supply line dynamics is shown in Figure 6-11. The transfer function of this circuit is:

$$E_{out} = \frac{1 + \tau_s}{1 + \frac{2\zeta}{\omega_n} S + \frac{1}{\omega_n^2} S^2} (E_{in.} - R\, i) \tag{6-43}$$

$$\omega_n^2 = \frac{1}{LC}$$

$$2\zeta\omega_n = \frac{R}{L}$$

$$\tau = \frac{L}{R}$$

Letting pressure be equivalent to voltage, and flow be equivalent to current, the circuit parameters become:

$$R_h = -\frac{\partial P'_s}{\partial \dot{W}_\rho}, \frac{\text{sec}}{\text{in.}^2}$$

$$L_h = \frac{\rho z}{\pi r_1^2}, \text{ lb sec}^2/\text{in.}^5$$

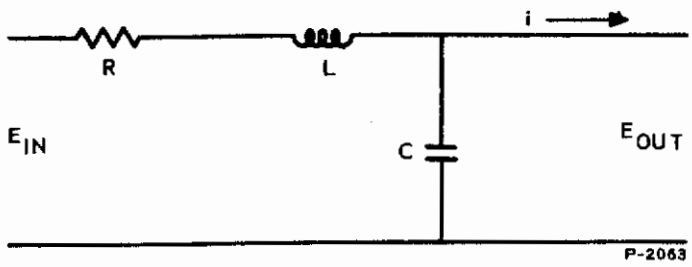

Figure 6-11 - Equivalent Circuit for Propellant Supply Line

$$\frac{1}{C_h} = \frac{B}{V_h} + \frac{1}{C_t}, \text{ lb/in.}^5$$

where: B = fluid bulk modulus, lb/in.^{2}

V_h = line volume, in.^{3}

z = line length, in.

r_l = line radius, in.

P'_s = line outlet pressure, psiu

C_t = line wall capacitance, in.^{5}/lb

and the resulting transfer function is:

$$P'_s = \frac{1 + \frac{L_h}{R_h} S}{1 + R_h C_h S + L_h C_h S^2} (P_s - \dot{W}_p R_h) \qquad (6\text{-}44)$$

The complete dynamics of the valve-combustor system is described by the block diagram shown in Figure 6-12. A computer simulation of this system is discussed in the subsection which follows.

6.4.3 Computer Simulation

The dynamic performance of the system consisting of the valve and combustion chamber was simulated on an analogue computer. The computer equations, operational diagram, and constants are discussed and given in Appendix VIII. The results of the computer runs are presented here.

Figures 6-13 through 6-25 show the step response traces obtained from the computer for various combinations of variables. Note that the time scale on these traces goes from right to left. Figure 6-13 shows the step response for the constants listed in Table 6-3. The remaining figures use these same constant values except that in each case one parameter is varied to determine its effect. Table 6-4 lists the respective variables and presents the important response characteristics.

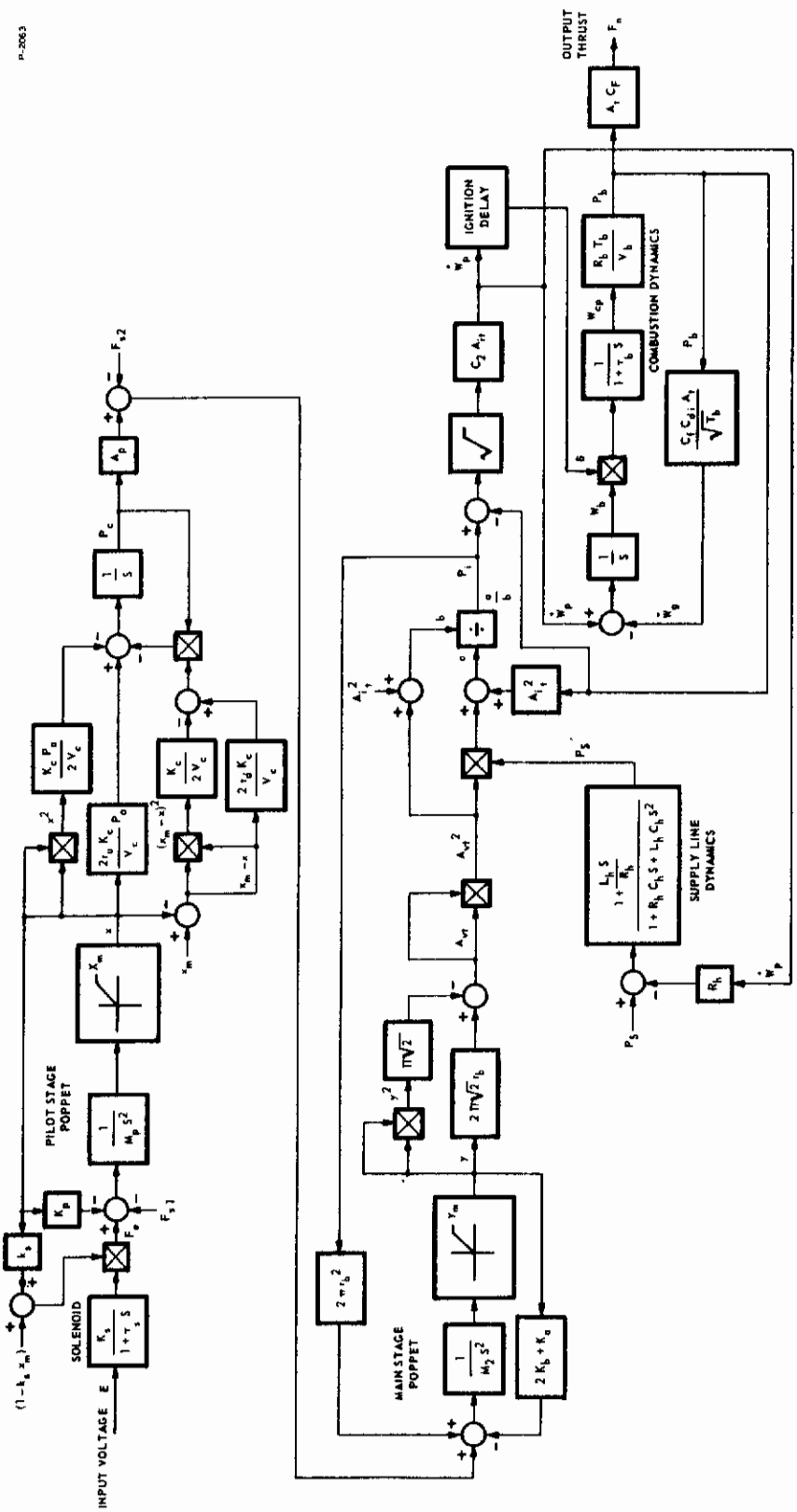

Figure 6-12 - Block Diagram of Valve-Combustor System

Table 6-4 - Effect of System Parameters Upon Response

Parameter	Value	Pressure Buildup Time (Milliseconds)	Pressure Decay Time (Milliseconds)	Pressure Overshoot (Percent)	Pressure Oscillations	Figure Number
r_i	0.0005	6.8	8.2	67	4	6-14
r_i	0.002	8.2	8.2	134	4	6-14
r_b	0.00075	7.0	7.5	116	3	6-15
r_b	0.003	8.2	9.8	92	5	6-15
V_b	28.1	6.8	7.7	142	6	6-16
V_b	112.4	7.2	8.0	58	3	6-16
A_t	1.41	8.1	8.6	75	4	6-17
A_t	5.64	7.8	8.1	54	4	6-17
x_m	0.012	6.9	8.1	61	4	6-18
x_m	0.048	6.9	8.3	64	4	6-18
y_m	0.050	6.8	7.8	65	4	6-19
y_m	0.150	6.8	7.8	77	4	6-19
V_c	0.01	7.2	8.5	74	4	6-20
V_c	0.015	7.6	9.2	74	4	6-20
F_{s1}	1.00	4.0	11.2	74	4	6-21
F_{s1}	5.19	7.0	7.6	74	4	6-21
F_{s2}	60.0	6.9	7.7	74	4	6-22
F_{s2}	100.0	7.1	7.6	74	4	6-22
P_a	400.0	7.0	7.6	74	4	6-23
P_a	800.0	6.8	7.7	74	4	6-23
P_s	300.0	7.2	8.1	53	4	6-24
P_s	600.0	8.1	7.8	45	4	6-24
With supply line dynamics		7.2	8.0	106	4	6-25
Without supply line dynamics		7.0	8.0	106	4	6-25

P-2063

The factors having the greatest effect on response time and stability were found to be the ignition time delay τ_i, combustion time constant τ_b, combustion chamber volume V_b, control volume V_c, and pilot stage preload F_{sl}. We do not have much control over τ_i and τ_b, and the volumes V_b and V_c are determined by other considerations. Therefore the remaining effective parameter, F_{sl}, determined the optimum system and was increased to give approximately the same response for charging and discharging the main stage. The resulting optimum response is shown in Figure 6-13.

Figure 6-14 shows that increasing the ignition time delay τ_i by a factor of 4 increases the pressure buildup time by about 20 percent and doubles the overshoot. Increasing the combustion time constant τ_b by a factor of 4 increased both the pressure buildup time and pressure decay time by about 17 percent, decreased the pressure overshoot 21 percent, decreased the natural frequency by 2.5, and reduced the damping, as shown in Figure 6-15. The results of varying the combustion chamber volume V_b by a factor of 4 are shown in Figure 6-16, where it is seen that the pressure buildup time increased 6 percent and the pressure decay time increased 4 percent. Also, the pressure overshoot decreased 50 percent and the damping increased. As shown in Figure 6-17, increasing the throat area by a factor of 4 decreases the pressure buildup time 4 percent, decreases the pressure decay time 6 percent, and decreases the pressure overshoot 28 percent. When x_m was increased from 0.012 inch to 0.048 inch, the pressure buildup time did not change, there was a slight increase in the pressure decay time and pressure overshoot as shown in Figure 6-18. The only effect of increasing y_m was a slight increase in pressure overshoot as shown in Figure 6-19. Figure 6-20 shows that increasing the control chamber volume results in a slight increase in both pressure buildup time and pressure decay time. Figure 6-21 shows that increasing the pilot stage preload F_{sl} by a factor of 4 increases the pressure buildup time by 75 percent and decreases the pressure decay time by 32 percent. Figure 6-22 shows that the result of increasing the main stage preload is a slight increase in pressure buildup time and a slight decrease in pressure decay time. Figure 6-23 shows the effect of increasing the inert gas supply pressure. There was a slight decrease of pressure buildup time and a slight increase of pressure decay time. The effect of increasing the fuel supply pressure is shown in Figure 6-24. The pressure buildup time increased 12 percent and the pressure decay time decreased 4 percent. The supply line dynamics increases the

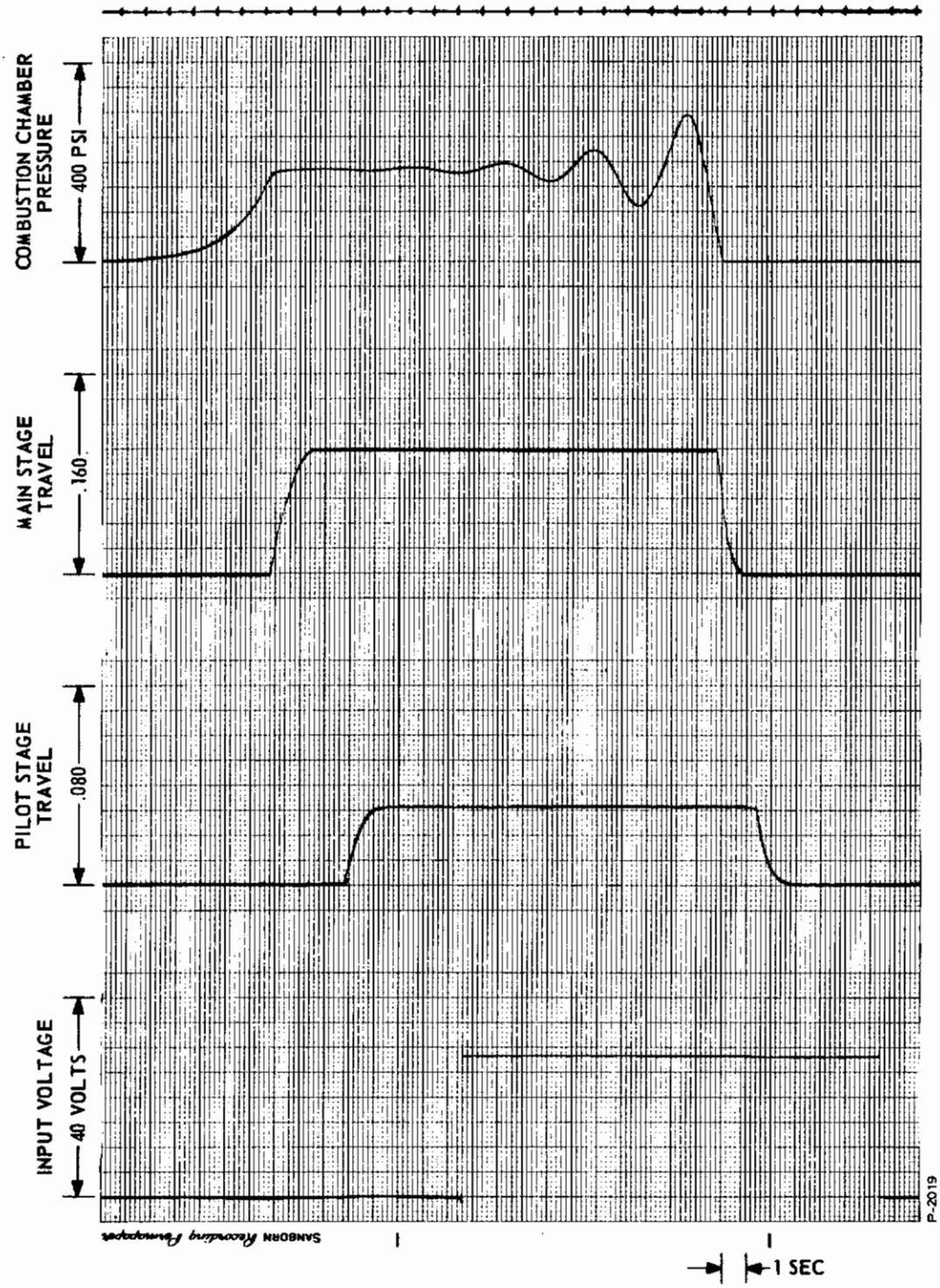

Figure 6-13 - Step Response of Optimum Valve - Combustor System

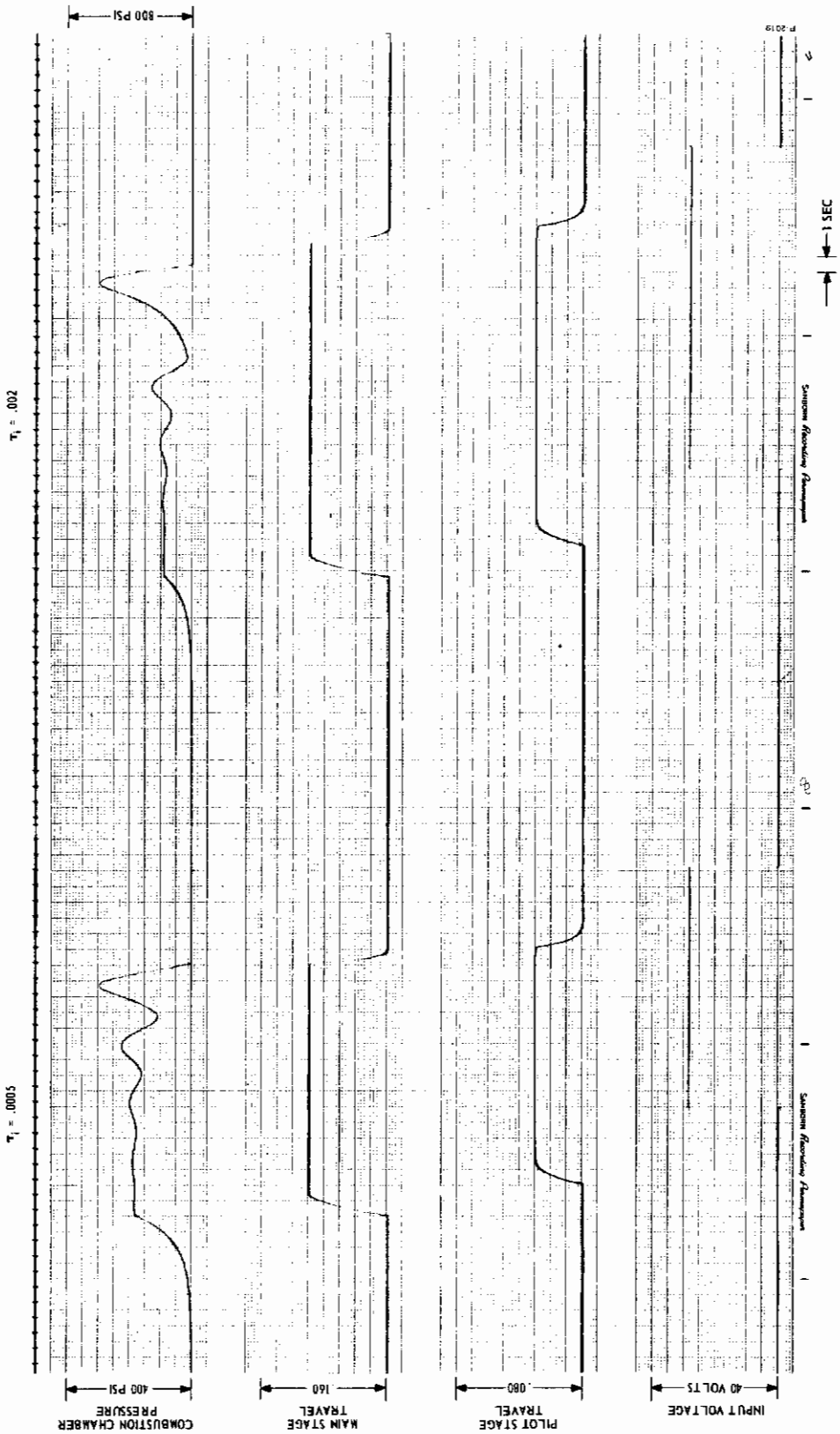

Figure 6-14 - Step Response of Valve-Combustor System for τ_i = 0.0005 sec and τ_i = 0.0020 sec

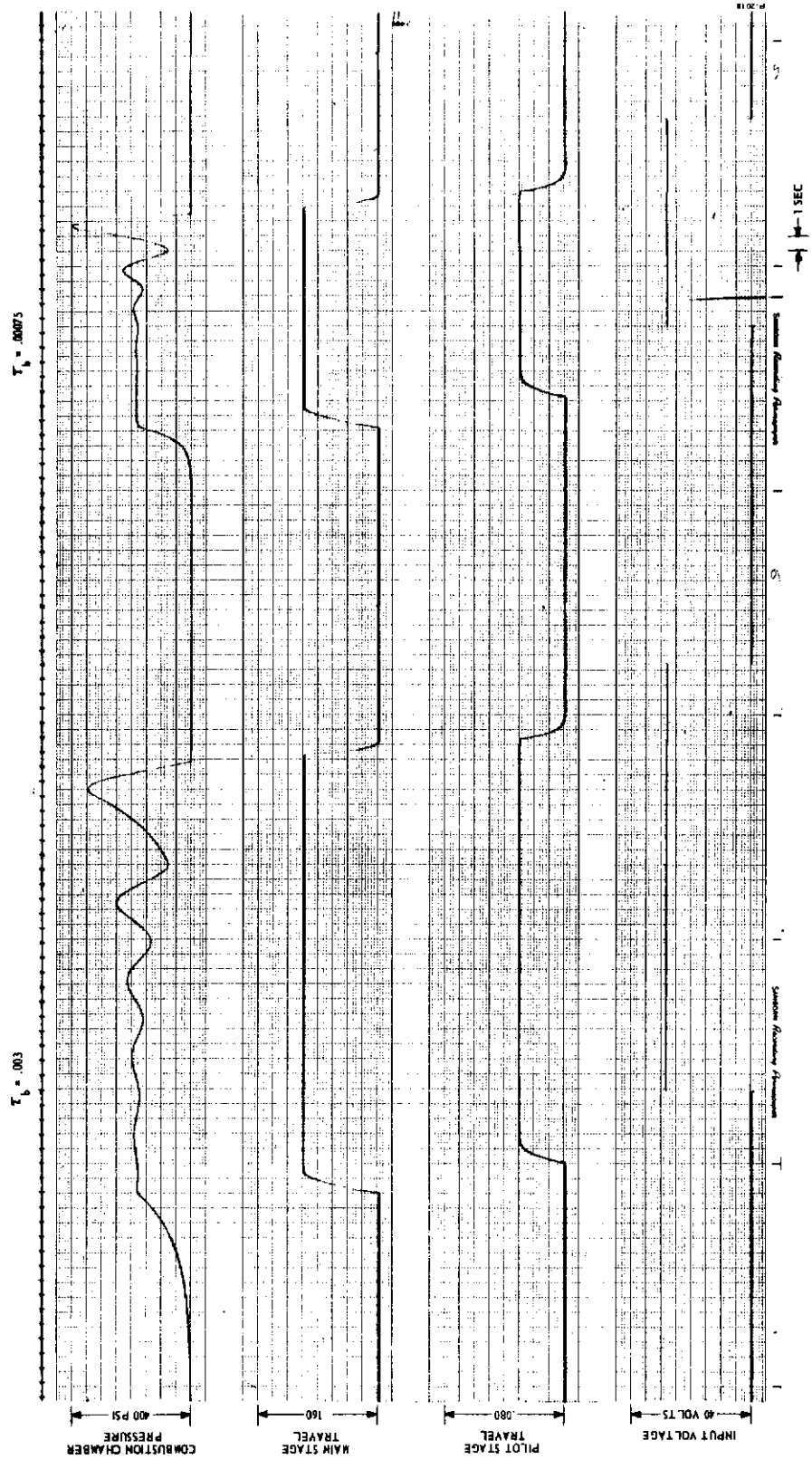

Figure 6-15 - Step Response of Valve-Combustor System for τ_b = 0.0030 sec and τ_b = 0.00075 sec

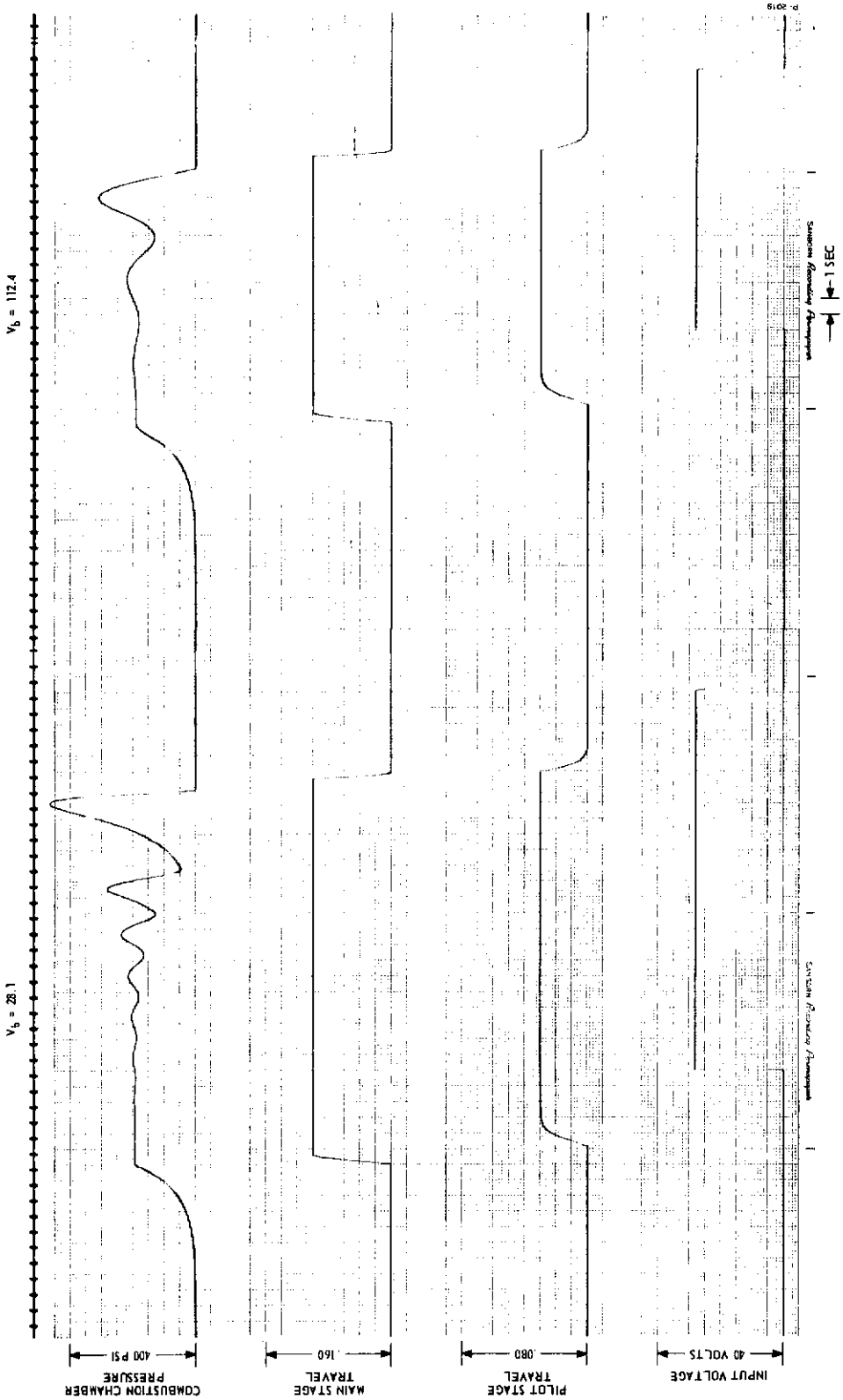

Figure 6-16 - Step Response of Valve-Combustor System for V_b = 28.1 in.^{3} and V_b = 112.4 in.^{3}

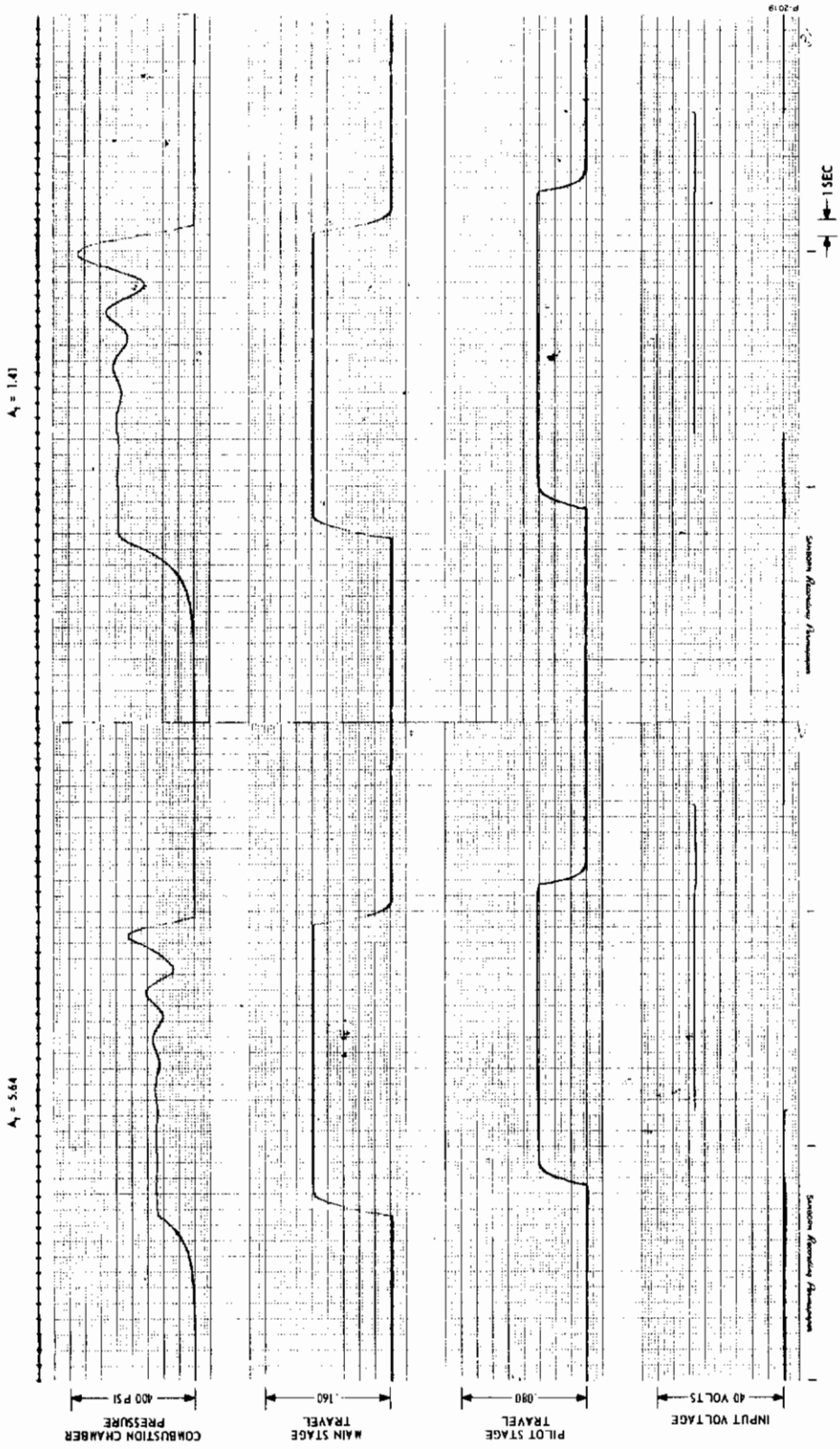

Figure 6-17 - Step Response of Valve-Combustor System for A_t - 5.64 in.^{2} and A_t = 1.41 in.^{2}

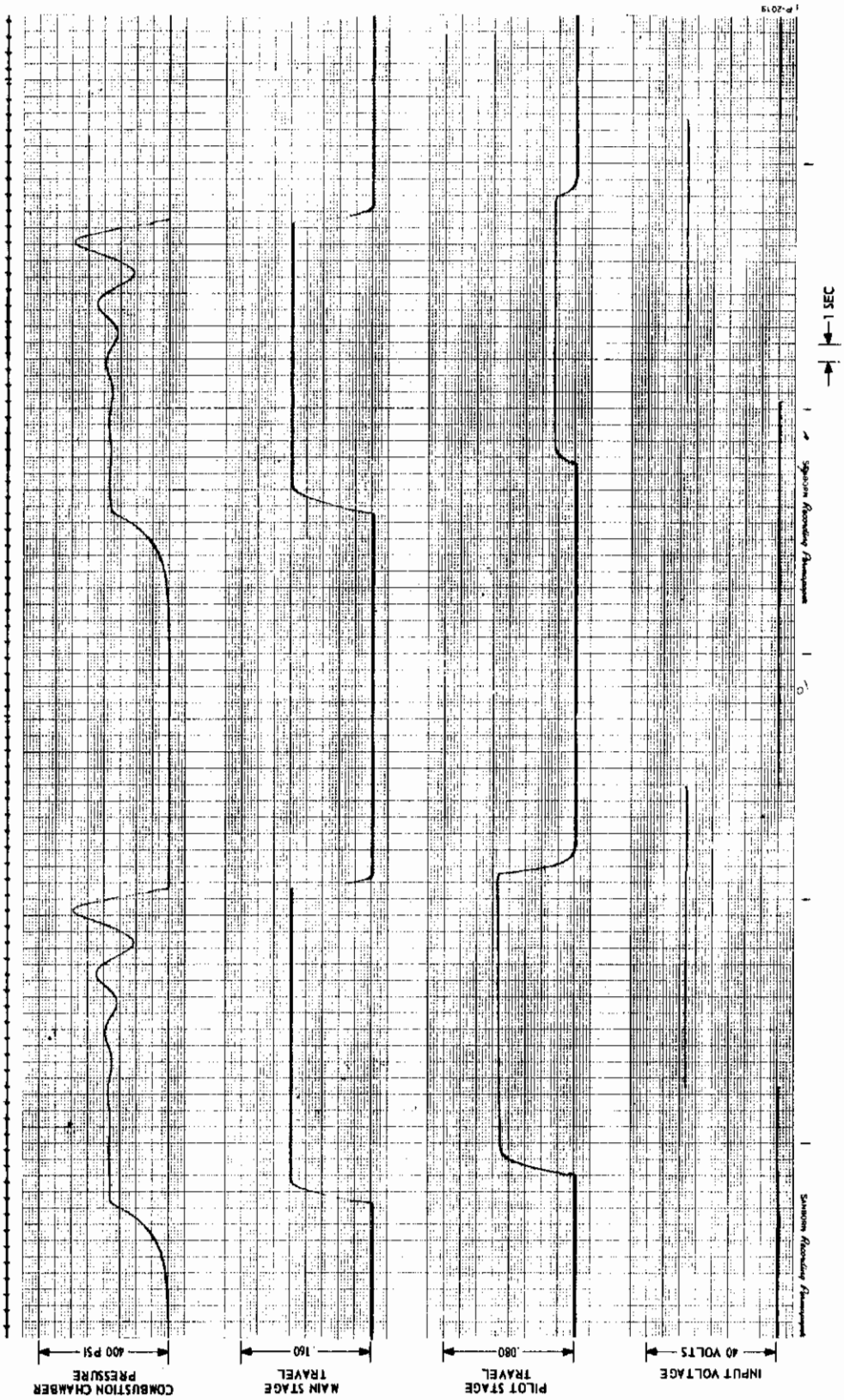

Figure 6-18 - Step Response of Valve-Combustor System for x_m = 0.012 in. and x_m = 0.048 in.

Figure 6-19 - Step Response of Valve-Combustor System for y_m = 0.050 in. and y_m = 0.150 in.

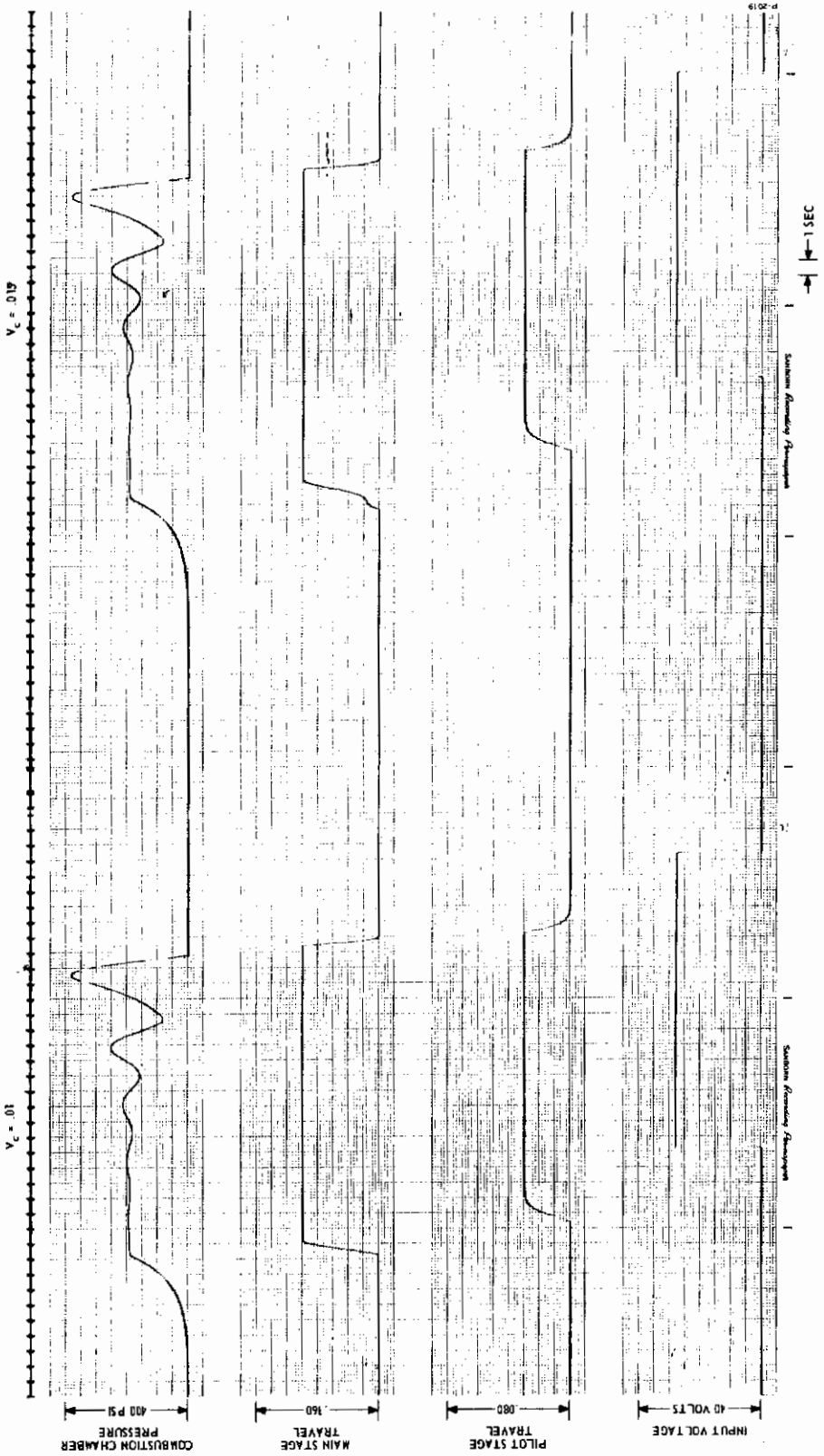

Figure 6-20 - Step Response of Valve-Combustor System for V_c = 0.010 in.^{3} and V_c = 0.015 in.^{3}

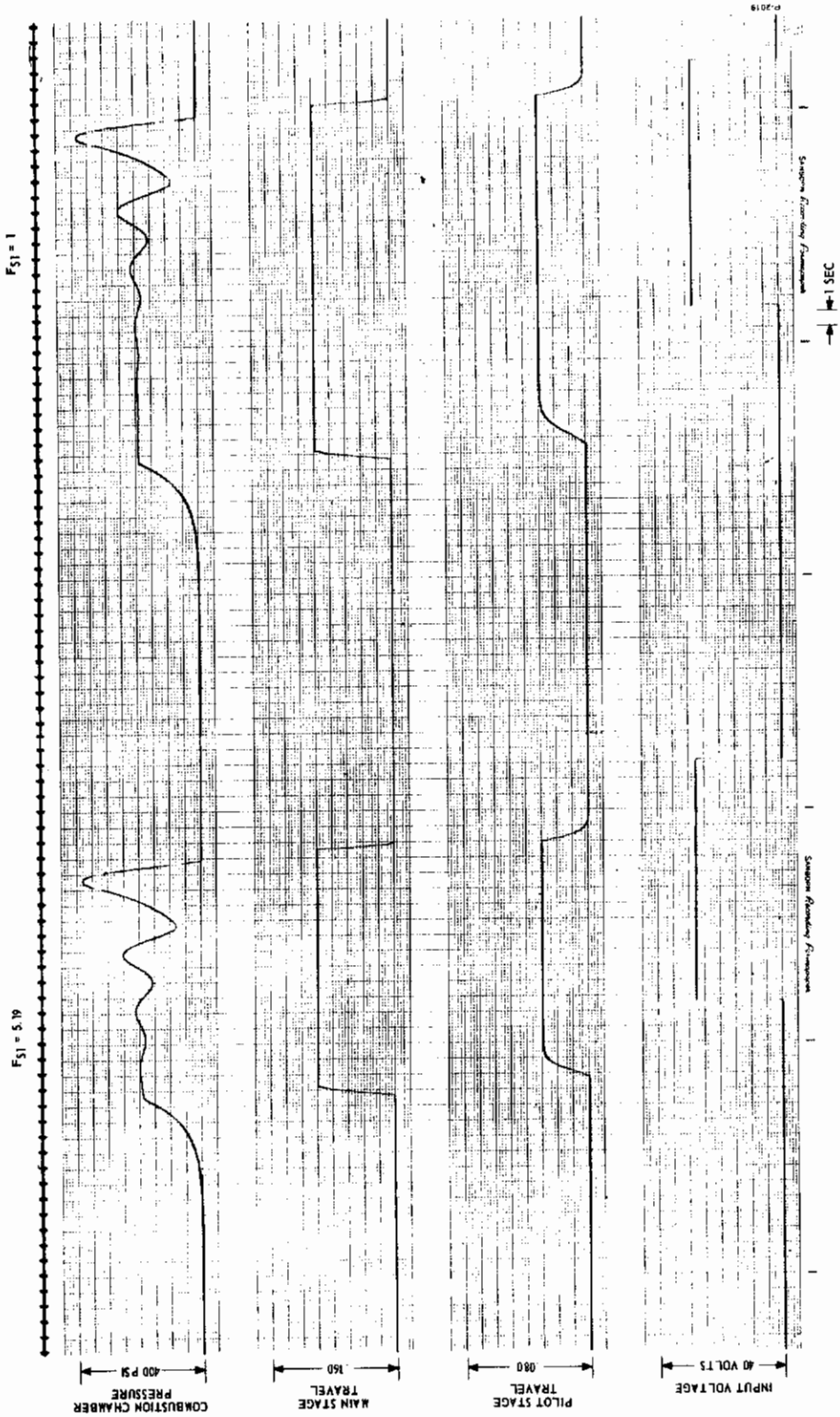

Figure 6-21 - Step Response of Valve-Combustor System for F_{s1} = 1.00 lb and F_{s1} = 5.19 lb

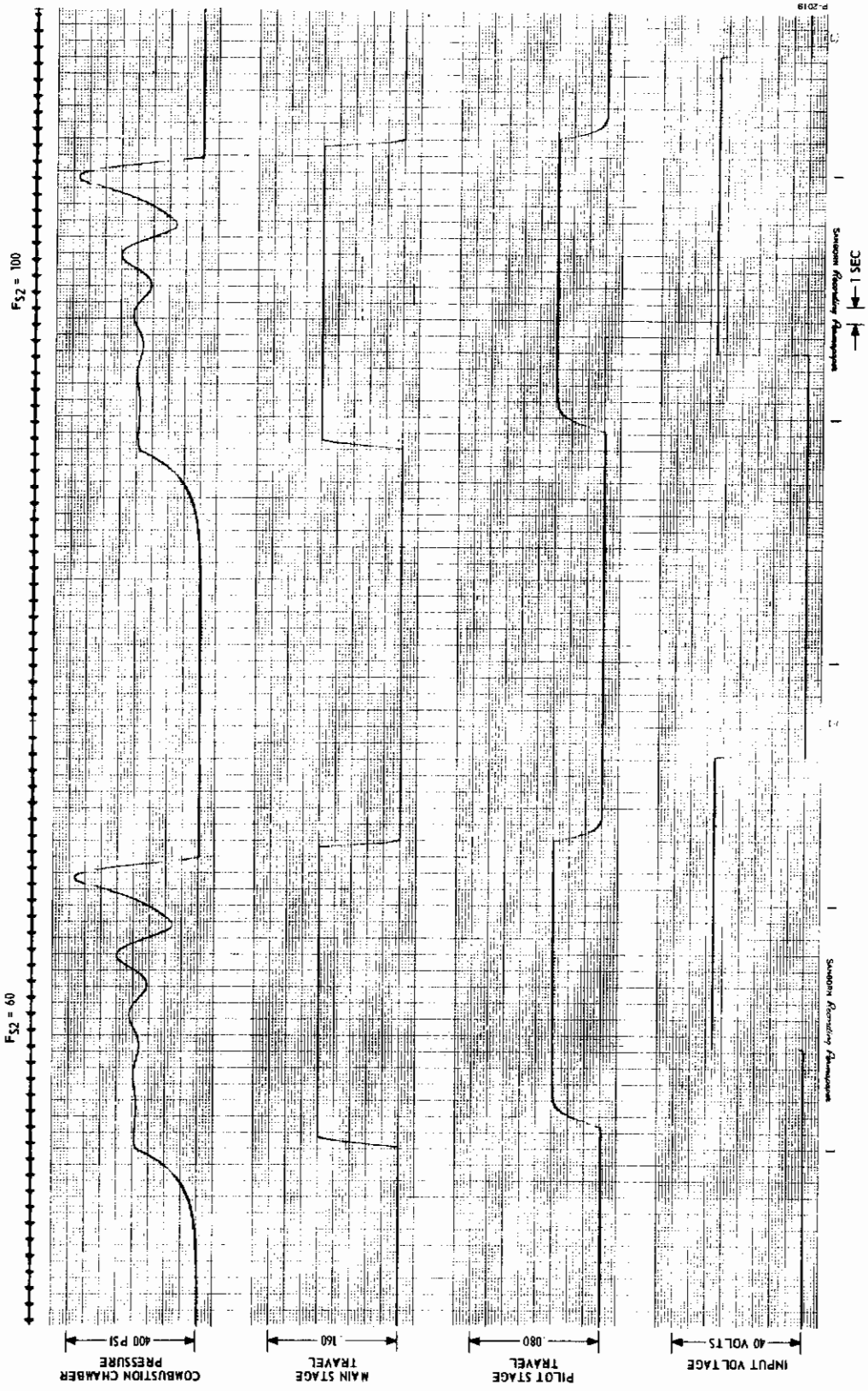

Figure 6-22 - Step Response of Valve-Combustor System for F_{s2} = 60 lb and F_{s2} = 100 lb

Figure 6-23 - Step Response of Valve-Combustor System for P_a = 800 psia and P_a = 400 psia

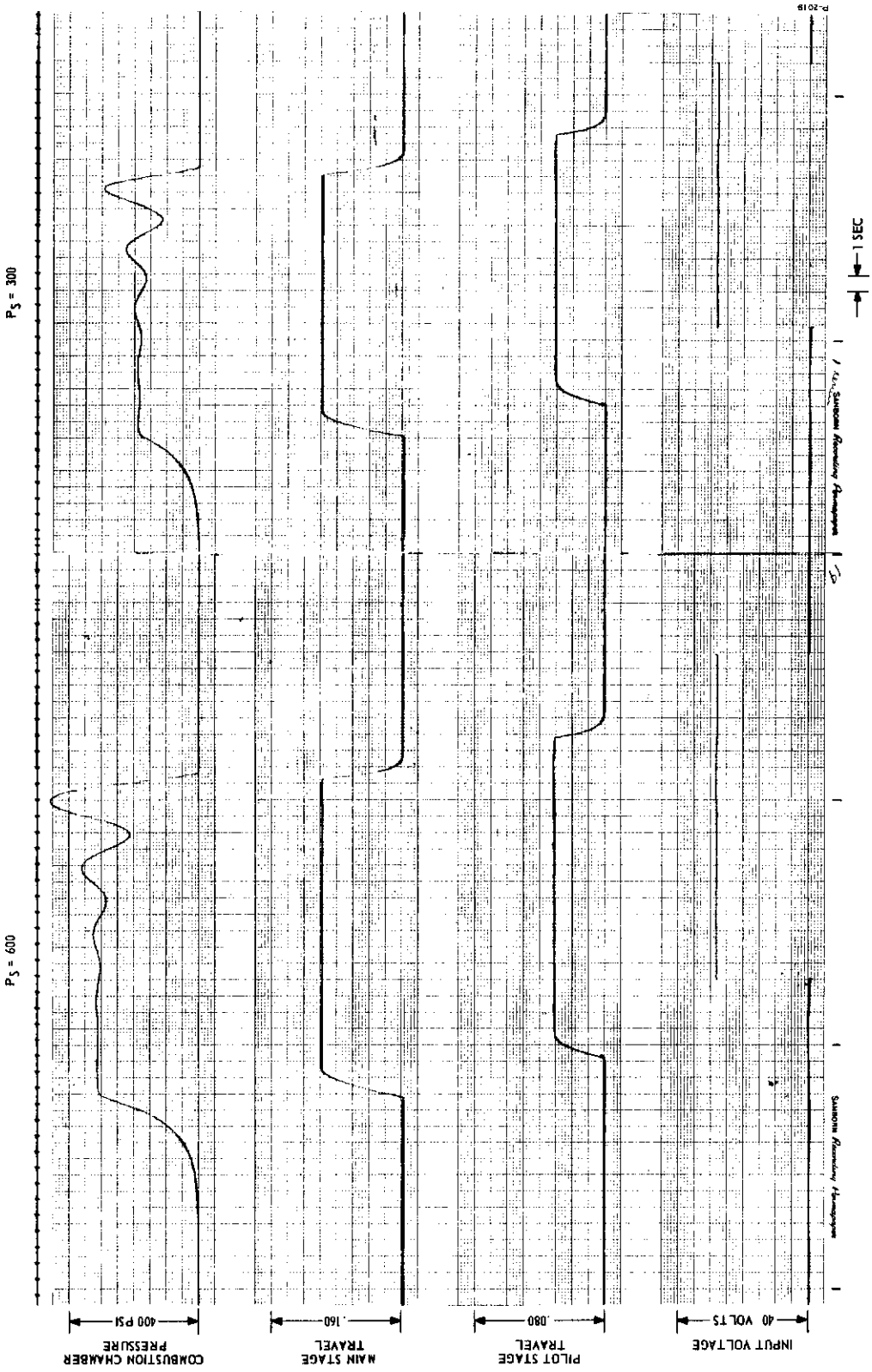

Figure 6-24 - Step Response of Valve-Combustor System for P_s = 600 psia and P_s = 300 psia

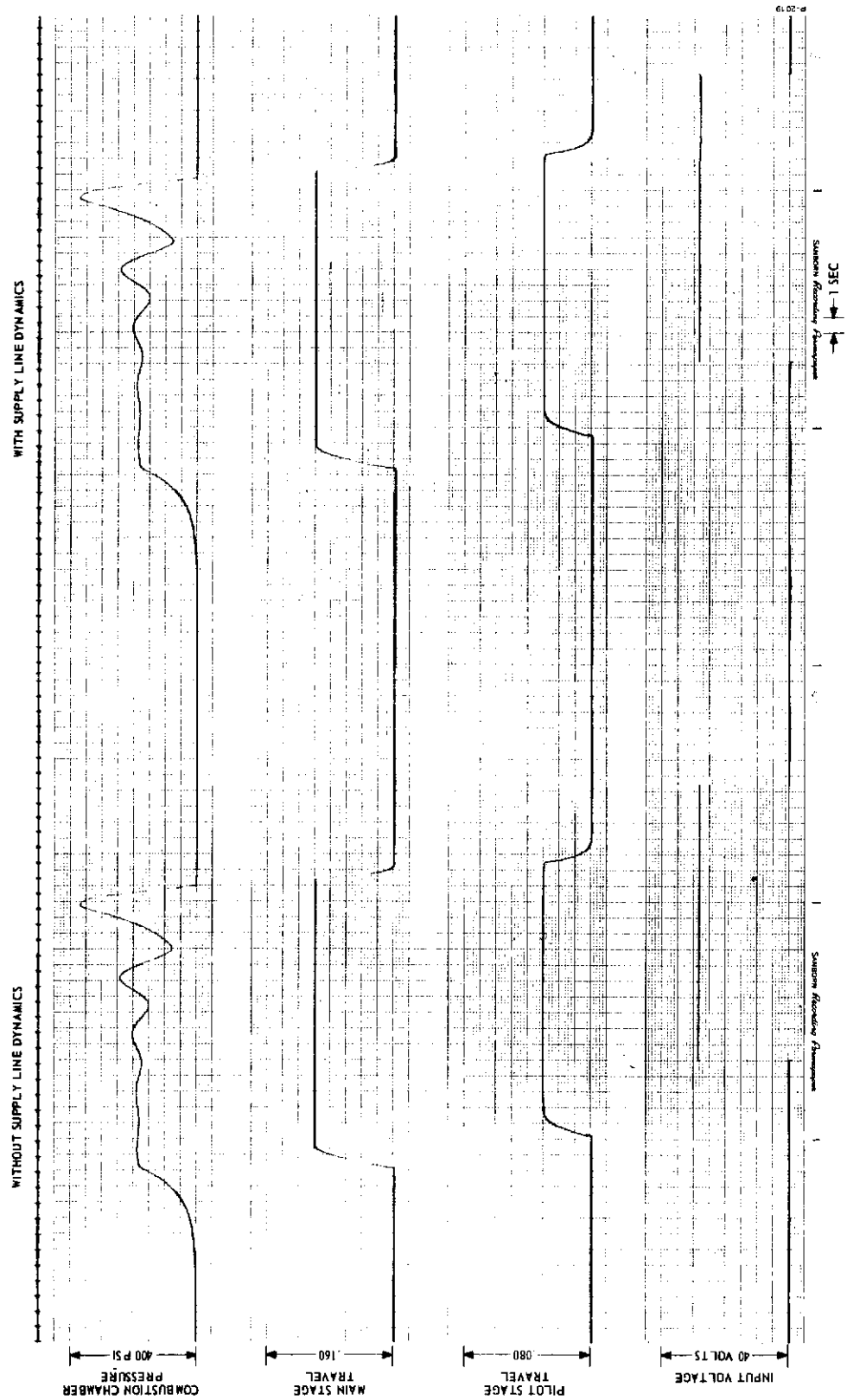

Figure 6-25 - Step Response of Valve-Combustor System With and Without Line Dynamics

pressure buildup time by 3 percent as shown in Figure 6-25. As was stated previously, the only significant parameter which can be arbitrarily changed to improve performance is the pilot stage preload F_{s1}.

The valve-combustor system as defined by Figure 6-12 is rather complex and would make the computer simulation of the complete attitude control system a difficult task. Its response, however, indicates that it can be represented by a simpler block diagram, so after a series of computer manipulations it was found that the system shown in Figure 6-26 provides essentially the same performance. The solenoid is represented by a linear first order transfer function, and the valve dynamics by a single integration, saturation, and positive feedback. The combustion process was simplified by leaving out the ignition time delay. The parameters were adjusted in the computer circuit for the simplified dynamics to get the same response time, overshoot, and same number of oscillations, as for the original complete simulation.

6.5 NOMENCLATURE

A_{if}	= area of fuel injector	$in.^2$
A_{io}	= area of oxidizer injector	$in.^2$
A_{it}	= injector total orifice area	$in.^2$
A_p	= area of main stage piston	$in.^2$

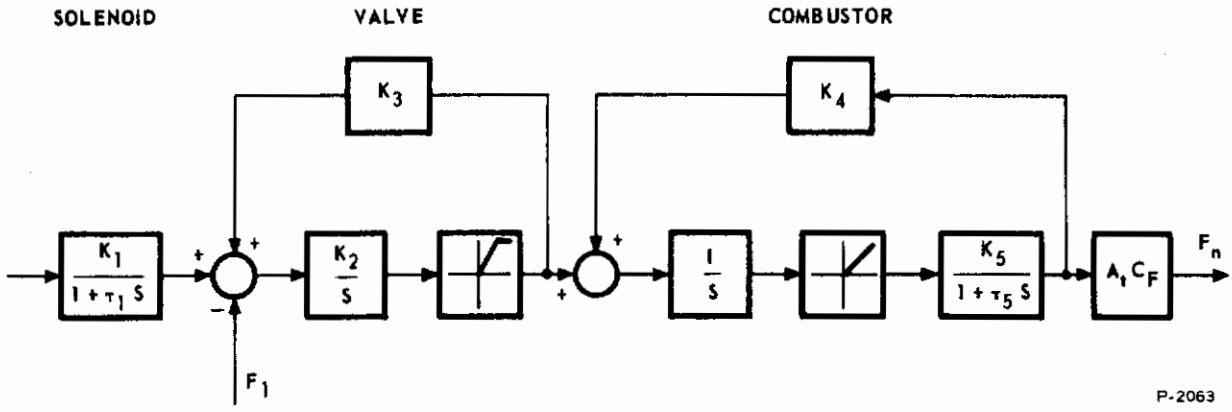

Figure 6-26 - Simplified Block Diagram of Valve and Combustion Dynamics

A_t	= nozzle throat area	$in.^2$
A_{vt}	= main stage total flow area	$in.^2$
B	= fluid bulk modulus	$lb/in.^2$
B_p	= maximum flux density in solenoid	$webers/meter^2$
C*	= characteristic velocity, ft/sec	
C_{di}	= orifice discharge coefficient for gas	
C_{dp}	= orifice discharge coefficient for propellant	
C_F	= thrust coefficient (refer to Equation 6-13)	
C_f	= flow coefficient for nozzle	$(°R)^{1/2}/sec$
C_h	= effective line capacitance	$in.^5/lb$
C_i	= flow coefficient for control gas	$(°R)^{1/2}/sec$
C_t	= line wall capacitance	$in.^5/lb$
C_2	= equivalent flow coefficient for liquid fuel and oxidizer	$(lb)^{1/2}/in.\ sec$
E	= solenoid input voltage	volts
F_e	= solenoid force output	lb
F_n	= nozzle thrust	lb
F_{s1}	= pilot stage preload	lb
F_{s2}	= main stage preload	lb
g	= acceleration of gravity	$in./sec^2$
I_{SP}	= specific impulse	sec
k_b	= specific heat ratio for combustion gas products	
k_i	= specific heat ratio for control gas	
k_s	= solenoid displacement gain	lb/in.
K_a	= rate of main stage return spring	lb/in.
K_b	= spring rate of main stage poppet bellows	lb/in.
K_p	= pilot stage spring rate	lb/in.

$K_c = \frac{1}{\sqrt{2}} C_i C_{di} \pi R_i \sqrt{T_i}$		in./sec
K_s	= solenoid force gain at full stroke	lb/volt
L_h	= effective line inductance	lb $sec^2/in.^5$
L_s	= solenoid coil inductance	henrys
M	= moleculor weight of combustion products	
M_2	= main stage mass	lb $sec^2/in.$
M_p	= pilot stage mass	lb $sec^2/in.$
N	= number of solenoid coil turns	
P_a	= control gas supply pressure	psia
P_b	= combustion chamber pressure	psia
P_c	= main stage control pressure	psia
P_e	= ambient pressure	psia
P_i	= pressure between main stage and injector orifice	psia
ΔP_i	= pressure drop across injector	psia
P_s	= propellant supply pressure	psia
P_s'	= propellant supply pressure at valve	psia
r	= oxidizer-to-fuel ratio by weight	
r_l	= radius of propellant supply line	in.
r_b	= radius of main stage poppet land	in.
r_d	= radius of pilot stage poppet downstream land	in.
r_s	= solenoid radius	meters
r_u	= radius of pilot stage poppet upstream land	in.
R_b	= gas constant for combustion products	in./°R
R_h	= effective line fluid resistance	$sec/in.^2$
R_i	= gas constant for control gas	in./°R

R_s	= solenoid coil resistance	ohms
t	= time	sec
T_b	= combustion chamber temperature	°R
T_i	= temperature of control gas	°R
V_b	= combustion chamber volume	$in.^3$
V_c	= main stage control chamber volume	$in.^3$
V_h	= supply line volume	$in.^3$
$\dot{W}_a$	= gas flow rate into main stage control volume	lb/sec
W_b	= total weight of propellants and gas in combustion chamber	lb
$\dot{W}_c$	= compressibility flow in main stage control volume	lb/sec
$\dot{W}_e$	= gas flow rate out of main stage control volume	lb/sec
$\dot{W}_f$	= weight flow rate of fuel into combustion chamber	lb/sec
$\dot{W}_g$	= flow rate of gas through nozzle	lb/sec
$\dot{W}_o$	= weight flow rate of oxidizer into combustion chamber	lb/sec
$\dot{W}_p$	= total flow rate of fuel and oxidizer into combustion tank	lb/sec
W_{cp}	= weight of combustion products in combustion chamber	lb
x	= pilot stage poppet travel	in.
x_m	= maximum value of x	in.
y	= main stage poppet travel	in.
y_m	= maximum value of y	in.
z	= length of supply line	in.
δ	= switching function	
δ_f	= specific gravity of fuel	
δ_o	= specific gravity of oxidizer	

θ	= poppet angle	deg
ρ	= mean effective propellant density	$lb/in.^3$
τ_b	= combustion time constant	sec
τ_i	= ignition time delay	sec
τ_s	= solenoid time constant	sec

SECTION 7

ATTITUDE CONTROL DURING RENDEZVOUS AND ORBITAL TRANSFER

7.1 INTRODUCTION

7.1.1 Objective

The objective of this study is to select and devise an attitude control system which will meet all of the requirements dictated by orbital transfer and rendezvous maneuvers. In meeting this objective, a simulation of the control loop and vehicle dynamics must be accomplished.

7.1.2 Requirements

During rendezvous, range rate and angular rate corrections are made at frequent intervals. The guidance logic computes the required corrections from measured values and accordingly commands thrust pulses from the guidance engines. The attitude control system properly aligns the guidance engines' thrust vectors with respect to the line-of-sight between the vehicle and target. If sizable attitude errors occur, large errors are introduced into the guidance system, resulting in an unsuccessful rendezvous.

The average accuracies required by the attitude control system during a rendezvous guidance correction were derived in Subsections 3.3.3 and 3.3.4 and are specified as follows:

Axis	Maximum Average Error
Pitch	$\pm$0.010 radians
Yaw	$\pm$0.010 radians
Roll	$\pm$0.020 radians

During orbital transfer, attitude errors of $\pm$0.020 radians about all axes can be tolerated. It is seen that the rendezvous accuracy requirements are the most stringent. On this basis, it will be assumed that a system which provides successful rendezvous performance will also be adequate for orbital transfer.

Representative moments of inertia about the three axes are:

Axis	Moment of Inertia
Pitch	4.36×10^6 lb-sec^2-ft
Yaw	5.22×10^6 lb-sec^2-ft
Roll	1.0×10^6 lb-sec^2-ft

Perfect alignment of the guidance control engines is impossible, therefore, each time a guidance engine is fired, an attitude disturbance will act on the vehicle for the duration of the firing. The attitude control system must be sized to correct these disturbances. A secondary injection thrust vector control loop will be incorporated with the main engine to handle the largest disturbance torques. Typical values for these disturbance torques are:

Axis	Maximum Main Engine Misalignment Torque
Pitch	400,000 ft-lb
Yaw	200,000 ft-lb
Roll	≈ 0

As rendezvous progresses, the angular dynamics of the line-of-sight and the disturbance torques acting on the vehicle vary. Table 7-1 gives the important values for angular acceleration of line-of-sight, $\ddot{\gamma}$, about the pitch axis and maximum disturbance torques, M_d, as the range, r, decreases.

Table 7-1 - Rendezvous Parameters

r ft	$\ddot{\gamma}$ rad/sec^2	M_{dp}(pitch) ft-lb	M_{dy}(yaw) ft-lb	M_{dx}(roll) ft-lb
220,000	-5.9×10^{-5}	50,000*	0*	25,000
15,000	-8.66×10^{-4}	50,000*	0*	25,000
9,200	-2.2×10^{-4}	58,000	25,000	4,000
1,500	-1.33×10^{-3}	58,000	25,000	4,000
900	-1.70×10^{-4}	8,600	4,000	300
100	-2.50×10^{-3}	8,600	4,000	300

*These values are exclusive of the contributions due to main engine misalignment.

For purposes of attitude simulation, the angular motion of rendezvous may be approximated by the curve given in Figure 7-1. The value of $\dot{\gamma}$ at the initiation of a guidance correction is always at or near 0.001 rad/sec, but $\ddot{\gamma}$ does change and is adequately defined in Table 7-1. In the actual case, $\dot{\gamma}$ is not quite reduced to zero, but the angular motion existing after the correction is negligible compared to that during the correction.

The desired control system must satisfy the functional requirements stated above, and in addition:

(a) Have a fast response time,

(b) Use a minimum amount of propellant in making attitude changes,

(c) Minimize the number of switchings of the attitude jets,

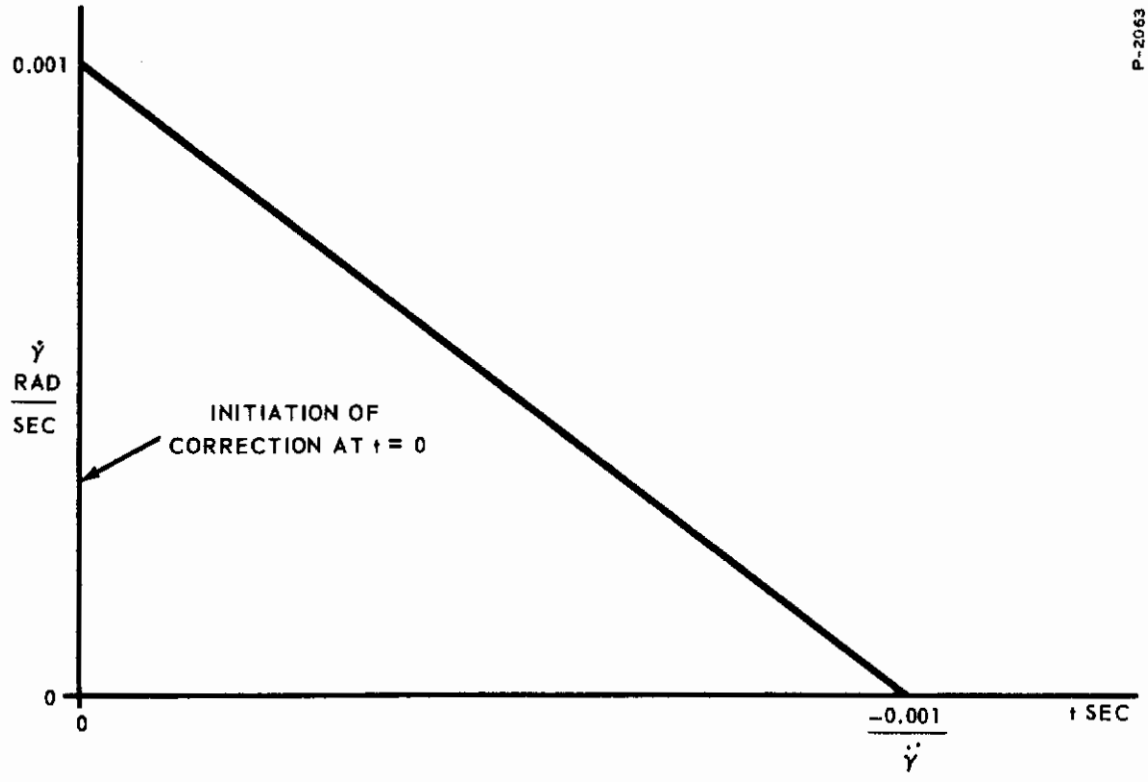

Figure 7-1 - Rendezvous Angular Motion Approximation

(d) Minimize the propellant consumption in the attitude limit cycle,

(e) Minimize the complexity of the system.

7.2 PRELIMINARY STUDY OF REACTION ENGINE CONTROL LOOP

7.2.1 Introduction

There are three basic types of reaction engine attitude control systems; on-off, on-off with more than one thrust level, and proportional. Without a control dead zone, an on-off control is always in one direction or the other and a proportional control is seldom at the neutral position. To prevent excessive propellant consumption, a dead zone must be used to reduce the time when the jets are on.

The undamped vehicle inertia contributes 180 degrees phase lag to the control loop at all frequencies. Unstable operation will result if the control loop phase lag is 180 degrees or greater at the frequency for which the loop gain is unity. Therefore, rate feedback or lead-lag compensation must be used to reduce the phase lag for a linear system. Stable operation can be obtained with no compensation by using logic circuitry to control the thrust impulses.

In all of the discussion which follows, the dynamics of the attitude engines and associated components are neglected. This simplification is considered to be reasonable, since the goal of this preliminary study is only to choose the basic type of control. Implementation and optimization of the complete control loop is carried out later in the report.

7.2.2 Possible Control Systems

7.2.2.1 On-Off Control

An on-off attitude control system with proportional plus rate feedback, shown in Figure 7-2, is discussed in (79)* and (82). With small values of rate feedback this system is underdamped. An objectional feature of this system is that, for small initial values of attitude error, the response may chatter, i.e., a number of control torque pulses are applied before the error changes sign.

*Numbers in parentheses refer to the references listed in Section 10.

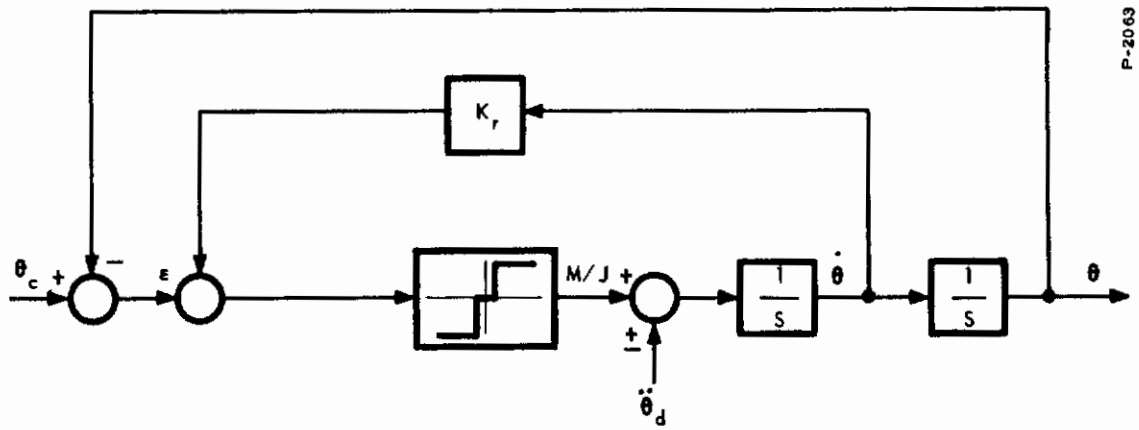

Figure 7-2 - Block Diagram - On-Off Attitude Control System with Rate Feedback

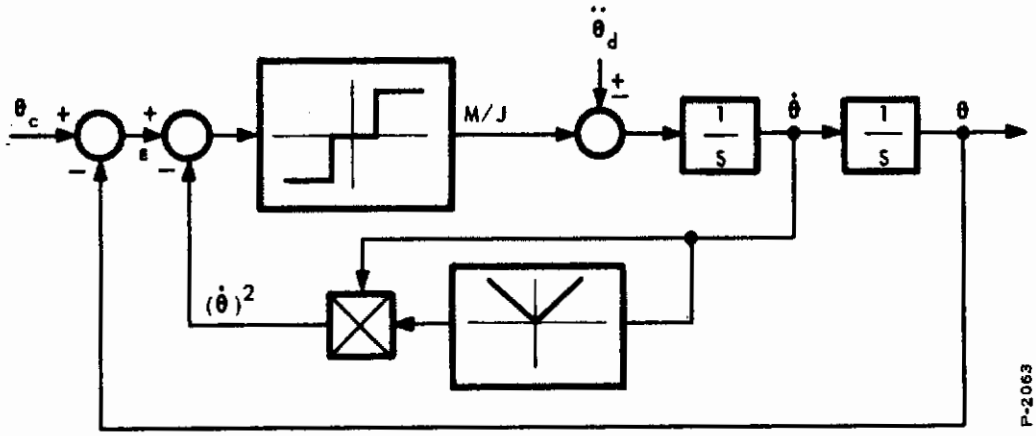

Figure 7-3 - Block Diagram - On-Off Control with Rate-Squared Feedback

On-off control with proportional plus rate-squared feedback is also discussed in (79) and is shown in Figure 7-3. For an initial error, the ideal response of this controller is control torque in one direction until the error is reduced to half its initial value and then reverse torque until the error and error rate become zero. This maneuver has the minimum response time, but there are several objections to it. The propellant consumption is excessive and the squaring circuit adds to the complexity. Also, the ideal performance can only be obtained when the control acceleration and the characteristics of the control system elements can be predicted exactly. If this cannot be done, the performance is degraded.

7.2.2.2 Proportional Control

In (83), the optimum value of control acceleration to minimize the total impulse for various initial conditions and disturbances is determined for an on-off system. The optimum value was seen to be different in each case. The optimum control system would therefore require an infinite number of values of control acceleration. Thus, the optimum system would appear to be a proportional controller.

The authors of (79) object to conventional proportional systems on the basis of complexity, leakage, and reliability. The proportional attitude control system proposed for this application eliminates or minimizes these objectional features as it has zero quiescent leakage and is of relatively simple construction.

7.2.2.3 Pulse Width Modulation and Pulse Amplitude Modulation

The requirements of fast response and low propellant consumption eliminate the pulse width and pulse amplitude modulated systems from consideration. A very low frequency during the limit cycle is required to minimize propellant consumption, and a high frequency required for fast response when there is a disturbance. Since these systems have a fixed carrier frequency, both requirements cannot be satisfied.

7.2.2.4 Logically Controlled Pulses

A method of obtaining stable operation with no compensation or rate feedback is described in (81). The operation of this system is best described by use of the phase plane plot of error versus error rate shown in Figure 7-4. The phase plane is divided into a number of vertical sections by switching lines. Starting with an initial error and error rate, the error increases until the first switching line is crossed. The controller then meters out the absolute minimum impulse, resulting in a decrease in error rate. If the error rate still has the same sign, the error keeps increasing until the next switching line is crossed. Then another impulse is generated and so on until the error rate changes sign. When the switching lines are crossed in the direction of decreasing error, they produce no control action. When the error passes through zero and reaches the switching line of opposite sign an impulse is generated and the system goes into a stable limit cycle. The basic idea of this system is to control the attitude of the spacecraft

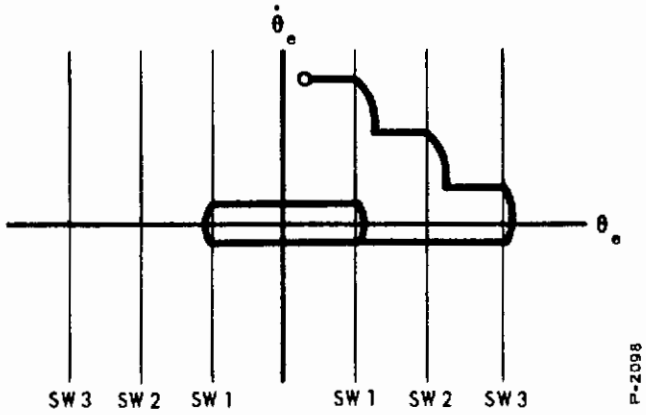

Figure 7-4 - Phase Plane Diagram for Logically Controlled Pulse System

with pulse torquing according to error limits and damping the motion in a nonlinear fashion by using phase plane quadrant information only. The knowledge of the quadrant is obtained from the property that an increasing error magnitude defines the first and third quadrants. The block diagram of this control system is shown in Figure 7-5.

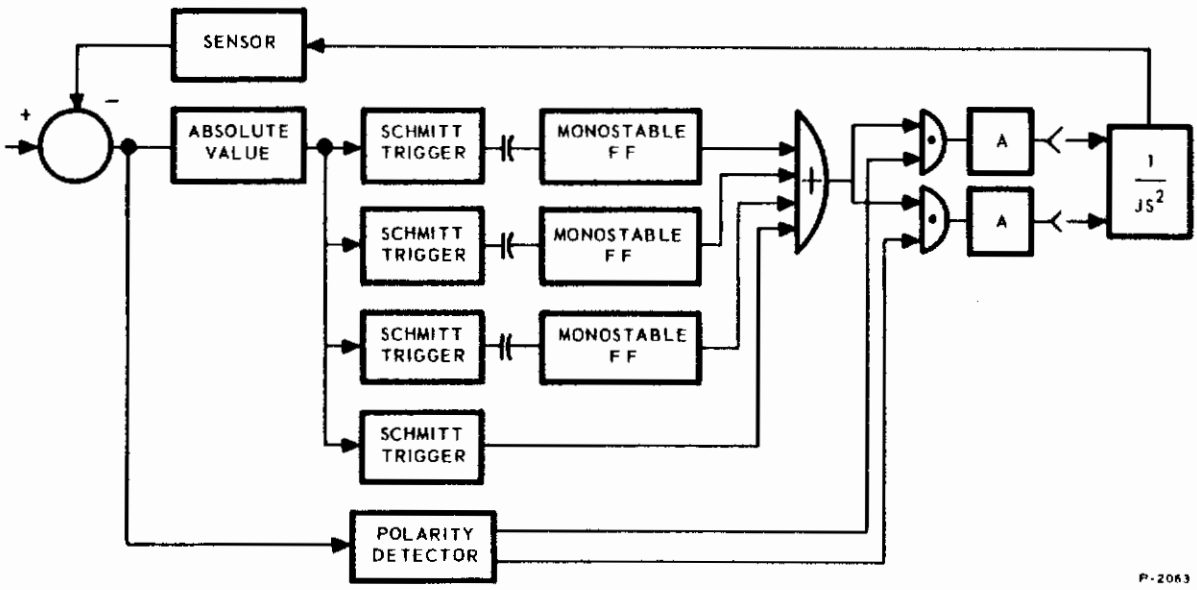

Figure 7-5 - Block Diagram of Logically Controlled Pulse System

7.2.2.5 Pulse Sequence Technique

The pulse sequence logic is based on the history of the previous pulses (80). It contains two separate logic sequences to cover the control of the vehicle during the maneuvering required to achieve a desired attitude (acquisition), and the maintenance of that attitude within specified limits (limit cycling). The acquisition logic controls the vehicle during the original attitude acquisition and during reacquisitions which become necessary following disturbance torques or maneuvering. Acquisition is accomplished by monitoring the time that the vehicle has been beyond the threshold limits. This time is used in commanding the proper corrective impulse sizes (actuator on-times) and the length of time between corrective impulses. The limit cycle logic is derived from a continuous investigation of the three previous pulses. A particular pulse width is maintained until the last three pulses contain an alternation of sign of either (+, -, +) or (-, +, -). Either of these sequences acts as a trigger signal to command a step down to the next smaller control impulse size. In the absence of a disturbance this process is continued until the pulse magnitude is reduced to its smallest value.

7.2.3 Comparison of Control System Types

The principal application for a control system using logic techniques is in the control of vehicle attitude during long periods of coasting when the disturbances are very small. The vehicle rates are below the threshold of rate sensing devices and thereforerate feedback is not practical. A typical limit cycle for a system of this type has a frequency of one cycle per hour. The logic systems are considerably more complex than rate feedback or lead-lag compensation. The vehicle rates during rendezvous are considerably above the threshold of rate sensors, therefore, rate feedback or lead-lag compensation should be used in preference to the logic techniques for stabilization. It appears that on-off control, proportional control, or a combination thereof would provide the best over-all performance.

7.2.4 Computer Simulation

7.2.4.1 On-Off Control

The block diagram of an on-off controller with rate feedback is shown in Figure 7-2, and the same controller with lead-lag compensation is shown in Figure 7-6. The on-off element can be either

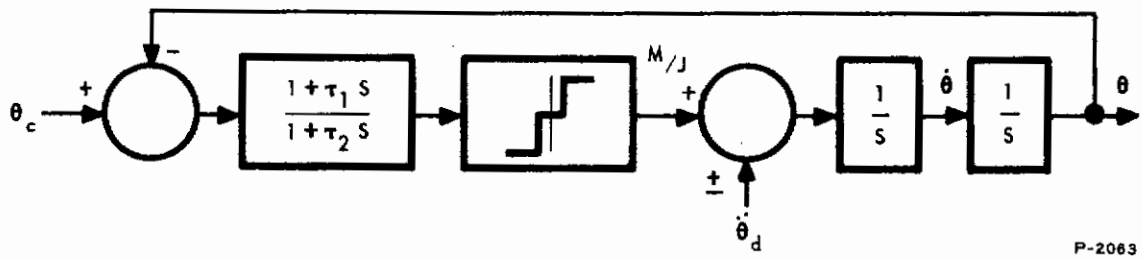

Figure 7-6 - Block Diagram - On-Off Attitude Control System with Lead-Lag Compensation

a solid state switch, relay, or high gain amplifier. Dead zone is included to reduce the total impulse during the limit cycle. The valve and combustion dynamics should appear between the on-off element and the vehicle inertia, but were omitted in this preliminary study.

The analogue computer simulation of the on-off system with rate feedback revealed a significant amount of chattering, which is in agreement with (79). The on-off system with lead-lag compensation did not chatter, so a more detailed investigation was made where it was assumed that a constant disturbance acceleration of 0.010 rad/sec^2 existed for 10 seconds.

It was found that the average attitude error during the disturbance duration decreased as the torque-to-inertia ratio M/J increased, but this was accompanied by an increase in total acceleration impulse I_{at}. The problem in selecting an optimum value for M/J results in a trade-off between acceptable values of attitude error and propellant consumption rate.

The response for M/J equal to 0.012 rad/sec^2 is shown in Figure 7-7 for zero initial error and in Figure 7-8 for an initial error equal to the limit cycle amplitude. This value of M/J is the mimumum value for zero initial attitude error which will hold the average attitude error within the required limit of 0.010 radian. In Figure 7-7, the average error is 0.0095 radian, while in Figure 7-8 it is 0.0277 radian. The value used for M/J is obviously too low to handle all possible initial conditions.

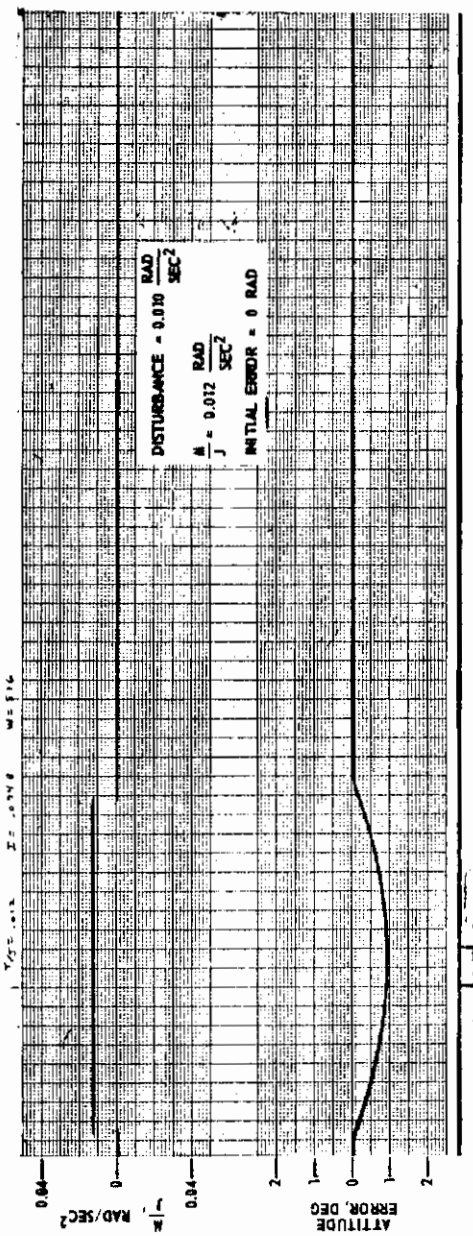

Figure 7-7 - Response of On-Off System with Lead-Lag Compensation

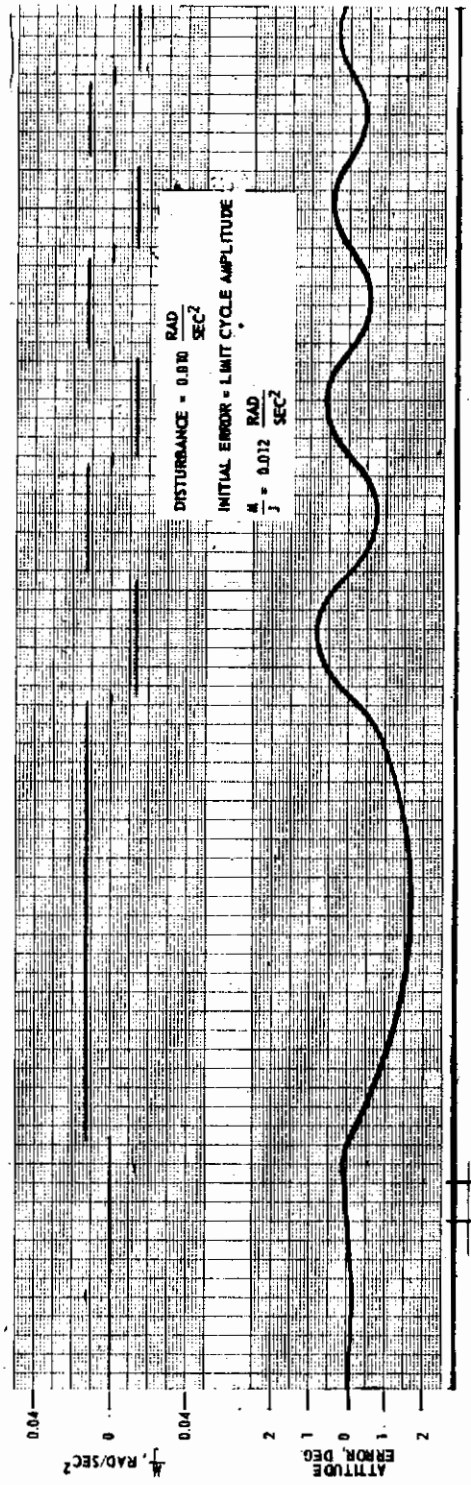

Figure 7-8 - Response of On-Off System with Lead-Lag Compensation

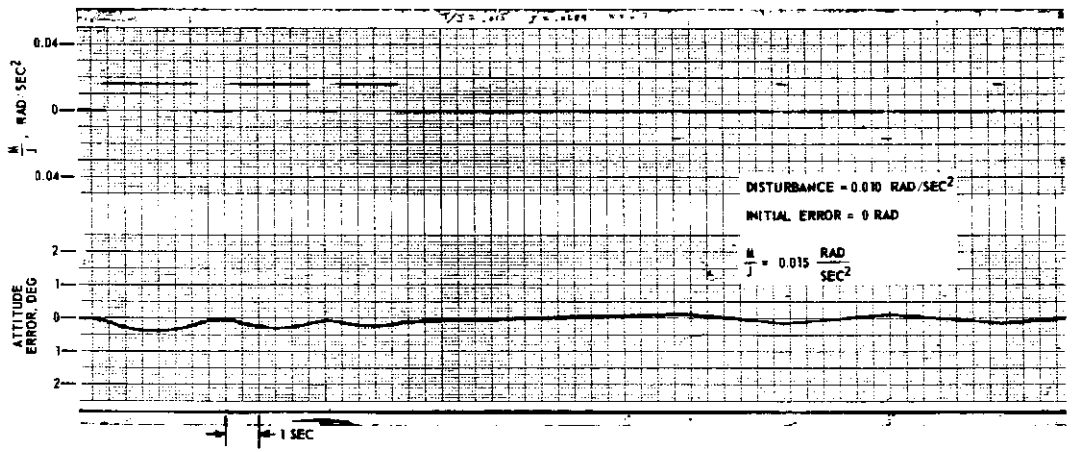

Figure 7-9 - Response of On-Off System with Lead-Lag Compensation

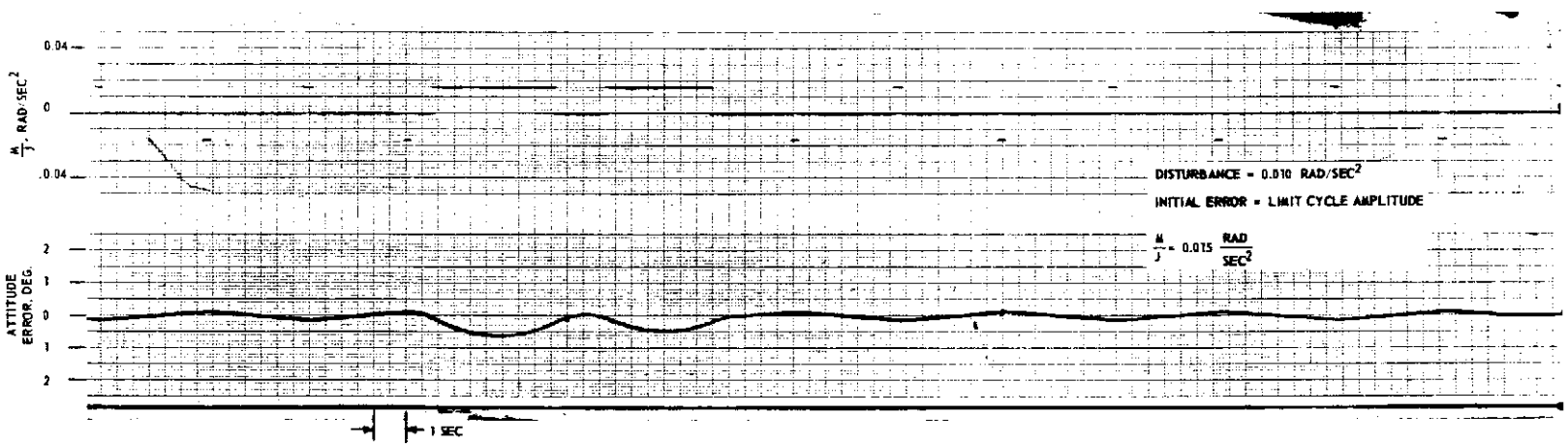

Figure 7-10 - Response of On-Off System with Lead-Lag Compensation

The response for M/J, equal to 0.015 rad/sec^2, is shown in Figure 7-9 for zero initial error and in Figure 7-10 for an initial error equal to the limit cycle amplitude. For these two cases, the average errors are 0.0028 radian and 0.0056 radian respectively and the total impulses are equal to 0.13 rad/sec. This system is acceptable within the accuracy of the simplifying assumptions used.

The on-off system with deadband described here is similar to pulse-width modulation since the pulse frequency during a disturbance does not differ appreciably from the frequency during the limit cycle with zero error. When the pulse amplitude is decreased, the limit cycle frequency decreases, but the error resulting from disturbances becomes greater. Thus the M/J ratio should be the smallest value that will hold the error within the desired limits.

If the time between disturbances is always sufficient to permit the system to attain a limit cycle, an optimum value of deadband exists. If the deadband is too small, the limit cycle frequency will be too high, and propellant consumption will be excessive during the limit cycle. As the deadband is increased, M/J must be increased to prevent large overshoots when a disturbance is applied at a peak of the limit cycle. The larger M/J also results in excessive propellant consumption.

7.2.4.2 Proportional Control

The block diagram for the proportional system studied is shown in Figure 7-11 with rate feedback, and in Figure 7-12 with lead-lag compensation. Dead-zone and nonlinear gain are used in each case to minimize the total impulse. The valve and combustion dynamics are omitted for this preliminary study.

It was found that the proportional control system with lead-lag compensation had an excessive pulse width during its limit cycle. A pulse-width limiter circuit was used to reduce the pulse width when the error was small, but this resulted in chattering when controlling during a disturbance.

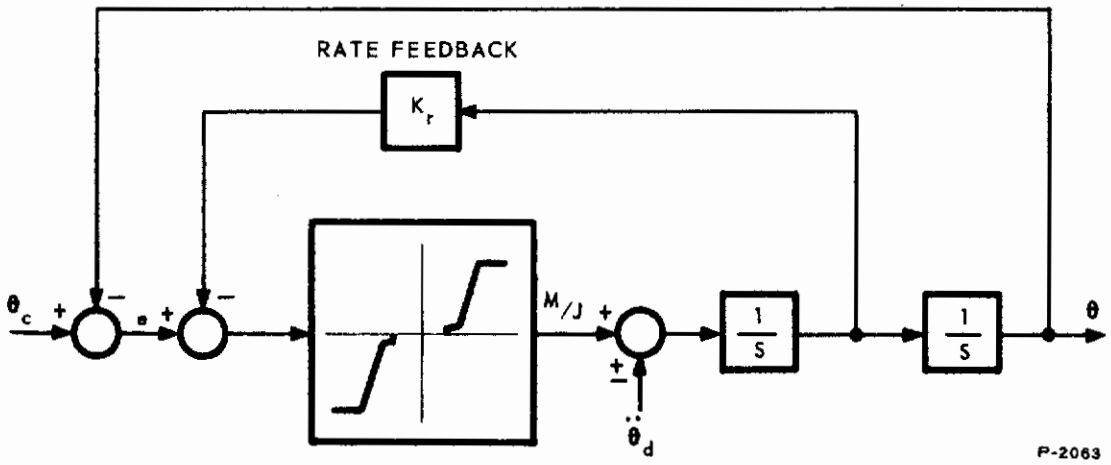

Figure 7-11 - Block Diagram of Proportional Attitude Control System with Rate Feedback

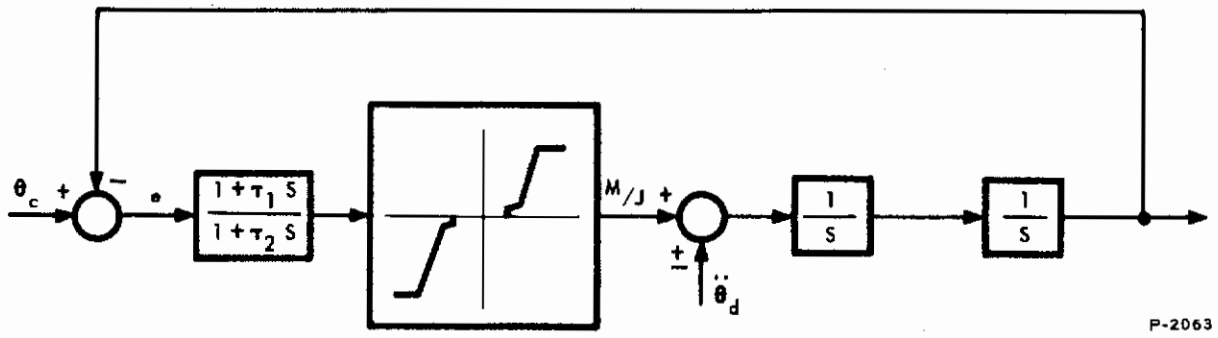

Figure 7-12 - Block Diagram of Proportional Attitude Control System with Lead-Lag Compensation

The proportional control system with rate feedback functioned acceptably without any additional logic. Figure 7-13 shows the system with an M/J of 0.015 rad/sec^2, and Figure 7-14 gives the response for M/J equal to 0.020 rad/sec^2. The average error given in Figure 7-13 is 0.0046 radian while that in Figure 7-14 is 0.0041 radian. The system described by Figure 7-13 has the lowest acceleration impulse, 0.11 rad/sec.

7.2.5 Conclusions

The proportional system with rate feedback appears to be superior to the on-off system with lead-lag compensation, based upon the preliminary study reported here. No specific conclusion can be made except that some promising control techniques have been defined.

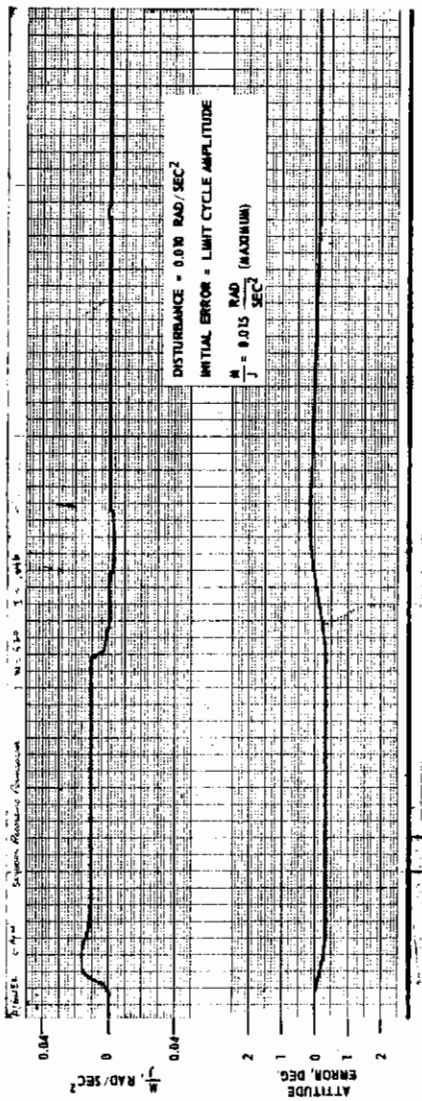

Figure 7-13 - Response of Proportional Control System with Rate Feedback

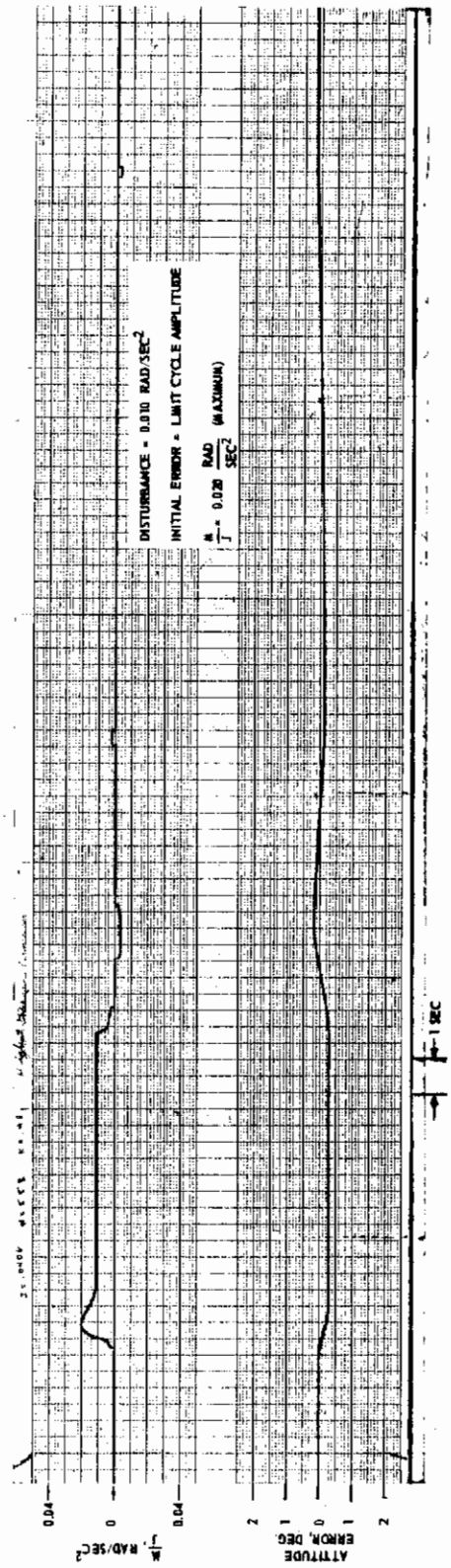

Figure 7-14 - Response of Proportional Control System with Rate Feedback

The information and experience obtained from this study should be valuable in selecting and optimizing the final system model where all dynamics are included.

Indications are that a reaction engine attitude control system can provide adequate attitude accuracy. This means that the added weight and complexity of a momentum exchange system is unnecessary.

7.3 COMPLETE STUDY OF REACTION ENGINE CONTROL LOOP

7.3.1 Introduction

The objective of this study is to define an attitude control loop that will meet the system requirements described in Subsection 7.1.2. Several promising control techniques were obtained from the preliminary study. To these systems, the predicted dynamics of a reaction engine are added.

7.3.2 Computer Simulation of On-Off System

7.3.2.1 System Description

The block diagrams for the on-off systems are shown in Figures 7-15 and 7-16. Figure 7-15 shows the system with lead-lag compensation in the forward loop for stabilization. Rate feedback for stabilization is shown in Figure 7-16. The deadband in both figures is incorporated to minimize propellant consumption during a limit cycle. The reaction engine dynamics which are described in Subsection 6.4 consist of a pure time delay, an underdamped quadratic for thrust rise, and a simple exponential thrust decay.

A computer diagram used for both compensation methods is shown in Figure 7-17. Two manual switches are provided, one consisting of a double pole set of contacts which is used to switch between lead-lag and rate feedback compensation. The second switch changes the sign of the initial condition of position error so that the problem can be started at either extreme of the limit cycle.

A set of operating conditions was selected for use in optimizing each of the systems. It would be too time consuming to optimize for every set of conditions listed in Table 7-1, and since the pitch axis has the most stringent requirements, all optimization was done about this axis. The operating conditions at a range of 9,200 feet were used, because they represent the maximum disturbance torque

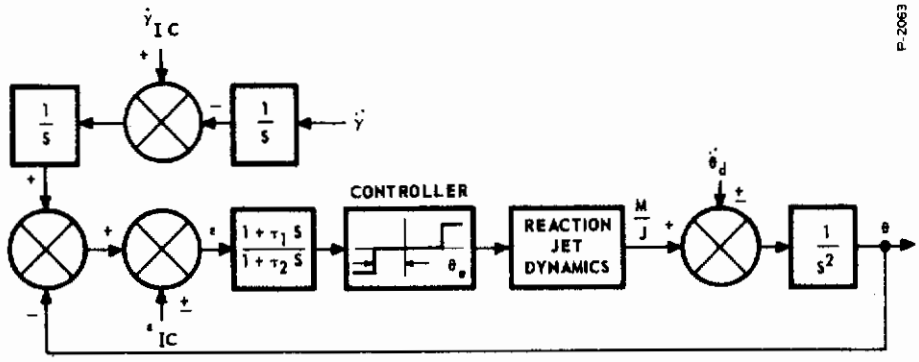

Figure 7-15 - Block Diagram of On-Off System with Lead-Lag Compensation

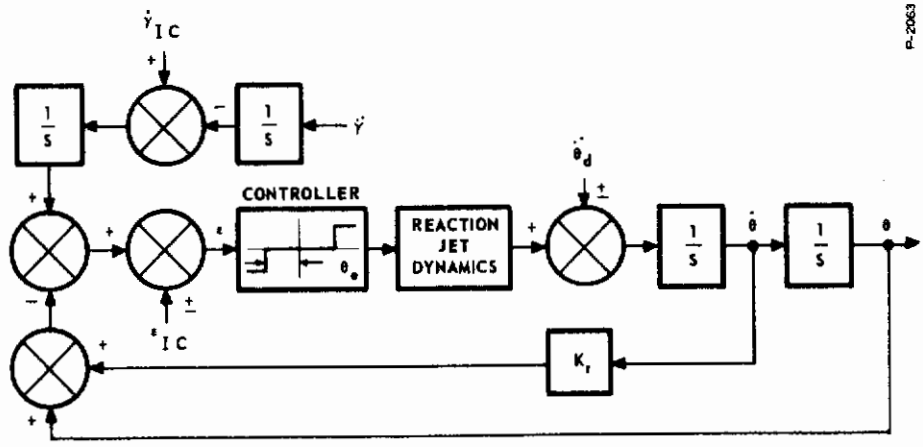

Figure 7-16 - Block Diagram of On-Off System with Rate Feedback Compensation

(without main engine misalignment) and a time duration of sufficient length to permit attitude error overshoot to be significant in affecting average error.

Four dependent variables were selected for recording: position error ϵ, ratio of moment-to-inertia M/J, integrated position error $\int_o^t \epsilon\, dt$, and integrated absolute value of moment-to-inertia $\int_o^t |M/J|\, dt$. The position error recording shows the amount of overshoot and the amplitude of the limit cycle. During the initial part of this study it was determined that a negative initial error resulted in a larger overshoot. This does not necessarily imply that the average error or the total propellant consumption will be more than for a positive initial error. In some cases the integrated negative error more than compensates

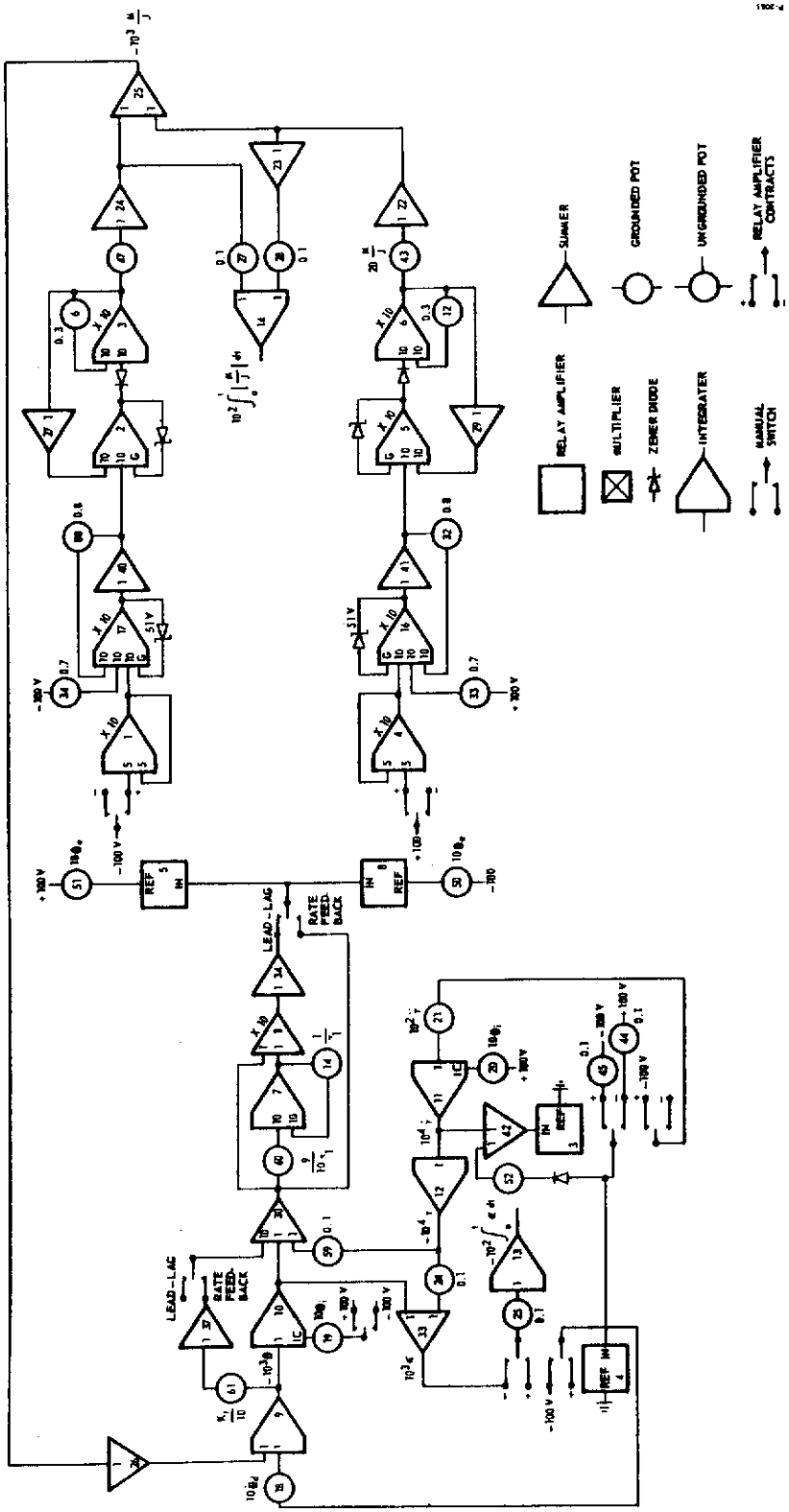

Figure 7-17 - Computer Diagram - On-Off Control System

for the additional overshoot in the positive direction. The reaction engine is off initially for a longer time for a negative initial error than for a positive initial error. However, the overshoot in error may require an excess of propellant to correct. Since it is not clear in advance which initial condition is the worst case, each set of data was taken for both initial conditions. The curves included in this section represent the worst case involving both average error and total propellant consumption. The moment-to-inertia channel recording gives an indication of control system stability. The number of times that the reaction jet controller turns on and off during a disturbance is a measure of its reliability. Certainly it is desirable to minimize the number of operations.

Position error is integrated for the duration of the correction of line-of-sight angular velocity. This time is $t_c = \dot{\gamma}_{I.C.}/\ddot{\gamma}$ where $\dot{\gamma}_{I.C.}$ is the angular velocity of the line-of-sight at which the correction begins. The correction continues until the angular velocity is at or near zero. For the corrective logic selected, $\dot{\gamma}_{I.C.} = 0.001$ radian/second so that the time for correcting is $t_c = 1/10^3\,\ddot{\gamma}$ seconds. The average error is then

$$\bar{\epsilon} = \frac{\int_o^t \epsilon \, dt}{t_c} \qquad (7\text{-}1)$$

This value must be kept as small as possible to insure rendezvous and must not exceed the values given in Subsection 7.1.2.

The integrated absolute value of moment-to-inertia ratio is proportional to the weight of fuel and oxidizer consumed.

$$W = \frac{J}{I_{SP}\,\ell} \int_o^t \left| \frac{M}{J} \right| dt \qquad (7\text{-}2)$$

For pitch axis control, the propellant consumption is approximately

$$W = 10^2 \int_o^t \left| \frac{M}{J} \right| dt \qquad (7\text{-}3)$$

7.3.2.2 Lead-Lag Compensation

In the simple block diagram of Figure 7-15, there are four parameters to be optimized; lead time constant τ_1, lag time constant τ_2, deadband θ_e, and maximum moment-to-inertia ratio M/J. One variable was eliminated by stipulating that the lag time constant shall be one-tenth (0.1) of the lead time constant. This is a reasonable assumption considering the practical design and operational problems in a lead network. If the lag time constant is reduced significantly, then this system will be similar to the rate feedback compensated system.

By varying each parameter, a set of variables was obtained which appeared to be near optimum. From this near optimum condition each parameter was then varied individually. Figure 7-18 shows the effect of varying the lead time constant. The increasing lead anticipates the need for correction, and thus, results in less overshoot. Since the disturbance is removed near the maximum value of the positional error, the smaller overshoot results in less corrective thrust. The smaller integrated acceleration $\int_o^t |M/J|\, dt$ amounts to a smaller total propellant consumption.

Variation of maximum thrust level is shown in Figure 7-19. The disturbance is 0.0133 rad/sec^2 so that the first set with M/J = 0.013 rad/sec^2 has a large error. If the thrust duration were longer, the average error could be excessive and prevent rendezvous. The minimum value of M/J must therefore be at least equal to the maximum disturbance. As the thrust level is increased, the overshoot and average error decreases. Above M/J = 0.017 rad/sec^2 the average error does not decrease significantly but the limit cycle frequency increases. The higher frequency limit cycle will use more propellant during the coast, or zero disturbance phase. The optimum control acceleration appears to be near M/J = 0.015 rad/sec^2.

The frequency at which a nonlinear system such as this will limit cycle depends upon the system dynamics, nature of the nonlinearity, and the loop gain. In general, an increase in loop gain results in an increase in frequency. For this system, inclusion of a deadband can be considered a reduction in loop gain. The curves shown in Figure 7-20 for different values of deadband show this. It appears that the largest amount of deadband will use the least amount of propellant but this is true only during coasting. As the deadband is increased, the overshoot increases. This results in a larger average error and a

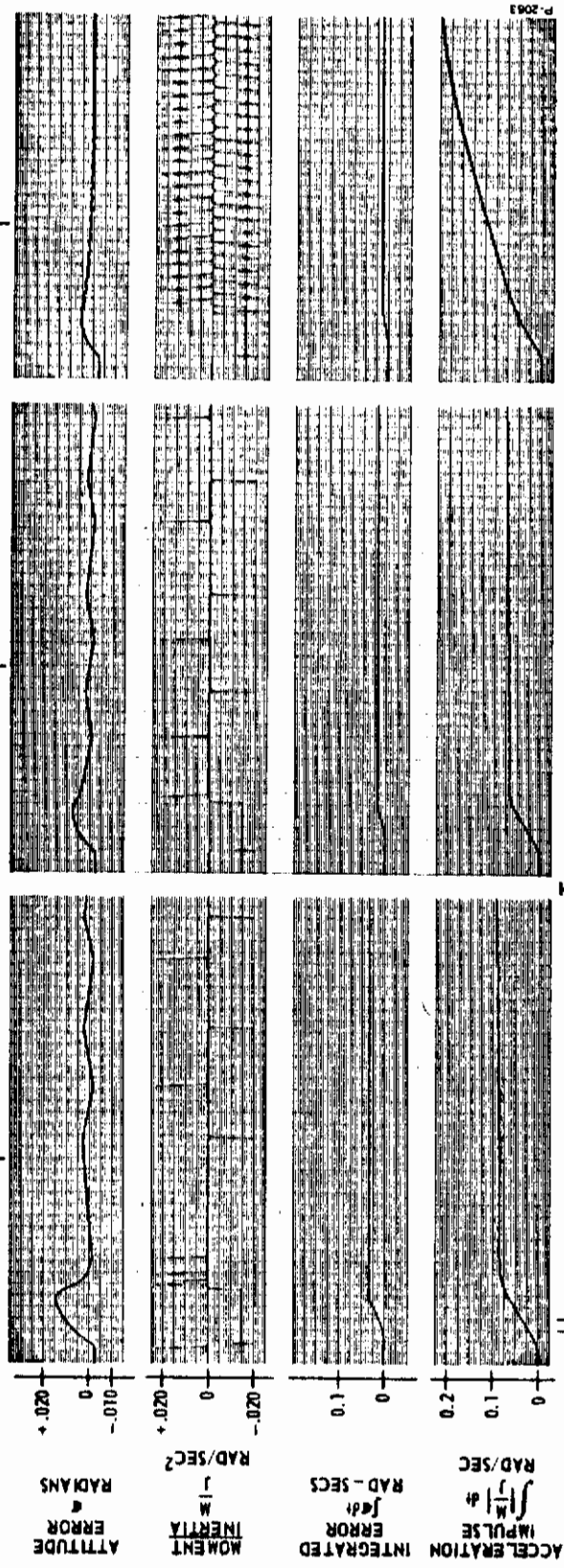

Figure 7-18 - On-Off System with Lead-Lag Compensation; Effect of Lead Time Constant upon Performance

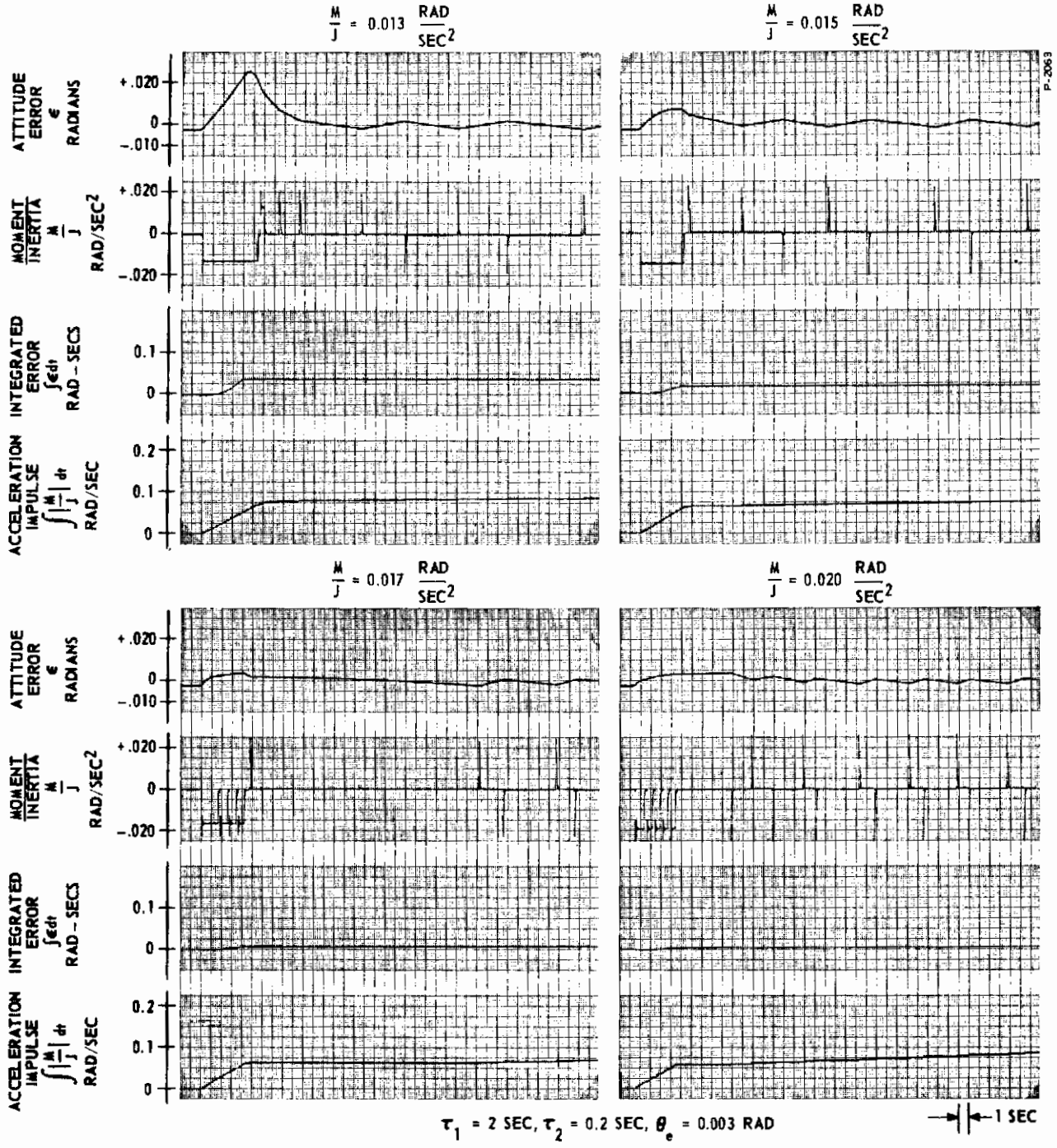

Figure 7-19 - On-Off System with Lead-Lag Compensation; Effect of Moment Level upon Performance

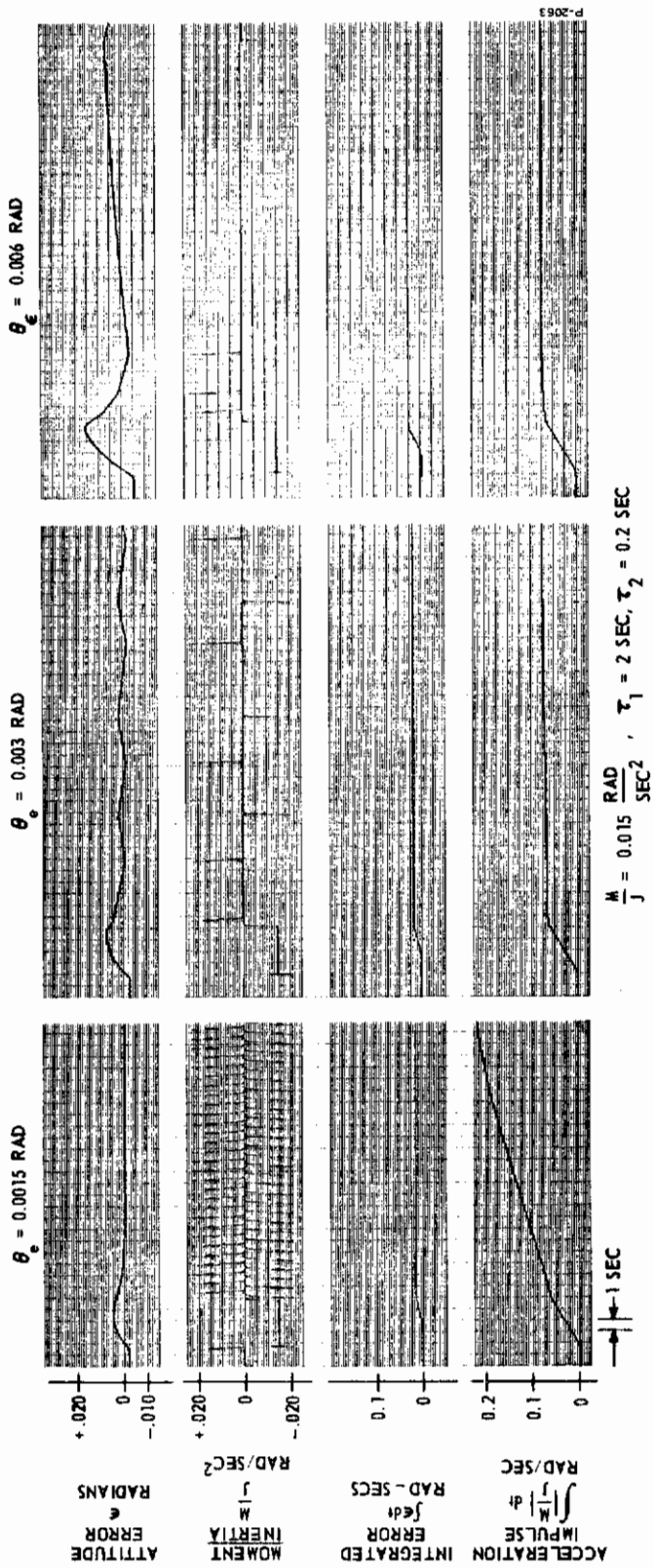

Figure 7-20 - On-Off System with Lead-Lag Compensation; Effect of Deadband upon Performance

requirement of more propellant to bring the system into the larger limit cycle region. The exact determination of the deadband magnitude is dependent upon the relative duration of disturbance correction and coast. A deadband of 0.003 radian appears to be reasonable for the assumed operating durations.

7.3.2.3 Rate Feedback Compensation

The block diagram of Figure 7-16 has three variables to be optimized; rate feedback gain K_r, deadband θ_e, and maximum moment-to-inertia ratio M/J. A comparison between the sets of data obtained by varying parameters in this system and in the lead-lag compensated system show the trends to be similar. The discussion which follows is almost identical to the one contained in the preceding subsection.

The effects of varying the rate feedback gain are shown in Figure 7-21. The rate feedback gain is denoted by K_r and it is similar in function to the lead time constant τ_1 in the lead-lag compensated system. The two systems would be identical if the lag time constant τ_2 were zero. An increase in rate gain anticipates the need for correction and therefore minimizes the overshoot in positional error. A rate gain of 4 increases the limit cycle frequency thereby consuming more propellant during the coast phase. A rate gain of 2 minimizes propellant consumption for the duration of disturbance and coast and still maintains an average error that is comparable to the higher rate gain condition.

As shown in Figure 7-22, the control moment must be greater than the disturbance. Again the disturbance is $\ddot{\theta}_d$ = 0.0133 rad/sec^2. There appears to be no improvement in average error by increasing M/J from 0.015 to 0.017 rad/sec^2. The higher thrust engine results in a higher frequency limit cycle and therefore more propellant consumption during coast. No additional propellant is used during the disturbance.

A small deadband reduces the average error but increases the propellant consumption during coast. As can be seen in Figure 7-23, the propellant used during the disturbance is about the same for each value of deadband. The only difference then is in the average error and the propellant used during the limit cycle. The system with a deadband of 0.006 radian did not get into a limit cycle in the time shown due to a combination of minimum impulse from the

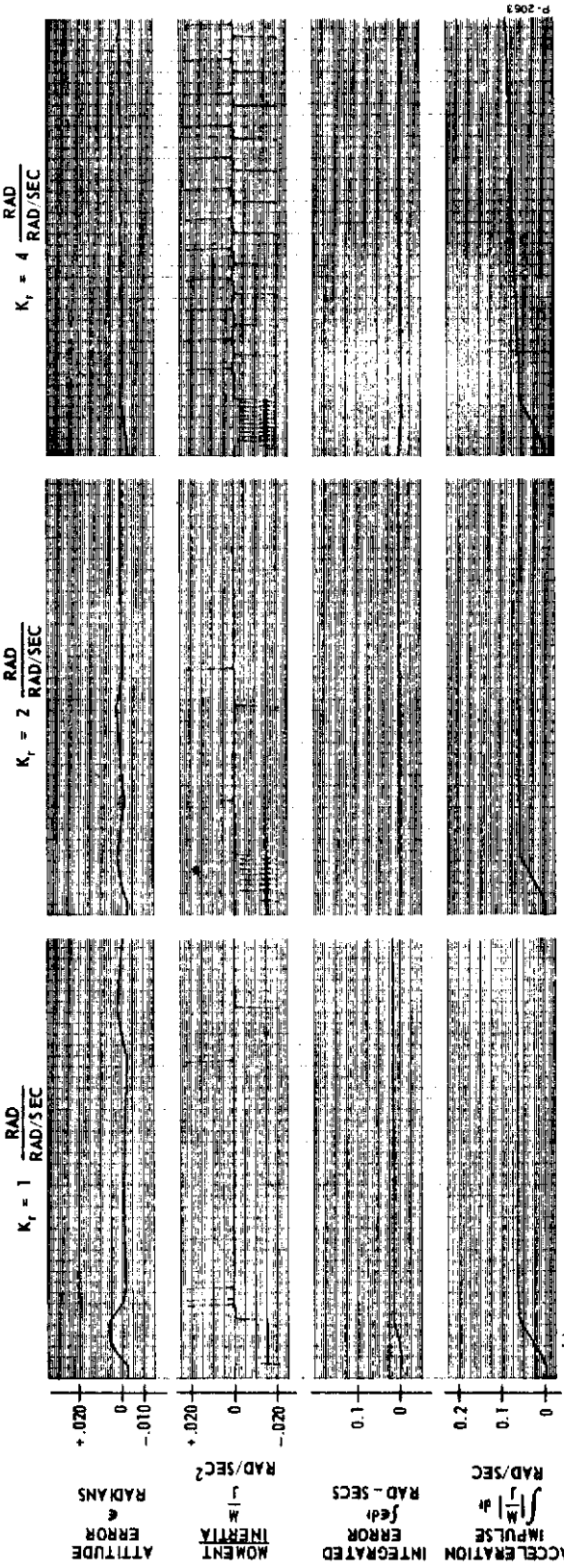

Figure 7-21 - On-Off System with Rate Feedback; Effect of Rate Feedback Gain upon Performance

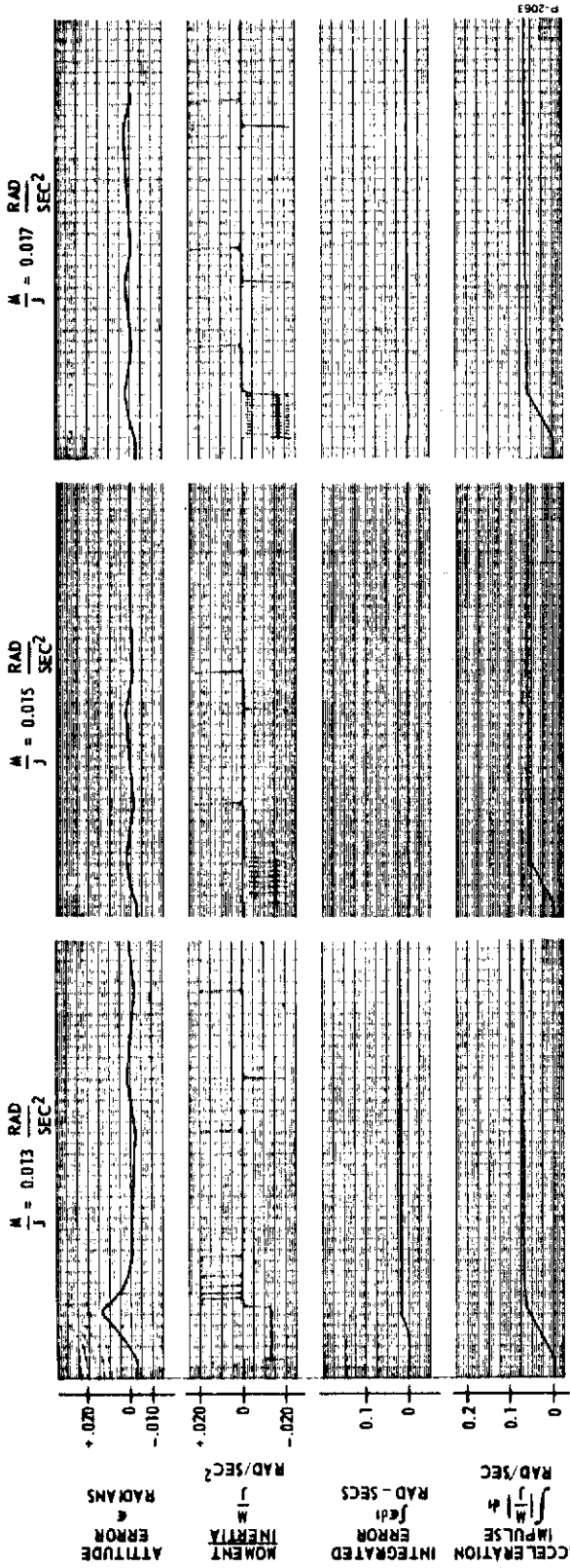

Figure 7-22 - On-Off System with Rate Feedback; Effect of Moment Level upon Performance

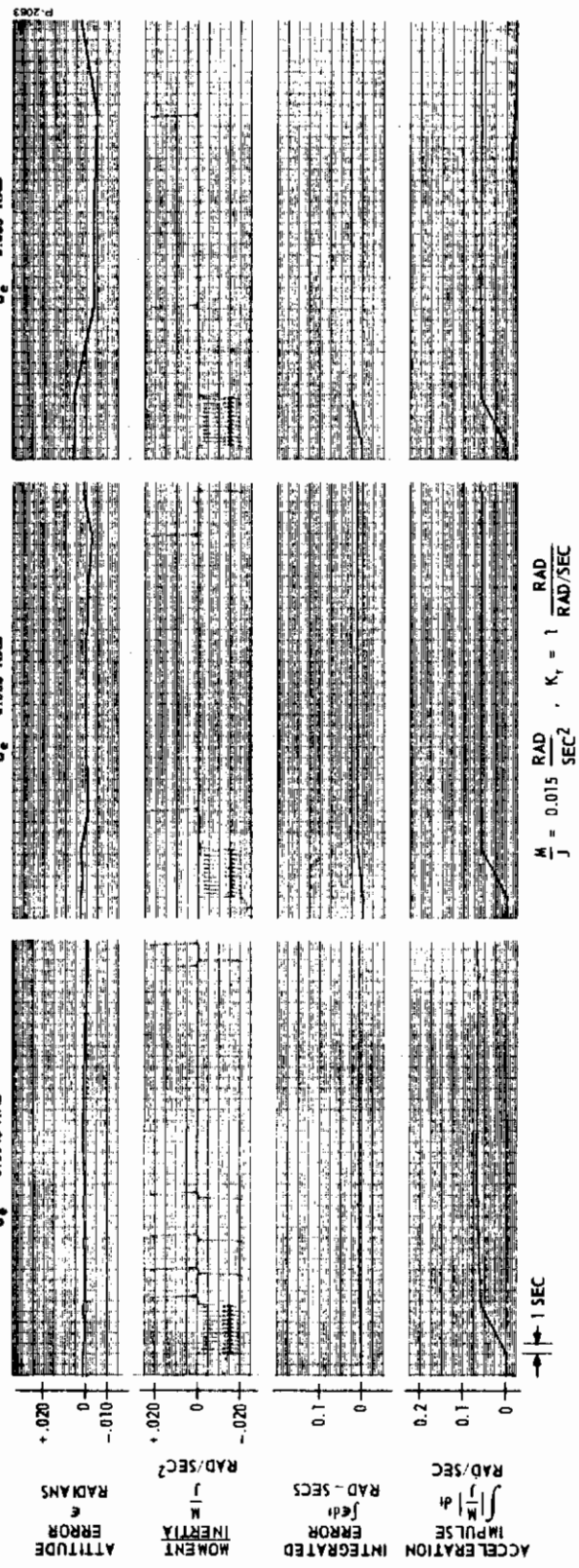

Figure 7-23 - On-Off System with Rate Feedback; Effect of Deadband upon Performance

reaction engines and the initial conditions at the beginning of coast. The traces for a negative initial error show a limit cycle where the propellant consumed for the 0.003 radian deadband is not significantly higher than for the 0.006 radian deadband.

7.3.2.4 Comparison of Compensation Methods

A comparison between the two methods of compensation can be made on the basis of average error and total propellant consumption. The choice in this case is clear from a performance point of view. The rate feedback compensated system has a smaller average error and less propellant consumption for every condition listed in Table 7-1. In addition, the above conclusion holds true for disturbances that are much less than the maximum expected disturbances. A number of curves are shown in Figure 7-24 to illustrate the differences. It is interesting to note that both systems have the same amount of lead compensation; i.e., $\tau_1 = K_r = 2$. The additional lag in the lead-lag compensated system slows down the response and degrades the performance.

7.3.3 Computer Simulation of Proportional System

7.3.3.1 System Description

A variable thrust system can be made from an on-off system by restricting the flow of fuel and oxidizer in venturi injectors. This method is described in Subsection 6.3.5.

A block diagram of the lead-lag compensated system is shown in Figure 7-25, and Figure 7-26 shows the rate feedback compensated system. A nonlinear gain device is used to limit total propellant consumption. The need for this device was determined from the preliminary study.

To convert the computer diagram of the on-off system to proportional operation, the propellant flow to the combustion chamber must be capable of attenuation. Figure 7-27 shows the computer diagram used. The use of multipliers as gain devices for the inputs to amplifiers 2 and 5 permit the output steady state moment-to-inertia ratio to be varied while retaining the pure time delay in turning the reaction engine on.

As in the cases of the on-off system, the same four dependent variables are recorded: position error, moment-to-inertia ratio, integrated position error, and integrated absolute value of

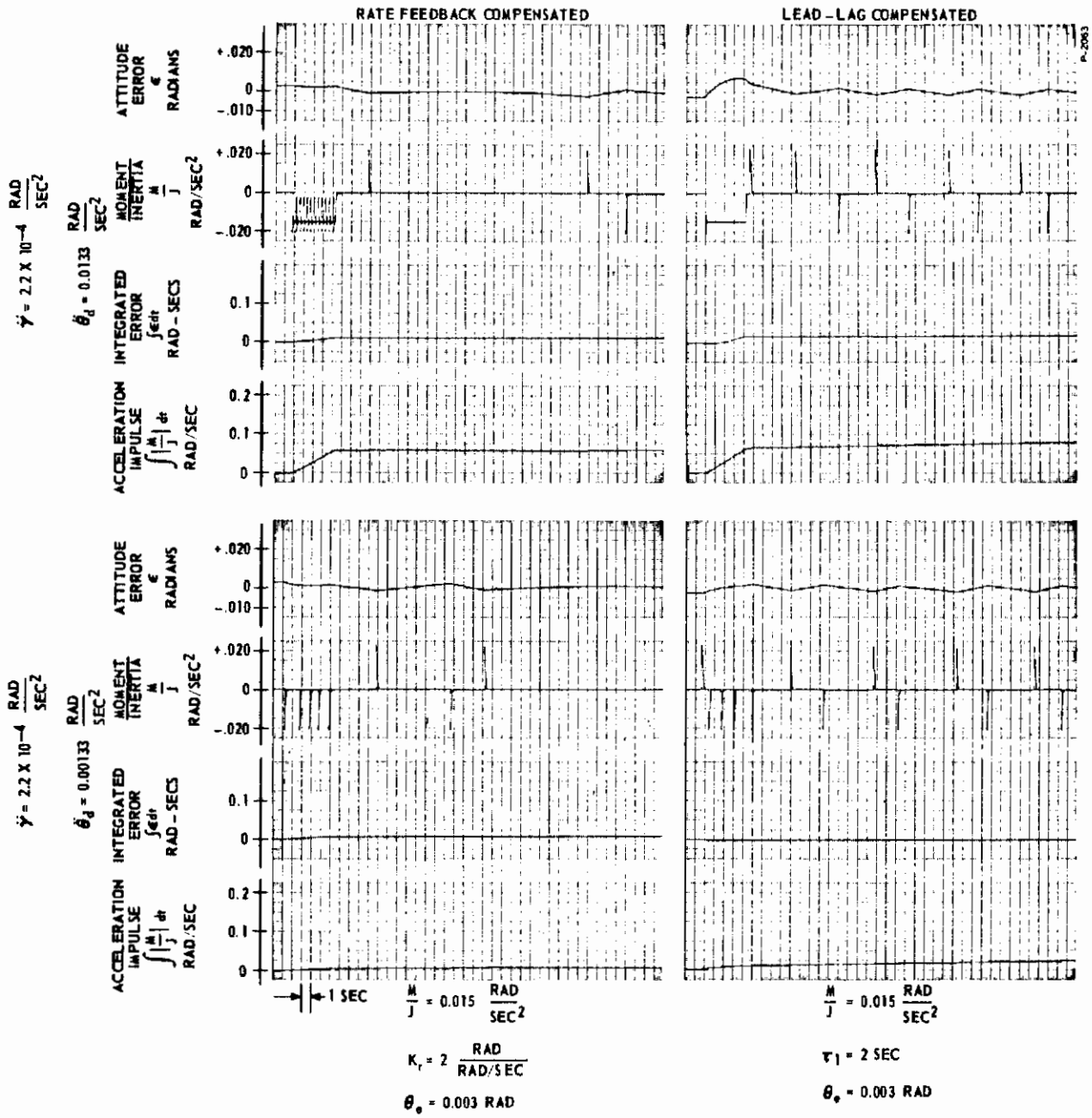

Figure 7-24(a) - Comparison of On-Off System Performance for Rate Feedback and Lead-Lag Compensation

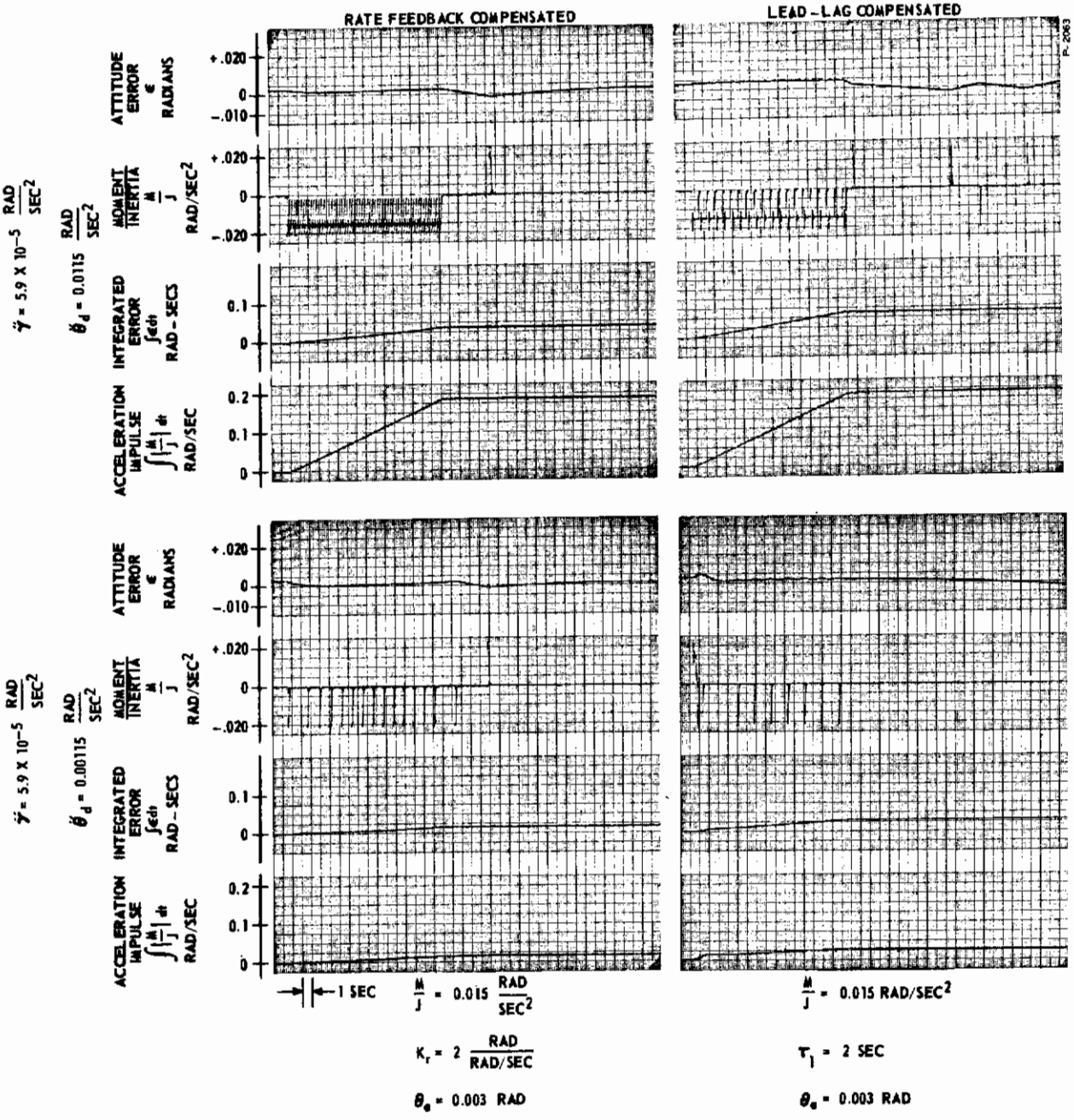

Figure 7-24(b) - Comparison of On-Off System Performance for Rate Feedback and Lead-Lag Compensation

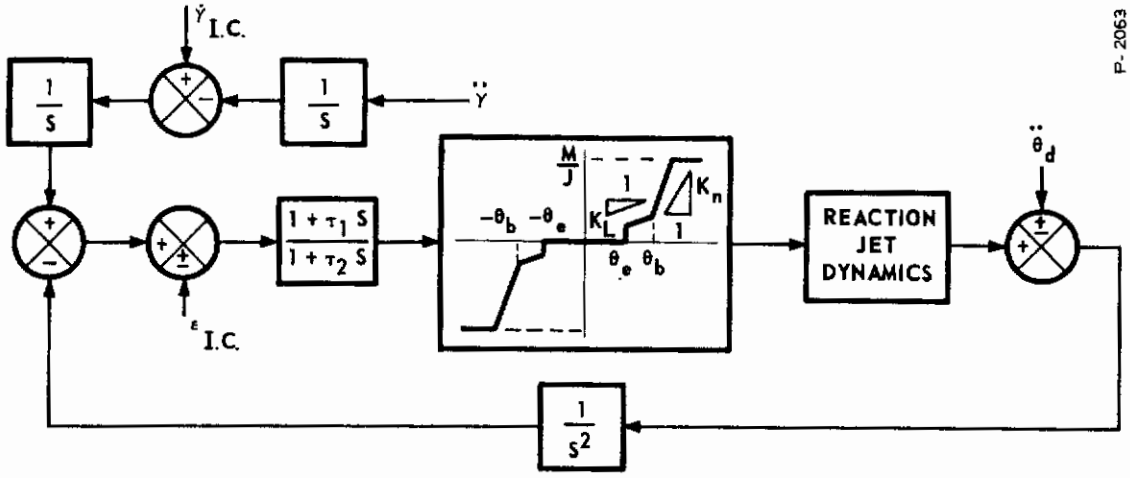

Figure 7-25 - Block Diagram of Proportional System with Lead-Lag Compensation

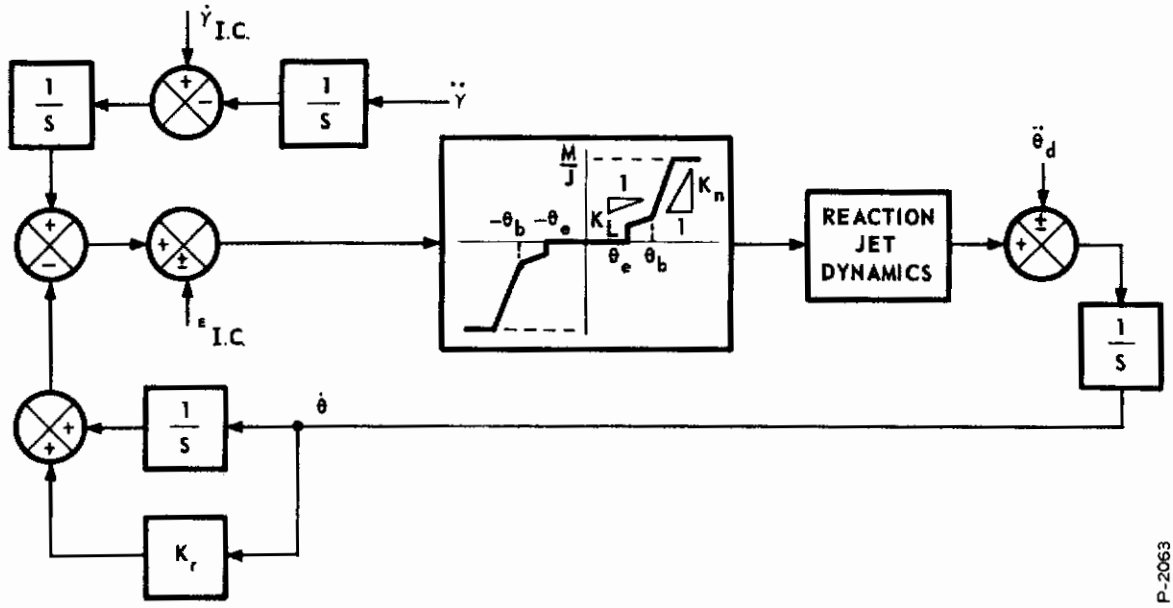

Figure 7-26 - Block Diagram of Proportional System with Rate Feedback

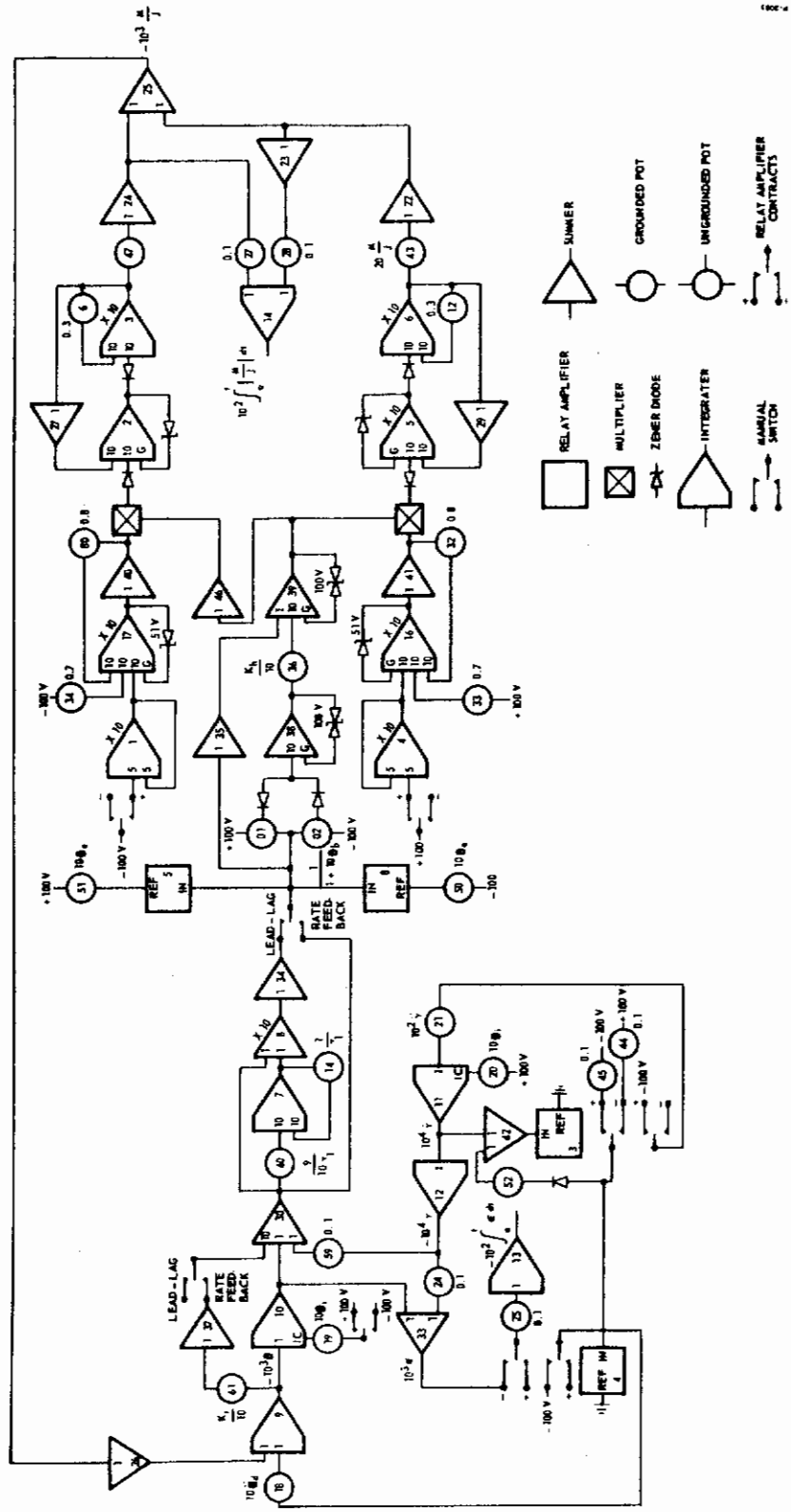

Figure 7-27 - Computer Diagram - Proportional Control System

moment-to-inertia. The variables to be optimized are those given previously plus the characteristics of the nonlinear gain device. Both the high and low end gains and the point at which the gain changes need to be determined.

7.3.3.2 Lead-Lag Compensation

The lead-lag compensated system was optimized by varying each parameter. Figure 7-28 shows the effect of changing the lead time constant. As in the case for the on-off system, the lag time constant is one-tenth of the lead time constant. Comparing the traces, the average error and propellant consumption are about the same for both 2 and 4 second lead time constants. The system with a 4 second lead time constant, turned on and off more times during coast than that with a 2 second lead time constant. From a reliability point of view, the 2 second lead time constant appears to be better.

A maximum moment-to-inertia level must be provided which is greater than the maximum expected disturbance. Larger size reaction engines will reduce the average error but will not use more propellant. From Figure 7-29, it can be seen that the largest controller size $M/J = 0.020$ rad/sec^2 had the most oscillations during the coast phase. The frequency of oscillation is a function of loop gain of which M/J is a part. The loop gain could be reduced for the larger engine by reducing the low end gain K_L of the nonlinear gain device. The trade-off criterion is then between decreasing average error and the increased size and weight of a larger engine. For this study it was felt that a 20 percent reduction in average error did not warrant an engine 33 percent larger. A moment-to-inertia ratio of 0.015 rad/sec^2 was considered reasonable.

On the basis of the above discussion, the gain at the low end of the nonlinear gain device was kept at unity during the entire study. The high end gain K_h was varied and the higher gain had the smallest average error. From Figure 7-30 it can be seen that a 12 db increase in gain improved the average error by only 23 percent. Although the final system comparison was based on a gain K_h of 20, consideration was given to the improvement possible with higher gain.

The location of the change in gain from K_L to K_h is determined from the curves shown in Figure 7-31. For a value of θ_b that is less than the deadband θ_e, the system is similar to an on-off system during coast. If θ_b is much larger than θ_e, the low gain

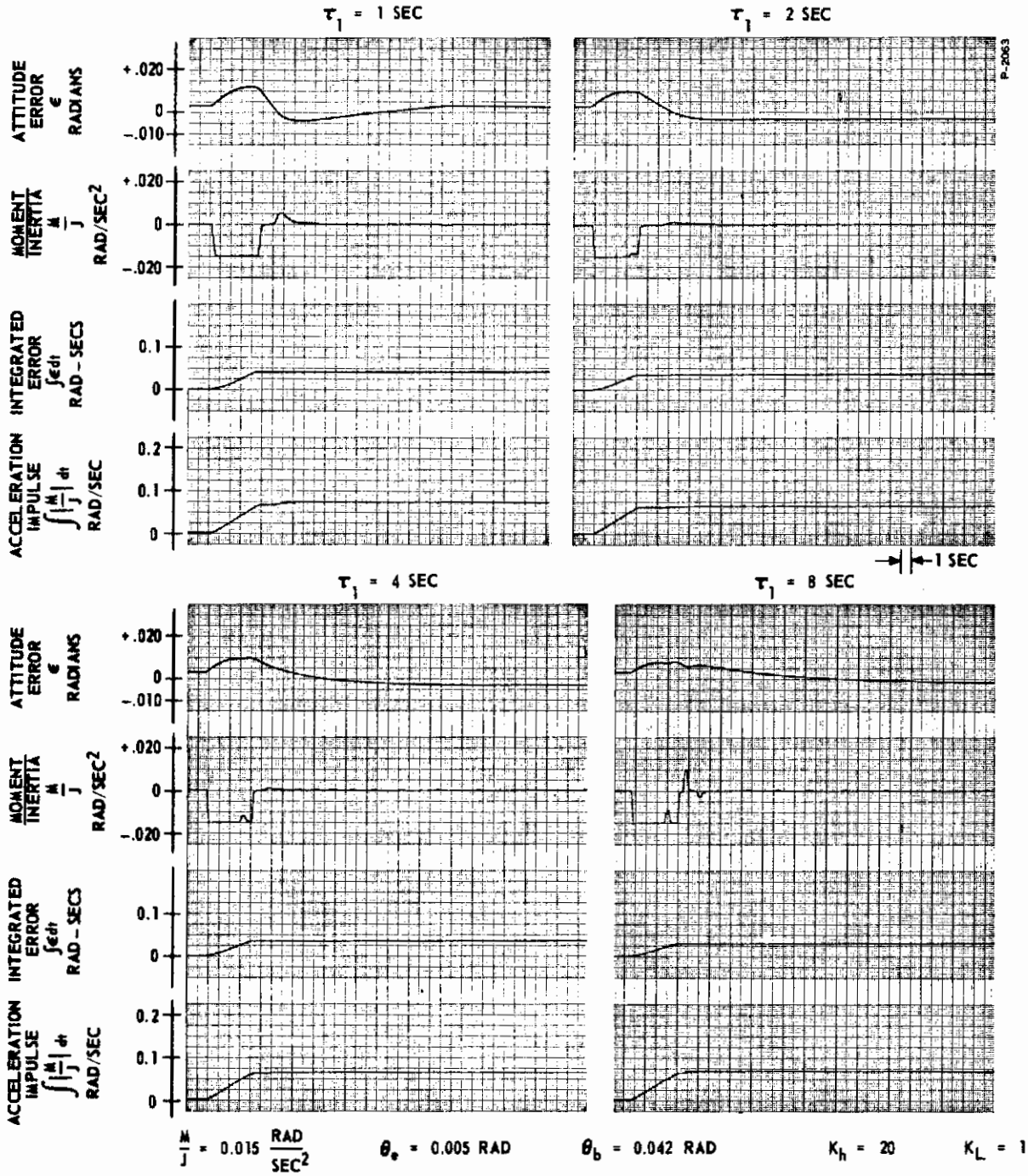

Figure 7-28 - Proportional System with Lead-Lag Compensation; Effect of Lead Time Constant upon Performance

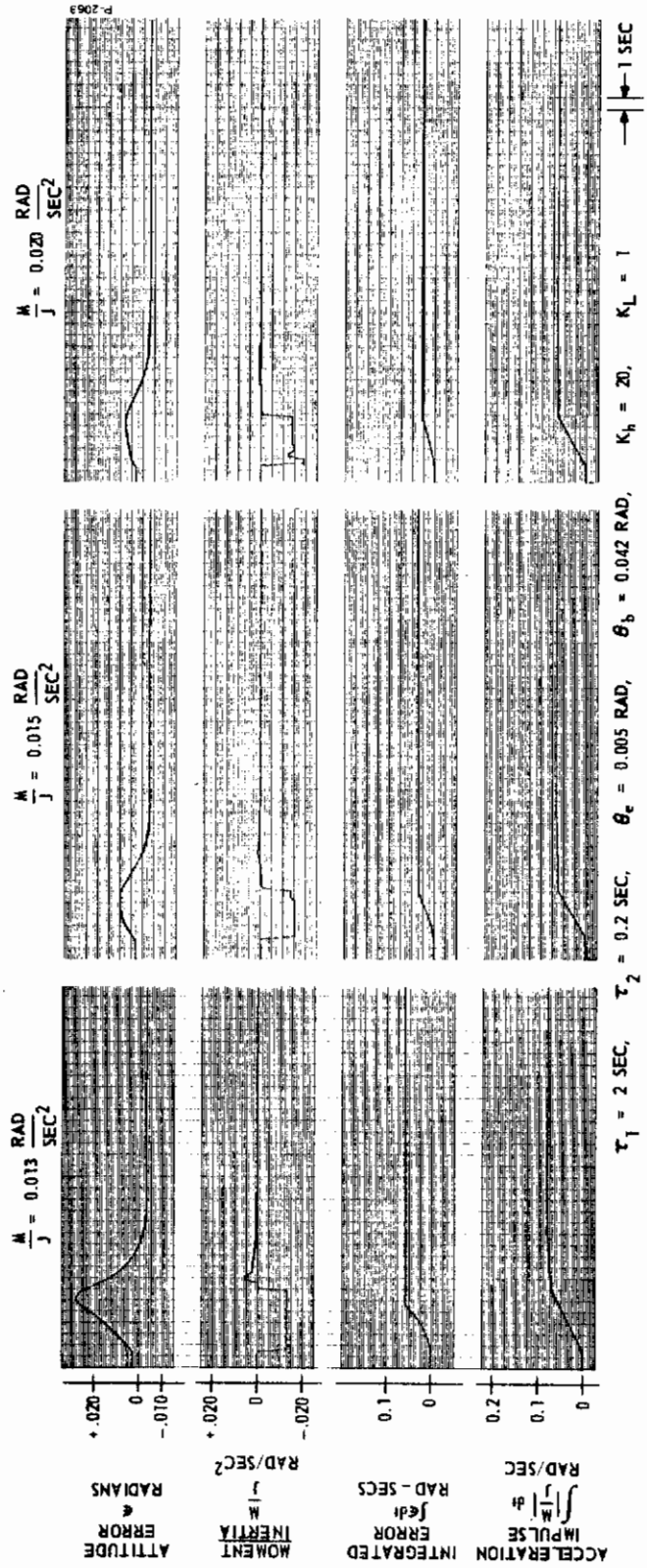

Figure 7-29 - Proportional System with Lead-Lag Compensation
Effect of Control Moment upon Performance

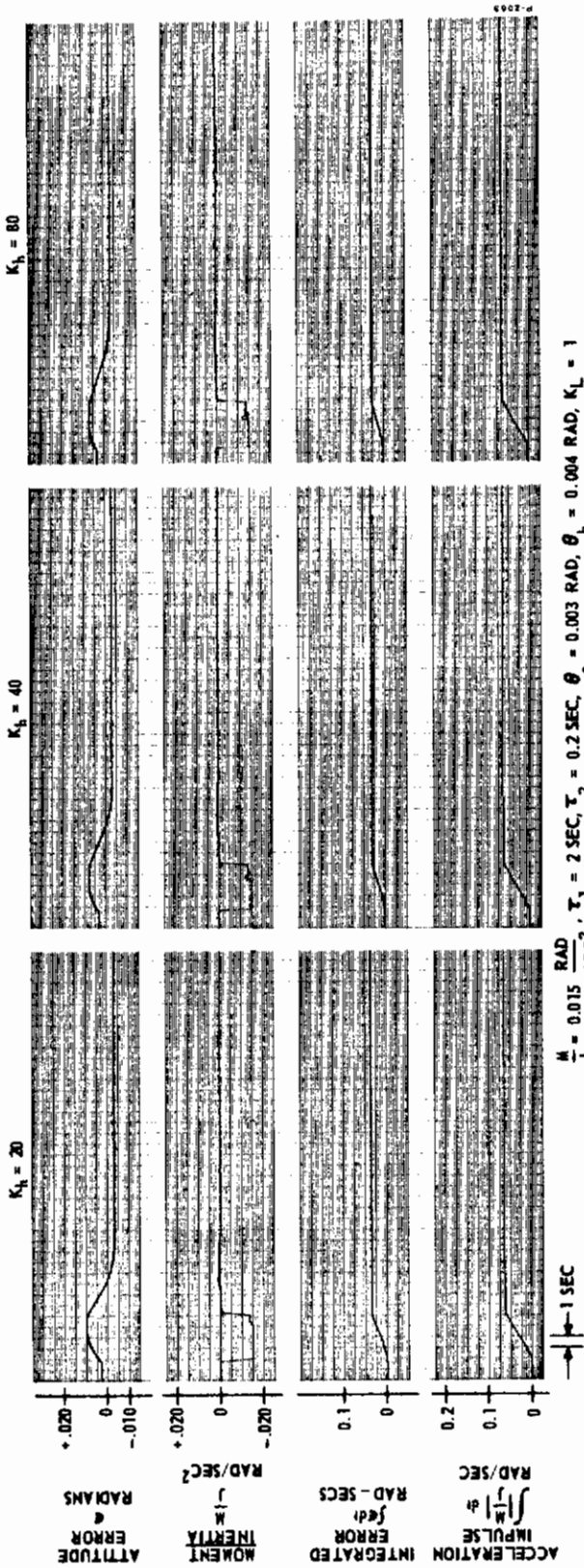

Figure 7-30 - Proportional System with Lead-Lag Compensation
Effect of High End Gain upon Performance

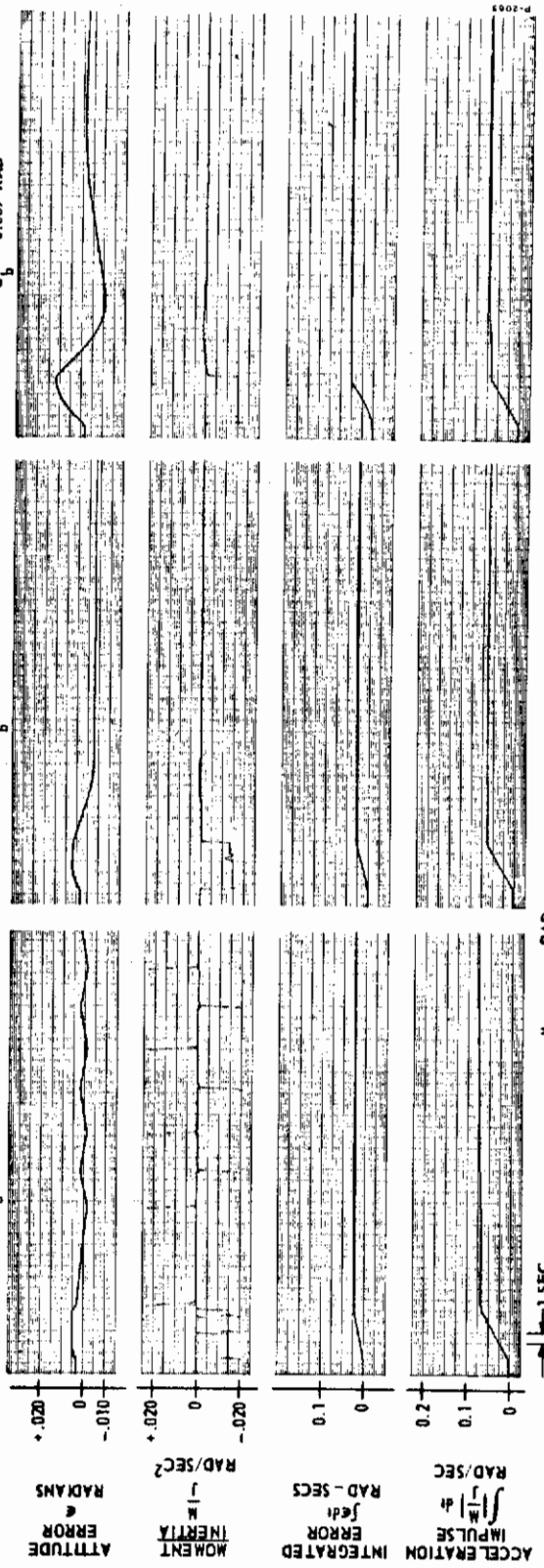

Figure 7-31 - Proportional System with Lead-Lag Compensation; Effect of Location of Nonlinear Gain Break Point upon Performance

characteristics during the initial part of a disturbance results in a large average error. The change in gain should therefore occur at a value that is slightly larger than θ_e. θ_b should be large enough so that the limit cycle will never get into the high gain region. The value of θ_b assumed to be near optimum is 0.004 radian.

The final parameter investigated is the deadband θ_e. From Figure 7-32 it appears that there is no problem operating the system with small deadband. The characteristics shown by the traces are not a true picture of the effect of this parameter variation for several reasons. The nonlinear gain break point θ_b was kept constant so that a deadband of 0.006 implies operation on the high gain only. A deadband of 0.0015 implies reaction engine throttling over a 66:1 range. Although it may be possible to control the fuel and oxidizer flow over this range, the performance in the engine combustion chamber is questionable. Control of 66:1 would be a considerable extension of the state-of-the-art. The scale factor on M/J does not permit the determination of the frequency of oscillation. It appears reasonable to assume, based on data for other systems, that the oscillation or limit cycle frequency will increase as the deadband is reduced. The selection of a deadband of 0.003 as near optimum does not affect the comparison criteria significantly.

7.3.3.3 Rate Feedback Compensation

The effect of parameter variation on the rate feedback compensated proportional system is shown in the accompanying figures. In Figure 7-33, the rate feedback gain is varied. The same amount of propellant is used in each case, but the average error decreases with increasing rate feedback. The higher rate feedback tends toward oscillations on the initial rise. A rate gain of 4 rad/rad-sec minimizes the oscillations while still maintaining the average error to about 55 percent of the maximum permissible.

The high end gain K_h of the nonlinear gain device affects the performance only during a disturbance. During coast, the error is never sufficiently high to operate in this region. As the high end gain is increased, average error decreases with no increase in propellant consumption. However, the relative damping decreases also. A high end gain of 20 appears reasonable. The traces are shown in Figure 7-34.

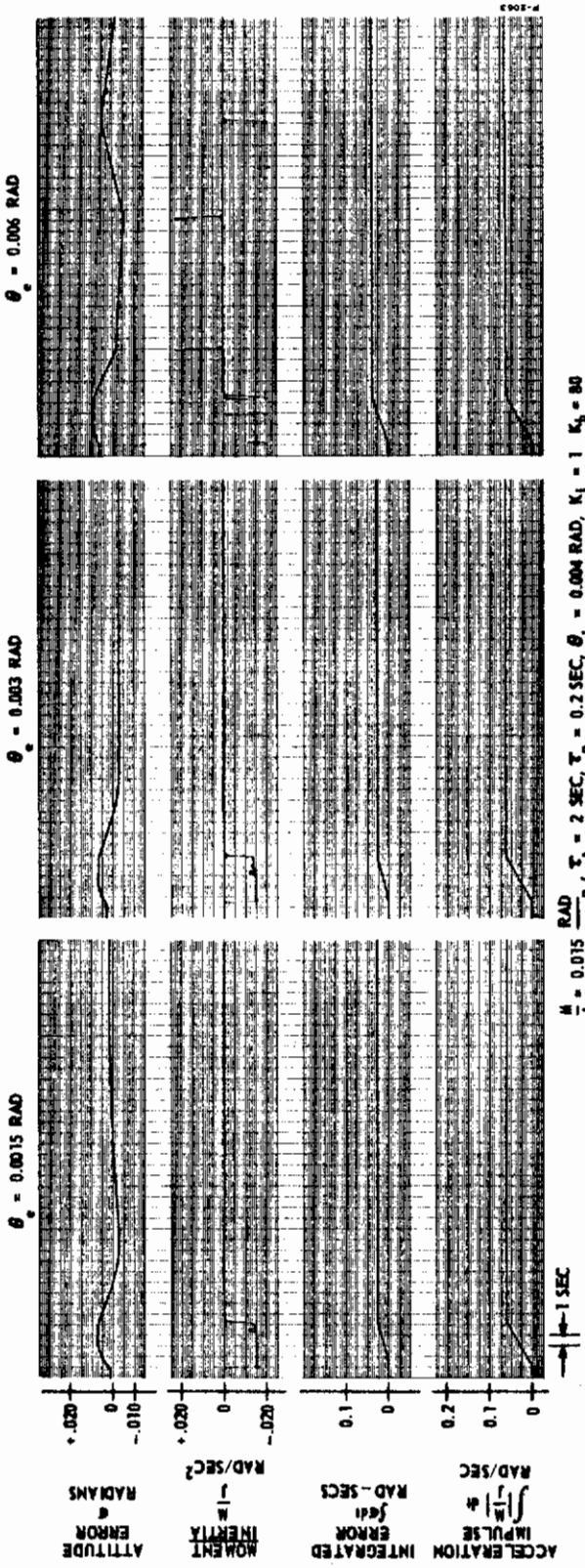

Figure 7-32 - Proportional System with Lead-Lag Compensation; Effect of Deadband upon Performance

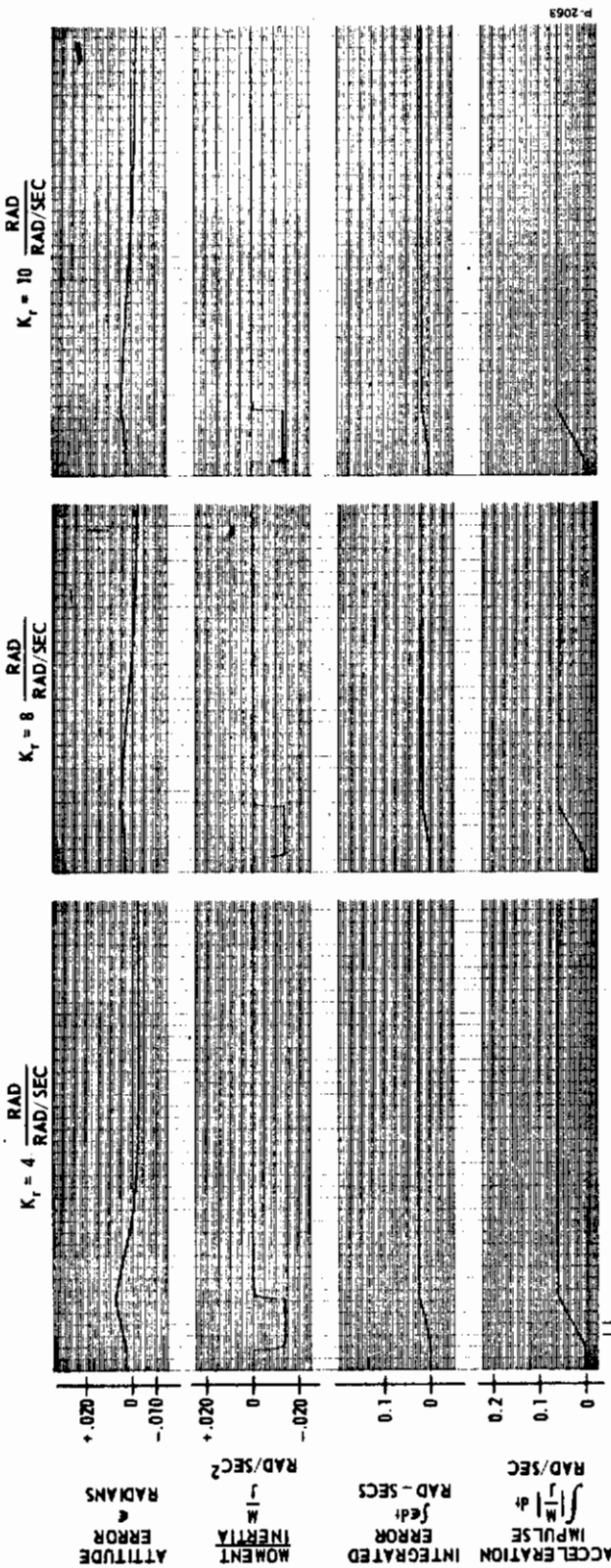

Figure 7-33 - Proportional System with Rate Feedback; Effect of Rate Feedback Gain upon Performance

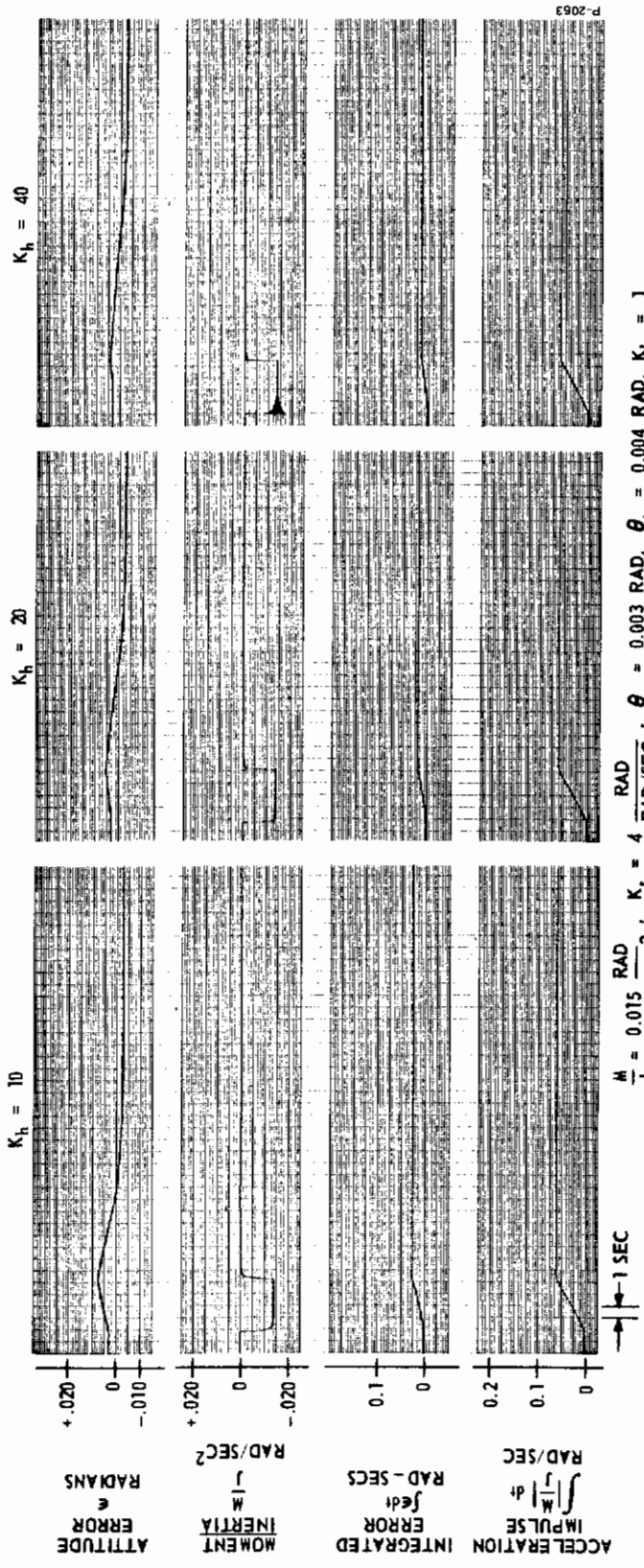

Figure 7-34 - Proportional System with Rate Feedback; Effect of High End Gain upon Performance

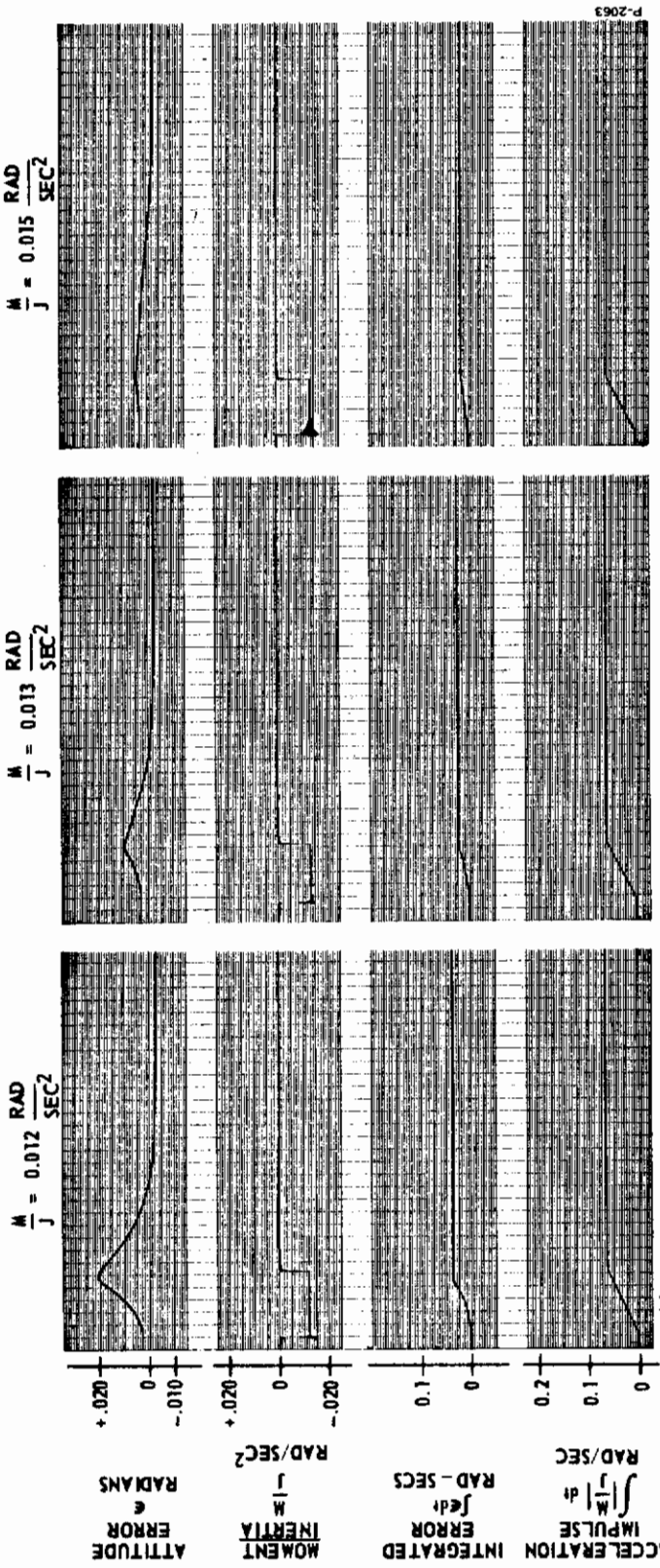

Figure 7-35 - Proportional System with Rate Feedback; Effect of Maximum Control Moment upon Performance

The effect of moment-to-inertia ratio on performance was determined with the high end gain K_h at 40. In Figure 7-35 it is seen that the propellant consumption is independent of the engine size even for a moment-to-inertia ratio of 0.012 rad/sec^2 which is less than the disturbance acceleration $\ddot{\theta}_d$ of 0.0133 rad/sec^2. There does not appear to be any problem in meeting the maximum average error criterion with a moment-to-inertia ratio of 0.012 rad/sec^2, however, the probability of rendezvous increases as the average error decreases. Considerable improvement can be realized with a 25 percent larger engine. For this study, a moment-to-inertia ratio of 0.015 rad/sec^2 was felt to be the more optimum value.

Variations in the amount of deadband θ_e affects average error and can affect propellant consumption. Propellant consumption is affected if the thrust-to-inertia ratio is not large enough to reduce the error to the deadband during a disturbance. For that case the reaction engines must remain on after the disturbance has been removed. For the case shown in Figure 7-36, the larger

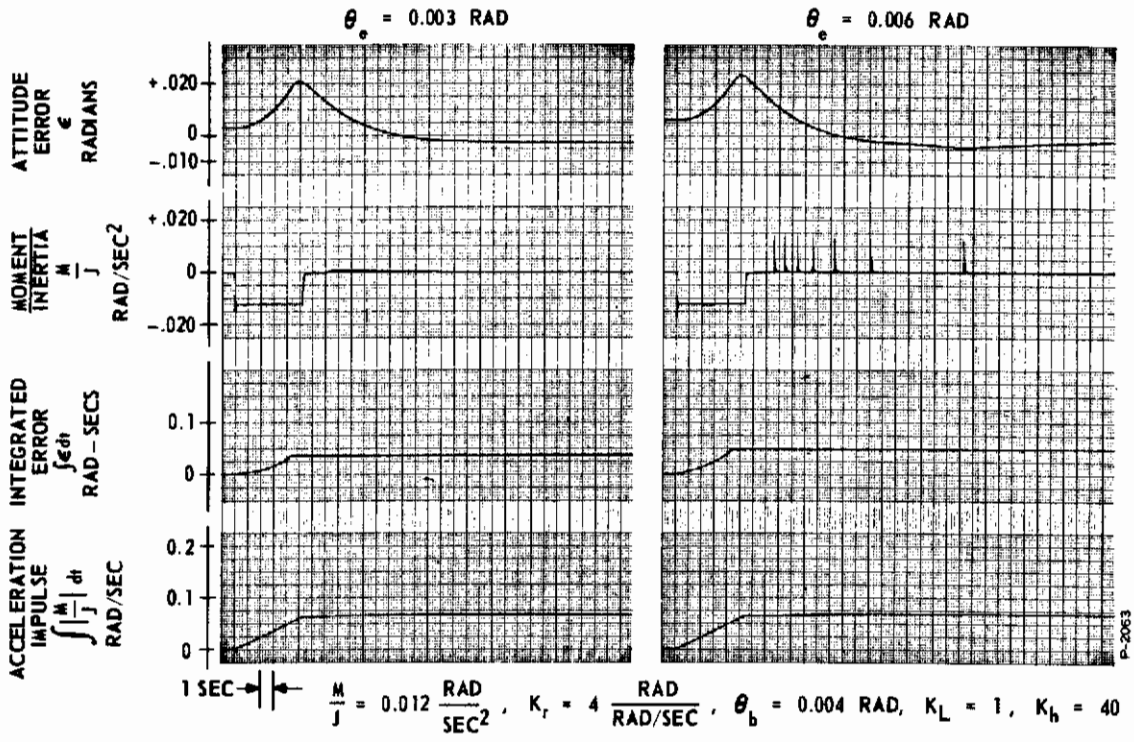

Figure 7-36 - Proportional System with Rate Feedback; Effect of Deadband upon Performance

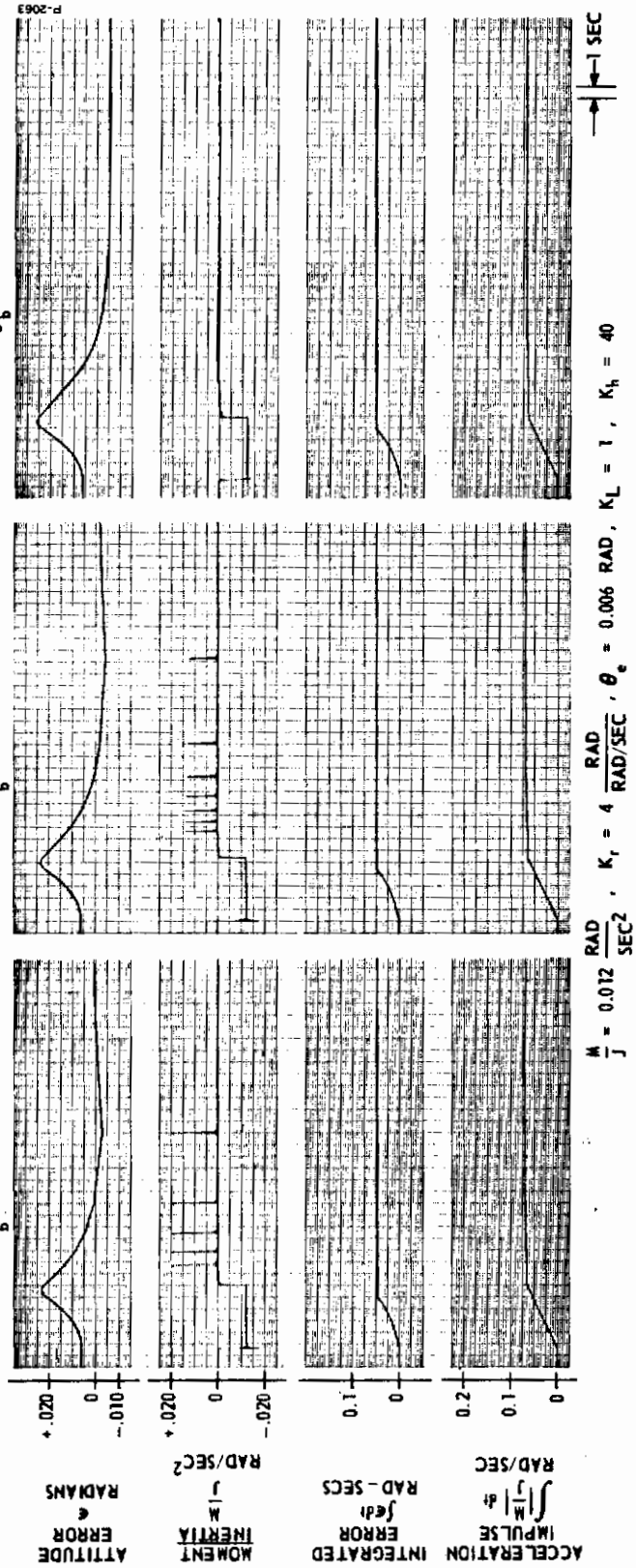

Figure 7-37 - Proportional System with Rate Feedback; Effect of Location of Nonlinear Gain Break Point upon Performance

deadband would result in slightly less propellant consumption if not for that required during coast. The high propellant consumption during coast is caused by θ_e = 0.006 radian being greater than the nonlinear gain breakpoint θ_b. The average error results indicate that the deadband should be kept as small as possible. A deadband smaller than 0.003 radian was not considered because of the arguments presented in Subsection 7.3.3.2.

Figure 7-37 shows the effect of moving the nonlinear gain breakpoint. The deadband for the three curves is 0.006 radian. All three cases use the same amount of propellant during the disturbance, but the propellant used during coast increases as the breakpoint is reduced. This is only true if the breakpoint is less than the deadband. For a breakpoint greater than the deadband, no change in limit cycle characteristics will occur if the breakpoint is moved further out. The average error is affected by breakpoint location because it determines how soon maximum corrective thrust will be applied. This is not easily seen on the curves for θ_b = 0.004 and θ_b = 0.0005 radian because the disturbance is applied when the gain is already at a high value. The optimum value for the nonlinear gain breakpoint θ_b should be larger than the deadband θ_e yet not too large so as to delay the full magnitude of corrective thrust when needed.

7.3.3.4 Comparison of Compensation Methods

It is a very simple matter to decide which of the two proportional systems has the better performance. With respect to average error and total propellant consumption, the rate feedback compensated system is superior to the lead-lag compensated system for every condition listed in Table 7-1. This holds true for disturbances that are much less than the maximum predicted disturbances. The curves shown in Figure 7-38 illustrate the differences. The two systems do not have the same lead compensation since τ_1 = 2 and K_r = 4 sec. However, from Figure 7-28 an increase in lead time constant to 4 did not improve either average error or propellant consumption. All of the other parameters are identical. The conclusion here, as in the case of the on-off system, is that the lag in the lead-lag compensated system is large enough to slow down system response. If the separation between lead and lag can be increased considerably from 10:1 in a practical system then the two systems would be identical.

7.3.4 Control Loop Selection

The choice of control loop can be based on three criteria: average error, total propellant consumption, and reliability. The maximum average errors given in Subsection 7.1.2 must not be exceeded. While this criterion is necessary to accomplish rendezvous, the probability of rendezvous is increased by decreasing the average error during corrective action by the guidance engines. The propellant consumption is a critical factor since it determines the payload available for the vehicle. Sufficient fuel and oxidizer must be carried to account for the maximum or worst conditions that could be encountered. In this case, the propellant requirements are not severe because the attitude control system uses the same propellant as used in the main propulsion system. The propellant requirements for attitude control for a short mission are much less than the guidance engine requirements. System reliability may be evaluated on the basis of equipment complexity and duty cycle. The additional valve and electronic equipment required to operate a proportional reaction engine certainly increase the chance of failure even if these components are well developed and proven components. On the other hand, if a reaction engine operates many times due to a high frequency limit cycle, the probability of failure increases.

From previous sub-sections of this section, rate feedback compensation has been shown to be better for both the on-off and the proportional systems. There remains the selection of one of the remaining two systems as an optimum system based on the previously mentioned criteria. The response of the two systems to the conditions of Table 7-1 are shown in Figure 7-39. In addition, two sets of data are given for the longest two correction durations with a disturbance one-tenth (0.1) of the maximum value. In each and every case the average error for the on-off-system is equal to, or less than, the average error for the proportional system. The two average errors are about the same at a range of 15,000 feet and at 100 feet the average errors are both negligible. On a propellant consumption basis, the proportional system generally uses less. This difference is due to the small amount of propellant consumed during the coasting limit cycle. It can be noted that the on-off system did not always go into a limit cycle immediately after removal of the disturbance. This certainly can occur given the proper minimum impulse obtainable and an appropriate set of initial conditions. For all comparisons of propellant consumption, it is assumed that the on-off system goes into a limit cycle immediately upon the removal of the disturbance and the accompanying data has been adjusted accordingly.

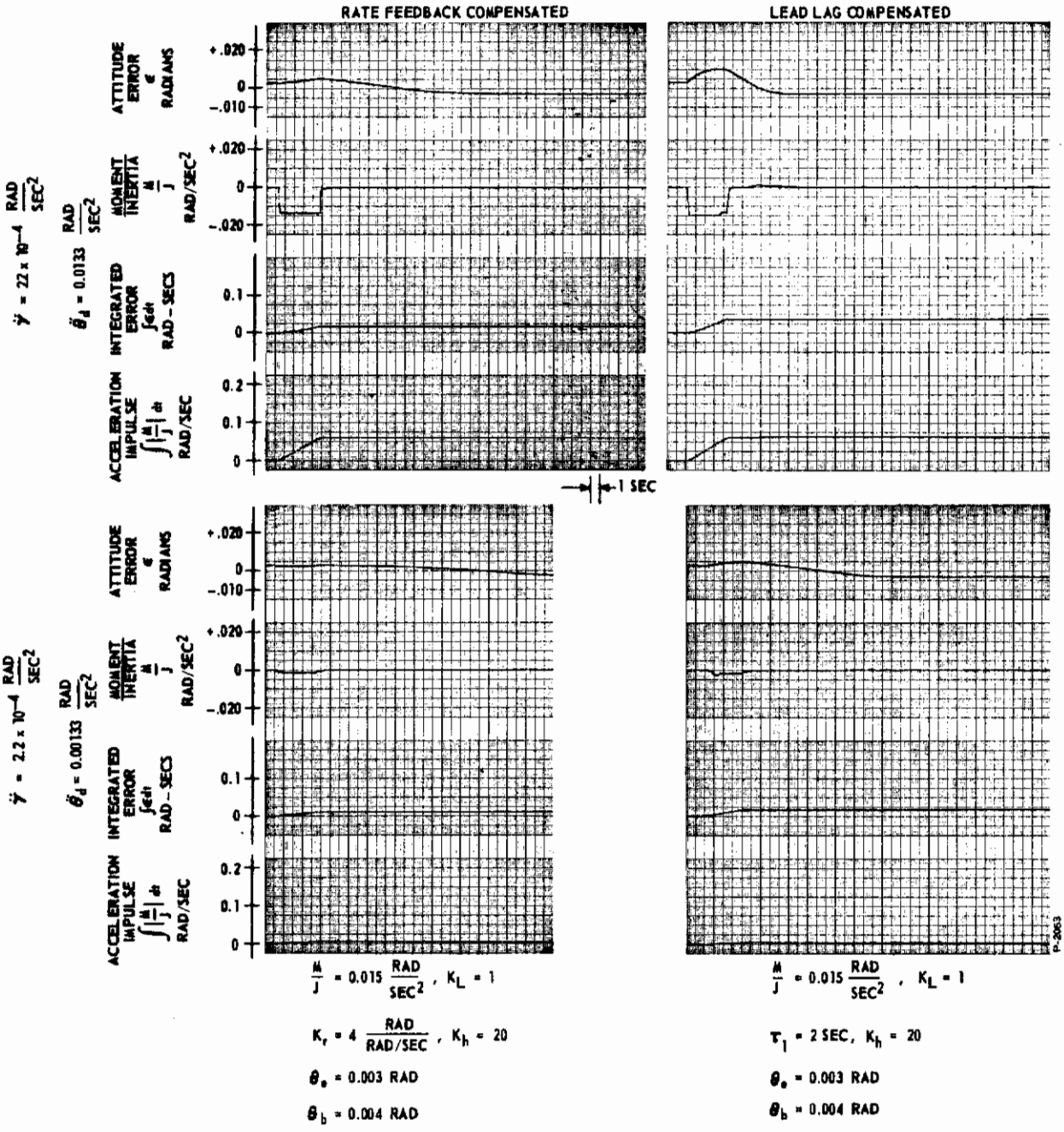

Figure 7-38(a) - Comparison of Proportional System Performance for Rate Feedback and Lead-Lag Compensation

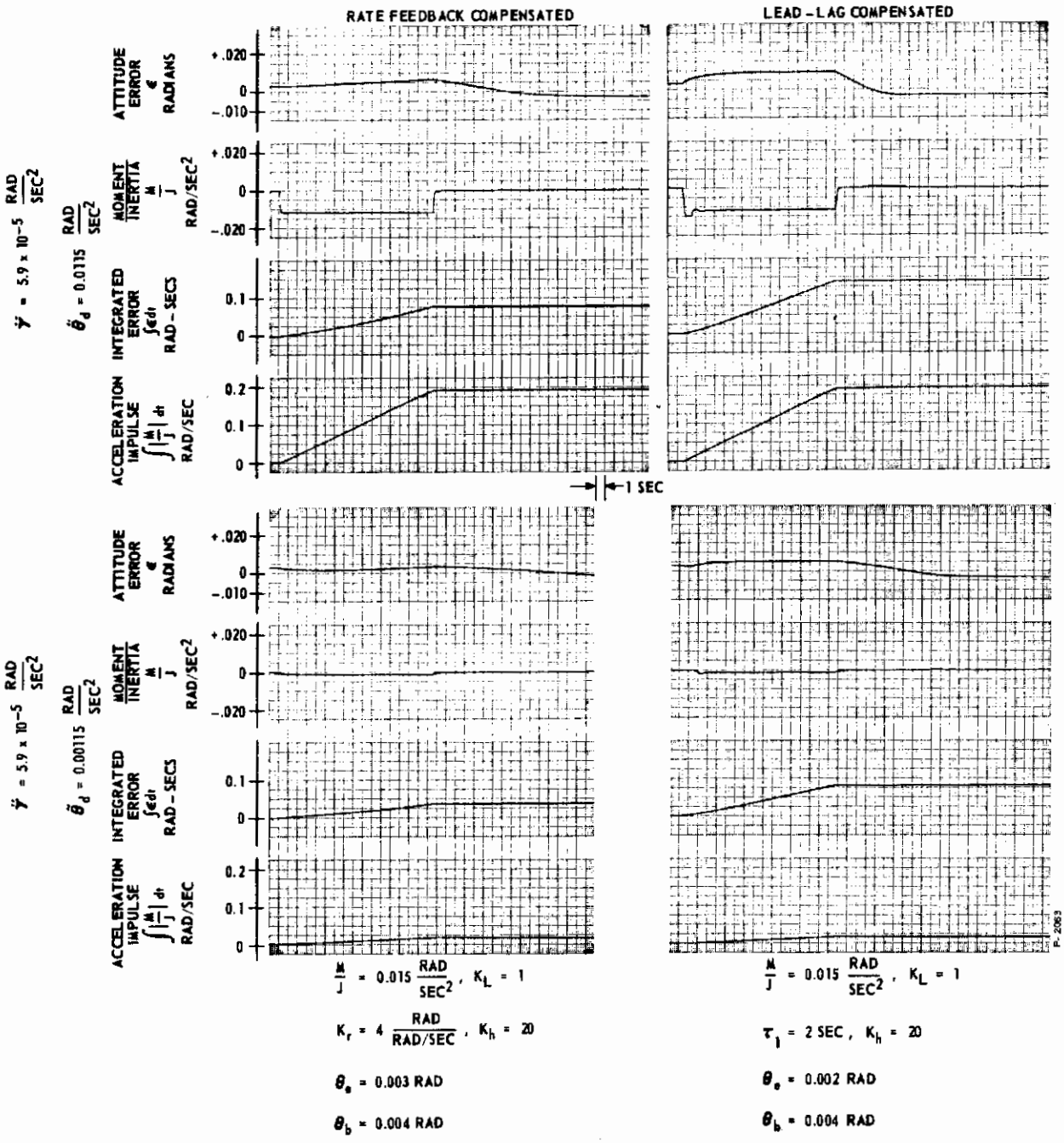

Figure 7-38(b) - Comparison of Proportioned System Performance for Rate Feedback and Lead-Lag Compensation

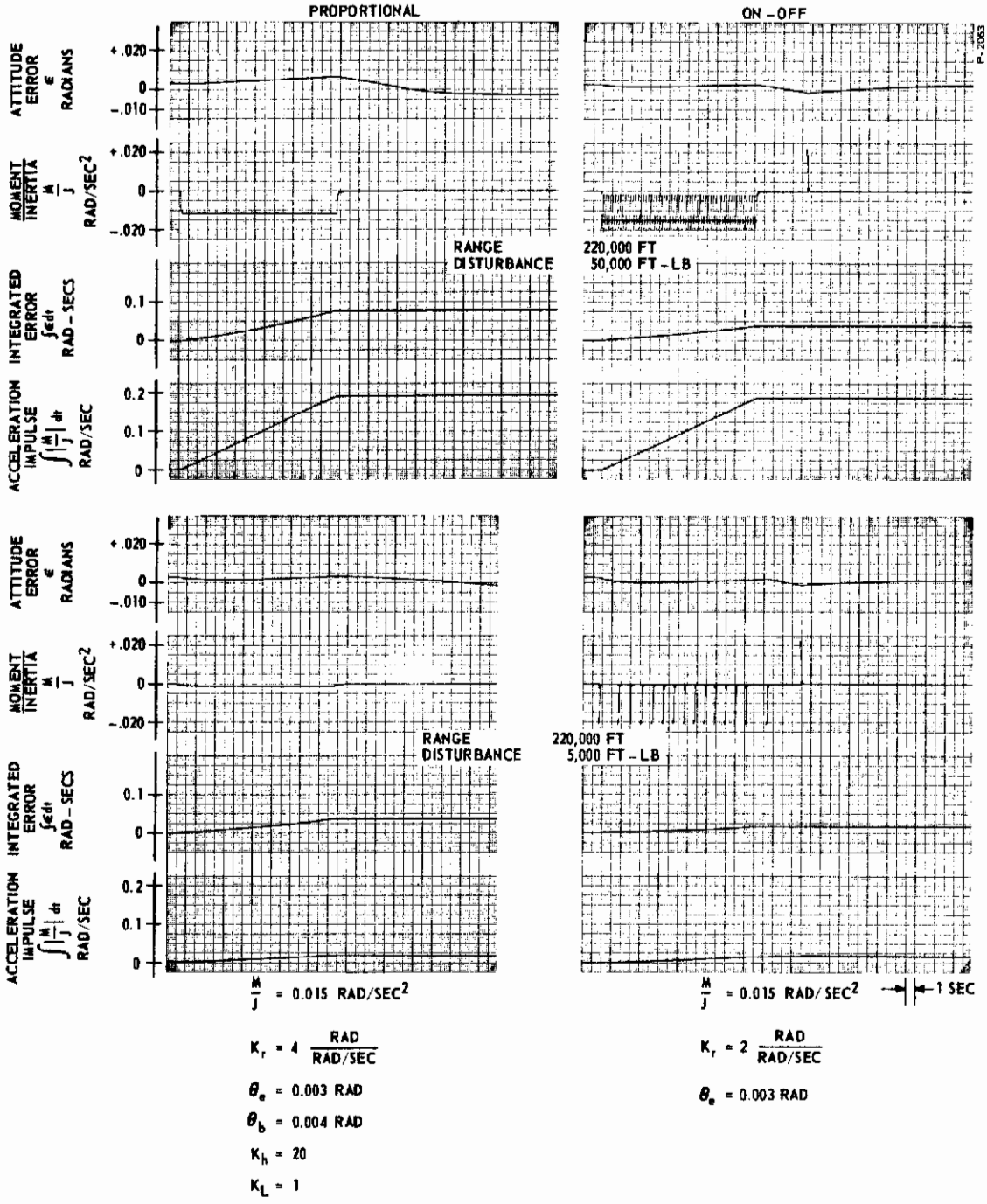

Figure 7-39(a) - Comparison of On-Off and Proportional Attitude Control Systems with Rate Feedback

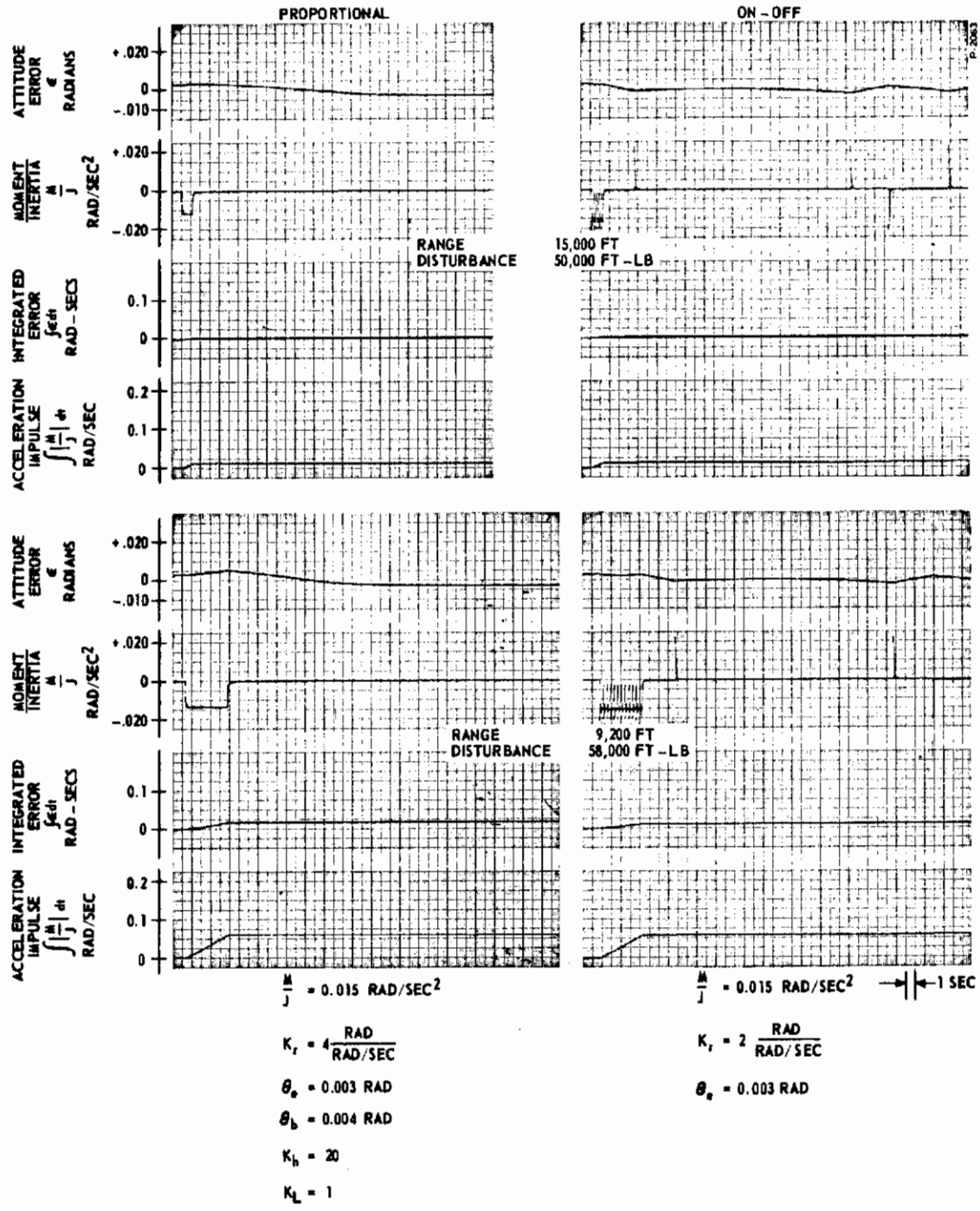

Figure 7-39(b) - Comparison of On-Off and Proportional Attitude Control Systems with Rate Feedback

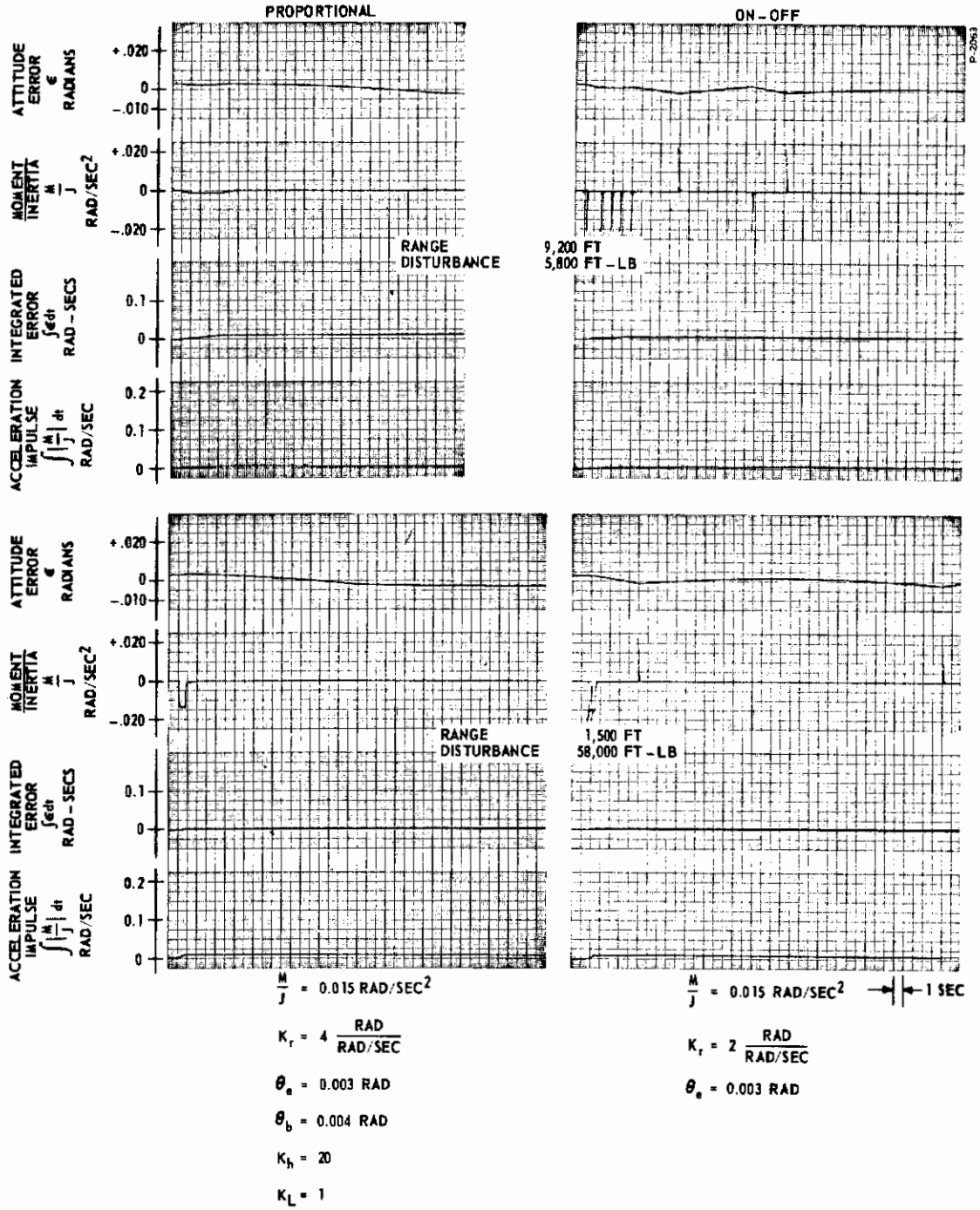

Figure 7-39(c) - Comparison of On-Off and Proportional Attitude Control Systems with Rate Feedback

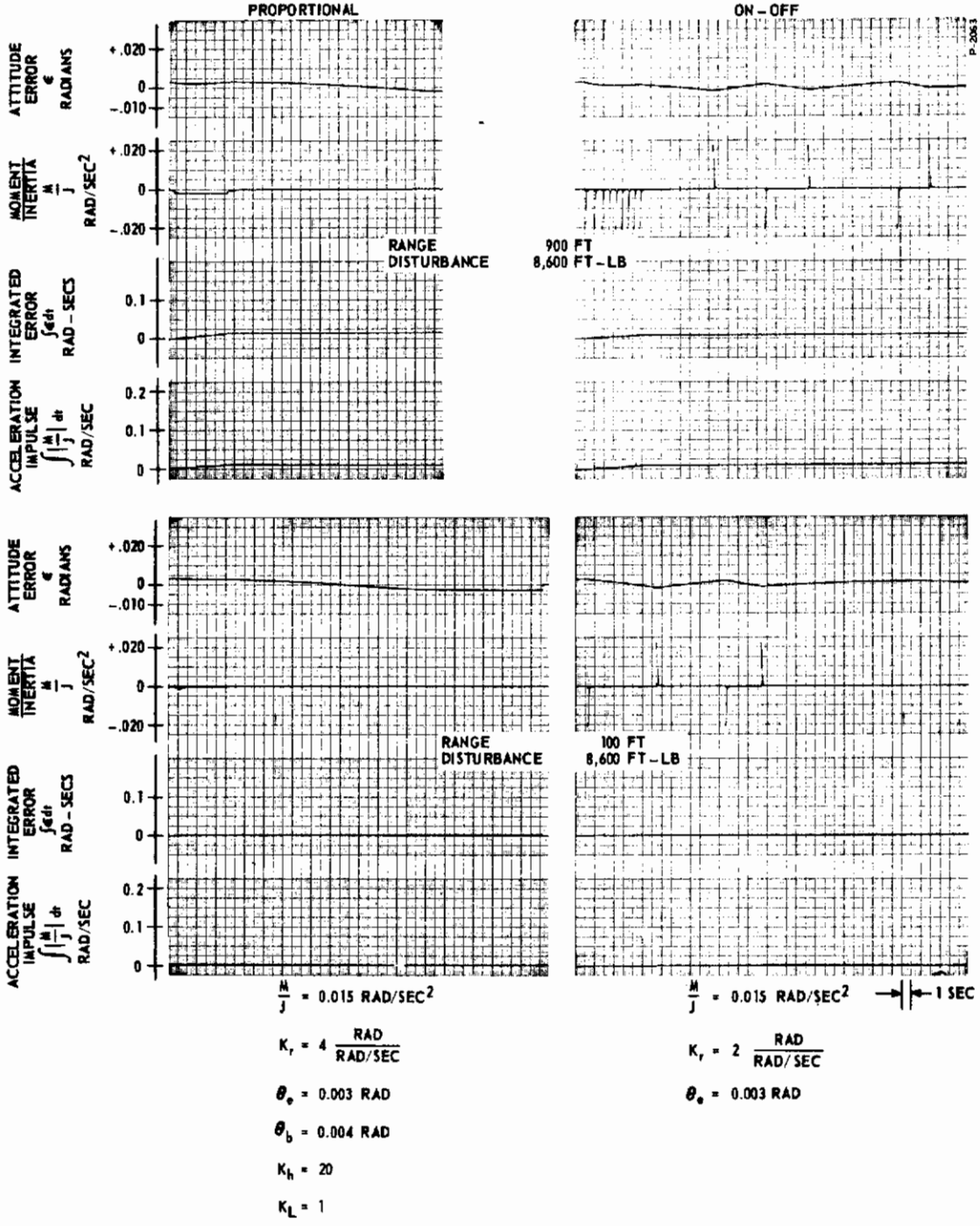

Figure 7-39(d) - Comparison of On-Off and Proportional Attitude Control Systems with Rate Feedback

If a rendezvous requires that, in each range, four guidance corrections are required, the total impulse or propellant consumption can be calculated based on maximum disturbances. For the proportional system, a total impulse of 1.15 rad/sec is required compared to 1.26 rad/sec for the on-off system. The 9.5 percent advantage amounts to about 11 pounds of propellant. This certainly is a small amount compared with the total amount of propellant that must be carried for the primary propulsion.

From a reliability point of view, the added complexity of the proportional system has already been mentioned. An interesting phenomenon can be seen during coasting with the proportional system. In all cases the controller chatters many more times than the equivalent on-off system. For each condition except one, there are more firings of the proportional engine than the on-off engine. The one exception is for the 220,000 foot range with maximum disturbance where there are probably more oscillations during the disturbance for the on-off system than during coast for the proportional system. The total number of operations or firings whether maximum or minimum thrust is a reliability criterion because in each case the pilot stage and main stage valves must operate full stroke.

On the basis of the above discussion, the on-off system with rate feedback compensation has been selected as the optimum attitude control system. The results of this section are considerably different than the results of the preliminary study. This can be attributed to the pure time delay associated with the real reaction control system and the thrust decay time. Both of these characteristics tend to slow down the system and reduce chattering. In addition, the average error criterion has been changed from ability to maintain the maximum permissible error to absolute minimization of average error.

7.3.5 Attitude Control about Roll and Yaw Axes

The control moment requirements about the yaw axis are considerably less severe than for the pitch axis. From Table 7-1 and the representative moment of inertia about the yaw axis, the maximum disturbance moment is 0.0048 rad/sec^2. This is less than half of the pitch axis maximum disturbance. Since the maximum average error requirements about the two axes are the same, no difficulty is encountered in using the same control loop with a smaller engine size for yaw axis attitude control. Using engines giving a corrective control moment

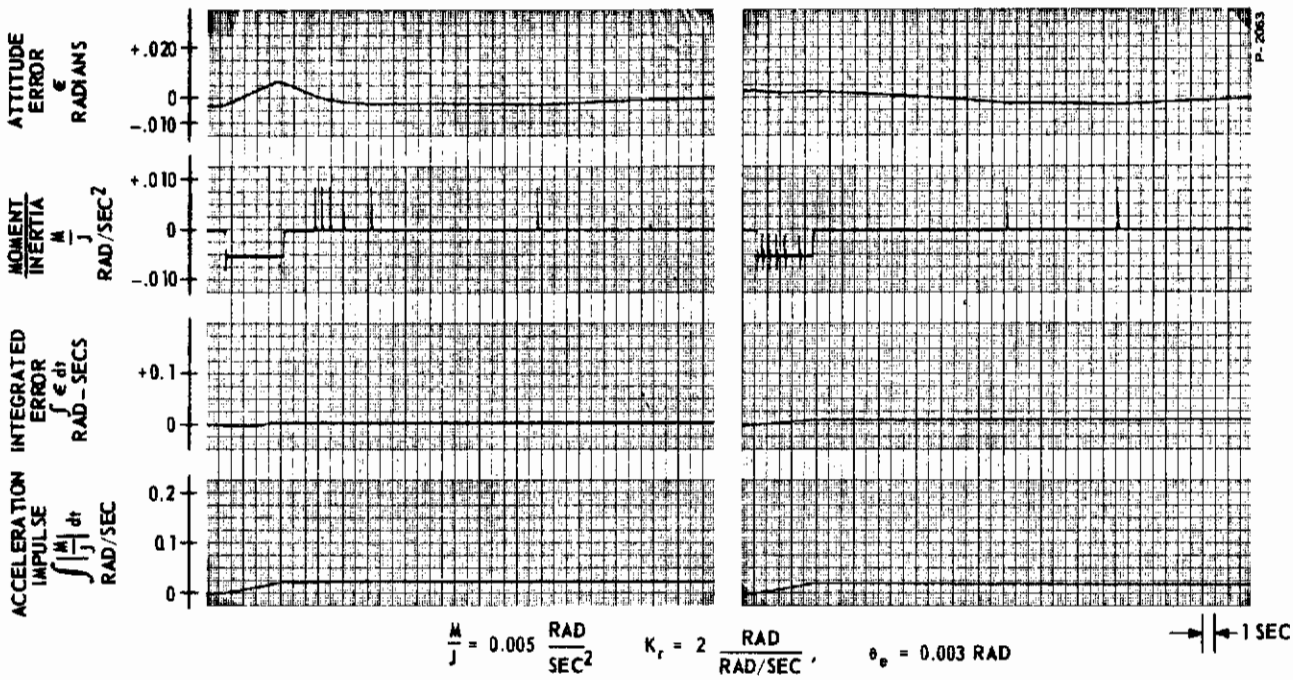

Figure 7-40 - Response of Attitude Control System about Yaw Axis

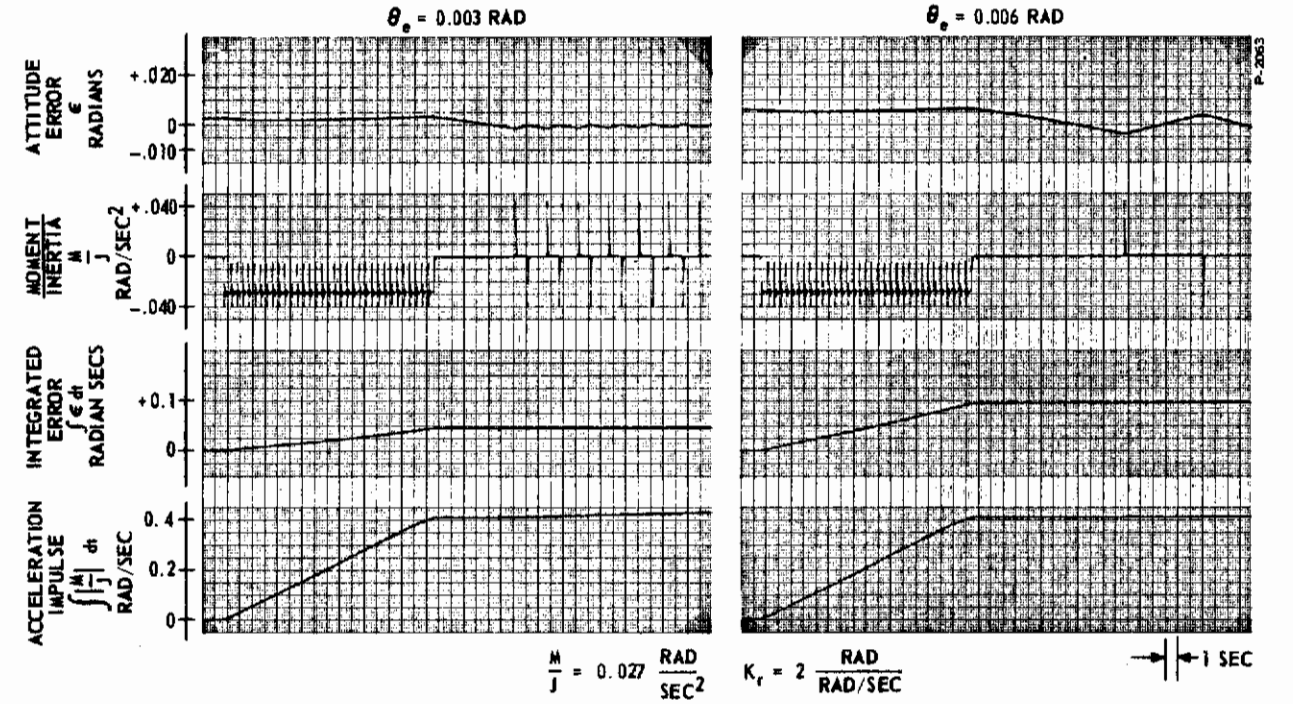

Figure 7-41 - Response of Attitude Control System about Roll Axis; Effect of Deadband

of 0.0050 rad/sec^2 results in a maximum average error of 0.0022 radian. This is about the same maximum average error obtained in the pitch axis for maximum disturbance in each range. Figure 7-40 shows the yaw axis response at a range of 9,200 feet for two different initial conditions of attitude error.

Although the maximum disturbance moment about the roll axis is less than for pitch, the lower vehicle inertia about roll demands a higher corrective acceleration. From Table 7-1 and the inertia about roll, the maximum disturbance about the roll axis is 0.025 rad/sec^2. For the pitch axis, the maximum disturbance acceleration is 0.0133 rad/sec^2. A simple design for the roll axis attitude control is obtained by using the basic control system optimized for the pitch axis but with an M/J of 0.027 rad/sec^2. The higher loop gain (M/J = 0.015 rad/sec^2 for the pitch axis) results in a higher frequency limit cycle during coast. The maximum average attitude error requirements about roll are 0.020 radian while for the other two axes 0.010 radian is the maximum. There is no reason why one axis should have better accuracy, percentage wise,

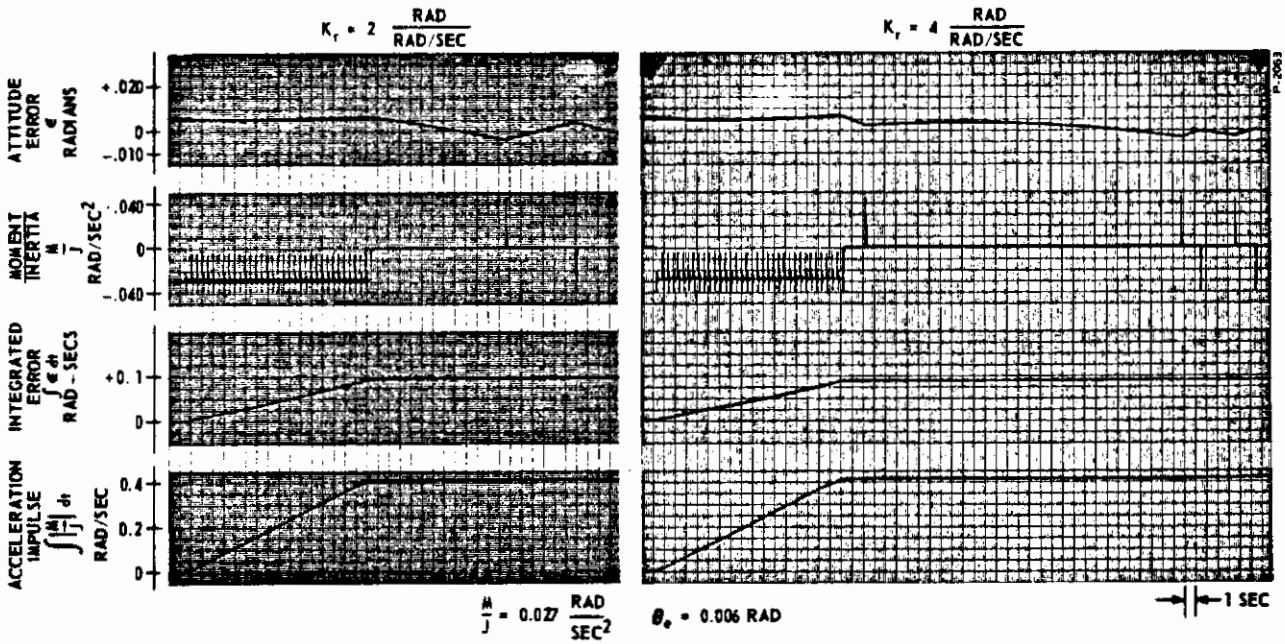

Figure 7-42 - Response of Attitude Control System about Roll Axis; Effect of Rate Feedback

than any other axis, so that an increase in deadband to 0.006 radian in roll is consistent with the total vehicle attitude requirements. Figure 7-41 shows that doubling the deadband increases the average error to slightly more than twice its original value. The average error for the 0.006 radian deadband is 0.0055 radian. The doubled deadband has reduced the limit cycle frequency about one quarter with a resultant decrease in propellant consumption. Increasing the amount of rate feedback as shown in Figure 7-42 improves the average error by about 5 percent but increases the limit cycle frequency by a factor of about two. No over-all advantage is obtained by increasing the rate feedback. Figure 7-43 shows the response at three different ranges.

7.3.6 Summary

An attitude control system has been determined which will meet the requirements of orbital transfer and rendezvous maneuvers. An on-off control system with rate feedback compensation has been selected as optimum based on the small number of criteria that were considered. All of the systems, proportional and on-off with rate feedback or lead-lag compensation will meet the requirements demanded for rendezvous and, consequently, orbital transfer. The selection of an attitude control system for a specific vehicle and mission will involve many more and different criteria than were considered.

Based on the systems selected and the vehicle geometry, Table 7-2 shows the engine sizes and moment arms for each axis.

Table 7-2 - Summary of Attitude Control Moment Requirements

Axis	M/J rad/sec^2	Moment Arm Between Engines, ft	Engine Thrust, lb
Pitch	0.015	100	655
Yaw	0.005	100	261
Roll	0.027	75	360

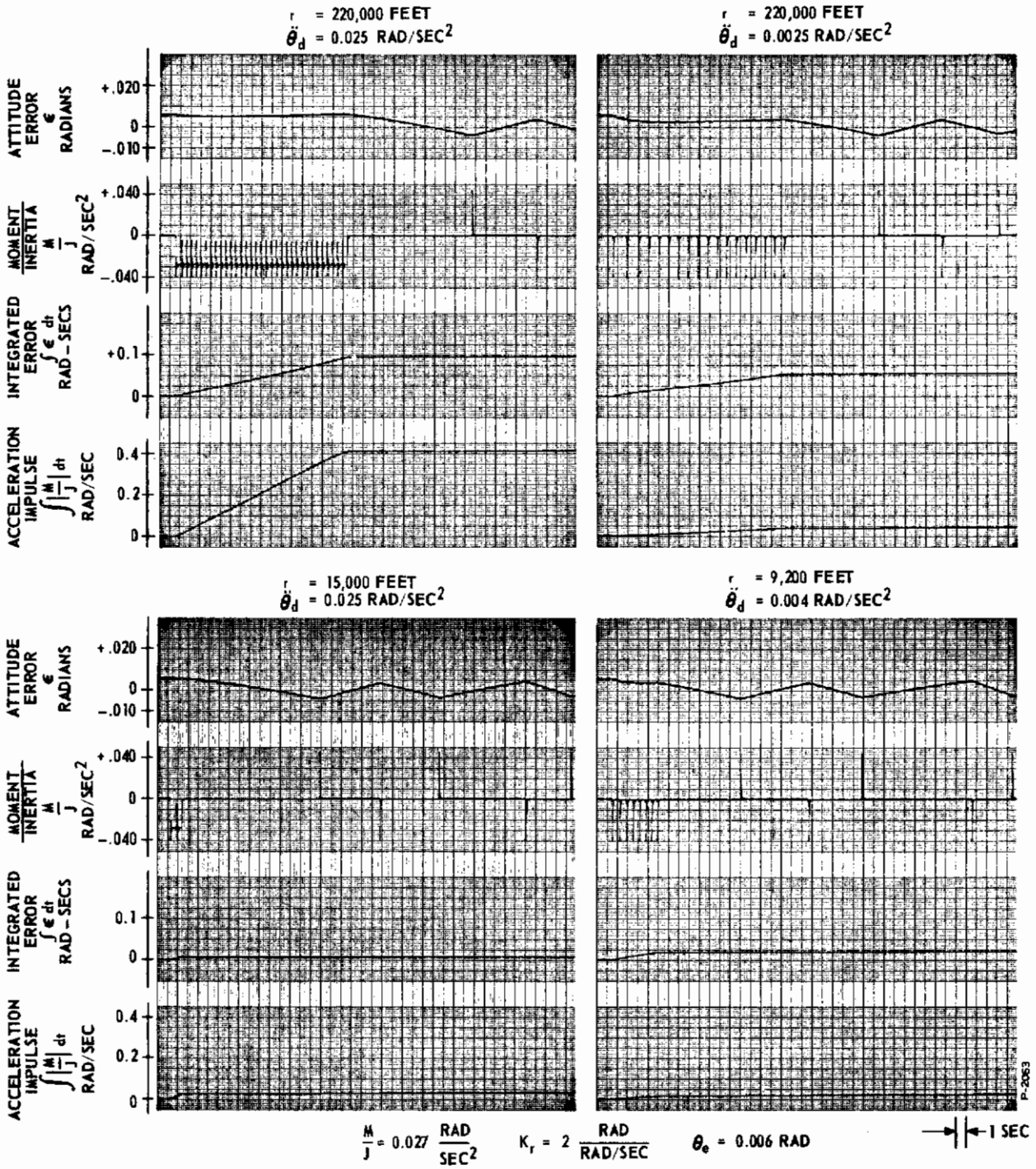

Figure 7-43 - Response of Attitude Control System about Roll Axis at Various Ranges

7.4 SECONDARY INJECTION THRUST VECTOR CONTROL LOOP

7.4.1 Introduction

Main engine misalignments can produce disturbances considerably larger than the corrective capability of the attitude control systems, because the attitude control engines are sized to correct for misalignments only in the small guidance engines. Considerable efficiency is obtained by using thrust vector control for large disturbances rather than by oversizing the attitude control engines. In this section the interaction between a thrust vector control system and an attitude control system, both acting to reduce the attitude error, is investigated.

7.4.2 Selection of Control Mode

A comparison was made in Section 5 between a poppet valve and a vortex valve for thrust vector control. The vortex valve was found to be superior, so it is used in this study. The selection of the control mode is based on the previous attitude control system study where it was found that rate feedback provides better performance than lead-lag compensation. On-off control resulted in smaller errors and less propellant consumption during a disturbance than proportional control. The propellant consumption during limit cycle or coast is not of interest in this study because thrust vector control is active only during main engine firing. The system selected for investigation then, is a vortex valve in an on-off rate feedback compensated loop.

7.4.3 Computer Simulation and Optimization

A block diagram of the combined thrust vector control and reaction engine attitude control systems is shown in Figure 7-44. Each control system has its own feedback and compensation. The desired attitude is common to both systems and cross coupling between systems occurs through the vehicle dynamics. The response of the vortex valve is assumed to be infinitely fast but as a practical matter the method of simulating on-off operation results in a finite operating time.

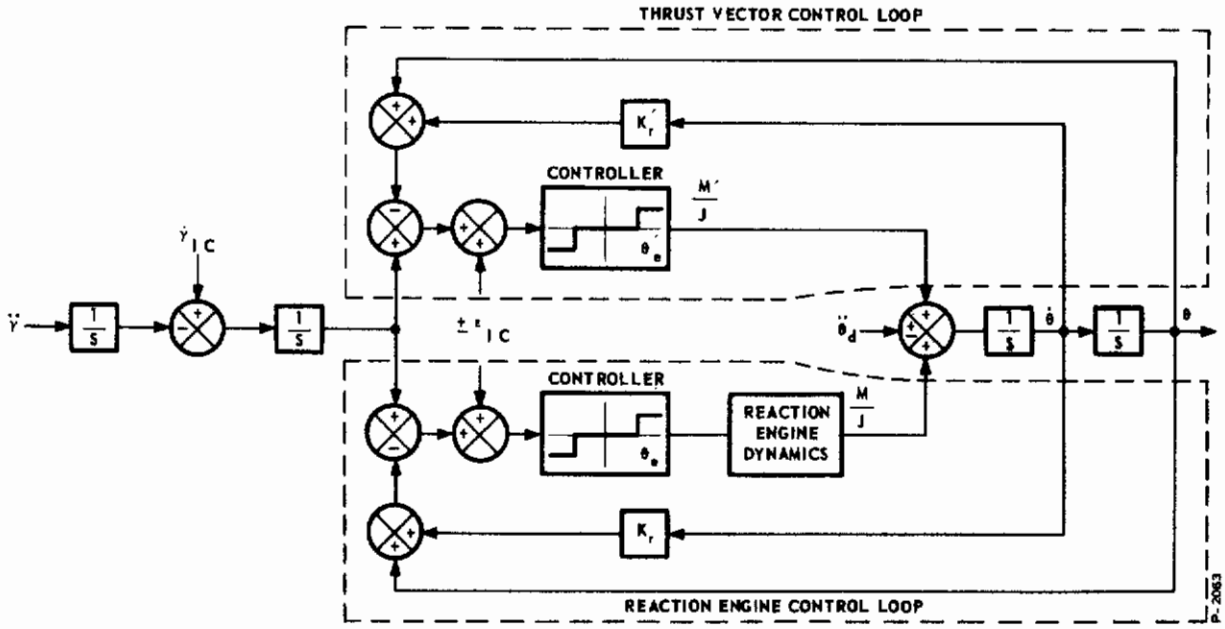

Figure 7-44 - Block Diagram of Combined Thrust Vector Control and Reaction Engine Attitude Control Systems

The computer diagram for the entire system is shown in Figure 7-45. This is similar to the computer diagram for the on-off attitude control system given in Figure 7-17. In addition, another error channel $\epsilon + K_r' \dot{\theta}$ is derived for driving two relay amplifiers to obtain deadband and on-off simulation. The relay amplifiers require three to five milliseconds for operation so this presents a dynamic lag to the thrust vector control loop. An additional relay is used to remove the disturbance $\ddot{\theta}_d$ and the thrust vector control acceleration M'/J when the line-of-sight angular velocity $\dot{\gamma}$ reaches zero.

Eight channels of recording were taken. Four channels are the same as for the reaction engine attitude control system study: attitude error ϵ, attitude control moment-to-inertia ratio M/J, integrated error $\int_o^t \epsilon \, dt$, and attitude control acceleration impulse $\int_o^t |M/J| \, dt$. In addition the thrust vector control moment-to-inertia ratio M'/J and acceleration impulse $\int_o^t |M'/J| \, dt$ are recorded. The last two recorded channels are line-of-sight angular velocity $\dot{\gamma}$ and attitude angular velocity $\dot{\theta}$. The line-of-sight angular velocity is merely the integral of $\ddot{\gamma}$ but it shows when the disturbance begins and ends (beginning and end of ramp respectively). The attitude velocity gives a better indication

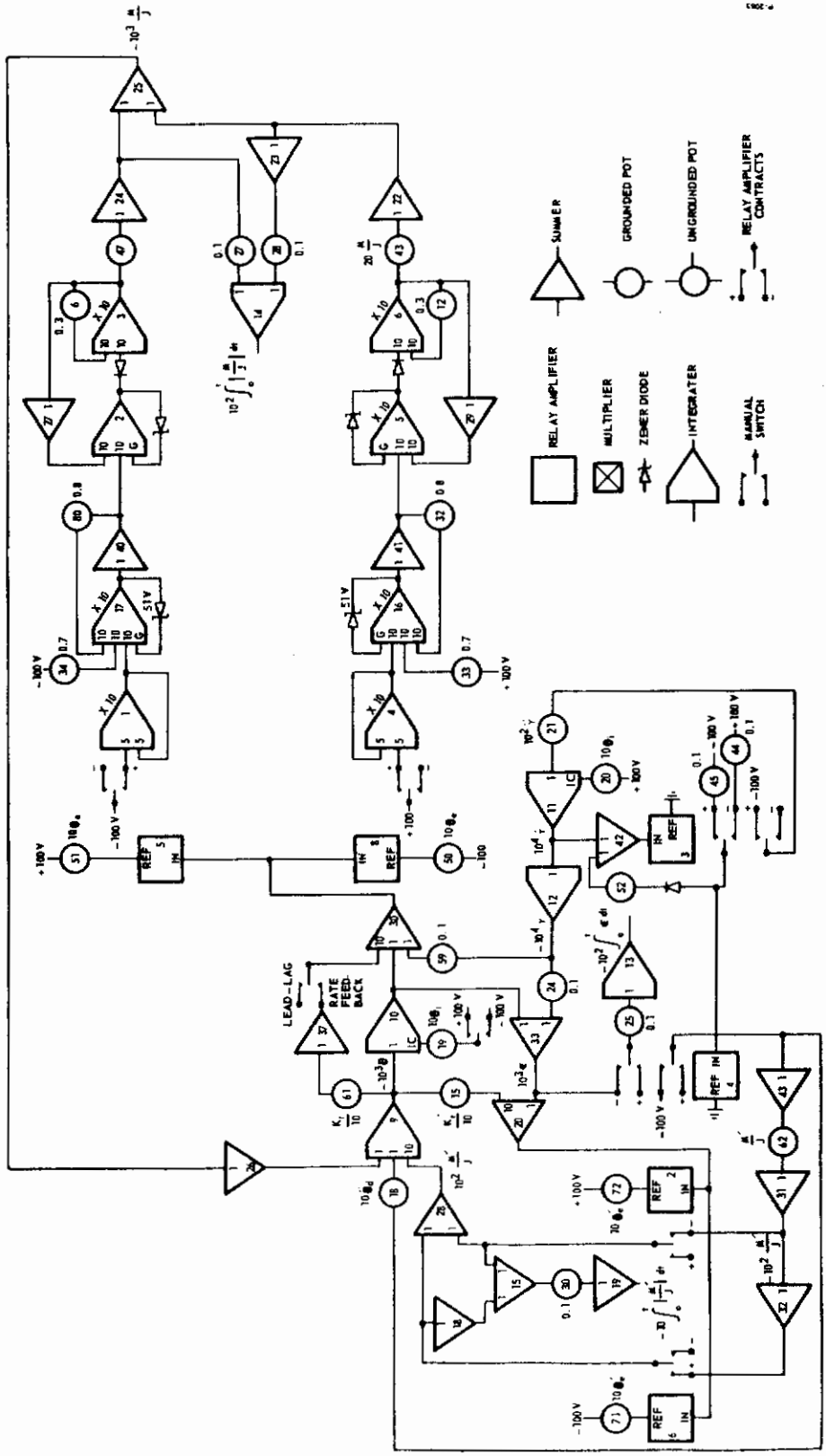

Figure 7-45 - Computer Diagram of Combined Thrust Vector Control and Reaction Engine Attitude Control Systems

of oscillations that are occurring than attitude error does. This is due to the scale factors that can be used and the fact that $\dot{\theta} = \omega\theta$, where ω is the angular velocity of oscillation. High frequency low amplitude oscillations show up very well on this type of recording.

The rendezvous parameters used for evaluating system performance about the pitch axis are at a range of 220,000 feet. This condition represents the maximum disturbance and the maximum time duration. The disturbance acceleration consists of 0.0115 rad/sec^2 due to normal engine misalignment and 0.0918 rad/sec^2 due to main engine misalignment.

The thrust vector control system (TVCS) was optimized and then a parameter variation study was performed. Although the thrust vector control system appears to be unstable at a frequency too high to be recorded conveniently, vehicle performance does not reflect this instability. The vortex valve with no moving parts is capable of high frequency operation reliability so that no attempt has been made to stabilize the system. A real system would be limited by the response capability of the resultant moment to the injected flow rate, but this information was not available for inclusion in the simulation.

A maximum disturbance of 0.1033 rad/sec^2 was set and the TVC moment-to-inertia ratio M'/J was varied. The total available corrective acceleration should be greater than the maximum disturbance. Two different approaches are possible: $M'/J > \ddot{\theta}_d$ or $M'/J + M/J > \ddot{\theta}_d$. Figure 7-46 shows the difference in the two methods. If $M'/J > \ddot{\theta}_d$ then the reaction engine attitude control system generally is inoperative during the disturbance. This is because the thrust reactor control system maintains an attitude error less than the deadband θ_e. The TVCS chatters in order to maintain an average acceleration about equal to the disturbance. In the second case $M'/J + M/J > \ddot{\theta}_d$, but $M'/J < \ddot{\theta}_d$. The TVCS is not capable of maintaining an attitude error within its deadband θ_e so the reaction engine attitude control system operates to maintain the error within its deadband θ_e. Average error has increased for this case although it is still very small. About 5 percent saving in TVC injectant results but this difference in acceleration impulse is provided by the attitude control system. The efficiency of TVC is very high because a small flow into the thrust stream can result in a large moment. It is therefore concluded that the thrust vector control system should be sized to correct for the maximum disturbance without regard for the reaction engine attitude control system capability.

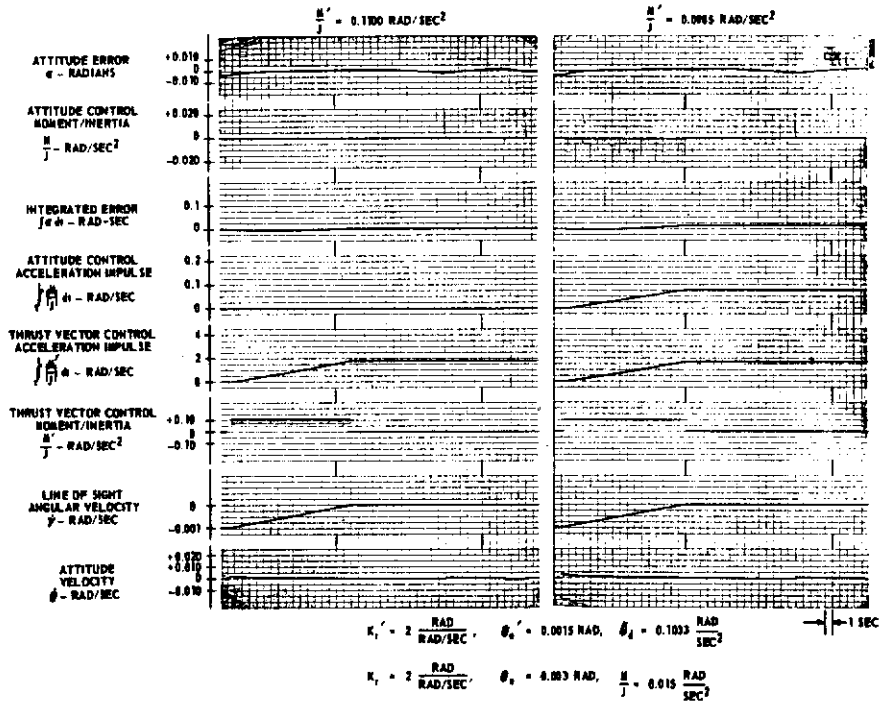

Figure 7-46 - Thrust Vector Control System; Effect of Moment-to-Inertia Ratio upon Performance

The effect of rate feedback can be seen from the three curves in Figure 7-47. A reduction in rate feedback results in attitude velocities sufficient to actuate the reaction engine attitude control system. In addition to the added propellant flow, the average error is also increased. A large reduction in rate gain to 0.15 rad/rad-sec results in attitude error overshoot. TVC injectant consumption is not changed noticeably but the reaction engine attitude control system uses considerably more propellant. A rate feedback gain greater than two was not considered because the average error was small and the propellant consumption optimum. Increased rate feedback could lead to instability.

The deadband θ_e' used with the thrust vector control system should be less than the reaction engine attitude control system deadband θ_e to keep the latter system from operating. From Figure 7-48 it can be seen that if the two control systems have the same deadband $\theta_e = \theta_e' = 0.003$ radian the average error increases. The saving in acceleration impulse by the thrust vector control system is obtained at the expense of an equal acceleration impulse by the attitude control

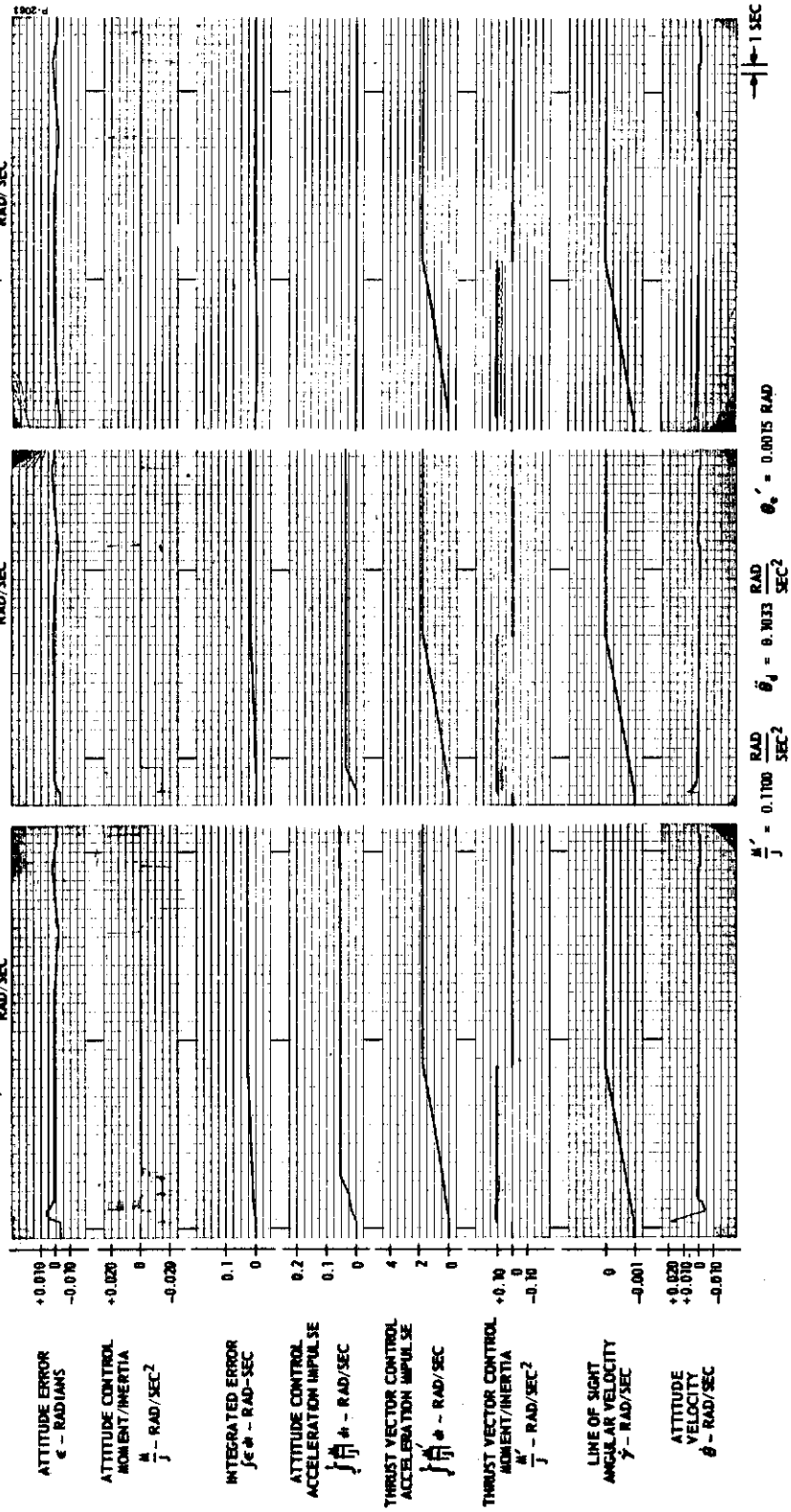

Figure 7-47 - Thrust Vector Control System; Effect of Rate Feedback upon Performance

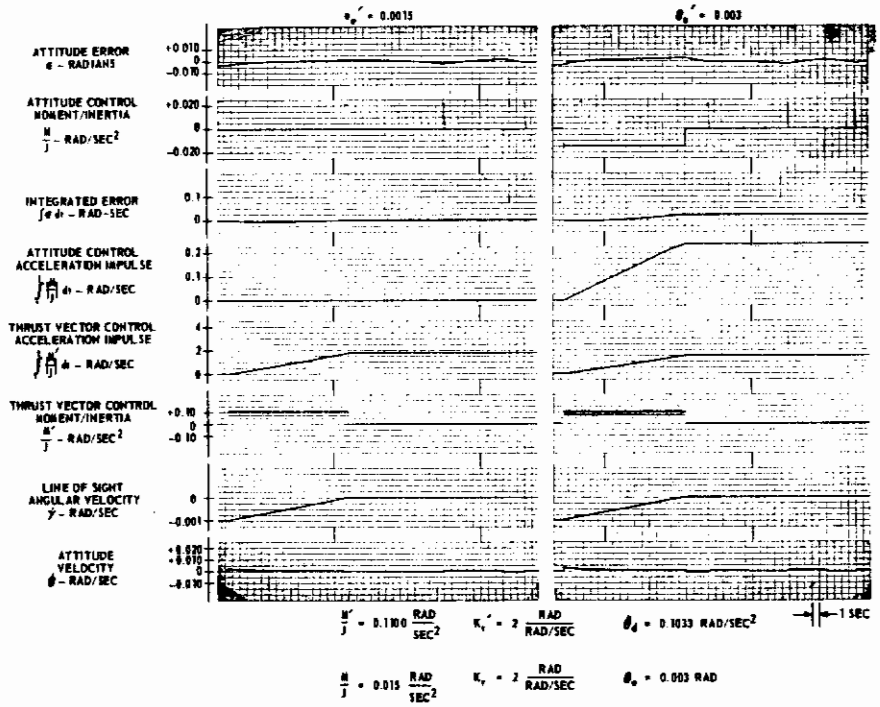

Figure 7-48 - Thrust Vector Control System; Effect of Deadband upon Performance

system. Because of the relative efficiencies, the thrust vector control system should have a smaller deadband than the attitude control system.

It was stated previously that the response of the control moment to injected flow was not available. Since any additional lag in the thrust vector control loop might lead to instability or interaction problems, a first order lag was added to the loop. As Figure 7-49 shows, the inclusion of dynamics to the thrust vectoring phenomena can result in interaction problems if the thrust vector control system is not maintained much faster than the attitude control system.

The final set of data in Figure 7-50, shows the response to various disturbances. Although the system chatters for large and small disturbances, the injectant consumption or acceleration impulse depends only upon the disturbance and its duration.

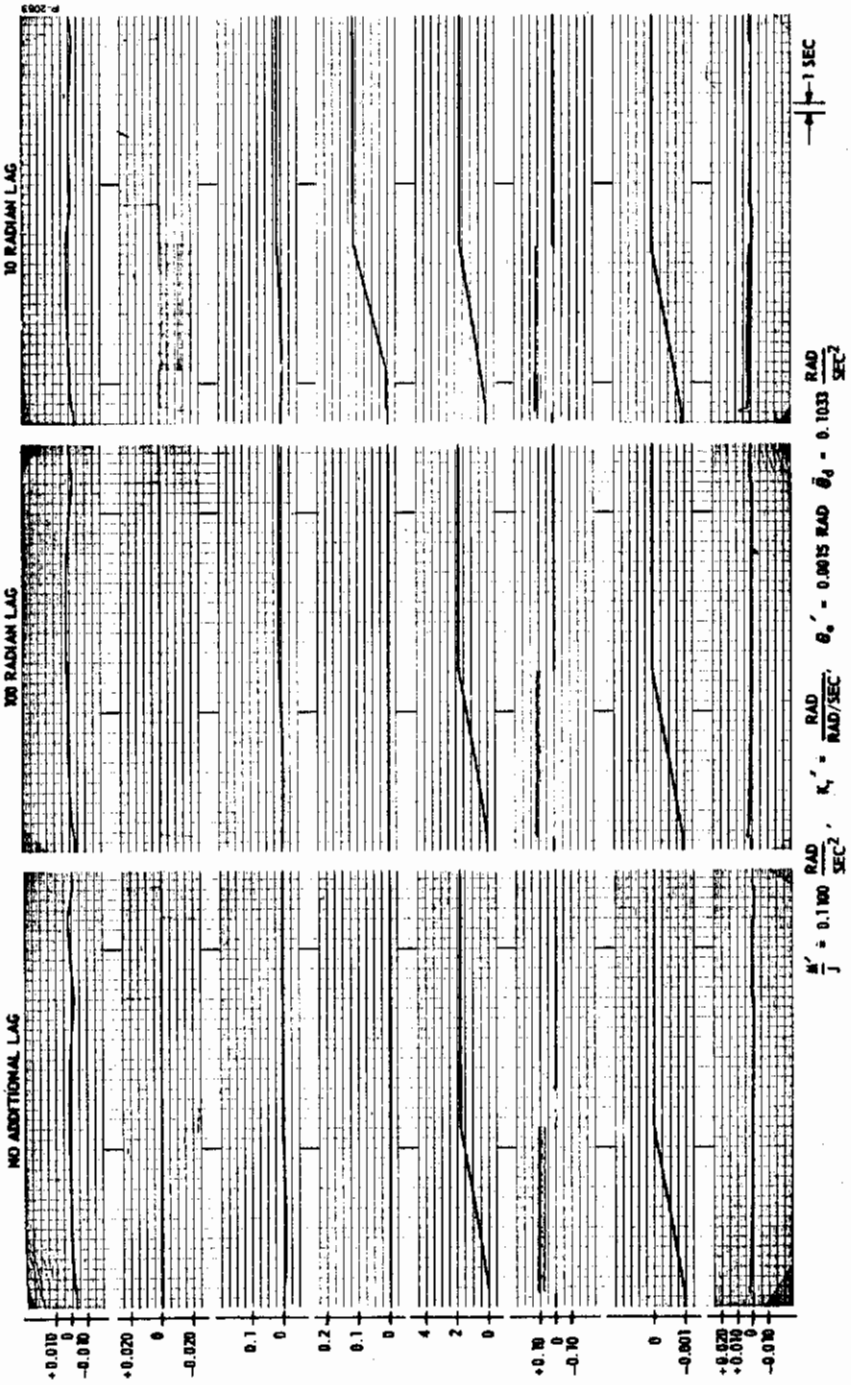

Figure 7-49 - Thrust Vector Control System; Effect of Dynamic Lag upon Performance

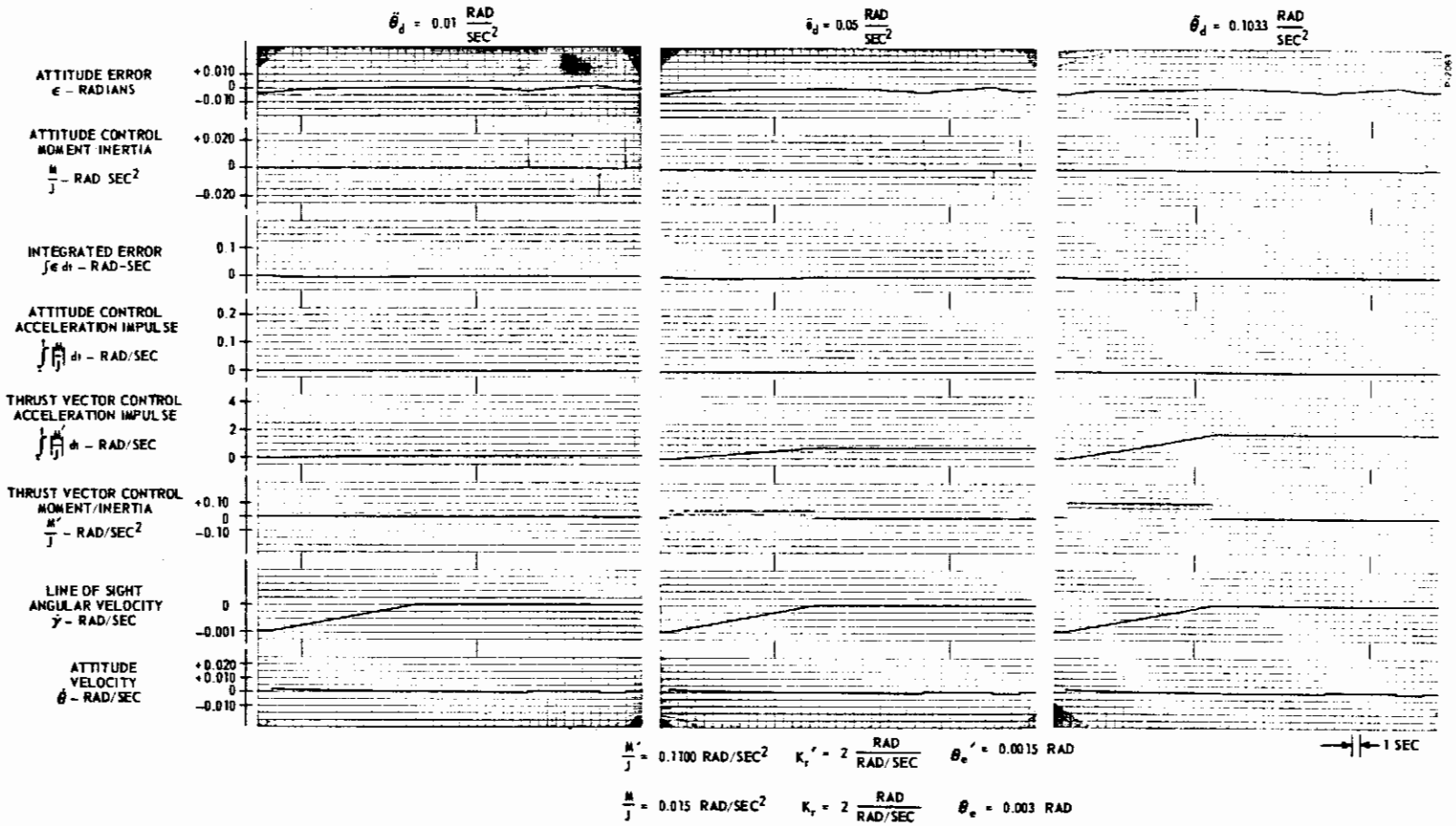

Figure 7-50 - Thrust Vector Control System; Response for Various Disturbances

7.4.4 Conclusions

As a result of this study it can be concluded that thrust vector control can be used during main engine firings to maintain average attitude errors within limits that will permit rendezvous. Due to the high performance capability of the vortex valve and no coasting requirements, the TVC can be designed to maintain better accuracy than an attitude control system with reaction engines. No interaction problems appear as long as the TVCS is much faster than the reaction engine attitude control system. If the TVCS is not fast, then it may be necessary to deactivate the attitude control system during main engine firings.

7.5 NOMENCLATURE

Symbol		Definition
I_{at}	=	Acceleration impulse, $\int_o^t \lvert M/J \rvert \, dt$, rad/sec
I_{SP}	=	Specific impulse of propellant, sec
J	=	Vehicle moment of inertia, lb-sec^2-ft
K_h	=	Initial slope of nonlinear gain device
K_L	=	Final slope of nonlinear gain device
K_r	=	Rate feedback gain
ℓ	=	Moment arm of reaction engines, ft
M	=	Control moment, ft-lb
M_d	=	Disturbance moment, ft-lb (subscripts p, y, r refer to pitch, yaw, and roll axes)
r	=	Range between vehicle and target, ft
S	=	Laplace operator, 1/sec
t	=	Time, sec
t_c	=	Duration of line-of-sight correction, sec
W	=	Weight of propellant consumed, lb
$\dot{\gamma}$	=	Angular velocity of line-of-sight, rad/sec
$\ddot{\gamma}$	=	Angular acceleration of line-of-sight, rad/sec^2

Symbol		Definition
ϵ	=	Attitude error, rad
θ	=	Inertial reference angle, rad
$\dot{\theta}$	=	Vehicle angular velocity, rad/sec
$\ddot{\theta}$	=	Vehicle angular acceleration, rad/sec^2
θ_b	=	Error at which nonlinear gain changes slope, rad
θ_e	=	Deadband in controller, rad
θ_c	=	Command vehicle attitude, rad
$\ddot{\theta}_d$	=	Disturbance acceleration, M_d/J, rad/sec^2
τ	=	Time constant, sec
τ_1	=	Lead time constant, sec
τ_2	=	Lag time constant, sec
$( )'$	=	Primed symbols refer to thrust vector control loop.

SECTION 8

ATTITUDE CONTROL DURING RE-ENTRY

8.1 INTRODUCTION

8.1.1 Objective

The attitude control system comprises one of the more important loops within the re-entry guidance system. In fact, its performance determines the degree of success of the entire re-entry maneuver, since the vehicle angle-of-attack (pitch attitude) controls the lift and drag acting on the vehicle. Errors in the angle-of-attack can cause the vehicle to enter the atmosphere too rapidly with excessive aerodynamic heating, or they can force the vehicle to skip out of the atmosphere into an undesirable orbit or trajectory. The performance of the attitude control system then, is most properly defined in terms of deviations of the trajectory characteristics from optimum or commanded values. Subsection 3.4.2 defines what is considered to be an optimum trajectory. Accordingly, the objective of this study is to analyze and define an attitude control system for re-entry which will allow the vehicle to closely follow this hypothetical trajectory.

8.1.2 Problem Definition

The aerodynamic forces and moments acting on the vehicle during re-entry are correlated by expressions which contain the dynamic pressure, q, as a factor. Thus, before any numerical calculation of moments acting on the vehicle can be performed, the dynamic pressures must be known. The dynamic pressure is given by:

$$q = \frac{\rho V^2}{2} \qquad (8\text{-}1)$$

Figure 8-1 gives a plot of dynamic pressure versus time for the trajectory selected in Subsection 3.4.2. It can be seen that during the early stages of re-entry, the dynamic pressure is small. Specifically, q is less than 2 psf for the first 96 seconds of re-entry and is never less than this value thereafter. This value of dynamic pressure is

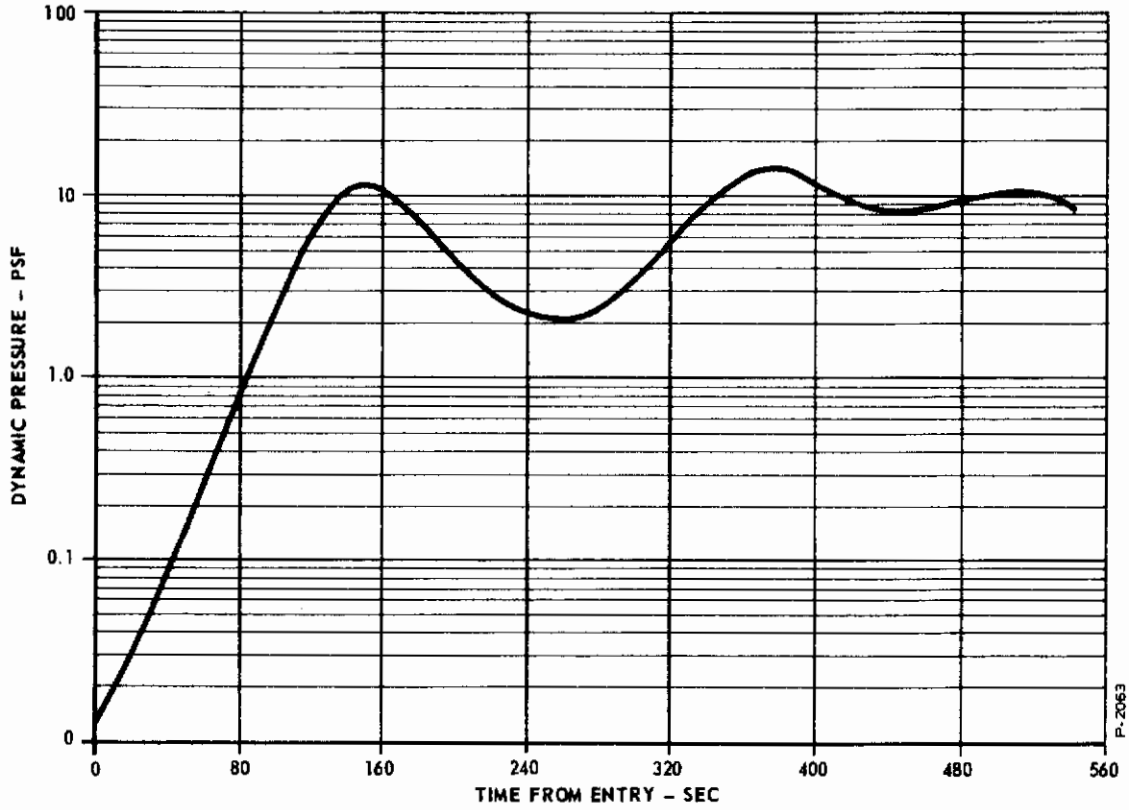

Figure 8-1 - Dynamic Pressure Versus Time for Selected Re-Entry Trajectory

considered adequate for complete aerodynamic control of attitude. It is therefore concluded that during the first 96 seconds of re-entry, an additional source of moments for attitude control is required. The re-entry maneuver is considered to be made up of two parts, the first part involving both aerodynamic and mass expulsion control and the second part using only aerodynamic control.

The vehicle attitude during the first part of re-entry is controlled primarily by moments created by small rocket motors. The initial altitude is 400,000 feet, the initial speed is 26,000 ft/sec, and the initial path angle is 2.5 degrees. This portion of the flight lasts approximately 96 seconds and finally achieves an altitude of approximately 294,000 feet and a speed of approximately 25,200 ft/sec. A limit of 2 g's path deceleration is set for the entire re-entry but is not approached during the initial 96 seconds; therefore, no angle-of-attack corrections are required. The flap angle δ_f is maintained at -30 degrees

(flap up) which causes the vehicle to naturally trim at an angle-of-attack of 77 degrees. The aerodynamic attitude control moments are too small to provide adequate response during this portion of the re-entry, so augmentation by mass expulsion is necessary.

The second part of re-entry begins after approximately 90 to 100 seconds when the dynamic pressure reaches a sufficient level to allow complete aerodynamic control of the vehicle attitude. During this time, the path deceleration first reaches 2 g's, thus causing the guidance system to move the aerodynamic flaps in commanding a new angle-of-attack. From this point on, the angle-of-attack is corrected until pilot control is initiated.

8.2 ANALYSIS OF FIRST PART OF RE-ENTRY

8.2.1 Attitude Control by Means of Mass Expulsion

Since aerodynamic forces are the least during the first 96 seconds of re-entry, attitude control by means of mass expulsion will be the most advantageous during this period. Quite obviously, the worst case for mass expulsion will be that in which no use whatsoever is made of aerodynamic forces to obtain the desired pitch angle.

The pitching moment about the vehicle center of gravity is given by:

$$M_p = C_m A_r \bar{C} q \qquad (8\text{-}2)$$

For the assumed vehicle, $A_r = 14{,}500\ ft^2$ and $\bar{C} = 141$ feet. The selected trajectory requires that $L/D = 0.307$ and $C_d = 1.40$ for the first 128 seconds of re-entry.

The aerodynamic characteristics of the assumed vehicle are given in Ref. (19).* For the case in which no use is made of aerodynamic control, $\delta_f = 0$, and from (19), at $C_d = 1.4$ and $\delta_f = 0$, $\alpha = 65°$ for a nose incidence of 10 degrees. With these conditions, $C_m = -0.085$ with the vehicle center of gravity located at $0.42\ \bar{C}$.

*Numbers in parentheses refer to the references listed in Section 10.

With $\delta_f = 0$, the vehicle will trim at an angle-of-attack of approximately 23 degrees. Thus, to maintain $\alpha = 65°$, a continuous thrust could be applied to overcome the aerodynamic pitching moment corresponding to this angle of attack. The value of this thrust is given by:

$$F_p = \frac{M_p}{x_p} \tag{8-3}$$

Substitution of Equation (8-2) into (8-3) gives:

$$F_p = \frac{C_m A_r \bar{C} q}{x_p} \tag{8-4}$$

Since the center of gravity of the vehicle, which has an over-all length of 204 feet, is 125 feet from the nose, the maximum distance of the aft pitch engine from the center of gravity is 79 feet. Since the engine cannot be located exactly at the end of the vehicle, a value of 75 feet will be assumed here. Since two engines are used to provide a pure couple, $x_p = 150$ ft.

With the numerical values just given, and with Figure 8-1 giving q as a function of time, the values of F_p for a single pitch engine versus time can be computed from Equation (8-4). This plot which is shown in Figure 8-2 can be graphically integrated to obtain the total impulse required to maintain the desired pitch angle during the first 100 seconds of re-entry. The graphical integration gives 50,500 lb-sec per engine or 101,000 lb-sec total. For a 400 second specific impulse, this amounts to approximately 250 pounds of propellants, which is not unreasonable.

The thrust versus time curve shown in Figure 8-2 can be interpreted in either of two ways. It can represent the thrust level of a continuously operating throttleable pair of engines or it can represent the effective output of a pair of pulsing engines. In the latter case the units of thrust would be more correctly denoted lb-sec/sec than lb.

For the case where t = 0 sec, Equation (8-4) gives F_p = 13.7 lb, and at t = 100 sec, F_p = 2860 lb. This is a 209:1 ratio, which is beyond the capabilities of either a throttling system or a pulsing system. Thus the limitation on the length of time after re-entry that mass expulsion can be used for attitude control is a function not of total propellant consumption, but of the ratio of minimum to maximum moments that can be produced by this means.

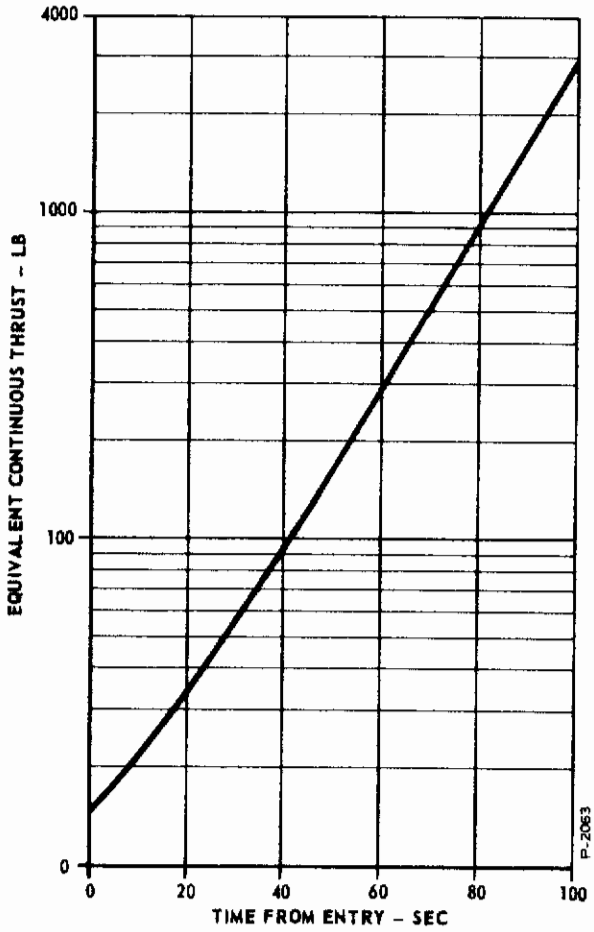

Figure 8-2 - Equivalent Thrust Versus Time

8.2.2 Attitude Control by Means of Aerodynamic Surfaces

In order to determine the length of time after initial entry during which mass expulsion must be used for attitude control, some idea of the performance of a pitch control system operating by purely aerodynamic means must be obtained. The model tested in (19) used a trailing edge flap with an area comprising 36 percent of the total wing area. This is, no doubt, too large to be practical, but should nevertheless serve to define the general characteristics of aerodynamic controls during the initial stages of re-entry.

From basic principles of mechanics:

$$J_p \frac{d^2\gamma}{dt^2} = -M_p + \frac{\partial M_p}{\partial \dot{\alpha}} \frac{d\alpha}{dt} \tag{8-5}$$

From Equation (III-6) of Appendix III we know that:

$$\frac{d\gamma}{dt} = \frac{d\theta}{dt} + \frac{V \cos\theta}{R} - \frac{d\alpha}{dt} \tag{8-6}$$

From the results of the trajectory calculations of Subsection 3.4.1 it can be seen that $d\theta/dt$ and $V \cos\theta/R$ are small compared with $d\alpha/dt$ during attitude adjustments. It will therefore be assumed that:

$$\frac{d\gamma}{dt} = \frac{-d\alpha}{dt} \tag{8-7}$$

Equation (8-5) then becomes:

$$J_p \frac{d^2\alpha}{dt^2} = +M_p - \frac{\partial M_p}{\partial \dot{\alpha}} \frac{d\alpha}{dt} \tag{8-8}$$

The damping term $\partial M_p/\partial \dot{\alpha}$, may, from Equation (8-2) be expressed as:

$$\frac{\partial M_p}{\partial \dot{\alpha}} = A_r \bar{C} q \frac{\partial C_m}{\partial \dot{\alpha}} \tag{8-9}$$

Equation (8-6) presumes that q is independent of $d\alpha/dt$.

Substitution of Equations (8-2) and (8-9) into (8-8) gives:

$$J_p \frac{d^2\alpha}{dt^2} = -C_m A_r \bar{C} q - A_r \bar{C} q \frac{\partial C_m}{\partial \dot{\alpha}} \frac{d\alpha}{dt} \tag{8-10}$$

From (19) it can be seen that for a range of either side of the trim value of α:

$$C_m = C_{m_o} - \frac{\partial C_m}{\partial \alpha} \alpha \tag{8-11}$$

with $\partial C_m/\partial \alpha$ being a constant.

From Figure 8-1, it can be seen that for the first 80 seconds:

$$q \quad q_i \quad e^{at} \tag{8-12}$$

If we define a term α' such that:

$$\alpha = \alpha_o + \alpha' \tag{8-13}$$

where α_o = value of α at which $C_m = 0$, we can say that:

$$\frac{d\alpha}{dt} = \frac{d\alpha'}{dt} \tag{8-14}$$

and

$$\frac{d^2\alpha}{dt^2} = \frac{d^2\alpha'}{dt^2} \tag{8-15}$$

Substitution of Equation (8-13) into (8-11) gives:

$$C_m = \frac{-\partial C_m}{\partial \alpha} \alpha' \tag{8-16}$$

Substitution of Equations (8-12), (8-14), (8-15), and (8-16) into Equation (8-10) yields:

$$J_p \frac{d^2\alpha'}{dt^2} = -\frac{\partial C_m}{\partial \alpha} \bar{C} A_r q_i e^{at} \alpha' - \frac{\partial C_m}{\partial \dot{\alpha}} A_r \bar{C} q_i e^{at} \frac{d\alpha'}{dt} \tag{8-17}$$

Rearrangement of Equation (8-17) gives:

$$\frac{J_p e^{-at}}{(\partial C_m/\partial \alpha) \bar{C} A_r q_i} \frac{d^2\alpha'}{dt^2} + \frac{(\partial C_m/\partial \dot{\alpha}')}{(\partial C_m/\partial \alpha)} \frac{d\alpha'}{dt} + \alpha' = 0 \tag{8-18}$$

Taking the Laplace transform of Equation (8-18) produces:

$$\left[\frac{J_p}{(\partial C_m/\partial\alpha)\,\bar{C}\,A_r\,q_i}\right]\left[(S+a)^2\,\alpha'(S) - \alpha_o'\,S - \left(\frac{\partial\alpha}{\partial t}\right)_o\right]$$

$$+\frac{(\partial C_m/\partial\dot{\alpha})}{(\partial C_m/\partial\alpha)}\,S\alpha'(S) + \alpha'(S) = 0 \qquad (8\text{-}19)$$

From which:

$$\alpha'(S) = \left[\alpha_o' S + \left(\frac{\partial\alpha}{\partial t}\right)_o\right]\left[\frac{J_p}{(\partial C_m/\partial\alpha)\,\bar{C}\,A_r\,q_i}\right]$$

$$\left\{\frac{S^2}{\left[a^2 + \left(\frac{\partial C_m}{\partial\alpha}\right)\left(\frac{\bar{C}\,A_r\,q_i}{J_p}\right)\right]} + \frac{2\,a\,s}{\left[a^2 + \left(\frac{\partial C_m}{\partial\alpha}\right)\left(\frac{\bar{C}\,A_r\,q_i}{J_p}\right)\right]}\right.$$

$$\left. + \left[\frac{\left(\frac{\partial C_m/\partial\dot{\alpha}}{\partial C_m/\partial\alpha}\right)S}{\frac{a^2 J_p}{(\partial C_m/\partial\alpha)\,\bar{C}\,A_r\,q_i} + 1}\right] + 1\right\} \qquad (8\text{-}20)$$

Of all the terms in Equation (8-20), the most difficult to evaluate is the term $\partial C_m/\partial\dot{\alpha}$. This term describes the aerodynamic damping and can be taken to be zero in the upper reaches of the atmosphere. If $\partial C_m/\partial\dot{\alpha} = 0$, the denominator of Equation (8-20) becomes:

$$\frac{S^2}{a^2 + \left(\frac{\partial C_m}{\partial\alpha}\right)\left(\frac{\bar{C}\,A_r\,q_i}{J_p}\right)} + \frac{2\,a\,S}{a^2 + \left(\frac{\partial C_m}{\partial\alpha}\right)\left(\frac{\bar{C}\,A_r\,q_i}{J_p}\right)} + 1$$

This is in the form:

$$\frac{S^2}{\omega_n^2} + \frac{2\zeta S}{\omega_n} + 1$$

and hence:

$$\omega_n = \sqrt{a^2 + \left(\frac{\partial C_m}{\partial \alpha}\right)\left(\frac{\bar{C} A_r q_i}{J_p}\right)} \qquad (8\text{-}21)$$

$$\zeta = \frac{a}{\sqrt{a^2 + \left(\frac{\partial C_m}{\partial \alpha}\right)\left(\frac{\bar{C} A_r q_i}{J_p}\right)}} \qquad (8\text{-}22)$$

From Figure 8-1: $a = 0.05 \text{ sec}^{-1}$

From (19): $\partial C_m / \partial \alpha = 0.358 \text{ rad}^{-1}$

From Subsection 3.4.2: $\bar{C} = 141$ ft.

$J_p = 4.13 \times 10^6$ lb-ft-sec^2

$A_r = 14{,}500$ ft^2

The values of q_i can be read from Figure 8-1 and correspond to the value of q for the time t at which values of ω_n and ζ are desired. For example:

$q_i = 0.012$ psf, $\omega_n = 0.068$ rad/sec, and $\zeta = 0.735$ @ t = 0

$q_i = 0.88$ psf, $\omega_n = 0.398$ rad/sec, and $\zeta = 0.126$ @ t = 80 sec.

After the initial stages of re-entry, the dynamic pressure ranges from 2 to 14 psf. Equation (8-12) no longer has any meaning and the natural frequency of the vehicle in pitch will be approximated by:

$$\omega_n = \sqrt{\left(\frac{\partial C_m}{\partial \alpha}\right)\left(\frac{\bar{C} A_r q}{J_p}\right)} \qquad (8\text{-}23)$$

Substitution of the values already assumed into Equation (8-23) gives $\omega_n = 0.595$ rad/sec for q = 2 psf and $\omega_n = 1.57$ rad/sec for q = 14 psf. These values are considered to be acceptable.

From the above analysis it can be concluded that during the first part of re-entry, pitch control with a 36 percent trailing edge flap will give a very low natural frequency. The damping in this period will be adequate because of the effect of increasing q, even if the usual aerodynamic damping coefficient is small. By the time 96 seconds from initial entry have elapsed, a fairly acceptable natural frequency will have been achieved. Damping due to the increase in q will be small, but it may be expected that aerodynamic damping will be at an acceptable value.

From this set of results and the set previously obtained, it may be concluded that neither attitude control by means of mass expulsion or by means of aerodynamic controls will alone be satisfactory during the first part of re-entry. It becomes necessary to examine the use of both methods.

8.2.3 Attitude Control by Means of Mass Expulsion and Aerodynamic Surfaces

If reaction controllers are in use during re-entry, the expression for the control moment M_p is:

$$M_p = C_m A_r \bar{C} q - F_p x_p \tag{8-24}$$

If aerodynamic damping is ignored, substitution of Equation (8-24) into Equation (8-8) gives:

$$J_p \frac{d^2\alpha}{dt^2} = C_m A_r \bar{C} q - F_p x_p \tag{8-25}$$

Combining Equations (8-12), (8-15), (8-16) and (8-25) yields:

$$J_p \frac{d^2\alpha'}{dt^2} = \frac{-\partial C_m}{\partial \alpha} \bar{C} A_r \alpha' q_i e^{at} - F_p x_p \tag{8-26}$$

Let

$$F_p(S) = k_t G_f(S) \alpha'(S) \tag{8-27}$$

Then following the steps taken previously to derive Equation (8-21), it can be seen that if $G_f(S)$ can be neglected:

$$\omega_n = \sqrt{a^2 + \left(\frac{\partial C_m}{\partial \alpha}\right)\left(\frac{\bar{C} A_r q_i}{J_p}\right) + \frac{k_t x_p}{J_p}} \qquad (8\text{-}28)$$

Using the previously estimated values for a, $(\partial C_m/\partial \alpha)$, $\bar{C}$, A_r, q_i, and J_p, it can be shown that $k_t x_p = 6.45 \times 10^5$ ft-lb/rad for $\omega_{n_3} = 0.4$ rad/sec at t = 0. If we assume that $x_p = 125$ ft, then $k_t = 5.13 \times 10^3$ lb/rad. This is not an unreasonable value, since a maximum value of $F_p = 1000$ lbs will allow α' to vary from 0 to ± 11 degrees without saturating the reaction control system.

The question of how the relationship $F_p = k_t \alpha'$ can be implemented should now be considered. Quite obviously, some method of measuring α' is required. The comments previously made regarding the advisability of measuring controlled variables by methods not requiring external probes or transducers are still valid. Thus it would be desirable to measure α' by measuring accelerations. The value of α, and hence α', is a function of L/D. Then, by measuring the lift acceleration and the drag acceleration, and dividing one by the other, a measure of the value of α' may be obtained.

Figure 8-3 shows the angular relationships involved with the measurement of lift-to-drag ratios. Figure 8-3(a) illustrates the situation for $\alpha' = 0$. The accelerometers used to measure lift and drag forces should be aligned to coincide with the directions of these forces for this case of $\alpha' = 0$. Figure 8-3(b) illustrates the situation for $\alpha < 0$. It can be seen that for $\alpha' \neq 0$, the axes of the accelerometers no longer coincide with the lift and drag directions. As a result, each accelerometer will measure a cosine component of the force it is intended to measure and sine component of the other force. That is:

$$D_{meas.} = D \cos \alpha' + L \sin \alpha \qquad (8\text{-}29)$$

$$L_{meas.} = L \cos \alpha' - D \sin \alpha \qquad (8\text{-}30)$$

Then:

$$\left(\frac{L}{D}\right)_{meas.} = \frac{L \cos \alpha' + D \sin \alpha'}{D \cos \alpha' - L \sin \alpha} \qquad (8\text{-}31)$$

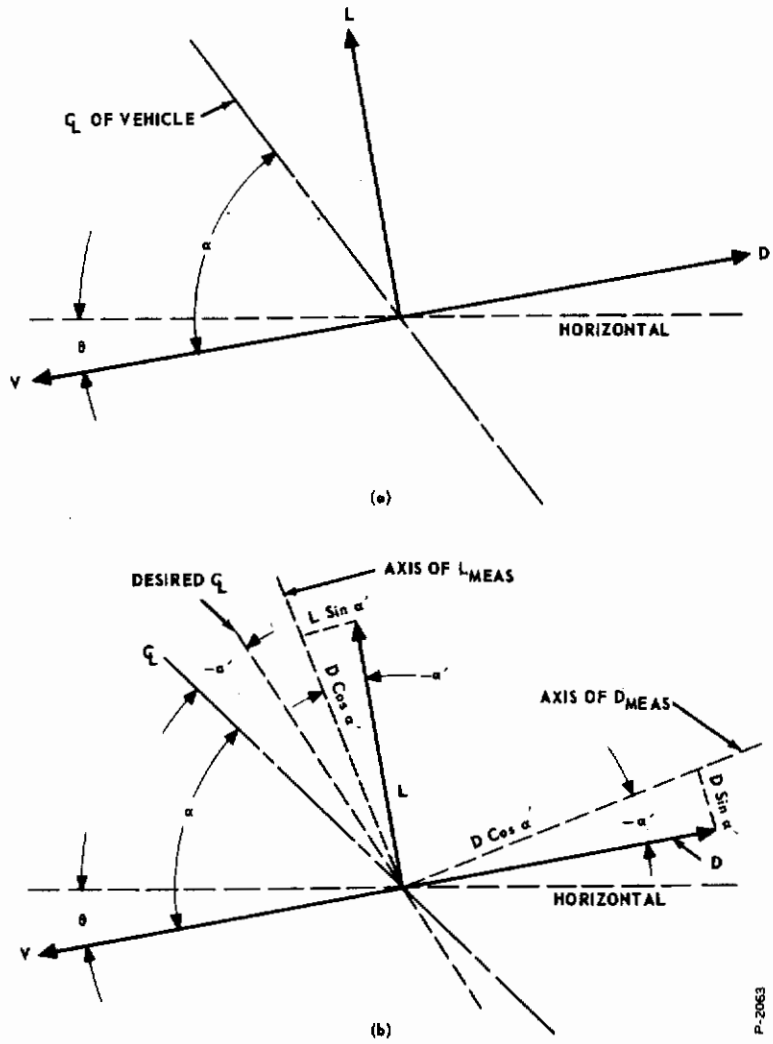

Figure 8-3 - Angular Relations for Measurement of α'

or

$$\left(\frac{L}{D}\right)_{meas.} = \frac{C_L}{C_D}\left[\frac{\cos\alpha' + (C_D/C_L)\sin\alpha'}{\cos\alpha' - (C_L/C_D)\sin\alpha'}\right] \qquad (8\text{-}32)$$

Values of C_L/C_D corresponding to $\delta_f = 30°$ and various values of α can be obtained from (19). These can be substituted into Equation (8-32) to obtain values of $(L/D)_{meas.}$ corresponding to various actual values of L/D. Such a plot is shown in Figure 8-4. For this data, $\alpha' = 0$ corresponds to $\alpha = 77°$. From Figure 8-4, it can be seen that

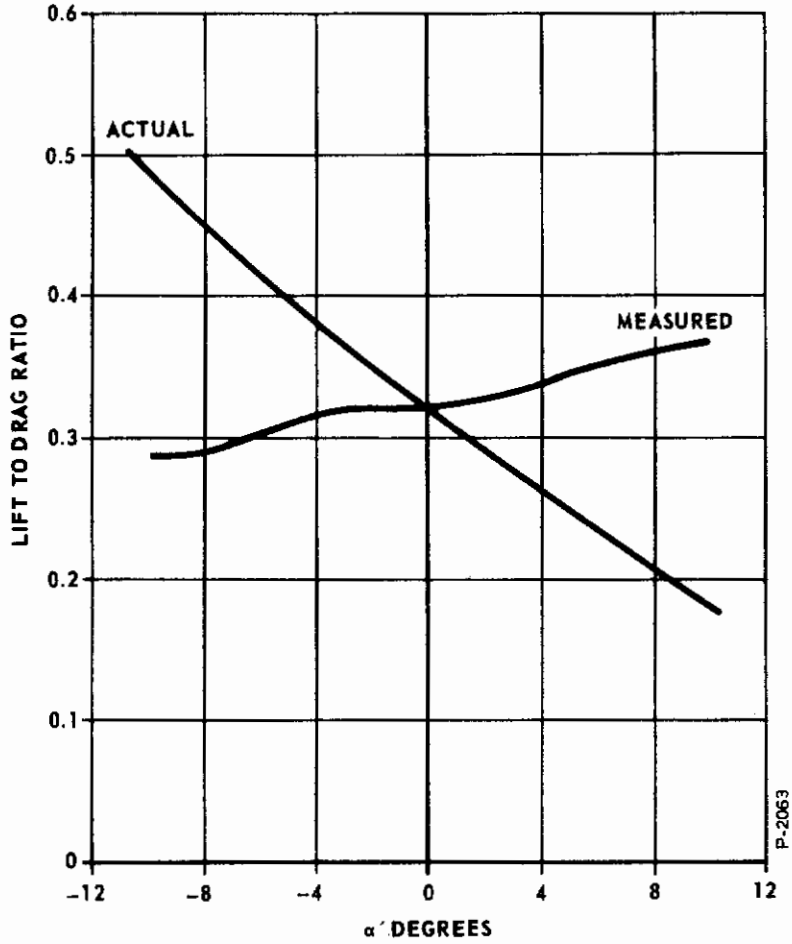

Figure 8-4 - Lift-to-Drag Versus α'

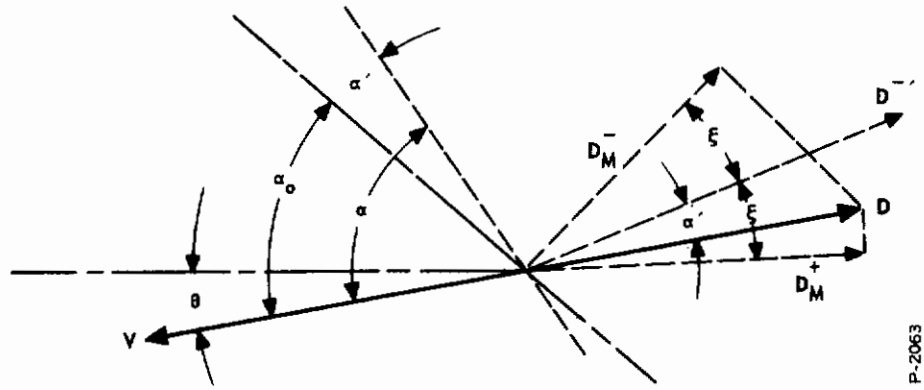

Figure 8-5 - Angular Relationships for Measurement of α' from Ratio of Two Drag Components

the effect of the sine and cosine terms in Equation (8-32) is to change the sign, reduce the slope, and delinearize the relationship between L/D and α'. These effects are generally undesirable, but this method is a usable means for measuring α'.

Another method for measuring angle of attack is to place two accelerometers at an angle ξ on either side of the direction of the drag force D at the desired angle of attack α. The angle of attack will then be a function of the ratio of the two measured decelerations. This is shown in Figure 8-5 where D_M^- and D_M^+ represent the outputs of the two accelerometers at an angle ξ to the desired drag direction represented by the vector $\overline{D}'$. From Figure 8-5, it can be seen that:

$$D_M^- = D \cos (\xi + \alpha') \tag{8-33}$$

and:

$$D_M^+ = D \cos (\xi - \alpha') \tag{8-34}$$

From Equations (8-33) and (8-34):

$$\frac{D_M^-}{D_M^+} = \frac{\cos (\xi + \alpha')}{\cos (\xi - \alpha')} \tag{8-35}$$

Plots of Equation (8-35) for $\xi = 15°$ and $\xi = 30°$ are shown in Figure 8-6. It can be seen that increasing ξ increases gain at the expense of linearity. On the whole, this approach appears to be preferable to measurement of α' from the nominal L/D components.

8.2.4 Dynamics

In the preceding sections it was established that there is an initial stage of re-entry in which the dynamic pressure, q, builds up from essentially zero to a level which is on the threshold of the range of values which it will assume for the remainder of the re-entry period. In the early stages of this initial period of re-entry, the level of dynamic pressure is so small that very low natural frequencies result if pitch control by purely aerodynamic means is attempted. On the other hand, if a zero flap deflection is assumed and an attempt to control pitch by using only mass expulsion is attempted, the required range of thrusts or impulse bits is excessively large. Thus the

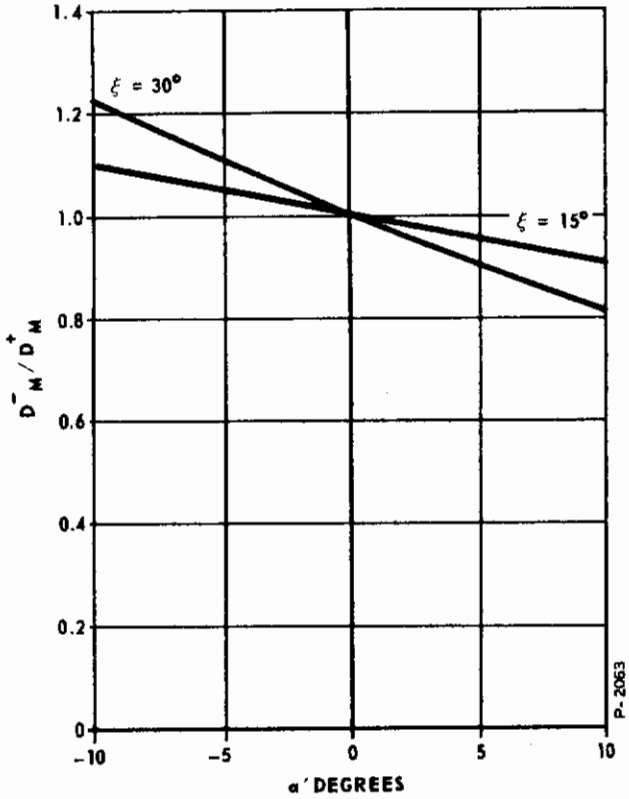

Figure 8-6 - D_M^- / D_M^+ Versus α'

conclusion is reached that a combination of the two modes of pitch control is required. A block diagram of the equations pertaining to the initial stages of re-entry is shown in Figure 8-7. This figure has been constructed from Equations (8-1), (8-5), (8-6), and (8-24).

If it is assumed that reaction controller response is very fast compared to vehicle response, Equation (8-27) becomes:

$$F_p = k_t (\alpha - \alpha_o) = k_t \alpha - F_{p_o} \tag{8-36}$$

From Appendix III, we have:

$$\frac{dV}{dt} = - \left[\frac{A_r}{m} \right] C_d q + g \sin \theta \tag{8-37}$$

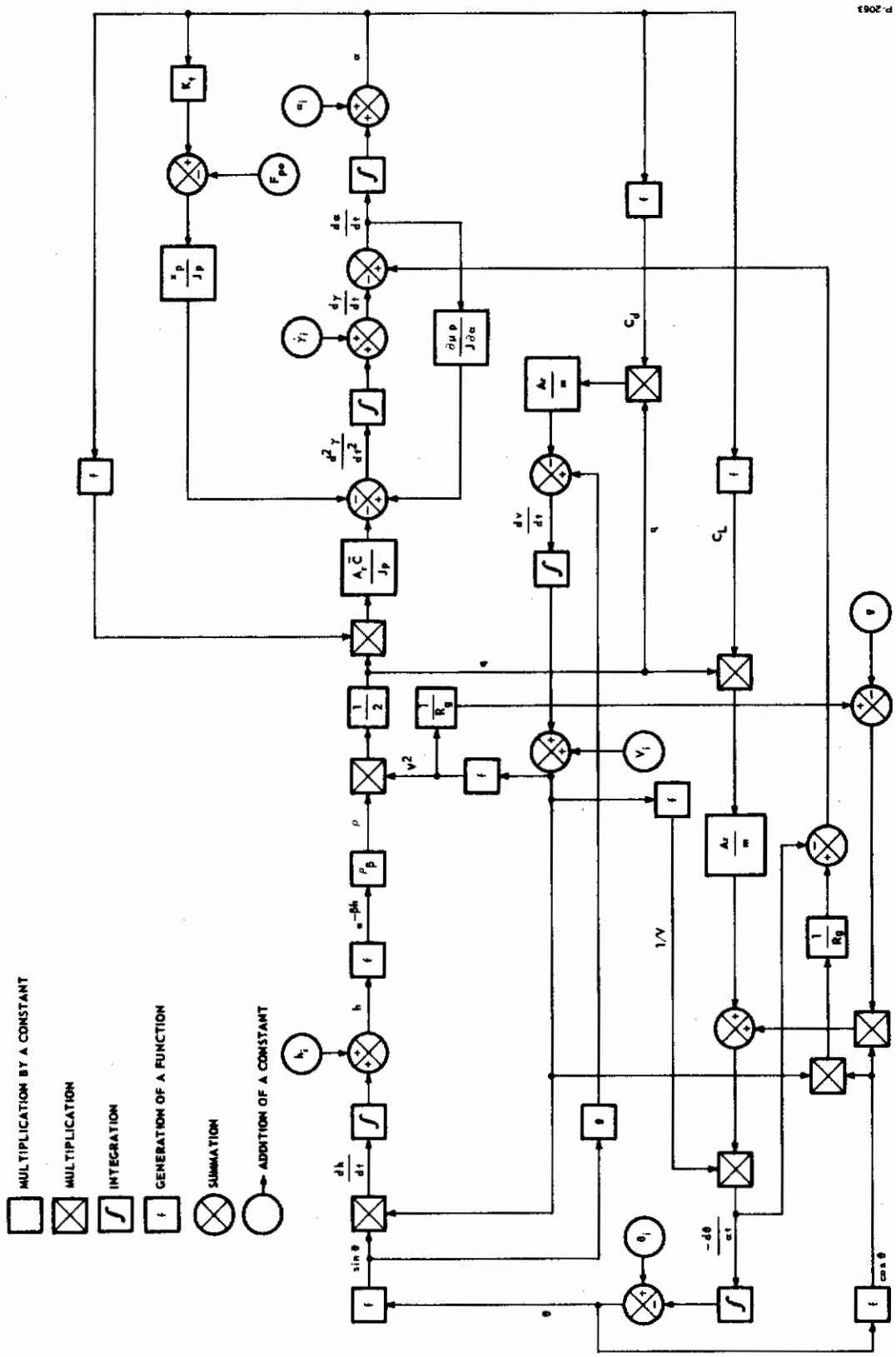

Figure 8-7 - Block Diagram of Equations for Initial Entry

$$- V \frac{d\theta}{dt} = \left[\frac{A_r}{m}\right] C_L q - g \cos \theta + \frac{V^2}{R} \cos \theta \tag{8-38}$$

$$\rho = \rho_\beta e^{-\beta h} \tag{8-39}$$

$$\frac{dh}{dt} = - V \sin \theta \tag{8-40}$$

If it is assumed that the aerodynamic coefficients are independent of Mach number and Reynolds number and that $d\delta_f/dt = 0$, we can say that:

$$C_d = f_d (\alpha) \tag{8-41}$$

$$C_L = f_L (\alpha) \tag{8-42}$$

$$C_m = f_m (\alpha) \tag{8-43}$$

The block diagram of Figure 8-7 is dependent on a limited number of assumptions. Additional simplifying assumptions can be made which make it more suitable for either analytical treatment or for incorporation into a computer program. For the specific case of the hypothetical vehicle being considered in this study, the following assumptions can be made for the first 90 seconds of re-entry.

$$\sin \theta = \theta \tag{8-44}$$

$$\cos \theta = 1 \tag{8-45}$$

$$\frac{dV}{dt} = 0 \tag{8-46}$$

It has already been assumed that:

$$C_m = C_{mo} + \frac{\partial C_m}{\partial \alpha} \alpha \tag{8-11}$$

Similarly, it can be assumed that:

$$C_L = C_{LO} + \frac{\partial C_L}{\partial \alpha} \alpha \tag{8-47}$$

$$C_d = C_{do} + \frac{\partial C_d}{\partial \alpha} \alpha \qquad (8\text{-}48)$$

The simplified block diagram resulting from the incorporation of these assumptions is shown in Figure 8-8. Note that because of the assumption $dV/dt = 0$, Equations (8-37) and (8-48) are no longer required.

8.3 ANALYSIS OF SECOND PART OF RE-ENTRY

8.3.1 Angle-of-Attack and Moment Requirements

The aerodynamic characteristics of the assumed vehicle are shown in Figure 8-9. This figure has been plotted from the data in (19) and hence applies to a 70 degree delta wing with 10 degrees nose incidence controlled by a trailing edge flap with an area 36 percent of the total wing area. The curve of δ_f versus α was obtained by plotting the values of α for which $C_m = 0$ at various values of δ_f. The values of C_d and C_L corresponding to the appropriate α and δ_f were then plotted.

Figure 3-2 of Subsection 3.4.1 gives the desired L/D ratios during re-entry. For the greatest part of the time, the minimum L/D ratio is required. This corresponds to $\alpha = 77°$ for the aerodynamic characteristics shown in Figure 8-9. Knowing the L/D ratios required and the values of α corresponding to the various L/D ratios permits one to plot a curve of α versus time during re-entry for the assumed vehicle. Figure 8-10, showing the values of α and q during adjustment of α, has been plotted on this basis. A greatly expanded scale has been used.

The curves of α versus t shown in Figure 8-10 can be graphically differentiated to obtain values of $d\alpha/dt$ versus t. These in turn can be graphically differentiated to obtain values of $d^2\alpha/dt^2$ versus t. These values of $d\alpha/dt$ and $d^2\alpha/dt^2$ have been plotted on Figure 8-11. It must be recognized that graphical differentiation introduces inaccuracies. Nevertheless, the values of angle of attack accelerations obtained should be representative of those required by a re-entry vehicle. From Figure 8-11, it can be seen that the maximum angular accelerations are required at the beginning and the end of each angle of attack adjustment. The maximum ptiching moment coefficients required may be calculated from the peak accelerations through the use of Equation (8-25), taking $F_p = 0$. With $F_p = 0$, Equation (8-25) becomes:

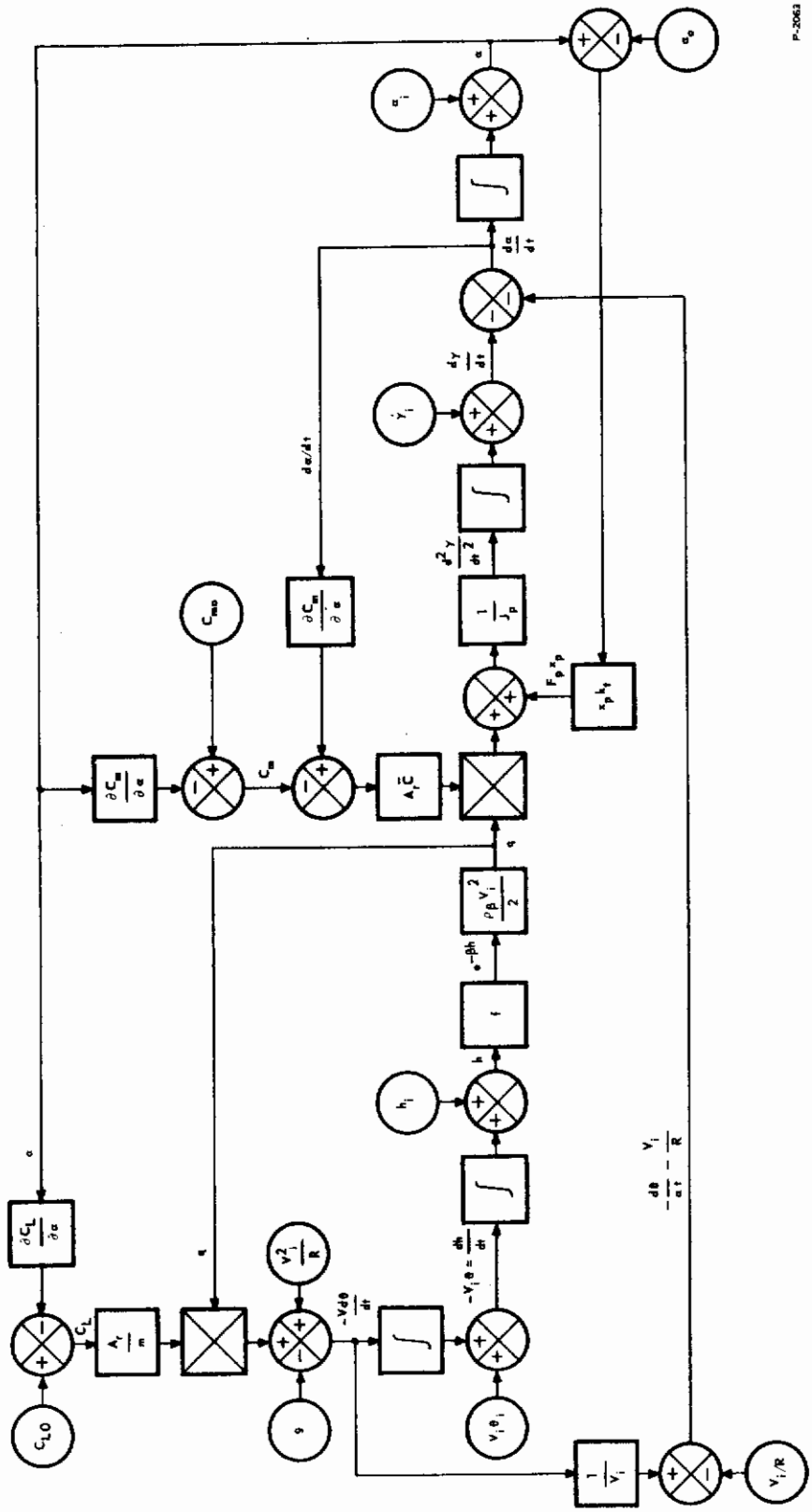

Figure 8-8 - Simplified Block Diagram of Equations for Initial Re-Entry

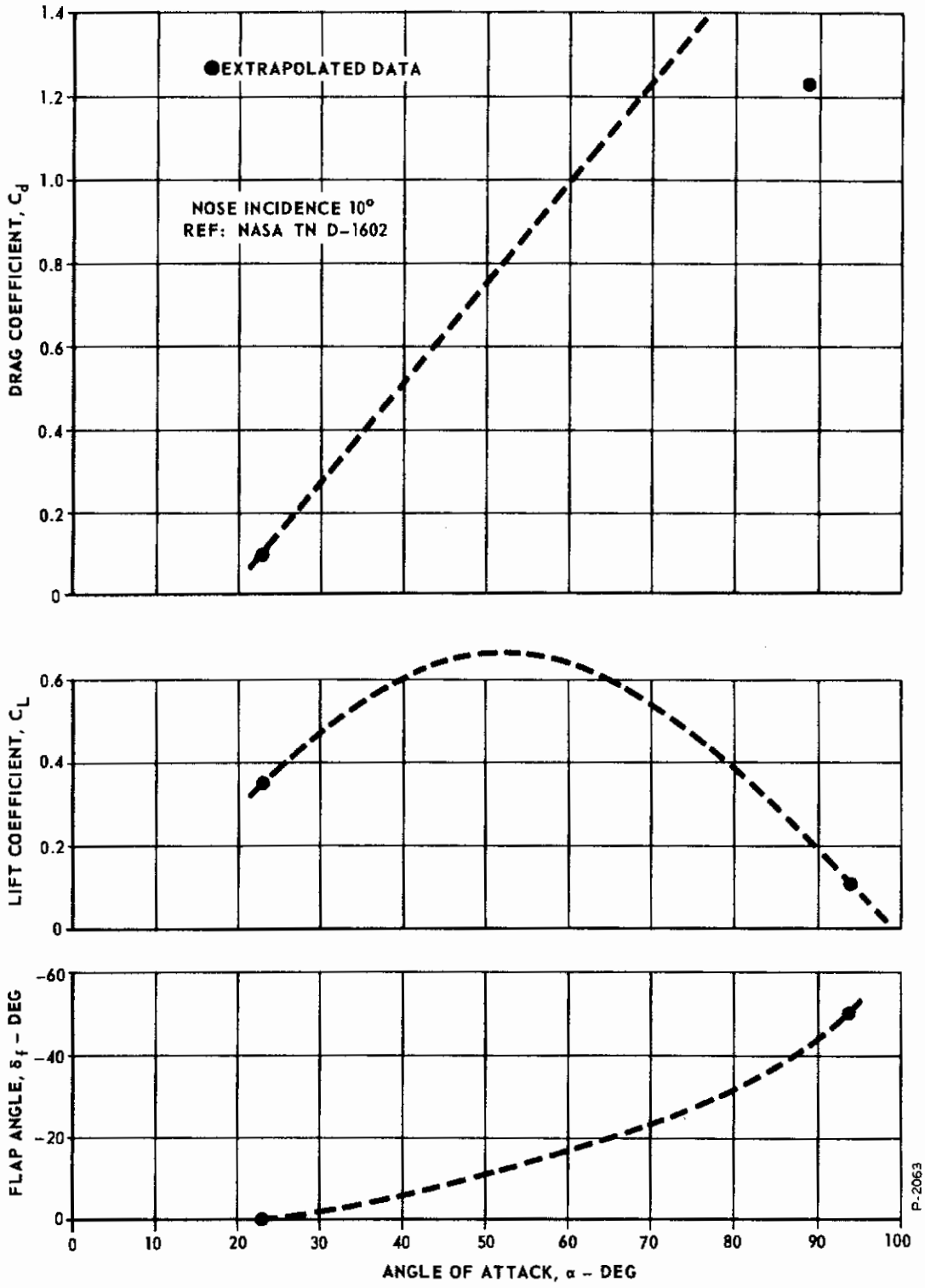

Figure 8-9 - Aerodynamic Characteristics of 70° Delta Wing Controlled by Trailing Edge Flap

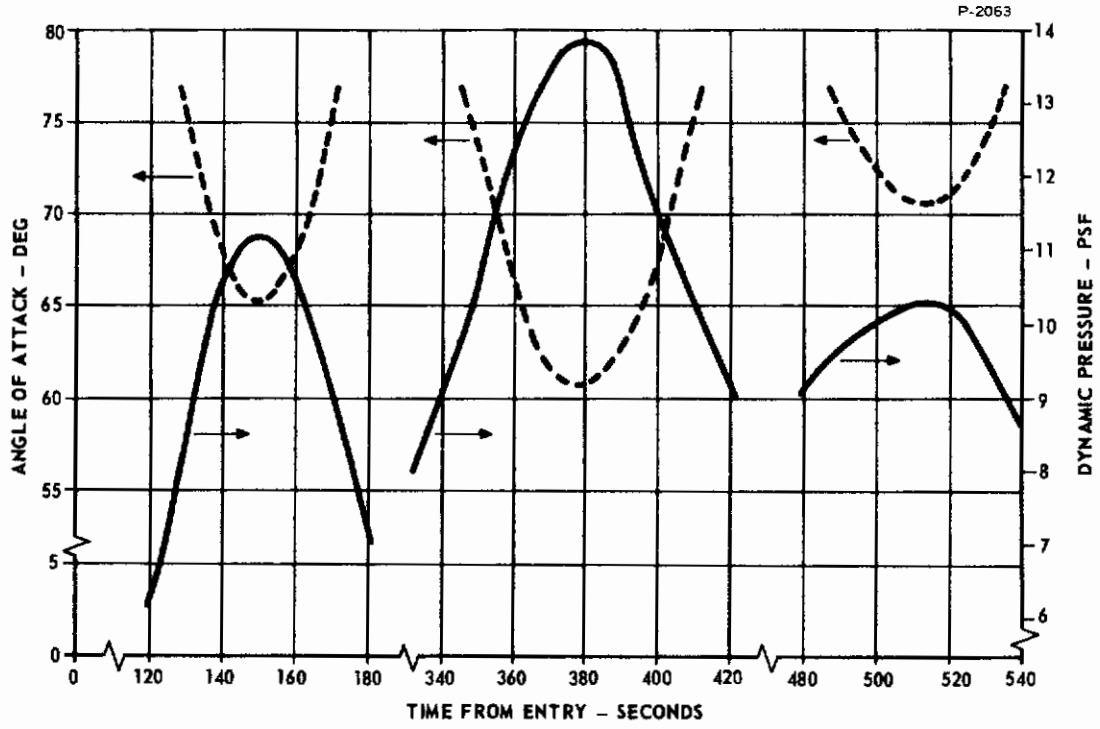

Figure 8-10 - Angle of Attack and Dynamic Pressure During Angle of Attack Adjustments

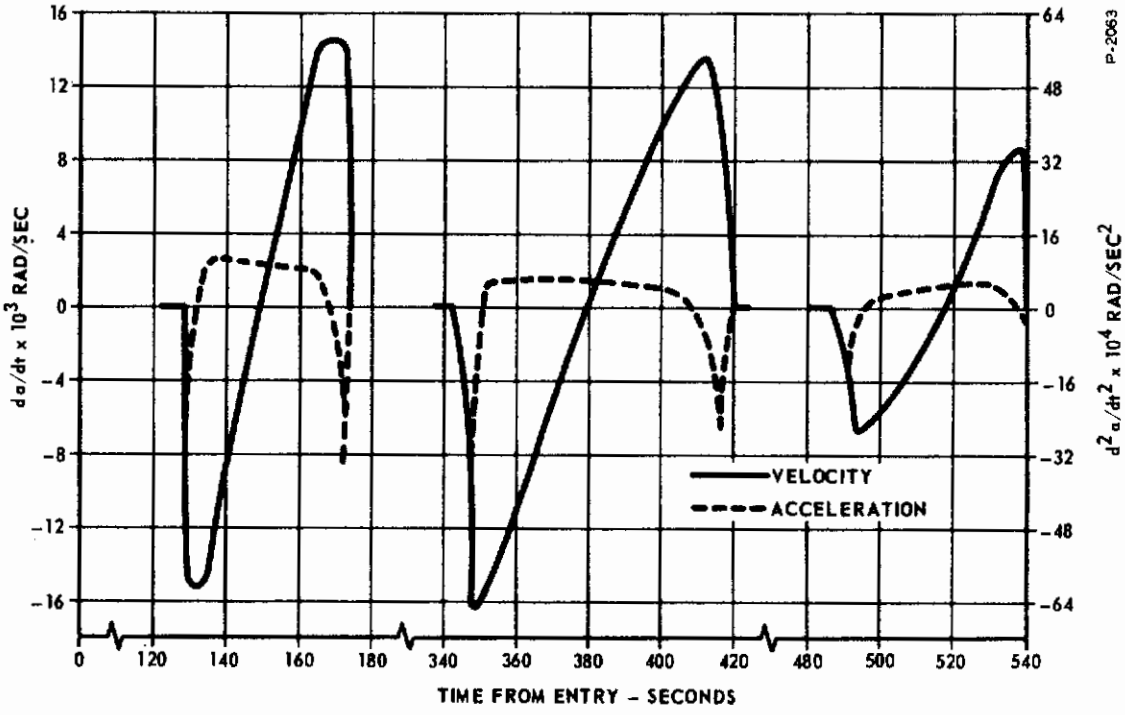

Figure 8-11 - Approximate Angular Velocity and Acceleration of Re-Entering Vehicle

$$J_p \frac{d^2\alpha}{dt^2} = C_m A_r \bar{C} q \qquad (8\text{-}49)$$

Table 8-1 summarizes the calculations of the maximum values of C_m required during the angle-of-attack adjustments.

Table 8-1

t sec	$d^2\alpha/dt^2$ rad/sec^2	q psf	C_m
129	0.0037	8.5	0.000873
172	0.0036	8.7	0.000830
348	0.0028	10.0	0.000561
414	0.0026	9.8	0.000532
488	0.0011	9.6	0.000229
540	0.0022	8.6	0.000513

For these calculations, the values of $\bar{C}$, A_r, and J_p are those previously used. The values of q have been obtained from Figure 8-10.

From Table 8-1, it can be seen that the values of C_m required to keep the vehicle on the previously computed trajectory are not unreasonable. It is probable that because of the time intervals selected in the numerical differentiation process, the angular accelerations given in Table 8-1 are on the low side. The point is, however, that even if the values of $d^2\alpha/dt^2$ were off by a factor of 10, the values of C_m required to keep the vehicle on the desired steady-state trajectory are quite easily obtainable, even with a reduced flap area. For the vehicle under consideration, values of C_m in the vicinity of 0.010 can be obtained.

8.3.2 Dynamics

Most of the equations used to derive the block diagram shown in Figure 8-7 are valid for the second part of re-entry. Repeating, these equations are:

$$q = \frac{\rho V^2}{2} \tag{8-1}$$

$$M_p = C_m A_r \bar{C} q \tag{8-2}$$

$$J_p \ddot{\gamma} = -M_p \tag{8-50}$$

$$\dot{\gamma} = \dot{\theta} + \frac{V \cos \theta}{R_e} - \dot{\alpha} \tag{8-6}$$

$$\dot{V} = -\frac{A_r}{m} C_d q + g \sin \theta \tag{8-37}$$

$$-V \dot{\theta} = -\frac{A_r}{m} C_L q - g \cos \theta + \frac{V^2}{R_e} \cos \theta \tag{8-38}$$

$$\rho = \rho_\beta e^{-\beta h} \tag{8-39}$$

$$\dot{h} = -V \sin \theta \tag{8-40}$$

Equation (8-50) is normally written as follows:

$$J_p \frac{d^2 \gamma}{dt^2} = -M_p + \frac{\partial M_p}{\partial \dot{\alpha}} \frac{d\alpha}{dt} \tag{8-5}$$

The second term on the right side is an aerodynamic damping term where:

$$\frac{\partial M_p}{\partial \dot{\alpha}} = A_r \bar{C} q \frac{\partial C_m}{\partial \dot{\alpha}} \tag{8-51}$$

Because of the difficulty of obtaining information on $\partial C_m / \partial \dot{\alpha}$ it will be assumed negligible. It was not considered important enough to be included in (19), and furthermore, it was shown in Equation (8-22) that damping is present on the vehicle with this same term again neglected.

Since the flap angle, δ_f, is no longer fixed as it was in the initial stages of re-entry, the aerodynamic coefficients are functions of δ_f as well as α.

$$C_d = f_d\ (\alpha, \delta_f)$$

$$C_L = f_L\ (\alpha, \delta_f)$$

$$C_m = f_m\ (\alpha, \delta_f)$$

During the trajectory computations described in Subsections 3.4.1, it was assumed that the aerodynamic control system limited the path deceleration to a value of 2 g's or less. The flap is to be positioned by means of a servomechanism sensitive to a signal related to the difference between the path deceleration and the desired value of 2 g's. It will be assumed that the flap is operated by a pneumatic actuator of either the piston-cylinder or expansion vane motor type. A general analysis applicable to either actuator will be made in order to determine its operating characteristics. The servo is assumed to consist of a servo amplifier, servo valve, actuator, transmission and a position-sensing transducer.

Consider the actuator as being represented by a expansion servo vane motor as shown in Figure 8-12. Writing the flow balance equation gives:

$$\frac{\partial Q}{\partial A} A - \frac{\partial Q}{\partial P} P = D_{mv} N + \frac{V_c}{k P_o} S P \qquad (8\text{-}52)$$

This equation states that the volumetric flow entering the actuator through the orifice area of the servo valve is dissipated by pressure-dependent leakage flow, displacement flow, and compressibility flow.

General equations for any pneumatic actuator are as follows:

$$Q = D_{mv} N \qquad (8\text{-}53)$$

$$T_m = D_{mt} \Delta P \qquad (8\text{-}54)$$

In Equations (8-53) and (8-54) the volumetric displacement D_{mv} is considered as being different from the torque displacement D_{mt}. This is true for expansion devices. For non-expansion actuators such as a piston-cylinder, D_{mv} is the same as D_{mt} and the subscripts, v, and t can be dropped. For purposes of generality, the subscripts will be retained. Substituting Equations (8-53) and (8-54) into (8-52) gives:

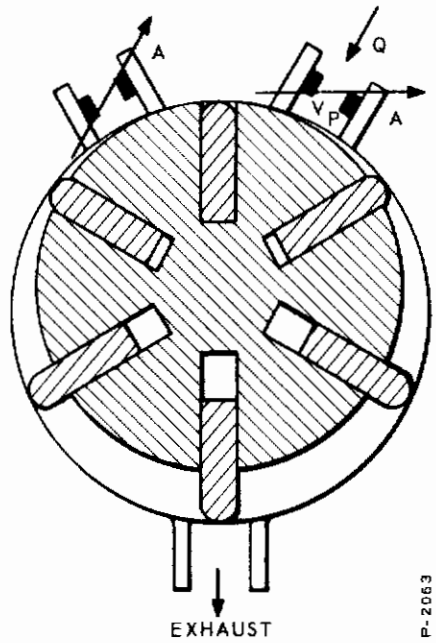

Figure 8-12 - Expansion Servo Vane Motor

$$N = \frac{\partial N}{\partial A} A - \left[1 + \left(\frac{V_c}{k P_o D_{mt} D_{mv}} \frac{\partial T_m}{\partial N}\right)\right] \frac{\partial N}{\partial T_m} T_m \quad (8\text{-}55)$$

In Equation (8-55) the following term is defined as the compressibility time constant, having the units of seconds:

$$\tau_c = \frac{V_c}{k P_o D_{mt} D_{mv}} \frac{\partial T_m}{\partial N} \quad (8\text{-}56)$$

Substituting Equation (8-56) into Equation (8-55) and rearranging gives:

$$T_m = \frac{1}{(1 + \tau_c S)} \left[\frac{\partial T_m}{\partial A} A - \frac{\partial T_m}{\partial N} N\right] \quad (8\text{-}57)$$

Using Equation (8-57) as a basis, the block diagram of the system is given in Figure 8-13. The interpretation is as follows: The demand flap position represented by a voltage signal $E_{\delta d}$ is compared to the actual output position δ_f, converted to a voltage $E_{\delta f}$ by the feedback gain K_f. The position error $E_{\delta e}$ is amplified by a gain K_a and converted to an electrical current in the coils of the torque-motor. The servo-valve is represented as a gain and a single lag $K_b/(1 + \tau_b S)$. In actuality, the servo-valve has dynamics of much higher order, but it is assumed that these dynamics are much faster than the servo system dynamics and can be neglected. The flow area A of the servo valve acts with the three-block system shown in Figure 8-13 to produce an output torque which is summed with the aerodynamic spring moment, M_h, and the friction torque, T_f. The aerodynamic spring load and the friction torque are shown unconnected because they are dependent upon the vehicle performance and must be properly connected to the over-all system block diagram of which Figure 8-13 is only a small part. The acceleration torque, T_a, is integrated and applied to the inertia to form the actuator shaft speed, N, which in turn is integrated again and converted to output position through a gear train.

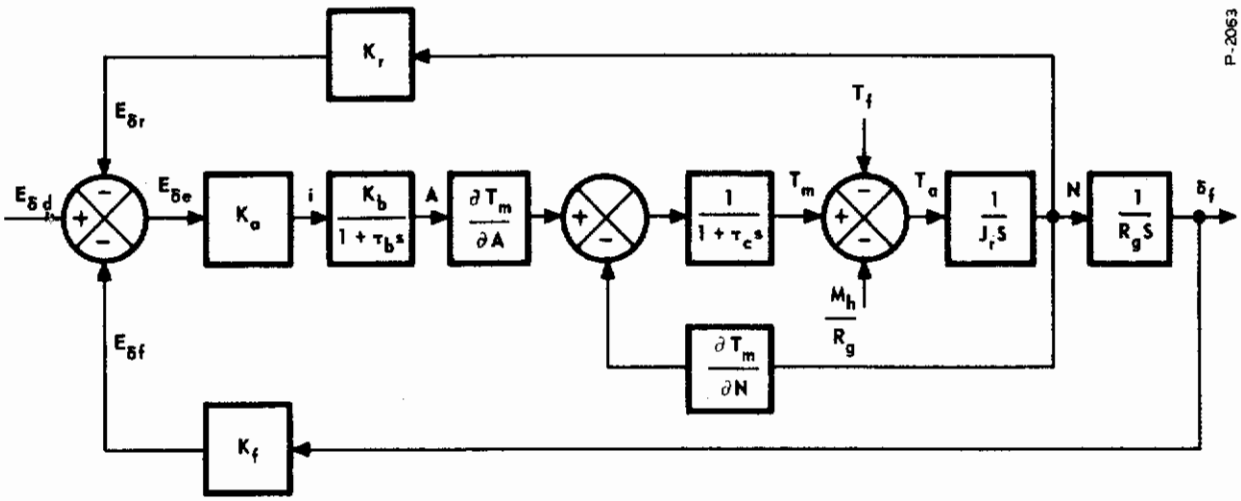

Figure 8-13 - Block Diagram of Flap Control Loop

Completing the system equations:

$$A = \frac{K_b}{1 + \tau_b S} \; i \tag{8-58}$$

$$i = K_a \, E_{\delta e} \tag{8-59}$$

$$E_{\delta e} = E_{\delta d} - E_{\delta f} - E_{\delta r} \tag{8-60}$$

$$T_m = T_a + T_f + M_h \tag{8-61}$$

$$N = \frac{T_a}{J_r S} \tag{8-62}$$

$$\delta_f = \frac{N}{R_g S} \tag{8-63}$$

Combining Equations (8-58), (8-59), and (8-60):

$$A = \frac{K_b}{1 + \tau_b S} \; K_a \, (E_{\delta d} - E_{\delta f} - E_{\delta r}) \tag{8-64}$$

Combining Equations (8-61), (8-62), and (8-63) gives:

$$T_m = J_r \, R_g \, \delta_f \, S^2 + T_f + M_h \tag{8-65}$$

Equations (8-57), (8-64) and (8-65) represent the servo system of Figure 8-13. They cannot be combined into a simple function of $\delta_f / E_{\delta d}$ because of the two extra variables T_f and M_h which are dependent on the vehicle.

The aerodynamic hinge moment is given by:

$$M_h = C_h \, q \, A_f \, \bar{C}_l \tag{8-66}$$

where:

$$C_h = f_h \, (a, \, \delta_f)$$

In order to prevent the vehicle from flipping over during periods when the dynamic pressure is not sufficiently high to build up the desired path deceleration, the flap must be mechanically restrained from exceeding the angle corresponding to the equilibrium value of the maximum desired angle-of-attack (77 degrees). Therefore:

$$0 \leq \delta_f \leq -30^\circ \tag{8-67}$$

A block diagram of the equations just given may be written. However, the resulting complexities interfere with a clear understanding of the process. A number of assumptions may be made which do not seriously affect the accuracy of the system of equations but which give a much simpler block diagram. Figure 3-6 of Subsection 3.4.1 shows that θ is within $\pm 5^\circ$ for almost the whole trajectory. It then can be assumed that:

$$\sin \theta = \theta$$

$$\cos \theta = 1$$

From (19) it is found that the following linearizations of the aerodynamic coefficients are reasonable:

$$C_m = C_{mo} + \frac{\partial C_m}{\partial \delta_f} (\delta_f - \delta_{fo}) + \frac{\partial C_m}{\partial \alpha} (\alpha - \alpha_o) \tag{8-68}$$

$$C_L = C_{LO} + \frac{\partial C_L}{\partial \delta_f} (\delta_f - \delta_{fo}) + \frac{\partial C_L}{\partial \alpha} (\alpha - \alpha_o) \tag{8-69}$$

$$C_d = C_{do} + \frac{\partial C_d}{\partial \delta_f} (\delta_f - \delta_{fo}) + \frac{\partial C_d}{\partial \alpha} (\alpha - \alpha_o) \tag{8-70}$$

$$C_h = C_{ho} + \frac{\partial C_h}{\partial \delta_f} (\delta_f - \delta_{fo}) + \frac{\partial C_h}{\partial \alpha} (\alpha - \alpha_o) \tag{8-71}$$

Hinge friction or, more properly, hinge stiction is an important consideration in vehicle performance. It can be simulated as follows: From previous experience it is known that stiction has the general no-load characteristics shown in Figure 8-14. This curve can be plotted on a function fitter. In order to make it useful for all loadings,

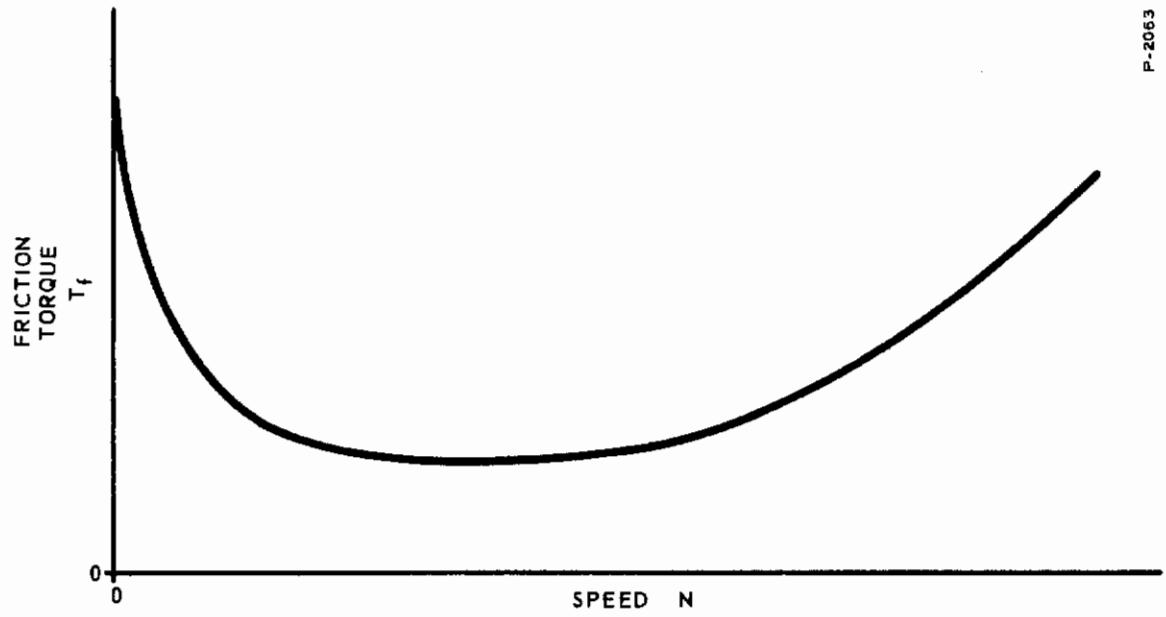

Figure 8-14 - Representative No-Load Stiction Characteristics

the aerodynamic loading is summed with unity (no load) and multiplied by the function-fitter output to obtain values of frictional torque for all speeds and loads.

A block diagram of the linearized system dynamics is shown in Figure 8-15. This representation of the aerodynamic attitude control system is discussed further in the articles contained in Subsection 8.5.

8.4 FLAP ACTUATOR SELECTION

8.4.1 Introduction

Three major methods of flap actuation are to be considered. They are as follows: reaction-jets on the flap edge, a piston-cylinder driving through a linkage, and an expansion vane motor driving through a suitable transmission.

8.4.2 Reaction Jets

The maximum aerodynamic spring load M_h on the flap is 5.58×10^5 ft-lb. Using a split flap for roll-control purposes, the torque per actuator is 2.79×10^5 ft-lb. The flap length is 41 feet, and assuming

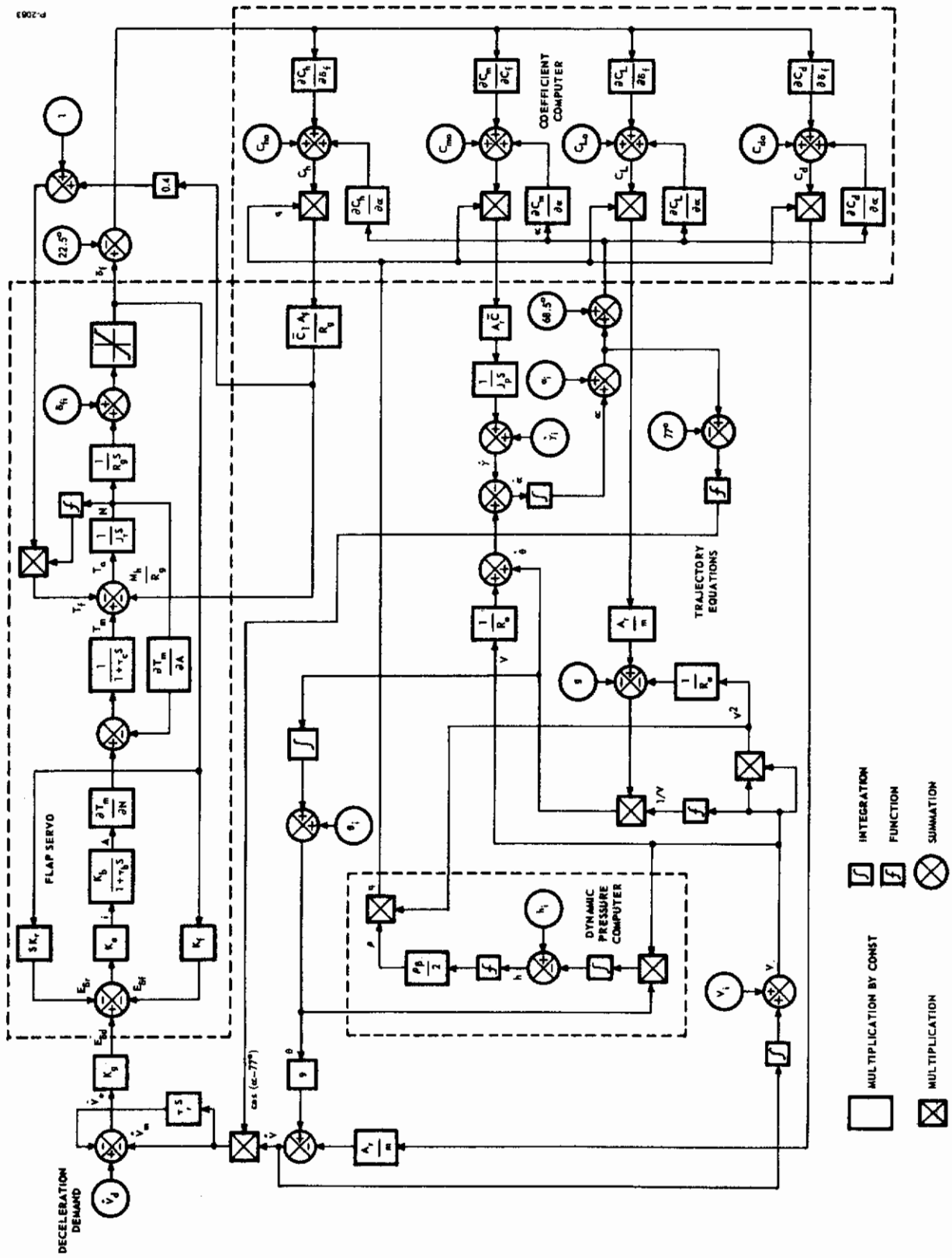

Figure 8-15 - Block Diagram for Equations Describing Second Part of Re-Entry

that the jets can be located within 4 feet from the outer edge, the moment arm is 37 feet and the required thrust is 7520 pounds. This is an enormous thrust, expending propellant at the rate of 18.8 lb/sec. This thrust will be in the direction to reduce the flap angle from 30 degrees to some lower value in an effort to decrease the vehicle angle of attack. There is danger however, that instead of reducing the angle of attack, the thrust may initially increase it through the hinge friction reaction on the vehicle. It is apparent that this method of flap actuation is uneconomical and rather complex, consequently it will be dropped from further consideration.

8.4.3 Rotary Motors Versus Piston-Cylinders

8.4.3.1 Summary

A few general comments will help clarify the differences between these two actuator concepts. Rotary actuators tend to have a higher response capability than equivalent piston-cylinder systems. High speed rotary motors generally have a small volume V_c under compression and require a high transmission ratio, often making the load inertia negligible. These factors, which tend to produce a high natural frequency ω_n are partially offset by the low quiscent pressure P_o, or rather the low bulk modulus k P_o of the pneumatic working medium. k is the ratio of specific heats for the gas and P_o is the instantaneous motor pressure. A low P_o is desirable to maintain low quiescent gas consumption since rotary devices tend to have large leakage areas. In addition, a low pressure produces low bearing loads that enhance servo threshold and resolution.

For a given size, a non-expansion rotary motor will have a higher power rating and natural frequency than an expansion motor of the same type. For example, if a non-expansion vane motor is redesigned to incorporate a 3 to 1 expansion ratio, its natural frequency will be reduced by approximately 50 percent.

The piston-cylinder actuator has a very large volume under compression. This handicap can be partially offset by the use of a high quiescent pressure. A high quiescent pressure can be used, as leakage areas are small and there is relatively little difficulty with bearing loads.

Friction and leakage affect motor performance significantly. Theoretically these losses, in addition to their effect on damping, tend to produce a small increase in natural frequency ω_n. In practice, however, leakage and friction produce a net reduction in ω_n because the inertia and volume under compression increase when a motor is sized to make up for internal losses. Despite high friction and leakage and the additional transmission inertia, a rotary servo usually exhibits better dynamic response than a piston-cylinder servo.

8.4.3.2 Dynamic Performance

The resonant frequency ω_n of a valve-actuator combination provides a measure of the attainable system performance. In practice, the bandpass of a servo cannot be much in excess of ω_n. With the servo valve sized for peak requirements, any attempt to obtain a significantly higher bandpass through system compensation will fail, since valve saturation will result for even extremely low system input signals. From the linearized equations for an ideal rotary actuator (expansion or nonexpansion) the expression for the open-loop natural frequency is:

$$\omega_n = \sqrt{\frac{k P_o D_{mv} D_{mt} R_g^2}{V_c J_L}} \qquad (8\text{-}72)$$

where R_g is the transmission ratio, P_o is the motor quiescent pressure, V_c is the volume under compression inside the valve-actuator, J_L is the total inertia reflected to the load, and k is the ratio of gas specific heats. The volumetric displacement D_{mv} is equal to the torque displacement D_{mt} except in the expansion-type motor. In all motors, D_{mv} is equal to the volume of gas entering the actuator per radian of rotation. In expansion motors, D_{mt} is larger than D_{mv} because in addition to the work derived from the volume flow into the motor, work is derived from internal energy of the gas.

For a piston-cylinder actuator, the expression for the open-loop natural frequency is:

$$\omega_n = \sqrt{\frac{k P_o A_p^2 Y^2}{V_c J_L}} \qquad (8\text{-}73)$$

where A_p is the piston area, and Y is the length of the moment arm.

In order to illustrate and compare the performances of rotary and piston-cylinder actuators, both actuators are sized to meet the following hypothetical system requirements:

Torque at peak power = 50,000 in.-lb

Velocity at peak power = 1 rad per sec

Load inertia J_L = 60 lb-in.-sec^2

Maximum rotation = plus or minus 0.6 rad

Supply pressure = 1,000 psi

Ratio of specific heats for gas = 1.26

A piston-cylinder actuator which meets these requirements would have the following minimum dimensions:

A_p = 40 in.^{2} V_c = 60 in.^{3}

Y = 2.5 in. P_o = 500 psi

Assuming the piston mass is negligible, the ω_n for the piston-cylinder is 41.8 rad/sec. If an expansion type of rotary vane motor is employed, a suitable design would have the following characteristics:

D_{mt} = 0.50 in.^{3} per rad J_L = 1,000 lb-in.-sec^2

D_{mv} = 0.25 in.^{3} per rad R = 500 (gear ratio)

V_c = 0.30 in.^{3} P_o = 50 psi

The natural frequency of this vane motor is 96.0 rad/sec. Thus the rotary servo has nearly twice the bandpass of the piston-cylinder servo. This result is typical for many applications.

8.4.3.3 Stiffness

Applications such as control of aerodynamic surfaces, where positional accuracy must be maintained in the face of severe load disturbances, require high output stiffnesses. A very high stiffness can be achieved by using a rotary servomotor and a high gear ratio. For many cases, rotary servos have been found to be 50 to 100 times stiffer than linear piston-cylinder servos of the same horsepower

rating. While the static stiffness of a piston-cylinder can be improved by using suitable compensation, the stiffness near resonance must remain low if adequate stability margin is to be maintained.

Adequate resolution and smooth low-speed operation can be a major problem in the design of a pneumatic servo, especially at high temperatures where conventional lubrication techniques cannot be used. In many cases the resolution requirement is on the order of 0.1 percent of maximum output displacement. This is difficult to obtain with a high temperature piston-cylinder due to the friction of the shaft and piston seals. Most rotary motors also exhibit high breakaway friction, but the high transmission ratio reduces the resolution problem.

8.4.3.4 Fuel Consumption

In any application where an independent gas source is required, fuel consumption is a major consideration, since for even a short mission, fuel and tankage may constitute a major part of the total weight. It is important, then, to select an actuator that has a low specific fuel consumption.

A nonexpansion actuator is a device that extracts only flow work from the gas in steady-state operation while an expansion actuator utilizes some of the internal energy of the gas. Clearly, an expansion actuator is preferred from the standpoint of efficiency.

With an ideal expansion motor, the specific fuel consumption is independent of motor speed. In a practical motor, however, the SFC varies widely, and minimum SFC occurs at some intermediate speed. As speed approaches zero, leakage causes the SFC to increase rapidly, while at high speeds friction produces a corresponding increase. It is difficult to generalize about leakage and friction since these parameters are strongly influenced by the size, implementation, and environment of a unit. Leakage is a greater problem with rotary motors than with piston-cylinder actuators because it is difficult to obtain an effective seal between parts moving at a high relative velocity.

The rotary motor is again at a disadvantage with regard to friction because of high velocity elements. As long as adequate lubrication can be maintained, actuator friction losses at practical speeds are usually small compared to leakage losses. Despite relatively high losses, rotary expansion-type actuators, such as the vane motor,

show substantially less fuel consumption than piston-cylinder actuators. For example, operating on 70°F nitrogen, the vane motor has shown a minimum SFC of 54 pounds per hp-hr, while the piston-cylinder has a minimum SFC on the order of 80 pounds per hp-hr.

8.4.3.5 Conclusions

The performance characteristics: fuel consumption, dynamic response and output stiffness have been compared for general types of pneumatic actuators. The relative importance of actuator characteristics can shift substantially from one application to another. For positioning aerodynamic surfaces, the important characteristics are over-all weight (including fuel), dynamic response and output stiffness. Operational life and resolution are also important but they are not readily predictable for comparative purposes.

An expansion-type vane motor is selected as the actuator because its characteristics most nearly fit the requirements. The expansion feature allows use of some of the gas internal energy. It has superior dynamic response when compared to the piston-cylinder actuator and its stiffness is also superior. A spool-type servo valve with inherent feedback is selected for use with the motor because of its economy and proven performance. Figure 8-16 shows a sketch of the valve-motor combination.

8.5 ANALYSIS AND DESIGN OF AERODYNAMIC CONTROL LOOP

8.5.1 Constants and Fixed Parameters

Constants and values for various fixed parameters which have been determined in previous articles are listed below. More constants pertinent to re-entry are determined in the articles which follow.

$$A_f = 5260 \text{ ft}^2$$

$$A_r = 14{,}600 \text{ ft}^2$$

$$C = 211 \text{ ft}$$

$$\bar{C} = 141 \text{ ft}$$

$$\bar{C}_1 = 41 \text{ ft}$$

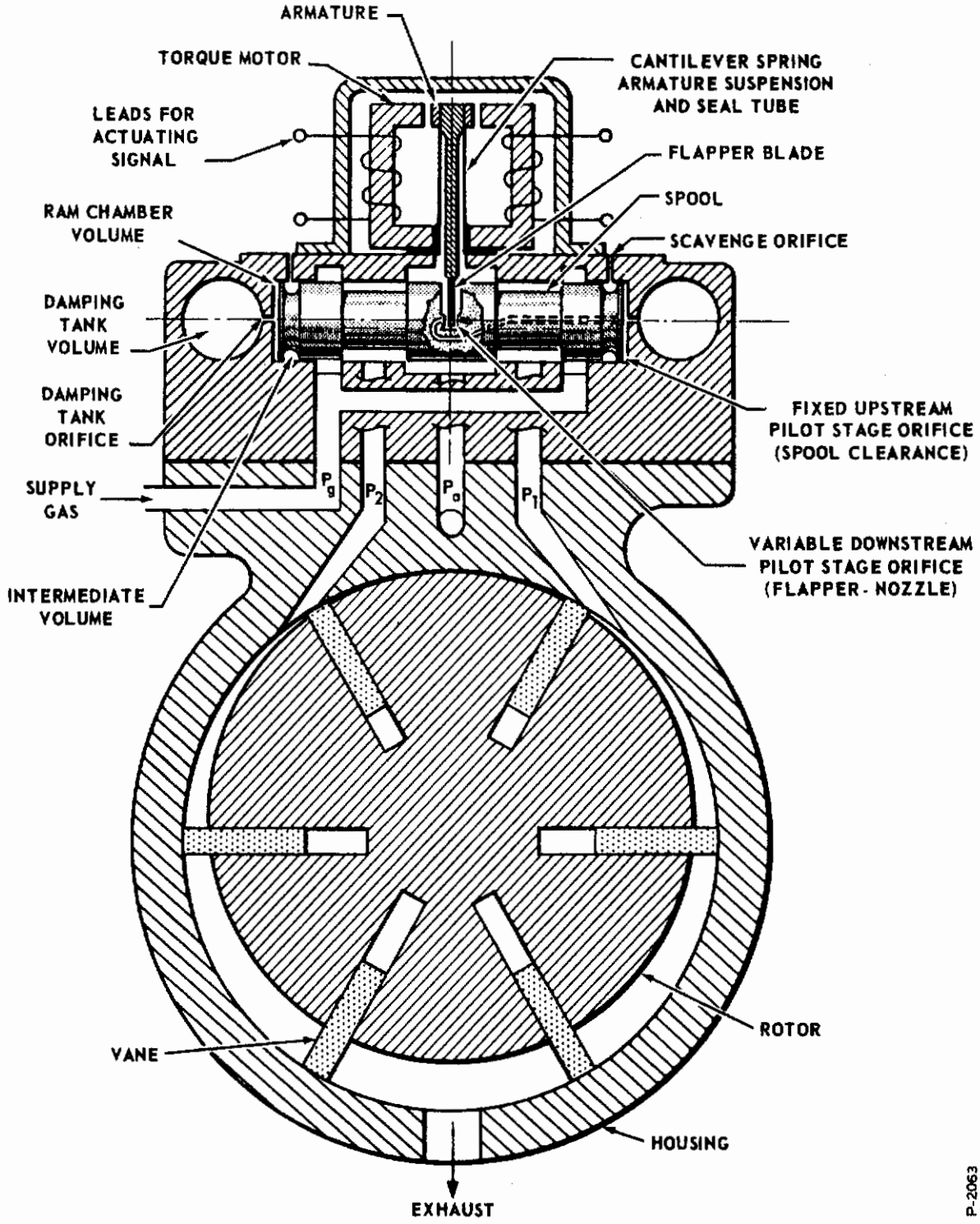

Figure 8-16 - Pneumatic Servo-Valve and Motor

$e = 2.71828$

$g = 31.4 \text{ ft/sec}^2$

$g_c = 32.2 \text{ ft/sec}^2$

$h_i = 294{,}000 \text{ ft}$

$J_p = 4.13 \times 10^6 \text{ ft-lb-sec}^2$

$k = 1.24$ (hydrogen-oxygen reaction)

$m = 3100 \text{ lb-sec}^2/\text{ft}$

$P_g = 600 \text{ psia}$

$V_i = 25{,}200 \text{ ft/sec}$

$\alpha_i = 77°$

$\beta^{-1} = 24{,}000 \text{ ft}$

$\delta_{fi} = -30°$

$\rho_\beta = 0.00238 \text{ lb-sec}^2/\text{ft}^4$

8.5.2 Selection of Vehicle Parameters

Figures 8-9 and 8-10 show that the angle-of-attack α and flap angle δ_f lie within the following ranges during steady-state conditions:

$$60° < \alpha < 77°$$

$$-15° > \delta_f > -30°$$

For the purpose of performing a linear analysis of the system, the operating point was selected as being defined by the conditions that:

$$\alpha_o = 68.5°$$

$$\delta_{fo} = 22.5°$$

which are arithmetic mid-points of the respective curves.

Curves relating the pitch moment coefficient, hinge moment coefficient, lift coefficient, and drag coefficient to the angle-of-attack and flap angle are shown in Figures 8-17 and 8-18. The dashed lines enclose the region defined by the ranges of flap angle and angle-of-attack, and the circled points represent the operating point selected for the analysis. From these curves, the following parameters are determined for the operating point:

$C_{LO} = 0.53$ $\quad \frac{\partial C_L}{\partial \delta_f} = 0.00447 \text{ deg}^{-1}$ $\quad \frac{\partial C_L}{\partial \alpha} = -0.00967 \text{ deg}^{-1}$

$C_{do} = 1.19$ $\quad \frac{\partial C_d}{\partial \delta_f} = 0.01268 \text{ deg}^{-1}$ $\quad \frac{\partial C_d}{\partial \alpha} = 0.0244 \text{ deg}^{-1}$

$C_{ho} = -0.196$ $\quad \frac{\partial C_h}{\partial \delta_f} = -0.00483 \text{ deg}^{-1}$ $\quad \frac{\partial C_h}{\partial \alpha} = -0.00487 \text{ deg}^{-1}$

$C_{mo} = -0.015$ $\quad \frac{\partial C_m}{\partial \delta_f} = -0.00656 \text{ deg}^{-1}$ $\quad \frac{\partial C_m}{\partial \alpha} = -0.00517 \text{ deg}^{-1}$

8.5.3 Flap Characteristics

The flap is assumed to have surface dimensions of 41 x 119 feet as shown in Figure 3-15. Its cross section is assumed to be a triangle with an 8-foot base. For an average density of 0.15 lb/ft^3, the flap weight is 3300 pounds. Using these values, the moment of inertia about the hinge is estimated to be 2.51×10^4 lb-ft-sec^2.

Figures 8-19 and 8-20 show the steady-state values of flap angle and flap angle rate during angle-of-attack adjustments. These curves are defined from the digital computer simulation of re-entry wherein all dynamics were neglected, so the results must be interpreted accordingly. Important values from these curves are:

$(\delta_f)_{max} = -16.6$ deg

$(\delta_f)_{min} = -29.0$ deg

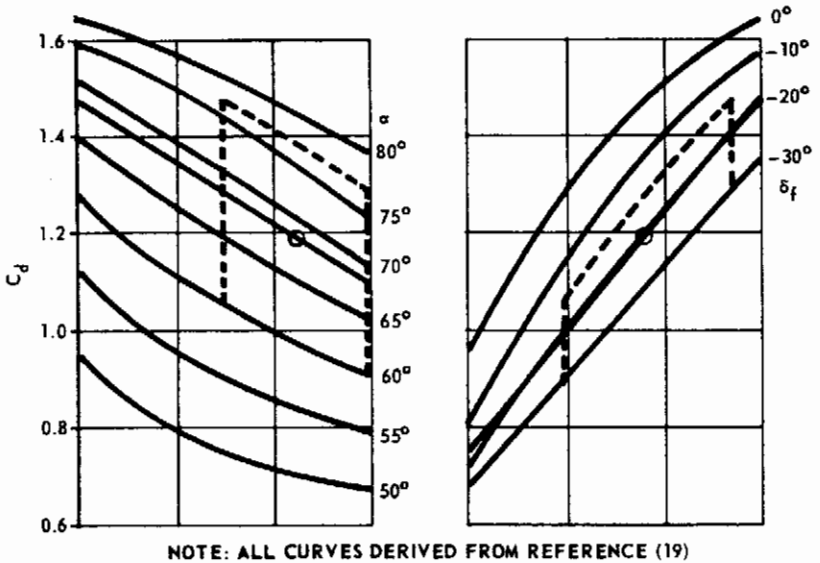

NOTE: ALL CURVES DERIVED FROM REFERENCE (19)

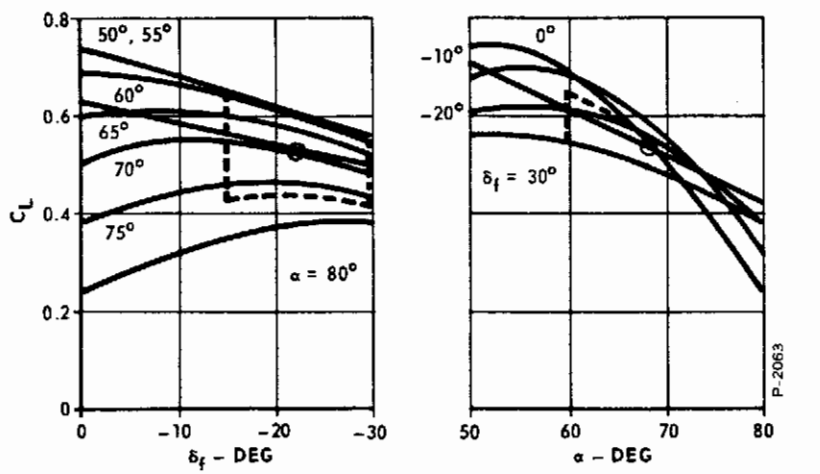

Figure 8-17 - Drag and Lift Coefficients Versus Angle-of-Attack and Flap Angle

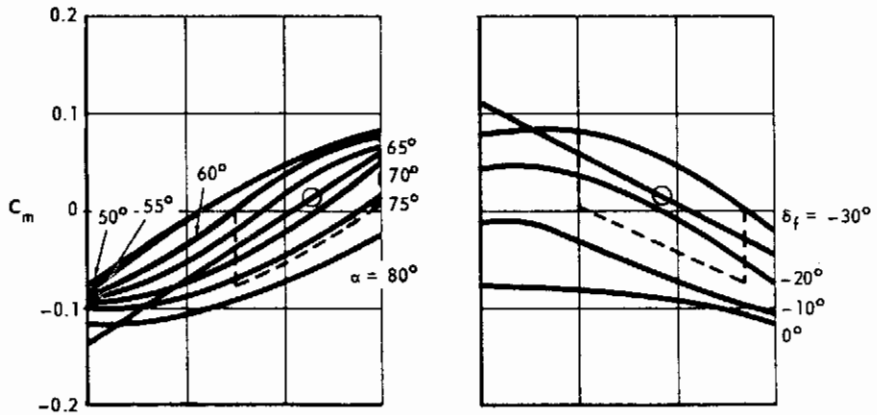

NOTE: ALL CURVES DERIVED FROM REF (19)

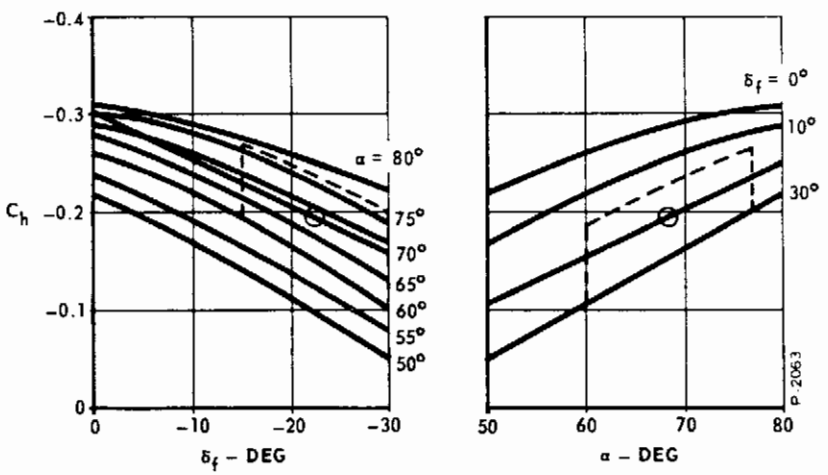

Figure 8-18 - Pitch Moment and Hinge Moment Coefficients Versus Angle-of-Attack and Flap Angle

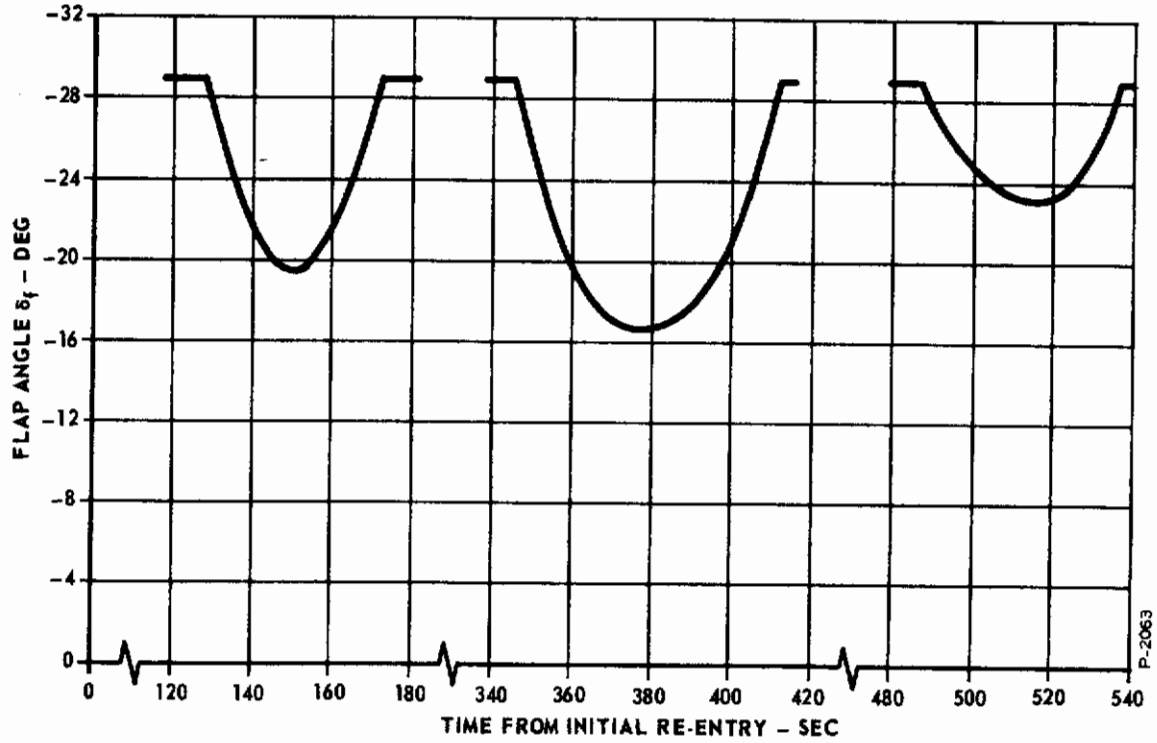

Figure 8-19 - Steady State Flap Angle During Angle of Attack Adjustments

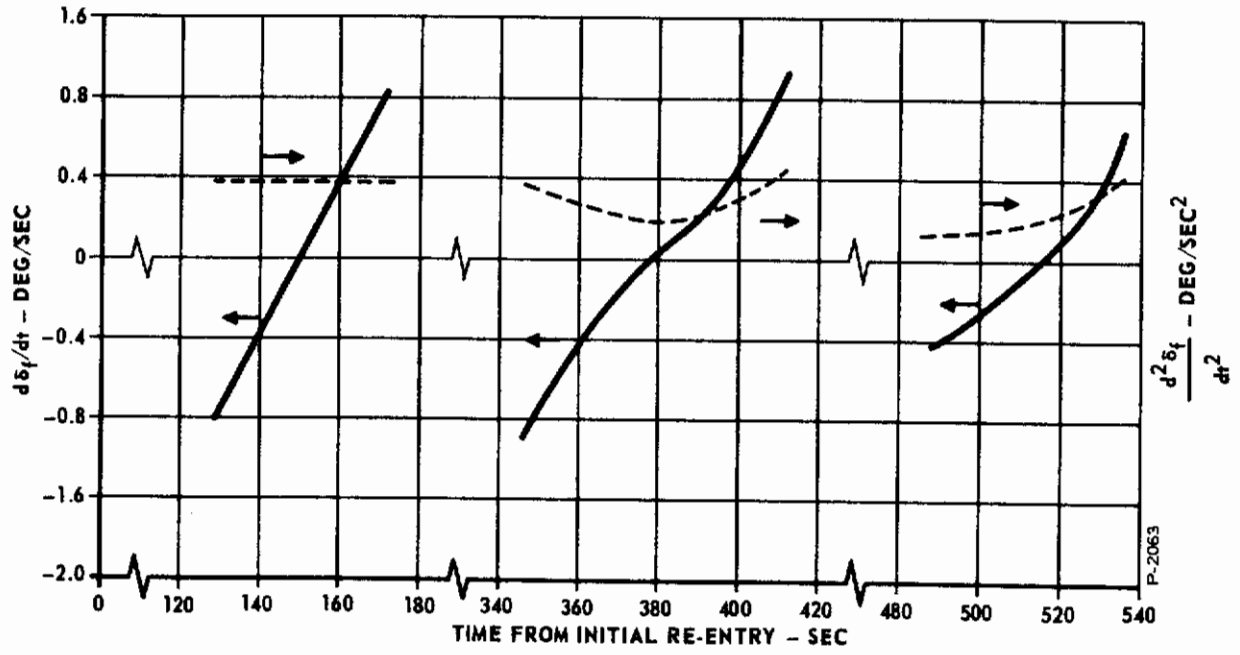

Figure 8-20 - Flap Angular Velocity and Acceleration During Angle-of-Attack Adjustments

$$\left(\frac{d\delta_f}{dt}\right)_{max} = 0.94 \text{ deg/sec}$$

$$\left(\frac{d^2\delta_f}{dt^2}\right)_{max} = 0.045 \text{ deg/sec}^2$$

Since these values represent essentially steady-state conditions, the flap control system must be capable of greater speeds and accelerations. A "safety factor" of approximately three will be used.

The flap will be split into two equal parts, each driven by a separate actuator. For pitch control, both actuators will move together, while roll control can be obtained by individual flap motions. This study is concerned with pitch control only, and differential flap motions will not be considered.

8.5.4 Actuator Requirements

Prior to designing the actuator, the torque and speed requirements imposed by external loads must be determined. The first load to be studied is the aerodynamic spring moment M_h, which is defined by:

$$M_h = \bar{C}_1 \, A_f \, C_h \, q \qquad (8\text{-}66)$$

where:

$$C_h = C_{ho} + \frac{\partial C_h}{\partial \alpha}(\alpha - \alpha_o) + \frac{\partial C_h}{\partial \delta_f}(\delta - \delta_{fo}) \qquad (8\text{-}71)$$

All of the constants in the above equations have been defined except for q, α, and δ_f. We will examine the condition where the dynamic pressure is the greatest. From Figures 8-10 and 8-19, it is seen that at 380 seconds after re-entry initiation,

$$q = 13.85 \text{ lb/ft}^2$$

$$\alpha = 60.6 \text{ deg}$$

$$\delta_f = -16.6 \text{ deg}$$

Substitution into Equations (8-60) and (8-71) reveals that:

$$M_h = 5.58 \times 10^5 \text{ ft-lb}$$

This is the total maximum aerodynamic load on the composite flap.

To assess the inertia load, it is assumed that the reflected motor inertia at the flap hinge is 30 times that of the flap and that the maximum required acceleration is 3 times the maximum steady-state value of 0.045 deg/sec^2 given in Subsection 8.5.3. The total moment required to accelerate the flap is calculated as 1826 ft-lb. It is seen that the acceleration load is small compared to the aerodynamic spring load.

In Subsection 8.5.3 it was shown that the maximum steady-state rotational speed of the flap is 0.94 deg/sec. It is assumed that the maximum speed under dynamic conditions is 2.82 deg/sec. For a maximum motor shaft speed of 4500 RPM, a gear ratio of 9580 to 1 is required. This ratio can be obtained by using a two-stage harmonic drive with a 98 to 1 ratio in each stage.

The maximum motor torque is estimated assuming a 50 percent efficiency for the high ratio transmission. Since two actuators will be used, the maximum motor torque per flap is computed as:

$$(T_m)_{max} = \frac{5.58 \times 10^5}{2 \times 9580 \times 0.5} = 58.5 \text{ ft-lb}$$

The maximum power requirement of each of the two actuators is estimated using the assumption that the torque and speed are 90 degrees out of phase. The power developed at the motor shaft is then:

$$(P_m)_{max} = (0.707)\left(\frac{4500 \times 2\pi}{60}\right)(0.707)(58.5) = 13{,}800 \text{ ft-lb/sec}$$

$$= 25 \text{ horsepower.}$$

The displacement of each motor is obtained using Equation (8-54). For a torque efficiency of 60 percent and a pressure differential of 400 psi, the torque displacement required to provide a maximum torque of 58.5 ft-lb is 2.92 in^3/rad.

8.5.5 Vane Motor Design

The design of the vane motor is based upon the following established relationships and parameters:

(a) Expansion ratio = 3 to 1 (approx.)

(b) Number of vanes = 6

(c) $D_{mt} = 2/3\ D_m$

(d) $D_{mv} = 1/3\ D_m$

(e) The rotor is square (d = b)

(f) $D_m = 0.6\ d^3$ (in units of $in.^3/rev$)

(g) $P = 2/3\ P_g$

In Subsection 8.5.4 it was established that the torque displacement D_{mt} must be 2.92 in^3/rad or 18.3 $in.^3/rev$. From Item (c) above we see that the expanded volume D_m is 4.38 $in.^3/rad$ or 27.5 $in.^3/rev$. Item (d) shows the volumetric displacement D_{mv} to be 1.46 $in.^3/rad$, and Item (f) shows that the rotor diameter d is 3.60 inches.

An approximate expression for the moment of inertia of the rotor is:

$$J_r = \frac{\pi d^4 b\sigma}{32\ g} \qquad (8\text{-}74)$$

where:

Rotor diameter $d = 3.60$ in.

Rotor length $b = 3.60$ in.

Specific Weight $\sigma = 0.30$ $lb/in.^3$

$g = 386$ $in./sec^2$

The result is $J_r = 0.0482$ $in.\text{-}lb\text{-}sec^2$, which when reflected to the flap hinge is 29.5 times the inertia of the flap. This is a good correlation with the previous assumption of thirty times the flap inertia.

The volumetric flow rate into the motor is defined by:

$$Q = \frac{D_{mv} N}{\eta_v} \tag{8-75}$$

where η_v is the volumetric efficiency.

For D_{mv} = 9.15 in.^{3}/rev, N = 4500 rev/min. and η_v = 0.80, the maximum volumetric flow rate is 858 in.^{3}/sec.

The weight flow rate through the motor is:

$$\dot{W}_m = \frac{P Q}{R' T_g} \tag{8-76}$$

where:

P = motor supply pressure, 400 psia

R' = gas constant, 3860 in./°R

T_g = gas temperature, 2060°R

The maximum weight flow rate is seen to be 0.0431 lb/sec

The specific fuel consumption is computed as follows:

$$SFC = \frac{0.0431 \times 3600}{25} = 6.2 \text{ lb/hp-hr}$$

The theoretical specific fuel consumption is obtained from:

$$(SFC)_t = \frac{2.38 \times 10^7}{\frac{D_{mt}}{D_{mv}} R' Tg \left(\frac{\Delta P}{P}\right)} \tag{8-77}$$

where:

ΔP = 400 psid

P = 400 psia

R' = 3860 in./°R

Tg = 2060°R

$$D_{mt} = 18.3 \text{ in.}^3/\text{rev.}$$

$$D_{mv} = 9.15 \text{ in.}^3/\text{rev.}$$

The result is:

$$(SFC)_t = 1.89 \ \frac{\text{lb}}{\text{hp-hr}}$$

From load considerations the maximum speed of the motor is set at 4500 RPM and the maximum torque is 702 in.-lb (58.5 ft-lb). These two parameters define the maximum power point of the load when each is reduced by the quadrature effect. It is desirable to design the motor such that its maximum power point occurs at the same speed as the maximum power demanded by the load. In the absence of leakage and friction, the maximum power out of the motor is obtained at one-half the speed at which the torque-speed curve intersects zero torque. This speed is 6360 RPM.

Using the maximum power point and the zero torque point, a straight line can be drawn through them which describes the motor torque-speed curve. It is seen that at 4500 RPM there is torque available to drive the load at its slewing speed. Additionally, the conditions at stall must be checked to determine if they are reasonable and in accord with other parameters. From Figure 8-21, "Expansion Vane Motor Torque-Speed Curve," it is seen that the stall torque is 1020 in.-lb. It is reasonable to assume that the pressure drop across the motor will be somewhat greater than that assumed at the maximum power point of 400 psi because the flow losses are very small. Assuming a pressure drop of 500 psi, the torque efficiency is computed to be 70 percent. This is higher than that assumed for the maximum power point (60 percent) and is reasonable because the rotating friction is absent. The torque-speed slope ($\partial T_m / \partial N$) is seen to be -0.165 in.-lb/rpm. This is an important motor characteristic which will be used later in defining the control loop.

Another important characteristic of the motor is the rate of change of torque with valve area. The valve area is defined by:

$$A = \frac{\dot{W}_m \sqrt{T_g}}{C_c C_2 P_g f_1\left(\frac{P}{P_g}\right)} \qquad (8\text{-}78)$$

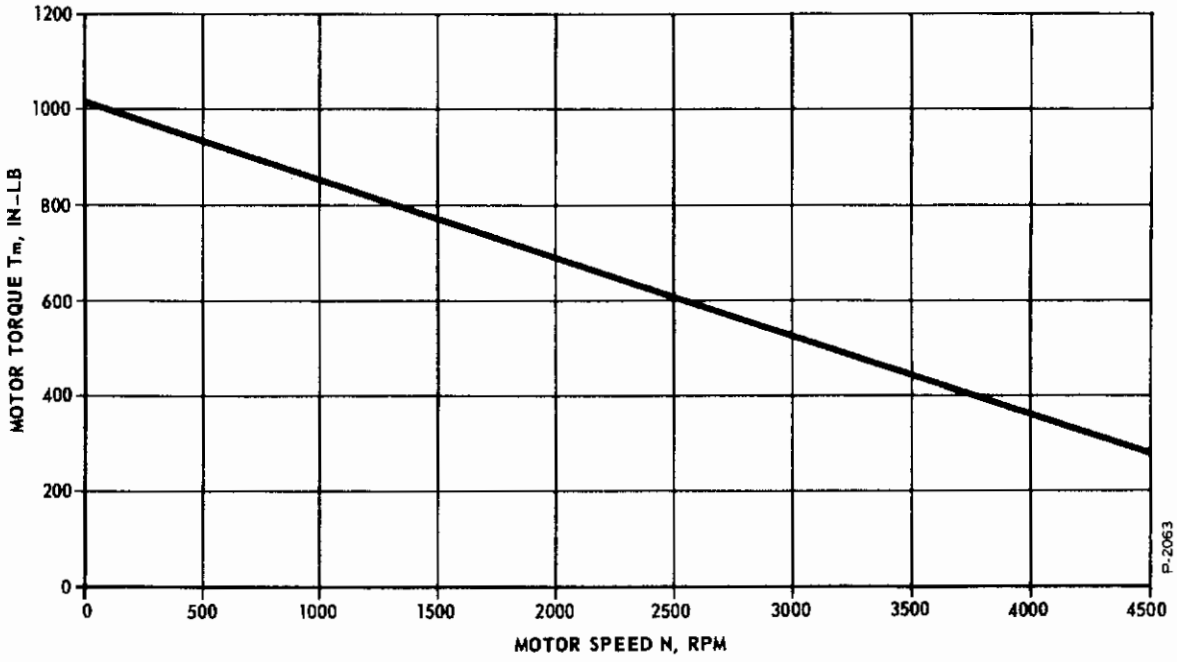

Figure 8-21 - Expansion Vane Motor Torque - Speed Curve

where:

P_g = pressure upstream of valve, 600 psia

P = pressure downstream of valve

T_g = gas temperature, 2060°R

C_c = orifice coefficient, 0.84

C_2 = gas flow constant, 0.211 °R/sec

$f_1\left(\frac{P}{P_g}\right)$ = orifice flow function.

For P = 400 psia, A = 0.0186 in^2. Using the motor torque at the maximum power point, the result is:

$$\frac{\partial T_m}{\partial A} = \frac{495}{0.0186} = 2.66 \times 10^4 \ \frac{in.\text{-}lb}{in.^2}$$

The compressibility time constant of the motor is defined by:

$$\tau_c = \frac{V_c}{k P_o D_{mt} D_{mv}} \frac{\partial T_m}{\partial N} \qquad (8\text{-}79)$$

where:

V_c = volume under compression, $in.^3$

k = ratio of specific heats of gas

P_o = quiescent motor pressure, psia

D_{mt} = torque displacement, $in.^3/rad$

D_{mv} = volumetric displacement, $in.^3/rad$

For the size motor being considered, a reasonable value for V_c is 0.5 in^3. The quiescent pressure is approximately defined by the expression:

$$D_{mt} P_o = \frac{M_{ho}}{R_g} \qquad (8\text{-}80)$$

The parameters used in Equation (8-80) are:

$$M_{ho} = 2.79 \times 10^5 \text{ ft-lb}$$

$$R_g = 9580$$

$$D_{mt} = 2.92 \text{ } in.^3/rad$$

the resultant quiescent pressure being 119 psia. Substitution into Equation (8-79) reveals that:

$$\tau_c = 0.00123 \text{ sec.}$$

8.5.6 Servo Valve and Vane Motor Characteristics

The servo valve transfer function is represented by:

$$\frac{A}{i} = \frac{K_b}{1 + \tau_b S} \qquad (8\text{-}81)$$

A_{max} is 0.0186 in.^{2}, and i_{max} is taken as 0.8 amps so that K_b = 0.0232 in.^{2}/amp. An accurate theoretical prediction of τ_b is not possible without going into a detailed design, but fortunately enough test data on similar valves is available to allow a reasonable estimate to be made. A typical set of frequency response curves is given in Figure 8-22. It is seen that the dynamics that produced curve No. 2 are of a higher order than a single lag, but because only the low frequency region is of interest, the single lag approximation is justified. It is seen that the 45 degree phase shift point occurs at approximately 80 cps. A good curve fit is obtained on both the amplitude ratio and phase angle curves at the lower frequencies for:

$$\tau_b = \frac{1}{2\pi \times 80} = 0.0020 \text{ sec.}$$

The entire valve transfer function is then:

$$\frac{A}{i} = \frac{0.0232}{1 + 0.002\,S} \quad \frac{\text{in}^2}{\text{amp}}$$

The servo loop of Figure 8-15 is simplified and represented by the block diagram shown in Figure 8-23. For the purpose of obtaining as much simplification as possible, the friction torque is not considered as its magnitude is small compared to the other torques involved. Further simplification of the block diagram is desirable to enable the loop to be analyzed by conventional techniques.

It is desirable to replace the circuit that generates the hinge coefficient C_h and hinge load M_h with a constant gain K_L defined by:

$$K_L = \frac{12}{R_g} \frac{d\,M_h}{d\,\delta_f} . \qquad (8\text{-}82)$$

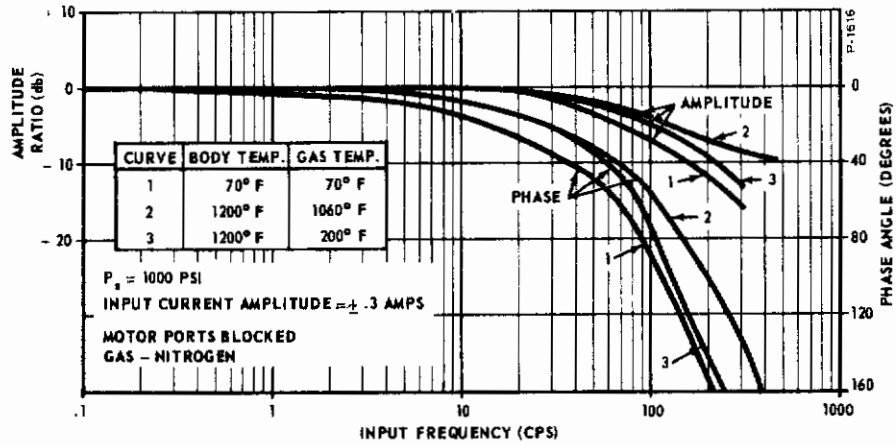

Figure 8-22 - Servo Valve Frequency Response at Various Temperatures

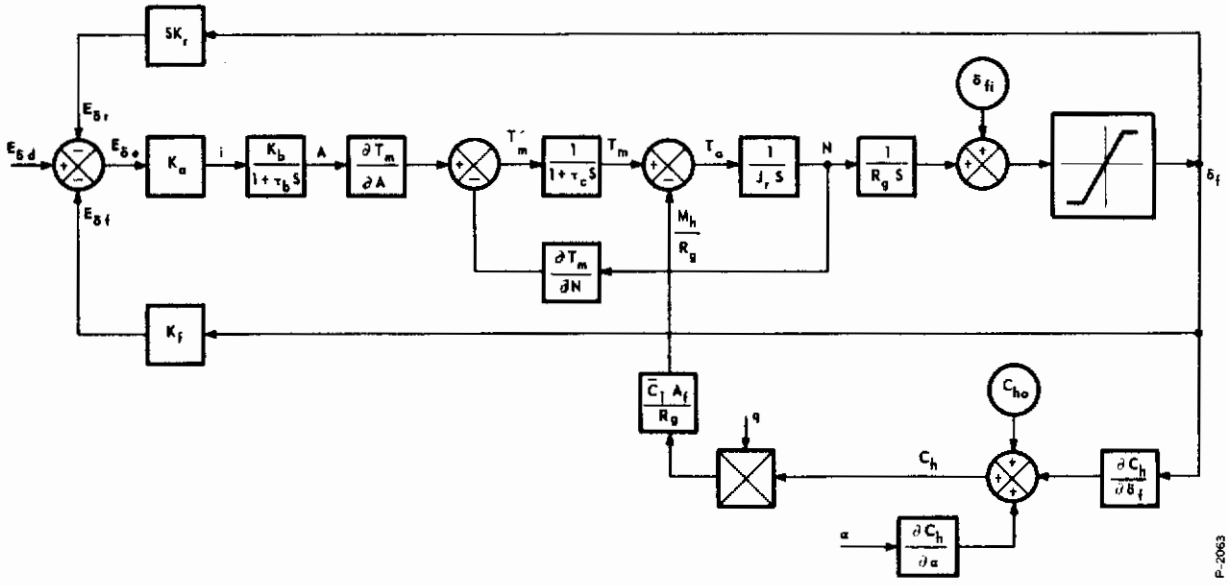

Figure 8-23 - Flap Servo System Block Diagram

To determine the aerodynamic spring moment gain $d M_h / d \delta_f$, Equations (8-66) and (8-71) are combined and differentiated letting q and α be constant. The resulting expression is:

$$\frac{\partial M_h}{\partial \delta_f} = \bar{C}_l A_f q \frac{\partial C_h}{\partial \delta_f} \tag{8-83}$$

Substitution of appropriate values reveals that:

$$K_L = 519 \text{ in.-lb/rad}$$

The undamped natural frequency of the motor is defined by:

$$\omega_n^2 = \frac{k P_o D_{mt} D_{mv}}{J_r V_c} \tag{8-82}$$

Substitution of appropriate parameters results in:

$$\omega_n = 163 \text{ rad/sec} = 25.9 \text{ cps}$$

Prior experience with this type of system has shown that the dynamic response cannot be extended much beyond the motor natural frequency.

Since the break frequency of the valve is significantly greater than the natural frequency of the motor, the valve dynamics will be neglected. This reduces the order of the system transfer function from four to three and simplifies the analysis of the system performance. Figure 8-24 shows the simplified block diagram of the servo loop.

8.5.7 Analysis of Closed Loop Transfer Function

The system equations represented by Figure 8-24 are:

$$E_{\delta e} = E_{\delta d} - S K_r \delta_f - K_f \delta_f \tag{8-83}$$

$$T_m' = K_b \frac{\partial T_m}{\partial A} K_a E_{\delta e} - \frac{\partial T_m}{\partial N} N \tag{8-84}$$

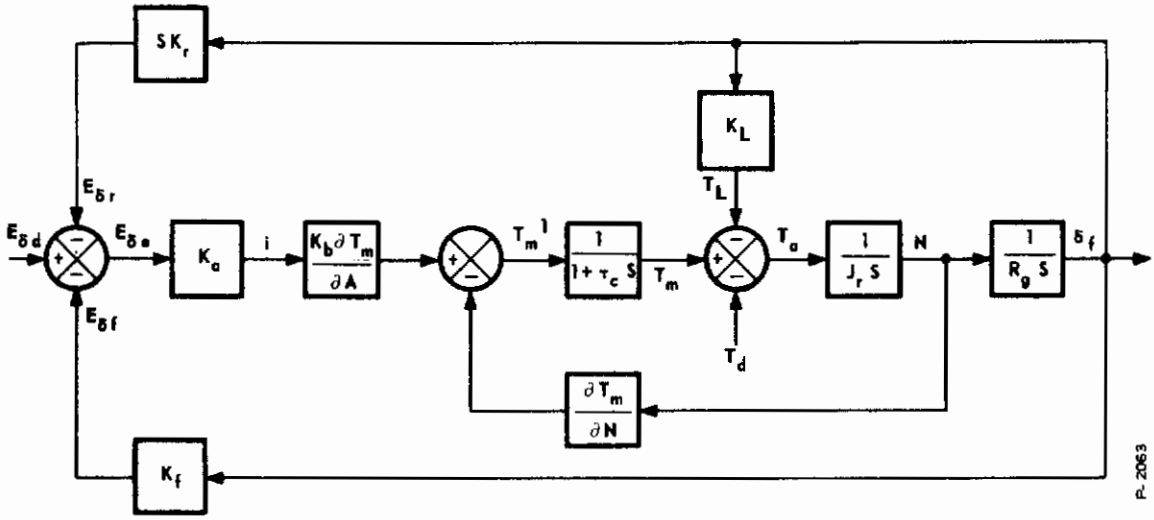

Figure 8-24 - Simplified Flap Servo System Block Diagram

$$T_m = \frac{T_m'}{1 + \tau_c S} \tag{8-85}$$

$$T_a = T_m - K_L \delta_f \tag{8-86}$$

$$N = \frac{T_a}{J_r S} \tag{8-87}$$

$$\delta_f = \frac{N}{R_g S} \tag{8-88}$$

By appropriately combining the above equations, the closed loop transfer function is found to be of the form:

$$\frac{\delta_f}{E_{\delta d}} = \frac{b_1}{a_3 S^3 + a_2 S^2 + a_1 S + a_o} \tag{8-89}$$

where:

$$b_1 = \frac{K_a K_b \frac{\partial T_m}{\partial A}}{K_L + K_a K_b K_f \frac{\partial T_m}{\partial A}}$$

$$a_3 = \frac{R_g J_r \tau_c}{K_L + K_a K_b K_f \frac{\partial T_m}{\partial A}}$$

$$a_2 = \frac{R_g J_r}{K_L + K_a K_b K_f \frac{\partial T_m}{\partial A}}$$

$$a_1 = \frac{K_L \tau_c + R_g \frac{\partial T_m}{\partial A} + K_a K_b K_r \frac{\partial T_m}{\partial A}}{K_L + K_a K_b K_f \frac{\partial T_m}{\partial A}}$$

$$a_o = 1$$

The system transfer function is of third order and can be analyzed by an established technique. Equation (8-89) is first rewritten as:

$$\frac{\delta_f}{b_1 E_{\delta d}} = \frac{B^*}{\left(\frac{S}{\omega_{ns}}\right)^3 + A^* \left(\frac{S}{\omega_{ns}}\right)^2 + \left(\frac{S}{\omega_{ns}}\right) + B^*} \qquad (8\text{-}90)$$

where:

$$\omega_{ns}^2 = \frac{a_1}{a_3}$$

$$B^* = \frac{a_o}{\omega_{ns}\, a_1}$$

$$A^* = \frac{a_2}{\omega_{ns}\, a_3}$$

Taking $K_f = 57.3$ volt/rad and substituting the known system parameters into the expressions for the coefficients results in:

$$a_3 = \frac{0.569}{519 + 35{,}200\, K_a}$$

$$a_2 = \frac{462}{519 + 35{,}200\, K_a}$$

$$a_1 = \frac{15{,}100 + 615\, K_a\, K_r}{519 + 35{,}200\, K_a}$$

$$a_o = 1$$

$$\omega_{ns} = \sqrt{\frac{15{,}100 + 615\, K_a\, K_r}{0.569}}$$

$$A^* = \sqrt{\frac{613}{15{,}100 + 615\, K_a\, K_r}}$$

$$B^* = \frac{1}{\sqrt{26{,}600 + 1082\, K_a\, K_r}\left(\frac{15{,}100 + 615\, K_a\, K_r}{519 + 35{,}200\, K_a}\right)}$$

It has been established that optimum system response results when $A^* = 0.7$ and $B^* = 0.35$. The expression for A^* shows that $K_a\, K_r$ must be 1220. Substitution of this into the expression for B^* results in:

$$K_a = 8780 \text{ amp/volt}$$

and

$$K_r = 0.139 \text{ volt-sec}$$

All of the parameters for the flap control servo loop have been selected and computed to obtain optimum performance. From Figure 8-25 it is seen that the system has a resonance peak of 2 db occurring at a frequency of 4.35 cps. The phase shift at this point is 135 degrees. The -3 db point occurs at 5.32 cps with a phase shift of 205 degrees. The transient response of this system has a 10% overshoot and four oscillations.

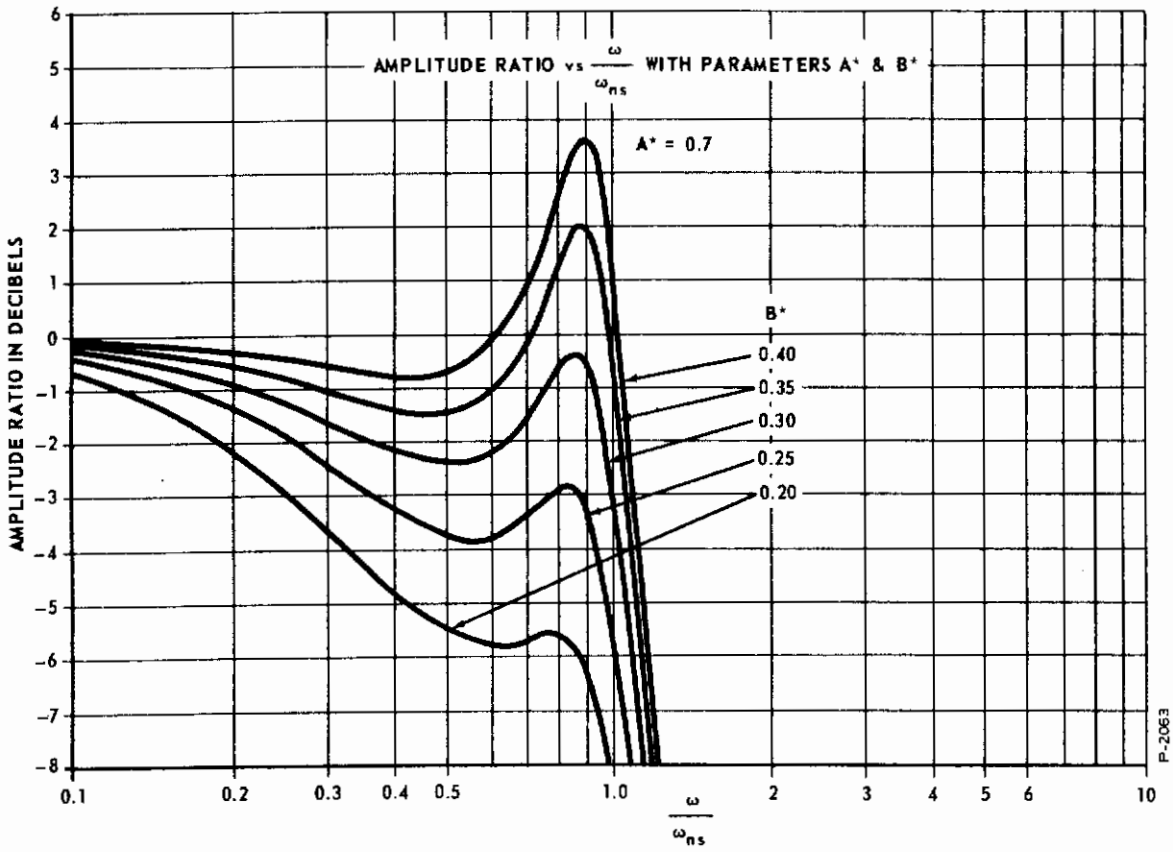

Figure 8-25 - Frequency Response of a Third Order System

8.6 SUMMARY AND CONCLUSIONS

The attitude control of a lifting re-entry vehicle requires the use of both mass expulsion and aerodynamic surfaces. At high altitudes where the dynamic pressure is low, aerodynamic control is insufficient and requires augmentation by control moments created by mass expulsion. At a later time, however, the dynamic pressure reaches a sufficient level to allow complete aerodynamic control of attitude.

There is no problem in maintaining attitude control during the initial part of re-entry where both mass expulsion and aerodynamic control are used. With the flap set to trim the vehicle at the required angle-of-attack, the mass expulsion system need only maintain stability and overcome extraneous disturbance torques exerted on the vehicle. The mass expulsion attitude control system which is used for the rendezvous maneuver will be more than adequate for re-entry.

Attitude control during the latter part of re-entry is dependent upon the servo system which actuates the flaps. Essentially, the frequency response of the servo system must be substantially greater than the 0.5 to 2 rad/sec aerodynamic natural frequency of the vehicle.

The actuator selected for driving the flaps is an expansion vane motor controlled by a spool-type servo valve. Reaction jets are completely out of the question for flap control because of the enormous quantities of fuel required. A piston-cylinder lacks the performance and fuel economy of an expansion vane motor.

A flap control system was designed which has adequate performance for controlling vehicle angle-of-attack during re-entry. Based upon a simplified mathematical model, the servo system has a frequency response at least an order of magnitude greater than the maximum aerodynamic natural frequency of the vehicle.

The analyses presented in this section involved a great deal of linearization and simplification. This was done because it allowed a preliminary system design to be readily accomplished without the expense of a complex computer simulation of re-entry. The accomplished work is considered to be adequate to the extent of defining and sizing the high moment-producing method and system required.

8.7 NOMENCLATURE

Symbol		Definition
a	=	constant defined by Equation (8-12)
A	=	orifice flow area of servo-valve, $in.^2$
A*	=	lumped constant (see text)
A_f	=	effective area of flap, ft^2
A_p	=	piston area, $in.^2$
A_r	=	vehicle wing area, ft^2
b	=	length of vane motor rotor, in.
B*	=	lumped constant (see text)
C	=	vehicle wing root chord, ft
C_2	=	gas flow constant, °R/sec
$\bar{C}$	=	mean aerodynamic chord of vehicle (2/3 C), ft
$\bar{C}_l$	=	mean aerodynamic chord of flap, ft
C_c	=	orifice coefficient
C_d	=	drag coefficient
C_h	=	aerodynamic hinge moment coefficient
C_L	=	lift coefficient
C_m	=	pitching moment coefficient
d	=	diameter of vane motor rotor, in.
D	=	drag force, lb
$\bar{D}'$	=	desired drag vector, lb
D_M	=	accelerometer measurement of drag, lb (refer to Figure 8-5)

D_m = theoretical motor displacement, $in.^3/rad$

D_{mt} = torque displacement of motor, $in.^3/rad$

D_{mv} = volumetric displacement of motor, $in.^3/rad$

e = base of natural logarithms

$E_{\delta d}$ = voltage command signal to servo-loop

$E_{\delta e}$ = error voltage in servo-loop

$E_{\delta f}$ = position feedback voltage

$E_{\delta r}$ = rate feedback voltage

F_p = thrust of attitude control engine acting about pitch axis, lb

g = gravitational acceleration, ft/sec^2

g_c = gravitational acceleration at sea level, ft/sec^2

G_f = function defined by Equation (8-27)

h = altitude above earth's surface, ft

i = electrical current to torque motor, amps

J_f = moment of inertia of flap with respect to hinge, $lb\text{-}ft\text{-}sec^2$

J_L = total system inertia reflected to the load, $lb\text{-}ft\text{-}sec^2$

J_p = vehicle moment of inertia about pitch axis, $lb\text{-}ft\text{-}sec^2$

J_r = moment of inertia of motor rotor, $lb\text{-}ft\text{-}sec^2$

k = ratio of specific heats of control gas

k_t = constant defined by Equation (8-27)

K_a = amplifier gain in servo-loop

K_b = gain of servo valve

K_g = input gain

K_f = position feedback gain in servo-loop

K_L = gain defined by Equation (8-82)

K_r = rate feedback gain

L = lift force, lb

m = vehicle mass, lb-sec^2/ft

M_h = aerodynamic spring moment about hinge, ft-lb

M_p = pitch control moment about vehicle center of gravity, ft-lb

N = motor shaft speed, rad/sec

P = motor supply pressure, psia

ΔP = pressure drop across motor, psid

P_g = valve supply pressure, psia

P_o = motor quiescent pressure, psia

q = dynamic pressure, lb/ft^2

q_i = dynamic pressure at initiation of re-entry, lb/ft^2

Q = volumetric flow rate into motor, in.^{3}/sec

R = distance from vehicle to earth's center, ft

R' = universal gas constant, in./°R

R_g = gear ratio between motor and load

R_e = earth's radius, ft

R_g = gear ratio between motor and load

S = Laplace operator, 1/sec

t = time, sec

T_a	=	torque acting to accelerate flap, ft-lb
T_f	=	friction torque at motor output, ft-lb
T_g	=	supply gas temperature, °R
T_m	=	motor torque output, ft-lb
V	=	velocity of vehicle along flight path, ft/sec
V_c	=	motor volume under compression, $in.^3$
$\dot{V}_m$	=	measured vehicle acceleration, ft/sec^2
$\dot{W}_m$	=	weight flow rate through motor, lb/sec
x_p	=	distance between pitch control engines, ft
Y	=	moment arm for piston-cylinder actuator, in.
α	=	vehicle angle of attack, rad
α_o	=	value of α when $C_m = 0$, rad
α'	=	variable term affecting α, rad
β	=	exponential factor in atmospheric density approximation. (refer to Equation (8-39))
γ	=	pitch angle from inertial reference, rad
δ_f	=	flap position angle, rad
ζ	=	damping ratio
η_v	=	motor volumetric efficiency
θ	=	flight path angle with respect to horizon, rad
ξ	=	accelerometer reference angle, rad (refer to Figure 8-5)
π	=	3.1416
ρ	=	atmospheric density, $lb\text{-}sec^2/ft^4$

ρ_β	=	base density used in atmospheric density approximation, $lb\text{-}sec^2/ft^4$
σ	=	specific weight of motor rotor, $lb/in.^3$
τ_b	=	lag time constant of servo valve, sec
τ_c	=	compressibility time constant of motor, sec
τ_r	=	compensation time constant, sec
ω_n	=	undamped natural frequency, rad/sec
$(\dot{})$	=	single dot above symbol denotes first derivative with respect to time
$(\ddot{})$	=	two dots above symbol denotes second derivative with respect to time
$\frac{\partial}{\partial}$	=	indicates partial derivative

Subscripts

i	=	initial value of a variable
o	=	mean value of a variable

SECTION 9

CONCLUSIONS AND RECOMMENDATIONS

9.1 CONCLUSIONS

A manned space vehicle which executes orbital transfer, rendezvous, and re-entry maneuvers has been studied with regard to its attitude control requirements and the means for meeting these requirements. For each maneuver, a particular trajectory or guidance logic was selected, the attitude control requirements were determined, and an attitude control system was selected and designed. For the relatively short mission duration of the hypothetical vehicle considered, the optimum attitude control system for space maneuvers employs mass expulsion reaction engines and uses secondary injection thrust vector control when necessary. The re-entry maneuver requires a combination of mass expulsion and aerodynamic control during the initial stages and pure aerodynamic control during latter stages of the maneuver.

Momentum exchange systems provide greater attitude accuracy than do mass expulsion systems, but they become large and complex when high control moments are required. Also, a momentum exchange system requires the presence of a properly integrated mass expulsion system to provide de-saturization. For the application studied in this report, a mass expulsion system can provide the necessary attitude control accuracy, thus eliminating the need for an auxiliary system.

A large space vehicle with a long mission duration might use a momentum exchange system to advantage, particularly for the lower moment control functions such as stabilization. For this case, control moment gyros are preferred to reaction wheels because of their significantly lower power requirements.

The guidance engines for the hypothetical vehicle were assumed to use liquid hydrogen and liquid oxygen as the propellant combination. A comparison of this fuel and oxidizer with other bipropellants reveals that liquid hydrogen and liquid oxygen are preferred for use with the attitude control reaction engines. Strong points in this argument are the advantages inherent in having a common propellant supply for all engines on board.

Secondary injection thrust vector control is a convenient and efficient means for compensating for engine misalignment and maintaining attitude control during main engine firing. Fast response of the secondary injectant flow is obtained by using an all-fluid valving system; however, sufficient information concerning the dynamic response of the thrust vector deflection phenomenon is not available to allow the complete loop characteristic to be accurately defined.

The selection of a control system for the rendezvous phase of a manned space vehicle with a space station has been studied and a conclusion formed on what constitutes a good control system. The final configuration selected consists of a secondary injection thrust vector control system for major corrections when the main engine is firing and a reaction control system for lower magnitude attitude corrections and orientation. The secondary injection system is a simple control loop which uses hot gases from the main engine combustion chamber. An optimum control loop for both the reaction engine system and the secondary injection thrust vector control system uses an on-off controller with deadband and rate feedback. The two systems cross-couple through the vehicle dynamics but function in complete harmony.

Attitude control during the latter part of re-entry is dependent upon the servo system which actuates the aerodynamic flaps. A linearized analysis indicates that a proportionally controlled pneumatic system using a closed center valve and an expansion vane motor will provide adequate response with low gas consumption.

9.2 RECOMMENDATIONS

Further study is desirable in some of the many areas covered by this report. It was not possible in all of the analyses and investigations to go into as much detail as possible, and in some cases, the selection of a particular component, system, or technique had to be made on the basis of intuitive judgment due to lack of information available. Specific recommendations for further research and study are contained in the following paragraphs.

It is altogether possible that certain guidance techniques have less stringent attitude control requirements than others. In particular, the rendezvous maneuver, including the docking phase, can be executed with a number of different logic schemes. Rendezvous guidance should be studied from the standpoint of performing a successful maneuver with

the least demands upon the attitude control system, the goal being to increase reliability and reduce propellant consumption. The scope of this study should include the analogue simulation of the complete dynamics of the integrated attitude control and guidance systems.

The use of liquid hydrogen and liquid oxygen as the propellant for attitude control engines should be studied further and in greater detail to more firmly establish feasibility and practicability. There are a number of problems involved in providing the propellant in a liquid state at the reaction engines. The application of efficient thermal insulation must be considered as well as the problems associated with the boil-off which will result due to heat transfer and heat generation. The effect of the cryogenic liquids upon the propellant supply system design and operation should be determined, particularly with regard to the dynamic elements.

Additional analysis of the reaction engine attitude control system is required, now that the system has been defined, to establish complete system design criteria with emphasis on the following considerations:

(1) Establish more realistic analytical expressions for the combustion dynamics.

(2) An often neglected part of this system is the tankage and manifolding. The valves and nozzles are remotely located from the propellant storage tanks. The line dynamics become complex and are significant in optimizing performance. A general design analysis anticipating the variety of operating conditions and configurations is required. A distributed parameter analysis and analog simulation would be invaluable in this area.

(3) Further analysis and analog computer simulation is required with regard to choice of the proportional or on-off control mode, since a more accurate description of system non-linearities is being achieved as the technology is advanced. The relative effects of significant parameters on performance must be defined to assure the best design based on tradeoff parameters such as accuracy, simplicity, weight and reliability. The basic control system models have been established, and further analysis would improve their validity and worth to the vehicle designer.

A computer simulation of the complete re-entry maneuver should be performed wherein all of the nonlinearities of the dynamics are included. This is a sizeable effort, but it is the logical next step beyond the work reported here. Such a simulation will allow the attitude control system to be optimized for all of the dynamic pressure conditions of the complete re-entry trajectory. Also, it will positively verify that the attitude control system will allow the vehicle to follow the desired trajectory.

SECTION 10

LIST OF REFERENCES

1. White, J. F., "Flight Performance Handbook for Powered Flight Operations," John Wiley and Sons, Inc., New York, 1963.
2. Wolverton, R. W., "Flight Performance Handbook for Orbital Operations," John Wiley and Sons, Inc., New York, 1963.
3. Gretz, R. W., "Error Sensitivities in Satellite Ascent and Orbital Transfer," ARS Journal, December 1962.
4. Raytheon Company Staff, "Guidance and Control for Manned Lunar Flight," Control Engineering, June 1962.
5. Denton, C. I., Sando, R. M. and Monhert, A. T., "Space Rendezvous Guidance and Docking Techniques," Westinghouse Engineer, July - September 1962.
6. Steffan, K. F., "Satellite Rendezvous Terminal Guidance System," ARS Journal, November 1961.
7. Straly, W. H., "The Phasing Technique in Rendezvous," ARS Journal, April 1962.
8. Shapiro, M., "Attenuated Intercept Satellite Rendezvous System," ARS Journal, December 1961.
9. Nason, M. L., "Terminal Guidance Technique for Satellite Interception Utilizing a Constant Thrust Rocket Motor," ARS Journal, September 1960.
10. Kidd, A. T. and Sonle, P. W., "Terminal Maneuvers for Satellite Ascent Rendezvous," ARS Journal, January 1962.
11. Edelbaum, T. N., "Propulsion Requirements for Controllable Satellites," ARS Journal, August 1961.
12. Duke, W. M., Goldberg, E. A. and Pfeffer, I., "Error Analysis Considerations for a Satellite Rendezvous," ARS Journal, April 1961.
13. Koelle, H. H., "Handbook of Astronautical Engineering," McGraw-Hill Book Company, New York, 1961.

14. Poor, J. G. and Dix, R. U., "Vehicle Dynamics Considerations at Parabolic Velocities," ARS Journal, December 1962.

15. Mandell, D. S., "Maneuvering Performance of Lifting Re-Entry Vehicles," ARS Journal, March 1962.

16. Mayo, E. E., "Static Longitudinal Stability Characteristics of a Blunted Glider Re-Entry Configuration having 79.5° Sweepback and 45° Dihedral at a Mach Number of 6.2 and Angles of Attack up to 20°," NASA Technical Memorandum TM X-222, October 1959. Declassified.

17. Clark, F. L. and Evans, J. M., "Some Aerodynamic and Control Studies of Lifting Re-Entry Configurations at Angle of Attack up to 90° at a Mach Number of 2.91," NASA Technical Memorandum TM X-338, November 1960. Declassified.

18. Foster, G. V., "Effect of Longitudinal and Lateral Controls on Aerodynamic Characteristics of a Winged Re-Entry Configuration at a Mach Number of 1.97 and Angles of Attack up to Approximately 90°," NASA Technical Memorandum TM X-449, February 1961. Declassified.

19. Fetterman, D. E. and Neal, L., Jr., "An Analysis of the Delta Wing Hypersonic Stability and Control Behavior at Angles of Attack Between 30° and 90°," NASA Technical Note TN D-1602, March 1963.

20. Bernot, P. T., "Pressure Distributions on Blunt Delta Wings at Angles of Attack up to 90° and Mach Number of 6.85," NASA Technical Note TN D-1954, July 1963.

21. Bertram, M. H. and Everhaut, P. E., "An Experimental Study of the Pressure and Heat Transfer Distribution on a 70° Slab Delta Wing in Hypersonic Flow," NASA Technical Report TR R-153 1963.

22. "U.S. Standard Atmosphere, 1962," prepared under the sponsorship of National Aeronautics and Space Administration, U.S.A.F., and United States Weather Bureau, 1962.

23. Schuler, J. M. and Pritchard, F. E., "Six-Degree-of-Freedom Equations of Motion for a Maneuvering Re-Entry Vehicle," U.S. Naval Training Device Center, Port Washington, New York, Tech. Report NAVTRADEVCEN 801 A 15 June 1962. ASTIA AD-283911

24. "High Moment Producing Techniques for Attitude Control and Stabilization of Manned Space Vehicles - Volume I - Moment Requirements and Techniques," Aeronautical Systems Division Technical Documentary Report No. ASD-TDR-62-737, October 1962.

25. Koelle, H. H., Editor., "Handbook of Astronautical Engineering," McGraw-Hill Book Company, Inc., 1961.

26. Row, P. V. and Fischel, J., "X-15 Flight-Test Experience," Astronautics and Aerospace Engineering, June 1963.

27. Chapman, D. R., "An Approximate Analytical Method for Studying Entry into Planetary Atmospheres," NASA Technical Report R-11, 1959.

28. Lovelace, U. M., "Charts Depicting Kinematic and Heating Parameters for a Ballistic Re-Entry at Speeds of 26,000 to 45,000 Feet per Second," NASA Technical Note D968, October 1961.

29. Sutton, G. W., "Ablation of Reinforced Plastics in Supersonic Flow," Journal of Aerospace Sciences Vol. 27 n 5 May 1960.

30. Boisseau, P. C., "Investigation of the Low-Subsonic Flight Characteristics of a Model of a Re-Entry Vehicle with a Thick Flat 75° Swept Delta Wind and a Half-Cone Fuselage," NASA Tech. Note TN D-1007 February 1962.

31. Foster, G. V., "Effect of Longitudinal and Lateral Controls on Aerodynamic Characteristics of a Winged Re-Entry Configuration at a Mach Number of 1.97 and Angles of Attack up to Approximately 90°," NASA Technical Memorandum TM X-449 February 1961. Declassified.

32. Etlein, B., "Dynamics of Flight," John Wiley and Sons, Inc., New York, 1959.

33. Mandell, D. S., "Maneuvering Performance of Lifting Re-Entry Vehicles," ARS Journal , Vol. 32, No. 3, March 1962.

34. Bryson, A. E. and Denham, W. F., "Guidance Scheme for Supercircular Re-Entry of a Lifting Vehicle," ARS Journal, Vol. 32, No. 6, June 1962.

35. Lees, L., Hartwig, F. W. and Cohen, C. B., "Use of Aerodynamic Lift During Entry into the Earth's Atmosphere," ARS Journal, Vol. 29, No. 9, September 1959.

36. Eggers, A. J., Jr., Allen, H. J. and Neice, S. E., "A Comparative Analysis of the Performance of Long-Range Hypervelocity Vehicles," NASA TN-4046, October 1957.

37. Allen, H. J. and Eggers, A. J., Jr., "A Study of the Motion and Aerodynamic Heating of Missiles Entering the Earth's Atmosphere at High Supersonic Speeds," NASA TN-4047, October 1957.

38. Loh, W. H. T., "Dynamics and Thermodynamics of Entry," Journal of Aerospace Sciences, Vol. 27, No. 10, October 1960, p. 748.

39. Loh, W. H. T., "Some Exact Analytical Solutions of Planetary Entry," AIAA Journal, Vol. 1, No. 4., April 1963, p. 836.

40. Brunner, M. J., "Aerodynamic and Radiant Heat Input to Space Vehicles which Re-Enter at Satellite and Escape Velocity," ARS Journal, Vol. 31, No. 8, August 1961, p. 1102.

41. Loh, W. H. T., "Dynamics and Thermodynamics of Planetary Entry," Prentice-Hall Inc., 1963.

42. Astronautics - Guidance and Control Issue, November 1961.

43. Bendix Report AP 293B, "Reaction Wheels for Stabilizations of Satellite Vehicles," May 1, 1961.

44. Braumiller, J., Lynn, G. E., Julich, R. M. and Wood, C. W., "Magnetic Torquers for Space Vehicle Control," ASD-TDR-63-74, January 1963.

45. Cannon, R. H., Jr., "Some Basic Response Relations for Reaction-Wheel Attitude Control," ARS Journal, Vol. 31, January 1961.

46. Cornille, H. J., Jr., "YO-YO Cuts Spacecraft Spin Rates," Space/Aeronautics Vol. 39, January 1963.

47. Deimel, R. F., "Mechanics of the Gyroscope," Dover Publications Inc., New York City, New York, 1950.

48. Gibson, J. E. and Tuteur, F. B., "Control Systems Engineering," McGraw-Hill Book Company Inc., New York, 1958 pp. 343-362.

49. Grasshoff, L. H., "A Method for Controlling the Attitude of a Spin-Stabilized Satellite," ARS Journal, May 1961.

50. Grasshoff, L. H., "Eddy Current Torque Compensation in a Spin Stablized Earth Satellite," ARS Journal, Vol. 31, March 1961.

51. Haeussermann, W., "Recent Advances in Attitude Control of Space Vehicles," ARS Journal, Vol. 32, February 1962.

52. Haseltine, W. R., "Nutation Damping Rates for a Spinning Satellite," Aerospace Engineering, Vol. 21, March 1962.

53. Haseltine, W. R., "Passive Damping of Wobbling Satellites: General Stability, Theory and Example," Journal of the Aerospace Sciences, Vol. 29, May 1962.

54. Holahan, J., "Progress Report: Attitude Control for Unmanned Spacecraft," Space/Aeronautics, Vol. 39, February 1963.

55. Kamm, L. J., "The Magnetorquer - A Satellite Orientation Device," ARS Journal, June 1961.

56. Klass, P. J., "New Gyro Technique Orients Satellites," Aviation Week and Space Technology, February 12, 1962.

57. McRuer, D. T. and Stapleford, R. L., "Power and Energy Requirements for a Fixed-Axis Inertia Wheel Attitude and Control System," ARS Journal, Vol. 31, 1961.

58. Ormsby, R. D., and Smith, M. C., "Capabilities and Limitations of Reaction Spheres for Attitude Control," ARS Journal, Vol. 31, June 1961.

59. Ormsby, R. D., "A Free Reaction Sphere Attitude Control System," Proc. IAS National Specialists Meeting on Guidance of Aerospace Vehicles, Boston, Mass., May 1960.

60. Pittman, W. C., "Dynamics of an Air-Supported Spherical Gyroscope," ARS Journal, July 1962.

61. Roberson, R. E., Editor., "Methods for the Control of Satellites and Space Vehicles - Vols. I and II," WADD 60-643, July 31, 1960.

62. Roberson, R. E., Leondes, C. T. and Aoki, M., "Analysis and Synthesis of a Particular Class of Satellite Attitude Control Systems - Parts I and II,"
Part I "System - Analysis Results"
Part II "Synthesis Results"
Journal of the Aerospace Sciences, December 1962.

63. Stuart, W. H., "Satellite Attitude Stabilization by Means of Flywheels," Aerospace Engineering, September 1961.

64. Taplin, L. B. and Teitelbaum, B. R., "The State-of-the-Art of Space Vehicle Attitude Control."

65. Wells, R. C., Sicko, J. S. and Courtney, F. M., "Gyroscopic Low Power Attitude Control for Space Vehicles," ASD-TDR-62-580, September 1962.

66. White, J. S. and Hansen, Q. M., "Study of Systems using Inertia Wheels for Precise Attitude Control of a Satellite," NASA D-691, April 1961.

67. White, J. S. and Hansen, Q. M., "Study of a Satellite Attitude Control System using Integrating Gyros as Torque Sources," NASA D-1073, September 1961.

68. Whitford, R. K., "Attitude Control of Earth Satellites," Control Engineering, February 1962.

69. Wing, W. G., "Pros and Cons on Fluid Rotor Gyros," Control Engineering, March 1963.

70. Broadwell, James E., "Analysis of the Fluid Mechanics of Secondary Injection for Thrust Vector Control," AIAA Journal, May 1963.

71. Chamay, A. J. and Sederquist, R. A., "An Experimental Investigation of Shock Vector Control with Gaseous Secondary Injection," ARS Paper No. 2216-61, 1961.

72. Walker, R. E., Stone, A. R. and Shandor, M., "Secondary Gas Injection in a Conical Rocket Nozzle," AIAA Journal, February 1963.

73. Bender, S. I., "Weight Factors in Rocket Vectoring," Astronautics and Aerospace Engineering, August 1963.

74. Karamcheti, K. and Hsia, H., "An Integral Approach to the Analysis of Thrust Vector Control by Secondary Injection," ARS Paper No. 2760-63, 1963.

75. Newton, J. R., Jr. and Spaid, F. W., "Interaction of Secondary Injectants and Rocket Exhaust for Thrust Vector Control," ARS Journal, August 1962.

76. Wu, J., Chapkis, R. L. and Mayer, A., "Approximate Analysis of Thrust Vector Control by Fluid Injection," ARS Journal, December 1961.

77. "Secondary Injection: Leading Technique for Thrust Vector Control," Space/Aeronautics, August 1962.

78. Green, C. J., "Fluid Injection Thrust Vector Control," Aerospace Fluid Power Conference, Detroit, Michigan, October 1962.

79. "A Study of Manual and Automatic Control Systems for the Terminal Phase of Orbital Rendezvous," ASD-TDR-62-82 June 1962.

80. Fenzel, L. R., Nichol, K. C. and Wood, L. R., "Research and Feasibility of Control Logic Techniques for Space Vehicle Attitude Controls," ASD-TDR-62-76, April 1962.

81. Gaylord, R. S. and Keller, W. N., "Attitude Control System Using Logically Controlled Pulses," ARS Guidance, Control and Navigation Conference, August 7-9, 1961.

82. Taylor, L. W.,Jr. and Smith, J. W., "An Analytical Approach to the Design of an Automatic Discontinuous Control System," NASA TN D-630, April 1961.

83. "Research Study to Determine Propulsion Requirements and Systems for Space Missions," Report No. 2150, Aerojet-General, December 1961.

84. Lineberry, E. C., Jr. and Foudriat, E. C., "Application of Describing Function Analysis to the Study of an On-Off Reaction Control System," NASA TN D-654, January 1961.

85. Brown, S. C., "Predicted Performance of On-Off Systems for Precise Satellite Attitude Control," NASA TN D-1040, July 1961.

86. Dahl, P. R., Herman and Aldrich, G. T., "Limit Cycles in Radiation Jet Attitude Control Systems Subject to External Torques," ASTIA AD 278162, April 1962.

87. Nicklas, J. C. and Vivian, H. C., "Derived-Rate Increment Stabilization: Its Application to the Attitude-Control Problem," JPL Tech. Report No. 32-69, July 31, 1961.

88. Rao, G. V. R., "Recent Developments in Rocket Nozzle Configurations," ARS Journal, November 1961.

89. Ahlberg, Hamilton, Migdal and Nilson, "Truncated Perfect Nozzles in Optimum Nozzle Design," ARS Journal, May 1961.

90. Barsere, Marcel, et.al., "Rocket Propulsion," Elsevies Publishing Company, New York, 1960.

APPENDIX I

ERROR ANALYSIS OF ORBITAL PLANE CORRECTION

It is desirable to know the effect of errors during the maneuver to eliminate the differential inclination of the vehicle and target orbital planes. Of most importance is the residual inclination which exists after the corrective maneuver; this analysis deals only with this facet.

From Figure 2-2 it can be deduced that the rotation of the velocity vector is defined by:

$$\psi = \arctan \frac{\Delta V_1 \cos \xi}{V_{ic} - \Delta V_1 \sin \xi} \tag{I-1}$$

As implied in Article 2.1.2, this equation becomes an identity when:

$$\Delta V_1 = 2 V_{ic} \sin \frac{\psi}{2} \tag{I-2}$$

$$\xi = \frac{\psi}{2} \tag{I-3}$$

To determine changes in ψ for small perturbations in ΔV_1 and ξ, the technique is used where partial differentiation is performed on Equation (I-1) about its optimum value.

Partial differentiation of Equation (I-1) gives:

$$\partial\psi = \frac{1}{1 + \left(\frac{\Delta V_1 \cos \xi}{V_{ic} - \Delta V_1 \sin \xi}\right)^2} \times \left[\frac{(V_{ic} - \Delta V_1 \sin \xi)(-\Delta V_1 \sin \xi \, \partial\xi) + (\Delta V_1 \cos \xi)}{(V_{ic} - \Delta V_1 \sin \xi)^2} \right.$$

$$\left. \frac{(\Delta V_1 \cos \xi \, \partial\xi)}{} + \frac{(V_{ic} - \Delta V_1 \sin \xi)(\partial \Delta V_1 \cos \xi) - (\Delta V_1 \cos \xi)(-\partial \Delta V_1 \sin \xi)}{(V_{ic} - \Delta V_1 \sin \xi)^2} \right] \tag{I-4}$$

Substitution of Equations (I-2) and (I-3) into Equation (I-4) results in:

$$\partial\psi = \frac{1}{1+\tan^2\psi}\left[\left(\frac{1-\cos\psi}{\cos^2\psi}\right)\partial\xi + \left(\frac{\cos\psi\cos\frac{\psi}{2}+\sin\psi\sin\frac{\psi}{2}}{\cos^2\psi}\right)\frac{\partial\Delta V_1}{V_{ic}}\right] . \quad \text{(I-5)}$$

Reducing Equation (I-5) and using δ for incremental notation gives:

$$\delta\psi = (1 - \cos\psi)\ \delta\xi + \cos\frac{\psi}{2}\ \frac{\delta(\Delta V_1)}{V_{ic}} . \quad \text{(I-6)}$$

APPENDIX II

LINEARIZATION OF RENDEZVOUS EQUATIONS

II.1 EQUATIONS OF MOTION

The equations for coplanar relative motion between two bodies can be written in polar coordinates as (refer to Subsection 2.2.3 and Figure 2-7):

$$\ddot{r} - r\,\dot{\gamma}^2 = a_r \tag{II-1}$$

$$r\ddot{\gamma} + 2\dot{r}\dot{\gamma} = a_n \tag{II-2}$$

The first step in linearizing these equations is to neglect certain cross-coupling terms. When considering the angular motion, it is assumed that $\ddot{r} \simeq 0$, with $\dot{r}$ assuming a constant value of $\dot{r}_o$. The motion along the line-of-sight is analyzed on the assumption that $r\dot{\gamma}^2 << a_r$. The equations of motion then become:

$$\ddot{r} = a_r \tag{II-3}$$

$$r\ddot{\gamma} + 2\dot{r}_o\dot{\gamma} = a_n \tag{II-4}$$

Consider first the angular motion of the line-of-sight. The expression for r is:

$$r = r_o + \dot{r}_o (t - t_o). \tag{II-5}$$

Substitution of Equation (II-5) into (II-4) gives

$$\ddot{\gamma} + \frac{2\dot{r}_o\dot{\gamma}}{r_o + \dot{r}_o \Delta t} = \frac{a_n}{r_o + \dot{r}_o \Delta t}, \tag{II-6}$$

where $\Delta t = t - t_o$.

Equation (II-6) is a linear differential equation with variable coefficients. The solution is:

$$\dot{\gamma} = \left(\frac{1}{r_o + \dot{r}_o \Delta t}\right)^2 \left[a_n \Delta t \left(r_o + \frac{\dot{r}_o}{2}\right) \Delta t + r_o^2 \dot{\gamma}_o\right], \qquad \text{(II-7)}$$

where $\dot{\gamma}_o$ is the angular rate prior to the application of a_n. Solving Equation (II-7) for Δt gives:

$$\Delta t = \left[1 - \sqrt{1 + \frac{(\dot{\gamma}_o - \dot{\gamma})\frac{2 r_o}{a_n}}{\tau_o + \frac{2 r_o \dot{\gamma}}{a_n}}}\right] \tau_o \, . \qquad \text{(II-8)}$$

When $\dot{\gamma} = \dot{\gamma}_b$, Δt becomes the thrusting time duration Δt_n for the normal correction. When $\dot{\gamma} = 0$, Equation (II-8) reduces to:

$$\Delta t_n = \tau_o \left(1 - \sqrt{1 + \frac{2 r_o \dot{\gamma}_o}{\tau_o a_n}}\right), \qquad \text{(II-9)}$$

where:

$$\tau_o = - \frac{r_o}{\dot{r}_o}$$

In Equation (II-8), an important parameter is seen to be r_o/a_n. Solving for r_o/a_n in terms of Δt_n gives:

$$\frac{r_o}{a_n} = \frac{\Delta t_n \left(1 - \frac{\Delta t_n}{2\tau_o}\right)}{\dot{\gamma}_b \left(1 - \frac{\Delta t_n}{\tau_o}\right)^2 - \dot{\gamma}_o} \qquad \text{(II-10)}$$

Close examination of Equations (II-8) and (II-10) reveals that when

$$\frac{r_o}{a_n} = -\frac{\tau_o}{2\dot{\gamma}_o} ,$$

$$\Delta t_n = \tau_o .$$

This means that the angular rate correction would not be completed until collision had occurred (providing that no range-rate corrections are made). It is therefore essential that:

$$\left|\frac{r_o}{a_n}\right| << \frac{\tau_o}{2\dot{\gamma}_o} \qquad \text{(II-11)}$$

It is also important to determine what happens to the relative motion during periods with no corrections. By conservation of angular momentum, the angular rate behaves as follows:

$$\dot{\gamma} = \left(\frac{r_1}{r}\right)^2 \dot{\gamma}_1 \qquad \text{(II-12)}$$

where r_1 is the range and $\dot{\gamma}_1$ is the residual angular rate at the termination of the last correction. It is seen that since r is decreasing, $\dot{\gamma}$ increases and will eventually have to be corrected again. It is obvious that a limit cycle could exist for $\dot{\gamma}$. The frequency of this limit cycle depends upon the guidance logic and the rate at which r decreases.

Further investigation of the angular rate limit cycle proceeds by writing Equation (II-12) as:

$$\dot{\gamma} = \frac{r_1^2 \dot{\gamma}_1}{\left[r_1 + \int_{t_b}^{t} \dot{r}\, dt\right]^2} \qquad \text{(II-13)}$$

Letting $\dot{r} = \dot{r}_1$, the expression becomes:

$$\dot{\gamma} = \frac{r_1^2 \dot{\gamma}_1}{\left[r_1 + \dot{r}_1 (t - t_b)\right]^2} \qquad \text{(II-14)}$$

Consider the situation at the initiation of the next correction, i.e., $\dot{\gamma} = \dot{\gamma}_o$ and $\tau_1 - \tau_o = t_o - t_b$. Equation (II-14) reduces to:

$$\frac{\dot{\gamma}_o}{\dot{\gamma}_1} = \left[\frac{\tau_1}{\tau_o}\right]^2 \qquad \text{(II-15)}$$

Equation (II-15) is a useful relationship between the control parameters of the range rate and angular rate control systems.

The motion along the line-of-sight is approximately described by Equation (II-3). Integration of this expression gives

$$\dot{r} = \dot{r}_o + a_r \Delta t \qquad \text{(II-16)}$$

$$r = r_o + \dot{r}_o \Delta t + \frac{1}{2} a_r (\Delta t)^2 \qquad \text{(II-17)}$$

The time-to-go parameter is:

$$\tau = -\frac{r}{\dot{r}} = -\frac{r_o + \dot{r}_o \Delta t + \frac{1}{2} a_r (\Delta t)^2}{\dot{r}_o + a_r \Delta t} \qquad \text{(II-18)}$$

Solving Equation (II-18) for Δt gives:

$$\Delta t = \frac{\left(1 - \frac{a_r \tau_o \tau}{r_o}\right) + \sqrt{1 - \frac{2 a_r \tau_o^2}{r_o} + \left(\frac{a_r \tau_o \tau}{r_o}\right)^2}}{\frac{a_r \tau_o}{r_o}} \qquad \text{(II-19)}$$

where:

$$\tau_o = -\frac{r_o}{\dot{r}_o}$$

For $\tau = \tau_b$, Equation (II-19) gives Δt_r, the pulse duration for range rate correction.

II.2 GUIDANCE EQUATIONS

In Subsection 2.2.4 the selected guidance logic was shown to require two continuous on-board computations. The associated equations were deliberately made simple so as to be easily handled by spaceborne computers. Justification for their use follows.

Equation (II-8) is an expression for the normal thrusting time. This equation is based upon a linearized analysis but is expected to have good accuracy. It is more complicated than is desirable for an on-board computation, so further linearization is in order. A binominal expansion of the square root term where all but the first two terms in the series are eliminated results in:

$$\Delta t_n = - \frac{(\dot{\gamma}_o - \dot{\gamma}_b)\, r_o\, \tau_o}{\tau_o + \frac{2\dot{r}_o \dot{\gamma}_b}{a_n}} \qquad \text{(II-20)}$$

Since we are really interested in an integrated accelerometer output, Equation (II-20) is rearranged to the following:

$$a_n \Delta t_n = - \frac{(\dot{\gamma}_o - \dot{\gamma}_b)\, r_o}{1 - \frac{2\dot{r}_o \dot{\gamma}_b}{a_n}} \qquad \text{(II-21)}$$

This equation is not particularly formidable, but the denominator is a little troublesome. Typical values of the denominator have been computed and tabulated below.

r_o	>75,000	15,000	1500
$\dot{\gamma}_b$	0.0004	0.0004	0.0004
$\dot{r}_o$	-1242	-375	-37.5
a_n	-13	-2	-0.150
$1 - \frac{2\dot{r}_o \dot{\gamma}_o}{a_n}$	0.924	0.850	0.800

The above results create the temptation to make the denominator of Equation (II-21) unity. The effect of doing this is investigated in the following paragraph.

Let the normal thrusting duration be dictated by:

$$\Delta t_n = - \frac{(\dot{\gamma}_o - \dot{\gamma}_b)\, r_o}{a_n} \qquad \text{(II-22)}$$

Let $\dot{\gamma}_b = \dot{\gamma}_1$ in Equation (II-8) and combine Equations (II-8) and (II-22) to eliminate Δt_n. The result can be arranged to give the "actual" $\dot{\gamma}$, e.g., $\dot{\gamma}_1$, existing after a correction for a given commanded value, $\dot{\gamma}_b$. This is written as:

$$\dot{\gamma}_1 = \frac{\dot{\gamma}_b a_n^2 + \frac{1}{2} \dot{r}_o a_n (\dot{\gamma}_o - \dot{\gamma}_b)^2}{\left[a_n - \dot{r}_o (\dot{\gamma}_o - \dot{\gamma}_b)\right]^2} \qquad \text{(II-23)}$$

Using the same parameter values as before, the results are as follows:

r_o	>75,000	15,000	15,000	1500
$\dot{\gamma}_o$	0.0010	0.0010	0.0010	0.0010
$\dot{\gamma}_b$	0.0004	0.0004	0.0004	0.0004
$\dot{r}_o$	-1242	-375	-375	-37.5
a_n	-13	-13	-2	-0.150
$\dot{\gamma}_1$	0.00046	0.00042	0.00053	0.00062

The deviation between $\dot{\gamma}_1$ and $\dot{\gamma}_b$ is particularly significant just after there has been a reduction in the normal thrust. This need not be serious, so long as the resulting coasting time is sufficiently long to allow adequate data smoothing. This appears to be the case. It is concluded that Equation (II-22) is adequate for on-board computation. (This conclusion was verified in computer runs. See Subsection 3.3.3).

Turning next to the longitudinal corrections, we have from Equation (II-19):

$$\Delta t_r = \frac{\left(1 - \frac{a_r \tau_o \tau_b}{r_o}\right) + \sqrt{1 - \frac{2a_r \tau_o^2}{r_o} + \left(\frac{a_r \tau_o \tau_b}{r_o}\right)^2}}{\frac{a_r \tau_o}{r_o}} \qquad \text{(II-24)}$$

Expanding the square root term in a binominal series and dropping all but the first two terms results in:

$$\Delta t_r = \frac{r_o}{a_r}\left[\frac{1}{\tau_o} - \frac{1}{\tau_b} + \frac{r_o}{2 a_r \tau_o^2 \tau_b}\right] \qquad \text{(II-25)}$$

Here again it is desirable to drop a rather complex term, the result being:

$$\Delta t_r = \frac{r_o}{a_r}\left[\frac{1}{\tau_o} - \frac{1}{\tau_b}\right] \qquad \text{(II-26)}$$

By setting $\tau_b = \tau_1$ in Equation (II-24) and combining Equations (II-24) and (II-26) to eliminate Δt_r, the following expression for τ_1 is obtained:

$$\tau_1 = \tau_b\left[1 + \frac{\dot{r}_o}{2\tau_o a_r} + \frac{r_o}{2a_r \tau_b^2}\right] \qquad \text{(II-27)}$$

Computations for the critical conditions reveals the following:

r_o	50,000	15,000	1500
$\dot{r}_o$	-1242	-375	-37.5
a_r	100	13	2
τ_o	40	40	40
τ_b	60	60	60
τ_1	55	48	52

The worst case allows eight seconds for data smoothing, which may be sufficient. If more smoothing time is required, τ_b can be increased at the expense of increasing the over-all maneuver time.

In conclusion, Equation (II-26) appears to provide an adequate firing command for the longitudinal engine. (This also was verified in Subsection 3.3.3.)

II.3 NOMENCLATURE

a_n = Acceleration created by transverse engine, ft/sec^2

a_r = Acceleration created by longitudinal engine, ft/sec^2

r = Range between vehicle and target during rendezvous, ft

r_o = Range at initiation of correction, ft

r_1 = Range at termination of correction, ft

$\dot{r}$ = Range rate, ft/sec

$\dot{r}_o$ = Range rate at the initiation of a correction, ft/sec

t = Time, sec

t_o = Total elapsed time at initiation of a correction, sec

t_b = Total elapsed time at termination of a correction, sec

Δt_n = Thrusting time of normal engine, sec

Δt_r = Thrusting time of longitudinal engine, sec

$\dot{\gamma}$ = Angular rate of rendezvous line-of-sight, rad/sec

$\dot{\gamma}_b$ = Desired or commanded angular rate at end of normal correction, rad/sec

$\dot{\gamma}_o$ = Angular rate at the initiation of a correction, rad/sec

$\dot{\gamma}_1$ = Actual angular rate at the termination of a normal correction, rad/sec

τ	=	Time-to-go parameter, $-r/\dot{r}$, sec
τ_b	=	Desired or commanded time-to-go at end of logitudinal correction, sec
τ_o	=	Time-to-go at the initiation of a correction, sec
τ_1	=	Actual time-to-go at the termination of a longitudinal correction, sec
$(\dot{})$	=	Denotes first derivative with respect to time
$(\ddot{})$	=	Denotes second derivative with respect to time

APPENDIX III

STATE-OF-THE-ART SURVEY OF RE-ENTRY ANALYSIS TECHNIQUES

III.1 BASIC ASSUMPTIONS

The assumptions commonly made in analytical studies of re-entry are:[24],[33]*

(1) The earth is a uniformly homogeneous, nonrotating sphere with the mass concentrated at the center.

(2) All trajectories lie in a plane containing the earth's center.

(3) Drag due to the atmosphere is negligible above 400,000 feet.

(4) Altitude of vehicle is negligible compared to radius of earth.

(5) Atmospheric density below 400,000 feet is given by:

$$\rho = \rho_B e^{-\beta h} \qquad \text{(III-1)}$$

where $\rho_B = \rho_{SL} = 0.00238$ slugs/ft^3

and $\beta = (1/24100)$ ft^{-1}

(6) Automatic re-entry control ceases at a vehicle velocity of 5000 fps and the pilot takes over to land the vehicle.

Assumption 2 is somewhat restrictive since it is possible that the mission requirements for an actual re-entry vehicle might call for a trajectory which at least partially follows a minor circle. However, following a minor circle trajectory requires that a continual side force be applied to the vehicle. Thus a great circle trajectory is a minimum energy trajectory. In addition, providing for other than great circle

---

* Numbers in parentheses refer to the reference listed in Section 10.

trajectories introduces mathematical complications which are probably best avoided until some of the more fundamental problems are solved.

The mathematical statement of assumption 4 is $r_e + h \approx r_e$. From this, it follows that $g \approx g_c$.

Assumption 5 is based on the atmosphere being isothermal and in hydrostatic equilibrium. Reference (24) shows the fit between the 1959 ARDC Model Atmosphere and Equation (III-1). The replacement of the 1959 ARDC Model Atmosphere by the 1962 U.S. Standard Atmosphere does not significantly change the accuracy of the fit.

III.2 FACTORS TO BE CONSIDERED DURING RE-ENTRY

There are several factors which must be considered during a re-entry study. These are for the most part related to the physical limitations of the vehicle or its contents.

The dynamic pressure is given by:

$$q = \frac{\rho V^2}{2} \qquad \text{(III-2)}$$

The value of q must not exceed the allowable value for the vehicle.

A similar limitation is that the maximum value of deceleration dV/dt must not exceed a given limit. The allowable limit on deceleration will undoubtably be that defined by the maximum which can be imposed upon the crew. Reference (34) gives a plot of time of useful consciousness versus acceleration level. This plot shows that although accelerations up to 10 or 12 g's can be withstood for short periods of time, accelerations must be limited to about 4 g's if consciousness is to be maintained for periods of time measured in minutes. Lesser values would be desirable from the standpoint of crew comfort and efficiency.

During the re-entry process, the various parameters associated with aerodynamic heating must be maintained within tolerable limits. Aerodynamic heating can be considered from the standpoint of: (1) the total heat input to the vehicle, (2) the time rate and maximum time rate of average heat input per unit area, and (3) the time rate and maximum time rate of local stagnation heat input per unit area. The values of these parameters and their allowable limits are quite sensitive to the actual construction of the vehicle and are thus difficult to handle during a general study except in a relative way.

III.3 EQUATIONS OF MOTION IN PITCH PLANE

The equations of motion in the pitch plane for a vehicle moving through a planetary atmosphere and following a great circle trajectory are:

$$m \frac{dV}{dt} = -D + mg \sin \theta \qquad \text{(III-3)}$$

$$-mV \frac{d\theta}{dt} = L - mg \cos \theta + \frac{mV^2 \cos \theta}{r} \qquad \text{(III-4)}$$

$$\frac{d^2 \gamma}{dt^2} = - \frac{M_p}{J_p} \qquad \text{(III-5)}$$

The derivation of Equations (III-3) and (III-4) is shown in Reference (35). Equation (III-5) is merely a statement of Newton's Law. The geometry of Equations (III-3) through (III-5) is shown in Figure 2-11. From this figure, it can be seen that:

$$\frac{d\gamma}{dt} = \frac{d\theta}{dt} + \frac{V \cos \theta}{r} - \frac{d\alpha}{dt} \qquad \text{(III-6)}$$

III.4 TRAJECTORY OF RE-ENTERING VEHICLE

If the vehicle is considered to be a point mass, Equations (III-3) and (III-4) define the pitch plane trajectory followed by the vehicle during re-entry. Various assumptions have been made in order to obtain solutions to these equations. Many of these solutions are based on negligible lift (ballistic entry) or on constant L/D ratio and are thus of little interest to the present investigation. Results based on zero lift and constant L/D are given in References (27), (36), and (37).

Various solutions for entry with variable values of L/D and constant values of $C_D A_R/m$ are reported in References (38) and (39). The solutions in Reference (38) are approximate, but apply to minor circle trajectories. The solutions given in Reference (39) are exact, but apply only to great circle trajectories. If the equations of Reference (38) are applied to great circle trajectories, the estimated error is < 6.2 percent for $V > 5000$ fps.

The solutions from References (38) and (39) cover the following cases:

(1) Constant dynamic pressure, ρV^2 = constant.

(2) Constant rate of average heat input per unit area or constant average equilibrium skin temperature, ρV^3 = constant.

(3) Constant rate of stagnation point heat input per unit area or constant stagnation radiation equilibrium temperature, ρV^6 = constant.

(4) Constant angle of inclination, θ = constant.

Reference (38) also includes:

(5) Constant rate of descent, dh/dt = constant.

One feature of interest is that re-entry at constant aerodynamic load (ρV^2 = constant) with $C_D A_R/m$ constant approximates re-entry at constant deceleration quite closely. In fact, with the approximate solutions given,[38] there is no difference for the two cases.

Since deceleration and dynamic pressure are two of the parameters which will have to be maintained during re-entry, the fact that holding one constant will tend to hold the other constant is of importance. Since these two parameters are fairly easy to measure, it is probable that one or the other will be the measured variable of the final control system selected.

III.5 DYNAMIC STABILITY OF RE-ENTERING VEHICLE

In order to take the pitch plane dynamic stability of the re-entering vehicle into account, Equation (III-5) and hence, Equation (III-6) must be used with Equations (III-3) and (III-4). This set of equations is sufficiently complex to preclude analytical solution without resorting to extreme simplifications.

By making the substitutions:

$$D = C_D q A_R = \frac{C_D \rho V^2 A_R}{2} \qquad \text{(III-7)}$$

$$L = C_L q A_R = \frac{C_L \rho V^2 A_R}{2} \qquad \text{(III-8)}$$

$$M_p = Fy + C_M q b A_R = \frac{C_M \rho V^2 b A_R}{2} \qquad \text{(III-9)}$$

into Equations (III-3), (III-4), and (III-5) we obtain:

$$m \frac{dV}{dt} = - \frac{C_D A_R \rho V^2}{2} + mg \sin\theta \qquad \text{(III-10)}$$

$$-mV \frac{d\theta}{dt} = \frac{C_L A_R \rho V^2}{2} - mg \cos\theta + \frac{mV^2 \cos\theta}{r} \qquad \text{(III-11)}$$

$$\frac{d^2\gamma}{dt^2} = - \frac{C_M \rho b A_R V^2}{2 J_p} - \frac{Fy}{J_p} \qquad \text{(III-12)}$$

Ideally, C_D and C_L would be functions of α only, while C_M would be a function of δ_e and α. If this were true, a fairly straightforward block diagram for the re-entering vehicle could be drawn. Unfortunately, C_L, C_D, and C_M are functions of α, V, ρ, δ_e, γ, dV/dt, $d\alpha/dt$, $d\delta_e/dt$, and probably other parameters. To take all these effects into account would seem to be impractical. Thus a decision must be made as to which can be safely ignored. It can be assumed that:

$$C_L = f_L (\alpha, M, \delta_e) \qquad \text{(III-13)}$$

$$C_D = f_D (\alpha, M, \delta_e) \qquad \text{(III-14)}$$

$$C_M = f_M (\alpha, M, \delta_e, \frac{d\alpha}{dt}) \qquad \text{(III-15)}$$

From Figure 2-11, it can be seen that:

$$\frac{dh}{dt} = V \sin\theta \qquad \text{(III-16)}$$

Also:

$$\frac{dM}{dt} = \frac{b}{a} \frac{dV}{dt} \qquad \text{(III-17)}$$

A block diagram describing the motion of the vehicle in the pitch plane can be constructed from Equations (III-1), (III-6), (III-10), (III-11), (III-12), (III-13), (III-14), (III-15), (III-16), and (III-17). This block

diagram abounds in non-linearities and feedbacks. Considerable simplification is required before the system represented by these equations can be treated analytically or even inserted in a analog computer. This simplification and the assigning of values to certain constants requires aerodynamic data on re-entry configurations at hypersonic velocities.

III.6 AERODYNAMIC HEATING

Aerodynamic heating is quite sensitive to the characteristics of both the trajectory and the vehicle. Thus, for the purposes of this study, heating need be considered only in a very relative fashion. The investigation of heating effects only have to be carried as far as is necessary to show that the trajectory selected does not have obviously impractical heat rates and inputs associated with it.

A fairly complete review of the subject of aerodynamic heating is contained in References (1), (40), and (41). Three types of heat inputs may be encountered during re-entry. These are:

(1) laminar convection

(2) turbulent convection

(3) radiation

Radiation heating is an important factor during entry at escape velocity. However, at satellite velocity, radiation heating is a small fraction of the convective heating. The ratio of radiation heat flux to laminar stagnation heat flux decreases with decreasing entry angle, decreasing $m/C_D A_R$, and increasing L/D. It appears that radiation heating would at most be a few percent of the convective heating for the vehicle in this study. Hence radiation heating can be neglected.

In the initial stages of re-entry, Reynolds numbers are low and laminar heating prevails. At the stagnation point, Reference (25) gives the following expression for laminar convective heat flux:

$$Q = 865 \frac{V^{3.15}}{10^4} \sqrt{\frac{\frac{\rho}{\rho_{SL}}}{R_n}} \qquad \text{(III-18)}$$

Convective heating at points away from the nose and leading edge will be significantly less than the value given by Equation (III-18).

The following general statements may be made regarding convective heating at satellite velocities.

(1) Both the laminar and turbulent convective heating rates increase as θ increases but the total time-integrated convective input decreases.

(2) An increase in $m/C_D A_R$ increases both the total time-integrated convective heat input and the convective heat input rates.

(3) Increasing L/D decreases convective heat input rates but increases total time-integrated convective heat input.

III.7 NOMENCLATURE

A_R = Reference area - ft^2

a = Local speed of sound - fps

b = Reference length for moment coefficient evaluation - ft

C_D = Gasdynamic drag coefficient - dimensionless

C_L = Gasdynamic lift coefficient - dimensionless

C_M = Pitching moment coefficient - dimensionless

D = Drag force - lbs

e = Base of natural logarithms - dimensionless

F = Reaction controller thrust - lbs

g = Gravitational acceleration - ft/sec^2

g_c = Gravitational acceleration at sea level = 32.174 fps

h = Geometric altitude - ft

J_p = Pitching moment of inertia about center of gravity - $ft\text{-}lb\text{-}sec^2/rad$

L = Lift force - lbs

m = Vehicle mass - slugs

M_p = Summation of pitching moments about center of gravity - ft-lbs

M = Mach number - dimensionless

q = Dynamic pressure - psf

r = Distance from vehicle to center of earth - ft

r_e = Radius of earth - ft

R_n = Radius of nose of vehicle - ft

S = Distance along flight path - ft

t = Time - sec

V = Vehicle velocity - ft/sec

y = Moment arm through which reaction controller operates - ft

α = Angle of attack - radians

β = Exponential factor used in Equation (III-1)(1/24.100) ft^{-1}

γ = Angle of pitch measured from inertial axis system - radians

δ_e = Elevator deflection - radians

ϵ = Angle defined by Figure 2-11 - radians

θ = Path angle with horizontal - radians

ρ = Atmospheric density - slugs/ft^3

ρ_{SL} = Atmospheric density at sea level = 0.00238 slugs/ft^3

ρ_B = Base density used in Equation (III-1)-slugs/ft^3

APPENDIX IV

ANALYSIS OF VEHICLE INERTIA

IV.1 WEIGHT DISTRIBUTION

Some estimate of the moments of inertia of the vehicle must be made in order to analyse the moment requirements. The estimate of the moments of inertia is dependent upon the way in which the weight is distributed among the various parts of the vehicle.

It will be assumed that the vehicle weighs 100,000 pounds at re-entry and prior to orbit contains 100,000 pounds of propellant with a specific impulse of 400 seconds. This is slightly less than the theoretical value which can be obtained with a hydrogen-oxygen rocket engine operating with an oxygen-fuel (O/F) ratio of 3.54 and a propellant bulk density of 0.264 g/cc. It should be noted that although this O/F ratio corresponds to the maximum specific impulse, an actual system would use a higher O/F ratio to obtain a better density impulse. Ten percent additional propellants will be assumed for ullage and reserve.

The initial weight of liquid oxygen will be

$$W_o = 100{,}000 \times 1.10 \times \frac{3.54}{(3.54 + 1)} = 85{,}800 \text{ lbs}$$

the initial weight of liquid hydrogen will be

$$W_h = 100{,}000 \times 1.10 \times \frac{1}{(3.54 + 1)} = 24{,}200 \text{ lbs}$$

Typically, liquid oxygen tankage may be expected to weigh on the order of 0.2 lb/lb O_2 and liquid hydrogen tanks may be expected to weigh on the order of 1.0 lb/lb H_2. Thus we have:

$$W_{to} = 0.2 \times 85{,}800 = 17{,}200 \text{ lbs}$$

and

$$W_{th} = 1.0 \times 24{,}200 = 24{,}200 \text{ lbs}$$

If the wing and structure is assumed to weigh 2.5 lbs/ft^2 of wing, we have

$$W_s = 2.5\ A_R = 2.5 \times 14{,}500 = 36{,}200 \text{ lbs}$$

A weight, W_e, of 4400 pounds will be assumed for the main propulsion engine. The other attitude control and thrust engines will be assumed to be covered by the weight allowance for the structure. Thus we have:

W_o	=	85,800 lbs
W_h	=	24,200
W_{to}	=	17,200
W_{th}	=	24,200
W_s	=	36,200
W_e	=	4,400
TOTAL		192,000 lbs

Thus a weight of 8000 pounds is left for the payload and power system weight, W_p.

IV.2 DIMENSIONS OF VEHICLE

It has already been assumed that the vehicle is a delta winged glider 200 feet long with a sweepback angle $\Lambda = 70$ degrees. An actual vehicle will not have a perfectly triangular platform, however. NASA has tested wings with taper ratios $\lambda = c_t/c_r$ of 0.174 to 0.296. It appears reasonable to say that the tip chord, c_t, should at least be as long as any trailing edge flap which may be used. The model used in Ref. (19)* had a trailing edge flap with an area 36 percent of the total wing area. This is admittedly larger than practical and may thus be used as a basis for selecting the maximum length of a trailing edge flap.

The following dimensions were selected for the wing:

Root chord	c_r = 204 ft
Tip chord	c_t = 41 ft
Taper ratio	$\lambda = c_t/c_r = 0.2$
Wing span	b = 119 ft

*Numbers in parentheses refer to the references listed in Section 10.

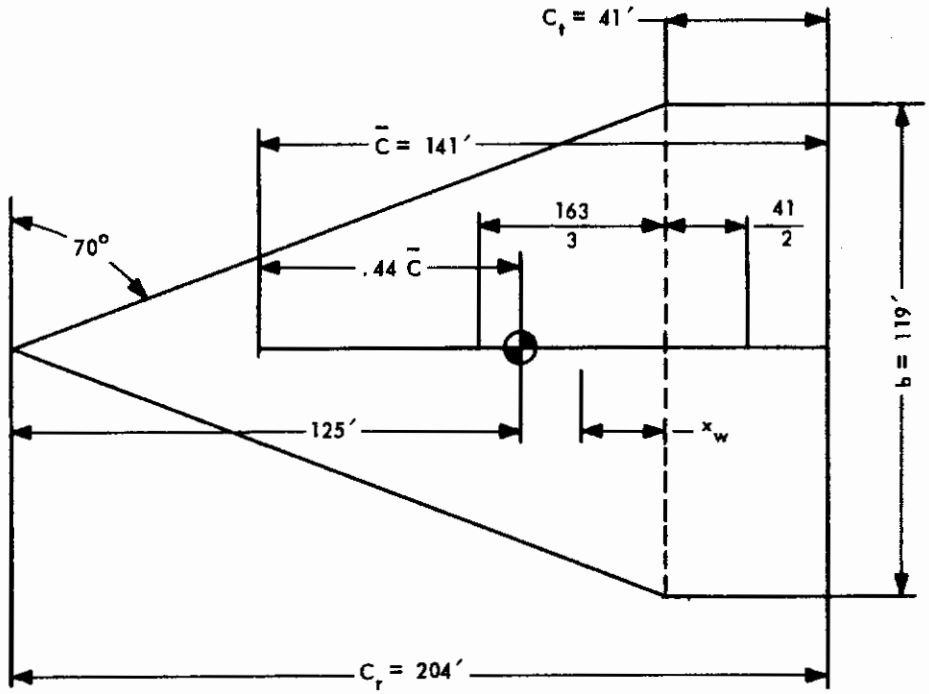

Figure IV-1 - Wing Dimensions

These are illustrated in Figure IV-1. From these dimensions the total wing area may be computed to be 14,600 ft^2. If the maximum trailing edge flap length is taken as being equal to the tip chord, the maximum area of the trailing edge flap will be 33 percent of the total wing area.

Two parameters frequently used in correlating aerodynamic data are the aspect ratio, b^2/A_R and the mean aerodynamic chord which from Ref. (32) is for a trapezoidal wing:

$$\bar{c} = \frac{2}{3} c_r \left[\frac{1 + \lambda + \lambda^2}{\lambda} \right] \qquad \text{(IV-1)}$$

For the dimensions selected, aspect ratio = 0.97 and $\bar{c}$ = 141 ft.

The trajectory computations reported in Subsection 3.4.1 were based on aerodynamic data.[19] This reference considered center of moment locations of 0.42 to 0.45 $\bar{c}$. The center of gravity of the hypothetical vehicle for this study has been located 125 feet from the nose. This corresponds to the 0.44 $\bar{c}$ position.

The 110,000 pounds of propellants carried by the vehicle at the beginning of the mission have a bulk density of 0.264 grams/cc and hence occupy a volume of 6690 ft^3. If the propellants are carried in cylindrical tanks with a diameter of 9 feet, a total tank length of 105 ft will be required. It would be extremely desirable to minimize the displacements of the vehicle center of gravity as the propellants are expended. Hence, the center of gravity of the tanks should coincide with center of gravity of the vehicle as closely as possible. Additionally, the hydrogen and oxygen compartments within the tanks should be located as symmetrically as possible. There appears to be no essential difficulty in locating the tank cg at the vehicle cg in the plane of the wing. However, if the wing is to be flat-bottomed, the tank cg must be located above the vehicle cg along the yaw axis. The weight of the structure, engine, and payload is $W_s + W_e + W_p = 48{,}600$ pounds. The cg of this portion of the vehicle will lie in the plane of the wing. If the tanks are to be located entirely above the wing platform, the cg of tanks and propellants will be a tank radius of 4.5 feet above the wing platform. The weight of tank and propellants is

$$W_h + W_o + W_{to} + W_{th} = 151{,}400 \text{ lbs.}$$

After the 100,000 pounds of propellants have been used the tank and propellant weight will be 51,400 pounds. This is illustrated in Figure IV-2. From this figure it can be ascertained that the location of the over-all cg of the vehicle along the yaw axis measured from the wing platform $\bar{z}_y$ will be 3.41 feet with full propellant tanks and 2.31 feet with empty tanks. Thus the total excursion of the cg will be 1.10 feet along the yaw axis as the 100,000 pounds of propellants are used. This does not seem to be too unreasonable. Since some constructional tolerances will be required, the actual movement of the cg used in calculations should be somewhat greater to be conservative.

From Figure IV-1, it can be calculated that the triangular portion of the wing has an area of 9700 ft^2 and the rectangular portion, an area of 4800 ft^2. The centroid of the triangular area will be located a distance of (204-41)/3 ft from the junction of the two wing sections. The centroid of the rectangular section of the wing will be 4 1/2 feet on the other side of the junction. Then from Figure IV-1 it can be seen that the centroid of the over-all wing will be located a distance x_w from the junction of the triangular and rectangular sections, where x_w is given by:

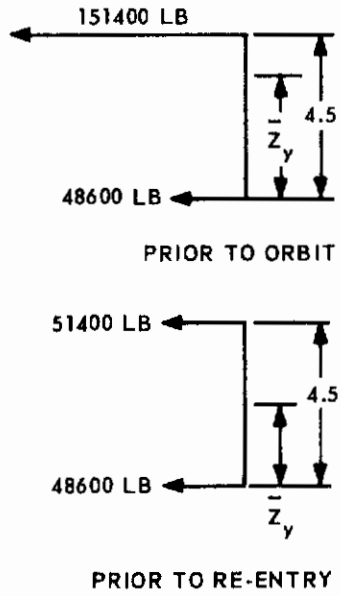

Figure IV-2 - Vertical Location of Vehicle CG

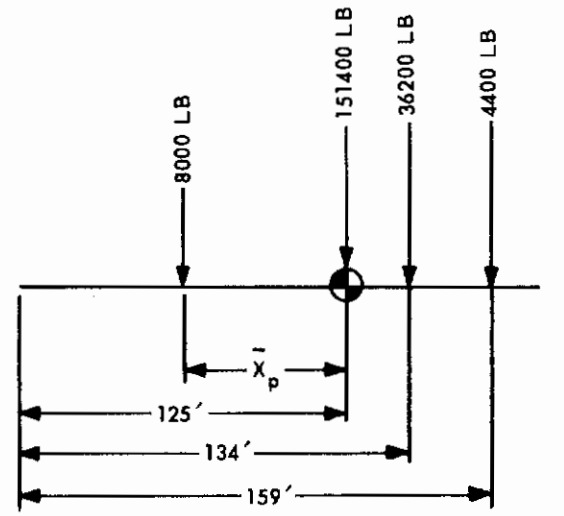

Figure IV-3 - Axial Location of Payload

$$x_w = \frac{\frac{(204 - 41)}{3} \times 9700 - \frac{41}{2} \times 4880}{9700 + 4880}$$

From which x_w = 29.2 feet.

The payload and engine must be located along the root chord in order to bring the over-all vehicle cg to its desired position 125 feet aft of the nose. The engine has been located 165 feet from the nose. Thus the location, $\bar{x}_p$, of the payload forward of the desired cg position is obtained from Figure IV-3.

$$\bar{x}_p = \frac{W_s (163 - 29 - 125) + W_e (165 - 125)}{W_p}$$

With W_s = 36,200 lbs, W_e = 3700 lbs, and W_p = 8000 lbs, $\bar{x}_p$ = 59.3 ft.

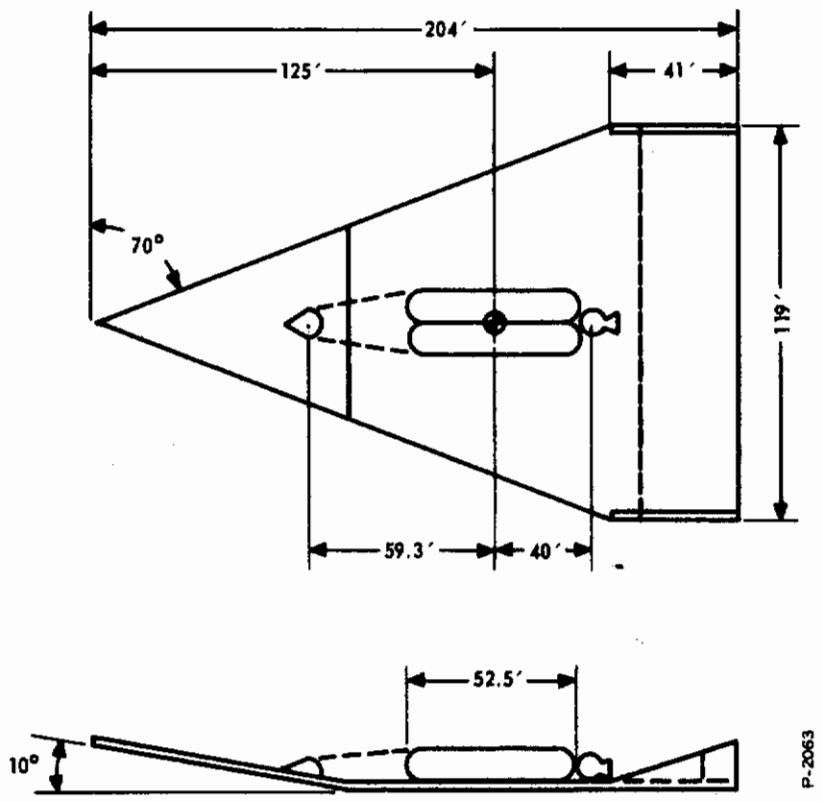

Figure IV-4 - Vehicle Configuration Schematic Diagram

A sketch of the hypothetical vehicle incorporating the results of the estimates made in this analysis is presented in Figure IV-4. In order for the cg of the propellant tanks to coincide with the vehicle cg in the wing plane, the total tank length required has been obtained with a side-by-side arrangement. A 10 degree nose incidence as indicated by Ref. (19) has been shown.

IV.3 ESTIMATE OF PRINCIPAL MOMENTS OF INERTIA

For purposes of estimating moments of inertia, the nose incidence and shift of the vehicle cg will be neglected. The vehicle cg will thus be assumed to be at its average position and a value of $\bar{z}_y$ = (3.41 + 2.31)/2 = 2.86 feet will be used. The propellant tanks will be considered as perfectly homogeneous bodies.

The moments of inertia in pitch are as follows:

$$J_{pp} = W_p (\bar{x}_p^2 + \bar{z}_y^2)$$

$$J_{pp} = 8000 (59.3^2 + 2.86^2) = 28.2 \times 10^6 \text{ lb-ft}^2$$

$$J_{pe} = W_e (\bar{x}_e^2 + \bar{z}_y^2)$$

$$J_{pe} = 3700 \left[(165 - 125)^2 + 2.86^2 \right] = 6.2 \times 10^6 \text{ lb-ft}^2$$

$$J_{pt}^* = \frac{b(c_r - c_t)^3 \sigma_w}{3}$$

$$J_{pt}^* = \frac{119 \times (204 - 41)^3 \times 2.5}{36} = 36.4 \times 10^6 \text{ lb-ft}^2$$

$$J_{pt} = J_{pt}^* + \left\{ \left[\frac{2}{3} (c_r - c_t) - \bar{x}_c \right]^2 + \bar{z}_y^2 \right\} \frac{b(c_r - c_t) \sigma_w}{2}$$

$$J_{pt} = 36.4 \times 10^6 + \left\{ \left[\frac{2}{3} (204 - 41) - 125 \right]^2 + 2.86^2 \right\} \frac{119(204 - 41 \times 2.5}{2}$$

$$J_{pt} = 42.8 \times 10^6 \text{ lb-ft}^2$$

$$J_{pr}^* = \frac{c_t^3 b \sigma_w}{12} = \frac{41^3 \times 119 \times 2.5}{12} = 1.7 \times 10^6 \text{ lb-ft}^2$$

$$J_{pr} = J_{pr}^* + c_t b \sigma_w \left\{ \left[\frac{c_t}{2} + (c_r - c_t) - \bar{x}_c \right]^2 + \bar{z}_y^2 \right\}$$

$$J_{pr} = 1.7 \times 10^6 + 41 \times 119 \times 2.5 \left\{ \left[\frac{41}{2} + (204 - 41) - 125 \right]^2 + 2.86^2 \right\}$$

$$J_{pr} = 43.6 \times 10^6 \text{ lb-ft}^2$$

$$J_{p\ell} = (W_o + W_h + W_{to} + W_{th}) \left[r^2 + \frac{a_T^2}{3} \right] \times \frac{1}{4}$$

$$J_{p\ell} = \frac{151000}{4} \left[4.5^2 + \frac{52.5^2}{3} \right] = 35.4 \times 10^6 \text{ lb-ft}^2$$

$$J_{p\ell} = J_{p\ell}^* + (W_o + W_h + W_{to} + W_{th}) \left[r^2 + (r - \bar{z}_y)^2 \right]$$

$$J_{p\ell} = 35.4 + 151000\left[4.5^2 + (4.5 - 2.86)^2\right]$$

$$J_{p\ell} = 38.9 \times 10^6 \text{ lb-ft}^2$$

$$J_{pc} = \frac{W_{to} + W_{th}}{W_o + W_h + W_{to} + W_{th}} \times J_{p\ell}$$

$$J_{pc} = \frac{51000}{151000} \times 38.9 \times 10^6 = 13.2 \times 10^6 \text{ lb-ft}^2$$

$$J_{pv\ell} = J_{pp} + J_{pe} + J_{pt} + J_{pr} + J_{p\ell}$$

$$J_{pv\ell} = (28.2 + 6.2 + 42.8 + 43.6 + 38.9) \times 10^6$$

$$J_{pv\ell} = 159 \times 10^6 \text{ lb-ft}^2 = \underline{4.94 \times 10^6} \text{ lb-ft-sec}^2$$

$$J_{pve} = J_{pp} + J_{pe} + J_{pt} + J_{pr} + J_{pc}$$

$$J_{pve} = (28.2 + 6.2 + 42.8 + 43.6 + 13.2) \times 10^6$$

$$J_{pve} = 133 \times 10^6 \text{ lb-ft}^2 = \underline{4.13 \times 10^6} \text{ lb-ft-sec}^2$$

The moments of inertia in roll are as follows:

$$J_{rp} = W_p \bar{z}_y^2$$

$$J_{rp} = 8000 \times 2.86^2 = 0.0655 \times 10^6 \approx 0.1 \times 10^6 \text{ lb-ft}^2$$

$$J_{re} = W_e \bar{z}_y^2$$

$$J_{re} = 4400 \times 2.86^2 = 0.0360 \times 10^6 \text{ lb-ft}^2 \approx 0$$

$$J_{rt}^* = \frac{2\,\sigma_w (c_r - c_t)\left(\frac{b}{2}\right)^3}{12}$$

$$J_{rt}^* = \frac{2 \times 2.5\,(204 - 41)\left(\frac{119}{2}\right)^3}{12} = 14.3 \times 10^6 \text{ lb-ft}^2$$

$$J_{rt} = J_{rt}^{*} + \frac{\sigma_w (c_r - c_t) b}{2} \bar{z}_y^2$$

$$J_{rt} = 14.3 \times 10^6 + \frac{2.5 (204 - 41) 119}{2} \times 2.86^2 = 14.5 \times 10^6 \text{ lb-ft}^2$$

$$J_{rr}^{*} = \frac{c_t b^3 \sigma_w}{12}$$

$$J_{rr}^{*} = \frac{41 \times 119^3 \times 2.5}{12} = 14.3 \times 10^6 \text{ lb-ft}^2$$

$$J_{rr} = J_{rr}^{*} + c_t b \sigma_w \bar{z}_y^2$$

$$J_{rr} = 14.3 \times 10^6 + 41 \times 119 \times 2.5 \times 2.86^2 = 14.4 \times 10^6 \text{ lb-ft}^2$$

$$J_{r\ell} = \frac{(W_o + W_h + W_{to} + W_{th}) r^2}{2}$$

$$J_{r\ell}^{*} = \frac{151000}{2} \times 4.5^2 = 1.5 \times 10^6 \text{ lb-ft}^2$$

$$J_{r\ell} = J_{r\ell}^{*} + (W_o + W_h + W_{th}) \left[r^2 + (r - z_y)^2 \right]$$

$$J_{r\ell} = 1.5 \times 10^6 + 151000 \left[4.5^2 + (4.5 - 2.86)^2 \right]$$

$$J_{r\ell} = 5.0 \times 10^6 \text{ lb-ft}^2$$

$$J_{rc} = \left[\frac{W_{to} + W_{th}}{W_o + W_h + W_{to} + W_{th}} \right] I_{r\ell}$$

$$J_{re} = \frac{51000}{151000} \times 5.0 \times 10^6 = 1.7 \times 10^6 \text{ lb-ft}^2$$

$$J_{rv\ell} = J_{rp} + J_{re} + J_{rt} + J_{rr} + J_{r\ell}$$

$$J_{rv\ell} = (0.1 + 0 + 14.5 + 14.4 + 5.0) \times 10^6$$

$$J_{rv\ell} = 34.0 \times 10^6 \text{ lb-ft}^2 = \underline{1.06 \text{ lb-ft-sec}^2}$$

$$J_{rve} = J_{rp} + J_{re} + J_{rt} + J_{rr} + J_{re}$$

$$J_{rve} = (0.1 + 0 + 14.5 + 14.4 + 1.7) \times 10^6$$

$$J_{rve} = 30.7 \times 10^6 \text{ lb-ft}^2 = \underline{0.95 \times 10^6} \text{ lb-ft-sec}^2$$

The moments of inertia in yaw are as follows:

$$J_{yp} = J_{pp} = 28.2 \times 10^6 \text{ lb-ft}^2$$

$$J_{ye} = J_{pe} = 6.2 \times 10^6 \text{ lb-ft}^2$$

$$J_{yt}^* = J_{pt}^* + J_{rt}^* = (36.4 + 14.3) \times 10^6 = 50.7 \times 10^6 \text{ lb-ft}^2$$

$$J_{yt} = J_{yt}^* + \left[\frac{2}{3}(c_r - c_t) - x_c\right]^2 \frac{(c_r - c_t)\, b\, \sigma_w}{2}$$

$$J_{yt} = 50.7 \times 10^6 + \left[\frac{2}{3}(204 - 41) - 125\right]^2 \frac{(204 - 41) \times 119 \times 2.5}{2}$$

$$J_{yt} = 56.9 \times 10^6 \text{ lb-ft}^2$$

$$J_{yr}^* = J_{pr}^* + J_{rr}^* = (1.7 + 14.3) \times 10^6 = 16.0 \times 10^6 \text{ lb-ft}^2$$

$$J_{yr} = J_{yr}^* + c_t\, b\, \sigma_w \left[\frac{c_t}{2} + c_r - c_t - x_c\right]^2$$

$$J_{yr} = 16.0 \times 10^6 + 119 \times 41 \times 2.5 \left[\frac{41}{2} + (204 - 41 - 125)\right]^2$$

$$J_{yr} = 57.7 \times 10^6 \text{ lb-ft}^2$$

$$J_{y\ell}^* = J_{y\ell}^* = 35.4 \times 10^6 \text{ lb-ft}^2$$

$$J_{y\ell} = J_{y\ell}^* + 4.5^2 (W_o + W_h + W_{to} + W_{th})$$

$$J_{y\ell} = 35.4 \times 10^6 + 4.5^2 \times 151000$$

$$J_{y\ell} = 38.5 \times 10^6 \text{ lb-ft}^2$$

$$J_{yc} = \left[\frac{W_{to} + W_{th}}{W_o + W_h + W_{to} + W_{th}}\right] J_{y\ell}$$

$$J_{yc} = \frac{51000}{151000} \times 38.5 \times 10^6 = 13.0 \times 10^6 \text{ lb-ft}^2$$

$$J_{yv\ell} = (J_{yp} + J_{ye} + J_{yt} + J_{yr} + J_{y\ell})$$

$$J_{yv\ell} = (28.2 + 6.2 + 56.9 + 57.7 + 38.5) \times 10^6$$

$$J_{yv\ell} = 186 \times 10^6 \text{ lb-ft}^2 = \underline{5.78 \times 10^6} \text{ lb-ft-sec}^2$$

$$J_{yve} = (J_{yp} + J_{ye} + J_{yt} + J_{yr} + J_{yc})$$

$$J_{yve} = (28.2 + 6.2 + 56.9 + 57.7 + 13.0) \times 10^6$$

$$J_{yve} = 161 \times 10^6 \text{ lb-ft}^2 = \underline{5.00 \times 10^6} \text{ lb-ft-sec}^2$$

IV.4 CONCLUSIONS

The ranges of the principal moments of inertia of the vehicle as determined by full and empty fuel tanks are:

$$J_p = 4.94 \times 10^6 \text{ lb-sec}^2\text{-ft} \text{ to } 4.13 \times 10^6 \text{ lb-sec}^2\text{-ft}$$

$$J_y = 5.78 \times 10^6 \text{ lb-sec}^2\text{-ft} \text{ to } 5.00 \times 10^6 \text{ lb-sec}^2\text{-ft}$$

$$J_r = 1.06 \times 10^6 \text{ lb-sec}^2\text{-ft} \text{ to } 0.95 \times 10^6 \text{ lb-sec}^2\text{-ft}$$

The center of gravity moves 1.10 feet along the yaw axis as the 100,000 pounds of propellant are used up.

IV.5 NOMENCLATURE

a_T = Propellant tank length - ft

A_R = Reference or wing area - ft

b = Wing span - ft

$\bar{c}$ = Mean aerodynamic chord - ft

c_r = Root chord - ft

c_t = Tip chord - ft

J = Moment of inertia - lb-ft-sec^2 (see below for subscripts)

r = Propellant tank radius - ft

W = Weight - lb (see below for subscripts)

x_w = Axial distance of centroid of wing from junction of triangular and sections - ft

$\bar{x}$ = Distance along roll axis from vehicle center of gravity - ft (see below for subscripts)

$\bar{z}_y$ = Distance of vehicle center of gravity from wing along yaw axis - ft

λ = Taper ratio - dimensionless

Λ = Sweepback angle - degrees

σ_w = Weight of wing per unit area - lb/ft^2

Subscripts for W

o = Weight of oxygen

h = Weight of hydrogen

to = Weight of oxygen tank

th = Weight of hydrogen tank

e = Weight of main engine

s = Weight of wing and structure

p = Weight of payload and power system

Subscripts for $\bar{x}$

c = Distance of cg from nose

e = Distance of main engine from cg

p = Distance of payload from cg

Subscripts for J

$\underline{p}$ = Pitch

$\underline{y}$ = Yaw

$\underline{r}$ = Roll

$\underline{\underline{p}}$ = Payload

$\underline{\underline{e}}$ = Engine

$\underline{\underline{t}}$ = Triangular section of wing

$\underline{\underline{r}}$ = Rectangular section of wing

$\underline{\underline{\ell}}$ = Loaded tanks

$\underline{\underline{c}}$ = Empty tanks

$\underline{\underline{v\ell}}$ = Vehicle with full propellant tanks

$\underline{\underline{ve}}$ = Vehicle with empty propellant tanks

*Superscript denotes that J is taken about cg of individual component. J without * superscript denotes that J is taken about cg of vehicle.

APPENDIX V

GUIDANCE ENGINE ORIENTATION

V.1 ENGINE SIZES

The thrust levels required for vehicle guidance at various times during the flight are:

(a) 400,000 lbs
(b) 50,000 lbs
(c) 8,000 lbs
(d) 600 lbs

The 400,000-pound thrust is used for plane change, orbital transfer and re-entry de-boost, while all thrust levels are required during the rendezvous maneuver. During rendezvous the following thrust combinations are required:

(a)	Longitudinal thrust:	400,000 lbs
	Normal thrust:	50,000 lbs
(b)	Longitudinal thrust:	50,000 lbs
	Normal thrust:	8,000 lbs
(c)	Longitudinal thrust:	8,000 lbs
	Normal thrust:	600 lbs

V.2 POSSIBLE LAYOUTS

For the thrust requirements defined above, the logical guidance engine locations are shown in Figure V-1. This arrangement requires at least six engines, assuming that constant thrust engines are used. This arrangement is the least demanding on the attitude control system because no vehicle rotations are required prior to changing thrust magnitude.

A second possible engine arrangement is described by Figure V-2. Here we see that the minimum number of engines has dropped to four, since the orthogonal guidance channels share engines. The disadvantage of this arrangement is that each change in thrust level must be preceded by a 90 degree pitch rotation and a 180 degree rotation about the yaw or

roll axis. Since these rotations must be fast, so as not to jeopardize the maneuver, large attitude control engines must be used.

A compromise between engine Layouts "A" and "B" is to use the five thrust vectors shown in Figure V-3. This is a better arrangement than Layout "A" because only one 50,000 pound engine is used, however a 90 degree pitch rotation is required prior to engine changes.

V.3 THRUST VECTOR MISALIGNMENTS

It is highly unlukely that the guidance engines and vehicle structure can be so mated that the thrust vectors always pass through the vehicle center of gravity. The firing of the guidance engines, therefore, produces disturbance torques which must be counteracted by the attitude control system. Table V-1 contains the estimated maximum moment arms which could exist and the resulting disturbance torques exerted on the vehicle for each of the various engines.

Table V-1 - Engine Misalignment Estimates

Engine Size, lb	400,000	50,000	50,000	8,000	8,000	600
Axis Location	Roll	Roll	Yaw	Roll	Yaw	Yaw
Max. Moment Arm about Roll, ft	0	0	0.5	0	0.5	0.5
Max. Roll Moment ft-lb	0	0	25,000	0	4,000	300
Max. Moment Arm about Pitch, ft	1	1	1	1	1	1
Max. Pitch Moment ft-lb	400,000	50,000	50,000	8,000	8,000	600
Max. Moment Arm about Yaw, ft	0.5	0.5	0	0.5	0	0
Max. Yaw Moment, ft-lb	200,000	25,000	0	4,000	0	0

Secondary injection thrust vector control will be incorporated into a separate attitude control loop to handle the large disturbance torques produced during the 400,000 pound thrust. The smaller engines will not use

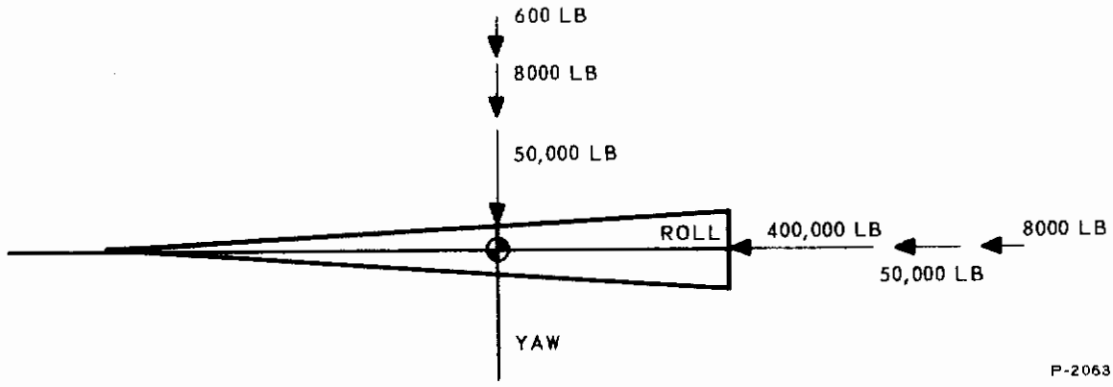

Figure V-1 - Guidance Engine Layout "A"

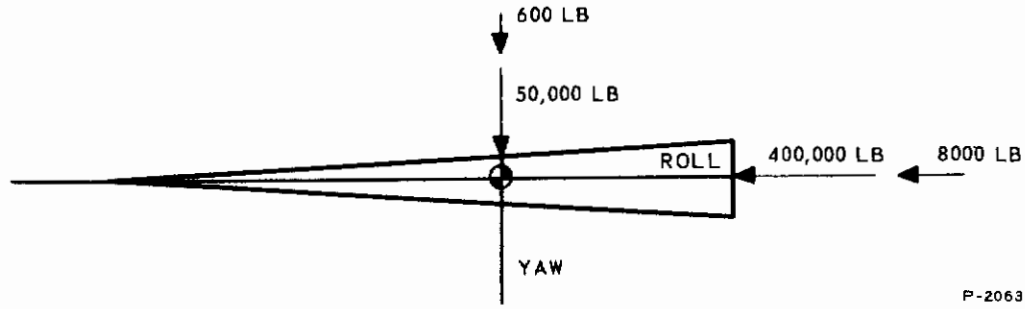

Figure V-2 - Guidance Engine Layout "B"

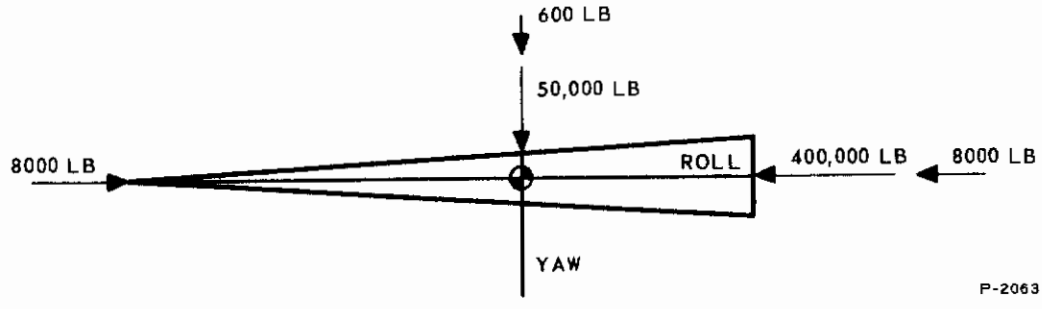

Figure V-3 - Guidance Engine Layout "C"

thrust vector control, consequently their disturbance torques will be imposed upon the normal attitude control system. Table V-2 shows the maximum total distrubance torques exerted by the smaller guidance engines.

Table V-2 - Total Disturbance Torques

	Engine Layout "A"	Engine Layout "B"	Engine Layout "C"
Maximum Pitch Moment, ft-lb	25,000	25,000	25,000
Maximum Yaw Moment, ft-lb	58,000	58,000	58,000
Maximum Roll Moment, ft-lb	25,000	4,000	4,000

V-4 CONTROL MOMENT REQUIREMENTS

For Layout "A" of the guidance engines, the attitude control moments must be somewhat greater than the corresponding values given in Table V-2. The added increment for each axis is determined by the moments required for attitude control during the various maneuvers.

The use of Engine Layout "B" requires sizable attitude changes in short periods of time. The expression which relates the minimum moment and the required time for single axis motion is:

$$M = \frac{4\,\theta\,J}{t^2} \qquad (V-1)$$

where M = Reaction moment, ft-lb

θ = Total angle traveled, radians

J = Moment of inertia, lb-sec^2-ft

t = Time duration, sec.

In view of the fact that the coasting durations in the rendezvous maneuver are around 20 seconds, the time duration for rotating the vehicle should not exceed 10 seconds. Using Equation (V-1) and the inertias defined in Subsection 3.5.2, we see that a 180 degree roll in 10 seconds requires a reaction moment of 126,000 ft-lb, a 180 degree yaw in 10 seconds requires a reaction moment of 650,000 ft-lb, and a 90 degree pitch in 10 seconds requires a 266,000 ft-lb moment. Actually, a simultaneous roll-pitch or yaw-pitch motion would be required, which could increase the moment requirements due to cross-coupling between axes. This type of maneuver does not appear to be desirable.

Engine Layout "C" offers a compromise between the othe two configurations. Only a 90 degree rotation about the pitch axis is required prior to engine changes, which requires at least a 266,000 ft-lb pitch control moment. Insofar as vehicle loads and passenger discomfort are concerned, this pitch maneuver would create a centripetal acceleration of only 12 ft/sec^2. The moment requirements about the roll and yaw axes are determined by the disturbance torques (Table V-2) and the moment requirements for attitude control.

V.5 RECOMMENDED ENGINE LOCATIONS

Engine Layout "A" appears to be the most practical. While it consists of the largest number of guidance engines, it does not require that large attitude control engines be used. The effect of large attitude engines upon the vehicle structure and weight is obvious. Also, without the large attitude changes characteristic of the other layouts, a less complex tracking system is required and greater rendezvous accuracy can be expected. While a detailed analysis of this area is beyond the scope of the present study, it is concluded that Layout "A" will provide the greatest accuracy and reliability with no greater weight penalty than the other layouts discussed.

APPENDIX VI

LITERATURE SURVEY OF MOMENTUM EXCHANGE CONTROL TECHNIQUES

VI.1 INTRODUCTION

The use of momentum exchange techniques for the attitude control of space vehicles has attained considerable prominence in the current engineering and scientific literature. The articles available can be classified into five basic categories: (1) survey articles, (2) control requirements, (3) specific momentum exchange systems, (4) momentum dumping techniques, and (5) general design articles. The content of the articles surveyed will be presented in this sequence.

The point should be made at this time that the primary intent of the literature search was to determine the most desirable momentum exchange system for large moments (in the order of 25 to 25,000 ft-lbs) as well as classifying the available design information on all current related systems. It was assumed at the beginning that satisfactory position and rate sensors will be available, the major function of the momentum-exchange system being to provide the necessary control moments for alignment or error control purposes.

VI.2 SURVEY LITERATURE

The survey literature in any field must always be weighed against the date of publication, attitude control being no exception. The earliest work to be reviewed was that by Roberson[61]* published July 31, 1960. The report is a combination literature survey and design criteria presentation, including material on sensors and sensing methods, torque sources, control systems, synthesis methods, dynamics of control and controlled elements, and complete system responses. The report contains no specific design information but rather presents in an analytical manner the operating principles, the suitability and limitations

*Numbers in parentheses refer to the references listed in Section 10.

weight. The authors also make the standard cry that more accurate attitude sensors are needed and it is in this area that the state-of-the-art of attitude control suffers the most. This is a summary article whose major contribution to the literature on attitude control is in the description of specific reference articles and the preliminary considerations which must be taken into account in a control system design. This includes such items as mission length, attitude requirements and available state-of-the-art systems.

The remaining survey article is that by Holohan[54] which covers the literature up to February 1963. The author lists the methods used for attitude control on all missiles and satellites which have been launched already or are now in the design and construction stage. This includes five planned satellites which have momentum exchange controls in the form of reaction wheels and a sixth series (the Samos and Midas) which will use gyros for the momentum exchange device. The state-of-the-art of the current active and passive attitude control systems are listed in tabular form along with the relative merits of each system. In particular, the momentum-exchange systems are well suited for applications where a large amount of impulse must be expended and the control torques are random in direction or cycles with fairly short periods. The state-of-the-art of the momentum exchange systems listed included gyros, flywheels, and reaction spheres. Gyro torque sources are given a very pessimistic rating in terms of attitude control based on spin bearing life and drift error accumulation. Reaction spheres are also listed as showing promise but lacking in adequate suspension and torqueing mechanisms. The only new device presented was a liquid flywheel being developed by General Electric. This article lacks sufficient references to be considered a good literature survey article. In this respect its major value lies in the presentation of specific systems now used or in the planning stage for satellite control.

Two more survey sources which will not be discussed here are Whitford[68] and the entire November 1961 Guidance and Control Issue of Astronautics[42].

VI.3 VEHICLE AND CONTROL REQUIREMENTS

In the area of vehicle and control requirements for specific vehicle missions and parameter magnitudes, there is one source which is particularly outstanding, this being the report by Roberson[61] as mentioned earlier. The two volumes by Roberson contain no specific magnitude or

design information but rather present in an analytical manner the operating principles of the subjects, the suitability and limitations of the same, and an outline of the areas in which information and/or design is most lacking. A fairly thorough treatment of the general dynamic equations of a free body are available for calculating the specific magnitudes if desired. Both volumes of the report do contain, however, general design information and environment parameters which are lacking in so much of the literature. The topics are purposely kept as general as possible to encourage further reference or later specific applications of the information. The only criticism would be the lack of sufficient background information in several of the derivations such as the coordinate system used for vehicle motion studies and the gravity gradient techniques.

There are several other articles worth rating such as those by Cannon[45] and McRuer[57] which analyze the general power requirements of flywheel systems. White and Hansen [66], [67] have also analyzed the control requirements of an Inertia Wheel Control System and an Integrating Gyro Control System which will be described in more detail in Article VI.5. The number of articles available, concerning vehicle mission requirements, is almost endless. Only the most pertinent general articles have been listed here.

VI.4 GENERAL DESIGN

The general design articles are presented as a separate subject in this listing because, while they describe the methods of obtaining the equations for various systems, usually only an order-of-magnitude study of the validity of the equations is included with no mention of specific hardware or vehicle configuration. A section of this type must also include what is felt to be the best references for general gyroscope theory, the assumption being made that the inertia wheel theory is understood well enough to be unnecessary.

Roberson has several articles in this category, the most general being the survey report published in 1960[61]. In this report the author points out that reaction wheels are well known and pose only physical design problems such as bearing wear. The equation of a vehicle using reaction wheels for attitude control is derived for both a single degree of freedom system and the standard three degree of freedom system. In the latter case, strong cross-coupling of control reaction results with two to three times the power requirement for rotation about one

axis as compared with the single degree of freedom system. This is an important consideration in any type of an earth-centered axis system. The primary advantage of reaction wheels on the other hand are the dynamic equations for system behavior. It is interesting to note that the author made a statement that no known commercial equipment was available capable of performing the necessary functions in a space environment. Within a year the literature reflects availability of commercial wheels. It was stated that gyro actuators enjoy a distinct advantage over reaction wheels in terms of power consumption, the gyros being capable of operation with control torques as low as 10^{-6} of the torque required for the reaction wheels. Also present state-of-the-art gyro accuracy for actuator usage is far better than required. The reaction sphere has certain advantages beyond this but lacks sufficient development for serious consideration at the time of the writing. Roberson also develops the equations for the dynamic behavior of the general space vehicle and presents the equations for earth-centered and inertia axis control requirements of the reaction wheels and the gyroscopes. The gyros are treated both with their momentum vectors orthogonal and also coplaner, the coplaner arrangement being advantageous in the elimination of precession torques in the case of an earth-centered or earth fixed orbit. A system of 3 gyropairs, 1 pair for each axis, is briefly discussed. The arrangement would have the advantage of avoiding mechanical coupling and avoiding precession torques. The comment is made that ultimately it might be expected that reaction wheels can never compete with gyros on a power-consumption basis.

A second article by Roberson, Leondes and Aoki[62], is concerned with the equations describing the behavior of a satellite attitude control system based upon yaw gyro and earth-centered sensors and reaction wheel actuators. The analytical treatment is very complete and the authors refrain from approximations to preserve the generality of the equations. The basic approach was to treat the entire vehicle, sensor and actuator system as an integrated unit from the very beginning. Part 1 of the article was concerned with the necessary synthesis equations with no limitations on size of satellite and equipment or expected vehicle maneuvers. Part II shows the results obtained for various vehicle scaling parameters and maneuvers. Several analog computer runs are included to demonstrate the validity of the equations. It should be mentioned that this was one of the most complete and useful analyses of the variables involved in the final satellite behavior to be

found in the literature search. Since the report involved a full twenty pages of detailed equations, no attempt will be made here to summarize the specific content. The continuity of the article was good. The authors fail to discuss specific hardware such as the reaction wheels but this could hardly be considered within the already crowded scope of the article.

Cannon[45] has presented the techniques necessary for analyzing the general response of a reaction-wheel satellite attitude control system in a fairly detailed manner. This includes impulse and sinusoidal response as well as power requirements. The paper is composed of two main sections. The first section covers the dynamics of a single axis model of a vehicle controlled by a reaction wheel. The second is concerned with the response of the standard three-axis system. The equations are set up for both an inertial and an orbit-oriented system. In either case the assumption is made that any rotation will occur about a single reference axis parallel to the orbit axis. Also all angles are considered small and the inertia ratios J/I, where J is for the reaction wheel and I is for the vehicle, are dropped for values less than 1. He shows that the reaction wheel activity may be 2 or 3 times greater for decoupling control of a 3-axis system than for a single axis case if the wheel speeds are high. The article is limited to a linear analysis although the limitations imposed by the author to obtain a concise analysis can easily be removed by following the general method from the initial equations. However, his major concern is the overall system and as such he ignores the system components, such as the reaction wheel motors, etc., thus limiting the final usefulness of the equations.

In the same line of thought is an article by McRuer and Stapleford[57] which presents an alternate method of computing the power requirements of a fixed-axis inertia wheel for attitude control. The control system function is set up in a standard manner for single axis control only. Then by use of the control equations, the total energy of the system was derived. The power requirements were realized by differentiating the energy. The author introduces two specific methods. The first is the straightforward method of designating the angular velocity of either the wheel or the vehicle as a function of time and using this relationship to find the system energy. The second method involves finding the energy by use of the complex convolution integral and is useful when no external torques act on the vehicle. For simple results it is laborious

but for complicated inputs or transfer functions it is claimed to be irreplaceable. A sample calculation is included in the article to substantiate the method. This is one of the several articles devoted to specific analytical techniques for the solution of attitude control problems. The method of the convolution integral seems to have definite merit for complicated systems, although no actual applications to complicated systems are presented to verify this merit.

Stuart[63] has presented a good article on the equations of motion for a vehicle-flywheel system designed for maintaining alignment of the vehicle axes with respect to a reference axes in terms of stability only. He makes the assumption that the reference frame will rotate at a constant angular velocity around a single axis with a fixed speed, ω. This is obviously incorrect as it would require a perfectly circular orbit, but the effect of any small rotational components would only introduce small variable torques in the motion equation depending on a particular orbit. All equations are also linearized and non-dimensionalized. The author points out that the resultant angular momentum in the system must be colinear with the ω axis. If not, the rotors would have to be constantly accelerated to offset the rate of change of the momentum vector. Several possible forcing torques which would influence the satellite are discussed in a quantitative manner. The author concluded that there are two control schemes available as follows:

1. Make flywheel torque proportional to angular rate,
2. Make angular momentum proportional to angular displacement.

The analysis was performed in terms of the system transient response. The author suggests a similar analysis be performed for a steady-state response to oscillations resulting from periodic forcing torque. The article presented a good introduction to the problems involved in designing a three-dimensional attitude control system. The linearization assumptions were pointed out very thoroughly and the basic equations could easily be used in a more rigorous analysis if desired. The article should serve as a good reference to avoid the early pitfalls in the design of an entire system.

One of the better publications on general gyroscopic theory is the book "Mechanics of the Gyroscope" by Deimel.[47] The book is mentioned here primarily because of its appearance in such a large

number of articles which pertain to any form of gyroscopic motion. It is accepted as one of the best handbooks on both gyroscopic behavior and rotational motion.

The best control function analysis of the gyroscope was found in "Control Systems Engineering" by Gibson and Tuteur[48]. The authors describe the motion and cause of the gyroscopic effect and present the transfer functions for linear motion of a gyro-gimbal combination. Schuler tuning is mentioned in conjunction with inertia damping considerations. A brief discussion of gyro applications is also given. This includes the differentiation between freee and rate gyros, angular velocity sensitive gyros, and restrained or rate gyros. Inertial navigation techniques are discussed in terms of an integrating gyro and accelerometer combination. The basic formulas for demonstrating the Schuler tuning in order to maintain inertial platform reference with respect to the earth are also presented.

Hansen and White[66], [67] should be mentioned in this category although their work is discussed in greater detail in Section VI.5 of this survey. Haseltine [52] is also mentioned for his work on the equations of motion for nutation and passive damping of a spin-stabilized satellite.

This is by no means a complete listing of the general design type of articles. Roberson has made several presentations at various conferences which were not available at the time of this writing. There is also considerable literature on the design of the Nimbus and Advent Satellite Series which have reaction-wheel attitude control. Several articles were also reviewed which are not discussed here as it was felt that the material was usually only a specific review of one of the topics in the general articles already presented.

VI.5 SPECIFIC MOMENTUM EXCHANGE SYSTEMS AND DEVICES

The most interesting and informative article on a specific momentum exchange system is the recent WADD Report by Wells, Courtney and Sicko[65]. This report covers the design of a particular gyro attitude control configuration using control system analysis. This was the only work of this kind found during the literature search in which system cross-coupling from large gyro angles was eliminated by correction computers. All other sources mentioned this possibility but limited their approach to small control angles. Basically, the proposed system used four gyros, located on the great circles of a sphere so as to provide a zero total momentum in the equilibrium position. A redundant control

system was used to torque the gyro(s) needed for the proper control. The saturation of the system was 3H (H being the momentum of one gyro) as compared to a saturation limit of H with a set of paired gyros. The report described a complete attitude control system, including the gyros, a star tracking device and a coupling computer. This system is suitable for a satellite in the 300 to 1000 lb weight class and has a maximum power consumption of 0.5 watt for a 320 lb vehicle with a maneuvering rate of 2 deg/secs. Damping is inherent. A disadvantage of this system is the weight, which amounts to 1 to 3%of the total vehicle weight depending upon the vehicle size. The method of using a redundant control system to extend the use of the gyros beyond the small angles normally allowed not only increased the ultimate saturation of the system, but also allows a considerable variation in system gain with very little effect on performance as compared to other momentum transfer systems.

White and Hansen have published two NASA reports[66], [67] which are very good examples of specific system design. The first report studies the use of the inertia wheels for attitude control while the second considers the use of integrating gyros for the torque sources instead of the inertia wheels. In the first report the authors analyze three inertia wheel configurations for attitude control of the OGO satellite series. The three configurations differed in the method of damping used; these being (1) a rate gyro, (2) an error-rate network and (3) a tachometer. The analysis consisted of a generalized linear analysis, a nonlinear analysis using a switching-time method and an analog computer study. An experimental design was also built as a means of verifying the date. The error-rate network system was shown to be superior because the threshold level with the gyro causes a significant amount of limit-cycle operation and the tachometer system was not available in the required dynamic range. In an experimental study under laboratory conditions a dynamic tracking error of less than ± 0.5 second of an arc was obtained. Reference is made to the fact that to maintain continuous control of the satellite, provision must be made for removing momentum to avoid saturation. This requires a system design which allows driving the wheel to maximum without the error exceeding tolerable limits. This can be accomplished either by having sufficient gain or by adding an integrator between the sensor and the motor. The full design equations for all three systems are contained in the report.

The second report[67] by the same authors analyzes vehicle attitude control using 3 single-degree-of-freedom integrating gyros

as torque sources. The analysis again pertains directly to the OGO satellite series. For the system described, the study demonstrated that the integrating gyros could be designed with reasonably rapid and well damped transients as well as very small steady state errors. Another advantage of the integrating gyro is its ability to behave as a rate sensor, thereby eliminating the need for an external error sensor or, when the target is occulated, an alternate reference. The gyro system, in question, did have the following disadvantages as compared to reaction wheels:

1. Only 5 percent (for a float angle of ±3°) of the gyro momentum is available for active control; thus a larger or faster turning wheel is required.
2. Additional moving parts and weight are required for the gyro float and case.
3. The float and case may have to be temperature controlled which also requires additional weight and power.

The first disadvantage results from limiting the float angle to ± 3° to eliminate any gyroscopic cross-coupling in the control equations. This would naturally impose a severe limitation on the amount of useful momentum. The article was an excellent source of the application of control-system procedures to attitude control. Several assumptions were made however which, appear to impose unfair limitations on the gyro system. First, as stated above, the ± 3° float angle rotation will eliminate cross-coupling but at the expense of useful momentum. The major reason for this is the work can be presented in terms of uncoupled single axis control equations. A control system such as this would be adequate for perturbation or small correction changes only. It is felt that a more useful system would result if larger angles were allowed with some means of compensation for the cross-coupling.

The high moment report by Bendix[24] presents an order-of-magnitude study of the use of a pair of gyros for each vehicle axis to furnish the necessary control torques. Most of the cross-coupling is inherently eliminated in the combination by having the angular momentum vectors in a back-to-back arrangement. This allows much greater gimbal movement and a corresponding increase in the useful saturation of the system. Unloading is still a problem. Also, as stated earlier, a more favorable system would have resulted if more time had been

allowed for large attitude maneuvers. In the Bendix report, a gyro combination capable of delivering a single axis impulse of 1000 ft-lb-sec in 20 seconds would weigh 0.63 percent of the total vehicle weight. System damping was not considered.

The use of twin gyros in this manner was also suggested by Klass[56] and Roberson[61]. The article by Klass, while more of a survey article on the work of the Instrumentation Laboratory at MIT, is listed here as it presents several specific gyro possibilities for combination active-passive attitude control systems, with the passive control being gravity gradient. The satellite is treated as a large inertia, slow speed gyro with an orbital rotating speed about its pitch axis. The smaller included gyros act only to dampen any transient conditions and provide stability around the yaw axis. Several techniques are described using one or two control gyros. Whenever a configuration is used such that the gyro spin axis(s) does not lie along the satellite pitch axis, a constant torque such as a torque motor or permanent magnet must be applied if the vehicle is to retain its earth-centered position. The point is also made that this type of gyro damping for a satellite is most efficient when the orbital angular momentum of the satellite equals the spin angular momentum of the gyro(s). The real value of the article is that it points out several novel gyro-satellite configurations which might have applications in other areas.

Typical reaction wheels for extreme space environment have been developed by the Bendix Corporation[48]. They are primarily intended for the OGO size of satellite and the current models produce angular momentum ranging from 5.5 slug-ft^2/sec at 800 rpm for the coarse models to 0.15 at 5000 rpm for very fine control.

Spin stabilization has been the most popular means of attitude control to date and as such has been widely published. While this is in the true sense a momentum-storage technique it was not included here because there is no provision for attitude changes using some form of active momentum exchange. The word active is purposely included because two passive systems using the magnetic field of the earth have been developed for attitude changes of a spinning satellite[49], [50].

Spherical gyros or reaction spheres have received considerable attention due to their theoretical ability to eliminate system cross-coupling, thereby simplifying the analytical techniques. They also have a theoretically infinite choice of torque application axes. These are the properties listed by Ormsby and Smith[58] in a 1961 article

"Capabilities and Limitations of Reaction Spheres". Three possible suspension systems are discussed; gas bearings, magnetic field suspension. An example of the potential of the device is the ability to turn a satellite with a moment of inertia of 1000 slug-ft^2 180° in 20 minutes using a 5 in. diameter, 1 in. thick wall 410 stainless steel rotor with a maximum speed of 10,000 rpm. The basic equations for the suspension system are presented along with the theoretical limitations of the device. The torque system equations are discussed and the final conclusion of the article is that the mutual dependence of the various parts of the system in determining the motion of the sphere in the cavity makes the design procedure a trial and error process. The title of the article is very misleading in that the limitations discussed are the theoretical limitations with little mention of actual practical limitations. This tends to confirm the opinion of other sources as to the non-practibility of the device at this time. Ormsby also provides a second source(59) for the equations of vehicle motion acting under reaction sphere control.

Recent advances in fluid gyros should also be mentioned at this time because it is apparent that some will soon be on the market. Wing(69) has a good article on the more recent advances in Fluid Rotor Gyros. The major advantage for using fluid gyros as torque sources was interpreted to be the use of an external drive motor, thus eliminating slip rings, flexible leads, spin bearings in the special case of a non-rotating container system, and a relative insensitivity to production tolerances. The disadvantages are thermal gradients in the fluid, inherent rate gyro characteristics (which may or may not be a disadvantage), and undoubtedly a complex fluid storage and pumping system. The report by Wing is concerned primarily with instrumentation gyroscopes.

This discussion has referenced only the literature which is commonly available with regard to specific momentum exchange systems and devices. There is undoubtedly additional information available from the current satellites such as the OGO series which use inertia wheel controllers. Most of the application techniques are confidential in nature, however, and have not received general publication.

VI.6 MOMENTUM DUMPING TECHNIQUES

This section contains a brief attempt to classify a few of the currently proposed momentum dumping techniques. The most obvious and efficient systems are the reaction jet systems. Since these are

well known and have proven application potential they will not be covered here. This immediately limits the discussion to primarily passive systems. (Photon or electron emission are considered completely impractical due to present power requirements.) For an earth-orbit satellite the two most popular dumping systems are those which interact with either the earth's magnetic field or the earth's gravitational field.

For large moment applications the use of the earth's gravitational field does not appear to be feasible. This result is postulated in[24] where it is shown that for the large vehicle in question, the theoretical ultimate moment produced would be 82.2 lb-ft. A moment of this magnitude (if always at its maximum which is impossible to begin with) could rotate the vehicle approximately 0.212 degrees in one hour. This is at an altitude of 150 miles and would decrease at higher altitudes.

The gravity gradient is not insignificant with smaller satellites. Klass[56] has already been mentioned as describing a system which utilized the gravity gradient. The survey articles by Roberson[61], Haessurman[51], Taplin and Teitelbaum[64], and Holohan[54] list several references for gravity gradient techniques on the smaller satellites.

A very promising method for initial orientation of a vehicle in terms of removing any spin resulting from the launching and/or injection into orbit is the Yo-Yo Technique as described by Cornille[46]. At some predetermined time after launch, diametrically opposite weights constrained by wires are freed from the vehicle by letting the spin of the vehicle unwind the wires. When the wires reach the full radial position, they are released. Further, the use of an elastic wire will actually cause a feedback effect during the de-spin process. This article was included because it describes an energy technique which could correct large initial errors of vehicle attitude, thus setting the stage for vernier control devices for the remainder of the mission. No significant design information was presented.

Solar pressure has also been suggested as a control source but for large moments it is again inadequate. This leaves the earth's magnetic field as the only remaining passive system which can be used to dump momentum. There are several references describing use of this method for small satellites. Braumuller, Lynn, Julich, and Wood[44] have published a report which includes descriptions of the magnetic field, regions or orbits with the most potential, and the physical weights and sizes of any necessary equipment. Here again the maximum vehicle

weight considered in the report is 1,414 lbs. The various survey articles also list several similar sources, a few of which are listed in Section 10 of this report. Reference (24) investigated the potential of this type of device and concluded that it is clearly inadequate if standard conductors are used. A control torque of 50 ft-lb would require a copper ring with a 10 ft inside diameter, a 3 ft rim thickness and a 6 ft length. Super-conductors are also discussed but in any case the use of the magnetic field for large moments has yet to reach practical state-of-the-art development.

The conclusion for this section is that, as far as the present state-of-the-art of passive attitude systems is concerned, none show immediate promise for any high moment application.

VI.7 CONCLUSIONS

The conclusions from the literature survey, regarding feasibility of a momentum exchange system for large moments, are as follows:

(1) Reaction wheels have reached an advanced state-of-the-art both in theory and in practice but the power requirement and physical size for any type of high moment work are very large.

(2) The use of gyroscopes as torque sources has yet to reach the state-of-the-art development of the reaction wheels, but the power requirement is predicted to be very much lower for equivalent performance. In the course of the literature search only one source was found which actually attempted to utilize the maximum amount of momentum available, this being the Glopac system[65]. The others were all limited to small angular displacements to reduce cross-coupling. The major problem in present system concepts is that of unloading.

(3) The various passive systems surveyed showed no promise for high moments except for super-conducting magnets which are considered impractical relative to the present state-of-the-art. They do show considerable future potential.

(4) The special devices such as reaction spheres and fluid gyros also suffer from a lack of development which makes a critical analysis impossible at this time.

APPENDIX VII

ANALYSIS OF GYRO MOMENTS

VII.1 INTRODUCTION

This analysis is concerned with defining the moments which a single-degree-of-freedom gyro system can exert on a space vehicle to effect attitude control. The objective is to obtain simple equations which will allow a reasonably accurate preliminary design to be made. A major simplifying feature of the analysis is the restriction that the gyro precession axes lie on, or parallel to, the principal axes of the vehicle. Other simplifications are made as the analysis progresses.

VII.2 GENERAL ANALYSIS

The basic equation for a gyro-vehicle system in the absence of external torques is:

$$\bar{H} + \bar{H}_v = \text{const.} \qquad \text{(VII-1)}$$

where $\bar{H}$ and $\bar{H}_v$ designate the angular momentum of the gyro and vehicle respectively and are inertial quantities. If the time derivative of the above equation is taken, then:

$$\left(\frac{d\bar{H}}{dt}\right)_{\text{inertial}} + \left(\frac{d\bar{H}_v}{dt}\right)_{\text{inertial}} = 0 \qquad \text{(VII-2)}$$

where:

$\left(\frac{d\bar{H}}{dt}\right)_{\text{inertial}}$ = torque or moment acting <u>on the gyro</u>

$\left(\frac{d\bar{H}_v}{dt}\right)_{\text{inertial}}$ = torque or moment acting <u>on the vehicle</u>

and the vehicle torques can be obtained from gyro motions by:

$$\bar{M}_v = \left(\frac{d\bar{H}_v}{dt}\right)_{\text{inertial}} = -\left(\frac{d\bar{H}}{dt}\right)_{\text{inertial}} \qquad \text{(VII-3)}$$

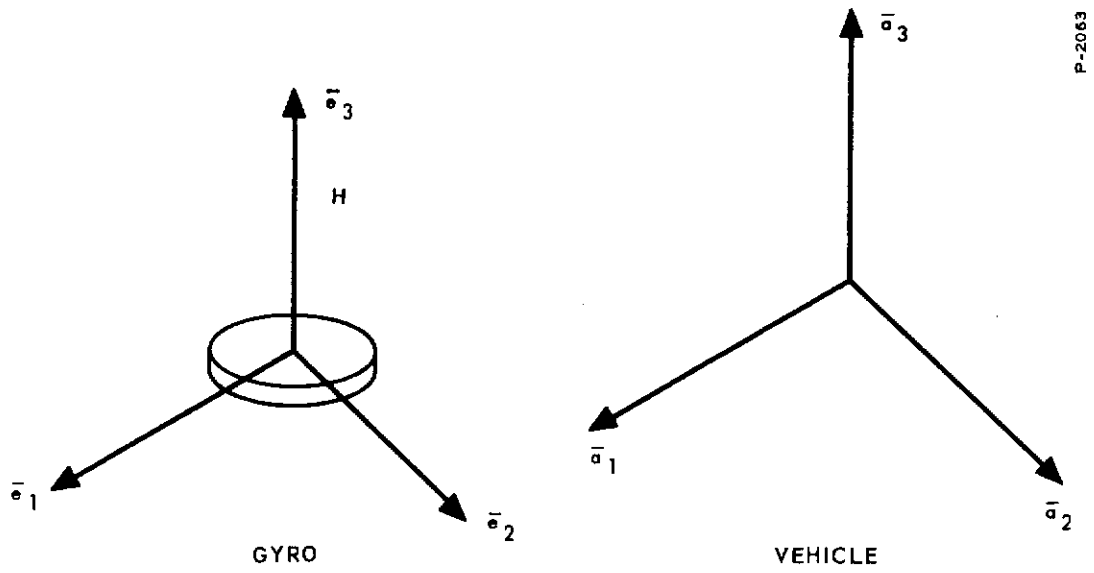

Figure VII-1 - Gyro Coordinate System

Figure (VII-1) shows a gyro with axes as determined by the unit vectors $\bar{e}_1$, $\bar{e}_2$ and $\bar{e}_3$ and a vehicle with axes $\bar{a}_1$, $\bar{a}_2$ and $\bar{a}_3$. The angular momentum of the gyro is written in terms of its reference axes and has the form:

$$\bar{H} = A\,p\bar{e}_1 + Aq\bar{e}_2 + C\,(\Omega + r)\,\bar{e}_3 \qquad \text{(VII-4)}$$

The time derivative of this quantity must account for both the change of H with respect to the $\bar{e}_1$, $\bar{e}_2$ and $\bar{e}_3$ frame and the rotation of the frame, that is:

$$\bar{M}_v = -\left(\frac{d\bar{H}}{dt}\right)_{\text{inertial}} = -\left(\frac{\partial \bar{H}}{\partial t}\right) - \bar{\omega}_{123} \times \bar{H} \qquad \text{(VII-5)}$$

where:

$\frac{\partial H}{\partial t}$ = a partial derivative in which $\bar{e}_1$, $\bar{e}_2$ and $\bar{e}_3$ are held fixed

$\bar{\omega}_{123}$ = the sum of the angular velocity of the gyro axes relative to the vehicle axes and the angular velocity of the vehicle axis $p\bar{e}_1 + q\bar{e}_2 + r\bar{e}_3$.

thus:

$$\bar{\omega}_{123} = \bar{\omega}\,\text{gyro/veh.} + \bar{\psi}$$

$$= \omega_1 \bar{e}_1 + \omega_2 \bar{e}_2 + \omega_3 \bar{e}_3 + \psi \qquad \text{(VII-6)}$$

In order to complete this expression, $\bar{\psi}$ veh must be expressed in terms of the gyro axes. This involves the determination of the direction cosines from the geometry of the particular system. This transformation can be written in matrix form:

	$\bar{e}_1$	$\bar{e}_2$	$\bar{e}_3$
$\bar{a}_1$	c_{11}	c_{12}	c_{13}
$\bar{a}_2$	c_{21}	c_{22}	c_{23}
$\bar{a}_3$	c_{31}	c_{32}	c_{33}

(VII-7)

and:

$$\psi_{veh} = \sum_{j=1}^{3} \bar{e}_j \left[\sum_{i=1}^{3} \psi i \;\; Cij \right]$$

$$= \psi_1 \bar{e}_1 + \psi_2 \bar{e}_2 + \psi_3 \bar{e}_3 \qquad \text{(VII-8)}$$

Equation (VII-6) can then be written:

$$\bar{\omega}_{123} = p\bar{e}_1 + q\bar{e}_2 + r\bar{e}_3$$

$$= (\omega_1 + \psi_1)\,\bar{e}_1 + (\omega_2 + \psi_2)\,\bar{e}_2 + (\omega_3 + \psi_3)\,\bar{e}_3 \qquad \text{(VII-9)}$$

and Equation (VII-9) can be used with Equations (VII-5) and (VII-6) to obtain the moments acting on the vehicle. Combining Equations (VII-5) and (VII-6):

$$M_v = -\left(\frac{d\bar{H}}{dt}\right)_{inertial}$$

$$= -\left[A\dot{p} + (C\Omega)\, q + (C - A)\, qr\right] \bar{e}_1$$

$$- \left[A\dot{q} - (C\Omega)\, p - (C - A)\, pr\right] \bar{e}_2$$

$$- \left[C\,(\dot{\Omega} + \dot{r})\right] \bar{e}_3 \qquad \text{(VII-10)}$$

The values of p, q and r are found from Equation (VII-9). Also $C\Omega$ is the spin angular momentum, H, of the gyro. Using these substitutions, Equation (VII-10) becomes:

$$\bar{M}_v = -\left[A\,(\dot{\omega} + \dot{\psi}_1) + H\,(\omega_2 + \psi_2) + (C - A)\,(\omega_2 + \psi_2)\,(\omega_3 + \psi_3)\right] \bar{e}_1$$

$$- \left[A\,(\dot{\omega}_2 + \dot{\psi}_2) - H\,(\omega_1 + \psi_1) - (C - A)\,(\omega_1 + \psi_1)\,(\omega_3 + \psi_3)\right] \bar{e}_2$$

$$- \left[C\,(\dot{\Omega} + \dot{\omega}_3 + \dot{\psi}_3)\right] \bar{e}_3 \qquad \text{(VII-11)}$$

This expression contains the gyro inertia terms as well as the rate of position change of the system angular momentum vector. In order to describe the vehicle motion, the moments must be transferred to the vehicle axes. Rewriting Equation (VII-11):

$$\bar{M}_v = M_{e1}\,\bar{e}_1 + M_{e2}\,\bar{e}_2 + M_{e3}\,\bar{e}_3 \qquad \text{(VII-12)}$$

and using the inverse transformation of Equation (VII-7) to express the moments in terms of the $\bar{a}_1$, $\bar{a}_2$ and $\bar{a}_3$ axes:

$$\bar{M}_v = M_{a1}\,\bar{a}_1 + M_{a2}\,\bar{a}_2 + M_{a3}\,\bar{a}_3 \qquad \text{(VII-13)}$$

VII.3 SINGLE-DEGREE-OF-FREEDOM GYROS

The equations for the single-degree-of-freedom gyro as shown in Figure 4-1 will now be developed using the general method described above. Assume the gyro to be initially located with its input axis, $\bar{e}_1$, along the vehicle $\bar{a}_1$ axis and its spin axis initially along the vehicle $\bar{a}_3$ axis. At any later period of time, the gyro will have processed about the $\bar{a}_1$ axis as shown in Figure 4-1 where θ_1 is the angle between the gyro $\bar{e}_3$ axis and the vehicle $\bar{a}_3$ axis as shown.

Referring to Equation VII-10, the moments acting on the vehicle are expressed in terms of the absolute angular velocities, p, q and r, of the gyro, where:

$$\bar{\omega}\,\text{gyro} = \bar{\omega}\,\text{gyro/veh} + \bar{\psi} \qquad \text{(VII-14)}$$

$$= p\bar{e}_1 + q\bar{e}_2 + r\bar{e}_3 \qquad \text{(VII-15)}$$

$$= (\omega_1 + \psi_1)\,\bar{e}_1 + (\omega_2 + \psi_2)\,\bar{e}_2 + (\omega_3 + \psi_3)\,\bar{e}_3 \qquad \text{(VII-16)}$$

The velocities ω_1, ω_2 and ω_3 which are the angular velocity components of the gyro, with respect to the vehicle, will contain a rotation about the $\bar{e}_1$ axis only due to the single-degree-of-freedom constraint. Thus

$$\omega\,\text{gyro/veh} = \dot{\theta}_1\, e_1 \qquad \text{(VII-17)}$$

and

$$\omega_1 = \dot{\theta}_1$$

$$\omega_2 = 0$$

$$\omega_3 = 0$$

The $\bar{e}$ axes components of the vehicle angular velocity, ψ_1, ψ_2 ψ_3 are found by the transformation as described in Equations (VII-7) and (VII-8). The transformation table is found by inspection of Figure 4-1 to be:

	$\bar{e}_1$	$\bar{e}_2$	$\bar{e}_3$
$\bar{a}_1$	1	0	0
$\bar{a}_2$	0	$\cos\theta_1$	$-\sin\theta_1$
$\bar{a}_3$	0	$\sin\theta_1$	$\cos\theta_1$

(VII-18)

Using Equation (VII-9) and the above transformation table, the absolute angular velocity components of the gyro rotor become:

$$p = \omega_1 + \psi_1 = \dot{\theta}_1 + \psi_1 \qquad \text{(VII-19)}$$

$$q = \omega_2 + \psi_2 = 0 + \psi_2 \cos\theta_1 + \psi_3 \sin\theta_1 \qquad \text{(VII-20)}$$

$$r = \omega + \psi_3 = 0 - \psi_2 \sin\theta_1 + \psi_3 \cos\theta_1 \qquad \text{(VII-21)}$$

Combining Equations (VII-10), (VII-19), (VII-20), and (VII-21), and letting $C_1\Omega_1 = H_1$, the following expression for the moments acting on the vehicle is obtained:

$$\begin{aligned} M_{v1} = & -\Big\{A_1(\ddot{\theta}_1 + \ddot{\psi}_1) + H_1(\psi_2 \cos\theta_1 + \psi_3 \sin\theta_1) \\ & + (C_1 - A_1)\left[(\psi_3^2 - \psi_2^2)\cos\theta_1 \sin\theta_1 + \psi_2\psi_3(\cos^2\theta_1 - \sin^2\theta_1)\right]\Big\}\bar{e}_1 \\ & - \Big\{A_1\left[(\dot{\psi}_2 + \psi_3\dot{\theta}_1)\cos\theta_1 + (\dot{\psi}_3 - \psi_2\dot{\theta}_1)\sin\dot{\theta}\right] - H_1(\dot{\theta}_1 + \dot{\psi}_1) \\ & - (C_1 - A_1)\left[(\psi_3\dot{\theta}_1 + \psi_1\psi_3)\cos\dot{\theta}_1 - (\psi_2\dot{\theta}_1 + \psi_1\psi_2)\sin\theta_1\right]\Big\}\bar{e}_2 \\ & - \Big\{C_1\Omega_1 + C_1\left[(\dot{\psi}_3 - \psi_2\dot{\theta}_1)\cos\theta_1 (\dot{\psi}_2 + \dot{\psi}_3\theta_1)\sin\theta_1\right]\Big\}e_3 \end{aligned} \qquad \text{(VII-22)}$$

These moments must now be transformed to the vehicle axes. Before this is done, the negligible terms will be dropped so that a simple easily handled expression is obtained. For the application at hand,

$$\dot{\psi}_1, \dot{\psi}_2, \dot{\psi}_3 \ll \dot{\theta}_1$$

$$\dot{\psi}_1, \dot{\psi}_2, \dot{\psi}_3 \ll \theta_1$$

$$\dot{\Omega} = 0$$

Simplification of Equation (VII-22) results in the following expression:

$$\bar{M}_{v1} = -A_1\dot{\theta}_1\bar{e}_1 + H_1\dot{\theta}_1\bar{e}_2 + (0)\bar{e}_3 \qquad \text{(VII-23)}$$

Transforming this expression, in terms of the vehicle principal axes, by means of Equation (VII-18) results in:

$$\bar{M}_{v1} = -A_1\dot{\theta}_1\bar{a}_1 + H_1\dot{\theta}_1\cos\theta_1\bar{a}_2 + H_1\dot{\theta}_1\sin\theta_1\bar{a}_3 \qquad \text{(VII-24)}$$

When three single-degree-of-freedom gyros (one along each axis) are used as shown in Figure 4-5, the moment equations for the other two gyros are:

$$\bar{M}_{v2} = H_2\dot{\theta}_2\sin\theta_2\bar{a}_1 - A_2\ddot{\theta}_2\bar{a}_2 + H_2\dot{\theta}_2\cos\theta_2\bar{a}_3 \qquad \text{(VII-25)}$$

$$\bar{M}_{v3} = H_3\dot{\theta}_3\cos\theta_3\bar{a}_1 + H_3\dot{\theta}_3\sin\theta_3\bar{a}_2 - A_3\dot{\theta}_3\bar{a}_3 \qquad \text{(VII-26)}$$

Neglecting cross-coupling between vehicle axes to eliminate the need for Euler's equations, the equations of motion for the vehicle become:

$$J_1\dot{\psi}_1 = -A_1\ddot{\theta}_1 + H_2\dot{\theta}_2 \sin\theta_2 + H_3\dot{\theta}_3\cos\theta_3 \qquad \text{(VII-27)}$$

$$J_2\dot{\psi}_2 = H_1\dot{\theta}_1 \sin\theta_1 + A_2\ddot{\theta}_2 H_3\dot{\theta}_3 \sin\theta_3 \qquad \text{(VII-28)}$$

$$J_3\ddot{\psi}_3 = H_1\dot{\theta}_1 \sin\theta_1 + H_2\dot{\theta}_2\cos\theta_2 - A_3\ddot{\theta}_3 \qquad \text{(VII-29)}$$

These three simplified equations are adequate for use in the preliminary analysis and design of a gyro attitude control system for the vehicle under consideration.

VII.4 NOMENCLATURE

Symbol	Definition
$\bar{a}_1, \bar{a}_2, \bar{a}_3$	Unit vectors along vehicle principal axes
A	Moment of inertia of gyro rotor about transverse axis, lb-ft-sec^2 (subscripts 1, 2, 3, refer to particular gyros)
C	Moment of inertia of gyro rotor about spin axis, lb-ft-sec^2 (subscripts 1, 2, 3, refer to particular gyros)
$\bar{e}_1, \bar{e}_2, \bar{e}_3$	Unit vectors along gyro rotor principal axes
H	Angular momentum of gyro rotor, lb-ft-sec (subscripts 1, 2, 3, refer to particular gyros)
H_v	Angular momentum of vehicle, lb-ft-sec
J	Principal moment of inertia of vehicle, lb-ft-sec^2 (subscripts 1, 2, 3, refer to principal axes)
M_v	Moment exerted on vehicle by gyro, ft-lb (subscripts 1, 2, 3, refer to particular gyros)
p, q, r	Absolute angular velocities of gyro axes about $\bar{e}_1$, $\bar{e}_2$, and $\bar{e}_3$ axes respectively, rad/sec
t	Time, sec
ω	Angular velocity of gyro rotor relative to vehicle, rad/sec (subscripts 1, 2, 3, refer to gyro principal axes)

θ	Gyro precision angle, rad (subscripts 1, 2, 3, refer to particular gyros)
ψ	Vehicle angular velocity, rad/sec (subscripts 1, 2, ψ, refer to vehicle principal axes)
$(\dot{\ })$	Denotes first derivative with respect to time
$(\ddot{\ })$	Denotes second derivative with respect to time
$(\bar{\ })$	Denotes vector quantity

APPENDIX VIII

COMPUTER PROGRAM FOR VALVE-COMBUSTOR SIMULATION

The basic equations describing the dynamic performance of the valve-combustor system are presented and discussed in Subsection 6.4. These equations are repeated here along with the corresponding equations which have been scaled for application on an analog computer.

The expression for solenoid force is:

$$F_c = \left[\frac{K_s E}{1 + \tau_s S}\right] \left[1 - k_s (x_m - x)\right] \qquad (6\text{-}24)$$

The corresponding computer equation is:

$$\frac{\dot{F}_e}{a_t} = \frac{K_s E}{a_t \tau_s} \left[1 - \frac{k_s}{10^3} (10^3 x_m - 10^3 x)\right] - \frac{F_e}{a_t \tau_s} \qquad (VIII\text{-}1)$$

where a_t is the time scale factor.

The equation of motion for the pilot stage poppet is:

$$M_p \ddot{x} + K_p x + F_{sl} = F_e \qquad (6\text{-}25)$$

The computer equation is:

$$\frac{\ddot{x}}{a_t^2} = \frac{F_e}{a_t^2 M_p} - \frac{K_p}{10^3 a_t^2 M_p} (10^3 x) - \frac{F_{sl}}{a_t^2 M_p} \qquad (VIII\text{-}2)$$

The equation describing the pressure in the main stage control volume is:

$$\frac{d P_c}{dt} = \frac{K_c}{V_c} \left\{ \left[2 r_u x - \frac{x^2}{2}\right] P_a - \left[2 r_d (x_m - x) - \frac{1}{2} (x_m - x)^2\right] P_c \right\} \qquad (6\text{-}29)$$

When scaled for the computer, this equation becomes:

$$\frac{\dot{P}_c}{10\, a_t} = \frac{2 K_c P_a r_u}{10^4\, a_t V_c}(10^3 x) - \frac{K_c P_a}{2(10^5) a_t V_c}(10^4 x^2) -$$

$$\left\{\frac{2 K_c r_d}{10^3\, a_t V_c}\left[10^3 (x_m - x)\right] - \frac{K_c}{2(10^4) a_t V_c}\left[10^4 (x_m - x)^2\right]\right\}\frac{P_c}{10} \qquad \text{(VIII-3)}$$

The equation of motion for the main stage mass is:

$$M_2 \ddot{y} + F_{s2} + (2K_b + K_a)\, y = A_p P_c + 2\pi r_b^2 P_i \qquad (6\text{-}30)$$

Scaling for the computer gives:

$$\frac{10^3 \ddot{y}}{2 a_t^2} = \frac{10^4 A_p}{2 M_2 a_t^2}\left(\frac{P_c}{10}\right) + \frac{2(10^4)\pi r_b^2}{2 M_2 a_t'^2}\left(\frac{P_i}{10}\right) -$$

$$\frac{2 K_b + K_a}{M_2 a_t^2}\left(\frac{10^3}{2} y\right) - \frac{10^3 F_{s2}}{2 M_2 a_t^2} \qquad \text{(VIII-4)}$$

The main stage poppet total flow area is given by:

$$A_{vt} = \sqrt{2}\,\pi\left(2 r_b y - \frac{y^2}{2}\right)$$

This expression scaled for the computer is:

$$10^2 A_{vt} = \frac{4\pi\sqrt{2}}{10} r_b \left(\frac{10^3}{2} y\right) - \frac{2\pi\sqrt{2}}{10^2}\left(\frac{10^4}{4} y^2\right) \qquad \text{(VIII-5)}$$

The respective equations for injection pressure are:

$$P_i = \frac{A_{vt}^2 P_s' + A_{it}^2 P_b}{A_{vt}^2 + A_{it}^2} \qquad (6\text{-}33)$$

$$\frac{P_i}{10} = \frac{1}{10^3 \left(A_{it}^2 + A_{vt}^2 \right)} \left[10^2 \left(A_{vt}^2 \; P_s' + A_{it}^2 \; P_b \right) \right] \qquad \text{(VIII-6)}$$

The expression for flow of propellant into the combustion chamber is:

$$\dot{W}_p = C_2 A_{it} \sqrt{P_i - P_b} \qquad (6\text{-}32)$$

Scaling for the computer gives:

$$\frac{20 \; W_p}{a_t} = \frac{2 \sqrt{10} \; C_2 \; A_{it}}{a_t} \left(10 \sqrt{\frac{P_i}{10} - \frac{P_b}{10}} \right) \qquad \text{(VIII-7)}$$

The combustion process is described by:

$$P_b = \frac{\delta}{1 + \tau_b S} \; \frac{R_b \; T_b \; W_b}{V_b} \qquad (6\text{-}37)$$

The corresponding computer equation is:

$$\frac{\dot{P}_b}{10 \; a_t} = \frac{\delta \; R_b \; T_b}{2(10^5) \; a_t \; \tau_b \; V_b} \left[2(10^4) \; W_b \right] - \frac{P_b}{10 \; a_t \; \tau_b} \qquad \text{(VIII-8)}$$

The rate of change of total weight within the combustion chamber is:

$$\dot{W}_b = \dot{W}_p - \frac{C_{di} \; C_f \; A_t \; P_b}{\sqrt{T_b}} \qquad (6\text{-}39)$$

For the computer this is:

$$\frac{2(10^4)}{a_t} \; \dot{W}_b = \frac{2(10^4)}{2 \; a_t} (20 \; \dot{W}_p) - \frac{2(10^5) \; C_{di} \; C_f \; A_t}{a_t \sqrt{T_b}} \; \frac{P_b}{10} \qquad \text{(VIII-9)}$$

The supply line dynamics is described by:

$$P_s' = \frac{1 + \frac{L_h}{R_h} S}{1 + R_h C_h S + L_h C_h S^2} (P_s - \dot{W}_p R_h) \qquad (6\text{-}44)$$

Since P_s is constant, this equation is programmed for the computer using the parameter $\Delta P_s = P_s - P_s'$. The result is:

$$\Delta P_s = \frac{R_h}{20 L_h C_h a_t^2} \frac{20 \dot{W}_p}{S^2} + \frac{1}{20 C_h a_t} \frac{20 \dot{W}_p}{S} - \frac{\Delta P_s}{a_t^2 L_h C_h S} \frac{R_h \Delta P_s}{a_t L_h S}$$

(VIII-10)

Equations (VIII-1) through (VIII-10) are combined to form the computer diagram shown in Figure VIII-1. The constants used in the computer simulation are given in Table VIII-1, and the respective potentiometer identifications and settings are given in Table VIII-2.

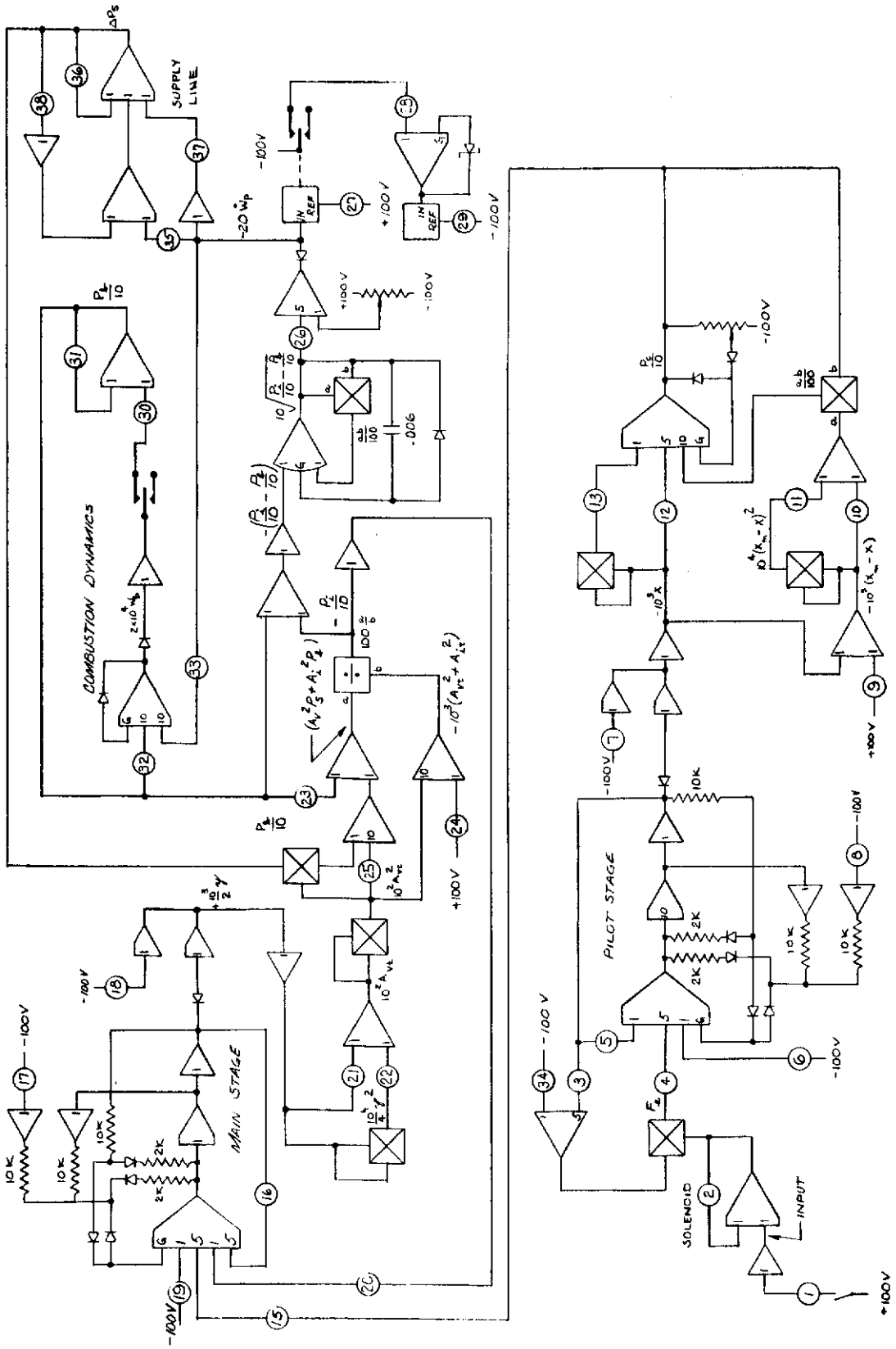

Figure VIII-1 - Computer Diagram for Valve-Combustor System

Table VIII-1 - Values of Computer Constants

Symbol	Value	Units	Symbol	Value	Units
A_{it}	0.0834	$in.^2$	M_p	8.663×10^{-5}	$lb\text{-}sec^2/in.$
A_p	1.225	$in.^2$	P_a	600	psia
A_t	2.79	$in.^2$	P_e	≈ 0	psia
C_d	0.85		P_s	300	psia
C_h	0.000178	$in.^5/lb$	r_b	0.375	in.
C_f	0.3075	$°R^{\frac{1}{2}}/sec$	rd	0.156	in.
C_i	0.523	$°R^{\frac{1}{2}}/sec$	r_u	0.0625	in.
C_2	3.16	lb/in.-sec	R_h	12.47	$sec/in.^2$
E	28.0 (max.)	volts	R_i	662	in/°R
F_{s1}	5.19	lb	R_b	1820	in./°R
F_{s2}	85.0	lb	T_b	5460	°R
k_i	1.4		T_i	100	°R
k_b	1.25		V_b	56.2	$in.^3$
k_s	18.5	1/in.	V_c	0.050	$in.^3$
K_a	1500	lb/in.	x_m	0.030	in.
K_b	300	lb/in.	y_m	0.100	in.
K_c	6530	in./sec	θ	45.0	deg.
K_p	50	lb/in.	τ_b	1.5×10^{-3}	sec
K_s	0.643	lb/volt	τ_i	0.001	sec
L_h	17.32	$lb\text{-}sec^2/in.^5$	τ_s	0.003	sec
M_2	0.00145	$lb\text{-}sec^2/in.$			

P-2063

Table VIII-2 - Potentiometer Settings

Pot No.	Equation	Value	Pot No.	Equation	Value	Pot No.	Equation	Value
1	$\frac{K_s\,(0.28)}{a_t\,\tau_s}$	0.060	14	$\frac{P_{c\,max}}{10^3}$	0.600	28	$100\,\tau_i$	0.100
						29	$0.1\,a_t\,\tau_i$	0.100
2	$\frac{1}{a_t\,\tau_s}$	0.333	15	$\frac{10^3\,A_p}{M_2\,a_t^2}$	0.845	30	$\frac{R_b\,T_b}{2(10^5)\,a_t\,V_b\,\tau_b}$	0.524
3	$\frac{k_s}{50}$	0.370	16	$\frac{2K_b + K_a}{5M_2\,a_t^2}$	0.290	31	$\frac{1}{a_t\,\tau_b}$	0.663
4	$\frac{20}{a_t^2\,M_p}$	0.231	17	$5\,Y_{max}$	0.500	32	$2\,(10^5)\,\frac{C_{di}\,C_f\,A_t}{a_t\,\sqrt{T_b}}$	0.200
5	$\frac{K_p}{10\,a_t^2\,M_p}$	0.0577	18	$5\,Y_{max}$	0.500	33	$\frac{10^2}{a_t}$	0.100
6	$\frac{F_{s1}}{a_t^2\,M_p}$	0.0597	19	$\frac{10\,F_{s2}}{2M_2\,a_t^2}$	0.293	34	$1 - k_s\,x_m$	0.445
7	$10\,x_m$	0.300	20	$\frac{10^4\,\pi\,r_b^2}{M_2\,a_t^2}$	0.768	35	$\frac{R_h}{20\,L_h\,C_h\,a_t^2}$	0.0202
8	$10\,x_m$	0.300						
9	$10\,x_m$	0.300	21	$0.4\,\pi\sqrt{2\,r_b}$	0.666	36	$\frac{R_h}{L_h\,a_t}$	0.0072
10	$\frac{2K_c\,r_d}{100 a_t\,V_c}$	0.408	22	$\frac{2\,\pi\sqrt{2}}{100}$	0.089	37	$\frac{1}{20\,C_h\,a_t}$	0.562
			23	$10\,A_{it}^2$	0.0153			
11	$\frac{K_c}{2(10^3)\,a_t\,V_c}$	0.0654	24	$10\,A_{it}^2$	0.0153	38	$\frac{1}{L_h\,C_h\,a_t^2}$	0.0324
12	$\frac{2K_c P_a\,r_u}{5(10^4)\,a_t\,V_c}$	0.1965	25	$\frac{P_s}{10^3}$	0.300			
			26	$2/5\sqrt{10\,C_2\,A_{it}}$	0.250			
13	$\frac{K_c\,P_a}{2(10^5)\,a_t\,V_c}$	0.392	27	———	0.010			

P-2063